DEVELOPMENT OF FUNCTIONAL MATERIALS FOR PHOTOCATALYTIC WATER-SPLITTING FOR HYDROGEN GENERATION

YAO XIAO

Doctor of Philosophy

The Hong Kong Polytechnic University

2023

The Hong Kong Polytechnic University

Department of Applied Biology and Chemical Technology

Development of Functional Materials for Photocatalytic Water-Splitting for Hydrogen Generation

YAO XIAO

A thesis submitted in partial fulfillment of the requirements for the degree of Doctor of Philosophy

Aug 2022

CERTIFICATE OF ORIGINALITY

I hereby declare that this thesis is my own work and that, to the best of my knowledge and belief, it reproduces no material previously published or written, nor material that has been accepted for the award of any other degree or diploma, except where due acknowledgement has been made in the text.

_____ _____ (Signed)

_____YAO XIAO_____ (Name of student)

Abstract

With the rising concerns of greater energy demand and a decrease in the global fossil fuel supply, exploring alternative energy sources has become an urgent and challenging research subject. Solar energy is considered one of the most promising solutions to our energy scarcity as it can be collected and transformed into different forms of power using photocatalytic devices, and that the solar-driven photocatalytic water-splitting can provide a clean pathway to produce hydrogen fuel. The first water-splitting system for hydrogen production using a TiO_2 photoanode ever reported was in 1972 by Fujishima and Honda. Following this pioneering research, water-splitting systems for hydrogen production have been developing rapidly throughout past decades.

Ruthenium(II) complexes have shown impressive performance for their potential applications in water-splitting systems due to the unusual metal-to-ligand charge transitions (MLCT) and unique photophysical properties. However, to realise the light-harvesting abilities in these photocatalytic systems remains a challenging task. Most systems can only use ultraviolet (UV) and partially visible light, accounting for only 5–7% of sunlight. To improve the water splitting for the hydrogen-production capability, I proposed a series of Ru(II) complexes with different ligands, such as isoquinoline or triphenylamine, which have been proven to significantly increase the hydrogen-production efficiency during water splitting. All the Ru(II) complexes have been used in water-splitting hydrogen-production experiments. Additionally, the influence of different anchoring groups, such as carboxylic acid anchors or phosphonate functional

groups of Ru(II) complexes in hydrogen production, are discussed in the thesis. With the best Ru(II) water-splitting system after 236 hours of irradiation, an H_2 turnover number (TON) of up to 14232 was recorded.

Compared to other metal dyes that include first- and second-row transition metals, Ir(III) cyclometalated complexes have taken on excellent ligand field stabilisation energies in their 5d valence shell. However, Ir(III) cyclometalated complexes often suffer from weak absorbance of visible light. Therefore, I synthesised a series of Ir(III) complexes with different functional groups, such as triphenylamine or aldehyde, for the Pt-TiO_2 system, which showed satisfactory hydrogen production results. Different anchoring groups were designed to test the working efficiency of the water-splitting system. Most of the developed Ir(III) photosensitisers for photocatalytic applications possess carboxylic acid anchors. However, these dyes might have poor stability under photocatalytic operating conditions. Furthermore, the hydrolysis characteristic of the carboxylate linkage site has been reported to inhibit electron transfer efficiency from Ir(III) complex to TiO_2. In this regard, the linkage of the phosphonate functional group to the TiO_2 surface has been presented with higher stability than that of the carboxylate group. A respectable hydrogen TON of 16483 in a platinised TiO_2 hydrogen-production system was demonstrated with the best Ir(III) water-splitting system.

In most traditional molecular water-splitting systems, expensive noble metals have been used. Such high cost may hinder industrial application of those water splitting systems. However, cadmium sulfide nanorod (CdS NRs) systems, which have large light-absorption coefficients, offer great research potential. Research has been

conducted on water-splitting systems with CdS and different earth-abundant metal complexes, particularly Ni. Different electron-donating or withdrawing ligands have been used on templates of salen-type or salophen-type Schiff bases to determine the physical and chemical properties of the earth-abundant metal complexes and their water-splitting performance for hydrogen production. This study has also examined the effects of the size and aspect ratio of the CdS NRs on hydrogen production. A photocatalytic system containing a metal-salophen complex based on nickel achieved a steady and impressive catalytic activity with a TON of 57238 and a turnover frequency (TOF) of 436.9 h^{-1} over 131 hours under blue-light irradiation.

Metal-organic cages (MOCs), assembled from diverse inorganic structures and organic linkers, have been in rapid development recently. MOCs are a new type of material with an individual nanoscale molecular structure assembled through weak interactions while possessing a great potential for photocatalytic water splitting. The supramolecular chemistry nature of MOCs makes them the ideal materials for binding catalyst centres with different linkers. Additionally, the catalytic properties of MOCs can be tuned effectively by proper structural design. In order to achieve effectively H_2 production, MOCs are expected to possess significant absorption characteristics. I have developed functional metal cages with various structures, such as phenyl, furan, and thiophene combined with Ni or Co. Their various water-splitting performances and physical and chemical characteristics are discussed in the thesis.

Publication Arising from the Thesis

Yao, X., Ho, P.-Y., Yiu, S.-C., Suramitr, S., Li, W. B., Ho, C.-L., & Hannongbua, S. (2022). Development of new thiocyanate-free Ruthenium (II) dyes bearing isoquinoline chromophores for hydrogen production via water splitting. *Dyes and Pigments*, *205*, 110508.

Acknowledgements

I would like to express my profound gratitude and sincere thanks to my supervisor, Dr. Ho Cheuk Lam, for her invaluable advice, encouragement, and support in my studies and daily life. Her precious comments and advice on the preparation of this thesis are gratefully acknowledged. Her devoted attitude in research has strongly impressed and inspired me, making my studies a truly rewarding experience.

I also offer sincere thanks to my co-supervisor, Prof. Yung Joseph, for his attention and guidance. Special thanks are given to Dr. So Pui Kin for his contributions with MS analysis, Dr. Li Wan Bo for TEM and SEM analysis, Dr. Li Bo for DFT calculations and Dr. Yan Kenneth for his help with NMR analysis. Also, I wish to express my great appreciation to all the technical staffs and administrative staffs: Ms. Wan Hoi Ying, Mr. Au You Kwok, Mr. Ho Chi Man, Mr. Shiu Yui Wah, Mr. Wan Koon Hung, Mr. Chan Arnold, Mr. Chan Hoi Ming, Miss Yeung Man Yu, Ms. Wong Oi Li, Ms. Kwok Peggy, Miss Chung Shadow, and Miss Tsui Iris.

I would also like to show my kind gratitude to our research members, Dr. Ho Po Yu, Dr. Yiu Sze Chun, Mr. Zheng Zhong, Miss. Han Shi Chun, Miss Fan Lin Yu and Mr. Zhang Qian, for their genuine care and guidance. Special acknowledgement will be given to Mr. Luo Hao Jie for his support and encouragement. Thanks also to Dr. Hau Sam from Chinese University of Hong Kong, Dr. Ren Kang Ning, and Prof. Jiang Ming from the

Hong Kong Baptist University for their attentive support.

Many thanks go to my best friends, Ms. Chan Ting Yu, Mr. Chen Xiong, Mr. Wu Gao Han, Miss Wu Yi Fan, Miss Zhang Dong, Miss Wang Yi Su, Miss Tang Yu Jing, Miss Weng Lin Shuang, Ms. Zeng Li Qin, Mr. Hung Zhi Hang, Mr. Feng Liang and Mr. Lin Yun Cong, for their kind support and help.

I would like to acknowledge the Hong Kong Polytechnic University for financial support. The Hong Kong Baptist University and all the professors in chemistry department are also gratefully acknowledge.

Finally, I want to express deep thanks to my cousins, Mr. Lin Jie Ming, Mr. Chen Jie, Mr. Huang Yi Cheng, Mr. Mao mao, Dr. Xie Bing Qing, Dr. Zheng Xue Fang, Dr. Zheng Xue Zhen, Dr. Lin Si Ning, and Dr. Wu Jia Wei. Most importantly, my whole-hearted gratitude must be dedicated to my family members, Prof. Zheng Jin Ping, Mr. Yao Qing Chun, Mr. Chen Xi Ming, and especially my grandmother, Ms. Kang Xia Gui and two lovely cats, for their care, comfort, and continuous support through everything.

Table of Contents

List of Tables

List of Figures

List of Schemes

List of Abbreviations and Symbols

THF	Tetrahydrofuran
$CHCl_3$	Chloroform
CH_2Cl_2	Dichloromethane
DMF	*N*,*N*-Dimethylformamide
MeOH	Methanol
HOMO	Highest occupied molecular orbital
LUMO	Lowest unoccupied molecular orbital
TLC	Thin layer chromatography
IR	Infra-red
NMR	Nuclear magnetic resonance
TMS	Trimethylsilyl
ppm	Part per million
Hz	Hertz
s	Singlet
d	Doublet
dd	Doublet of doublet
t	Triplet
m	Multiple
MS	Mass spectrometry
M^+	Molecular ion

m/z	Mass to charge ratio
h	Hour
E_g	Energy gap
MLCT	Metal-to-ligand charge transfer
UV/Vis	Ultraviolet–visible
CV	Cyclic voltammetry
Fc	Ferrocenyl
phen	Phenylacetylene
bpy	Bipyridine
ppy	2-Phenylpyridine
dcbpy	2,2′-Bipyridyl-5,5′-dicarboxylic acid
a.u.	Arbitrary unit
eV	Electron volt
r.t.	Room temperature
J	Modulus of the coupling constant
ε	Molar absorptivity
LC	Liquid chromatography
EIS	Electrospray ionisation
TOF	Time of flight
C^N	Cyclometalating ligand
TPA	Triphenylamine
MeCN	Acetonitrile

N^N	Anchoring group
Q	Quadrupole
DFT	Density functional theory
MO	Molecular orbital
SED	Sacrificial electron donor
EIS	Electrochemical impedance spectroscopy
FTO	Fluorine-doped tin oxide
GC	Gas chromatography
Å	Angstrom
ICP-OES	Inductively coupled plasma optical emission spectroscopy
TEM	Transmission electron microscopy
SEM	Scanning electron microscopy
TON	Turnover number
TOF	Turnover frequency
AQY%	Apparent quantum yield percentage
TEOA	Triethanolamine
CO_2	Carbon dioxide
H_2	Hydrogen
OER	Oxygen evolution reaction
HER	Hydrogen evolution reaction
VB	Valance band

CB	Conduction band
AA	Ascorbic acid
EDTA	Ethylenediaminetetraacetic acid
TEA	Triethylamine
NRs	Nanorods
MOFs	Metal–organic frameworks
COFs	Covalent organic frameworks
MOCs	Metal–organic cages

Chapter 1: Introduction

1.1. Background

In the modern era, fossil fuels are the major energy source used to power human activity.[1] The worldwide demand for fuel energy has experienced rapid growth. The U.S. Energy Information Administrations latest International Energy Report identified that world energy consumption will grow by 28% between 2015 and 2040 (**Fig. 1.1**).[2, 3] Based on the 2018 metrics, energy consumption has increased by more than three times since 1980.[4] According to data from the U.S. Energy Information Administration, the current reserve of petroleum is estimated to be unable meet the demand in 2030.[2] Under these conditions, the search to find alternative energy sources has become more and more crucial.

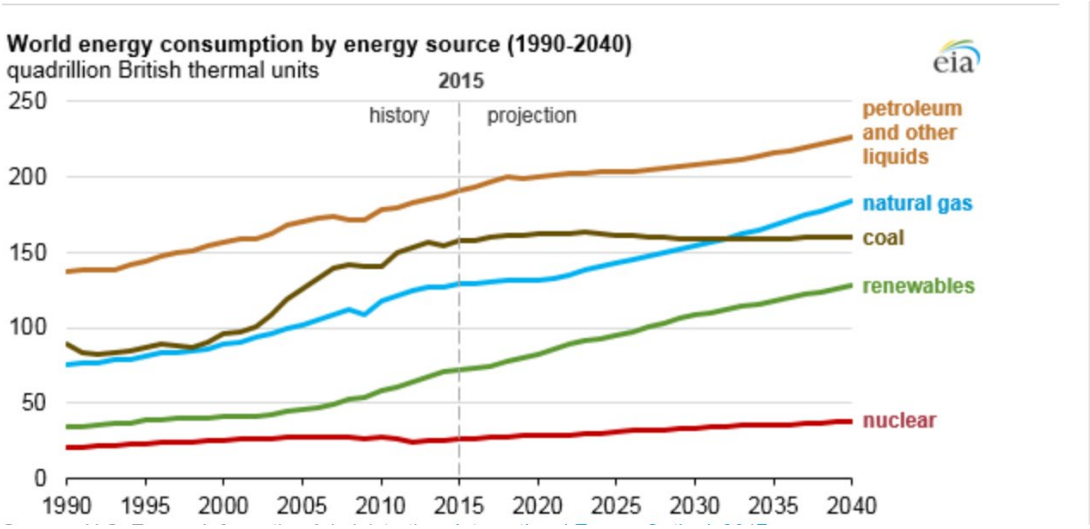

Fig. 1.1. World energy consumption categorised by energy source. Source: U.S. Energy Information Administration.[2, 3]

Due to the huge consumption of traditional energy sources, environmental problems have become increasingly serious. More than 80% of energy generated comes from carbon-based fossil fuels, resulting in a huge increase in the concentration of carbon dioxide (CO_2) in the atmosphere.[5] In 2019, the carbon dioxide average concentration reached 409.8 ppm (**Fig. 1.2**), which is higher than the value at any other point in the past 800,000 years.[6-8] In addition, acid rain, stratospheric pollution and other environmental issues caused by the consumption of traditional energy sources have led to more adverse impacts.[9] Therefore, corresponding measures must be taken to solve the aforementioned issues. Renewable energy is a worthwhile and important avenue to pursue.

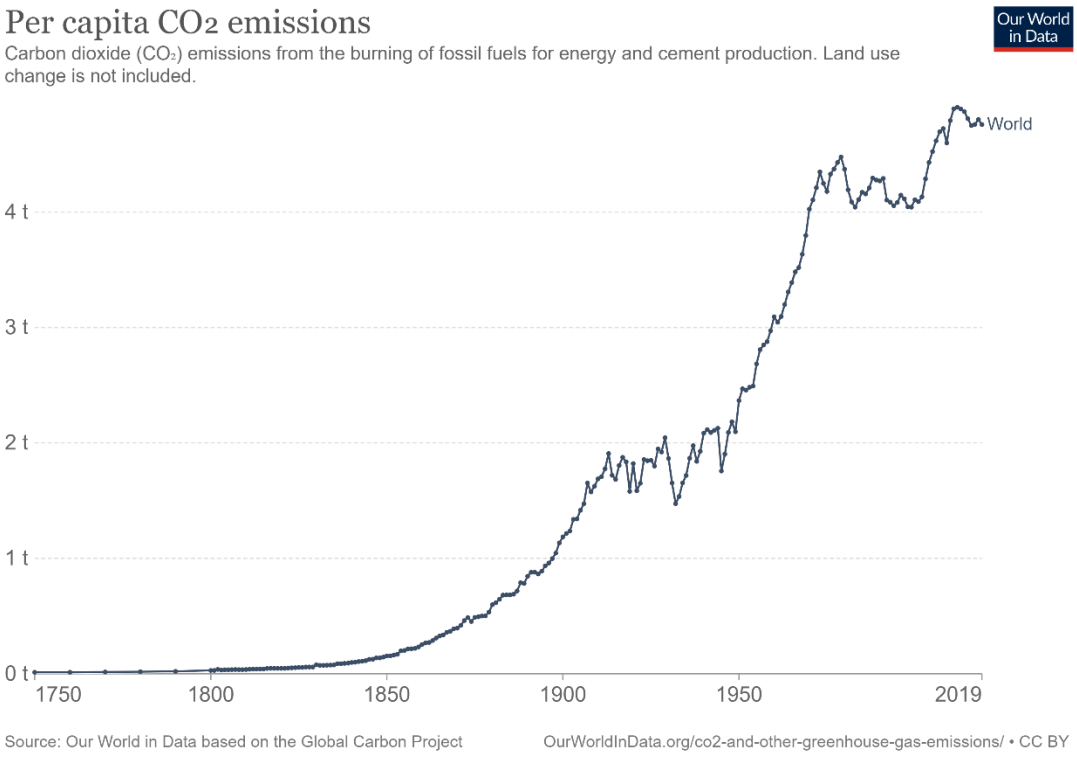

Fig. 1.2. Atmospheric CO_2 concentration. Source: Our World in Data based on the

Global Carbon Project, University of Oxford.[6-8]

Renewable energy, defined as the energy collected from renewable resources,[3] is quite common and has different storage forms. Renewable energies include hydrogen energy, wind energy, solar energy, geothermal heat energy and so on.[10] Hydrogen (H_2), an environmentally friendly and easy-to-store energy source, will play a very important role in the 21st century. As the cleanest fuel source, hydrogen causes no pollution to the environment during the energy-providing process. It produces only water when energy is consumed. Furthermore, it has the highest specific energy content.[11, 12] The thermodynamic conversion efficiency of hydrogen is much higher than that of petroleum products. The energy yield of hydrogen can reach up to 122 kJ/g, which is 2.75 times higher than that of hydrocarbon fuels.[13] Additionally, liquid hydrogen has a very low density of 0.07 g/cm^3, which is one tenth that of gasoline.[14] This makes hydrogen much easier to transport and store. Nowadays, hydrogen have been widely used in many fields, such as hydrogen fuel cars,[15] ferrous metallurgy[16] and so on. Therefore, hydrogen is considered an ideal energy source by the scientific community.

1.2. Water Splitting for Hydrogen Production

There are a variety of methods used to produce hydrogen gas. The most common method used in the industry is steam methane reforming, which generally produces about half of the global supply of hydrogen.[17] This method is based on a reaction

between steam and natural gas or methane, which is then used to produce hydrogen.[14] However, it is not an attractive production route because it results in the emission of carbon dioxide and has a high temperature requirement.[18] Hydrogen can be produced industrially via its separation and purification from hydrogen-rich industrial emissions (such as chlor-alkali tail gas and coke oven gas) as the raw material as well. [18] However, this approach is not applicable domestically because of carbon dioxide emissions and the high cost.[18] Hydrogen can also be produced by bio-material conversion technology. However, this technology is still in the demonstration stage as it has strict requirements for enzymes and a high cost. [12, 14, 19]

Hydrogen production with the support of photocatalysts has been reported to be an ideal method.[20] The water splitting involves two half-reactions: the oxidation of water to form oxygen (oxygen evolution reaction, OER) and the reduction of protons to form hydrogen (hydrogen evolution reaction, HER). Those two half reaction can be invigilated separately. For the HER, Fujishima and Honda demonstrated the first water splitting hydrogen generation system in 1972.[21] Following this pioneering research, water-splitting systems for hydrogen production have improved dramatically.[22] Solar-driven photocatalytic water splitting provides an attractive pathway for production of hydrogen because (i) it is a very simple reaction that directly converts photon energy into hydrogen energy without the emission of any pollutants; (ii) the experimental setup is simple and easy; (iii) the reaction proceeds in mild conditions and (iv) the cost of water splitting for hydrogen production is much lower than that of other methods.[22]

1.3. Sacrificial Electron Donors

Because of the rapid recombination of electrons and holes, the light-driven water-splitting hydrogen production efficiency is not high.[5] Adding sacrificial electron donors, which can react with the holes in the valance band (VB) level, can enhance the photocatalytic electron/hole separation and promote hydrogen production.[23] There are various sacrificial electron donors, such as ascorbic acid (AA), triethylamine (TEA), triethanolamine (TEOA), and ethylenediaminetetraacetic acid (EDTA) (**Fig 1.3**).[24, 25]

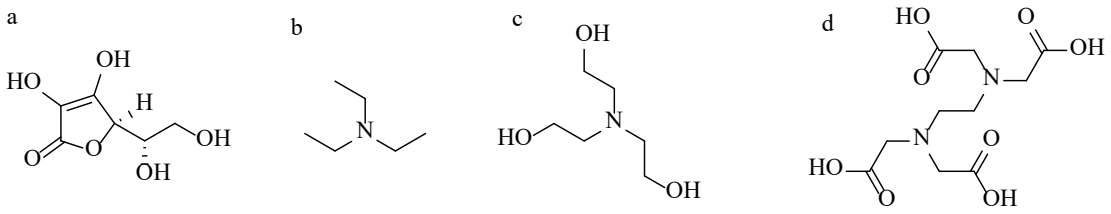

Fig. 1.3. The chemical structures of (a) ascorbic acid, (b) triethylamine, (c) triethanolamine, and (d) ethylenediaminetetraacetic acid.

EDTA is a tertiary diamine with four carboxyl functional groups that acts as a double-electron sacrificial donor.[26] The degradation of EDTA has been extensively explored.[27] Its oxidised amine radical can undergo a series of transformations to form carbon-centered reduction radical EDTA. However, the stability of the radicals towards degradative processes is pH-dependent.[28] TEA and TEOA form positively charged aminyl radicals upon oxidation,[29] both of which are good oxidants that can in principle react with any reduced species.[30] However, those systems bearing TEA or TEOA need to operate at pH values above 8,[26] which limits their applicability.[31] Furthermore,

TEA and TEOA are not water-soluble, so they cannot be used in aqueous environments. AA is well known to be a natural antioxidant used in the preservation of food and drinks.[32] In addition, It has previously been successfully used as a SED in water splitting hydrogen generation.[33] The working mechanism for AA is shown in **Fig. 1.4**. HA^- is first oxidised to $HA^{\bullet}$ [34] which was quickly dissociates into $A^{-\bullet}$ and H^+,[35] After that, $A^{-\bullet}$disproportionate into dehydroascorbic acid A and ascorbate A^{2-}.[26, 36] One of the most important reasons for choosing AA for the current research is its water solubility, and thus it can be used in aqueous environments. Furthermore, unlike traditional SEDs that require basic pH conditions, AA can work at neutral and acidic pH values.

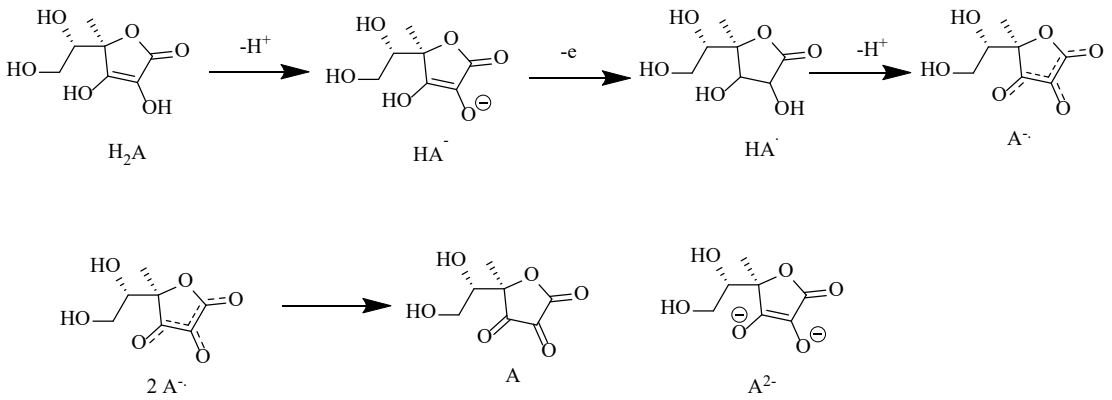

Fig. 1.4. The mechanism of ascorbic acid degradation.

1.4. Hydrogen Production in TiO_2 System

1.4.1. Introduction

In 1972, Fujishima and Honda demonstrated the first water-splitting hydrogen generation system using TiO_2. Following this pioneering research, TiO_2 has become the

most widely used semiconductor for water-splitting hydrogen generation.[5] It has many attractive properties such as having high thermal and chemical stability, as well as being cheap and non-toxic.[37]

The key technique in a water-splitting hydrogen generation system is the use of a semiconductor. The electronic structure of a semiconductor is a crucial point in photocatalytic water splitting. A semiconductor possesses a valence band and a conduction band. The energy gap between the two energy levels is called the band gap (E_g). Without excitation, both electrons and holes are in the VB level. When semiconductors are excited by photons with an energy that is equal to or greater than the band gap, electrons in the VB level receive the energy and are promoted to the conduction band (CB) level.

The photo-generated electrons and holes can undergo recombination in bulk or on the surface of the semiconductor very quickly, releasing energy in the form of heat or photons. Unreacted electrons and holes on the surface of semiconductors can reduce and oxidise the reactants adsorbed by the semiconductor, respectively. The reduction reaction is the basic mechanism of photocatalytic hydrogen production.[5] Therefore, according to the mechanism, the VB level should be more positive than the water oxidation level, while the CB level should be more negative than the reduction level (**Fig. 1.5**).

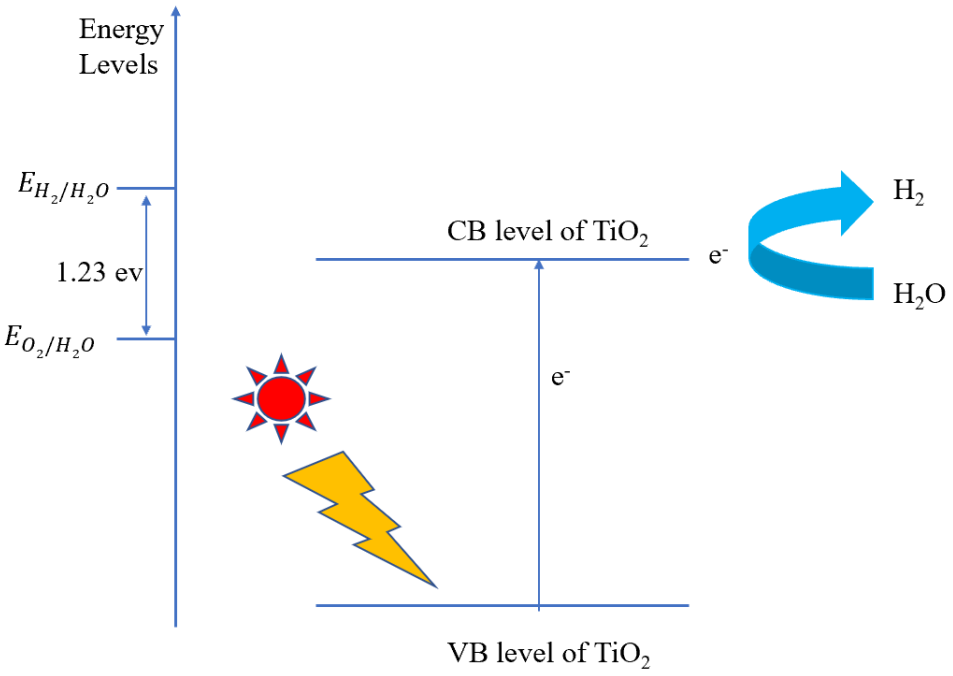

Fig. 1.5. Water-splitting mechanism for hydrogen production in TiO_2 system.

However, the photocatalytic water splitting for hydrogen production efficiency is still not high enough because of the following reasons:[5]

(i) Rapid recombination of electron/hole pairs: electrons in the CB level can recombine with holes in the VB level very quickly and can release energy in the form of heat or photons.

(ii) Inability to utilise visible light: common semiconductors, such as TiO_2, can only utilise UV light, which accounts for only about 4% of the solar light.

To enhance the photocatalytic water splitting for hydrogen generation, continuous efforts have been made to improve the photocatalytic activity. Adding sacrificial electron donors,[38] Pt loading,[39] dye sensitisation[40] and other techniques have been investigated and have proved useful for enhancing hydrogen production.

1.4.2. Techniques to enhance hydrogen production in TiO_2 system

1.4.2.1. Platinum loading

Loading of noble metals, especially Pt and Au, are highly effective for enhancing the photocatalytic performance of TiO_2.[41-44] Bamwenda et al.[42] compared hydrogen production performance from a water/ethanol system using Au-loaded TiO_2 or Pt-loaded TiO_2 as the photocatalyst. The result shows that Pt loading worked better than Au loading for water-splitting hydrogen generation.

The electron trap mechanism is organized through the Schottky barrier formation (**Fig. 1.6**).[45] The photo-generated electrons from the CB energy level of TiO_2 can easily migrate to the metal via the Schottky barrier while the metal acts as an electron sink.[46-48] Band bending at the semiconductor junction with the metal can occur due to electron transfer.[49] This phenomenon is the shifting of the energy band edges of the semiconductor due to the electric field/charge transfer between the semiconductor and the metal.[50] Electrons are generally transferred from the material with a higher Fermi level to one with a lower Fermi level until thermodynamic equilibrium is achieved.[44] The Fermi level of the metal is lower than that of TiO_2, and so electrons are transferred from the latter to the former.[44] Accumulated electrons on the metal particles can then be transferred to protons adsorbed on the surface, which can reduce the electron–hole recombination and thereby promote hydrogen production.[5, 51]

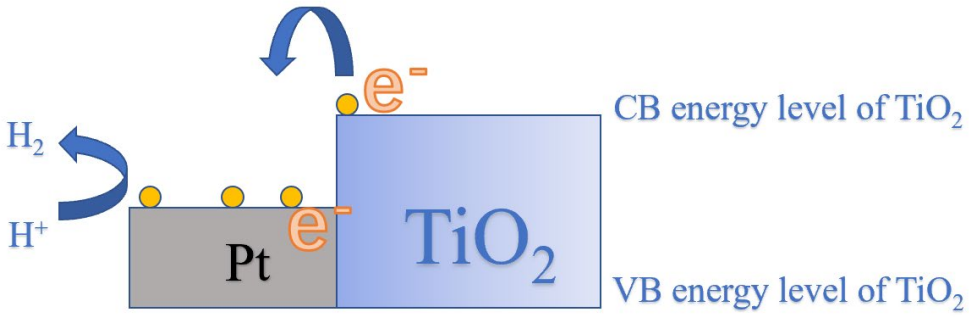

Fig.1.6. Schematic representation of electron transfer via Schottky barrier formation.

1.4.2.2. Dye sensitisation

Another effective approach to extend the proportion of solar irradiation harvesting by semiconductors is utilising a photosensitiser.[5] These absorb visible light and UV light, and transfer energy to the semiconductor.[52] Moreover, a photosensitiser can increase the lifetime of excited states of dyes by ensuring efficient charge separation, which can enhance water-splitting hydrogen generation.[53]

Fig. 1.7 describes the mechanism of the water-spitting system with Ru(II) dye as an example**.** In the light-driven hydrogen generation reaction, the photosensitiser undergoes photoexcitation under light irradiation, followed by electron injection into the CB energy level of TiO_2. The injected electrons move to the Pt nanoparticles loaded on TiO_2, thereby reducing the protons to release hydrogen. The oxidised photosensitiser is then reduced to the ground state by AA serving as a sacrificial electron donor.[54]

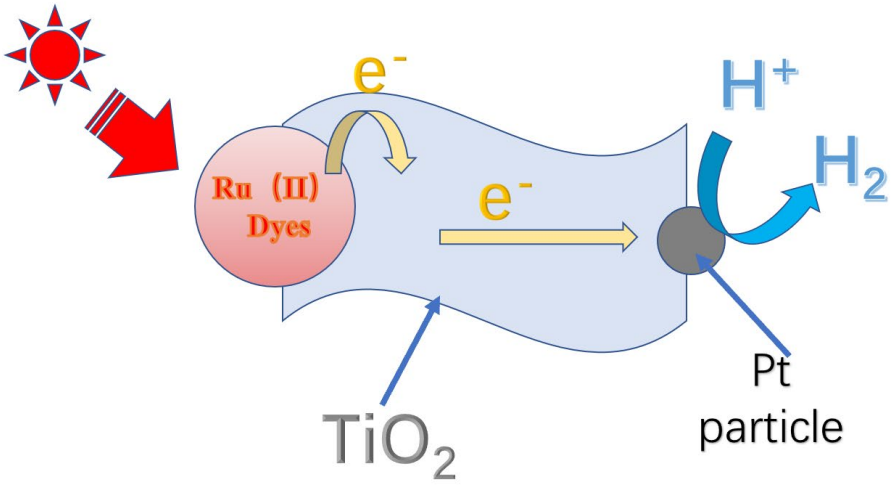

Fig. 1.7. A schematic of hydrogen evolution from water using Pt-TiO_2 and a Ru(II) complex photosensitiser under visible light.[54]

In general, high-performance photosensitizers require the following properties:[55]

i. A broad absorption band and high molar extinction coefficient.

ii. Anchoring groups that can be bonded to the surface of TiO_2 to avoid dye desorption and provide an efficient channel for electron injection.

iii. Suitable energy levels.

iv. High photochemical, electrochemical and thermal stability to avoid unwanted degradation.

Metal-based photosensitizers such as cyclometalated Ru(II) or Ir(III) complexes, Zn(II)

porphyrins, and Pt(II) diimine dithiolates have shown promising results in light-harvesting applications.[40, 56-60] Chanda et al.[61] investigated zinc porphyrin@TiO_2 for photocatalytic hydrogen production, and showed a satisfactory photocatalytic hydrogen production result with the activity of 9793.5 μmol g^{-1} h^{-1} with TEOA as SED. However, the photocatalytic activity of Zn-porphyrin-sensitized TiO_2 was greatly affected by factors such as the concentrations of Pt, electron donor, as well as the pH and temperature of the suspension, which makes the system unsuitable for long-term photocatalytic water splitting.[61-64] Zhu et al.[65-67] reported a catalyst with Pt-porphyrin nanoparticles that achieved the TON of 6311. However, the long-term stability of these complexes acting as photosensitizers is not satisfactory (only 12 h) due to decomposition after oxidation.[65-67]

In particular, Ru(II) complexes are the most studied metal-based photosensitizers due to intense light absorption along with a long-lived low-energy metal-to-ligand charge transfer (MLCT) transition,[60] which enhances hydrogen generation from photocatalytic water splitting.[60] Moreover, Ir(III) cyclometalated complexes are attracting attention because of their excellent ligand field stabilisation energy due to their 5d valence shell,[68-71] which makes them stable in water-splitting systems.[72]

1.4.2.2.1. Ru(II) complexes attached to TiO_2 as photosensitizers

Shortly after Fujishima and Honda's report of a water-splitting system with TiO_2 photo-anodes, the basis for artificial photosynthesis was investigated when $[Ru(bpy)_3]^{2+}$ (**Fig. 1.8**, bpy = 2,2'-bipyridine) complexes were found to efficiently enhance hydrogen

production.[73, 74] Since then, related Ru(II) dyes, such as **N3** and **N719** (**Fig. 1.8**), have been studied and have undergone rapid development.[75-77]

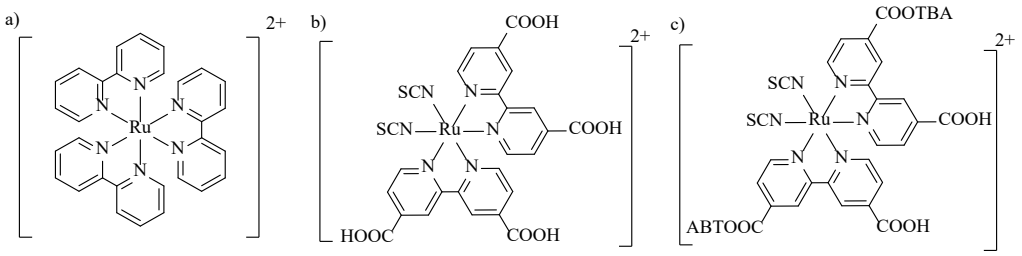

Fig. 1.8. Chemical structures of the (a) $[Ru(bpy)_3]^{2+}$ molecule, (b) **N3** molecule and (c) **N719** molecule.

This type of photosensitiser possesses several attractive characteristics. First, it displays a broad absorption of visible light.[78] Furthermore, their light absorption can be controlled by varying the ligands.[79, 80] Therefore, some of the most common dyes, such as **N3** and **N719**, have been successfully designed and synthesised based on the template of ruthenium bipyridyl complexes.[81]

However, some of these Ru(II) dyes contain monodentate isothiocyanate ligands, which are labile under thermal or light stress.[82] To obtain kinetically inert photosensitizers, isothiocyanate-free Ru(II) complexes with bidentate-donating ligands are preferable. On the other hand, these photocatalytic systems have relatively short lifetimes in service.[83] There is still room for improvement and unlimited potential in the hydrogen evolution performance of Ru-based photosensitizers. Efficient and stable Ru(II) photosensitizers are urgently required to accelerate the reaction rate for hydrogen generation.

1.4.2.2.2. Ir(III) complexes as photosensitizers attached onto TiO_2

After the initial investigations into Ir(III) cyclometalated complexes $[Ir(ppy)_2(bpy)]^+$ (ppy = 2-phenylpyridinato, bpy = 2,2′-bipyridine, **Fig. 1.9.**) by Bernhard et al.,[68, 84-86] Ir(III) cyclometalated complexes have become attractive dyes, and different structures have evolved.[68] Compared to other metal dyes that include first- and second-row transition metals, Ir(III) cyclometalated complexes take on excellent ligand field stabilisation energies in their 5d valence shell.[68, 70] Furthermore, the stability of Ir(III) cyclometalated complex water-splitting systems can be enhanced by C^N ligands because of metal-linked carbon σ-donations that increase the electron density in the metal centre.[68, 87] Owing to their advantageous photophysical properties, cyclometalated Ir(III) complexes have achieved widespread attention as photosensitizers.[88]

However, Ir(III) cyclometalated complexes often suffer from weak visible light absorbance, and visible light accounts for about 40% of the sunlight.[88-91] The structures of Ir(III) cyclometalated complexes should be better designed to enhance their hydrogen output.

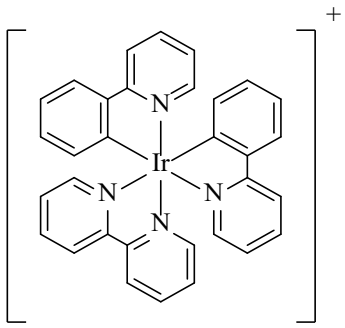

Fig. 1.9. Molecular structure of complex $[Ir(ppy)_2(bpy)]^+$.

1.4.2.2.3. Anchoring groups in Ru(II) and Ir(III) dyes

The photosensitizer should possess anchoring group(s) to enable efficient chemisorption onto a semiconductor. The nature of the anchoring group is important for determining the photocatalytic performance[92, 93] as it affects the electronic communication between the dye and TiO_2.[94] **Fig.1.10** presents the most common anchoring groups, [2,2 -bipyridine]-4,4 -dicarboxylic acid and tetraethyl [2,2 -bipyridine]-4,4 -diylbis(phosphonate). However, Ru(II) and Ir(III) photosensitizers with carboxylic acid anchoring groups are unstable under long-term photocatalytic operating conditions.[95] Moreover, it has been reported that hydrolysis of the carboxylate linkage sites inhibits the efficiency of electron transfer from the photosensitizer to TiO_2.[81] In this regard, linking the photosensitizer to the TiO_2 surface via phosphonate functional groups provides higher stability than via carboxylate groups.[81]

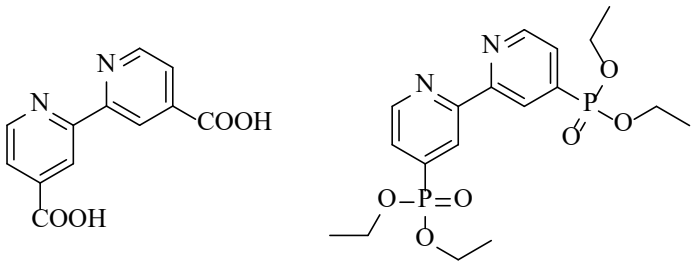

Fig. 1.10. The molecular structure of [2,2 -bipyridine]-4,4 -dicarboxylic acid and tetraethyl [2,2 -bipyridine]-4,4 -diylbis(phosphonate).

1.5. Hydrogen Production in CdS Nanorods Systems

Since the first water-splitting system for hydrogen production using a TiO_2 photoanode in 1972,[21] many catalytic systems have been developed.[96-99] However, in the majority of these traditional molecular water-splitting systems, expensive noble metals such as Pt[100, 101], Ru[91, 102, 103] or Ir[104, 105] have been used. Therefore, developing catalysts based on earth-abundant metals to replace noble metals is of great interest.[106] Although molecular catalysts comprising the first transition metal series, such as Ni[107-116], Zn[117-119] and Cu[120-122] are potential alternatives to noble metals, most of them have shown relatively moderate activity in pure aqueous proton reduction systems.[123-126]

On the other hand, it has been reported that cadmium sulphide (CdS) nanorods (NRs) and CdS quantum dots (QDs) are highly efficient and robust photosensitizers for photocatalytic systems.[127-129] They possess larger light-absorption coefficients, more tuneable optical and redox properties, a higher propensity for photo-induced electron transfer, broader absorption across the visible light spectrum and relatively higher photostability as compared to molecular photosensitizers.[130, 131] Moreover, the size of CdS NRs is easier to control than that of CdS QDs.[132] Hence, CdS NRs warrant further exploration for their potential as water-splitting photosensitizers.

1.6. Hydrogen Production in Metal–Organic Cages Systems

Because of the rapid recombination of photo-generated electrons and holes, the photocatalytic activity of the traditional water splitting for hydrogen production system is limited and must be improved. Many attempts have been made to address this limitation. Porous photocatalysts could suppress the electron–hole recombination due

to exposed active sites and accessibility to the substrate.[133] Therefore, metal–organic frameworks (MOFs) and covalent organic frameworks (COFs) were developed to improve the activity of the catalysts.[134-138] However, the carrier shell around the metal complex reduces the flexibility and accessibility of the photocatalytic centre, which may lower the catalytic activity.[139] Therefore, it is urgent to develop stable metal-complex catalysts without sacrificing their immanent high activity.

In recent years, metal–organic cages (MOCs) have been widely developed as inorganic clusters and organic connectors.[140] The supramolecular assembly of predesigned inorganic and organic building blocks is an excellent tool for constructing well-defined, nanosized molecular vessels that catalyse special chemical transformations.[141-143] With individual nanostructures linked by weak interactions, MOCs acquire high efficiency of photocatalytic activity.[137, 144, 145] Furthermore, the simple modification properties make it convenient to combine catalyst centres with different organic linkers.[134] In addition, the discrete nature of MOCs provides an efficient way to achieve higher catalytic activity and stability.

Recently, MOCs as heterogeneous catalysts have performed effectively in photocatalytic reactions.[146-148] In 2019, Su and co-workers reported **MOC-16 (Fig.1.11)**, which showed outstanding photocatalytic efficiency and cyclic stability for hydrogen evolution under visible-light irradiation with H_2O/MeCN environment (about 32 mmol g^{-1}).[149] In 2022, Lv and co-workers described a series of MOC photocatalytic systems **(Fig.1.11)** that showed high hydrogen production efficiency (6.423 mmol $h^{-1}g^{-1}$ in 5 h for the best one, **MOC-Q2**).[150] Hence, the potential application of MOCs

to water-splitting hydrogen generation warrants further exploration.

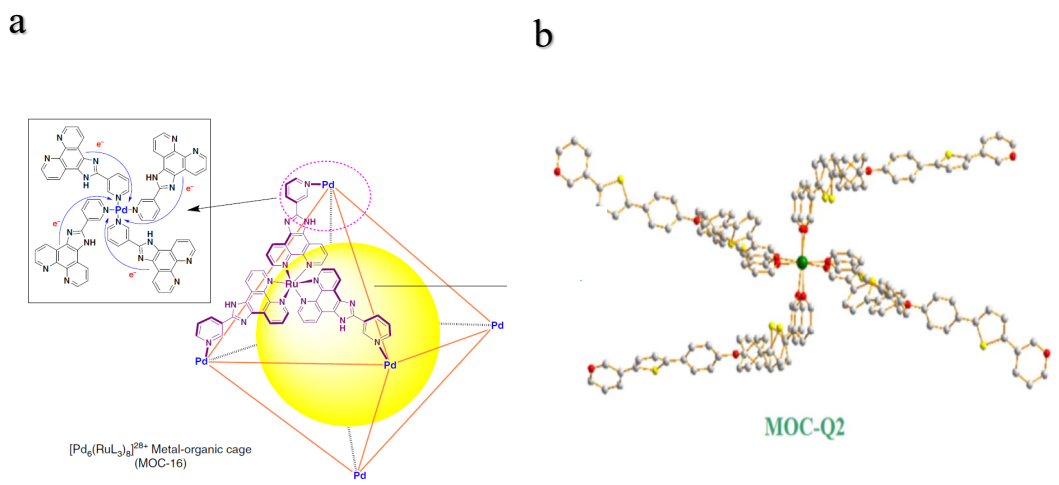

Fig. 1.11. The chemical structures of (a) **MOC-16**, [149] (b) **MOC-Q2**[150]

1.7. Scope of the Thesis

Since the first demonstration of a water-splitting system with TiO_2 as the semiconductor, Ru(II) complexes as photosensitizers for Pt-TiO_2 water-splitting systems have been designed and investigated. Ru(II) complexes have shown impressive performance for their potential applications in water-splitting systems because of their unusual MLCT and unique photophysical properties.[78, 151] However, fully utilising the light-harvesting abilities and stability of these photocatalytic systems remains a challenging task.[152] To improve water splitting for hydrogen production, a series of Ru(II) complexes with different ligands, such as isoquinoline or triphenylamine, which have been proven to significantly increase the hydrogen-production efficiency during water splitting[153-155] have been designed and explored. All these Ru(II) complexes have been used in water splitting for hydrogen production experiments. The influence of different anchoring

groups, such as carboxylic acid anchors or phosphonate functional groups of Ru(II) complexes (**Fig. 1.12**) in hydrogen production, are also discussed in the thesis. With the best Ru(II) water-splitting system, after 236 hours of irradiation, an H_2 TON of up to 14 232 was recorded.

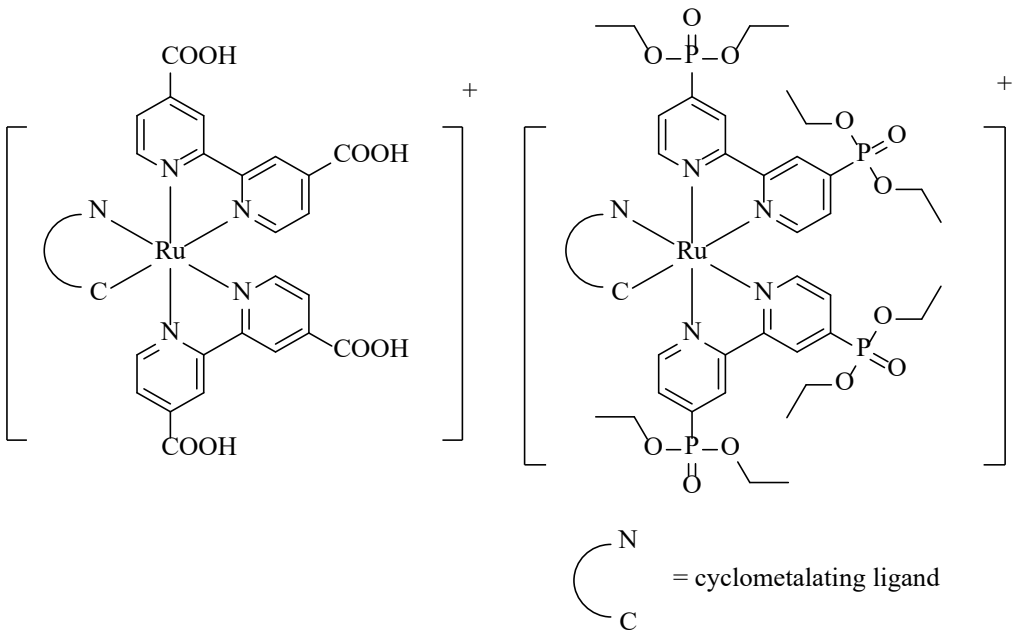

Fig. 1.12. Chemical structures of Ru(II) complexes.

Compared to other metal dyes that include first- and second-row transition metals, Ir(III) cyclometalated complexes possess excellent ligand field stabilisation energies with their 5d valence shell.[68, 70] However, Ir(III) cyclometalated complexes often suffer from weak absorbance of visible light. Therefore, I synthesised a series of Ir(III) complexes with different functional groups, such as triphenylamine or aldehyde, for the Pt-TiO_2 system, which showed satisfactory hydrogen production results.[104, 156, 157] Different anchoring groups were designed to test the working efficiency of the water-

splitting system (**Fig. 1.13**). Most of the previous Ir(III) photosensitizers for photocatalytic applications possess carboxylate acid anchors. However, these dyes may have poor stability under photocatalytic operating conditions.[158] In this regard, the linkage of the phosphonate functional group to the TiO_2 surface has been found to more effective and stable than that of the carboxylate group.[94, 159] A respectable hydrogen TON of 15 509 in a platinised TiO_2 hydrogen-production system was demonstrated with the best Ir(III) water-splitting system.

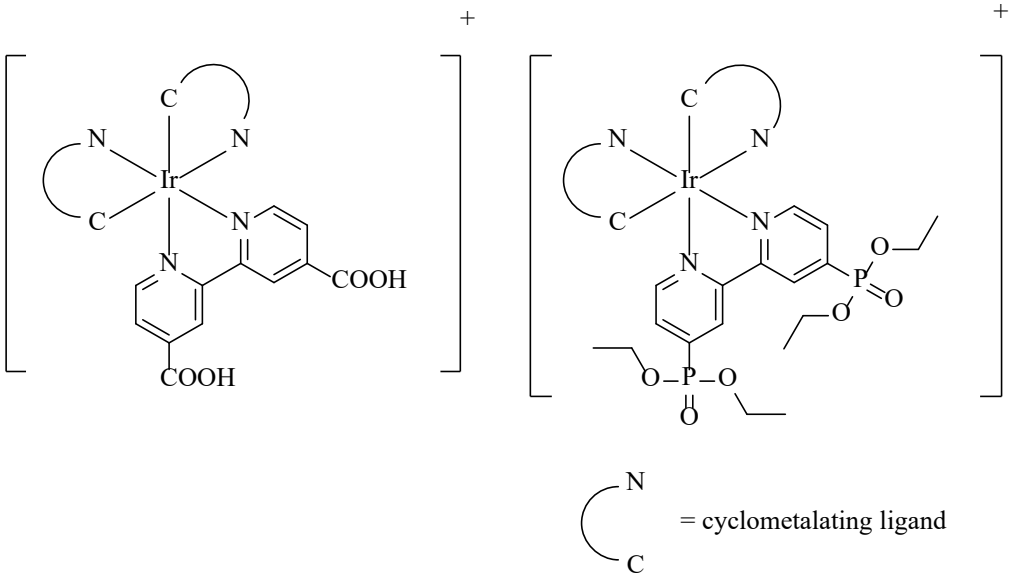

Fig. 1.13. Chemical structures of Ir(III) complexes.

In most traditional molecular water-splitting systems, expensive noble metals have been used.[100, 101] Such high costs may hinder the industrial application of those water-splitting systems.[102, 103] CdS NRs systems, which have large light-absorption coefficients, offer great potential.[160] Research has been conducted on water-splitting systems with CdS NRs and different earth-abundant metal complexes, particularly

Ni.[161] Different electron-donating or -withdrawing ligands have been used on templates of salen-type or salophen-type Schiff bases (**Fig. 1.14**) to determine the physical and chemical properties of the earth-abundant metal complexes and their water-splitting performance for hydrogen production. This study also examined the effects of the size and aspect ratio of the CdS NRs on hydrogen production. A photocatalytic system containing a metal-salophen complex based on nickel achieved a steady and impressive catalytic activity with a TON of 57 238 and a turnover frequency (TOF) of 436.9 h^{-1} over 131 hours under blue-light irradiation.

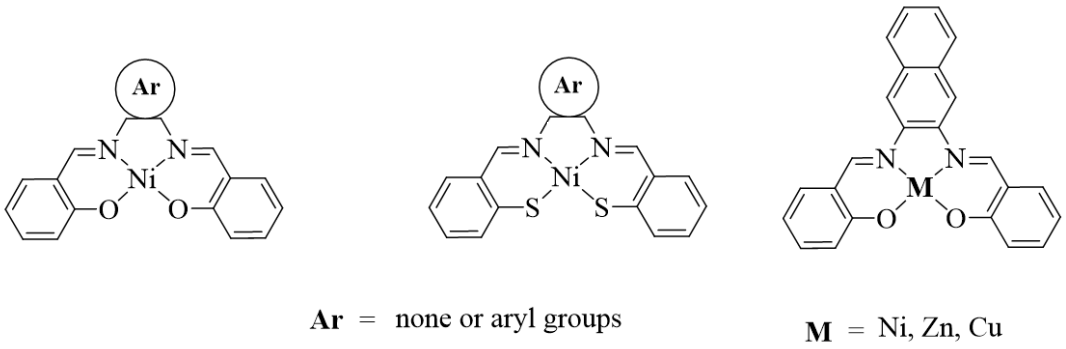

Fig. 1.14. Chemical structures of earth-abundant metal complexes.

MOCs, assembled from diverse inorganic structures and organic linkers, have recently been in rapid development.[140] Additionally, the catalytic properties of MOCs can be tuned effectively with a proper structural design.[136] In order to ensure the efficient production of H_2, the photocatalyst must possess a high charge transfer ability and strong absorption of visible light.[146, 147] Inspired by previous studies,[139, 140] two sets of metal−organic cages build with triphenylamine or benzene as the framework backbone with Ni or Co were designed and synthesised (**Fig. 1.15**). Their various water-

splitting performances and physical and chemical characteristics are discussed in this thesis.

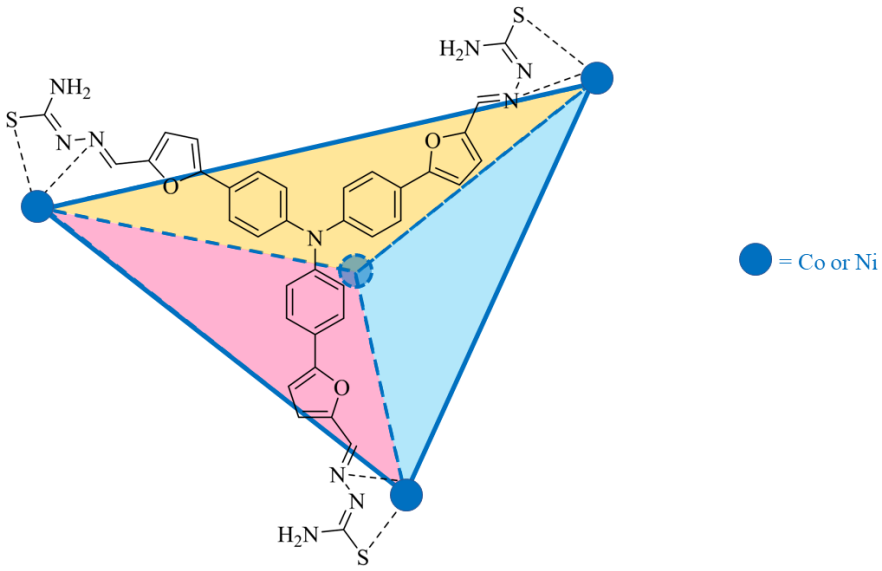

Fig. 1.15. Representative chemical structures of metal organic cage.

1.8. References

[1] A.-D. Pham, N.-T. Ngo, T. T. H. Truong, N.-T. Huynh, N.-S. Truong, *J. Clean. Prod.* **2020**, *260*, 121082.

[2] M. S. Kırlı, M. Fahrioğlu, *Energy Sources, Part A* **2019**, *41*, 1739-1751.

[3] A. Sieminski, *EIA.* **2014**, *18*, 1-24.

[4] P. Ciancarini, S. Ergasheva, Z. Kholmatova, A. Kruglov, G. Succi, X. Vasquez, E. Zuev, *Electronics* **2020**, *9*, 1678.

[5] M. Ni, M. K. H. Leung, D. Y. C. Leung, K. Sumathy, *Renewable Sustainable Energy Rev.* **2007**, *11*, 401-425.

[6] C. G. Hoehne, M. V. Chester, *Energy* **2016**, *115*, 646-657.

[7] W. W. Kellogg, *Climate change and society: consequences of increasing atmospheric carbon dioxide*, Routledge, London, **2019**.

[8] R. M. Andrew, G. P. Peters, *The Global Carbon Project's fossil CO_2 emissions dataset*, Zenodo, Geneva, Switzerland, **2021**.

[9] S. Bilgen, İ. Sarıkaya, *Renewable Sustainable Energy Rev.* **2015**, *51*, 1115-1131.

[10] H. Lund, *Energy* **2007**, *32*, 912-919.

[11] M. Balat, M. Balat, *Int. J. Hydrog. Energy* **2009**, *34*, 3589-3603.

[12] M. Balat, *Int. J. Hydrog. Energy* **2008**, *33*, 4013-4029.

[13] I. K. Kapdan, F. Kargi, *Enzyme Microb. Technol.* **2006**, *38*, 569-582.

[14] S. Sharma, S. K. Ghoshal, *Renewable Sustainable Energy Rev.* **2015**, *43*, 1151-1158.

[15] D. K. Ross, *Vacuum* **2006**, *80*, 1084-1089.

[16] J. Bilík, P. Pustejovska, S. Brozova, S. Jursova, *Sci. Iran.* **2013**, *20*, 337-342.

[17] F. Barbir, *Energy* **2009**, *34*, 308-312.

[18] S. Trasatti, *J. Electroanal. Chem.* **1999**, *476*, 90-91.

[19] T. Bessho, E. Yoneda, J.-H. Yum, M. Guglielmi, I. Tavernelli, H. Imai, U. Rothlisberger, M. K. Nazeeruddin, M. Grätzel, *J. Am. Chem. Soc.* **2009**, *131*, 5930-5934.

[20] L. Li, L. Duan, Y. Xu, M. Gorlov, A. Hagfeldt, L. Sun, *Chem. Commun.* **2010**, *46*, 7307-7309.

[21] A. Fujishima, K. Honda, *Nature* **1972**, *238*, 37-38.

[22] M. Watanabe, *Sci. Technol. Adv. Mater.* **2017**, *18*, 705-723.

[23] J. Schneider, D. W. Bahnemann, *J. Phys. Chem. Lett.* **2013**, *4*, 3479-3483.

[24] Y. Li, G. Lu, S. Li, *Chemosphere* **2003**, *52*, 843-850.

[25] A. A. Nada, M. H. Barakat, H. A. Hamed, N. R. Mohamed, T. N. Veziroglu, *Int. J. Hydrog. Energy* **2005**, *30*, 687-691.

[26] Y. Pellegrin, F. Odobel, *C. R. Chim.* **2017**, *20*, 283-295.

[27] D. R. Prasad, M. Z. Hoffman, *J. Am. Chem. Soc.* **1986**, *108*, 2568-2573.

[28] Q. G. Mulazzani, M. Venturi, M. Z. Hoffman, *J. Phys. Chem.* **1985**, *89*, 722-728.

[29] E. D. Cline, S. E. Adamson, S. Bernhard, *Inorg. Chem.* **2008**, *47*, 10378-10388.

[30] P. J. DeLaive, T. K. Foreman, C. Giannotti, D. G. Whitten, *J. Am. Chem. Soc.* **1980**, *102*, 5627-5631.

[31] P.-Y. Ho, Y. Wang, S.-C. Yiu, W.-H. Yu, C.-L. Ho, S. Huang, *Org. Lett.* **2017**, *19*, 1048-1051.
[32] F. Légalité, D. Escudero, Y. Pellegrin, E. Blart, D. Jacquemin, O. Fabrice, *Dyes Pigm.* **2019**, *171*, 107693.
[33] C. V. Krishnan, C. Creutz, D. Mahajan, H. A. Schwarz, N. Sutin, *Isr. J. Chem.* **1982**, *22*, 98-106.
[34] C. Creutz, *Inorg. Chem.* **1981**, *20*, 4449-4452.
[35] M. T. Craw, M. C. Depew, *Rev. Chem. Intermed.* **1985**, *6*, 1-31.
[36] M. Raula, M. H. Rashid, T. K. Paira, E. Dinda, T. K. Mandal, *Langmuir* **2010**, *26*, 8769-8782.
[37] A. Fujishima, T. N. Rao, D. A. Tryk, *J. Photochem. Photobiol. C* **2000**, *1*, 1-21.
[38] F. Costantino, P. V. Kamat, *ACS Energy Lett.* **2021**, *7*, 242-246.
[39] K. Sayama, H. Arakawa, *J. Chem. Soc., Chem. Commun.* **1992**, *1992*, 150-152.
[40] X. Yao, P.-Y. Ho, S.-C. Yiu, S. Suramitr, W.-B. Li, C.-L. Ho, S. Hannongbua, *Dyes Pigm.* **2022**, *205*, 110508.
[41] M. R. St. John, A. J. Furgala, A. F. Sammells, *J. Phys. Chem.* **1983**, *87*, 801-805.
[42] G. R. Bamwenda, S. Tsubota, T. Nakamura, M. Haruta, *J. Photochem. Photobiol. A* **1995**, *89*, 177-189.
[43] S. Sakthivel, M.V. Shankar, M. Palanichamy, B. Arabindoo, D. Bahnemann, V. Murugesan, *Water Res.* **2004**, *38*, 3001-3008.
[44] V. Kumaravel, S. Mathew, J. Bartlett, S. C. Pillai, *Appl. Catal. B* **2019**, *244*, 1021-1064.
[45] J. Ran, J. Zhang, J. Yu, M. Jaroniec, S. Z. Qiao, *Chem. Soc. Rev.* **2014**, *43*, 7787-7812.
[46] M. R. Gholipour, C.-T. Dinh, F. Béland, T.-O. Do, *Nanoscale* **2015**, *7*, 8187-8208.
[47] V. Maslova, A. Fasolini, M. Offidani, S. Albonetti, F. Basile, *Catal. Today* **2021**, *380*, 147-155.
[48] G. Colón, *Appl. Catal. A* **2016**, *518*, 48-59.
[49] J. Liqiang, S. Xiaojun, S. Jing, C. Weimin, X. Zili, D. Yaoguo, F. Honggang, *Sol. Energy Mater. Sol. Cells* **2003**, *79*, 133-151.
[50] Z. Zhang, J. T. Yates Jr, *Chem. Rev.* **2012**, *112*, 5520-5551.
[51] V. Subramanian, E. E. Wolf, P. V. Kamat, *J. Am. Chem. Soc.* **2004**, *126*, 4943-4950.
[52] R. M. Navarro, M. C. Alvarez-Galván, J. A. V. d. l. Mano, S. M. Al-Zahrani, J. L. G. Fierroa, *Energy Environ. Sci.* **2010**, *3*, 1865.
[53] S. Peiris, H. B. de Silva, K. N. Ranasinghe, S. V. Bandara, I. R. Perera, *J. Chin. Chem. Soc.* **2021**, *68*, 738-769.
[54] K. Maeda, G. Sahara, M. Eguchi, O. Ishitani, *ACS Catal.* **2015**, *5*, 1700-1707.
[55] J. F. Huang, Y. Lei, T. Luo, J. M. Liu, *ChemSusChem* **2020**, *13*, 5863-5895.
[56] P. G. Bomben, K. C. D. Robson, B. D. Koivisto, C. P. Berlinguette, *Coord. Chem. Rev.* **2012**, *256*, 1438-1450.
[57] I. N. Mills, J. A. Porras, S. Bernhard, *Acc. Chem. Res.* **2018**, *51*, 352-364.

[58] Y.-J. Yuan, Z.-T. Yu, D.-Q. Chen, Z.-G. Zou, *Chem. Soc. Rev.* **2017**, *46*, 603-631.
[59] J.-H. Shon, T. S. Teets, *ACS Energy Lett.* **2019**, *4*, 558-566.
[60] S.-C. Yiu, P.-Y. Ho, Y.-Y. Kwok, X. He, Y. Wang, W.-H. Yu, C.-L. Ho, S. Huang, *Chem. Eur. J.* **2022**, *28*, e202104575.
[61] N. Chanda, D. Koteshwar, S. Gonuguntla, S. Bojja, U. Pal, L. Giribabu, *Mater. Adv.* **2021**, *2*, 4762-4771.
[62] E. A. Malinka, A. M. Khutornoi, S. V. Vodzinskii, Z. I. Zhilina, G. L. Kamalov, *React. Kinet. Catal. Lett.* **1988**, *36*, 407-410.
[63] X. Chen, S. Shen, L. Guo, S. S. Mao, *Chem. Rev.* **2010**, *110*, 6503-6570.
[64] T. Shimidzu, *Nouv. J. Chim.* **1983**, *7*, 21-27.
[65] V. S. Zakharenko, A. V. Bulatov, V. N. Parmon, *React. Kinet. Catal. Lett.* **1988**, *36*, 295-300.
[66] P. Jarosz, P. Du, J. Schneider, S.-H. Lee, D. McCamant, R. Eisenberg, *Inorg. Chem.* **2009**, *48*, 9653-9663.
[67] M. Zhu, Y. Lu, Y. Du, J. Li, X. Wang, P. Yang, *Int. J. Hydrog. Energy* **2011**, *36*, 4298-4304.
[68] M. Yang, J. E. Yarnell, K. El Roz, F. N. Castellano, *ACS Appl. Energy Mater.* **2020**, *3*, 1842-1853.
[69] N. Serpone, D. Lawless, J. Disdier, J.-M. Herrmann, *Langmuir* **1994**, *10*, 643-652.
[70] J. C. Deaton, F. N. Castellano, in *Iridium (III) in optoelectronic and photonics applications* (Ed.: ZYSMAN-COLMAN E), John Wiley & Sons, Hoboken, **2017**, pp. 1-69.
[71] D. W. Bahnemann, in *Photochemical Conversion and Storage of Solar Energy* (Eds.: PELIZZETTI E, SCHIAVELLO M), Springer Netherlands, Dordrecht, **1991**, pp. 251-276.
[72] R. Bevernaegie, L. Marcélis, B. Laramée-Milette, J. De Winter, K. Robeyns, P. Gerbaux, G. S. Hanan, B. Elias, *Inorg. Chem.* **2018**, *57*, 1356-1367.
[73] R. A. Marcus, N. Sutin, *Biochim. Biophys. Acta.* **1985**, *811*, 265-322.
[74] V. Balzani, *Tetrahedron* **1993**, *48*, 10443-10514.
[75] R. Arakawa, K. Abe, M. Iwai, T. Fukuo, Y. Nakabayashi, *J. Mass Spectrom. Soc. Jpn.* **2001**, *49*, 183-187.
[76] D. G. Whitten, *Acc. Chem. Res.* **1980**, *13*, 83-90.
[77] M. D. Kärkäs, T. M. Laine, E. V. Johnston, B. Åkermark, in *Applied Photosynthesis: New Progress* (Ed.: NAJAFPOUR M), IntechOpen, London, **2016**, pp. 189-219.
[78] E. Erdmann, A. Villinger, B. König, W. W. Seidel, *Photochem. Photobiol. Sci.* **2018**, *17*, 1056-1067.
[79] G. Li, K. Hu, K. C. D. Robson, S. I. Gorelsky, G. J. Meyer, C. P. Berlinguette, M. Shatruk, *Chem. Eur. J.* **2015**, *21*, 2173-2181.
[80] Y. Liu, R. Hammitt, D. A. Lutterman, L. E. Joyce, R. P. Thummel, C. Turro, *Inorg. Chem.* **2009**, *48*, 375-385.
[81] E. Bae, W. Choi, J. Park, H. S. Shin, S. B. Kim, J. S. Lee, *J. Phys. Chem. B*

2004, *108*, 14093-14101.
[82] S. Aghazada, M. K. Nazeeruddin, *Inorganics* **2018**, *6*, 52.
[83] C. Ma, S. Piccinin, S. Fabris, *ACS Catal.* **2012**, *2*, 1500-1506.
[84] J. I. Goldsmith, W. R. Hudson, M. S. Lowry, T. H. Anderson, S. Bernhard, *J. Am. Chem. Soc.* **2005**, *127*, 7502-7510.
[85] M. S. Lowry, S. Bernhard, *Chem. Eur. J.* **2006**, *12*, 7970-7977.
[86] M. S. Lowry, J. I. Goldsmith, J. D. Slinker, R. Rohl, R. A. Pascal, G. G. Malliaras, S. Bernhard, *Chem. Mater.* **2005**, *17*, 5712-5719.
[87] E. A. Juban, A. L. Smeigh, J. E. Monat, J. K. McCusker, *Coord. Chem. Rev.* **2006**, *250*, 1783-1791.
[88] S.-y. Takizawa, C. Pérez-Bolívar, P. Anzenbacher Jr, S. Murata, *Eur. J. Inorg. Chem.* **2012**, *2012*, 3975-3979.
[89] Y. Wang, X. Zhao, Y. Zhao, T. Yang, X. Liu, J. Xie, G. Li, D. Zhu, H. Tan, Z. Su, *Dyes Pigm.* **2019**, *170*, 107547.
[90] J. Zhao, W. Wu, J. Sun, S. Guo, *Chem. Soc. Rev.* **2013**, *42*, 5323-5351.
[91] C.-H. Siu, C.-L. Ho, J. He, T. Chen, X. Cui, J. Zhao, W.-Y. Wong, *J. Organomet. Chem.* **2013**, *748*, 75-83.
[92] E. Bae, W. Choi, *J. Phys. Chem. B* **2006**, *110*, 14792-14799.
[93] H. Park, E. Bae, J. J. Lee, J. Park, W. Choi, *J. Phys. Chem. B* **2006**, *110*, 8740-8749.
[94] M. Zalas, B. Gierczyk, A. Bossi, P. R. Mussini, M. Klein, R. Pankiewicz, M. Makowska-Janusik, Ł. Popenda, W. Stampor, *Dyes Pigm.* **2018**, *150*, 335-346.
[95] T. N. Murakami, E. Yoshida, N. Koumura, *Electrochim. Acta.* **2014**, *131*, 174-183.
[96] V. Artero, M. Chavarot-Kerlidou, M. Fontecave, *Angew. Chem. Int. Ed. Engl.* **2011**, *50*, 7238-7266.
[97] V. S. Thoi, Y. Sun, J. R. Long, C. J. Chang, *Chem. Soc. Rev.* **2013**, *42*, 2388-2400.
[98] C.-B. Li, Z.-J. Li, S. Yu, G.-X. Wang, F. Wang, Q.-Y. Meng, B. Chen, K. Feng, C.-H. Tung, L.-Z. Wu, *Energy Environ. Sci.* **2013**, *6*, 2597-2602.
[99] L.-Z. Wu, B. Chen, Z.-J. Li, C.-H. Tung, *Acc. Chem. Res.* **2014**, *47*, 2177-2185.
[100] P. Du, K. Knowles, R. Eisenberg, *J. Am. Chem. Soc.* **2008**, *130*, 12576-12577.
[101] W.-G. Wang, F. Wang, H.-Y. Wang, C.-H. Tung, L.-Z. Wu, *Dalton. Trans.* **2012**, *41*, 2420-2426.
[102] S. Ott, M. Kritikos, B. Åkermark, L. Sun, *Angew. Chem. Int. Ed. Engl.* **2003**, *42*, 3285-3288.
[103] W.-N. Cao, F. Wang, H.-Y. Wang, B. Chen, K. Feng, C.-H. Tung, L.-Z. Wu, *Chem. Commun.* **2012**, *48*, 8081-8083.
[104] K. He, N. Su, Y. Junting, Y. Liu, W. Xiong, Z. Hao, D. Ma, W. Zhu, *Tetrahedron* **2016**, *72*, 7164-7169.
[105] P.-Y. Ho, S.-Y. Lee, C. Kam, J. Zhu, G.-G. Shan, Y. Hong, W.-Y. Wong, S. Chen, *Adv. Healthc. Mater.* **2021**, *10*, 2170116.
[106] M. L. Helm, M. P. Stewart, R. M. Bullock, M. R. DuBois, D. L. DuBois, *Science* **2011**, *333*, 863-866.

[107] A. D. Wilson, R. K. Shoemaker, A. Miedaner, J. T. Muckerman, D. L. DuBois, M. R. DuBois, *Proc. Natl. Acad. Sci. U. S. A.* **2007**, *104*, 6951-6956.
[108] J. Kuczyńska, B. Nieradko-Iwanicka, *Biomed. Pharmacother.* **2021**, *139*, 111608.
[109] M. L. Helm, M. P. Stewart, R. M. Bullock, M. R. DuBois, D. L. DuBois, *Science* **2011**, *333*, 863-866.
[110] Z. J. Han, W. R. McNamara, M. -S. Eum, P. L. Holland, R. Eisenberg, *Angew. Chem. Int. Ed. Engl.* **2012**, *51*, 1667-1670.
[111] Z. J. Han, F. Qiu, R. Eisenberg, P. L. Holland, T. D. Krauss, *Science* **2012**, *338*, 1321-1324.
[112] Y. Yamada, T. Miyahigashi, H. Kotani, K. Ohkubo, S. Fukuzumi, *Energy Environ. Sci.* **2012**, *5*, 6111-6118.
[113] J.-M. Lei, S.-P. Luo, S.-Z. Zhan, S.-P. Wu, *Inorg. Chem. Commun.* **2018**, *95*, 158-162.
[114] Y.-J. Lei, S. Liu, G.-L. Hu, R. Hu, R.-T. Yan, Y.-B. Lu, H.-Y. Wang, *Int. J. Hydrog. Energy* **2019**, *44*, 20079-20084.
[115] X. L. Ho, H. Y. Shao, Y. Y. Ng, R. Ganguly, Y. P. Lu, H. S. Soo, *Inorg. Chem.* **2019**, *58*, 1469-1480.
[116] U. J. Kilgore, J. A. S. Roberts, D. H. Pool, A. M. Appel, M. P. Stewart, M. R. DuBois, W. G. Dougherty, W. S. Kassel, R. M. Bullock, D. L. DuBois, *J. Am. Chem. Soc.* **2011**, *133*, 5861-5872.
[117] I. P. Oliveri, G. Malandrino, S. D. Bella, *Dalton. Trans.* **2014**, *43*, 10208-10214.
[118] H.-Y. Yin, J. Tang, J.-L. Zhang, *Eur. J. Inorg. Chem.* **2017**, *2017*, 5085-5093.
[119] G. Consiglio, S. Failla, I. P. Oliveri, R. Purrello, S. D. Bella, *Dalton. Trans.* **2009**, *2009*, 10426-10428.
[120] C.-Y. Chiang, K. Aroh, N. Franson, V. R. Satsangi, S. Dass, S. Ehrman, *Int. J. Hydrog. Energy* **2011**, *36*, 15519-15526.
[121] A. Paracchino, N. Mathews, T. Hisatomi, M. Stefik, S. D. Tilley, M. Grätzel, *Energy Environ. Sci.* **2012**, *5*, 8673-8681.
[122] C.-Y. Chiang, Y. Shin, S. Ehrman, *Energy Procedia* **2014**, *61*, 1799-1802.
[123] P. W. Du, R. Eisenberg, *Energy Environ. Sci.* **2012**, *5*, 6012-6021.
[124] Y. Yan, B. Y. Xia, B. Zhao, X. Wang, *J. Mater. Chem. A* **2016**, *4*, 17587-17603.
[125] L. Yuan, C. Han, M.-Q. Yang, Y.-J. Xu, *Int. Rev. Phys. Chem.* **2016**, *35*, 1-36.
[126] M. Wang, L. Chen, L. Sun, *Energy Environ. Sci.* **2012**, *5*, 6763-6778.
[127] A. Vaneski, J. Schneider, A. S. Susha, A. L. Rogach, *J. Photochem. Photobiol. C* **2014**, *19*, 52-61.
[128] K. Wu, T. Lian, *Chem. Soc. Rev.* **2016**, *45*, 3781–3810.
[129] Z. Han, F. Qiu, R. Eisenberg, P. L. Holland, T. D. Krauss, *Science* **2012**, *338*, 1321–1324.
[130] Y. Xu, Y. Huang, B. Zhang, *Inorg. Chem. Front.* **2016**, *3*, 591-615.
[131] Z.-R. Tang, B. Han, C. Han, Y.-J. Xu, *J. Mater. Chem. A* **2017**, *5*, 2387-2410.
[132] S. Y. Park, H. U. Lee, E. S. Park, S. C. Lee, J.-W. Lee, S. W. Jeong, C. H. Kim, Y.-C. Lee, Y. S. Huh, J. Lee, *ACS Appl. Mater. Interfaces* **2014**, *6*, 3365-3370.

[133] J.-D. Xiao, Q. Shang, Y. Xiong, Q. Zhang, Y. Luo, S.-H. Yu, H.-L. Jiang, *Angew. Chem. Int. Ed. Engl.* **2016**, *55*, 9389-9393.
[134] C. Ji, W. Wang, E.-S. M. El-Sayed, G. Liu, Y. Si, K. Su, Z. Ju, F. Wu, D. Yuan, *Appl. Catal. B* **2021**, *285*, 119782.
[135] M. Zhao, Y. Huang, Y. Peng, Z. Huang, Q. Ma, H. Zhang, *Chem. Soc. Rev.* **2018**, *47*, 6267-6295.
[136] G. Liu, Y. Di Yuan, J. Wang, Y. Cheng, S. B. Peh, Y. Wang, Y. Qian, J. Dong, D. Yuan, D. Zhao, *J. Am. Chem. Soc.* **2018**, *140*, 6231-6234.
[137] M. Sun, C. Sun, X. Wang, Z. Su, *Catal. Commun.* **2020**, *137*, 105930.
[138] H. Liu, C. Xu, D. Li, H.-L. Jiang, *Angew. Chem. Int. Ed. Engl.* **2018**, *130*, 5477-5481.
[139] C. Shi, M. Dubois, Y. Chen, L. Cheng, H. Ramezani, Y. Wang, X. Zhang, *Nat. Commun.* **2016**, *7*, 11110.
[140] X. Jing, C. He, Y. Yang, C. Duan, *J. Am. Chem. Soc.* **2015**, *137*, 3967-3974.
[141] R. Chakrabarty, P. S. Mukherjee, P. J. Stang, *Chem. Rev.* **2011**, *111*, 6810-6918.
[142] S. Leininger, B. Olenyuk, P. J. Stang, *Chem. Rev.* **2000**, *100*, 853-908.
[143] S. R. Seidel, P. J. Stang, *Acc. Chem. Res.* **2002**, *35*, 972-983.
[144] H. S. Lee, S. Jee, R. Kim, H.-T. Bui, B. Kim, J.-K. Kim, K. S. Park, W. Choi, W. Kim, K. M. Choi, *Energy Environ. Sci.* **2020**, *13*, 519-526.
[145] T.-F. Chen, S.-Y. Han, Z.-P. Wang, H. Gao, L.-Y. Wang, Y.-H. Deng, C.-Q. Wan, Y. Tian, Q. Wang, G. Wang, *Appl. Catal. B* **2019**, *259*, 118047.
[146] M. Zhou, S. Bao, A. J. Bard, *J. Am. Chem. Soc.* **2019**, *141*, 7327-7332.
[147] J. Liu, Y. Li, X. Zhou, H. Jiang, H. G. Yang, C. Li, *J. Mater. Chem. A* **2020**, *8*, 17-26.
[148] F. Li, D. Wang, Q.-J. Xing, G. Zhou, S.-S. Liu, Y. Li, L.-L. Zheng, P. Ye, J.-P. Zou, *Appl. Catal. B* **2019**, *243*, 621-628.
[149] Y.-C. Luo, K.-L. Chu, J.-Y. Shi, D.-J. Wu, X.-D. Wang, M. Mayor, C.-Y. Su, *J. Am. Chem. Soc.* **2019**, *141*, 13057-13065.
[150] C. Lv, S. Qin, Y. Lei, X. Li, J. Huang, J. Liu, *Nanomaterials* **2022**, *12*, 890.
[151] J. H. Alstrum-Acevedo, M. K. Brennaman, T. J. Meyer, *Inorg. Chem.* **2005**, *44*, 6802-6827.
[152] C. Ma, S. Piccinin, S. Fabris, *ACS Catal.* **2012**, *2*, 1500-1506.
[153] A. Mahmood, *Sol. Energy* **2016**, *123*, 127-144.
[154] S. Roquet, A. Cravino, P. Leriche, O. Alévêque, P. Frere, J. Roncali, *J. Am. Chem. Soc.* **2006**, *128*, 3459-3466.
[155] Q. Liu, L. Wu, M. Chen, Y. Guo, T. Xie, P. Wang, *Catal. Commun.* **2019**, *122*, 38-42.
[156] M. W. Ha, M.-H. Park, J. Y. Hwang, J. Kim, D.-H. Kim, T.-W. Lee, Y.-H. Kim, *Dyes Pigm.* **2021**, *185*, 108880.
[157] L. Flamigni, B. Ventura, E. Baranoff, J.-P. Collin, J.-P. Sauvage, *Eur. J. Inorg. Chem.* **2007**, *2007*, 5189-5198.
[158] K. L. Materna, R. H. Crabtree, G. W. Brudvig, *Chem. Soc. Rev.* **2017**, *46*, 6099-6110.
[159] R. A. Wahyuono, S. Amthor, C. Müller, S. Rau, B. Dietzek, *ChemPhotoChem*

2020, *4*, 618-629.
[160] Y. Fan, B. Yang, X. Song, X. Shao, M. Zhao, *J. Phys. D: Appl. Phys.* **2018**, *51*, 395501.
[161] D. Aggoun, Z. Messasma, B. Bouzerafa, R. Berenguer, E. Morallon, Y. Ouennoughi, A. Ourari, *J. Mol. Struct.* **2021**, *1231*, 129923.

Chapter 2: Synthesis, Structures, Characterisations and Water-Splitting Hydrogen Generation Experiments with Ruthenium(II) Cyclometalated Complexes

2.1. Introduction

The first water-splitting system for hydrogen production that used a TiO_2 photoanode was reported in 1972 by Fujishima and Honda.[1] Following this pioneering research, such systems have progressed dramatically.[2] Ruthenium(II) complexes such as **$[Ru(bpy)_3]^{2+}$**,[3-6] **N3**[7] and **N719**[8-10] (**Fig.2.1**) are attractive for their potential applications as photosensitizers in water-splitting systems due to their unusual metal-to-ligand charge transitions (MLCT) and unique photophysical properties.[3-6, 11] However, their light-harvesting ability in terms of efficacy when processing sunlight remains a prevalent challenge since most of them can only utilise UV light, which accounts for merely 5–7% of sunlight.[3-5, 12] In addition, some Ru(II) dyes contain monodentate isothiocyanate ligands, which are labile under thermal or light stress.[13] Although isothiocyanate-free Ru(II) complexes with bidentate donating ligands are preferable for obtaining kinetically inert photosensitizers, they have relatively short lifetimes.[14] Hence, there is still room for improvement and unlimited potential in their hydrogen evolution reaction performance. Efficient and stable Ru(II) photosensitizers are urgently required to accelerate the reaction rate for hydrogen generation.

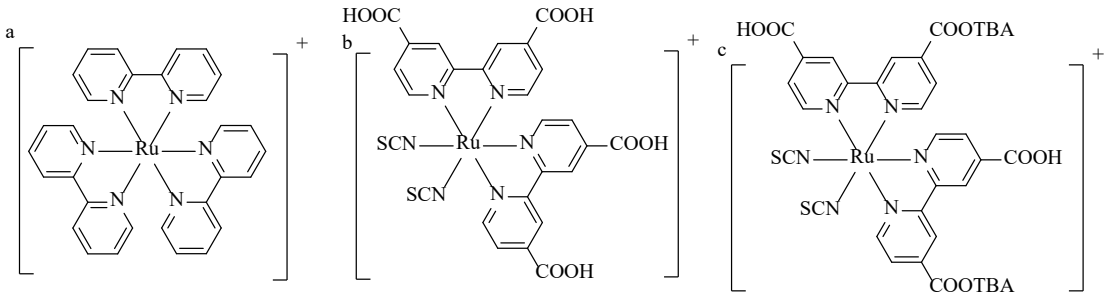

Fig. 2.1. Chemical structures of the (a) **[Ru(bpy)$_3$]$^{2+}$** molecule, (b) **N3** molecule and (c) **N719** molecule.

The recent development of Ru(II) photosensitizers has been focused on the structural modification by using cyclometalating and ancillary ligands to alter their photophysical and electrochemical properties.[3, 15] Their light-harvesting ability, electron injection efficiency and durability can be improved through judicious selection of chromophores and careful design of their molecular architecture. Thiophene rings with peculiar structural and electronic properties are widely used in photocatalysts.[16] Thiophene has lower resonance energy than benzene[17] because its π-excessive heteroaromatic five-membered ring aids charge transfer between the donors and acceptors.[18-20] Therefore, thiophene-based ligands are commonly used in the design of dyes for water-splitting hydrogen generation.[21] Furthermore, introducing pyridine functional groups causes the absorption spectrum to redshift slightly, which can improve the absorption of light in the visible region and increase hydrogen generation.[22, 23] Isoquinoline functional groups have also been extensively applied in dyes for water-splitting reactions because of their remarkable charge transfer ability.[24-26] Researchers have shown that the highly extended and polarisable π system in isoquinoline functional groups can greatly

increase hydrogen-production efficiency during water-splitting.[27-29] An appropriate donor on the cyclometalating ligands of Ru(II) photosensitizers leads to a better spectral response and faster charge injection efficiency, consequentially improving their performance for photocatalytic hydrogen generation.[30] Among various electron-donating moieties, triphenylamine (TPA) is one of the most popular, and its subsequent modification is desirable.[31, 32] In addition, TPA is an effective hole-transporting chromophore that can increase the charge-separated state lifetime by delocalising the generated cation over a planar amine unit, therefore, the stabilities and performance of their photocatalytic applications can be improved.[33, 34] These discoveries provide an attractive opportunity to develop highly efficient dyes for water-splitting systems.

On the other hand, a photosensitizer requires anchoring groups to enable efficient chemisorption onto a mesoporous oxide such as TiO_2. The nature of the anchoring group is an important factor in photocatalysis[35, 36] as it affects electronic communication between the dye and the TiO_2 semiconductor.[37] Although carboxylic acid anchors have been used in most Ru(II) photosensitizers so far, their use can incur instability during long-term photocatalysis.[38] Since the hydrolysing characteristic of the carboxylate linking site inhibits the efficiency of electron transfer from the Ru(II) complex to TiO_2,[39] the phosphonate functional group has been used instead, which has been shown to improve stability.[39]

In the present study, a new series of Ru(II) complexes (**Fig. 2.2**) with different functional groups were designed with the goal of increasing hydrogen production; either 4,4′ -dicarboxylic acid-2,2′ -bipyridine or tetraethyl[2, 2′ -bipyridine]-4,4′ -

diylbis(phosphonate) were used to anchor to TiO_2. Moreover, the photophysical and electrochemical properties of the new cyclometalated Ru(II) complexes along with their photocatalytic performance for hydrogen production via water-splitting were studied. Herein, the relationship between the anchoring groups and their hydrogen-production activities is also discussed.

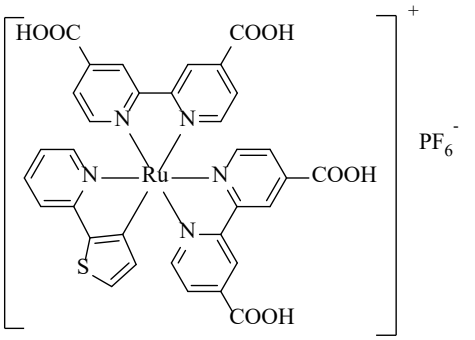

Ru1

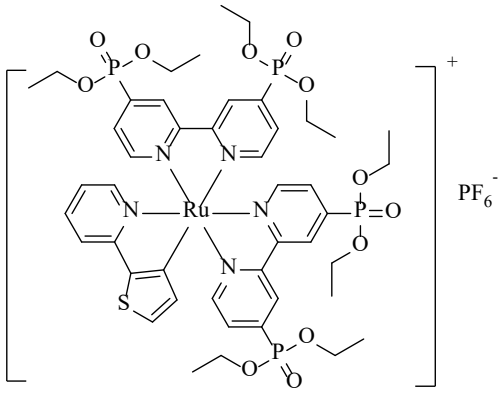

Ru2

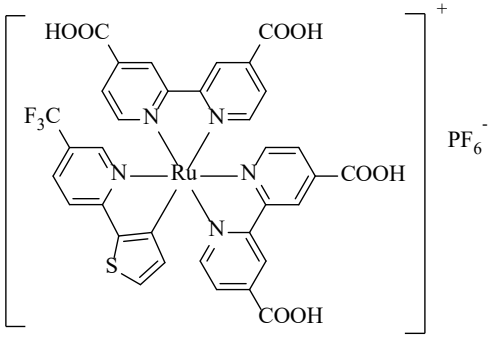

Ru3

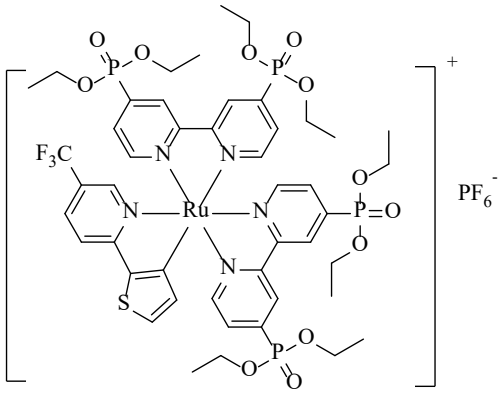

Ru4

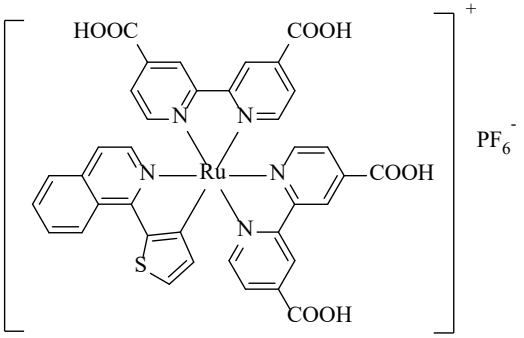

Ru5

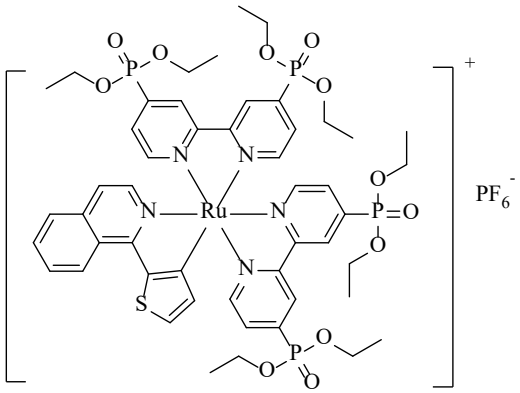

Ru6

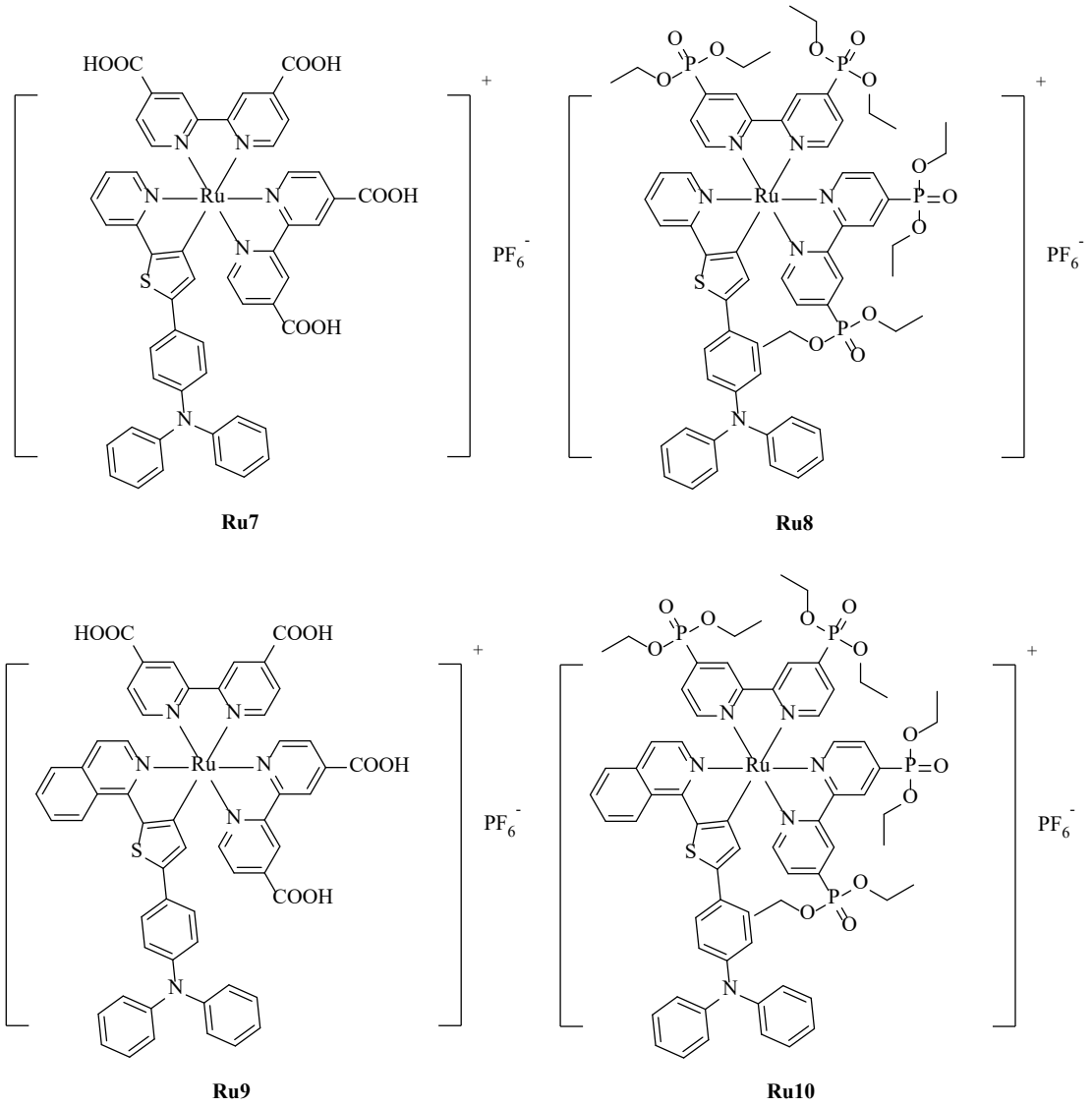

Fig. 2.2. The chemical structures of Ru(II) dyes **Ru1**–**Ru10**.

2.2. Synthesis

2.2.1. Synthesis of C^N ligands for the Ru(II) complexes

These were prepared by using the classical Suzuki reaction. C^N ligands were obtained from different boronic acids containing the corresponding bromo- or chloro-substituents starting in tetrahydrofuran solution with 2M K_2CO_3 solution and $Pd(PPh_3)_4$.

The synthetic pathways are shown in **Scheme 2.1**.

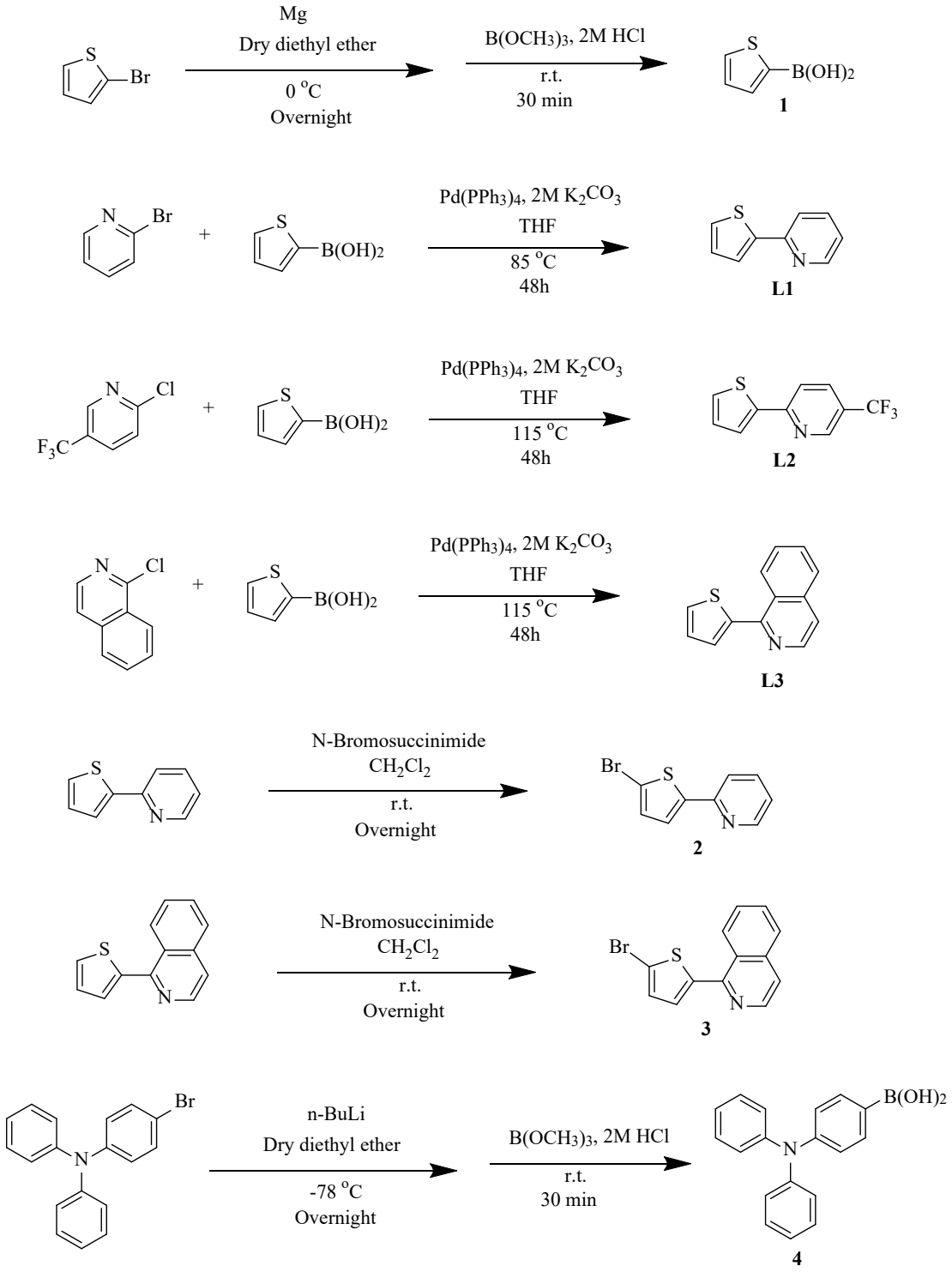

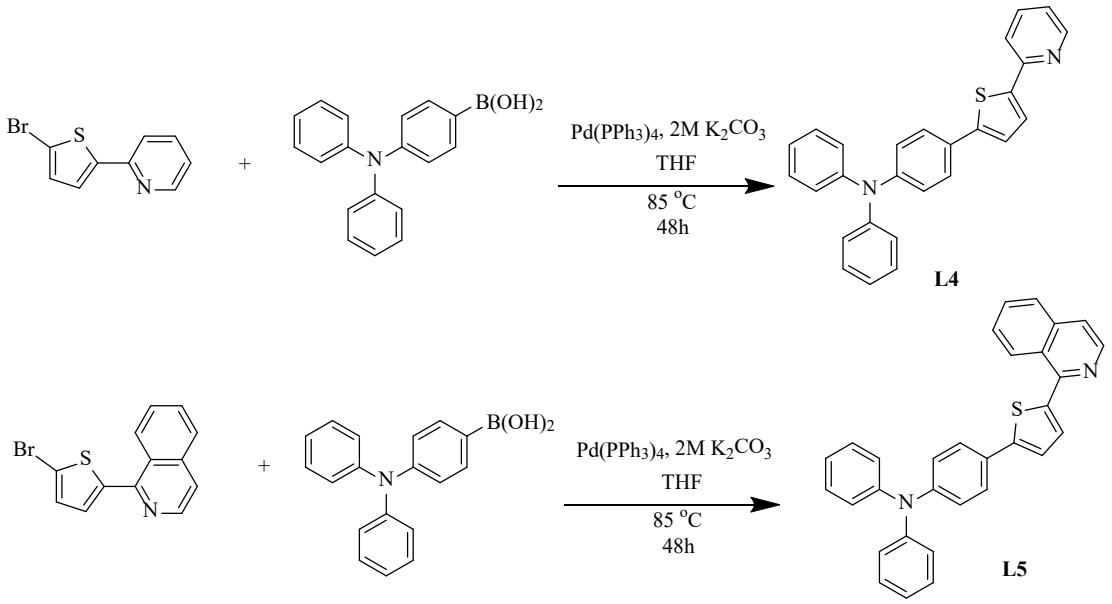

Scheme 2.1. Synthetic pathways for the C^N ligands.

2.2.2. Synthesis of the Ru(II) complexes

The synthetic routes for the Ru(II) photosensitizers are depicted in **Scheme 2.2**. All of the dyes are composed of a Ru(II) metal centre coordinated with one C^N cyclometalating ligand and two 2,2′-bipyridine-4,4′-dicarboxylic acid or tetraethyl[2,2′-bipyridine]-4,4′-diylbis(phosphonate) N^N ancillary ligands as anchoring groups. Preparation of the target Ru(II) dyes involved two steps.[40] $[RuCl_2(p\text{-cymene})]_2$ was first reacted with the corresponding C^N ligand to yield $[Ru(C^N)(MeCN)_4]PF_6$, which was then treated with the corresponding N^N ancillary ligands to obtain final products **Ru1** to **Ru10**. All of the complexes prepared in this study are stable as solids in air.

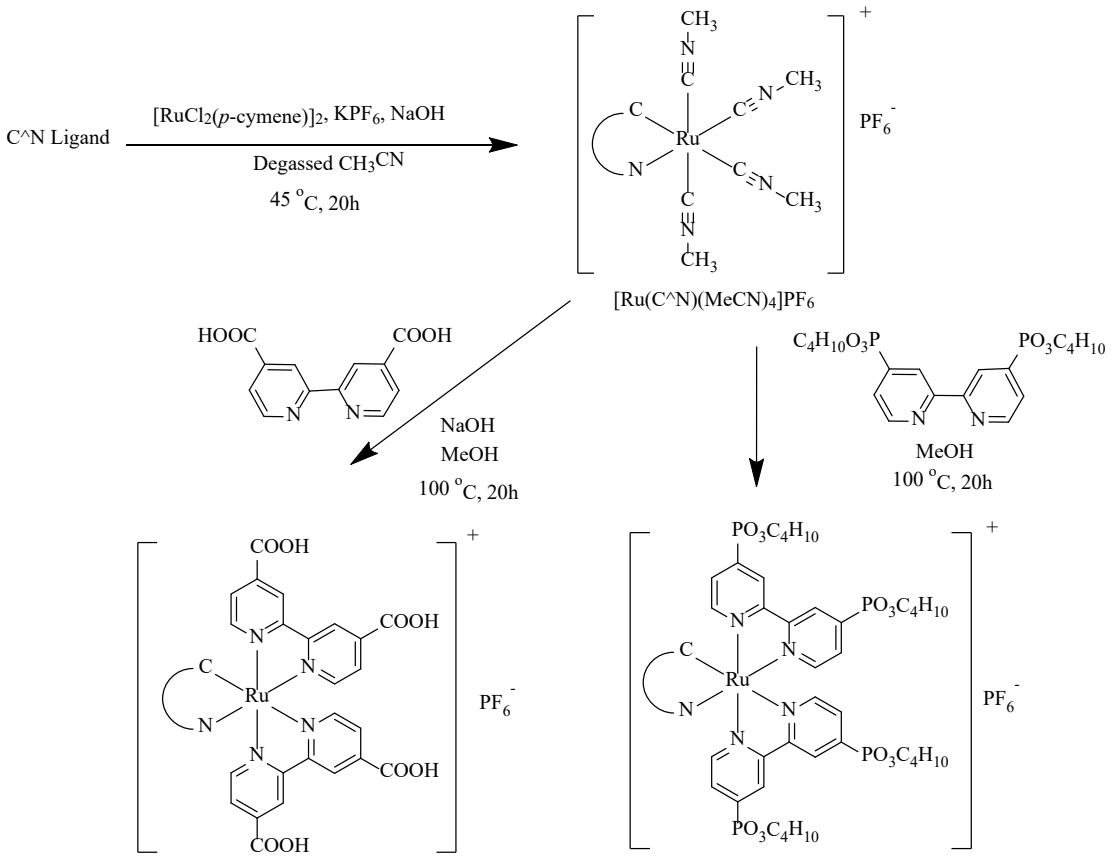

Scheme 2.2. Synthetic pathways for the Ru(II) complexes.

2.3. Spectroscopic Characterisation

All of the organic C^N ligands show characteristic ^{1}H NMR spectra and indicate a clear structure for each compound. For example, **Fig. 2.3** shows a ^{1}H NMR spectrum of **L3** with the signal at approximately 8.58 ppm being attributed to the ortho proton of isoquinoline.[27]

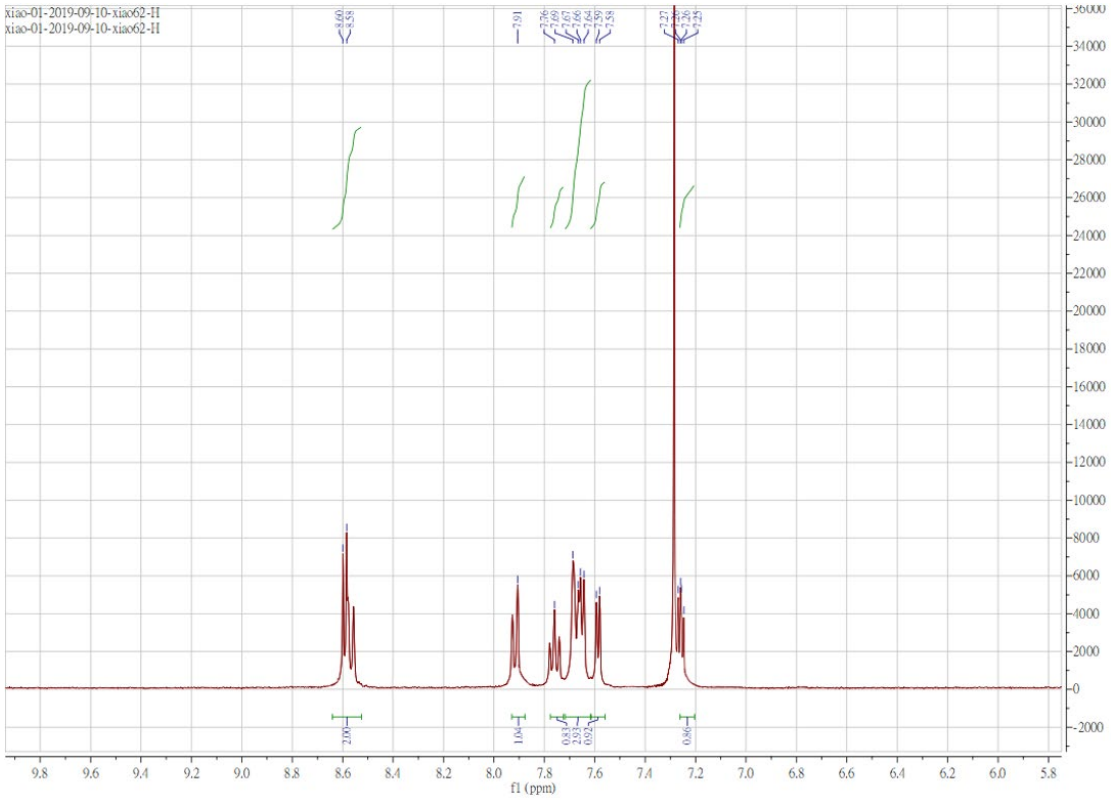

Fig. 2.3. ^{1}H NMR spectrum of **L3** in $CDCl_3$.

Because the solubility of the final Ru(II) complexes are not enough for ^{13}C NMR, only ^{13}C NMR data for C^N complexes could be obtained. The carbon NMR spectra show the structures. For example, **Fig. 2.4** exhibits a ^{13}C NMR spectrum of **L2**.

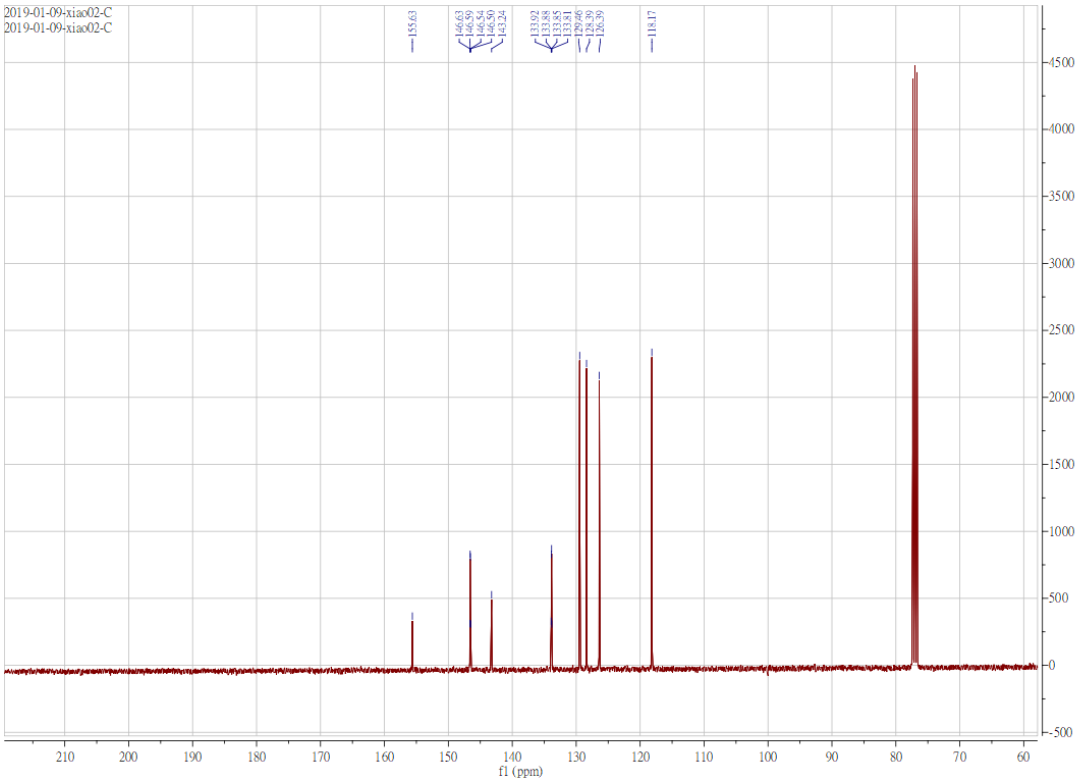

Fig. 2.4. ^{13}C NMR spectrum of **L2** in $CDCl_3$.

The Ru(II) complexes were also characterised by using ^{1}H NMR spectroscopy. All of the aromatic protons in the ^{1}H NMR spectra of **Ru1** to **Ru10** were chemically unique due to a lack of molecular symmetry, indicating that the two N^N ligands in them were magnetically non-equivalent. **Fig. 2.5** shows an NMR spectrum of **Ru8** as an example. These results preview the anticipated structure of those metal complexes.

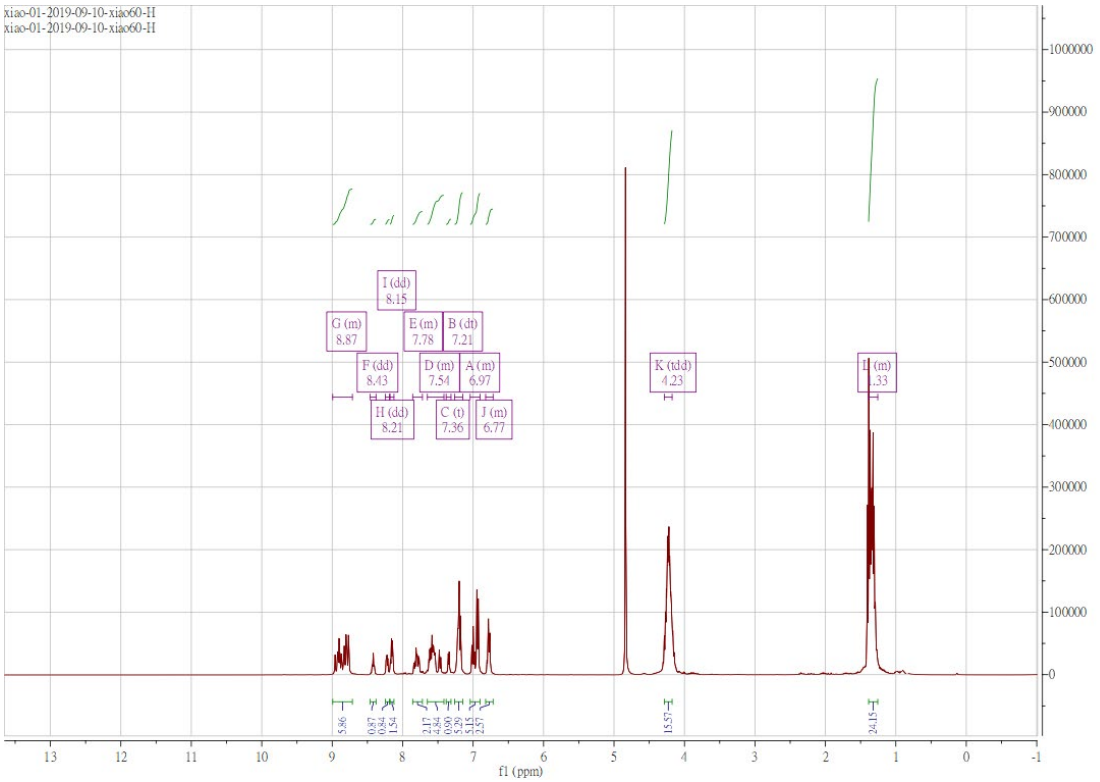

Fig. 2.5. ^{1}H NMR spectrum of **Ru8** in MeOD.

2.4. Mass Spectrum Characterisation

Liquid chromatography-electrospray ionisation quadrupole-time of flight (LC-ESI-Q-TOF) mass spectrometry was used to analyse the C^N ligand and the final products. For example, **Figs. 2.6** and **2.7** show the MS results for **L2** and **Ru8**, respectively. The main peaks of MS results match with the molecular ion peaks, indicating the correct synthesized of each compound.

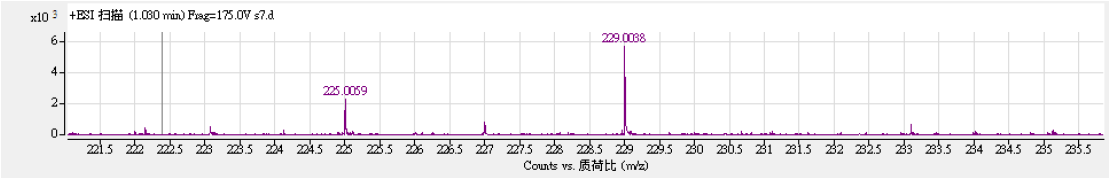

Fig. 2.6. MS results for **L2**.

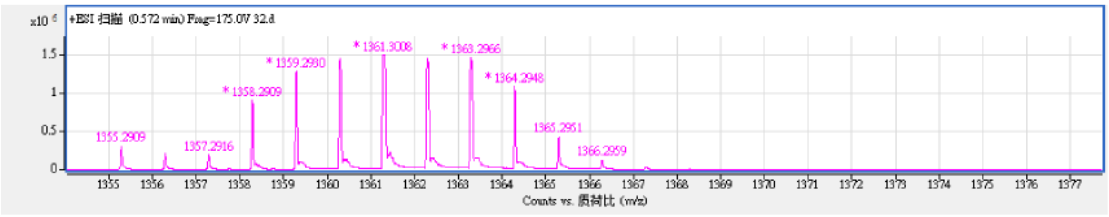

Fig. 2.7. MS results for **Ru8**.

2.5. Photophysical Properties

The photophysical properties of all of the Ru(II) dyes in MeOH were studied. Their UV/Vis absorption spectra are shown in **Fig. 2.8** and **Fig. 2.9** and the corresponding characteristic spectral data are tabulated in **Table 2.1**. In general, the absorption spectra of all of the dyes are dominated by an intense UV band at around 300 nm, which is attributed to the ligand-centred (LC) π-to-π* transitions of the ligands.[41] Broad absorption bands that are characteristic of metal-to-ligand charge transfer (MLCT) transitions can be seen in the visible region.[42] The lowest energy MLCT bands for all of the complexes were red-shifted from those of classical Ru(II) dyes **[Ru(bpy)$_3^{2+}$]** (λ_{max} = 454 nm)[43] and **N719** (λ_{max} = 500 nm),[44] which was attributed to the presence of electron donors with extended π-conjugation in the C^N ligand and the directionality of the excited state obtained by perfectly tuning the ligand highest occupied molecular

orbital (HOMO) energy level via donating groups in the dyes.[45] As the ε of the dye in the visible region serves as one of the key factors in determining the light-harvesting capacity of the photosensitizer in photocatalytic hydrogen generation, the ε of the ruthenium(II) complexes were measured. All of which were higher than that of **$[Ru(bpy)_3]^{2+}$** [46] and **N719,**[8-10] which indicates that the light-harvesting capabilities of the photosensitizers in the present study are better. Noteworthily, the effect of anchoring groups on the absorption properties of the Ru(II) dyes was marginal.[35, 36, 39, 47-49]

Fig. 2.8 presents the absorption spectra of **Ru1** to **Ru4**, the corresponding data for which are summarised in **Table 2.1**. Both spectra of **Ru3** and **Ru4** exhibit slight red shifting and marginally higher ε values compared to **Ru1** and **Ru2**, respectively, due to the introduction of the electron-withdrawing trifluoro functional group in the C^N ligand, which can enhance electron mobility.[50]

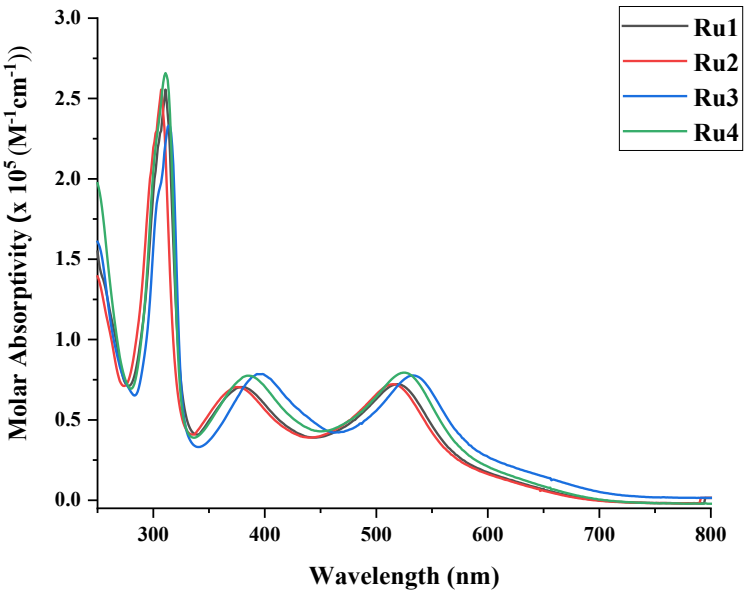

Fig. 2.8. UV/Vis absorption spectra of **Ru1** to **Ru4** in MeOH at 293 K.

Fig. 2.9 presents the absorption peaks of **Ru5** to **Ru10**, the corresponding data for which are summarised in **Table 2.1**. The enhanced ε value in the visible region is likely due to the presence of a strong σ-donating C^N ligand, especially for those bearing TPA functionalities (**Ru7** to **Ru10**). The extended π-conjugation guaranteed by the electron-donating TPA group in Ru(II) dyes results in broader absorption spectra with higher ε values compared to **Ru5** and **Ru6** at approximately 400 to 650 nm.[51-56] One of the generally accepted criteria for an ideal photosensitizer for photocatalytic applications is that the material should have strong absorption with a high ε value at a longer wavelength. Given that the incorporated TPA moiety enhanced photocatalytic hydrogen generation of the dye, **Ru9** and **Ru10** exhibited slight red shifting compared to **Ru7** and **Ru8** because of the isoquinoline in the C^N ligand containing extended π-conjugation,[57, 58] which can enhance water-splitting hydrogen generation.

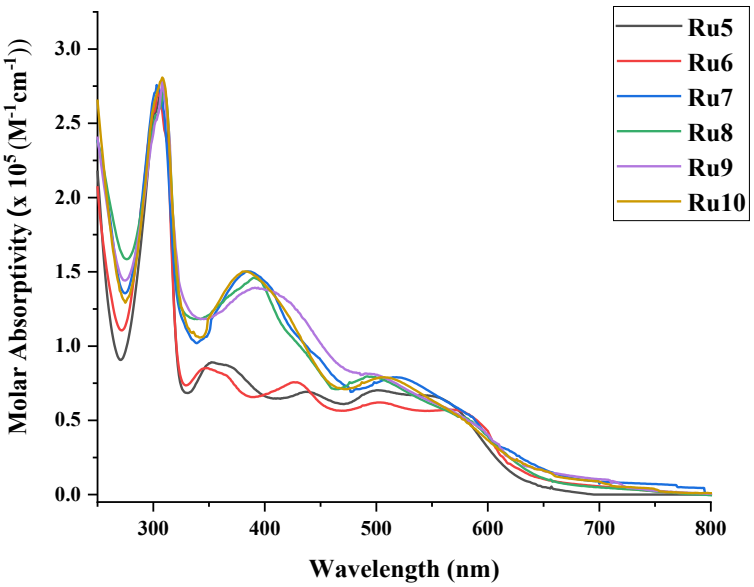

Fig. 2.9. UV/Vis absorption spectra of **Ru5** to **Ru10** in MeOH at 293 K.

Table 2.1. UV/Vis absorption parameter values of **Ru1** to **Ru10** in MeOH at 293 K.

Dye	λ_{max} /nm (ε /10^5 M^{-1} cm^{-1})	λ_{onset} /nm
Ru1	310 (2.55), 381 (0.70), 519 (0.73)	610
Ru2	305 (2.56), 376 (0.71), 515 (0.72)	604
Ru3	313 (2.33), 394 (0.78), 533 (0.78)	642
Ru4	311 (2.63), 386 (0.77), 522 (0.79)	628
Ru5	309 (2.72), 352 (0.88), 437 (0.71), 500 (0.70), 562 (0.62)	658
Ru6	306 (2.74), 346 (0.85), 429 (0.75), 501 (0.62), 577 (0.54)	634
Ru7	304 (2.74), 383 (1.51), 521 (0.80), 588 (0.52)	730
Ru8	308 (2.71), 388 (1.45), 492 (0.81), 582 (0.54)	709
Ru6	308 (2.78), 393 (1.39), 503 (0.81), 578 (0.51)	773
Ru10	308 (2.79), 381 (1.50), 509 (0.80), 582 (0.49)	734

2.6. Density Functional Theory Calculations

The DFT calculation for four selective Ru(II) dyes have been calculated. DFT was computed with the CAM-B3LYP functional for all the ruthenium(II) complexes, which provide an insight into the electron injection from the photoexcited dye into the TiO_2

for hydrogen generation. In this type of ruthenium(II) complex, the 4d ruthenium center is surrounded by two pairs of nitrogen atoms of bipyridines with one carbon and one nitrogen atom of C^N ligand. Such a configuration would be of great help for photoexcitations and electronic transitions. Usually, the primary photoexcitation in the visible region occurs from the transfer of one of the transition-metal d electrons to an unoccupied π* molecular orbital (MO) of the conjugated ligands, coupled with the transition from the ground state to an excited state favoring the MLCT. A detailed analysis of the HOMOs and LUMOs of all the ruthenium-based complexes by DFT is obtained.

Table 2.2. Calculated HOMO, LUMO, energy gap (ΔE) of the ruthenium(II) complexes. All values were calculated in eV.

Compounds	HOMO	LUMO	ΔE
Ru5	–5.76	–2.94	2.82
Ru6	–5.73	–2.78	2.95
Ru9	–5.44	–2.94	2.50
Ru10	–5.43	–2.75	2.68

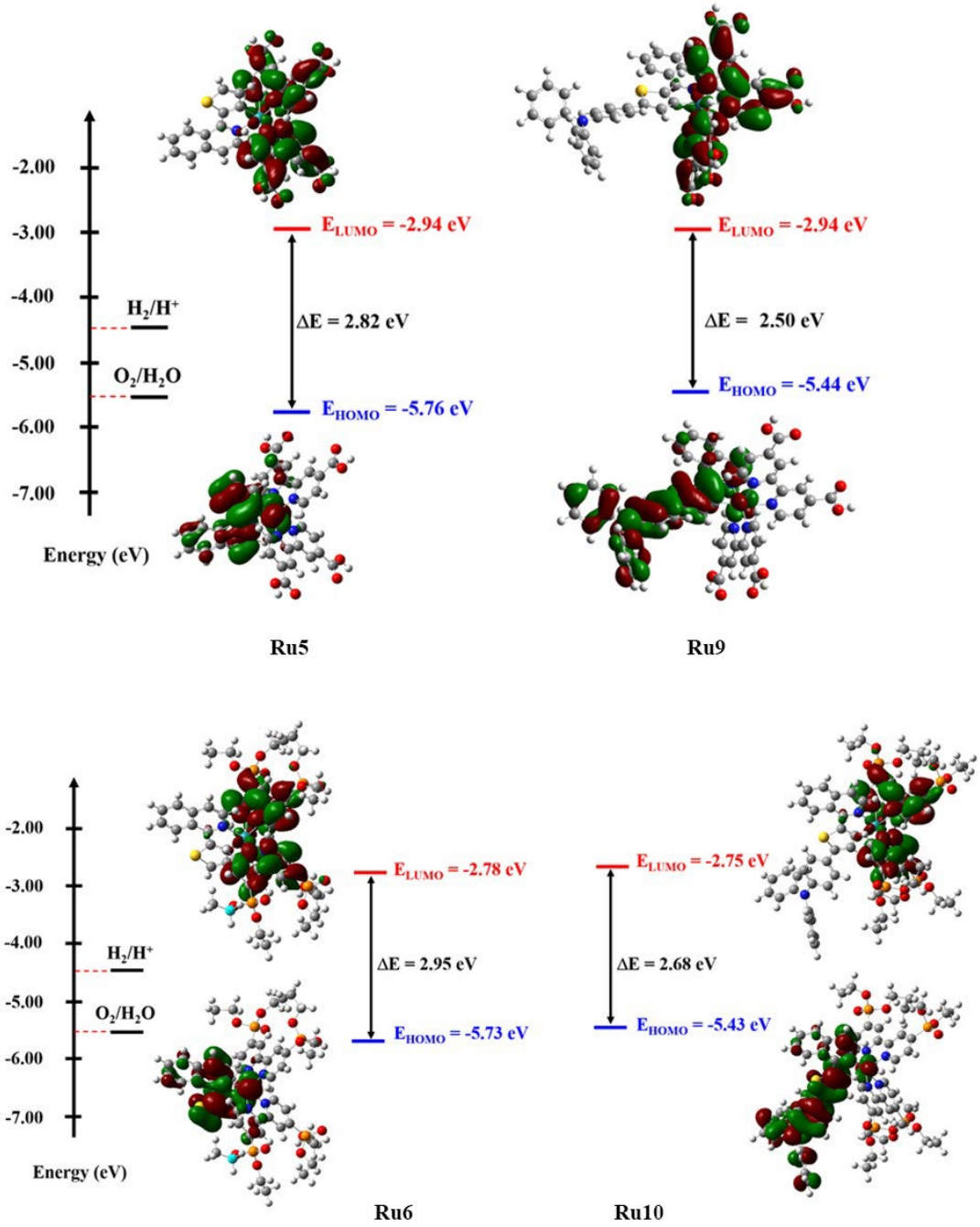

Fig. 2.10. Frontier molecular orbitals of **Ru5**, **Ru6**, **Ru9** and **Ru10** calculated at the CAM-B3LYP functional.

Generally, the orbital contributions of the HOMOs and LUMOs for these complexes are similar (**Fig. 2.10**). Analysis of the orbital diagrams indicates that the HOMOs are largely composed of π orbitals of C^N ligands and the ruthenium metal system, while

the LUMOs are delocalized over the carboxylic or phosphonate unit through bipyridine. As for the calculated HOMO energy levels, the orbital energies vary from –5.76 to –5.44 eV for **Ru5** to **Ru9** (from –5.73 to –5.43 eV for **Ru6** to **Ru10**), showing that the addition of the TPA donor group attached to thiophene moiety affects the composition of the HOMO remarkably. The electron-donating ability of the TPA functional group of C^N ligand in complexes **Ru9** and **Ru10** extends the conjugation range, which elevates the HOMO energy and lessens the HOMO-LUMO gap from 2.82 eV of **Ru5** to 2.50 eV of **Ru9** and 2.95 eV of **Ru6** to 2.68 eV of **Ru10**, which coincides with the experimental results. On the other hand, similar LUMO orbital energy levels are observed for the ruthenium(II) complexes bearing the same anchoring group, which are consistent with the conclusion that LUMOs are delocalized over the carboxylic or phosphonate unit. Molecular-orbital calculations of these dyes strongly suggest that the electrons move from the C^N ligand to the carboxylic or phosphonate moiety through photoexcitation of the dye and are injected into the conduction band of TiO_2 via the anchoring groups. Accordingly, the changes in the electron distribution induced by photoexcitation result in efficient charge separation. Those computational results match well with their electrochemical data.

2.7. Electrochemical Properties

Apart from the light-harvesting ability, proper energy gaps between the ruthenium(II) dyes and the semiconductor TiO_2 and sacrificial electron donor are essential for

hydrogen generation via water-splitting. If the lowest unoccupied molecular orbital of the ruthenium(II) dye is more positive than that of the conduction band of the semiconductor while the corresponding highest occupied molecular orbital is more negative than that of the SED, then the electron injection and charge separation are more efficient.[59] Cyclic voltammetry (CV) experimentation using the ruthenium(II) dyes was performed on thin films in a conventional three-electrode configuration system, wherein a glassy carbon electrode functioned as the working electrode, platinum wire as the counter electrode and an Ag/AgCl electrode functioned as the reference electrode. The measurements were performed in acetonitrile containing 0.1 M tetrabutylammonium hexafluorophosphate at a scan rate of 100 mV s^{-1}. The corresponding electrochemical behaviours of the dyes are recorded in **Table 2.3**.

Table 2.3. Electrochemical data and energy levels of **Ru1**−**Ru10**.

Dye	E_{Ox}^{Max} /V	E_{HOMO} [a] /eV	E_g[b] /eV	E_{ox*}[c] /V	E_{LUMO} [d] /eV
Ru1	1.22	−5.54	2.03	−0.81	−3.51
Ru2	1.17	−5.50	2.06	−0.89	−3.44
Ru3	0.85	−5.42	1.93	−1.08	−3.49
Ru4	0.74	−5.40	1.97	−1.23	−3.43
Ru5	0.60	−5.40	1.88	−1.28	−3.52
Ru6	0.59	−5.39	1.96	−1.37	−3.43
Ru7	0.91	−5.21	1.70	−0.79	−3.51
Ru8	0.90	−5.20	1.75	−0.85	−3.45
Ru9	0.31	−5.11	1.60	−1.29	−3.51
Ru10	0.29	−5.09	1.69	−1.40	−3.40

[a] Calculated from $-(E_{Ox}^{Max} + 4.8)$. [b] The energy bandgap (E_g) was determined from the onset of absorption. [c] $E_{ox*} = E_{Ox}^{Max} - E_g$. [d] $E_{LUMO} = E_{HOMO} + E_g$.

From the CV results, the conduction band edge level of semiconductor TiO_2 (−4.4 eV)

was more negative than that of the E_{LUMO} levels of all of the Ru(II) dyes (ranging from −3.40 to −3.52 eV), thereby enabling efficient electron injection for light-driven H_2 generation.[60] On the other hand, the E_{HOMO} levels of **Ru1** to **Ru10** were between –5.09 and –5.54 eV, which are more negative than the redox potential level of ascorbic acid (AA) (–4.65 eV, pH ~ 4) used as a SED in the water-splitting experiments. This allowed effective dye regeneration from the SED.[60] Thus, the energy levels of all of the Ru(II) dyes meet the requirements for effective electron injection and charge separation, thus highlighting their attractiveness for hydrogen generation via water-splitting.

According to previous research, HOMO energy levels are located at the Ru centre and on cyclometalating C^N ligands and can be easily adjusted. Meanwhile, LUMO energy levels are distributed across the anchoring N^N groups.[61] Compared with **Ru1** and **Ru2**, the HOMO levels of **Ru3** and **Ru4** are more positive due to the presence of trifluoromethyl groups on the cyclometalating ligand impoverishing the electron density and largely stabilising the HOMO level.[62-64] Moreover, the HOMO levels of **Ru5** and **Ru6** are more positive than those of **Ru1** and **Ru2** as a result of introduction of the extended π-conjugation isoquinoline functional group in the C^N ligand.[65] The HOMO destabilisation was expected with the introduction of strong electron-donating TPA groups in the C^N ligands of **Ru7** to **Ru10**, which affected the electronic properties of the metal centre and reduced their HOMO–LUMO gaps.[66] Phosphonic acid anchoring groups in Ru(II) dyes cause cathodic shifts of the C^N ligand reductions[47, 67] and also provide stronger chemical linking to the TiO_2 surface,[35, 39, 67, 68] which tunes the LUMO energy level and enhances water-splitting hydrogen generation.

2.8. Electrochemical Impedance Spectroscopy

To further investigate the charge recombination properties of our dyes, electrochemical impedance spectroscopy (EIS) for selective Ru(II) dyes was employed.[69, 70] The measurements were conducted on an electrochemical workstation according to the previous work.[69, 70] Ag/AgCl was served as reference electrode with the platinum electrode as a counter electrode, 0.5 M Na_2SO_4 solution as electrolyte and fluorine-doped tin oxide glass (FTO) with the attachment of ruthenium(II) dyes as the working electrode. The EIS Nyquist plot for all the ruthenium(II) dyes is shown in **Fig. 2.11**. It is well known that the smaller arc radius of the Nyquist plot indicates lower electric charge transfer resistance in the samples, which may lead to better hydrogen production performance.[69-72] Overall, the arc radius of **Ru9** and **Ru10** was smaller than that of **Ru5** and **Ru6**, which suggest of better transfer of charge carriers of the former dyes,[73] due to the presence of the TPA moiety in their ligands.[74] The results match well with the water-splitting hydrogen production performance.

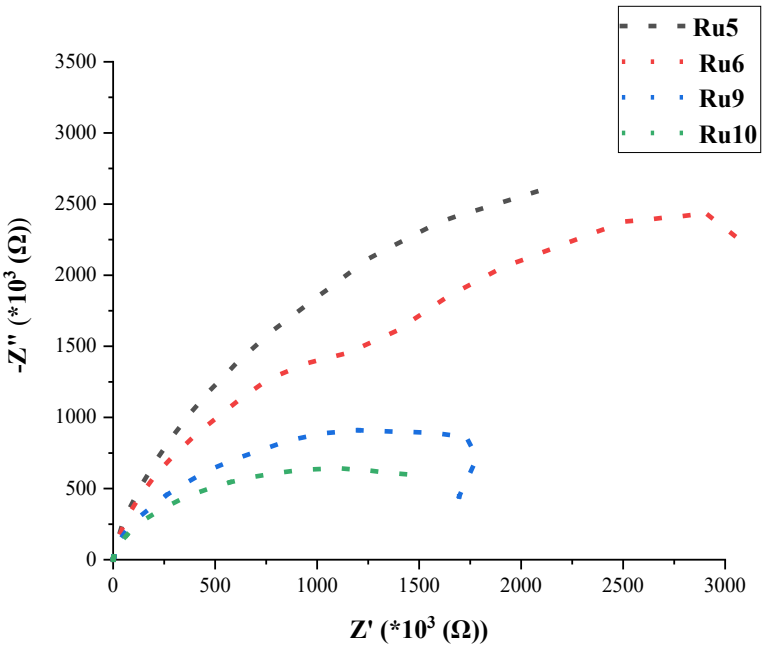

Fig. 2.11. EIS Nyquist plot for **Ru5**, **Ru6**, **Ru9** and **Ru10**.

2.9. Light-Driven Hydrogen Generation with Ru(II) Dyes @Pt–TiO_2

The photocatalytic hydrogen production via water-splitting by using Ru(II) dyes as photosensitizers were carried out. The detailed procedure for the preparation of the platinized TiO_2, the attachment of Ru(II) dyes onto the platinized TiO_2, and photocatalytic water-splitting reaction studies are described as below and in **Chapter 7**.

2.9.1. Calibration curve

Various of proportions of hydrogen and methane were used to plot the calibration curve obtained the area ratio obtained from gas chromatography (GC, Agilent 6890 Series GC System with a molecular sieve 5 Å column and thermal conductivity detector). **Fig.**

2.12 presents the calibration curve. The relationship between the signal area ratio (H_2/CH_4) and amount of H_2 produced is y = 0.4473x with Correlation Coefficient 0.9978.

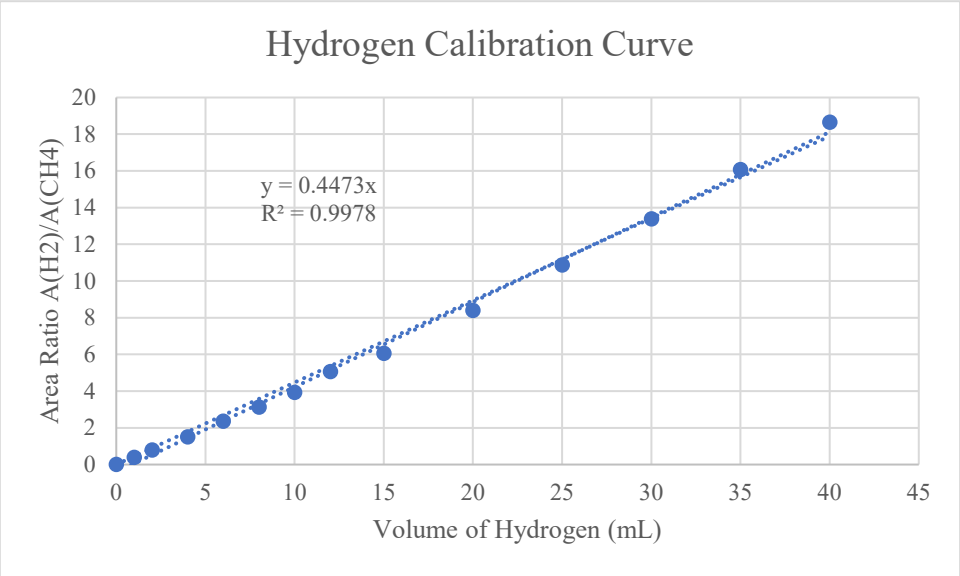

Fig. 2.12. Calibration plot of the signal ratio (H_2/CH_4) vs. amount of H_2 obtained from GC analysis.

2.9.2. Preparation of platinized TiO_2

To a one-neck round bottom flask containing 1.6 g of titanium oxide powder (anatase, < 25 nm particle size, 99.7% trace metals basis, Sigma-Aldrich) and 0.1 mL of H_2PtCl_6 aqueous solution (8 wt%), 40 mL MeOH was added. The reaction mixture was then subjected to radiation by a 300 W Hg lamp (HF300PD, EYE Lighting) for 24 h with stirring. The mixture was undergone centrifugation at 4000 rpm for 5 minutes and the solid obtained was washed with MeOH three times. The remaining solid was dried under vacuum in darkness overnight. The ICP-OES analysis have been performed and

the results have been shown in **Table 2.4** and **Table 2.5**. From the ICP-OES results, it can be found that the Pt nanoparticles was almost completely attached to the TiO_2. Furthermore, we have conducted the TEM characterization of Pt-TiO_2 (**Fig. 2.13**). As the TEM images of Pt-TiO_2 suggest, Pt nanoparticles were loaded uniformly on the TiO_2 nanoparticle surface.[75]

Table 2.4. ICP-OES analysis result of the intensity for standard solution.

Label	Std Conc.	intensity
Blank	0	2.7104
Standard 1	2.825	36.6453
Standard 2	5.650	70.4079
Standard 3	8.475	110.6560
Standard 4	11.300	143.3450

The relationship between the intensity and concentration is y = 12.5 x + 2.4 with Correlation Coefficient: 0.9995

Table 2.5. ICP-OES analysis result of the intensity for before and after Pt loading.

Label	Int. (c/s)	Calc Conc.	Units
Before	62.1622	4.76143	ppm
After	2.6553	0.020483	ppm

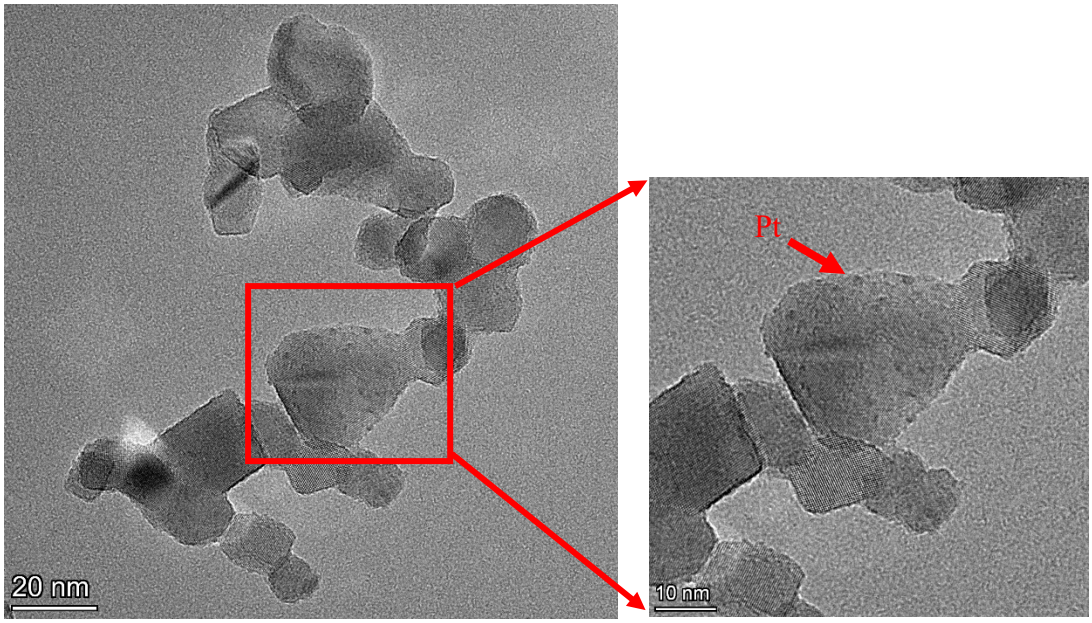

Fig. 2.13. TEM images of Pt−TiO_2.

2.9.3. Adsorption of ruthenium(II) photosensitizer onto platinized TiO_2

To a centrifuge tube containing 20 mg of Pt-TiO_2, 2.5 mL of 50 μM photosensitizer in MeOH solution was added, and the mixture was then sonicated for 30 mins. The solution was decolorized and became clear gradually (**Fig. 2.14**), while the grey color solid was changed to pink (**Fig. 2.15**). The tube was centrifuged at 4000 rpm for 15 mins and the liquid layer was removed by a dropper. The remaining solid was dried in darkness overnight. The whole dried pellet was directly utilized in the photocatalytic reaction. The dye-loading percentage was estimated by comparing the absorbance of the absorption peaks between the supernatant and the original photosensitizer solution at low energy region. **Fig. 2.16** presents the UV-Vis spectrum of **Ru1** before and after dye loading. It was found to be completely attached to the platinized TiO_2.

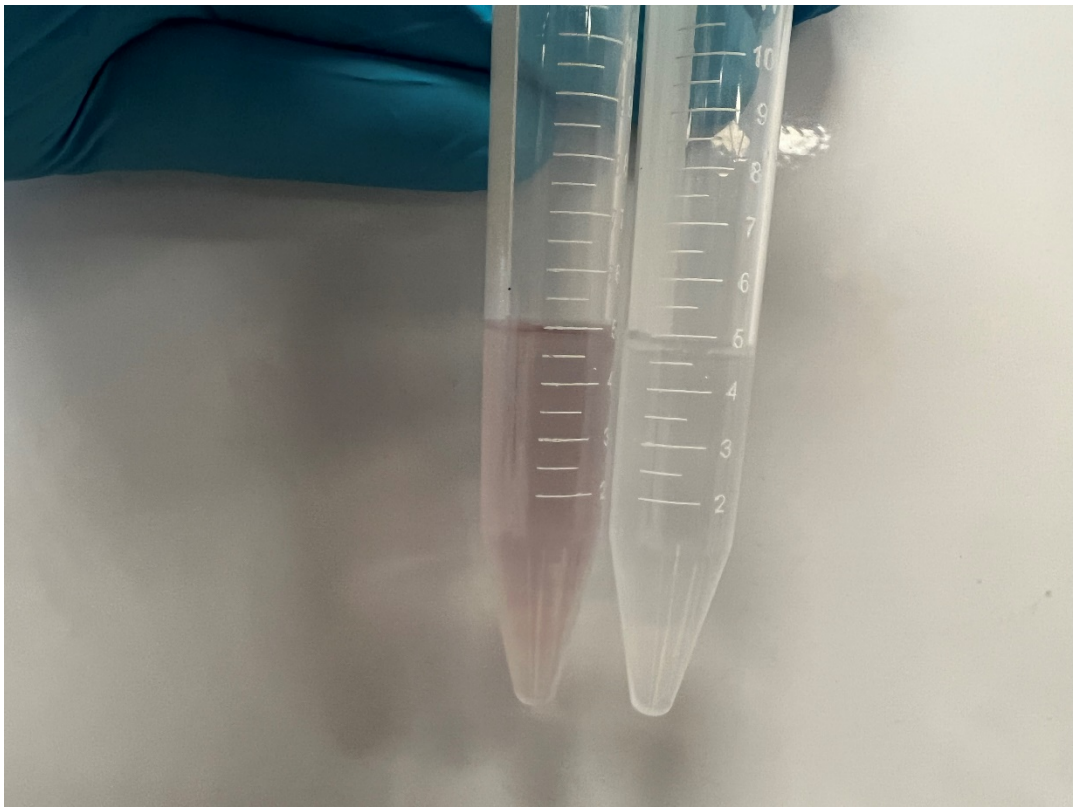

Fig. 2.14. **Ru1** solution (in MeOH) before (left) and after (right) dye loading.

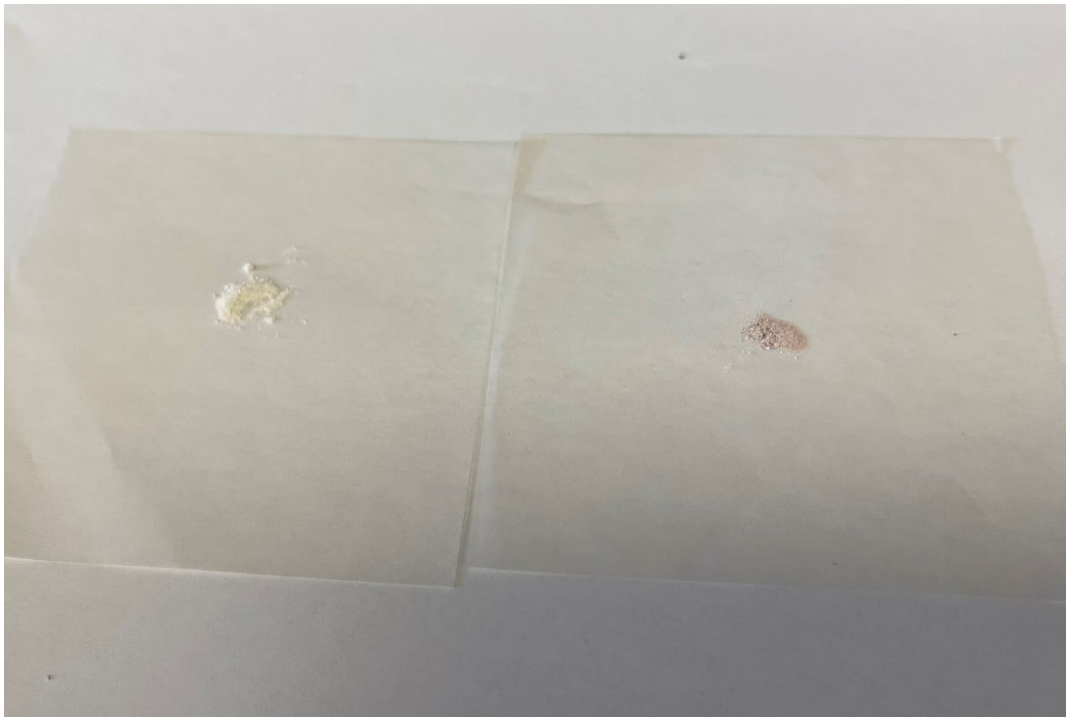

Fig. 2.15. Pt-TiO_2 before (left) and after (right) dye loading.

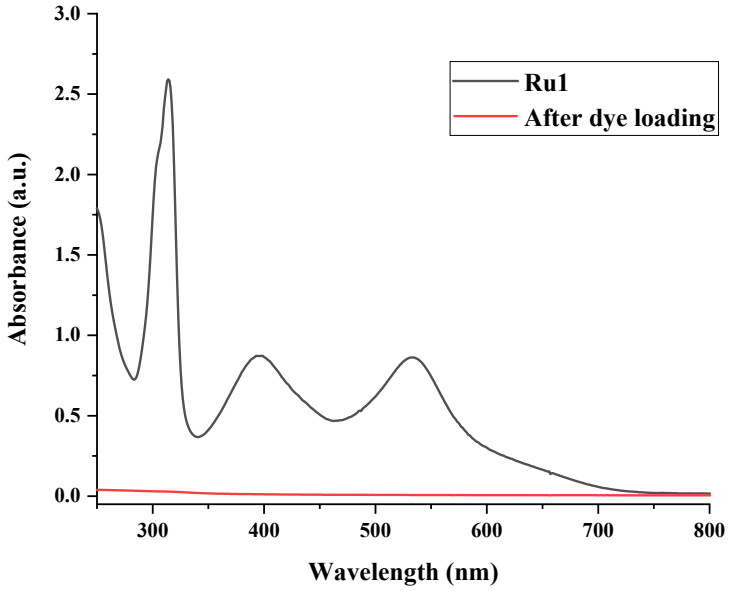

Fig. 2.16. UV/Vis absorption spectra of **Ru1** before and after dye loading in MeOH solution at 293 K.

2.9.4. Light-driven H_2 production experiment

To a one-neck pear-shaped round bottom flask containing the dye-adsorbed platinized TiO_2, 5 mL of 0.5 M of AA (pH = 4) was added as the hole scavenger. The flask was then sealed by rubber septa and was purged with a mixture of argon/methane (80:20 mol%) for 15 mins. The methane present in the gas mixture was served as an internal standard for GC analysis of each experiment. The flask was steadily stirred and continuously radiated from the bottom with green (*ca.* 520 nm) or blue (*ca.* 470 nm) light-emitting diodes inside a just-fit container, which blocks the stray light from the environment. The light power was measured using a thermal sensor and power meter (Model: BIM-7203-0100F & BIM-7001; Hangzhou Brolight Technology Co., Ltd.) and estimated to be 50 mW for each reaction. The produced hydrogen was measured by GC

(Agilent 6890 Series GC System with a molecular sieve 5 Å column and thermal conductivity detector) at different time points from the headspace of reaction mixtures and was quantified using a calibration plot of the integrated amount of hydrogen relative to the methane. The LED radiation is assumed to be monochromatic at emission intensity maximum (470 nm and 520 nm for blue and green LEDs, respectively)

2.9.5. Common parameters

There are various common parameters in the photocatalytic water splitting hydrogen generation experiment, such as turnover number (TON), turnover frequency (TOF), initial photocatalytic activity ($activity_i$), and apparent quantum yield percentage (AQY%), which are introduced below.

(i). Turnover Number (TON)

Turnover number (TON) for Light-driven H_2 production is usually defined by twice of the number of reacted molecules to that of an active site,[76] as given by equation below.

$$TON = \frac{2 \times \text{Number of reacted molecules}}{\text{Number of active sites}}$$

(ii). Turnover Frequency (TOF)

Similarly, the turnover frequency (TOF) for is described as the number of reacted molecules per hour to that of an active site,[77] as shown by equation below.

$$TOF = \frac{TON}{\text{Time}} \text{ or } TOF = \frac{2 \times \text{Number of reacted molecules per hour}}{\text{Number of active sites}}$$

(iii). Initial Photocatalytic Activity ($activity_i$)

Initial photocatalytic activity ($activity_i$) is defined as the number of micromoles of H_2 evolved per gram of platinum loaded per hour,[78] as given by equation below.

$$\text{Initial Photocatalytic Activity} = \frac{\text{Number of micromoles of } H_2 \text{ evolved per hour}}{\text{Number of gram of platinum loaded}}$$

(iv). Apparent Quantum Yield Percentage (AQY%)

Apparent quantum yield percentage (AQY%) is calculated as twice of the rate of hydrogen production to that of incident photons,[79] as given by equation below.

$$\text{AQY\%} = \frac{2 \times \text{Rate of hydrogen production}}{\text{Rate of incident photons}} \times 100\%$$

2.9.6. Light-driven H_2 production result studies

The hydrogen generation curves (vs time) for each sample are shown in **Fig. 2.17** to **Fig. 2.20**. The corresponding data are presented in **Tables 2.6**–**2.9**.

In this setting, the photosensitizer undergoes photoexcitation under light irradiation, followed by electron injection to the conduction band energy level of TiO_2. The injected electrons move to Pt nanoparticles loaded on the TiO_2, thereby reducing protons to release H_2. The oxidised photosensitizer is then reduced by a SED to the ground state.[80]

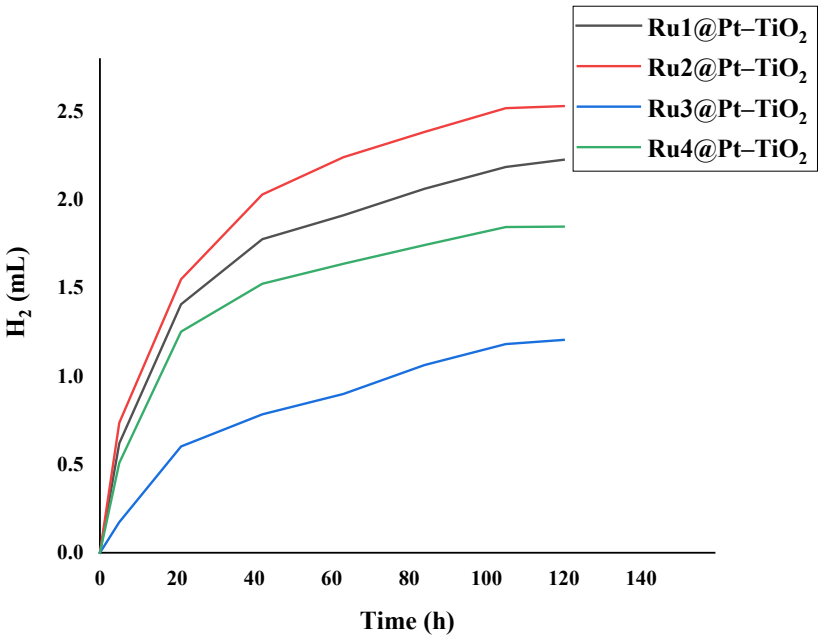

Fig. 2.17. Photocatalytic H_2 generation curves of **Ru1–Ru4@Pt–TiO₂** under blue LED irradiation (50 mW).

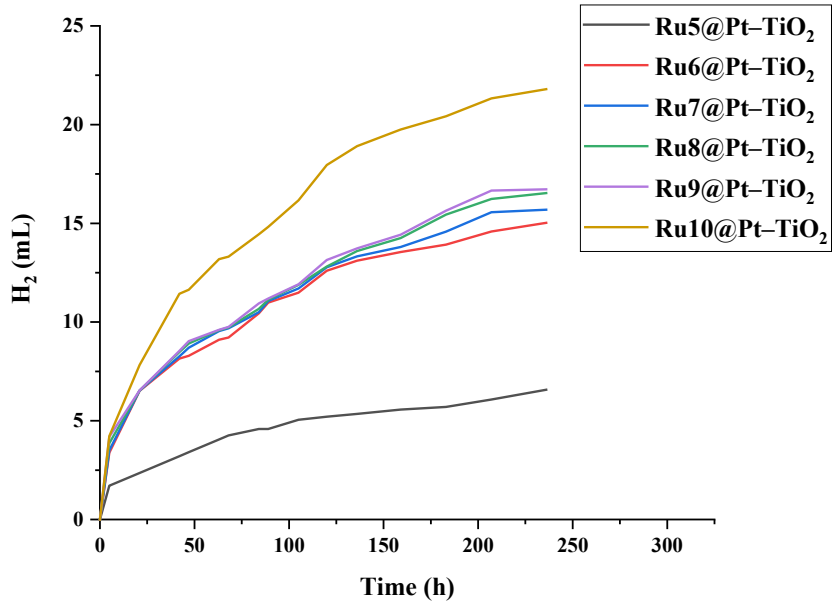

Fig. 2.18. Photocatalytic H_2 generation curves of **Ru5–Ru10@Pt–TiO₂** under blue LED irradiation (50 mW).

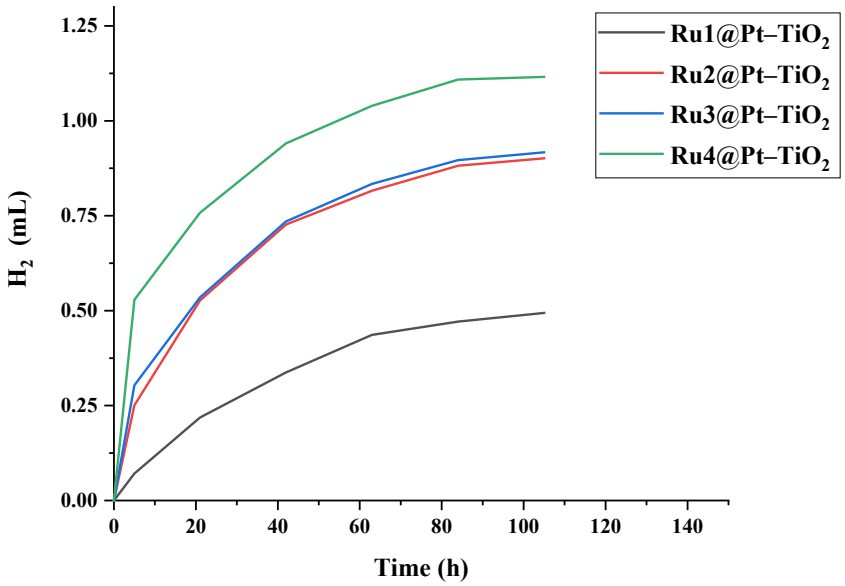

Fig. 2.19. Photocatalytic H_2 generation curves of **Ru1–Ru4@Pt–TiO₂** under green LED irradiation (50 mW).

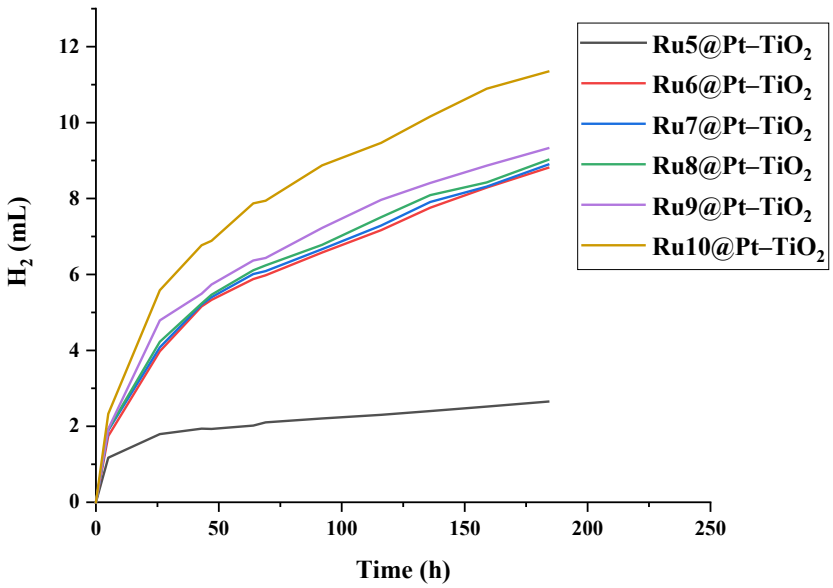

Fig. 2.20. Photocatalytic H_2 generation curves of **Ru5–Ru10@Pt–TiO₂** under green LED irradiation (50 mW).

Table 2.6. Photocatalytic H_2 generation data with different ruthenium(II) dyes attached on platinized TiO_2 (**Ru1–Ru4@Pt–TiO₂**) under blue light irradiation.

Dye	Time /h	H_2 /mL	TON[a]	TOF[b] /h^{-1}	TOF_i[c] /h^{-1}	$Activity_i$[d] /μmol g^{-1} h^{-1}	AQY%[e]
Ru1	120	2.2	1456	12.2	81.1	50656	0.70
Ru2	120	2.5	1655	13.8	96.3	60162	0.80
Ru3	120	1.2	789	3.4	22.7	14183	0.38
Ru4	120	1.9	1209	10.1	66.5	41570	0.58

[a] Turnover number (TON) of H_2 was calculated as twice of the number of moles of H_2 produced over the number of moles of PS attached to platinized TiO_2. [b] Turnover frequency (TOF) was calculated per hour. [c] Initial turnover frequency (TOF_i) in the first 5 h. [d] Initial photocatalytic activity ($Activity_i$) is defined as the number of micromoles of H_2 evolved per gram of platinum loaded per hour. [e] Apparent quantum yield percentage (AQY%).

Table 2.7. Photocatalytic H_2 generation data with different ruthenium(II) dyes attached on platinized TiO_2 (**Ru5–Ru10@Pt–TiO₂**) under blue light irradiation.

Dye	Time /h	H_2 /mL	TON[a]	TOF[b] /h^{-1}	TOF_i[c] /h^{-1}	$Activity_i$[d] /μmol g^{-1} h^{-1}	AQY%[e]
Ru5	236	6.6	4,290	18.2	223.3	139,563	1.04
Ru6	236	15.0	9,813	41.6	441.5	275,921	2.38
Ru7	236	15.7	10,245	43.4	457.3	285,837	2.48
Ru8	236	16.5	10,795	45.7	504.3	315,163	2.60
Ru9	236	16.7	10,922	46.3	547.3	342,041	2.63
Ru10	236	21.8	14,232	60.3	551.2	344,490	3.44

[a] Turnover number (TON) of H_2 was calculated as twice of the number of moles of H_2 produced over the number of moles of PS attached to platinized TiO_2. [b] Turnover frequency (TOF) was calculated per hour. [c] Initial turnover frequency (TOF_i) in the first 5 h. [d] Initial photocatalytic activity ($Activity_i$) is defined as the number of micromoles of H_2 evolved per gram of platinum loaded per hour. [e] Apparent quantum yield percentage (AQY%).

Table 2.8. Photocatalytic H_2 generation data with different ruthenium(II) dyes attached on platinized TiO_2 (**Ru1–Ru4@Pt–TiO₂**) under green light irradiation.

Dye	Time /h	H_2 /mL	TON[a]	TOF[b] /h^{-1}	TOF_i[c] /h^{-1}	$Activity_i$[d] /μmol g^{-1} h^{-1}	AQY%[e]
Ru1	105	0.5	323	3.1	9.3	5805	0.18
Ru2	105	0.9	589	5.6	32.8	20495	0.32
Ru3	105	0.9	599	5.7	39.7	24775	0.32
Ru4	105	1.1	729	7.0	69.1	43166	0.39

[a] Turnover number (TON) of H_2 was calculated as twice of the number of moles of H_2 produced over the number of moles of PS attached to platinized TiO_2. [b] Turnover frequency (TOF) was calculated per hour. [c] Initial turnover frequency (TOF_i) in the first 5 h. [d] Initial photocatalytic activity ($Activity_i$) is defined as the number of micromoles of H_2 evolved per gram of platinum loaded per hour. [e] Apparent quantum yield percentage (AQY%).

Table 2.9. Photocatalytic H_2 generation data with different ruthenium(II) dyes attached on platinized TiO_2 (**Ru5–Ru10@Pt–TiO₂**) under green light irradiation.

Dye	Time /h	H_2 /mL	TON[a]	TOF[b] /h^{-1}	TOF_i[c] /h^{-1}	$Activity_i$[d] /μmol g^{-1} h^{-1}	AQY%[e]
Ru5	184	2.7	1732	9.4	153.1	95654	0.54
Ru6	184	8.8	5754	31.3	227.5	142199	1.75
Ru7	184	8.9	5808	31.6	247.6	154759	1.77
Ru8	184	9.0	5891	32.0	250.1	156325	1.79
Ru9	184	9.3	6090	33.1	252.4	157758	1.85
Ru10	184	11.4	7409	40.3	304.2	190119	2.27

[a] Turnover number (TON) of H_2 was calculated as twice of the number of moles of H_2 produced over the number of moles of PS attached to platinized TiO_2. [b] Turnover frequency (TOF) was calculated per hour. [c] Initial turnover frequency (TOF_i) in the first 5 h. [d] Initial photocatalytic activity ($Activity_i$) is defined as the number of micromoles of H_2 evolved per gram of platinum loaded per hour. [e] Apparent quantum yield percentage (AQY%).

Under irradiation with green or blue LED, all of the dyes promoted hydrogen

production via photocatalytic water-splitting. The amount of hydrogen produced under blue light irradiation (450–500 nm) was much greater than that under green light irradiation (495–570 nm) which may be attributed to the higher light-absorbing ability of these dyes in the blue light region than in the green (**Fig. 2.8** and **Fig. 2.9**). The **Ru10@Pt–TiO$_2$** system exhibited the highest hydrogen generation activity under both blue and green light irradiation (TONs of 14,232 and 7,409, respectively), while **Ru9@Pt–TiO$_2$** also provided attractive results (TONs of 10,922 and 6,090, respectively). All of the dyes had higher hydrogen generation than those previously reported for Ru(II)-based dyes **[Ru(bpy)$_3$]$^{2+}$**[6] and **N719**,[8-10] which was probably due to their improved light-harvesting abilities with a broader absorption range and enhanced ε.

Compared with **Ru1@Pt–TiO$_2$** and **Ru2@Pt–TiO$_2$**, **Ru3@Pt–TiO$_2$** and **Ru4@Pt–TiO$_2$** have one trifluoromethyl group in the pyridine group, which is a strong electron-withdrawing group that makes the electron injection step slower because of the weak charge pushing effect,[81] thereby lowering the hydrogen-production volumes and TON values. Indeed, Ru(II) dyes with the isoquinoline functional group, such as **Ru5@Pt–TiO$_2$** and **Ru6@Pt–TiO$_2$**, achieved higher hydrogen generation than those with the pyridine functional group, such as **Ru1@Pt–TiO$_2$** and **Ru2@Pt–TiO$_2$**, since the former dyes are more effective for charge transfer.[24, 26, 82] Moreover, the Ru(II) dyes with the TPA functional group as a photosensitizer (e.g., **Ru9@Pt–TiO$_2$** and **Ru10@Pt–TiO$_2$**) were more effective in promoting hydrogen generation than those without it (e.g., **Ru5@Pt–TiO$_2$** and **Ru6@Pt–TiO$_2$**). Hence, strong electron-donating TPA coupled

with electron-withdrawing isoquinoline through π-linker thiophene effectively induced intramolecular charge transfer (ICT) ability with high molar extinction coefficients, which improved hydrogen production.[83, 84]

Ru(II) dyes bearing phosphonate anchoring groups were more effective in promoting hydrogen production than those with carboxylate ones because the former bound more strongly to the TiO_2 semiconductor.[35, 39] Similar results have also been reported in the literature.[68] In addition, by comparing the photocatalytic reaction mixture of **Ru10@Pt–TiO_2** before and after the irradiation (**Figs. 2.21**), the TiO_2 composite material still remained the original color and the AA aqueous solution changed from colorless to pale yellow due to the presence of dehydroascorbic acid (DHA) resulting from the dye-regeneration reaction. This indicated that issues regarding dye desorption and photobleaching of PS were not observed in our case.[85] In combination with the H_2 generation curve, it is reasonable to expect the photocatalytic system with **Ru10@Pt–TiO_2** is still highly active even under a longer duration of illumination.

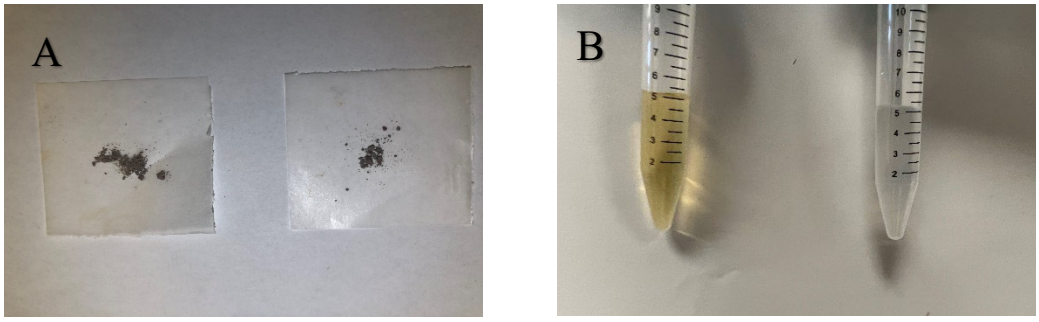

Fig. 2.21. (A) TiO_2 composite material with **Ru10** before (left) and after (right) irradiation. (B) AA aqueous solution before (right) and after (left) irradiation.

We have also performed the photocatalytic water-splitting experiments for **N3** and **N719**, in which **N3** and **N719** are ruthenium complexes containing thiocyanate groups. The experimental results are shown in **Fig. 2.22** and **Table 2.10**. From the results, the photocatalytic hydrogen generation of our new complexes are more efficient with higher stability than that of the ruthenium complexes containing thiocyanate groups. Furthermore, we revisited the literatures and sorted out the performance data of similar Ru complexes as **Table 2.11**. Compared with the reported literatures, our complexes, especially **Ru10**, shows a significant improvement in light-driven hydrogen evolution. These results also indicate that the thiocyanate-free cyclometalated ruthenium(II) complexes are promising candidate for highly stable photocatalytic application.

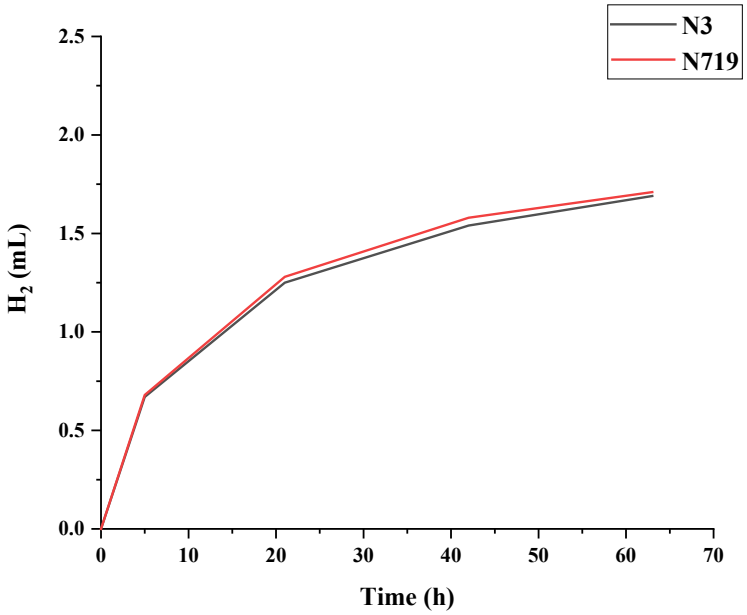

Fig. 2.22. Photocatalytic H_2 generation curves of **N3** and **N719** under blue LED irradiation (50 mW).

Table 2.10. Photocatalytic H_2 generation data with **N3** and **N719** under blue light irradiation.

Dye	Time /h	H_2 /mL	TON[a]	TOF[b] /h^{-1}	TOF_i[c] /h^{-1}	$Activity_i$[d] /μmol g^{-1} h^{-1}	AQY_i%[e]
N3	63	1.69	1100	17.5	87.5	54693	1.00
N719	63	1.71	1120	17.7	88.8	55510	1.01

[a] Turnover number (TON) of H_2 was calculated as twice of the number of moles of H_2 produced over the number of moles of PS attached to platinized TiO_2. [b] Turnover frequency (TOF) was calculated per hour. [c] Initial turnover frequency (TOF_i) in the first 5 h. [d] Initial photocatalytic activity ($Activity_i$) is defined as the number of micromoles of H_2 evolved per gram of platinum loaded per hour. [e] Initial apparent quantum yield percentage (AQY_i).

Table 2.11. Performance for light-driven hydrogen evolution based on different Ru dyes systems.

Dye	SED	H2 evolution rate (for first 5 or 6 h) [μmol g^{-1} h^{-1}]	reference
$[Ru_2(bpy)_4(BL)](ClO_4)_2$/P25	TEOA	236.4	[10]
$[Ru_2(dcbpy)_4(BL)](ClO_4)_2$/P25	TEOA	31.7	[10]
N719/P25	TEOA	15.3	[10]
$Ru(bpy)_2(him)_2$	TEOA	48.8	[8]
$Ru(bpy)_2(him)_2$	CH_3OH	561.3	[8]
N719	TEOA	43.7	[8]
N719	CH_3OH	271	[8]
$Ru(bpy)_3^{2+}$	TEOA (pH=11)	10.77	[6]
$Ru(bpy)_3^{2+}$	TEOA (pH=7.3)	5.63	[6]
$Ru(bpy)_3^{2+}$	TEOA (pH=6.0)	0.16	[6]
$Ru(bpy)_3^{2+}$	Ascorbic acid	0.33	[6]
$Ru(bpy)_3^{2+}$	Acetone	0.24	[6]
Ru10	Ascorbic acid (pH=4)	1722.49	This study

2.10. Conclusions

Ten new Ru(II) photosensitizers with either phosphonate or carboxylic acid anchoring groups were synthesised. All of them were fully characterised and their ability to promote hydrogen production via water-splitting in an aqueous environment was assessed. The introduction of TPA functional groups in the dyes effectively intensified and extended absorption in the visible region, which enhanced their light-harvesting ability and promoted hydrogen production. A TON of up to 14,231 was achieved by the **Ru10@Pt–TiO_2** system under blue LED irradiation. The results demonstrate the importance and advantages of introducing the TPA functional group to the Ru(II) complex, which can induce strong intramolecular charge transfer when coupled with the isoquinoline moiety. In addition, the Ru(II) dyes with phosphonate anchoring groups for attaching to the TiO_2 semiconductor achieved higher TON values than those with carboxylic acid anchors, thereby identifying the former as a promising replacement for the latter in designing highly effective Ru(II) photosensitizers with excellent stability for photocatalytic hydrogen generation from water.

2.11. References

[1] A. Fujishima, K. Honda, *Nature* **1972**, *238*, 37-38.

[2] R. Singh, S. Dutta, *Fuel* **2018**, *220*, 607-620.

[3] M. Watanabe, *Sci. Technol. Adv. Mater.* **2017**, *18*, 705-723.

[4] M. D. Kärkäs, T. M. Laine, E. V. Johnston, B. Åkermark, in *Applied photosynthesis: New progress* (Ed.: M. Najafpour), InTech, Croatia, **2016**, pp. 189-218.

[5] M. D. Karkas, O. Verho, E. V. Johnston, B. R. Åkermark, *Chem. Rev.* **2014**, *114*, 11863-12001.

[6] K. Hirano, E. Suzuki, A. Ishikawa, T. Moroi, H. Shiroishi, M. Kaneko, *J. Photochem. Photobiol. A. Chem.* **2000**, *136*, 157-161.

[7] Y. Chen, Y. Liu, Z. Ma, *Colloids Surf. A. Physicochem. Eng. Asp.* **2021**, *614*, 126119.

[8] T. Y. Peng, K. Dai, H. B. Yi, D. N. Ke, P. Cai, L. Zan, *Chem. Phys. Lett.* **2008**, *460*, 216-219.

[9] T. Y. Peng, D. N. Ke, P. Cai, K. Dai, L. Ma, L. Zan, *J. Power Sources* **2008**, *180*, 498-505.

[10] X. H. Zhang, U. Veikko, J. Mao, P. Cai, T. Y. Peng, *Chem. Eur. J.* **2012**, *18*, 12103-12111.

[11] R. Quint, N. Getoff, *Int. J. Hydrogen Energy* **1988**, *13*, 269-276.

[12] H. Tong, S. X. Ouyang, Y. P. Bi, N. Umezawa, M. Oshikiri, J. H. Ye, *Adv. Mater.* **2012**, *24*, 229-251.

[13] S. Aghazada, M. K. Nazeeruddin, *Inorganics* **2018**, *6*, 52.

[14] C. R. Ma, S. Piccinin, S. Fabris, *ACS Catal.* **2012**, *2*, 1500-1506.

[15] A. O. Adeloye, P. A. Ajibade, *Molecules* **2014**, *19*, 12421-12460.

[16] B. Cecconi, N. Manfredi, R. Ruffo, T. Montini, I. Romero-Ocaña, P. Fornasiero, A. Abbotto, *ChemSusChem* **2015**, *8*, 4216-4228.

[17] E. Campaigne, *J. Chem. Educ.* **1986**, *63*, 860.

[18] T. Debnath, P. Maity, H. Lobo, B. Singh, G. S. Shankarling, H. N. Ghosh, *Chem. Eur. J.* **2014**, *20*, 3510-3519.

[19] B.-G. Kim, K. Chung, J. Kim, *Chem. Eur. J.* **2013**, *19*, 5220-5230.

[20] M. Liang, J. Chen, *Chem. Soc. Rev.* **2013**, *42*, 3453-3488.

[21] A. Abbotto, N. Manfredi, *Dalton Trans.* **2011**, *40*, 12421-12438.

[22] M. Pagliai, G. Mancini, I. Carnimeo, N. De Mitri, V. Barone, *J. Comput. Chem.* **2017**, *38*, 319-335.

[23] Y. Law, A. Hassanali, *J. Chem. Phys.* **2018**, *148*, 102331.

[24] L. Duan, C. M. Araujo, M. S. Ahlquist, L. Sun, *Proc. Natl. Acad. Sci. U.S.A.* **2012**, *109*, 15584-15588.

[25] Q. Liu, L. Wu, M. Chen, Y. Guo, T. Xie, P. Wang, *Catal. Commun.* **2019**, *122*, 38-42.

[26] K. S. Joya, Y. F. Joya, K. Ocakoglu, R. Van De Krol, *Angew. Chem. Int. Ed.* **2013**, *52*, 10426-10437.

[27] C. J. Wang, Y. Chen, W.-F. Fu, *Dalton Trans.* **2015**, *44*, 14483-14493.

[28] B. J. Timmer, O. Kravchenko, T. Liu, B. Zhang, L. Sun, *Angew. Chem.* **2021**, *113*, 14625-14632.
[29] T.-T. Li, Y. Chen, F.-M. Li, W.-L. Zhao, C.-J. Wang, X.-J. Lv, Q.-Q. Xu, W.-F. Fu, *Chem. Eur. J.* **2014**, *20*, 8054-8061.
[30] S. H. Wadman, J. M. Kroon, K. Bakker, R. W. Havenith, G. P. Van Klink, G. Van Koten, *Organometallics* **2010**, *29*, 1569-1579.
[31] S. Haid, M. Marszalek, A. Mishra, M. Wielopolski, J. Teuscher, J.-E. Moser, R. Humphry-Baker, S. M. Zakeeruddin, M. Grätzel, P. Bäuerle, *Adv. Funct. Mater.* **2012**, *22*, 1291-1302.
[32] L.-L. Tan, H.-Y. Chen, L.-F. Hao, Y. Shen, L.-M. Xiao, J.-M. Liu, D.-B. Kuang, C.-Y. Su, *Phys. Chem. Chem. Phys.* **2013**, *15*, 11909-11917.
[33] I. M. Abdellah, T. H. Chowdhury, J.-J. Lee, A. Islam, A. El-Shafei, *Sol. Energy* **2020**, *206*, 279-286.
[34] C. H. Teh, R. Daik, E. L. Lim, C. C. Yap, M. A. Ibrahim, N. A. Ludin, K. Sopian, M. a. M. Teridi, *J. Mater. Chem. A* **2016**, *4*, 15788-15822.
[35] E. Bae, W. Choi, *J. Chem. Phys. B* **2006**, *110*, 14792-14799.
[36] H. Park, E. Bae, J.-J. Lee, J. Park, W. Choi, *J. Phys. Chem. B* **2006**, *110*, 8740-8749.
[37] M. Zalas, B. Gierczyk, A. Bossi, P. R. Mussini, M. Klein, R. Pankiewicz, M. Makowska-Janusik, Ł. Popenda, W. Stampor, *Dyes Pigm.* **2018**, *150*, 335-346.
[38] T. N. Murakami, E. Yoshida, N. Koumura, *Electrochim. Acta.* **2014**, *131*, 174-183.
[39] E. Bae, W. Choi, J. Park, H. S. Shin, S. B. Kim, J. S. Lee, *J. Chem. Phys. B* **2004**, *108*, 14093-14101.
[40] Y. Liu, R. Hammitt, D. A. Lutterman, L. E. Joyce, R. P. Thummel, C. Turro, *Inorg. Chem.* **2009**, *48*, 375-385.
[41] C.-H. Siu, C.-L. Ho, J. He, T. Chen, X. N. Cui, J. Z. Zhao, W.-Y. Wong, *J. Organomet. Chem.* **2013**, *748*, 75-83.
[42] Q. W. Wang, W. J. Wu, C.-L. Ho, L. Q. Xue, Z. Y. Lin, H. Li, Y. H. Lo, W.-Y. Wong, *Eur. J. Inorg. Chem.* **2014**, *2014*, 5322-5330.
[43] S. P. Pitre, C. D. Mctiernan, W. Vine, R. Dipucchio, M. Grenier, J. C. Scaiano, *Sci. Rep.* **2015**, *5*, 1-10.
[44] M. Hočevar, U. O. Krašovec, M. Berginc, M. Topič, *Acta. Chim. Slov.* **2010**, *57*.
[45] S. X. Wei, X. Q. Lu, X. F. Shi, Z. G. Deng, Y. Shao, L. M. Zhao, W. Y. Guo, C.-M. L. Wu, *Int. J. Photoenergy* **2014**, *2014*, 280196.
[46] S. Wallin, J. Davidsson, J. Modin, L. Hammarström, *J. Phys. Chem. A* **2005**, *109*, 4697-4704.
[47] S. Zakeeruddin, M. K. Nazeeruddin, P. Pechy, F. Rotzinger, R. Humphry-Baker, K. Kalyanasundaram, M. Grätzel, V. Shklover, T. Haibach, *Inorg. Chem.* **1997**, *36*, 5937-5946.
[48] A. Sen, A. Groß, *Int. J. Quantum Chem.* **2019**, *119*, e25963.
[49] T. M. Suzuki, H. Tanaka, T. Morikawa, M. Iwaki, S. Sato, S. Saeki, M. Inoue, T. Kajino, T. Motohiro, *Chem. Commun.* **2011**, *47*, 8673-8675.
[50] Q.-L. Xu, C.-C. Wang, T.-Y. Li, M.-Y. Teng, S. Zhang, Y.-M. Jing, X. Yang, W.-

N. Li, C. Lin, Y.-X. Zheng, *Inorg. Chem.* **2013**, *52*, 4916-4925.
[51] L.-L. Tan, J.-F. Huang, Y. Shen, L.-M. Xiao, J.-M. Liu, D.-B. Kuang, C.-Y. Su, *J. Mater. Chem. A* **2014**, *2*, 8988-8994.
[52] K. Q. He, N. Su, J. T. Yu, Y. Liu, W. J. Xiong, Z. R. Hao, D. G. Ma, W. G. Zhu, *Tetrahedron* **2016**, *72*, 7164-7169.
[53] P.-Y. Ho, S.-Y. Lee, C. Kam, J. F. Zhu, G.-G. Shan, Y. I. Hong, W.-Y. Wong, S. J. Chen, *Adv. Healthcare Mater.* **2021**, 2100706.
[54] A. Mahmood, M. Hussaintahir, A. Irfan, B. Khalid, A. G. Al-Sehemi, *Bull. Korean Chem. Soc.* **2015**, *36*, 2615-2620.
[55] Y. Y. Tang, Y. Q. Wang, X. Li, H. Ågren, W.-H. Zhu, Y. S. Xie, *ACS Appl. Mater. Interfaces* **2015**, *7*, 27976-27985.
[56] R. Balasaravanan, K. Duraimurugan, J. Sivamani, V. Thiagarajan, A. Siva, *New J. Chem.* **2015**, *39*, 7472-7480.
[57] S. Y. Takizawa, C. Pérez-Bolívar, P. Anzenbacher Jr, S. Murata, *Eur. J. Inorg. Chem.* **2012**, *2012*, 3975-3979.
[58] D. Aggoun, Z. Messasma, B. Bouzerafa, R. Berenguer, E. Morallon, Y. Ouennoughi, A. Ourari, *J. Mol. Struct.* **2021**, *1231*, 129923.
[59] C. Sreekala, I. Jinchu, K. Sreelatha, Y. Janu, N. Prasad, M. Kumar, A. K. Sadh, M. Roy, *IEEE J. Photovolt.* **2012**, *2*, 312-319.
[60] X. Li, J. G. Yu, J. X. Low, Y. P. Fang, J. Xiao, X. B. Chen, *J. Mater. Chem. A* **2015**, *3*, 2485-2534.
[61] Y. Wang, X. Zhao, Y. Zhao, T. Yang, X. Liu, J. Xie, G. Li, D. Zhu, H. Tan, Z. Su, *Dyes Pigm.* **2019**, *170*, 107547.
[62] N. M. Shavaleev, F. Monti, R. Scopelliti, N. Armaroli, M. GräTzel, M. K. Nazeeruddin, *Organometallics* **2012**, *31*, 6288-6296.
[63] P. Coppo, E. A. Plummer, L. De Cola, *Chem. Commun.* **2004**, 1774-1775.
[64] R. Bevernaegie, L. Marcélis, B. Laramée-Milette, J. De Winter, K. Robeyns, P. Gerbaux, G. S. Hanan, B. Elias, *Inorg. Chem.* **2018**, *57*, 1356-1367.
[65] P. S. Kim, S. Choi, S.-Y. Kim, J. H. Jo, Y. S. Lee, B. Kim, W. Kim, W. Choi, C. H. Kim, H.-J. Son, *Chem. Eur. J.* **2019**, *25*, 13609-13623.
[66] D. P. Hagberg, T. Marinado, K. M. Karlsson, K. Nonomura, P. Qin, G. Boschloo, T. Brinck, A. Hagfeldt, L. Sun, *J. Org. Chem.* **2007**, *72*, 9550-9556.
[67] R. A. Wahyuono, S. Amthor, C. Müller, S. Rau, B. Dietzek, *ChemPhotoChem* **2020**, *4*, 618-629.
[68] I. Gillaizeau-Gauthier, F. Odobel, M. Alebbi, R. Argazzi, E. Costa, C. A. Bignozzi, P. Qu, G. J. Meyer, *Inorg. Chem.* **2001**, *40*, 6073-6079.
[69] P. Tian, X. He, L. Zhao, W. X. Li, W. Fang, H. Chen, F. Q. Zhang, Z. H. Huang, H. L. Wang, *Int. J. Hydrogen Energy* **2019**, *44*, 788-800.
[70] P. Tian, X. He, L. Zhao, W. X. Li, W. Fang, H. Chen, F. Q. Zhang, Z. H. Huang, H. L. Wang, *Sol. Energy* **2019**, *188*, 750-759.
[71] H. Y. Wang, C. Y. Gao, R. Li, Z. K. Peng, J. H. Yang, J. Gao, Y. P. Yang, S. H. Li, B. J. Li, Z. Y. Liu, *ACS Sustainable Chem. Eng.* **2019**, *7*, 18744-18752.
[72] Y. Wang, P. Zheng, M. X. Li, Y. R. Li, X. Zhang, J. Chen, X. Fang, Y. J. Liu, X. L. Yuan, X. P. Dai, *Nanoscale* **2020**, *12*, 9669-9679.

[73] R. Acharya, B. Naik, K. Parida, *Beilstein J. Nanotechnol.* **2018**, *9*, 1448-1470.
[74] S. Roquet, A. Cravino, P. Leriche, O. Alévêque, P. Frere, J. Roncali, *J. Am. Chem. Soc.* **2006**, *128*, 3459-3466.
[75] S. Furugori, A. Kobayashi, A. Watanabe, M. Yoshida, M. Kato, *ACS Omega* **2017**, *2*, 3901-3912.
[76] A. Kudo, Y. Miseki, *Chem. Soc. Rev.* **2009**, *38*, 253-278.
[77] X. Li, J. Yu, J. Low, Y. Fang, J. Xiao, X. Chen, *J. Mater. Chem. A* **2015**, *3*, 2485-2534.
[78] S.-C. Yiu, P.-Y. Ho, Y.-Y. Kwok, X. He, Y. Wang, W.-H. Yu, C.-L. Ho, S. P. Huang, *Chem. Eur. J.* **2022**, *28*, e202104575.
[79] X. Yao, P.-Y. Ho, S.-C. Yiu, S. Suramitr, W. B. Li, C.-L. Ho, S. Hannongbua, *Dyes Pigm.* **2022**, *205*, 110508.
[80] K. Maeda, G. Sahara, M. Eguchi, O. Ishitani, *ACS Catal.* **2015**, *5*, 1700-1707.
[81] P. Piatkowski, C. Martin, M. R. Di Nunzio, B. Cohen, S. Pandey, S. Hayse, A. Douhal, *J. Phys. Chem. C* **2014**, *118*, 29674-29687.
[82] L. Wang, K. Fan, H. Chen, Q. Daniel, B. Philippe, H. Rensmo, L. Sun, *Catal. Today* **2017**, *290*, 73-77.
[83] P. Shen, Y. H. Tang, S. H. Jiang, H. J. Chen, X. Y. Zheng, X. Y. Wang, B. Zhao, S. T. Tan, *Org. Electron.* **2011**, *12*, 125-135.
[84] A. J. Sindt, B. A. Dehaven, D. F. Mceachern, D. M. M. Dissanayake, M. D. Smith, A. K. Vannucci, L. S. Shimizu, *Chem. Sci.* **2019**, *10*, 2670-2677.
[85] P.-Y. Ho, Y. Wang, S.-C. Yiu, W.-H. Yu, C.-L. Ho, S. P. Huang, *Org. Lett.* **2017**, *19*, 1048-1051.

Chapter 3: Synthesis, Structure, Characterisation, and Water-Splitting Hydrogen Generation Performance of Iridium(III) Cyclometalated Complexes

3.1 Introduction

Iridium(III) cyclometalated complexes are attractive candidates for preparing dyes and have made outstanding contributions to photocatalytic hydrogen production. Compared to other metal dyes containing first- and second-row transition metals, Ir(III) cyclometalated complexes exhibit excellent ligand-field stabilisation energies with their 5*d* valence shell.[1, 2] Bernhard et al.[1, 3-5] have investigated the iridium(III) complexes with general formula of $[Ir(C^N)_2(N^N)]^+$ (C^N = cyclometalating ligand, N^N = anchoring group) for their uses in photochemical water-splitting hydrogen generation systems. A TON of 800 was achieved with 50 μM of **$[Ir(ppy)_2(bpy)]^+$** as photosensitizers in water:acetonitrile (1:1, *v*/*v*) solvent mixture.[3, 6-9] Since then, iridium(III) cyclometalated complexes, such as **$[Ir(ppy)_2(bpy)]^+$**, **$[Ir(ppy)_2(dcbpy)]^+$** and **$[Ir(bzq)_2(bpen)]^+$** have drawn interest for their potential applications as photosensitisers (**Fig. 3.1**).[10] The stability of these complexes can be enhanced by the C^N ligands, owing to σ-donation from the metal-linked carbon, which increases the electron density on the metal centre and allows them more stable under photocatalytic experiments.[1, 11] Moreover, physicochemical properties such as energy gaps can be effectively tuned by varying the ligands.[12, 13] These favourable properties make Ir(III) cyclometalated complexes attractive candidates as dyes for H_2 production *via* water

splitting. However, Ir(III) cyclometalated complexes often suffer from weak absorption of visible light, which accounts for approximately 40% of the sunlight spectrum.[13-16] The structures of Ir(III) cyclometalated complexes should thus be adjusted to overcome these disadvantages and enhance their hydrogen output.

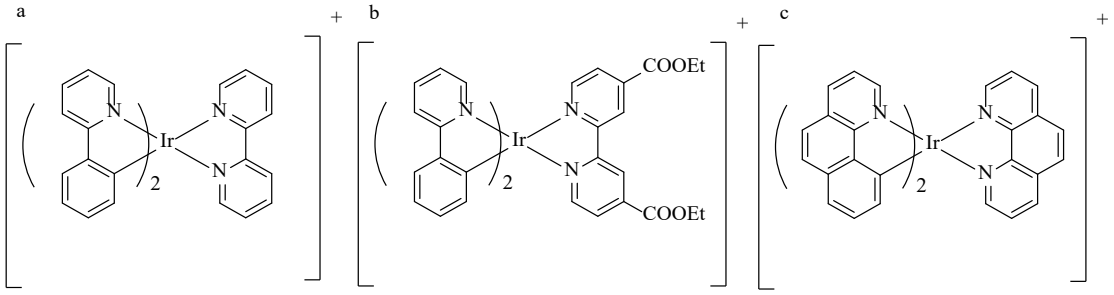

Fig. 3.1. Chemical structures of (a) **[Ir(ppy)$_2$(bpy)]$^+$** molecule, (b) **[Ir(ppy)$_2$(dcbpy)]$^+$** molecule and (c) **[Ir(bzq)$_2$(bpen)]$^+$** molecule.

Thiophene rings, with peculiar structural and electronic properties, are widely used in photocatalytic experiments.[17] Thiophene has a lower resonance energy than benzene,[18] because its π electron-rich heteroaromatic five-membered ring facilitates charge transfer between the donor and the acceptor.[19-21] Therefore, thiophene-based ligands are commonly used in the design of dyes for hydrogen generation based on water splitting.[22] Furthermore, the pyridine functional group leads to a red shift in the absorption spectrum of these compounds, which can help to improve the absorption of visible light.[23, 24] The attractive properties of triphenylamine functional groups have also stimulated intense research.[25] The high molar absorption coefficient of triphenylamine functional groups can result in largely improved photocatalytic

properties, highlighting the promising potential of these ligands in photocatalytic applications.[26] Moreover, the triphenylamine groups can control the energy levels (highest occupied molecular orbital and lowest unoccupied molecular orbital) of conjugated metal dyes, enhancing their reaction efficiency.[27, 28] Triphenylamine has also been shown to enhance the intramolecular energy- and charge-transfer properties.[29] Isoquinoline functional groups have been extensively applied in dyes for water-splitting reactions, owing to their remarkable charge transfer ability.[30-32] Previous studies have shown that the highly extended and polarisable π system of isoquinoline functional groups can greatly increase the hydrogen production efficiency during water splitting.[33-35] Owing to its red shift of the absorption spectrum, the aldehyde functional group has been applied in iridium compounds.[36-40] These findings provide an attractive opportunity to develop highly efficient Ir(III) cyclometalated dyes for water-splitting systems.

Previous studies of Ir(III) cyclometalated complexes have found that different anchoring groups on N^N ligands can be used to obtain highly efficient and stable water-splitting systems.[41, 42] Various anchoring groups, including carboxylate or phosphonic acid can be introduced in the bipyridine ligand of $[Ir(C^N)_2(N^N)]^+$-type dyes[42] to immobilise their linkage with the semiconductor. The 2,2′-bipyridine ligand in the anchoring group endows the complexes with large molar extinction coefficients, which can contribute to their light-harvesting efficiency for the photocatalytic conversion of water to hydrogen.[43] Anchoring ligands with a carboxyl functional group can help anchoring semiconductors such as TiO_2, improving the electron

transport and hydrogen production, as well as increasing the water solubility of Ir(III) cyclometalated complexes because of the presence of an acid–base equilibrium.[44-47] However, these dyes might have drawbacks in terms of stability under photocatalytic operating conditions.[48] The hydrolysis of the carboxylate linkage site has been reported to reduce the efficiency of the electron transfer from photosensitisers to TiO_2.[49] In this regard, the linkage of the phosphonate functional group to the TiO_2 surface has been found to exhibit higher stability than that of the carboxylate group.[49] In this work, a new series of iridium(III) complexes (**Fig. 3.2**) with different functional groups was designed and synthesized. Ir(III) complexes bearing either diethyl [2,2 -bipyridine]-4,4 -dicarboxylate or tetraethyl[2,2′-bipyridine]-4,4′-diylbis(phosphonate) anchoring units were designed and synthesized as photosensitisers for photocatalytic hydrogen generation from water. In addition, the photophysical and electrochemical properties of the new Ir(III) cyclometalated complexes were studied, and their photocatalytic performance in hydrogen production *via* water splitting was systematically investigated.

.

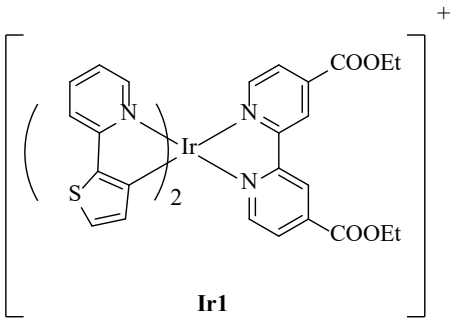

Ir1

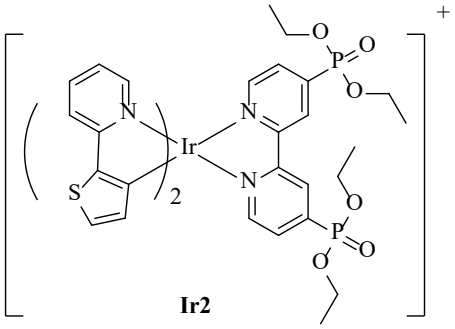

Ir2

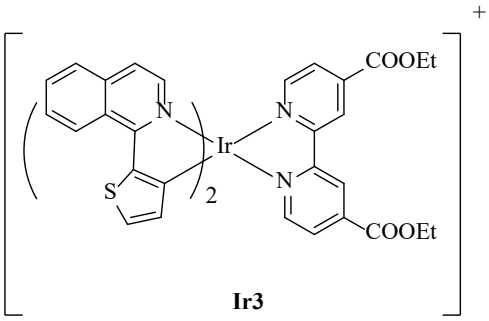

Ir3

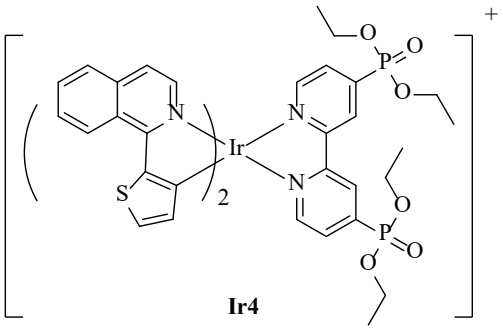

Ir4

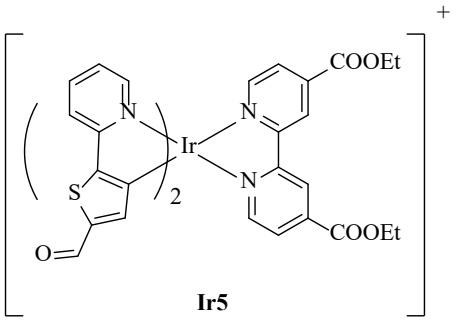

Ir5

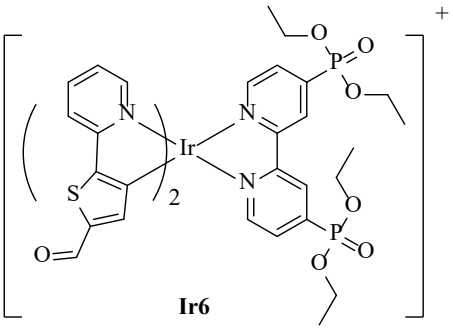

Ir6

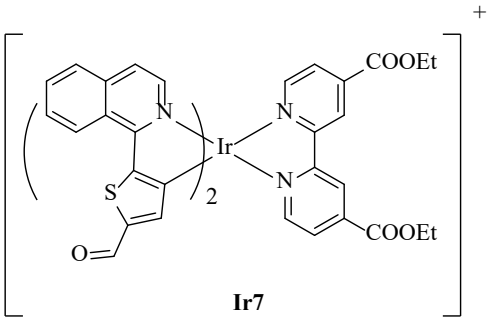

Ir7

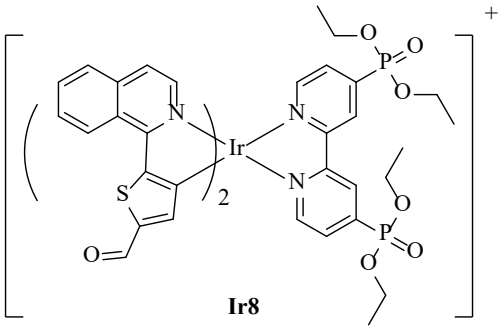

Ir8

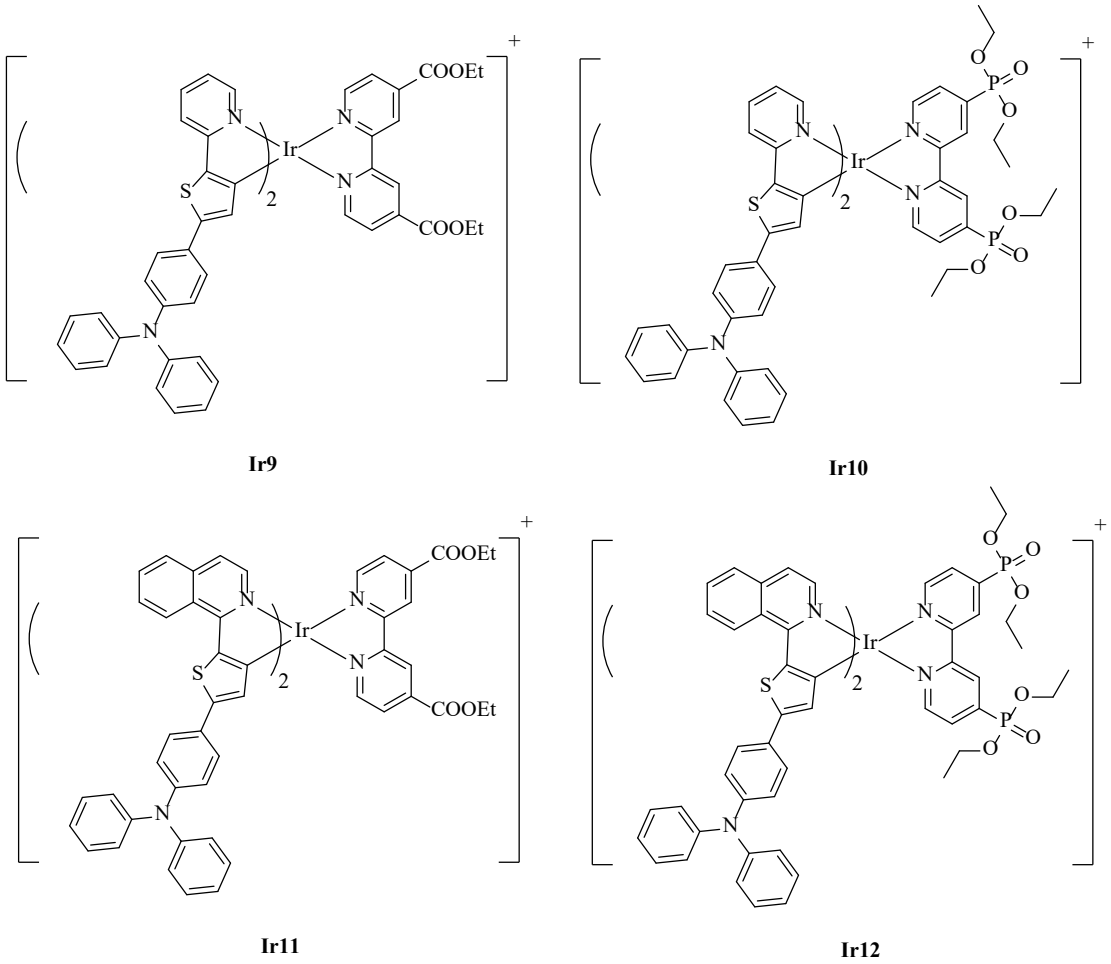

Fig. 3.2. Chemical structures of iridium(III) dyes **Ir1**–**Ir12**.

3.2 Synthesis

3.2.1 Synthesis of C^N ligands and anchoring group

Iridium(III) complexes with C^N ligands were generally prepared by the classical Suzuki reaction. C^N ligands were obtained from different boronic acids with corresponding organic compounds containing the bromo- or chloro- substituents. Part of the synthetic route is the same as that shown in **Scheme 2.1** in **Chapter 2**. The other part of the synthetic route is shown in **Scheme 3.1**.

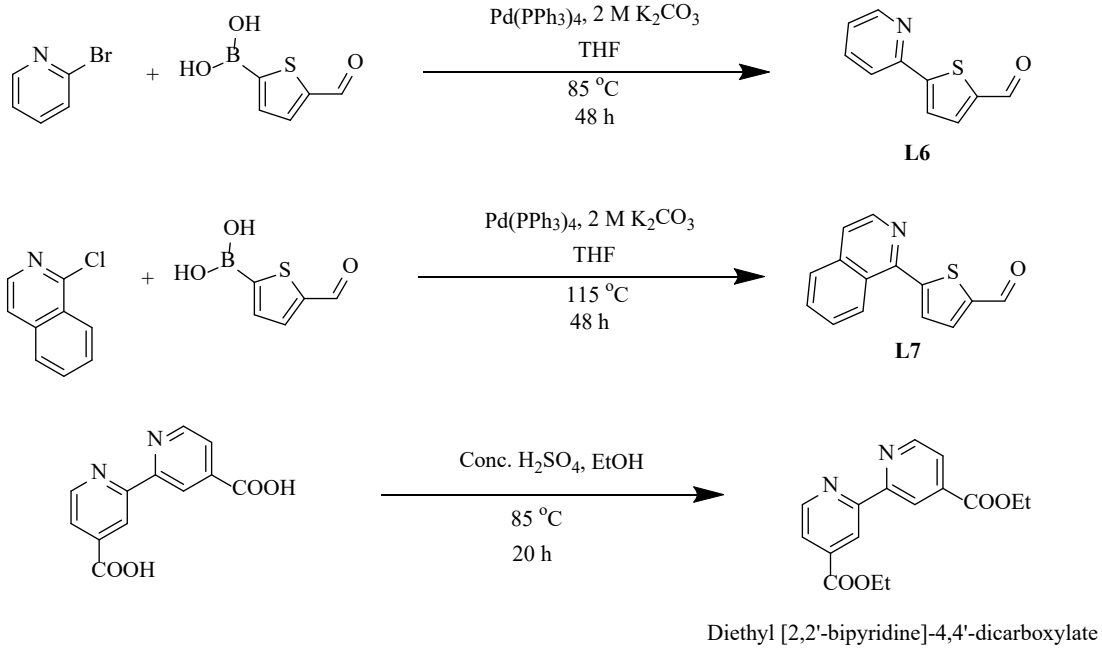

Scheme 3.1. Synthetic routes of C^N ligands and anchoring group.

3.2.2 Synthesis of iridium(III) complex precursors

The cyclometalated Ir(III) dye precursors $[Ir(C^N)_2Cl]_2$ were prepared according to a procedure described in previous literature.[50] The chloride-bridged metal dimer was obtained by refluxing $IrCl_3 \cdot 3H_2O$ with different C^N ligands in a mixture of 2-ethoxyethanol/water (3:1, *v/v*) overnight. The synthetic route is shown in **Scheme 3.2**.

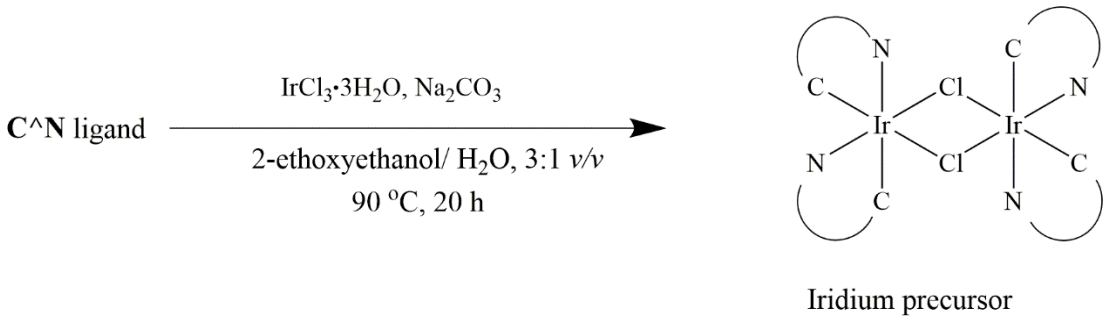

Scheme 3.2. Synthetic route of iridium(III) complex precursor.

3.2.3 Synthesis of iridium(III) complexes

The final cyclometalated Ir(III) dyes were prepared according to a previous literature.[50] The dimer precursors with the N^N ligands and Na_2CO_3 in a MeOH/CH_2Cl_2 (1:1, *v/v*) mixture were refluxed for 6 h to afford the final product. The synthetic route is presented in **Scheme 3.3**. All of the complexes prepared in this study are stable as solids in air.

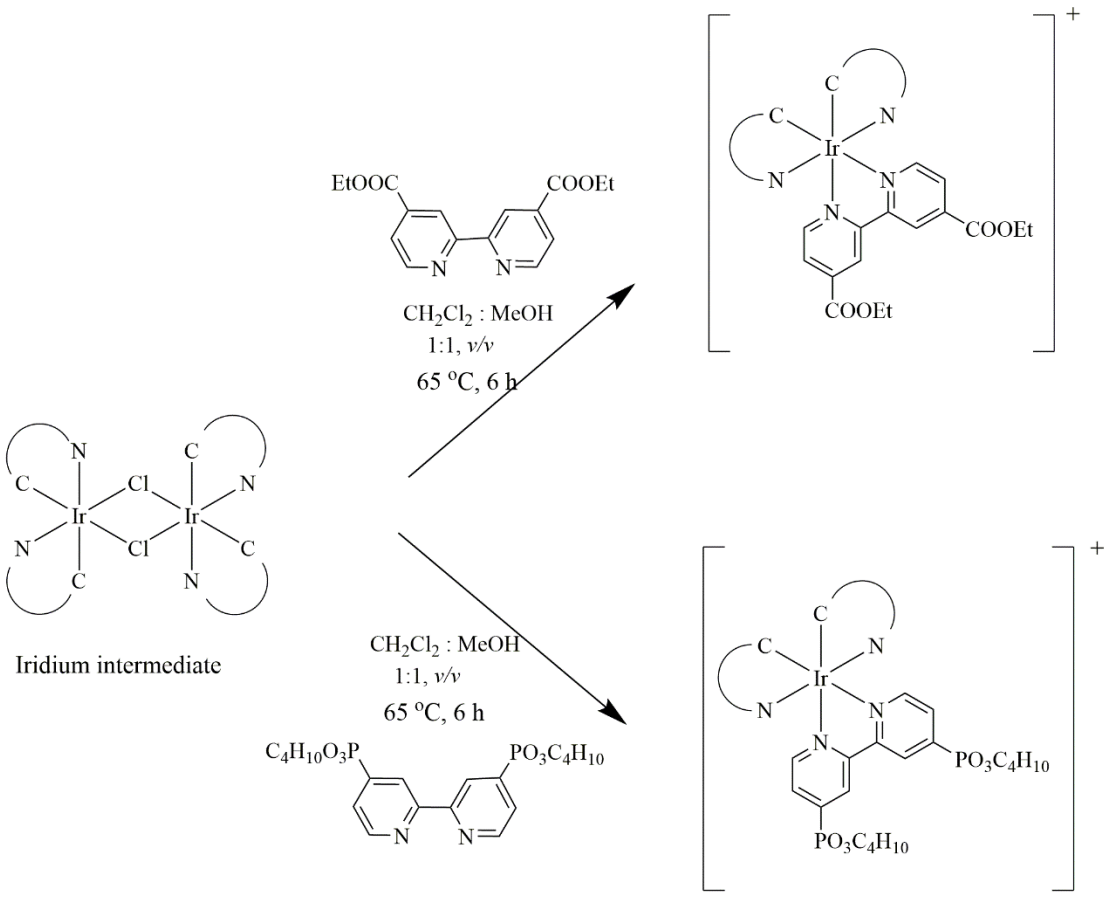

Scheme 3.3. Synthetic route of iridium(III) complexes.

3.3 Spectroscopic Characterisation

All the organic C^N ligands showed characteristic ^{1}H NMR spectra, and a clear structure was identified for each compound. For example, **Fig. 3.3** shows the ^{1}H NMR spectrum of **L6**, showing a singlet at approximately 9.95 ppm attributed to the proton of the aldehyde.[51]

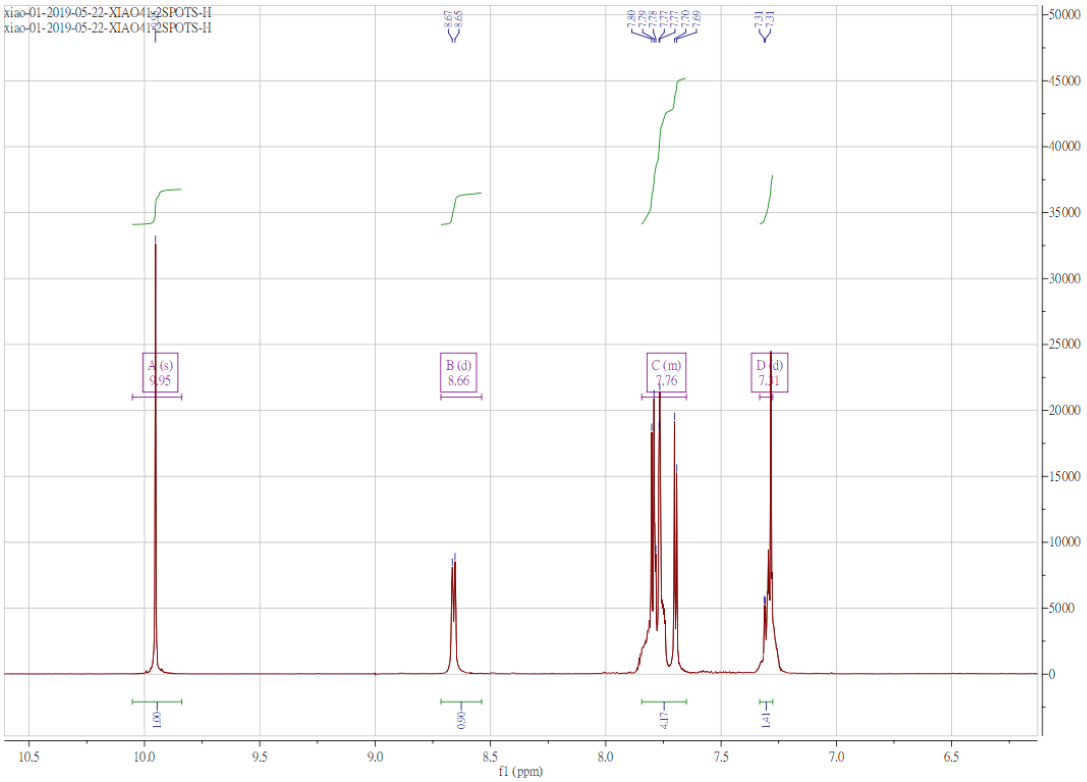

Fig. 3.3. ^{1}H NMR spectrum of **L6** in $CDCl_3$.

Because the solubility of the final iridium(III) complexes are not enough for ^{13}C NMR, only ^{13}C NMR data for the C^N compounds and anchoring group could be obtained. The corresponding NMR spectra reveal the structures of these compounds. For example, **Fig. 3.4** shows the ^{13}C NMR spectrum of **L7**.

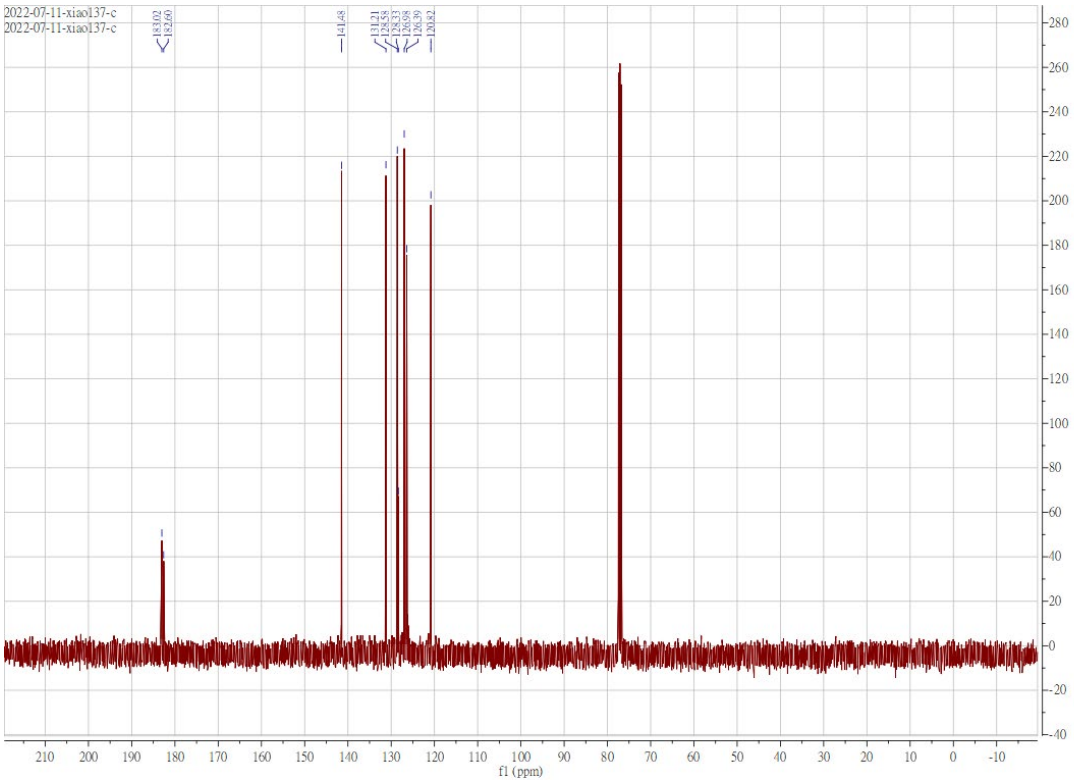

Fig. 3.4. ^{13}C NMR spectrum of **L7** in $CDCl_3$.

The Ir(III) complexes were characterised by ^{1}H NMR spectroscopy. Due to the lack of molecular symmetry, all aromatic protons in the ^{1}H NMR spectra of **Ir1**–**Ir12** were chemically unique, indicating that the two C^N ligands in these Ir(III) complexes were magnetically non-equivalent. **Fig. 3.5** shows the NMR spectrum of **Ir1** as an example. These results clearly confirm the expected structures of the present metal complexes.

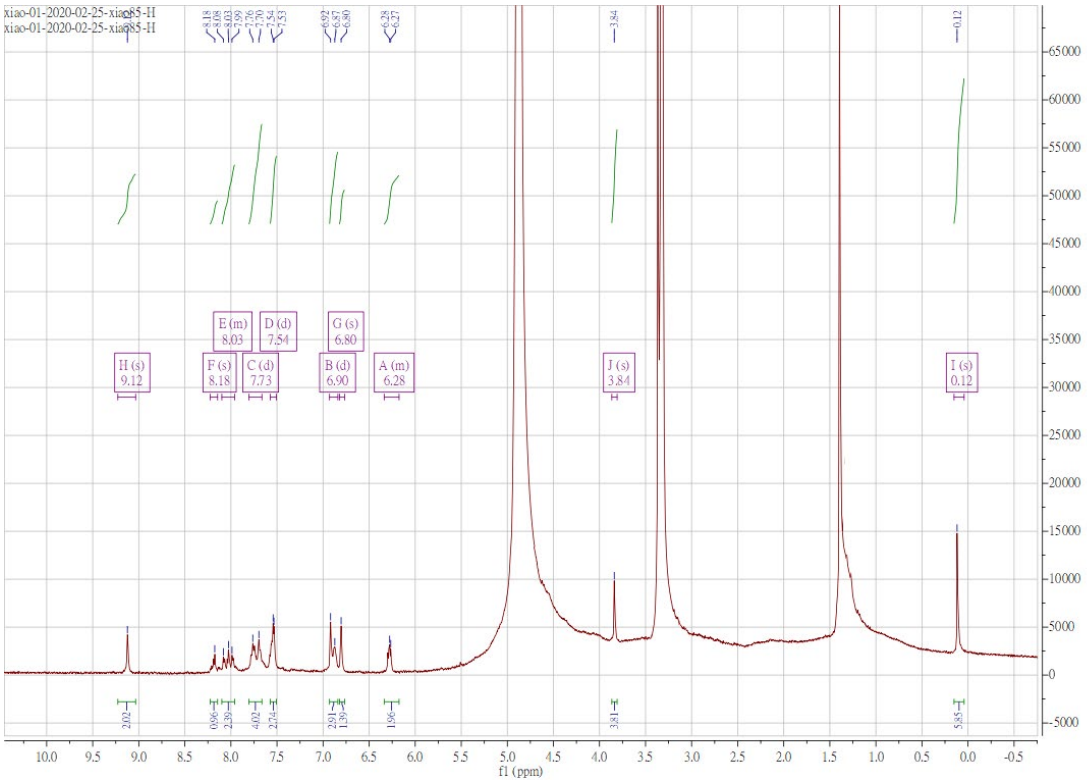

Fig. 3.5. ^{1}H NMR spectrum of **Ir1** in $CDCl_3$.

3.4 Mass Spectroscopy Characterisation

Liquid chromatography–electrospray ionisation–quadrupole time-of-flight mass spectrometry was used to characterise the C^N ligands, anchoring group and the final products. **Fig. 3.6** and **Fig. 3.7** show the mass spectra of **L6** and **Ir1**, respectively. The main peaks of MS results match with the molecular ion peaks, indicating the correct synthesized of each compound.

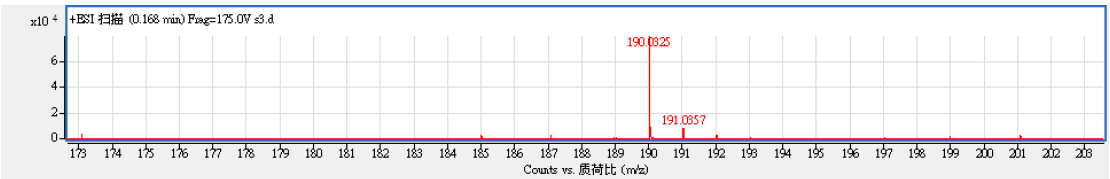

Fig. 3.6. Mass spectrum of **L6**.

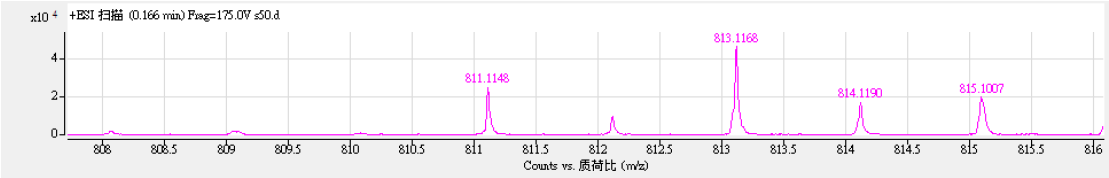

Fig. 3.7. Mass spectrum of **Ir1**.

3.5 Photophysical Properties

To investigate the absorptivity of different Ir(III) dyes, UV–Vis absorption spectra of **Ir1** to **Ir14** were measured in CH_2Cl_2 solvent at room temperature. Their UV–Vis absorption spectra are shown in **Fig. 3.8** and **Fig. 3.9** and the corresponding characteristic spectral data are tabulated in **Table 3.1**.

These compounds showed higher absorption intensities in the visible region than the **[Ir(ppy)$_2$(dcbpy)]$^+$** complex.[12] This difference demonstrates that these Ir(III) dyes had better light-harvesting ability, indicating their better hydrogen production ability than **[Ir(ppy)$_2$(dcbpy)]$^+$**. All Ir(III) dyes displayed strong absorption in the UV region at about 290–310 nm, originating from intra-ligand charge transfer transitions.[52] The intense and band at about 380 nm were originated from spin-allowed π to π* ligand centred electronic transitions on both the C^N and N^N ligand.[53] The broad absorption bands above 400 nm were ascribed to the mixture of MLCT and LLCT transition.[41]

In **Fig. 3.8**, compared with **Ir1** and **Ir2**, the π-conjugation of isoquinoline rather than pyridine of the cyclometalating ligand in **Ir3** and **Ir4** demonstrated a red shifted absorption band with a slightly higher molar absorptivity. [14, 54] The introduction of an aldehyde moiety into the Ir(III) dyes also induced an apparent redshift, but this was accompanied by lower absorptivity[37]. What is more, it should be noticed that for those

Ir(III) complexes, the spectra of Ir(III) dyes with different N^N anchoring groups and the same C^N ligand showed similar absorption peaks, implying that the N^N groups had a minimal influence on the absorption.[50]

In **Fig. 3.9**, it should be noticed that the extended π-conjugation guaranteed by the electron-donating TPA group in Ir(III) dyes resulted in broader absorption spectra with higher ε values at approximately 350 to 550 nm.[29, 55-59] In addition, **Ir10** and **Ir12** had two maximum absorption peaks in visible light, while **Ir9** and **Ir11** only had one peak. This was due to the introduction of heteroatom P atom into the anchoring ligand, which affected its electron density and finally formed a new peak near the wavelength at about 390 to 490 nm.[55-59] Although the conjugated system of **Ir11** and **Ir12** was larger, isoquinoline had greater steric hindrance to the system than pyridine, which led to the hypochromic effect and further reduced its molar extinction coefficient.[55-59] This result matched with the DFT calculation (**Fig. 3.10** and **Table 3.2**).

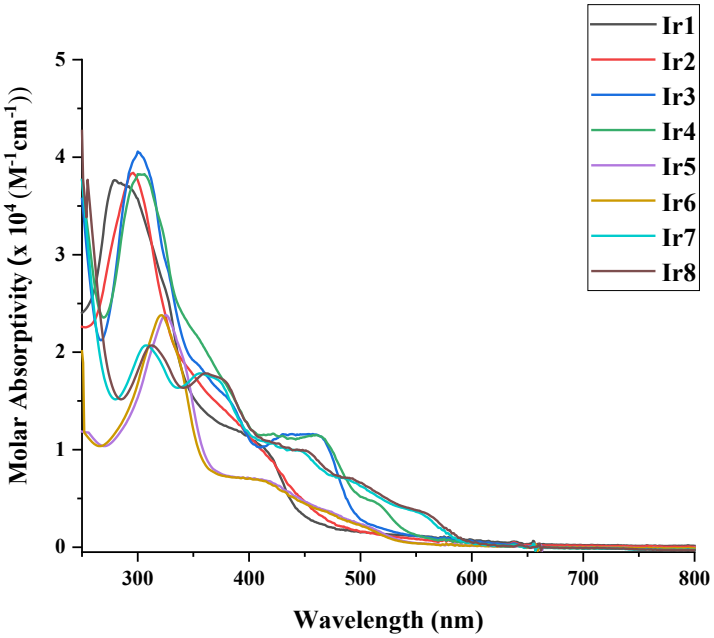

Fig. 3.8. UV–Vis absorption spectra of **Ir1** to **Ir8** in CH_2Cl_2 at 293 K.

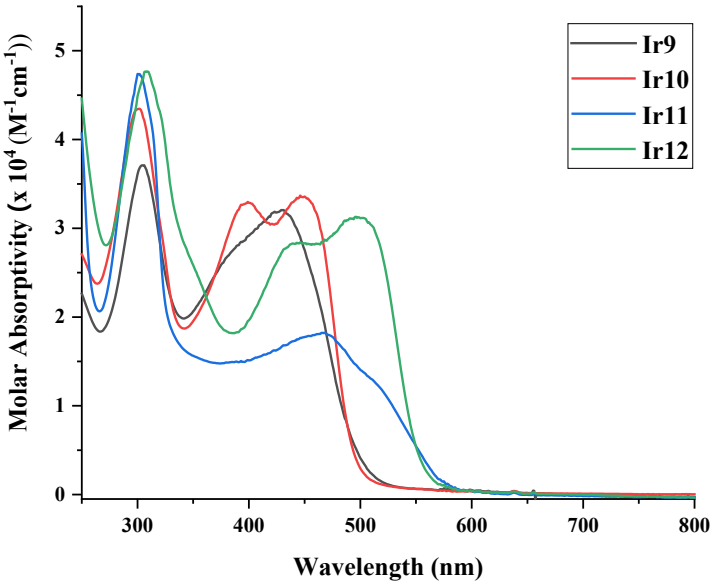

Fig. 3.9. UV–Vis absorption spectra of **Ir9** to **Ir12** in CH_2Cl_2 at 293 K.

Table 3.1. UV–Vis absorption parameter values of **Ir1** to **Ir12** in CH_2Cl_2 at 293 K.

Dye	λ_{max} /nm (ε /10^4 M^{-1} cm^{-1})	λ_{onset} /nm
Ir1	280(3.74), 410(0.96),	476
Ir2	294(3.82), 423(0.91)	500
Ir3	301(4.08), 384(1.49), 466(1.12)	533
Ir4	303(3.84), 385(1.64), 467(1.14), 525(0.41)	566
Ir5	319(2.38), 417(0.68)	539
Ir6	323(2.39), 418(0.70)	551
Ir7	306(2.07), 353(1.78), 448(0.98), 557(0.33)	576
Ir8	312(2.06), 359(1.80), 452(1.00), 566(0.29)	589
Ir9	304(3.69), 429(3.23)	537
Ir10	302(4.37), 401(3.29), 449(3.36)	520
Ir11	301(4.74), 467(1.82)	586
Ir12	309(4.75), 439(2.85), 498(3.13)	579

3.6. Density Functional Theory Calculations

The DFT calculation for two selective Ir(III) dyes have been performed. The Gaussian 16 suite of programs[60] was used to optimize the configurations. Structural optimization and molecular orbitals were performed using the b3lyp functional with the 6–311G(d) basis set for non-metal elements and SDD for Ir. The result was present in **Fig. 3.10** and **Table 3.2**. As for the calculated HOMO energy levels, the orbital energies vary from –6.60 eV, and –6.62 eV, respectively, for complexes **Ir11** and **Ir12**. The energy gaps between frontier molecular orbits between the HOMO–LUMO gap ($DE_{H–L}$) for **Ir11** and **Ir12** are 2.02 eV and 2.06 eV.

Table 3.2. Calculated HOMO, LUMO, energy gap (ΔE) of **Ir11** and **Ir12**. All values were calculated in eV.

Compounds	HOMO	LUMO	ΔE
Ir11	–6.60	–4.58	2.02
Ir12	–6.62	–4.55	2.06

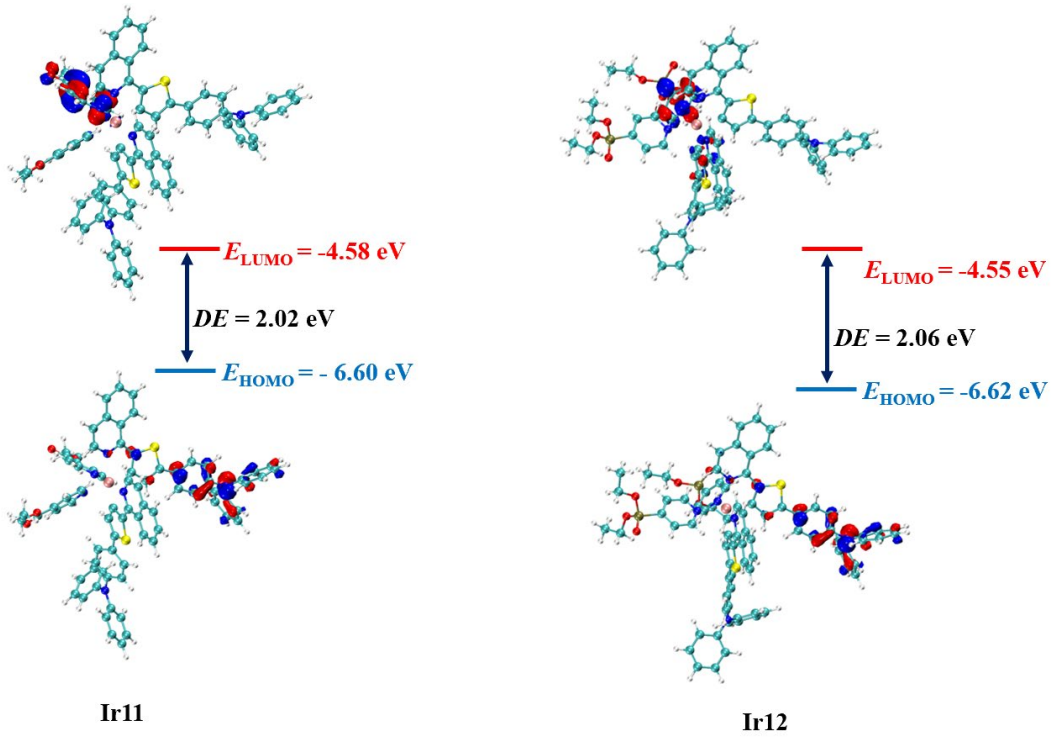

Fig. 3.10. Frontier molecular orbitals of **Ir11** and **Ir12** calculated at the b3lyp functional.

3.7 Electrochemical Properties

An appropriate energy gap between the TiO_2 semiconductor and the sacrificial electron donor in the Ir(III) dyes is crucial for producing hydrogen by water splitting. Electron injection and charge separation are more efficient when the LUMO energy level of the Ir(III) dye is more positive than that of the conduction band of the semiconductor, and when the corresponding HOMO energy level is more negative than that of the SED. Cyclic voltammetry experiments were performed to further investigate the energy

levels of the Ir(III) dyes. These measurements were performed in a conventional three-electrode configuration. A glassy carbon electrode served as the working electrode, whereas a platinum wire and an Ag/AgCl electrode were used as the counter and reference electrodes, respectively. The measurements were performed in dichloromethane containing 0.1 M tetrabutylammonium hexafluorophosphate, at a scan rate of 100 mV s^{-1}. The corresponding parameters of the dyes are shown in **Table 3.3**.

Table 3.3 Electrochemical data and energy levels of **Ir1**−**Ir12**.

Dye	E_{Ox}^{Max} /V	E_{HOMO}[a] /eV	E_g[b] /eV	E_{ox*}[c] /V	E_{LUMO}[d] /eV
Ir1	0.74	−5.54	2.48	−1.74	−3.06
Ir2	0.77	−5.57	2.61	−1.84	−2.96
Ir3	0.41	−5.21	2.19	−1.78	−3.02
Ir4	0.42	−5.22	2.33	−1.91	−2.89
Ir5	0.82	−5.62	2.25	−1.43	−3.37
Ir6	0.81	−5.61	2.3	−1.49	−3.31
Ir7	0.72	−5.52	2.11	−1.39	−3.41
Ir8	0.69	−5.49	2.15	−1.46	−3.34
Ir9	0.45	−5.25	2.31	−1.86	−2.94
Ir10	0.47	−5.27	2.33	−1.86	−2.94
Ir11	0.38	−5.18	2.12	−1.74	−3.06
Ir12	0.39	−5.19	2.13	−1.74	−3.06

[a] Calculated as $-(E_{Ox}^{Max} + 4.8)$. [b] Energy band gap, determined from the onset of absorption. [c] $E_{ox*} = E_{Ox}^{Max} - E_g$. [d] $E_{LUMO} = E_{HOMO} + E_g$.

The CV results were markedly different from those obtained for **[Ir(ppy)$_2$(dcbpy)]$^+$**, demonstrating that the energy gaps in Ir(III) dyes were effectively affected by the different ligands.[12, 13] According to the CV results, the CB level of the TiO_2 semiconductor (−4.4 eV) was more negative than the E_{LUMO} levels of all Ir(III) dyes (ranging from −2.94 to −3.37 eV), enabling an efficient electron injection during light-

driven hydrogen generation.[61] The E_{HOMO} values of **Ir1–Ir12** were between −5.18 and −5.62V, thus more negative than the redox potentials of the SED (AA) (−4.65 eV, pH ~ 4),[25, 62] enabling the effective dye regeneration from the SED. The energy levels of all Ir(III) dyes met the requirements for effective electron injection and charge separation, highlighting their promising potential for hydrogen generation *via* water splitting.

The HOMO energy levels of **Ir3** and **Ir4** were more positive than those of **Ir1** and **Ir2**, due to the extended π-conjugation of the isoquinoline functional group in the C^N ligand.[63] Furthermore, the HOMO energy levels of the Ir(III) dyes with the aldehyde moiety were much lower than those of the Ir(III) dyes with the same C^N ligand but without the aldehyde, such as **Ir3** and **Ir4** compared with **Ir7** and **Ir8**. The electron-withdrawing aldehyde group results in a larger energy gap, which may reduce the charge transfer ability and decrease the hydrogen production by water splitting.[37, 39, 64-67] For **Ir9** to **Ir12,** the HOMO destabilisation was expected with the introduction of the triphenylamine group facilitating intermolecular charge transfer, which can affect the electronic properties of the metal centre, resulting in a narrowing of their HOMO–LUMO gaps and enhanced hydrogen generation by water splitting.[68, 69] The trend matched the DFT calculation (**Fig. 3.10** and **Table 3.2**).

3.8. Electrochemical Impedance Spectroscopy

To further investigate the charge recombination properties of those Ir(III) dyes, electrochemical impedance spectroscopy for selective Ir(III) dyes was employed [70].

The measurements were conducted on an electrochemical workstation according to the previous work [71, 72]. Ag/AgCl was served as the reference electrode with the platinum electrode as the counter electrode, 0.5 M Na_2SO_4 solution as the electrolyte and fluorine-doped tin oxide glass (FTO) with the attachment of Ir(III) as the working electrode. The detail procedures are described in **Chapter 7**. The EIS Nyquist plots for **Ir9** to **Ir12** are shown in **Fig. 3.11**. It is well known that a smaller arc radius in the Nyquist plot indicates lower electric charge transfer resistance which leads to better HER performance [71-74]. Overall, **Ir12** had smaller arc radius than the other, indicating a better charge transfer ability[75] and better hydrogen generation performance. The results matched with the water-splitting hydrogen production performance.

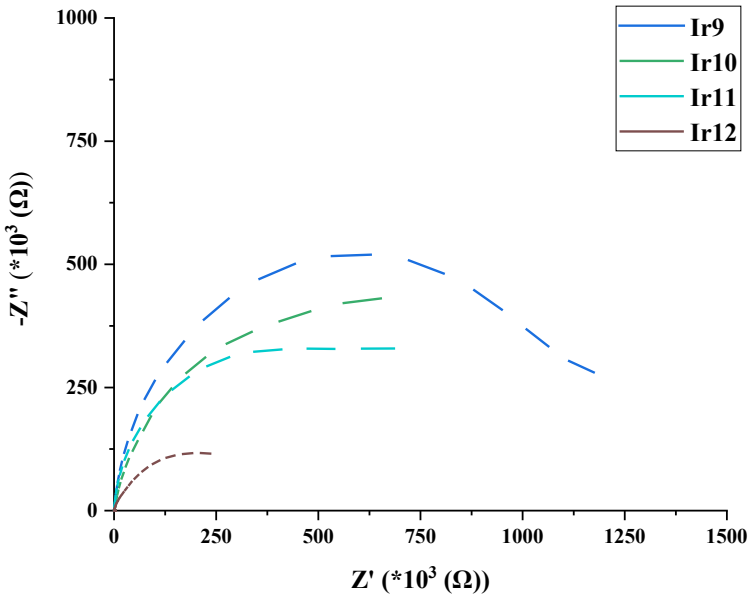

Fig. 3.11. EIS Nyquist plots for complexes **Ir9** to **Ir12**.

3.9 Light-Driven Hydrogen Generation with Ir(III) Dyes @Pt-TiO_2

Hydrogen was produced by photocatalytic water splitting using Ir(III) dyes as photosensitisers. The detailed procedures are the same as those employed for the Ru(II) dyes and can be found in **Chapter 2** and **Chapter 7**. The hydrogen generation curves (*vs.* time) for each sample are shown in **Fig. 3.12** and **Fig. 3.13**. The corresponding data (turnover number, turnover frequency, initial turnover frequency, initial photocatalytic activity, and apparent quantum yield percentage) are listed in **Tables 3.4** and **3.5**.

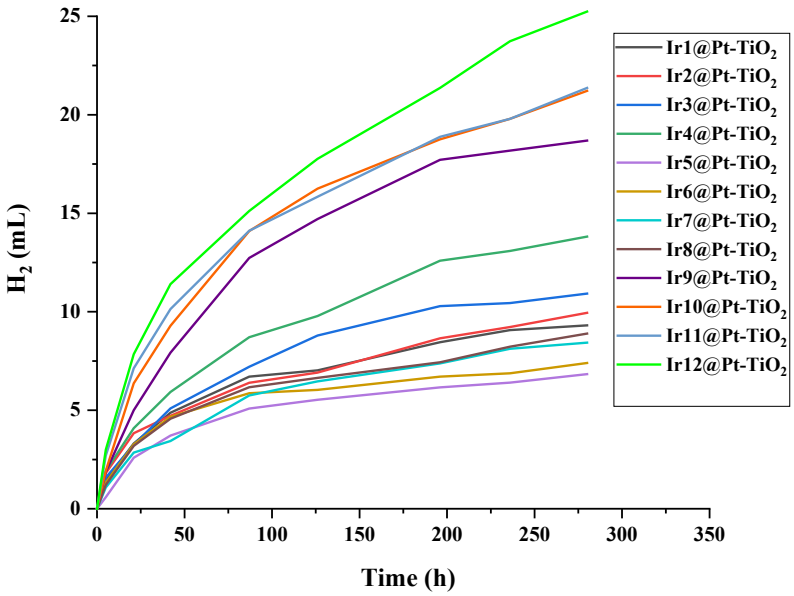

Fig. 3.12. Photocatalytic H_2 generation curves of **Ir1–Ir12@Pt-TiO$_2$** under blue LED irradiation (50 mW).

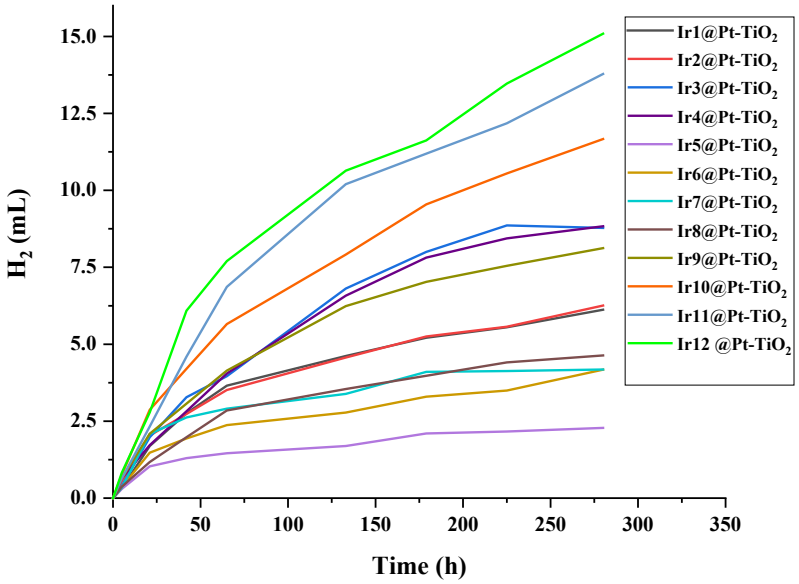

Fig. 3.13. Photocatalytic H_2 generation curves of **Ir1–Ir12@Pt-TiO₂** under green LED irradiation (50 mW).

Table 3.4. Photocatalytic H_2 generation data for different Ir(III) dyes attached on platinized TiO_2 (**Ir1–Ir12@Pt-TiO₂**) under blue light irradiation.

Dye	Time /h	H_2 /mL	TON[a]	TOF[b] /h^{-1}	TOF_i[c] /h^{-1}	$Activity_i$[d] /µmol g^{-1} h^{-1}	AQY_i%[e]
Ir1	280	9.31	6079	21.7	188.0	117551	1.24
Ir2	280	9.95	6494	23.2	236.6	147870	1.32
Ir3	280	10.92	7132	25.4	206.9	129306	1.45
Ir4	280	13.81	9024	32.3	250.8	156734	1.84
Ir5	280	6.83	4462	16.0	76.9	48052	0.91
Ir6	280	7.40	4834	17.3	124.0	87734	0.98
Ir7	280	8.44	5509	19.7	141.1	88163	1.13
Ir8	280	8.89	5809	20.8	158.3	98939	1.19
Ir9	280	18.68	12205	43.6	244.8	153037	2.48
Ir10	280	21.22	13856	49.4	252.4	157715	2.83
Ir11	280	21.36	13950	49.8	353.2	220732	2.84
Ir12	280	25.24	16483	58.9	391.8	244898	3.98

[a] Turnover number (TON) of H_2 was calculated as twice of the number of moles of H_2 produced over the number of moles of PS attached to platinized TiO_2. [b] Turnover frequency (TOF) was calculated per hour. [c] Initial turnover frequency (TOF_i) in the first 5 h. [d] Initial photocatalytic activity ($Activity_i$) is defined as the number of

micromoles of H_2 evolved per gram of platinum loaded per hour. [e] Apparent quantum yield percentage (AQY%).

Table 3.5. Photocatalytic H_2 generation data for different Ir(III) dyes attached on platinized TiO_2 (**Ir1–Ir12@Pt-TiO₂**) under green light irradiation.

Dye	Time /h	H_2 /mL	TON[a]	TOF[b] /h^{-1}	TOFi[c] /h^{-1}	Activity$_i$[d] /µmol g^{-1} h^{-1}	AQY$_i$%[e]
Ir1	280	6.12	3996	14.2	41.8	26122	0.80
Ir2	280	6.26	4086	14.6	70.2	43904	0.82
Ir3	280	8.78	5734	20.4	52.2	32654	1.15
Ir4	280	8.84	5770	20.6	84.0	52470	1.16
Ir5	280	2.28	1492	5.4	39.2	24490	0.30
Ir6	280	4.18	2728	9.8	47.0	29388	0.55
Ir7	280	4.18	2730	9.8	44.4	27756	0.55
Ir8	280	4.64	3028	10.8	48.6	30326	0.61
Ir9	280	8.12	5304	19.0	83.2	52024	1.06
Ir10	280	11.66	7620	27.2	98.8	61714	1.52
Ir11	280	13.78	9000	32.2	83.6	52244	1.80
Ir12	280	15.09	9853	35.1	107.9	67428	1.97

[a] Turnover number (TON) of H_2 was calculated as twice of the number of moles of H_2 produced over the number of moles of PS attached to platinized TiO_2. [b] Turnover frequency (TOF) was calculated per hour. [c] Initial turnover frequency (TOF_i) in the first 5 h. [d] Initial photocatalytic activity ($Activity_i$) is defined as the number of micromoles of H_2 evolved per gram of platinum loaded per hour. [e] Apparent quantum yield percentage (AQY%).

The Ir(III) dyes used in this study enhanced the hydrogen production *via* water splitting and achieved satisfactory hydrogen generation under both green and blue LED irradiation. The volume of hydrogen produced under blue light irradiation was much higher than that generated under green light. The hydrogen production results were consistent with the UV–Vis absorption spectra, which showed a better light-absorbing ability in the blue than in the green light region (**Fig. 3.8** and **Fig. 3.9**). The **Ir12@Pt-TiO₂** system exhibited the highest hydrogen generation ability both under blue and

green light irradiation, with corresponding TON values of 16483 and 9853, respectively, followed by the **Ir11@Pt-TiO$_2$** system, with TON values of 13950 and 9000 for blue and green light irradiation, respectively.

In the present study, Ir(III) dyes with isoquinoline exhibited a superior hydrogen production ability than those with pyridine, under both blue and green light irradiation. For example, the **Ir3@Pt-TiO$_2$** system presented TON values of 7132 and 5734 under blue and green light irradiation, respectively, which were much higher than those of the **Ir1@Pt-TiO$_2$** system (6079 and 3996, respectively). The same differences were also observed in **Ir4@Pt-TiO$_2$** and **Ir2@Pt-TiO$_2$,** owing to the high charge transfer ability of the isoquinoline functional group.[30, 32, 76] The UV–Vis spectra (**Fig. 3.8** and **Fig. 3.9**) also showed that **Ir3@Pt-TiO$_2$** and **Ir4@Pt-TiO$_2$** had higher light absorption ability than **Ir1@Pt-TiO$_2$** and **Ir2@Pt-TiO$_2$**. Ir(III) dyes with triphenylamine ligands were more effective than other Ir(III) dyes in promoting hydrogen generation under both blue and green LED irradiation, as observed for **Ir9@Pt-TiO$_2$** and **Ir10@Pt-TiO$_2$** compared to **Ir1@Pt-TiO$_2$** and **Ir2@Pt-TiO$_2$**. Previous research has shown that triphenylamine and its derivatives provide an improved hydrogen production capacity, owing to their excellent donor characteristics and favourable hole transport properties.[77, 78] Furthermore, triphenylamine has been reported to be a good light harvester, as confirmed by its broad absorption peak in the UV–Vis spectrum (**Fig. 3.8** and **Fig. 3.9**).[78]

Notably, the aldehyde functionality reduced the Ir(III)-promoted hydrogen production, likely due to its poor absorptivity (**Fig. 3.8** and **Fig. 3.9**) and large energy gap (**Table**

3.3). For example, the system based on **Ir6@Pt-TiO$_2$**, resulted in TONs of 4834 and 2728 under blue and green LED irradiation, respectively, were much less than that compared to the 9024 and 5770 values obtained with **Ir4@Pt-TiO$_2$**. This suggests that incorporating aldehydes into Ir(III) dyes reduces the hydrogen generation efficiency. Higher hydrogen production was obtained with Ir(III) dyes bearing phosphonate than carboxylate anchoring groups. Ir(III) dyes with a phosphonate anchoring group have been found to improve hydrogen production, due to the higher anchoring ability by the phosphonate group.[41, 69, 79, 80] Similar results have also been observed in the reported literature. [42, 48]

The photocatalytic water-splitting experiments for **[Ir(ppy)$_2$(dcbpy)]$^+$** have also been performed. The experimental results are shown in **Fig. 3.14** and **Table 3.6**. The results suggest that our new complexes show more efficient photocatalytic hydrogen generation and higher stability than **[Ir(ppy)$_2$(dcbpy)]$^+$**. Furthermore, we revisited the literatures and sorted out the performance data of similar Ir complexes as **Table 3.7**. Compared with the reported literatures, our complexes, especially **Ir12**, show a significant improvement in light-driven hydrogen evolution. These results also indicate that our new Ir(III) dyes are promising candidate for highly stable photocatalytic applications.

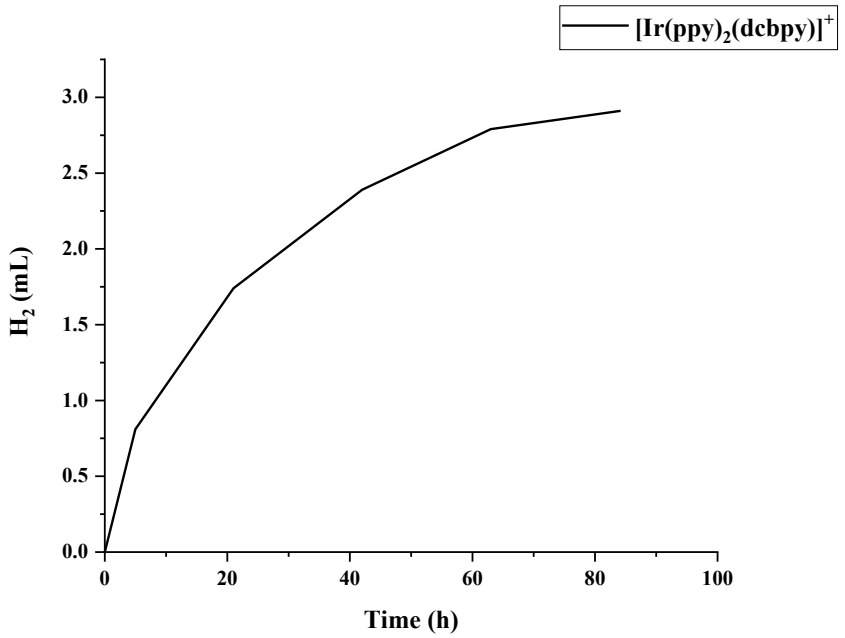

Fig. 3.14. Photocatalytic H_2 generation curves of **[Ir(ppy)$_2$(dcbpy)]$^+$** under blue LED irradiation (50 mW).

Table 3.6. Photocatalytic H_2 generation data with **[Ir(ppy)$_2$(dcbpy)]$^+$** under blue light irradiation.

Dye	Time /h	H_2 /mL	TON[a]	TOF[b] /h^{-1}	TOF_i[c] /h^{-1}	$Activity_i$[d] /μmol g^{-1} h^{-1}	AQY_i%[e]
[Ir(ppy)$_2$(dcbpy)]$^+$	84	2.91	1900	22.6	105.8	66122	0.42

[a] Turnover number (TON) of H_2 was calculated as twice of the number of moles of H_2 produced over the number of moles of PS attached to platinized TiO_2. [b] Turnover frequency (TOF) was calculated per hour. [c] Initial turnover frequency (TOF_i) in the first 5 h. [d] Initial photocatalytic activity ($Activity_i$) is defined as the number of micromoles of H_2 evolved per gram of platinum loaded per hour. [e] Initial apparent quantum yield percentage (AQY_i).

Table 3.7. Performance for light-driven hydrogen evolution based on different Ir(III) dye systems.

Dye	SED	TON (Time)	reference
$[Ir(ppy)_2(3\text{-}PhCHObpy)]PF_6$	TEA	6364 (5h)	[81]
$[Ir(ppy)_2(dtbbpy)]^+$	MeCN	289 (72h)	[82]
$[Ir(ppy)_2(dtbbpy)]^+$	EtOAc	233 (72h)	[82]
$[Ir(ppy)_2(dtbbpy)]^+$	DMSO	13 (72h)	[82]
$[Ir(ppy)_2(dtbbpy)]^+$	THF	52 (72h)	[82]
$[Ir(ppy)_2(dtbbpy)](PF_6)$	MeOH	About 1000 (18h)	[83]
$[Ir(ppy)_2(dtbbpy)](PF_6)$	THF	About 1200 (18h)	[83]
$[Ir\text{-}(Fmppy)_2(dtbbpy)](PF_6)$	MeOH	About 800 (18h)	[83]
$[Ir\text{-}(Fmppy)_2(dtbbpy)](PF_6)$	THF	About 800 (18h)	[83]
Ir12	Ascorbic acid (pH=4)	16483 (280h)	This study

3.10 Conclusions

In summary, this chapter reports new Ir(III) photosensitisers based on triphenylamine, pyridine, isoquinoline, or aldehyde, with either phosphate linker or carboxylic acid anchoring groups. All Ir(III) dyes were characterised and tested for their hydrogen generation rates *via* water splitting. The UV–Vis absorption spectra of the Ir(III) dyes showed markedly increased intensities and extended towards the visible region, especially in the case of those with triphenylamine functional groups, which enhanced their light-harvesting ability and hydrogen production.

The results of hydrogen generation *via* water splitting tests showed that the largest TON of 16483 was achieved by the **Ir12@Pt-TiO$_2$** system under blue LED irradiation, because this system contained triphenylamine and isoquinoline groups with phosphate anchoring groups. This result clearly demonstrates the beneficial effects of

triphenylamine and isoquinoline, owing to their strong intramolecular charge transfer ability. In addition, the Ir(III) dye systems with a phosphate anchoring group achieved higher TON values than those with the same C^N ligand but containing carboxylic acid. Therefore, the phosphate anchoring group is crucial for designing highly effective photosensitisers with excellent stability.

3.11 References

[1] M. Yang, J. E. Yarnell, K. El Roz, F. N. Castellano, *ACS Appl. Energy Mater.* **2020**, *3*, 1842-1853.

[2] J. C. Deaton, F. N. Castellano, in *Iridium (iii) in optoelectronic and photonics applications* (Ed.: E. Zysman-Colman), WilEy-VCH, WeinHeim, **2017**, pp. 1-69.

[3] J. I. Goldsmith, W. R. Hudson, M. S. Lowry, T. H. Anderson, S. Bernhard, *J. Am. Chem. Soc.* **2005**, *127*, 7502-7510.

[4] M. S. Lowry, S. Bernhard, *Chem. Eur. J.* **2006**, *12*, 7970-7977.

[5] M. S. Lowry, J. I. Goldsmith, J. D. Slinker, R. Rohl, R. A. Pascal, G. G. Malliaras, S. Bernhard, *Chem. Mater.* **2005**, *17*, 5712-5719.

[6] P. N. Curtin, L. L. Tinker, C. M. Burgess, E. D. Cline, S. Bernhard, *Inorg. Chem.* **2009**, *48*, 10498-10506.

[7] L. L. Tinker, N. D. Mcdaniel, P. N. Curtin, C. K. Smith, M. J. Ireland, S. Bernhard, *Chem. Eur. J.* **2007**, *13*, 8726-8732.

[8] L. L. Tinker, S. Bernhard, *Inorg. Chem.* **2009**, *48*, 10507-10511.

[9] S. Metz, S. Bernhard, *Chem. Commun.* **2010**, *46*, 7551-7553.

[10] G. B. Bodedla, D. N. Tritton, X. Chen, J. Zhao, Z. Guo, K. C.-F. Leung, W.-Y. Wong, X. Zhu, *ACS Appl. Energy Mater.* **2021**, *4*, 3945-3951.

[11] E. A. Juban, A. L. Smeigh, J. E. Monat, J. K. Mccusker, *Coord. Chem. Rev.* **2006**, *250*, 1783-1791.

[12] P. Wang, S. Guo, H. J. Wang, K. K. Chen, N. Zhang, Z. M. Zhang, T. B. Lu, *Nat. Commun.* **2019**, *10*, 1-12.

[13] Y. Wang, X. Zhao, Y. Zhao, T. Yang, X. Liu, J. Xie, G. Li, D. Zhu, H. Tan, Z. Su, *Dyes Pigm.* **2019**, *170*, 107547.

[14] S.-Y. Takizawa, C. Pérez-Bolívar, P. Anzenbacher Jr, S. Murata, *Eur. J. Inorg. Chem.* **2012**, *2012*, 3975-3979.

[15] J. Zhao, W. Wu, J. Sun, S. Guo, *Chem. Soc. Rev.* **2013**, *42*, 5323-5351.

[16] C.-H. Siu, C.-L. Ho, J. He, T. Chen, X. N. Cui, J. Z. Zhao, W.-Y. Wong, *J. Organomet. Chem.* **2013**, *748*, 75-83.

[17] B. Cecconi, N. Manfredi, R. Ruffo, T. Montini, I. Romero-Ocaña, P. Fornasiero, A. Abbotto, *ChemSusChem* **2015**, *8*, 4216-4228.

[18] E. Campaigne, *J. Chem. Educ.* **1986**, *63*, 860.

[19] T. Debnath, P. Maity, H. Lobo, B. Singh, G. S. Shankarling, H. N. Ghosh, *Chem. Eur. J.* **2014**, *20*, 3510-3519.

[20] B.-G. Kim, K. Chung, J. Kim, *Chem. Eur. J.* **2013**, *19*, 5220-5230.

[21] M. Liang, J. Chen, *Chem. Soc. Rev.* **2013**, *42*, 3453-3488.

[22] A. Abbotto, N. Manfredi, *Dalton Trans.* **2011**, *40*, 12421-12438.

[23] M. Pagliai, G. Mancini, I. Carnimeo, N. De Mitri, V. Barone, *J. Comput. Chem.* **2017**, *38*, 319-335.

[24] Y. Law, A. Hassanali, *J. Chem. Phys.* **2018**, *148*, 102331.

[25] Z. Ji, G. Natu, Y. Wu, *ACS Appl. Mater. Interfaces* **2013**, *5*, 8641-8648.

[26] Z. Wang, M. Liang, Y. Tan, L. Ouyang, Z. Sun, S. Xue, *J. Mater. Chem. A* **2015**,

3, 4865-4874.
[27] D. P. Hagberg, T. Marinado, K. M. Karlsson, K. Nonomura, P. Qin, G. Boschloo, T. Brinck, A. Hagfeldt, L. Sun, *J. Org. Chem.* **2007**, *72*, 9550-9556.
[28] M. Marszalek, S. Nagane, A. Ichake, R. Humphry-Baker, V. Paul, S. M. Zakeeruddin, M. Grätzel, *J. Mater. Chem.* **2012**, *22*, 889-894.
[29] L.-L. Tan, J.-F. Huang, Y. Shen, L.-M. Xiao, J.-M. Liu, D.-B. Kuang, C.-Y. Su, *J. Mater. Chem. A* **2014**, *2*, 8988-8994.
[30] L. Duan, C. M. Araujo, M. S. Ahlquist, L. Sun, *Proc. Natl. Acad. Sci. U.S.A.* **2012**, *109*, 15584-15588.
[31] Q. Q. Liu, L. L. Wu, M. Z. Chen, Y. Guo, T. Z. Xie, P. S. Wang, *Catal. Commun.* **2019**, *122*, 38-42.
[32] K. S. Joya, Y. F. Joya, K. Ocakoglu, R. Van De Krol, *Angew. Chem. Int. Ed.* **2013**, *52*, 10426-10437.
[33] C. J. Wang, Y. Chen, W.-F. Fu, *Dalton Trans.* **2015**, *44*, 14483-14493.
[34] B. J. Timmer, O. Kravchenko, T. Liu, B. Zhang, L. Sun, *Angew. Chem.* **2021**, *113*, 14625-14632.
[35] T.-T. Li, Y. Chen, F.-M. Li, W.-L. Zhao, C.-J. Wang, X.-J. Lv, Q.-Q. Xu, W.-F. Fu, *Chem. Eur. J.* **2014**, *20*, 8054-8061.
[36] K. K.-W. Lo, C.-K. Chung, N. Y. Zhu, *Chem. Eur. J.* **2003**, *9*, 475-483.
[37] H. Chen, Q. Zhao, Y. Wu, F. Li, H. Yang, T. Yi, C. Huang, *Inorg. Chem.* **2007**, *46*, 11075-11081.
[38] Y. H. Liu, Q. Q. Wang, M.-J. Li, *J. Organomet. Chem.* **2019**, *898*, 120874.
[39] Y. Ma, S. Liu, H. Yang, Y. Wu, C. Yang, X. Liu, Q. Zhao, H. Wu, J. Liang, F. Li, *J. Mater. Chem.* **2011**, *21*, 18974-18982.
[40] M. Fukui, A. Tanaka, K. Hashimoto, H. Kominami, *Chem. Commun.* **2017**, *53*, 4215-4218.
[41] A. Kobayashi, S. Watanabe, M. Yoshida, M. Kato, *ACS Appl. Energy Mater.* **2018**, *1*, 2882-2890.
[42] R. A. Wahyuono, S. Amthor, C. Müller, S. Rau, B. Dietzek, *ChemPhotoChem* **2020**, *4*, 618-629.
[43] V. Marin, E. Holder, R. Hoogenboom, U. S. Schubert, *Chem. Soc. Rev.* **2007**, *36*, 618-635.
[44] Y.-J. Yuan, Z.-T. Yu, X.-Y. Chen, J.-Y. Zhang, Z.-G. Zou, *Chem. Eur. J.* **2011**, *17*, 12891-12895.
[45] W. Jiang, Y. Gao, Y. Sun, F. Ding, Y. Xu, Z. Bian, F. Li, J. Bian, C. Huang, *Inorg. Chem.* **2010**, *49*, 3252-3260.
[46] Y. Himeda, N. Onozawa-Komatsuzaki, H. Sugihara, K. Kasuga, *Organometallics* **2007**, *26*, 702-712.
[47] J. Zhao, S. Ji, W. Wu, W. Wu, H. Guo, J. Sun, H. Sun, Y. Liu, Q. Li, L. Huang, *RSC Adv.* **2012**, *2*, 1712-1728.
[48] T. N. Murakami, E. Yoshida, N. Koumura, *Electrochim. Acta.* **2014**, *131*, 174-183.
[49] E. Bae, W. Choi, J. Park, H. S. Shin, S. B. Kim, J. S. Lee, *J. Chem. Phys. B* **2004**, *108*, 14093-14101.

[50] L.-X. Yang, W.-F. Yang, Y.-J. Yuan, Y.-B. Su, M.-M. Zhou, X.-L. Liu, G.-H. Chen, X. Chen, Z.-T. Yu, Z.-G. Zou, *Chem. Asian J.* **2018**, *13*, 1699-1709.

[51] L. Abis, E. Dalcanale, A. Du Vosel, S. Spera, *J. Org. Chem.* **1988**, *53*, 5475-5479.

[52] Y.-J. Yuan, J.-Y. Zhang, Z.-T. Yu, J.-Y. Feng, W.-J. Luo, J.-H. Ye, Z.-G. Zou, *Inorg. Chem.* **2012**, *51*, 4123-4133.

[53] S.-C. Yiu, P.-Y. Ho, Y.-Y. Kwok, X. J. He, Y. Wang, W.-H. Yu, C.-L. Ho, S. P. Huang, *Chem. Eur. J.* **2022**, *28*, e202104575.

[54] D. Aggoun, Z. Messasma, B. Bouzerafa, R. Berenguer, E. Morallon, Y. Ouennoughi, A. Ourari, *J. Mol. Struct.* **2021**, *1231*, 129923.

[55] K. Q. He, N. Su, J. T. Yu, Y. Liu, W. J. Xiong, Z. R. Hao, D. G. Ma, W. G. Zhu, *Tetrahedron* **2016**, *72*, 7164-7169.

[56] P.-Y. Ho, S.-Y. Lee, C. Kam, J. F. Zhu, G.-G. Shan, Y. I. Hong, W.-Y. Wong, S. J. Chen, *Adv. Healthcare Mater.* **2021**, 2100706.

[57] A. Mahmood, M. HussainTahir, A. Irfan, B. Khalid, A. G. Al-Sehemi, *Bull. Korean Chem. Soc.* **2015**, *36*, 2615-2620.

[58] Y. Y. Tang, Y. Q. Wang, X. Li, H. Ågren, W.-H. Zhu, Y. S. Xie, *ACS Appl. Mater. Interfaces* **2015**, *7*, 27976-27985.

[59] R. Balasaravanan, K. Duraimurugan, J. Sivamani, V. Thiagarajan, A. Siva, *New J. Chem.* **2015**, *39*, 7472-7480.

[60] M. J. Frisch, G. W. Trucks, H. B. Schlegel, G. E. Scuseria, M. A. Robb, J. R. Cheeseman, G. Scalmani, V. Barone, G. A. Petersson, H. Nakatsuji, X. Li, M. Caricato, A. Marenich, J. Bloino, B. G. Janesko, R. Gomperts, B. Mennucci, H. P. Hratchian, J. V. Ortiz, A. F. Izmaylov, J. L. Sonnenberg, D. Williams-Young, F. Ding, F. Lipparini, F. Egidi, J. Goings, B. Peng, A. Petrone, T. Henderson, D. Ranasinghe, V. G. Zakrzewski, J. Gao, N. Rega, G. Zheng, W. Liang, M. Hada, M. Ehara, K. Toyota, R. Fukuda, J. Hasegawa, M. Ishida, T. Nakajima, Y. Honda, O. Kitao, H. Nakai, T. Vreven, K. Throssell, J. A. Montgomery Jr, J. E. Peralta, F. Ogliaro, M. Bearpark, J. J. Heyd, E. Brothers, K. N. Kudin, V. N. Staroverov, T. Keith, R. Kobayashi, J. Normand, K. Raghavachari, A. Rendell, J. C. Burant, S. S. Iyengar, J. Tomasi, M. Cossi, J. M. Millam, M. Klene, C. Adamo, R. Cammi, J. W. Ochterski, R. L. Martin, K. Morokuma, O. Farkas, J. B. Foresman, D. J. Fox, *Gaussian 09, Revision E.01*, Gaussian, Inc., Wallingford CT, **2009**.

[61] T. Bessho, E. Yoneda, J.-H. Yum, M. Guglielmi, I. Tavernelli, H. Imai, U. Rothlisberger, M. K. Nazeeruddin, M. GräTzel, *J. Am. Chem. Soc.* **2009**, *131*, 5930-5934.

[62] S. Sebata, S.-Y. Takizawa, N. Ikuta, S. Murata, *Dalton Trans.* **2019**, *48*, 14914-14925.

[63] P. S. Kim, S. Choi, S.-Y. Kim, J. H. Jo, Y. S. Lee, B. Kim, W. Kim, W. Choi, C. H. Kim, H.-J. Son, *Chem. Eur. J.* **2019**, *25*, 13609-13623.

[64] A. Maity, B. L. Anderson, N. Deligonul, T. G. Gray, *Chem. Sci.* **2013**, *4*, 1175-1181.

[65] X. Q. Wu, J. Zhao, L. P. Wang, M. M. Han, M. L. Zhang, H. B. Wang, H. Huang, Y. Liu, Z. H. Kang, *Appl. Catal. B* **2017**, *206*, 501-509.

[66] N. Lin, H.-D. Ou, Q. Y. Xu, Y. Jin, W. Deng, Z.-J. Yao, *ACS Omega* **2020**, *5*, 4636-4645.
[67] K. K.-W. Lo, J. S.-W. Chan, C.-K. Chung, V. W.-H. Tsang, N. Zhu, *Inorg. Chim. Acta* **2004**, *357*, 3109-3118.
[68] C. Hierlinger, D. B. Cordes, A. M. Slawin, A. Colombo, C. Dragonetti, S. Righetto, D. Roberto, D. Jacquemin, E. Zysman-Colman, V. Guerchais, *Dalton Trans.* **2018**, *47*, 8292-8300.
[69] F. Légalité, D. Escudero, Y. Pellegrin, E. Blart, D. Jacquemin, O. Fabrice, *Dyes Pigm.* **2019**, *171*, 107693.
[70] X. Yao, P.-Ho, S.-C. Yiu, S. Suramitr, W. B. Li, C.-L. Ho, S. Hannongbua, *Dyes Pigm.* **2022**, *205*, 110508.
[71] P. Tian, X. He, L. Zhao, W. Li, W. Fang, H. Chen, F. Zhang, Z. Huang, H. Wang, *Int. J. Hydrogen Energy* **2019**, *44*, 788-800.
[72] P. Tian, X. He, L. Zhao, W. X. Li, W. Fang, H. Chen, F. Q. Zhang, Z. H. Huang, H. L. Wang, *Sol. Energy* **2019**, *188*, 750-759.
[73] H. Y. Wang, C. Y. Gao, R. Li, Z. K. Peng, J. H. Yang, J. Gao, Y. P. Yang, S. H. Li, B. J. Li, Z. Y. Liu, *ACS Sustainable Chem. Eng.* **2019**, *7*, 18744-18752.
[74] Y. Wang, P. Zheng, M. X. Li, Y. R. Li, X. Zhang, J. Chen, X. Fang, Y. J. Liu, X. L. Yuan, X. P. Dai, *Nanoscale* **2020**, *12*, 9669-9679.
[75] R. Acharya, B. Naik, K. Parida, *Beilstein J. Nanotechnol.* **2018**, *9*, 1448-1470.
[76] L. Wang, K. Fan, H. Chen, Q. Daniel, B. Philippe, H. Rensmo, L. Sun, *Catal. Today* **2017**, *290*, 73-77.
[77] M. Watanabe, *Sci. Technol. Adv. Mater.* **2017**, *18*, 705-723.
[78] Z. Li, Y. J. Chen, Y. K. Du, X. M. Wang, P. Yang, J. W. Zheng, *Int. J. Hydrogen Energy* **2012**, *37*, 4880-4888.
[79] M. W. Ha, M.-H. Park, J. Y. Hwang, J. Kim, D.-H. Kim, T.-W. Lee, Y.-H. Kim, *Dyes Pigm.* **2021**, *185*, 108880.
[80] K. L. Materna, R. H. Crabtree, G. W. Brudvig, *Chem. Soc. Rev.* **2017**, *46*, 6099-6110.
[81] Y.-J. Wang, G. Chang, Q. Y. Chen, G.-J. Yang, S.-Q. Fan, B. Z. Fang, *Chem. Commun.* **2015**, *51*, 685-688.
[82] A. C. Brooks, K. Basore, S. Bernhard, *Inorg. Chem.* **2013**, *52*, 5794-5800.
[83] I. N. Mills, H. N. Kagalwala, D. N. Chirdon, A. C. Brooks, S. Bernhard, *Polyhedron* **2014**, *82*, 104-108.

Chapter 4: Synthesis, Structures, Characterisations of Earth-Abundant Metal Complexes and Their Water-Splitting Hydrogen Generation Experiments in CdS Nanorod System

4.1 Introduction

Most traditional hydrogen generation systems via water-splitting use expensive noble metals[1-4] such as Pt,[5, 6] Ru,[7-9] and Ir,[10, 11] which significantly increases the cost. Therefore, substantial interest has been shown in developing catalysts based on earth-abundant metals instead of noble metals.[12] Catalysts using first-row transition metals such as Ni,[13-22] Zn,[23-25] and Cu[26-28] have been reported in hydrogen generation via water-splitting. Eisenberg and co-workers used molecular photosensitisers with nickel complexes (**Fig. 4.1**) to generate hydrogen with ascorbic acid (pH=4.5) as the SED in CH_3CN/H_2O solution. This system achieved satisfactory results (highest TON 7335) in 30 h.[29, 30] However, most earth-abundant metal complexes exhibit relatively moderate activity and low photostability in pure aqueous hydrogen generation systems.[31-34]

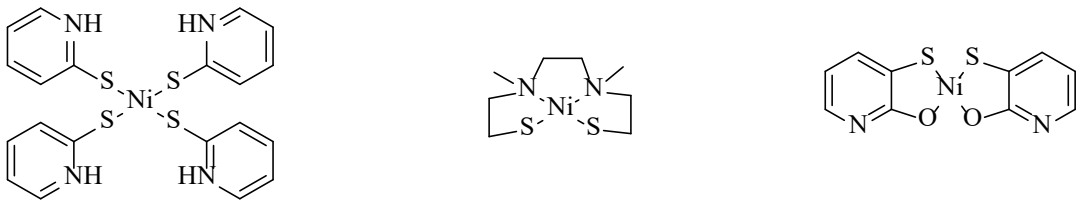

Fig. 4.1. Chemical structures of some Ni complexes for the evolution of light-driven hydrogen.

Transition metal complexes with salen-type Schiff base ligands are considered as promising electrode materials.[35] Salen-type ligands possess attractive properties, including high thermal stability, reversible electrochemical oxidation in a wide potential window, and high electronic conductivity.[36, 37] Thiasalen-type Schiff base (salen-type Schiff base with N2S2 ligating sites) has also attracted wide attention and has been applied in several fields, such as in organic synthesis catalysts or photocatalysts.[38-40] The S atom in the thiasalen Schiff base can act as electron donors for coordination to the metal centre, improving the catalyst efficiency in hydrogen generation via water splitting.[30, 41] However, the influence of the substituent group on the structure and photocatalytic performance of these complexes has not been systematically investigated.[40] Salophen (*N*,*N*-bis(salicylidene)phenylenediamine), a ligand used extensively in coordination chemistry,[42] contains two phenolic hydroxyl groups that can form complexes with transition metals in different oxidation states with different coordination numbers and geometries.[43, 44] Combining salophen with metals allows tuning of the catalytic, optical, electrical, and biological properties of the resulting complexes.[45, 46] Application of these metal complexes in hydrogen generation systems using water-splitting is of significant interest. In this chapter, three different sets of earth-abundant metal complexes (**Fig. 4.2**) have been designed and synthesised for photocatalytic hydrogen evolution from water.

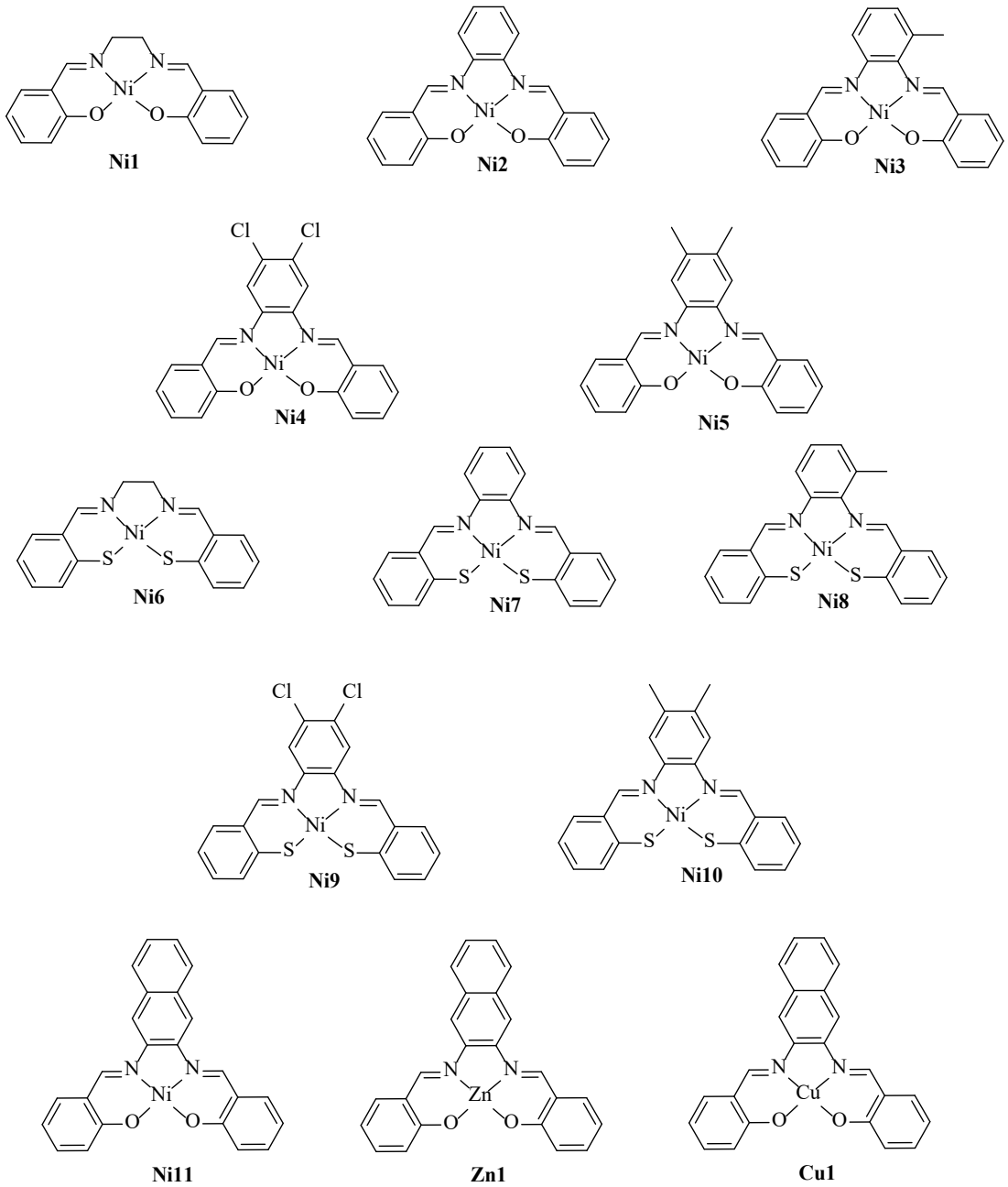

Fig. 4.2. Chemical structures of earth-abundant metal complexes **Ni1**–**Ni11, Zn1** and **Cu1**.

Common noble metal-free catalysts used as photosensitisers in hydrogen evolution reaction systems include dyes such as eosin Y (EY^{2-}),[47, 48] erythrosin B (EB^{2-}),[49] fluorescein (Fl^{2-}),[49] and rhodamine B,[50] along with nanorods (NRs) and quantum dots

(QDs).[51] It has been reported that CdS QDs and CdS NRs are highly efficient and robust photosensitisers for photocatalytic systems.[51-53] They possess larger light absorption coefficients, more tuneable optical and redox properties, higher efficiency for photoinduced electron transfer, broader absorption across the visible light spectrum, and higher photostability than molecular photosensitisers.[54, 55] Compared with CdS QDs, CdS NRs are easier to control in terms of size.[56] Hence, the potential application of CdS NRs in water-splitting hydrogen generation warrants further exploration.

Herein, efficient photocatalytic systems for hydrogen production in an aqueous solution composed of ligand-free CdS NRs and earth-abundant metal complexes are presented in this chapter. The electrochemical and photophysical properties of these metal complexes are investigated. The effects of the size and aspect ratio of the CdS NRs on the hydrogen production efficiency are also discussed.

4.2 Synthesis

4.2.1. Synthesis of CdS NRs

The solvothermal synthetic procedure is adopted from a previous study[57, 58] and the experiment details are described in **Chapter 7**. The synthetic pathway is shown in **Scheme 4.1**. The ligand-free CdS NRs samples were prepared via a solvothermal route in ethylenediamine under a solvent coordination molecular template (SCMT) mechanism.[57, 58]

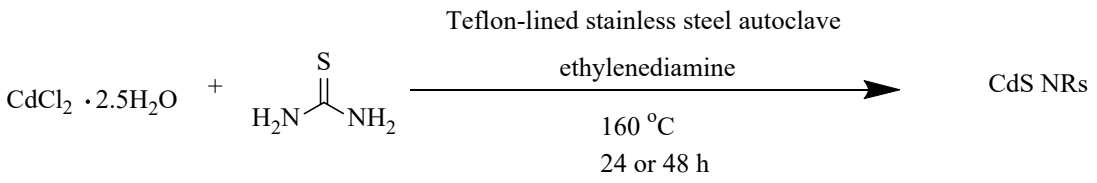

Scheme 4.1. Synthetic routes for CdS NRs.

4.2.2. Synthesis of metal complexes

Complexes **1**−**13** were synthesised according to procedures reported in the literature,[59, 60], as shown in **Schemes 4.2**–**4.4**. The procedures are described in **Chapter 7**. For complexes with an N2O2 structure (**Ni1**–**Ni5**, **Ni11**, **Zn1,** and **Cu1**), the Schiff base ligand was obtained from the reaction of 2-hydroxybenzaldehyde and the corresponding diamine. The final metal complex was synthesised from the reaction of the Schiff base and metal acetate. Complexes with an N2S2 structure (**Ni6**–**Ni10)**, 2,2'-disulfanediyldibenzaldehyde, bis(cyclooctadiene)nickel(0) were mixed with the corresponding diamine and stirred for 5 days to produce the final product. All complexes prepared in this study were stable as solids in air.

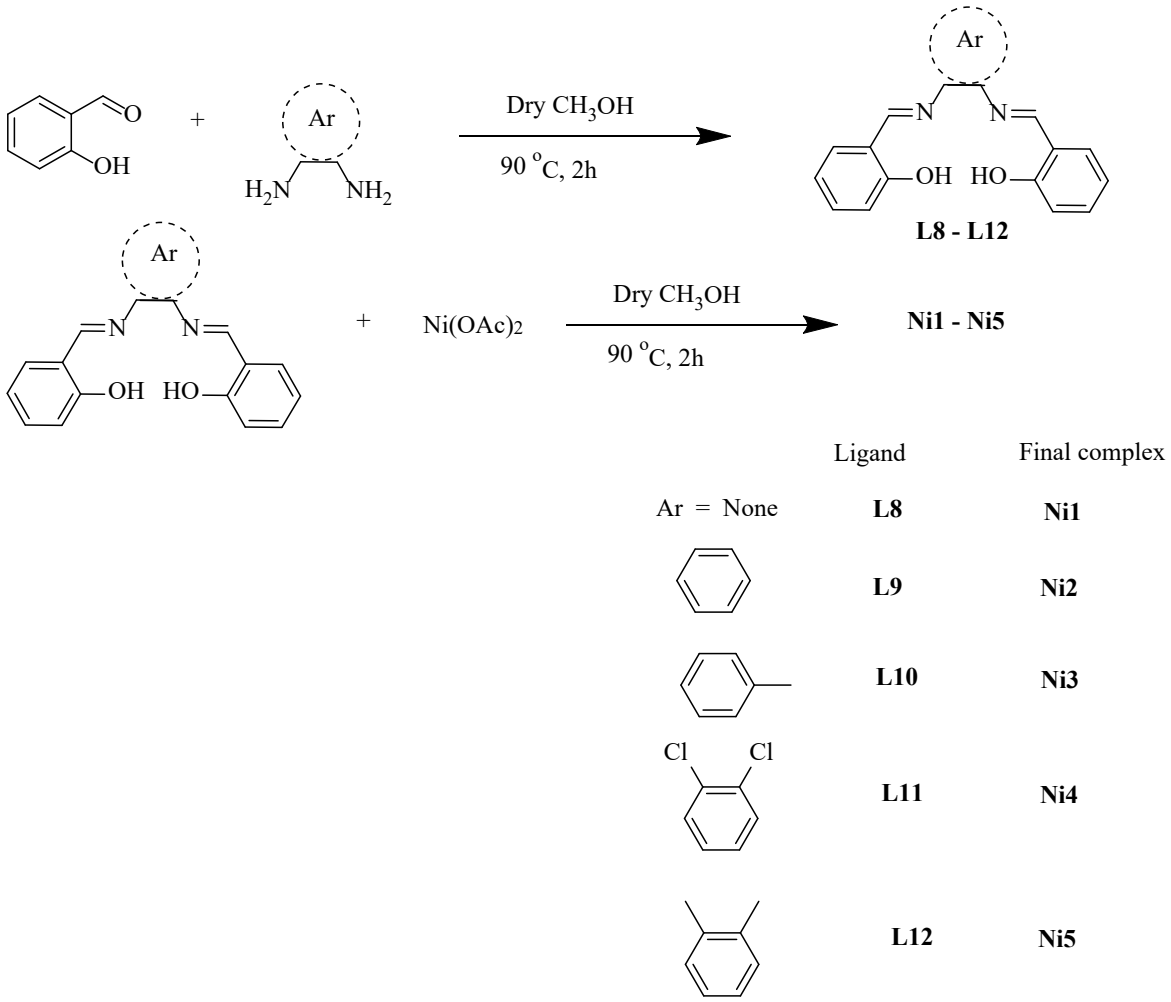

Scheme 4.2. Synthetic routes for **Ni1**–**Ni5** complexes.

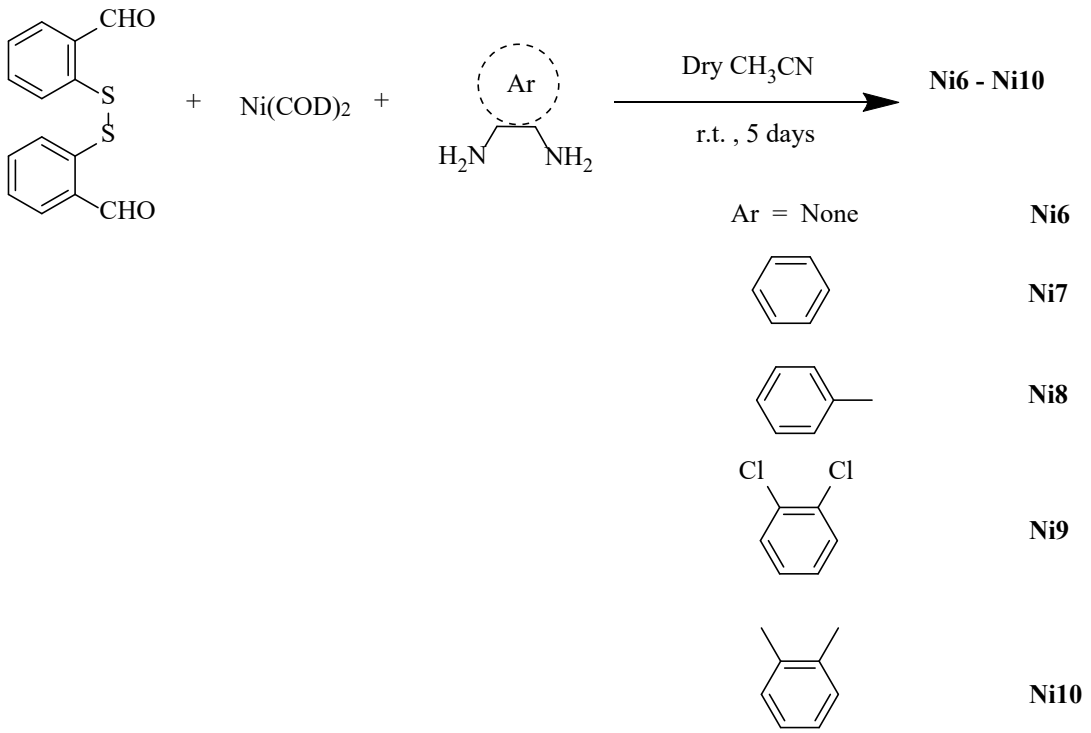

Scheme 4.3. Synthetic routes for **Ni6**–**Ni10** complexes.

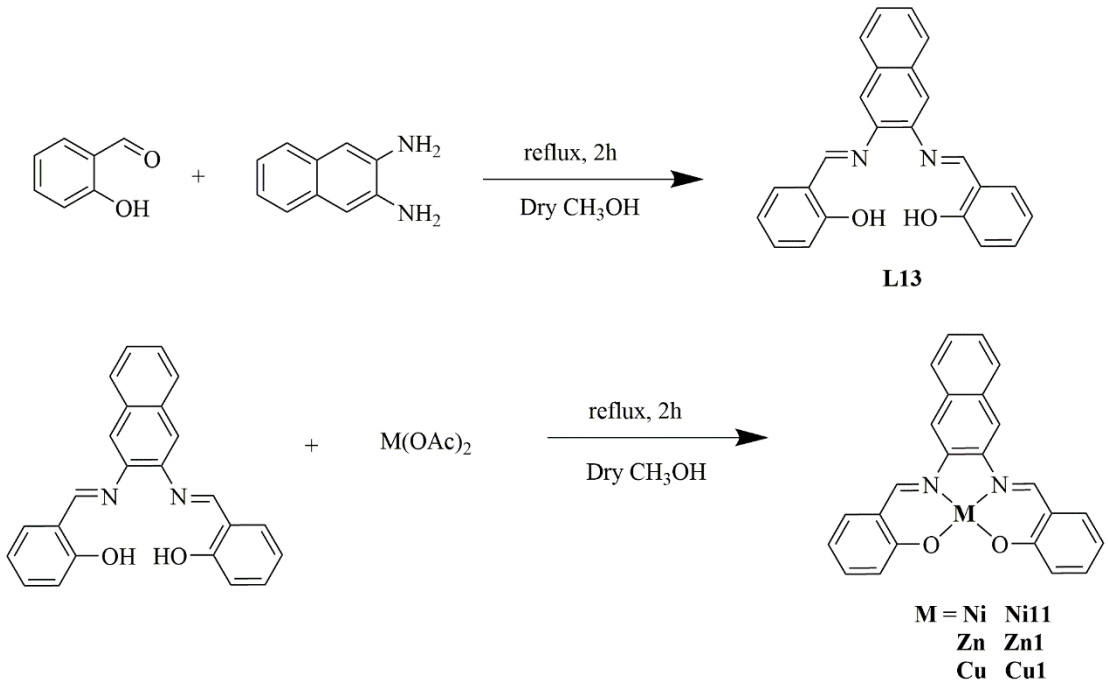

Scheme 4.4. Synthetic routes for **Ni11**, **Zn1** and **Cu1** complexes.

4.3 Spectroscopic Characterisation

All organic Schiff bases exhibited characteristic ^{1}H NMR spectra, indicating a clear structure for each compound. **Fig. 4.3** shows the ^{1}H NMR spectrum for compound **L13** with a signal at 9.08 ppm attributed to a hydroxyl proton. [61]

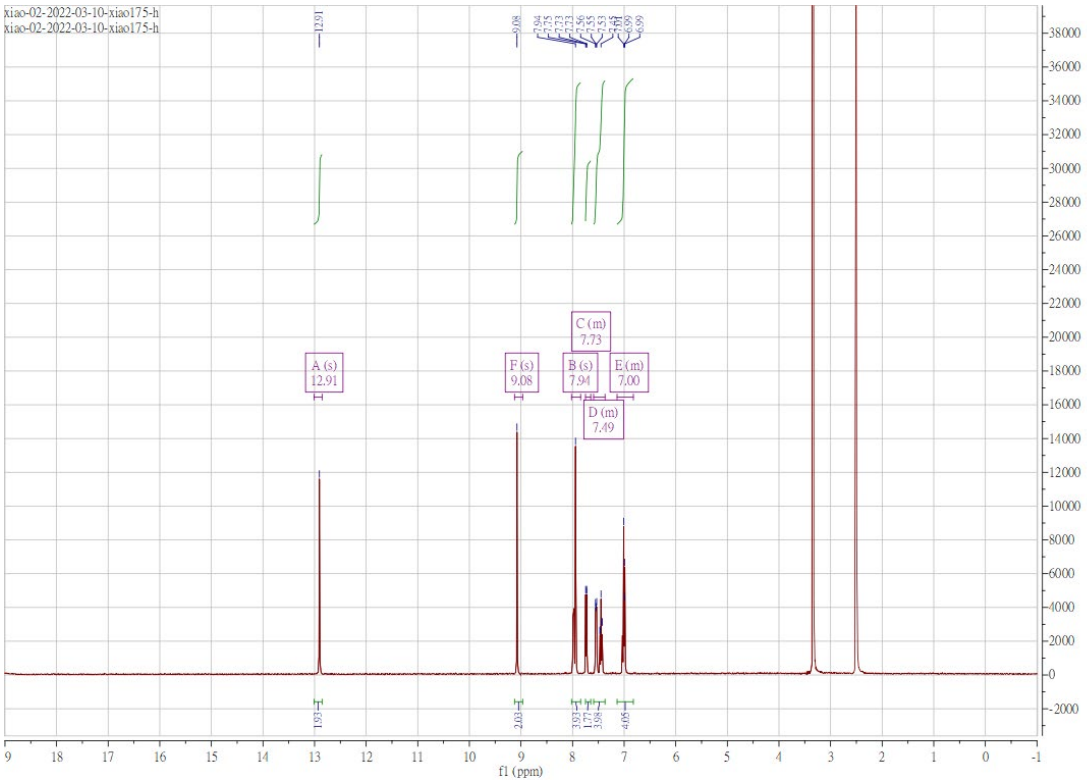

Fig. 4.3. ^{1}H NMR spectrum of compound **L13** in DMSO-d6.

With the poor solubility of the final metal complexes, only ^{13}C NMR data for organic Schiff bases could be obtained. The carbon NMR spectra show the structures. **Fig. 4.4** shows the ^{13}C NMR spectrum for compound **L13**.

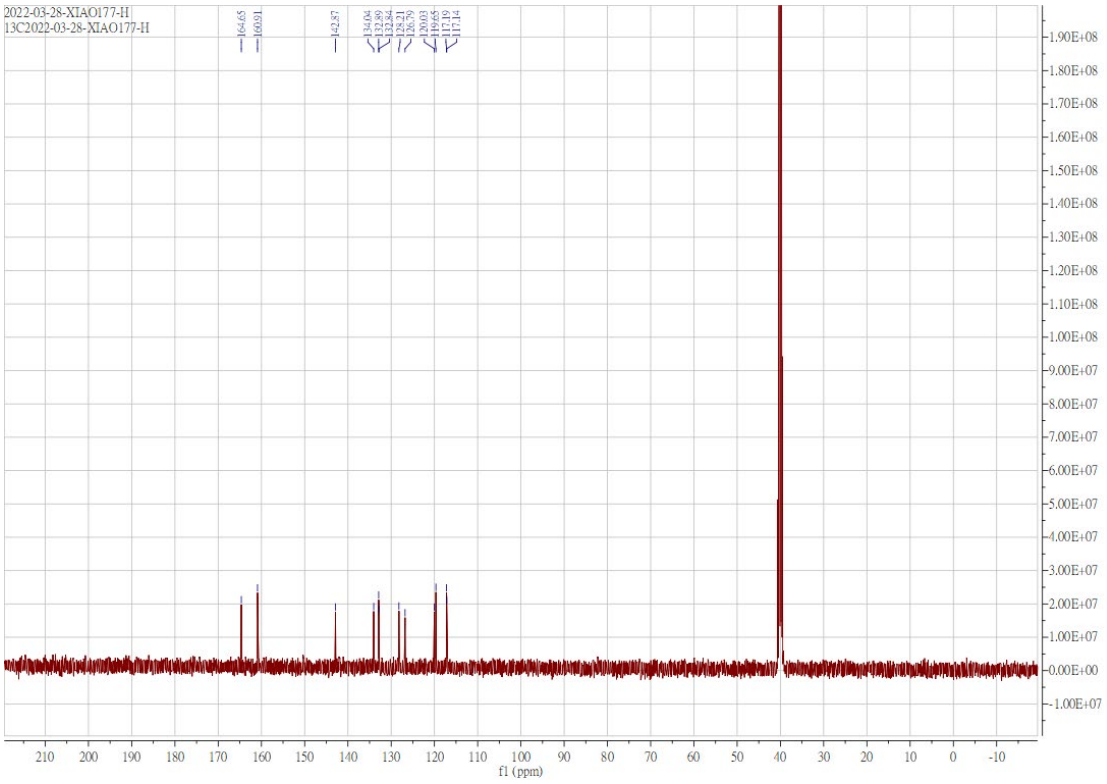

Fig. 4.4. ^{13}C NMR spectrum of compound **L13** in DMSO-d6.

The metal complexes were also characterised by ^{1}H NMR spectroscopy, indicating a clear structure. **Fig. 4.5** shows the ^{1}H NMR spectrum for complex **Zn1**. The signal at 9.90 ppm corresponds to the proton of the azomethine linkage. [61]

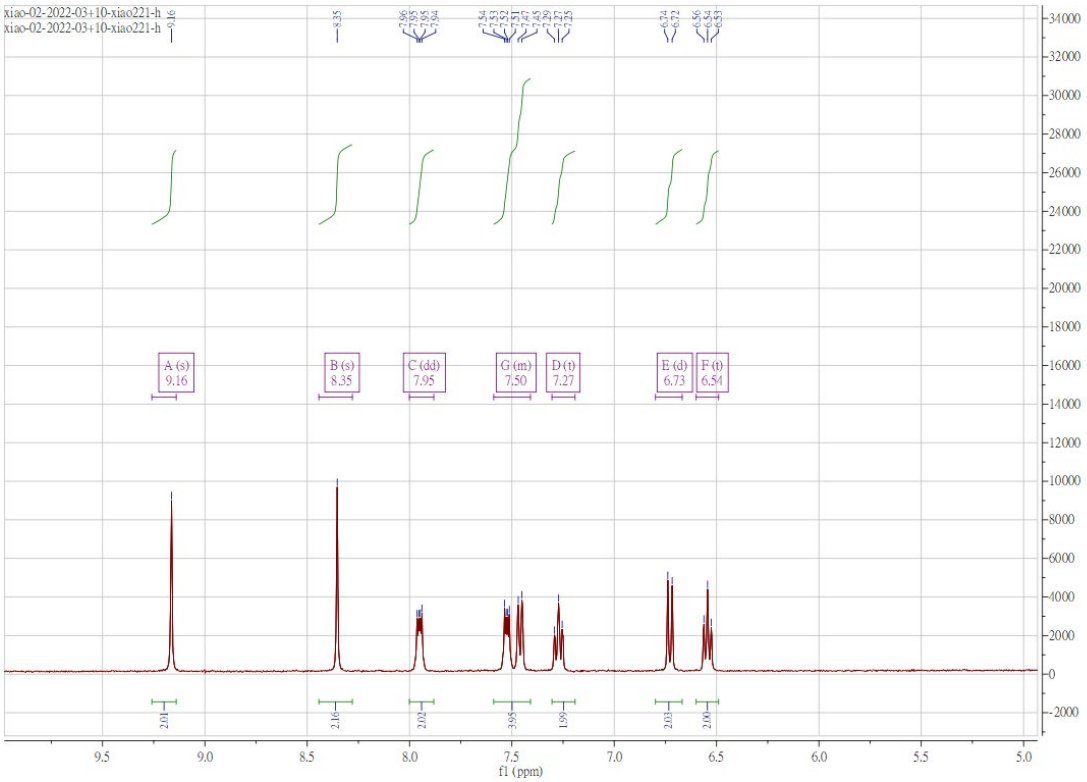

Fig. 4.5. ^{1}H NMR spectrum of complex **Zn1** in DMSO-d6.

4.4 Mass Spectroscopy Characterisation

High-resolution liquid chromatography–electrospray ionisation–quadrupole time-of-flight mass spectrometry measurements were conducted to confirm the structures of all ligands and final metal products. **Fig. 4.6** and **Fig. 4.7** show the MS results for compound **L8** and complex **Ni7**, respectively, as representative examples. The results match the molecular ion peaks and indicate the correct structures.

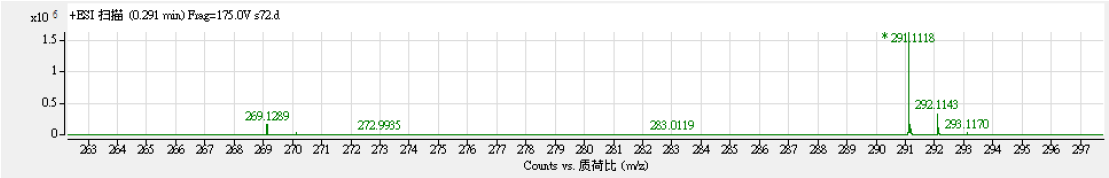

Fig. 4.6. MS profile of compound **L8**.

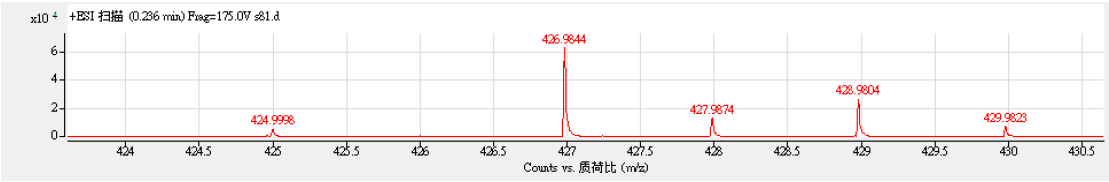

Fig. 4.7. MS profile of complex **Ni7**.

4.5. Scanning Electron Microscopy Characterization of the CdS NRs

Scanning electron microscopy (SEM) characterisation of CdS NRs was performed. **Fig. 4.8** shows SEM images of the CdS NRs prepared at 160 °C for solvothermal reaction times of 24 h and 48 h. The sample obtained at 160 °C for 24 h [CdS NRs (L/D = 12)] exhibits a nanorod morphology with an average length of 320 nm. Doubling the solvothermal reaction time [CdS NRs (L/D = 18)] also results in a nanorod morphology but with a significant increase in the average length of CdS NRs, reaching 550 nm. It was found that the CdS NRs (L/D = 12) and CdS NRs (L/D = 18) both retain diameters of approximately 25–30 nm. All of the characterisation information supports the conclusion that the obtained nanomaterials are composed of Cd and S atoms with crystalline order [57, 58, 62, 63]. These CdS NRs appear as a yellow powder (**Fig. 4.9**).

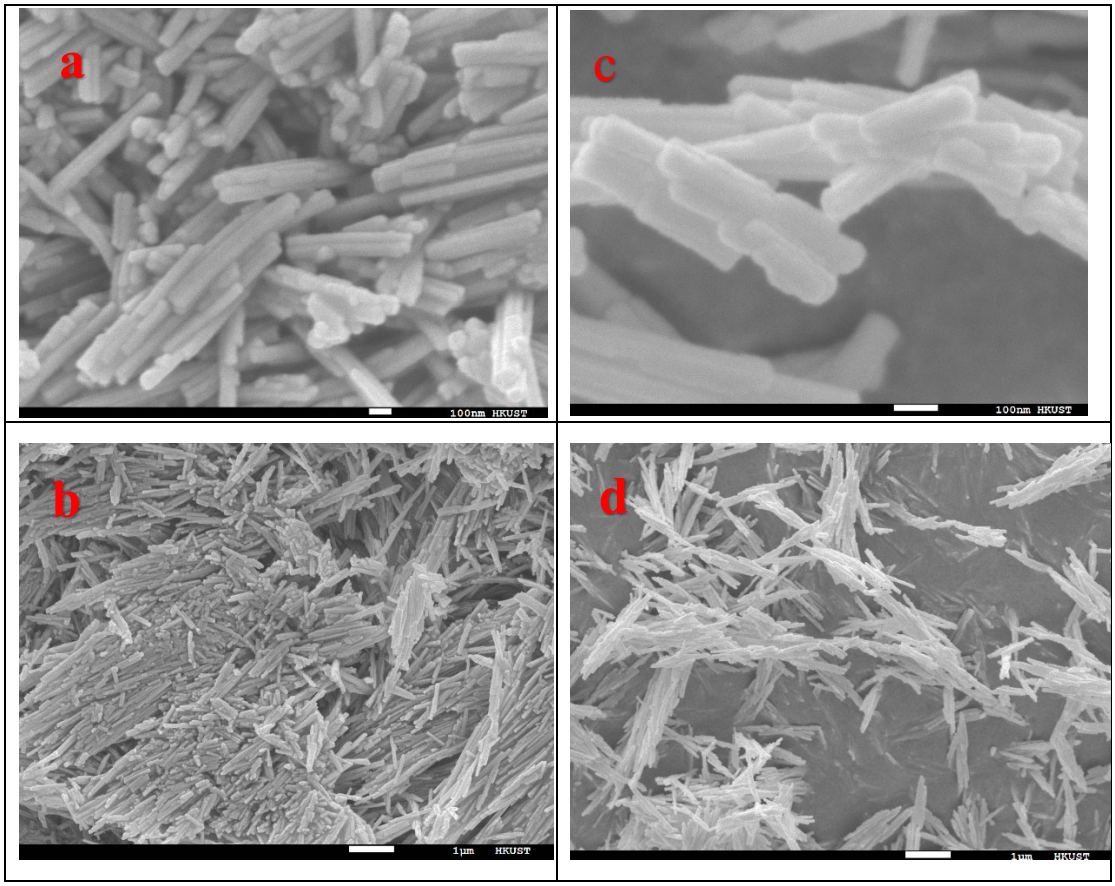

Fig. 4.8. SEM images of (a,b) CdS NRs (L/D = 12) and (c,d) CdS NRs (L/D = 18).

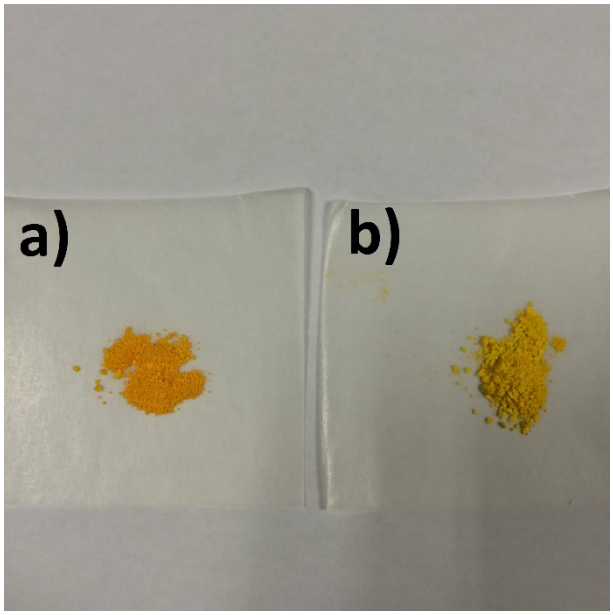

Fig. 4.9. Photo image illustrating the appearance of (a) CdS NRs (L/D = 12) and (b) CdS NRs (L/D = 18).

4.6 Photophysical Properties

One of the key factors determining the hydrogen production ability of a water-splitting system is the absorptivity. **Fig. 4.10** to **Fig. 4.12** show the UV–Vis absorption spectra of the **Ni1–Ni5, Ni6**–**Ni10**, as well as **Ni11, Zn1**, **Cu1** complexes, respectively, in DMSO solution and the corresponding spectral data are listed in **Table 4.1**.

In general, the high-energy bands from 260 to 340 nm correspond to spin-allowed intraligand (π–π*) transitions.[64] The broad low-energy bands with maxima ranging from 350 to 430 nm correspond to spin-allowed d–d transitions of the metal atoms.[64] Compared with complex **Ni1**, **Ni2** to **Ni5** exhibited a slight red shift at 260–340 nm, due to the addition of the phenyl functional group. The introduction of the electron withdrawing chloro functional groups into the phenyl ring resulted in a lower absorptivity for complex **Ni4** at 260–340 nm. Compared with the spectra of **Ni3** and **Ni5** complexes, the effect of the number of methyl groups on the phenyl absorption ability appears to be very marginal. The same trend is the observed for complexes **Ni6**–**Ni10**.

Compared with **Ni11**, the absorption bands at 350–430 nm for complexes **Zn1** and **Cu1** exhibited small red shifts, due to the increased electron delocalisation of the macrocycle in the complexes.[65] Notably, complex **Ni11** exhibited a slightly higher ε for these absorption bands compared with the other complexes, which is desirable for enhancing the photocatalytic HER performance. Furthermore, complex **Ni11** displayed one additional absorption band at 430–530 nm, which originated from the d orbitals of the Ni(II) ion involved in the electronic transitions,[61, 65, 66] and could promote the hydrogen

production.

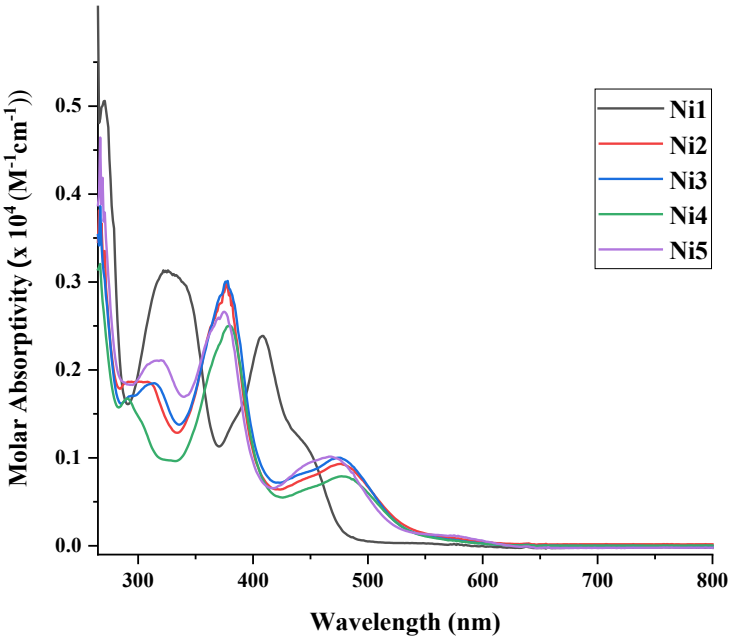

Fig. 4.10. UV-Vis absorption spectra of complexes **Ni1**–**Ni5** in DMSO at 293 K.

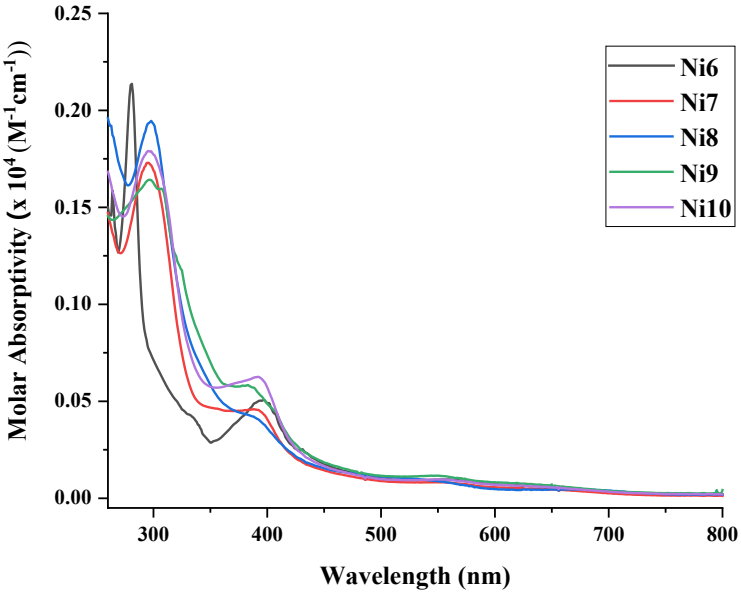

Fig. 4.11. UV-Vis absorption spectra of complexes **Ni6–Ni10** in DMSO solution at 293 K.

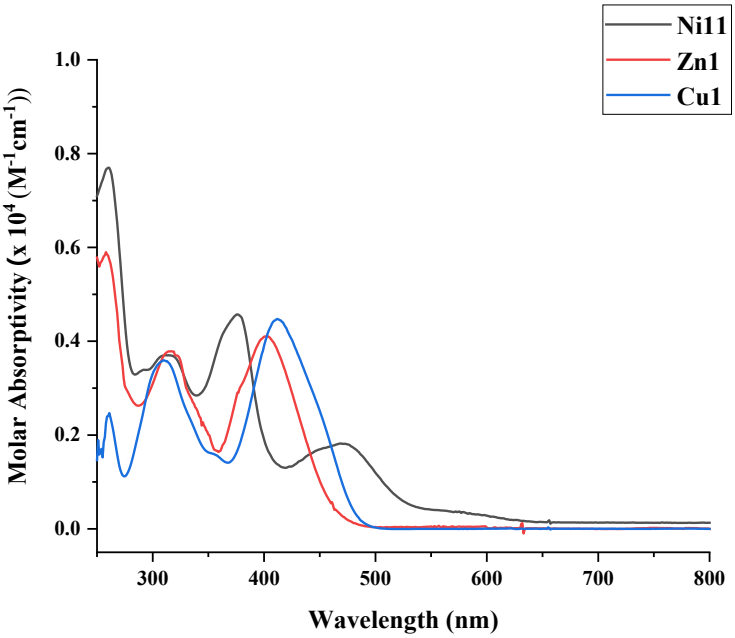

Fig. 4.12. UV-vis absorption spectra of complexes **Ni11**, **Zn1,** and **Cu1** in DMSO solution at 293 K.

Table 4.1. UV-vis absorption parameters of complexes **Ni1 - Ni11, Zn1** and **Cu1** in DMSO at 293 K.

Complex	λ_{max}/nm ($\varepsilon/10^5$ M^{-1} cm^{-1})	λ_{onset}/nm
Ni1	270(0.51), 325(0.32), 409(0.23), 452(0.10)	490
Ni2	295(0.19), 376(0.29), 475(0.09)	571
Ni3	317(0.19), 378(0.30), 476(0.10)	554
Ni4	292(0.17), 377(0.25), 481(0.08)	519
Ni5	321(0.21), 375(0.27), 472(0.10)	559
Ni6	282(0.21), 397(0.06),	506
Ni7	296(0.17), 395(0.05)	502
Ni8	297(0.20), 394(0.04)	506
Ni9	298(0.16), 385(0.06)	515
Ni10	297(0.18), 395(0.06)	506
Ni11	259 (0.77), 310 (0.37), 376 (0.46), 472 (0.18)	546
Zn1	259 (0.59), 314 (0.38), 403 (0.41)	495
Cu1	261 (0.24), 311 (0.36), 412 (0.45)	506

4.7 Density Functional Theory Calculations

Density Functional Theory calculation for three selective metal complexes **Ni11 Zn1** and **Cu1** have been performed. DFT was computed with the B3PW91-D3BJ functional and the def2-TZVPP basis set for all the complexes, which provided insight into the energy level for hydrogen generation. As for the calculated HOMO energy levels (**Fig. 4.13** and **Table 4.2**), the orbital energies vary from –5.68, –5.77 and –5.73 eV, respectively, for complexes **Ni11**, **Zn1** and **Cu1**, indicating that the HOMOs were affected by the uncoupled spin electrons. The number of uncoupled spin electrons are 3 for Ni, 0 for Zn, and 1 for Cu, which further elevated the HOMO energy and lessened the HOMO-LUMO gap from 3.20 of Complex **Ni11**, 3.28 of complex **Zn1** and 3.22 of Complex **Cu1**, which coincides with the CV experimental results (**Table 4.3**). The narrowest energy gap between HOMO and LUMO of complex **Ni11** might be the key

factor impacting the hydrogen catalysis.[67]

Table 4.2. Calculated HOMO, LUMO, and energy gap (ΔE) of the complexes **Ni11**, **Zn1** and **Cu1**. All values were calculated in eV.

Compounds	HOMO	LUMO	ΔE
Ni11	–5.68	–2.48	3.20
Zn1	–5.77	–2.49	3.28
Cu1	–5.73	–2.51	3.22

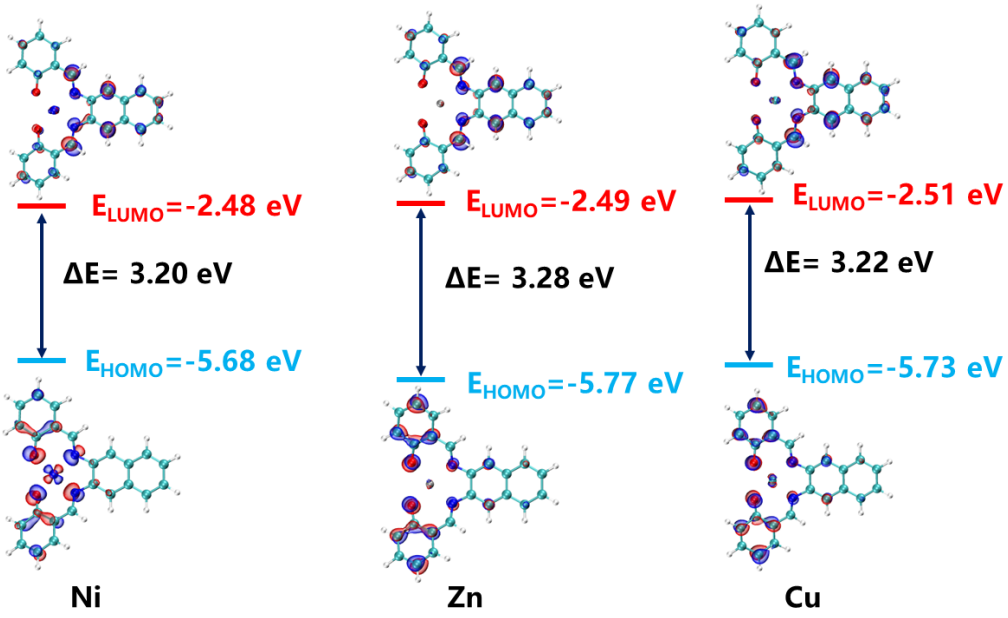

Fig. 4.13. Frontier molecular orbitals of complexes **Ni11**, **Zn1** and **Cu1** calculated at the B3PW91-D3BJ functional.

4.8 Electrochemical Properties

Cyclic voltammetry experiments of complexes **Ni1**–**Ni11, Zn1** and **Cu1** were performed in a conventional three-electrode configuration. A glassy carbon electrode functioned as the working electrode, platinum wire as the counter electrode, and

Ag/AgCl served as the reference electrode. The measurements were performed in dry DMSO containing 0.1 M tetrabutylammonium hexafluorophosphate at a scan rate of 100 mV s^{-1}. The corresponding electrochemical behaviours of the complexes are recorded in **Table 4.3**.

Table 4.3. Electrochemical data and energy levels of complexes **Ni1**–**Ni11, Zn1** and **Cu1**.

Complex	E_{Ox}^{Max} /V	E_{HOMO} [a] /eV	E_g [b] /eV	E_{ox*} [c] /V	E_{LUMO} [d] /eV
Ni1	0.29	–5.09	2.53	–2.24	–2.56
Ni2	0.39	–5.19	2.17	–1.78	–3.02
Ni 3	0.39	–5.19	2.24	–1.85	–2.95
Ni 4	0.40	–5.20	2.39	–1.99	–2.81
Ni 5	0.36	–5.16	2.22	–1.86	–2.94
Ni 6	0.22	–5.02	2.45	–2.23	–2.57
Ni 7	0.38	–5.18	2.47	–2.09	–2.71
Ni 8	0.23	–5.03	2.45	–2.22	–2.58
Ni 9	0.49	–5.29	2.41	–1.92	–2.88
Ni 10	0.25	–5.05	2.45	–2.20	–2.60
Ni 11	0.33	–5.13	2.28	–1.95	–2.85
Zn1	0.55	–5.35	2.49	–1.94	–2.86
Cu1	0.54	–5.34	2.46	–1.92	–2.88

[a] Calculated from $-(E_{Ox}^{Max} + 4.8)$; [b] Energy bandgap (E_g) determined from the onset of the absorption spectrum; [c] $E_{ox*} = E_{Ox}^{Max} - E_g$; and [d] $E_{LUMO} = E_{HOMO} + E_g$.

If the lowest unoccupied molecular orbital of the metal complexes is more positive than that of the conduction band of the semiconductor, while the corresponding highest occupied molecular orbital is more negative than that of the SED, then the electron injection and charge separation would be more efficient[68]. All the metal complexes in our water-splitting systems meet the requirements for electron injection and charge separation, which allows effective dye regeneration[69].

The addition of the phenyl functional group to the salen structure also reduced its

electron density and oxidation potential.[70] Therefore, complex **Ni1** had the lowest oxidation potential in **Ni1** to **Ni5**. Owing to the introduction of electron-withdrawing nature of chlorine substituents on the phenyl group, complex **Ni4** showed the highest oxidation potential in **Ni1** to **Ni5**, which may reduce its photocatalytic activity.[70] Notably, the CV data of complexes **Ni3** and **Ni5** were almost identical, indicating the migrally effect of methyl functional group in the phenyl. The same situation can be observed in complexes **Ni6** to **Ni10**. Furthermore, complex **Ni11** exhibited the smallest energy gap, which favors charge transfer and may facilitate hydrogen generation by water splitting.[67] **Zn1** exhibited the largest energy gap compared with **Ni11** and **Cu1**, which coincides with the DFT calculation results (**Fig. 4.13** and **Table 4.2**).

4.9 Electrochemical Impedance Spectroscopy

To further investigate the charge recombination properties of those metal complexes, electrochemical impedance spectroscopy was employed.[71] The measurements were conducted on an electrochemical workstation according to the previous work. [72, 73] Ag/AgCl was served as reference electrode with the platinum electrode as a counter electrode, 0.5 M Na_2SO_4 solution as electrolyte and fluorine-doped tin oxide glass (FTO) with the attachment of metal complex as the working electrode. The detail procedures can be found in **Chapter 7**. The EIS Nyquist plots for complexes by three systems, **Ni1** to **Ni5, Ni6** to **Ni10**, and **Ni11, Zn1**, **Cu1** were shown in **Fig. 4.14** to **Fig. 4.16** respectively. It is well known that a smaller arc radius in the Nyquist plot indicates

lower electric charge transfer resistance that leads to better HER performance.[72-75] Overall, the arc radius of complex **Ni1**, complex **Ni6** and complex **Ni11** were smaller than those of others in their systems, which suggested that it has better charge carrier transfer properties.[76] Compared with complexes **Ni1** and **Ni6**, **Ni1** was smaller than complex **Ni6**, indicating a better charge transfer ability and better hydrogen generation performance. The results match well with the water-splitting hydrogen production performance.

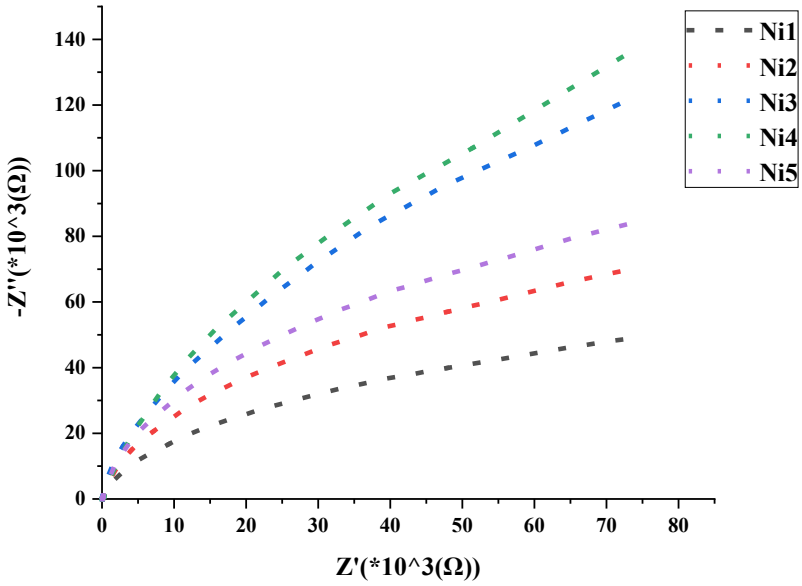

Fig. 4.14. EIS Nyquist plots for complexes **Ni1** to **Ni5**.

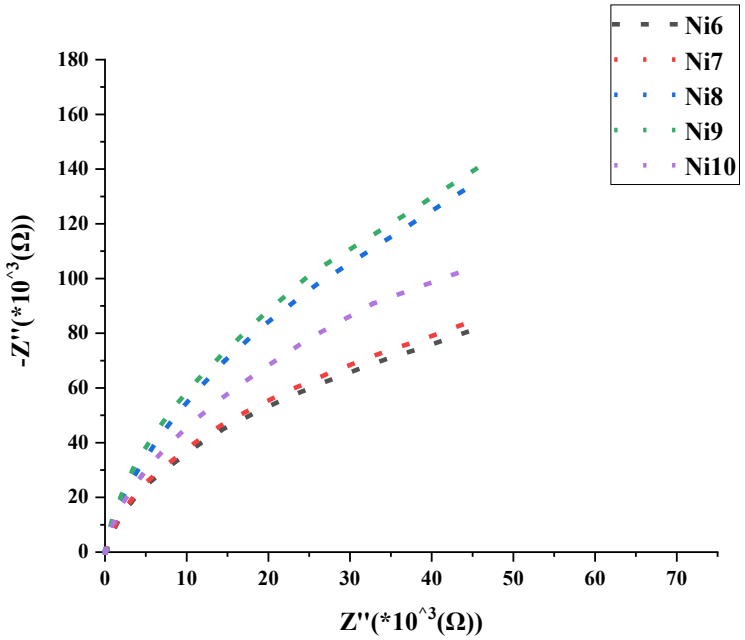

Fig. 4.15. EIS Nyquist plots for complexes **Ni6** to **Ni10**.

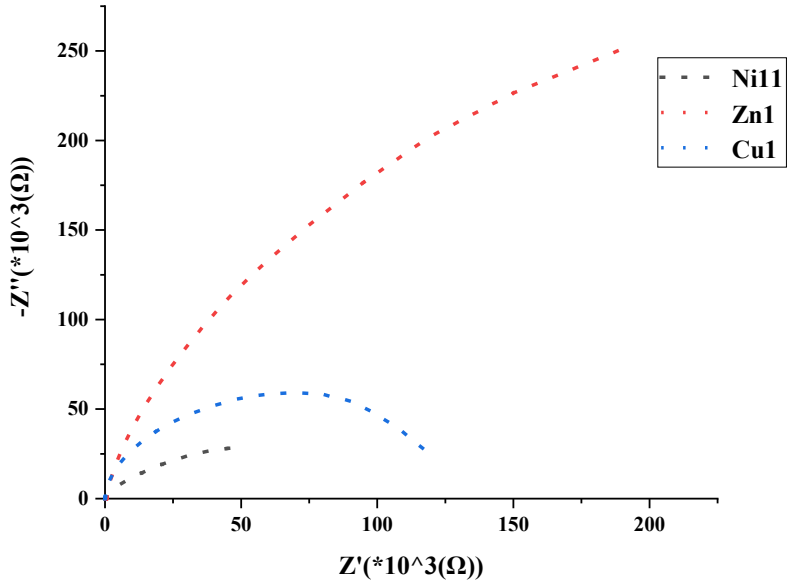

Fig. 4.16. EIS Nyquist plots for complexes **Ni11**, **Zn1** and **Cu1**.

4.10 Photocurrent Measurements

Photocurrent measurements were carried out to test the stability and charge separation

efficiency of the present metal complexes.[77] Photocurrent measurements were conducted according to a previously reported procedures.[78] Ag/AgCl was served as reference electrode with the platinum electrode as a counter electrode, 0.5 M Na_2SO_4 solution as electrolyte and fluorine-doped tin oxide glass (FTO) with the attachment of metal complex as the working electrode. All the experiments were conducted under a 300W Xe lamp condition. The detail procedure can be found in **Chapter 7**. A uniform and fast photocurrent response during light-on and light-off tests denotes stable photocatalytic activities,[79] while a higher photocurrent density reveals a higher charge separation efficiency,[80] which can enhance hydrogen production. **Fig. 4.17** to **Fig. 4.19** show the photocurrent responses of the three groups of complexes examined in the previous section under visible light irradiation for six on–off cycles, which can provide clear evidence of the electron transfer efficiency within the formed heterojunctions.[78] A photocurrent response during the light-on and light-off test of a complex indicates a stable photocatalytic activity.[79] Complexes **Ni1**, **Ni6**, and **Ni11** exhibited a significantly higher photocurrent intensity during irradiation, and the photocurrent decreased with a noticeable delay after the light was turned off, which indicated a superior charge separation efficiency and hydrogen generation performance.[78, 79, 81, 82] Compared with **Ni1** and **Ni6**, complex **Ni1** showed a higher photocurrent intensity, indicating a superior hydrogen generation performance.

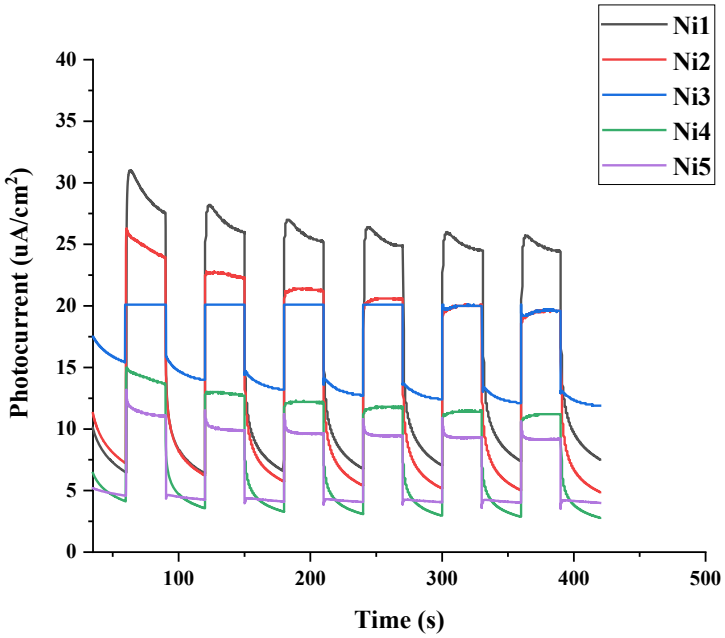

Fig. 4.17. Photocurrent responses of complexes **Ni1**–**Ni5**.

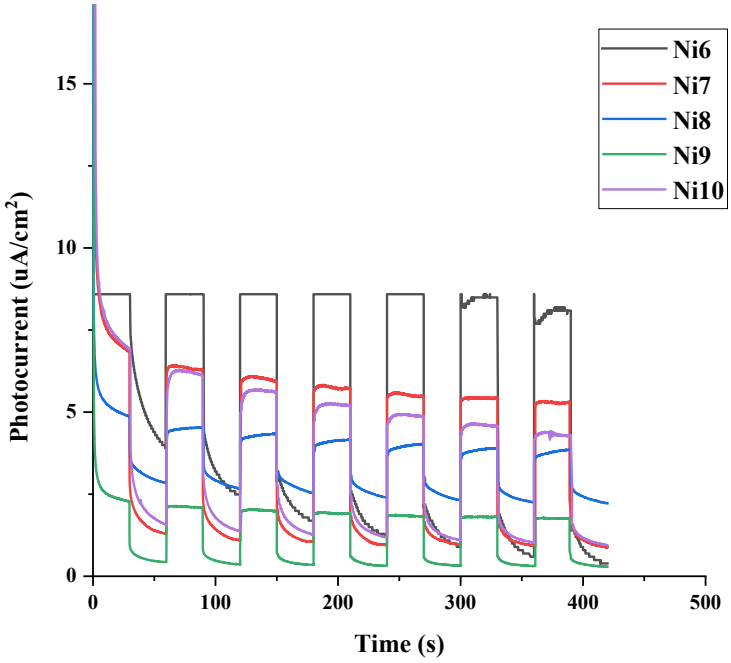

Fig. 4.18. Photocurrent responses of complexes **Ni6**–**Ni10**.

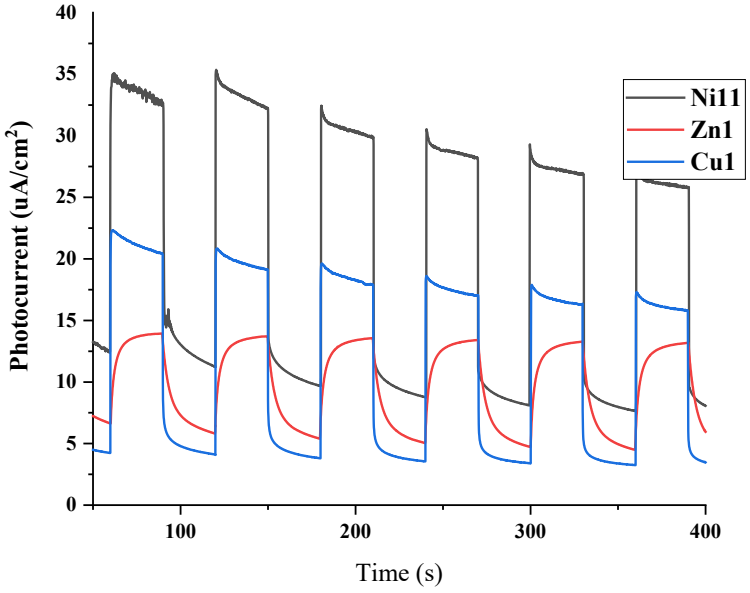

Fig. 4.19. Photocurrent responses of complexes **Ni11**, **Zn1**, and **Cu1**.

4.11 Light-Driven Hydrogen Generation of Metal Complex and CdS NRs

Hydrogen was produced by photocatalytic water splitting system with metal complex as catalyst and CdS NRs as photosensitizers. The detailed procedural references for photocatalytic water-splitting hydrogen production studies can be found in the experimental section of **Chapter 7**. The water splitting system containing 1 mg of CdS NRs, 10 μM of metal complex and 5 mL of 0.5 M of AA (pH = 4). The hydrogen generation curves (vs. time) for each sample are shown in **Fig. 4.20** to **Fig. 4.25**. The corresponding data (TON, TOF, TOF_i, and $Activity_i$) are tabulated in **Tables 4.4** and **4.5.**

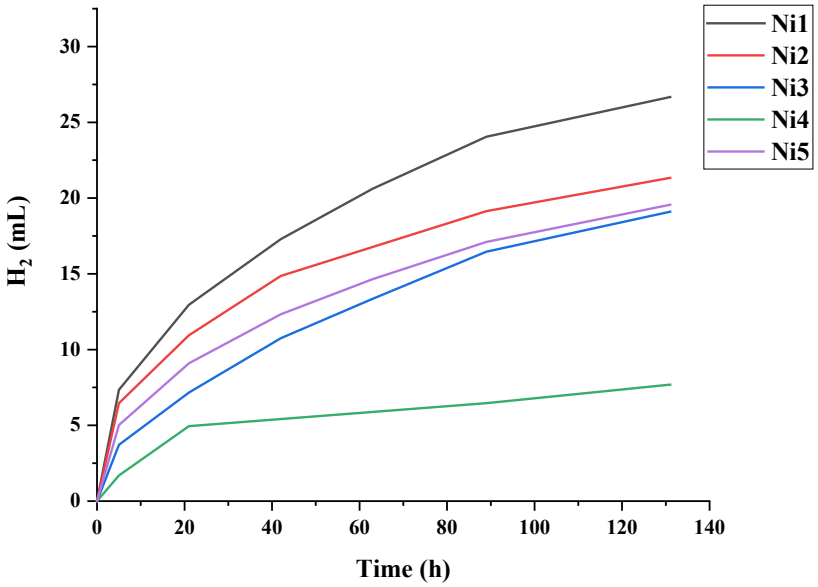

Fig. 4.20. Photocatalytic hydrogen evolution by metal complex **Ni1** to **Ni5** (10 μM), /CdS NR (L/D = 12; 1 mg) /AA (0.5 M) catalysts from H_2O (5 mL) upon irradiation with a 470-nm LED at 19°C, pH 4.0, and 1 atm initial pressure of N_2:CH_4 (80:20 mol%) with CH_4 as the internal standard for hydrogen quantification via GC.

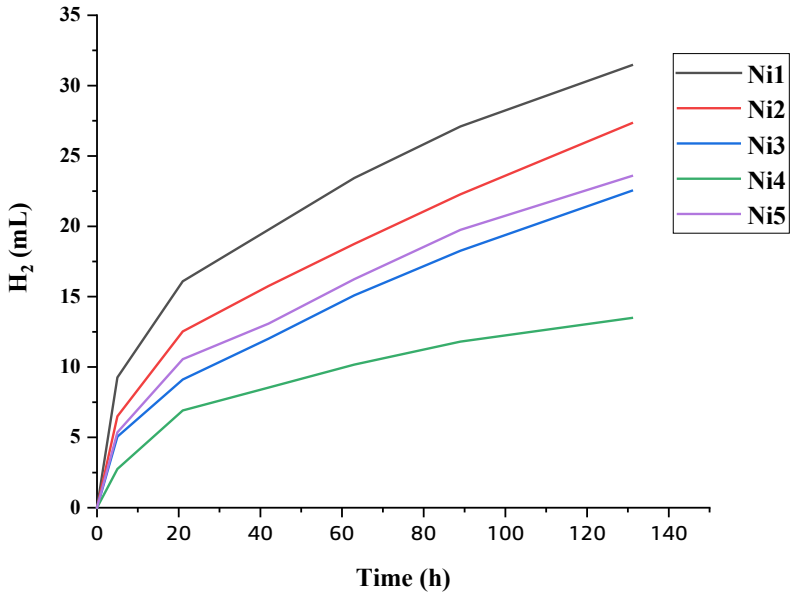

Fig. 4.21. Photocatalytic hydrogen evolution by metal complex **Ni1** to **Ni5** (10 μM)/ CdS NR (L/D = 18; 1 mg)/ AA (0.5 M) catalysts from H_2O (5 mL) upon irradiation

with a 470-nm LED at 19°C, pH 4.0, and 1 atm initial pressure of N_2:CH_4 (80:20 mol%) with CH_4 as the internal standard for hydrogen quantification via GC.

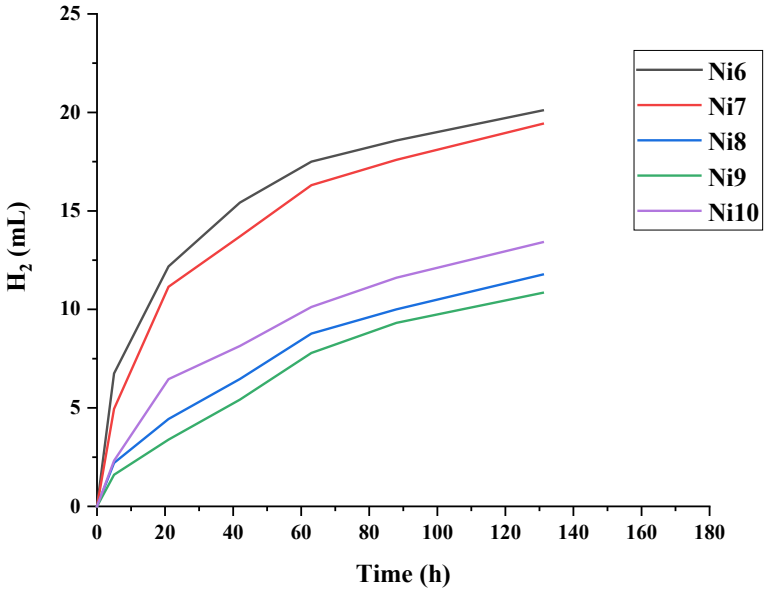

Fig. 4.22. Photocatalytic hydrogen evolution by metal complexes **Ni6** to **Ni10** (10 μM), /CdS NR (L/D = 12; 1 mg) /AA (0.5 M) catalysts from H_2O (5 mL) upon irradiation with a 470-nm LED at 19°C, pH 4.0, and 1 atm initial pressure of N_2:CH_4 (80:20 mol%) with CH_4 as the internal standard for hydrogen quantification via GC.

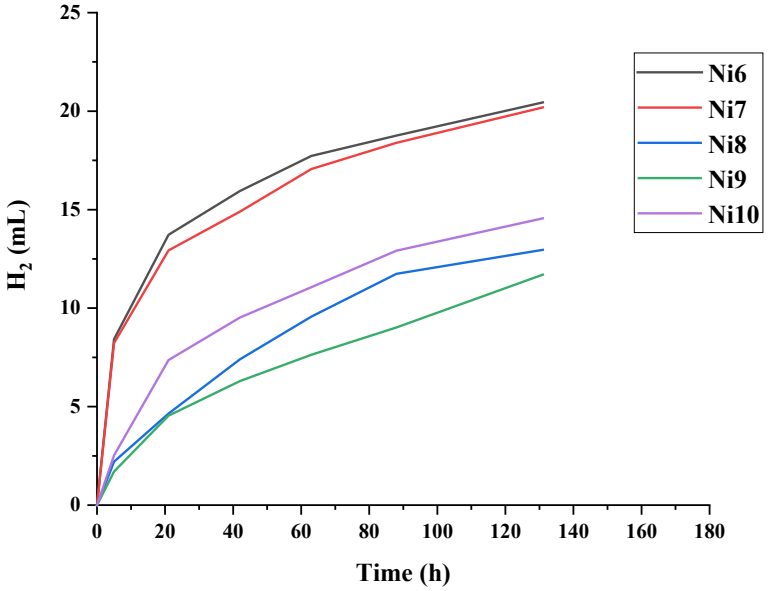

Fig. 4.23. Photocatalytic hydrogen evolution by metal complex **Ni6** to **Ni10** (10 μM)/ CdS NR (L/D = 18; 1 mg)/ AA (0.5 M) catalysts from H_2O (5 mL) upon irradiation with a 470-nm LED at 19°C, pH 4.0, and 1 atm initial pressure of N_2:CH_4 (80:20 mol%) with CH_4 as the internal standard for hydrogen quantification via GC.

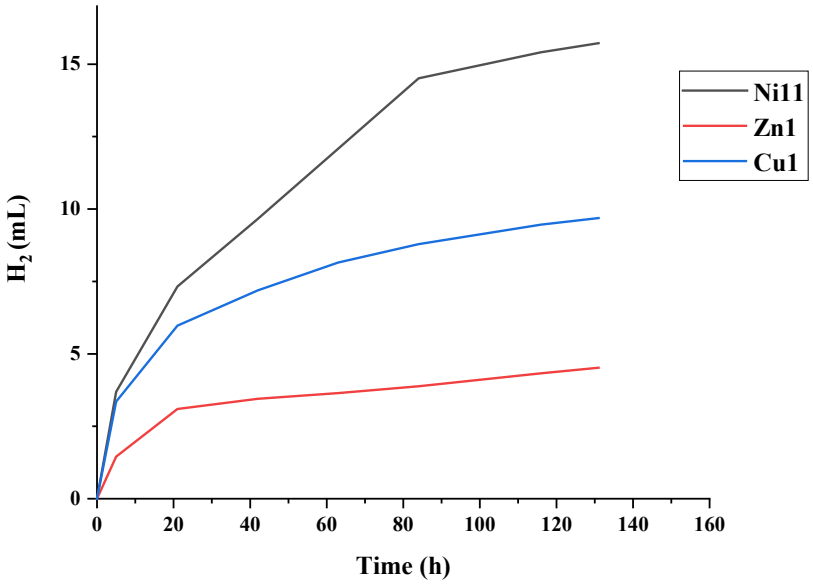

Fig. 4.24. Photocatalytic hydrogen evolution by metal-salophen complex **Ni11**, **Zn1** and **Cu1** (10 μM) / CdS NR (L/D = 12; 1 mg) / AA (0.5 M) catalysts from H_2O (5 mL)

upon irradiation with a 470 nm LED at 19°C, pH 4.0, and 1 atm initial pressure of N_2:CH_4 (80:20 mol%) with CH_4 as the internal standard for hydrogen quantification via GC.

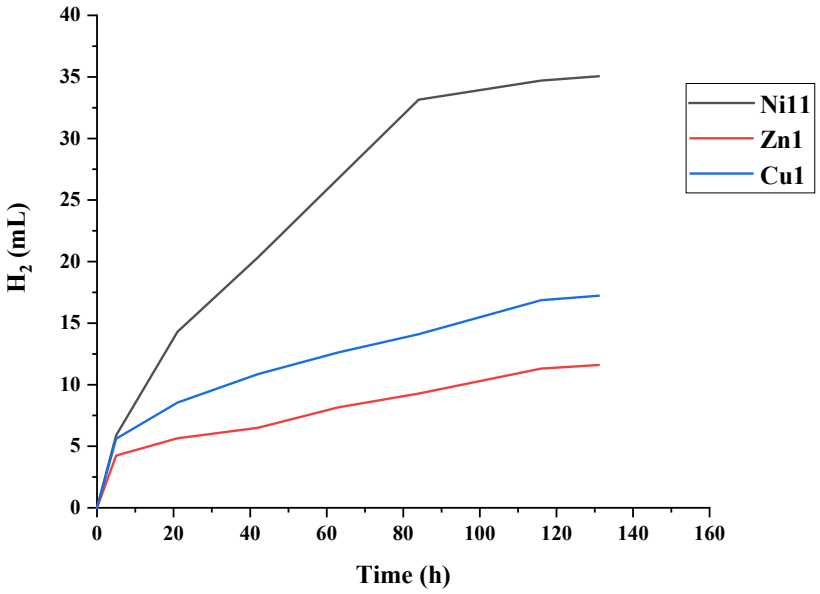

Fig. 4.25. Photocatalytic hydrogen evolution by metal complex **Ni11**, **Zn1** and **Cu1** (10 μM) / CdS NR (L/D = 18; 1 mg) / AA (0.5 M) catalysts from H_2O (5 mL) upon irradiation with a 470 nm LED at 19°C, pH 4.0, and 1 atm initial pressure of N_2:CH_4 (80:20 mol%) with CH_4 as the internal standard for hydrogen quantification via GC.

Table 4.4. Photocatalytic hydrogen evolution by metal-salophen complex/ CdS NRs (L/D = 12)/ AA catalysts under blue light irradiation.

Complex	Time /h	H_2 /mL	TON[a]	TOF[b] /h^{-1}	TOF_i[c] /h^{-1}	$Activity_i$[d] /µmol g^{-1} h^{-1}
Ni1	131	26.7	43538	332.4	2399.1	599763
Ni 2	131	21.3	34830	265.9	2111.0	527745
Ni 3	131	19.1	31181	238.0	1214.1	303531
Ni 4	131	7.7	12548	95.8	551.9	137981
Ni 5	131	19.6	31928	243.7	1640.4	410112
Ni 6	131	20.1	32828	250.6	2204.1	551018
Ni 7	131	19.4	31715	242.1	1617.9	404487
Ni 8	131	11.8	19213	146.7	721.0	180242
Ni 9	131	10.8	17704	135.1	523.7	130920
Ni 10	131	13.4	21894	167.1	758.0	189504
Ni 11	131	15.7	25676	196.0	1205.2	301291
Zn1	131	4.5	7384	56.4	473.6	118397
Cu1	131	9.7	15814	120.7	1095.0	273747

[a] Turnover number for hydrogen is calculated as twice the number of moles of hydrogen produced divided by the number of mols of the complex catalyst. [b] Turnover frequency calculated per hour. [c] Initial turnover frequency for the first five hours. [d] The photocatalytic activity of the system is defined as the number of micromoles of H_2 evolved per mg of CdS NRs loaded per hour.

Table 4.5. Photocatalytic hydrogen evolution by metal-salophen complex/ CdS NRs (L/D = 18)/ AA catalysts under blue light irradiation.

Dye	Time /h	H_2 /mL	TON[a]	TOF[b] /h^{-1}	TOF_i[c] /h^{-1}	$Activity_i$[d] /µmol g^{-1} h^{-1}
Ni1	131	31.5	51350	392.0	3022.9	755737
Ni 2	131	27.3	44624	340.6	2123.0	530740
Ni 3	131	22.5	36785	280.8	1650.1	412533
Ni 4	131	13.5	22027	168.1	899.6	224896
Ni 5	131	23.6	38502	293.9	1749.7	437425
Ni 6	131	20.4	33376	254.8	2751.5	687885
Ni 7	131	20.2	32960	251.6	2686.2	671558
Ni 8	131	13.0	21163	161.6	721.3	180320
Ni 9	131	11.7	19107	145.9	557.4	139338
Ni 10	131	14.6	23772	181.5	824.4	206102
Ni 11	131	35.1	57238	436.9	1923.7	480918
Zn1	131	11.6	18947	144.6	1386.5	346629
Cu1	131	17.2	28128	214.7	1831.8	457951

[a] Turnover number for hydrogen calculated as twice the number of moles of hydrogen produced divided by the number of mols of the complex catalyst. [b] Turnover frequency calculated per hour. [c] Initial turnover frequency for the first five hours. [d] The photocatalytic activity of the system is defined as the number of micromoles of H_2 evolved per mg of CdS NRs loaded per hour.

For **Ni1** to **Ni5**, among the catalytic systems containing CdS NRs (L/D = 12), those with complexes **Ni1** and **Ni2** achieved TONs of 43538 and 34830 and TOFs of 332.5 and 265.9 h^{-1} over 131 h, respectively. The catalytic systems containing longer CdS NRs (L/D = 18) produced much higher amounts of hydrogen than those with shorter CdS NRs (L/D = 12). In particular, the highest TON and TOF values of 51350 and 392.0 h^{-1}, respectively, were obtained with the system based on complex **Ni1**, followed by that containing complex **Ni2** (44624 and 340.6 h^{-1}, respectively) in the systems containing longer CdS NRs (L/D = 18). The TON values of the complexes followed the order **Ni1** > **Ni2** > **Ni5** > **Ni3** > **Ni4**. The system based on complex **Ni1** exhibited the highest hydrogen generation activity using either aspect ratio of CdS NRs, because the diamine bridge did not contain an electron-withdrawing phenyl group.[35, 40, 83] The replacement of hydrogen with an electron-donating methoxy group in the phenyl rings resulted in an enhanced hydrogen generation compared with the electron-withdrawing chloro functional group, as seen for complexes **Ni5** and **Ni4**.[84] The comparison of the hydrogen generation data of complexes **Ni3** and **Ni5** showed that the number of methyl groups had a very minor effect on the phenyl absorption ability.

For **Ni6** to **Ni10**, among the catalytic systems containing CdS NRs (L/D = 12), those with complexes **Ni6** and **Ni7** achieved TONs of 32828 and 31715 and TOFs of 250.6 and 242.1 h^{-1} over 131 h, respectively. The catalytic systems containing longer CdS

NRs (L/D = 18) produced the highest TON and TOF values of 33376 and 254.8 h^{-1}, respectively, with the system based on complex **Ni6**. The TON values of the complexes followed the order **Ni6** > **Ni7** > **Ni10** > **Ni8** > **Ni9**. The trend is the same as **Ni1** to **Ni5**. Furthermore, complex **Ni1** showed a higher hydrogen generation performance than complex **Ni6**, as confirmed by the EIS and photocurrent tests.

For **Ni11**, **Zn1** and **Cu1**, among the catalytic systems containing CdS NRs (L/D = 12), complexes **Ni11** and **Cu1** achieved TONs of 25676 and 15814 h^{-1} and TOFs of 196.0 and 120.7 h^{-1} over 131 h, respectively. The catalytic systems containing longer CdS NRs (L/D = 18) produced much higher amounts of hydrogen than those with shorter CdS NRs (L/D = 12). More specifically, the highest TON and TOF values of 57238 and 436.9 h^{-1} were obtained with the system containing complex **Ni11**, followed by that containing complex **Cu1** (28128 and 214.7 h^{-1}, respectively) in systems containing longer CdS NRs (L/D = 18). The TON values of the complexes followed the order **Ni11** > **Cu1** > **Zn1**. It possibly due to the superior charge transfer ability of **Ni11**, which has been confirmed by the EIS and photocurrent characterization (**Fig. 4.14** and **Fig. 4.19**, respectively).

The photocatalytic water-splitting experiments for control system with only selective metal complex **Ni11**, **Zn1**, **Cu1** or CdS NRs have been performed. The experimental results are shown in **Table 4.6**. From the results, it can be found that the photocatalytic hydrogen generation of the water splitting system containing both metal complex and CdS NRs are more efficient. The mechanism of metal complex and CdS NRs were described in the discussion part. Furthermore, we revisited the literatures and sorted out

the performance data of similar metal complexes as **Table 4.7**. Compared with the reported literatures, my complexes, especially **Ni11**, shows a significant improvement in light-driven hydrogen evolution. These results also indicate that the metal complexes with CdS NRs system are promising candidate for highly stable photocatalytic application.

Table 4.6. Photocatalytic hydrogen evolution by **Ni11**, **Zn1**, **Cu1**, CdS NRs and AA under blue light irradiation.

Complex	Time /h	H_2 /mL
Ni11	131	3.2
Zn1	131	1.5
Cu1	131	2.1
CdS (L/D = 12)	84	0.9
CdS (L/D = 18)	84	1.0

Table 4.7. Performance for light-driven hydrogen evolution based on different metal complex systems.

Metal complex	Water splitting system	H_2 performance	refer
NiS	CdS nanorods/g-C_3N_4 and TEOA (10 vol%)	H_2 (mmol g^{-1} h^{-1}) 2.563	[85]
NiS	g-C_3N_4/WO_3 and TEOA (15 vol%)	H_2 (mmol g^{-1} h^{-1}) 2.929	[86]
Ni-salen	g-C_3N_4 nanosheet/ CdS Na_2S and Na_2SO_3	H_2 (mmol g^{-1} h^{-1}) 22.3	[87]

$[BzPyN(CH_3)_2]_2[Ni(i\text{-}mnt)_2]$	CdS clusters, and ascorbic acid (pH 3.7).	H_2 (mmol g^{-1} h^{-1}) 1.375 (around)	[88]
Ni-salen	EY^{2-} and 10 % TEA, at pH 10.	H_2 (mmol g^{-1} h^{-1}) 0.27 (around)	[89]
Ni-salen	EY^{2-} and 10 % TEOA, at pH 10.	H_2 (mmol g^{-1} h^{-1}) 0.039 (around)	[89]
[Cu(TMPA)Cl]Cl	Ir-based PS, and 0.45 M TEA in Ar saturated CH_3CN/H_2O (9 : 1)	TON 4400	[90]
$[Cu(Cl\text{-}TMPA)Cl_2]$	Ir-based PS, and 0.45 M TEA in Ar saturated CH_3CN/H_2O (9 : 1)	TON 10014	[90]
$[Cu(DQPD)]_2$	fluorescein and [TEA] = 0.36 M in DMF/H_2O (80 : 20, v/v).	TON 2135	[91]
[6,60 -(2,20 -bipyridine-6,60 -diyl)bis(1,3,5-triazine2,4-diamine)](nitrato-O)copper	1 M for triethanolamine (TEOA), 0.1 M for (HBF_4), 0.56 M for water, 0.1 mM for the photosensitizer $[Ru(bpy)_3]$ $(PF_6)_2$	TON 47	[92]
N_3O_2 type of Schiff-base with Zn	MeOH/H_2O (1:2; *v/v*; 6.0 mL) solution containing 1.0 mM EY^{2-} and TEOA (10% v/v)	H_2 (mmol g^{-1} h^{-1}) 0.012 (around)	[93]
N_3O_2 type of Schiff-base with Zn	MeOH/H_2O (1:2; *v/v*; 6.0 mL) solution containing 1.0 mM EY^{2-} and TEA (10% v/v)	H_2 (mmol g^{-1} h^{-1}) 0.005 (around)	[93]
Complex Ni11	CdS NRs, and ascorbic acid (pH 4).	TON 57239 H_2 (mmol g^{-1} h^{-1}) 48	This study

4.12. Discussions

4.12.1. Proposed mechanism for hydrogen generation by metal complexes with N2O2 structure

The photocatalytic hydrogen generation mechanism of some similar metal complexes has been reported in previous studies.[48, 77, 94] In the current study, as shown in **Fig. 4.26**, under visible light irradiation, Cd^{2+} was excited to $*Cd^{2+}$; the latter received an electron from ascorbic acid (AscH-) to form Cd^{+}. After that, the present metal complex underwent an endothermic one-electron reduction by Cd^{+} to form **Int1**, which was then protonated at one of the phenolic O atoms by bonding with H_3O^{+} to form **Int2**. In the following step, a proton was transferred from the phenolic O atom of $\mathbf{M^{2+}}$ **(Int2)** to form $\mathbf{M^{3+}}$ **(Int3)**, which mediates with H_2O as a proton shuttle because of its low activation energy. As Cd^{+} transferred electrons to $\mathbf{M^{3+}}$ to form Cd^{2+}, $\mathbf{M^{3+}}$ transformed into $\mathbf{M^{2+}}$ **(Int4)**. Finally, the $\mathbf{M^{2+}}$ ion with the negatively charged H^{-} species was readily protonated, releasing a H_2 molecule and thus regenerating hydrogen.

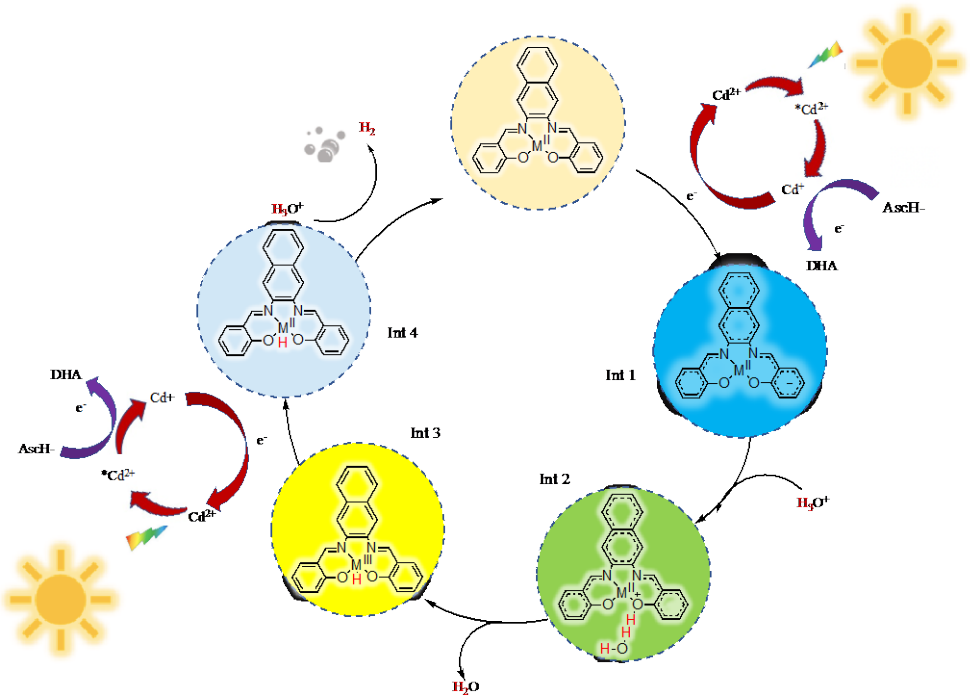

Fig. 4.26. Proposed pathway for hydrogen generation by complexes with N2O2 structure.

4.12.2. Proposed mechanism for hydrogen generation by metal complexes with N2S2 structure

The photocatalytic hydrogen generation mechanism of some similar metal complexes has been described in previous studies.[95] As shown in **Figure 4.27**, the one-electron reduction of the nickel complex generated a Ni^{I} species, $[(bpte)Ni]^{+}$. Then, the incorporation of H^{+} resulted in the formation of a Ni^{III}-H species, $[H\text{-}Ni^{III}(bpte)]^{2+}$. An additional one-electron reduction of the Ni^{III}-H species led to the formation of a Ni^{II}-H species, $[H\text{-}Ni^{II}(bpte)]^{+}$. Further incorporation of H^{+} into $[H\text{-}Ni^{II}(bpte)]^{+}$ produced a H_2 molecule and regenerated the starting complex.

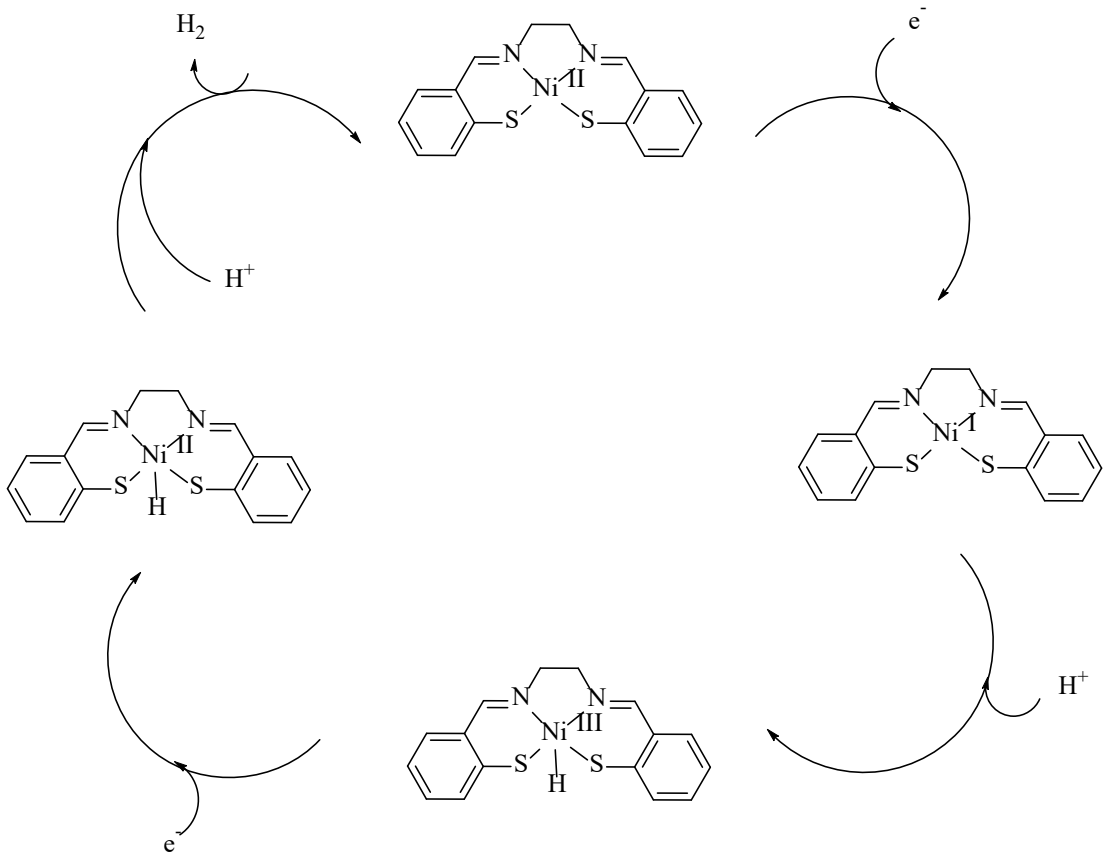

Fig. 4.27. Proposed pathway for hydrogen generation by complexes with N2S2 structure.

4.13. Conclusions

Three sets of earth-abundant metal–salophen complexes were synthesised and combined with ligand-free CdS NRs to create photocatalytic water-splitting hydrogen generation systems in a fully aqueous environment. The highest TON and TOF values of 51350 and 392.0 h^{-1}, respectively, were obtained with the system containing complex **Ni1**. The catalytic system containing complex **Ni6** achieved TON and TOF values of 33376 and 254.8 h^{-1} over 131 h, respectively. The system based on complex **Ni11** (at 10 μM concentration) and the longer CdS NRs (L/D = 18) achieved a TON of 57239

h^{-1} and a TOF of 436.9 h^{-1} over 131 h of blue light irradiation. These three systems exhibited the best performance among their respective sets of metal complexes. The present results indicate that controlling the length of the CdS NRs could be a potential route to optimise the efficiency of photocatalytic systems for water-splitting hydrogen generation.

4.14. References

[1] V. Artero, M. Chavarot-Kerlidou, M. Fontecave, *Angew. Chem. Int. Edit.* **2011**, *50*, 7238-7266.

[2] V. S. Thoi, Y. Sun, J. R. Long, C. J. Chang, *Chem. Soc. Rev.* **2013**, *42*, 2388-2400.

[3] C.-B. Li, Z.-J. Li, S. Yu, G.-X. Wang, F. Wang, Q.-Y. Meng, B. Chen, K. Feng, C.-H. Tung, L.-Z. Wu, *Energy Environ. Sci.* **2013**, *6*, 2597-2602.

[4] L.-Z. Wu, B. Chen, Z.-J. Li, C.-Tung, *Acc. Chem. Res.* **2014**, *47*, 2177-2185.

[5] P. Du, K. Knowles, R. Eisenberg, *J. Am. Chem. Soc.* **2008**, *130*, 12576-12577.

[6] W.-G. Wang, F. Wang, H.-Y. Wang, C.-H. Tung, L.-Z. Wu, *Dalton Trans.* **2012**, *41*, 2420-2426.

[7] S. Ott, M. Kritikos, B. Åkermark, L. Sun, *Angew. Chem. Int. Edit.* **2003**, *42*, 3285-3288.

[8] W.-N. Cao, F. Wang, H.-Y. Wang, B. Chen, K. Feng, C.-H. Tung, L.-Z. Wu, *Chem. Commun.* **2012**, *48*, 8081-8083.

[9] C.-H. Siu, C.-L. Ho, J. He, T. Chen, X. N. Cui, J. Z. Zhao, W.-Y. Wong, *J. Organomet. Chem.* **2013**, *748*, 75-83.

[10] K. He, N. Su, Y. Junting, Y. Liu, W. Xiong, Z. Hao, D. Ma, W. Zhu, *Tetrahedron* **2016**, *72*, 7164-7169.

[11] P.-Y. Ho, S.-Y. Lee, C. Kam, J. Zhu, G.-G. Shan, Y. Hong, W.-Y. Wong, S. Chen, *Adv. Healthcare Mater.* **2021**, *10*, 2100706.

[12] M. L. Helm, M. P. Stewart, R. M. Bullock, M. R. Dubois, D. L. Dubois, *Science* **2011**, *333*, 863-866.

[13] A. D. Wilson, R. K. Shoemaker, A. Miedaner, J. T. Muckerman, D. L. Dubois, M. R. Dubois, *Proc. Natl. Acad. Sci. U.S.A.* **2007**, *104*, 6951-6956.

[14] J. Kuczynska, *Russ. Lit.* **1990**, *27*, 253-258.

[15] U. J. Kilgore, J. A. Roberts, D. H. Pool, A. M. Appel, M. P. Stewart, M. R. Dubois, W. G. Dougherty, W. S. Kassel, R. M. Bullock, D. L. Dubois, *J. Am. Chem. Soc.* **2011**, *133*, 5861-5872.

[16] M. L. Helm, M. P. Stewart, R. M. Bullock, M. R. Dubois, D. L. Dubois, *Science* **2011**, *333*, 863-866.

[17] Z. J. Han, W. R. Mcnamara, M.-S. Eum, P. L. Holland, R. Eisenberg, *Angew. Chem. Int. Edit.* **2012**, *51*, 1667-1670.

[18] Z. J. Han, F. Qiu, R. Eisenberg, P. L. Holland, T. D. Krauss, *Science* **2012**, *338*, 1321-1324.

[19] Y. Yamada, T. Miyahigashi, H. Kotani, K. Ohkubo, S. Fukuzumi, *Energy Environ. Sci.* **2012**, *5*, 6111-6118.

[20] J.-M. Lei, S.-P. Luo, S.-Z. Zhan, S.-P. Wu, *Inorg. Chem. Commun.* **2018**, *95*, 158-162.

[21] Y.-J. Lei, S. Liu, G.-L. Hu, R. Hu, R.-T. Yan, Y.-B. Lu, H.-Y. Wang, *Int. J. Hydrogen Energy* **2019**, *44*, 20079-20084.

[22] X. L. Ho, H. Y. Shao, Y. Y. Ng, R. Ganguly, Y. P. Lu, H. S. Soo, *Inorg. Chem.*

2019, *58*, 1469-1480.
[23] I. P. Oliveri, G. Malandrino, *Dalton Trans.* **2014**, *43*, 10208-10214.
[24] G. Consiglio, S. Failla, I. P. Oliveri, R. Purrello, *Dalton Trans.* **2009**, 10426-10428.
[25] H.-Y. Yin, J. Tang, J.-L. Zhang, *Eur. J. Inorg. Chem.* **2017**, *2017*, 5085-5093.
[26] C.-Y. Chiang, K. Aroh, N. Franson, V. R. Satsangi, S. Dass, S. Ehrman, *Int. J. Hydrogen Energy* **2011**, *36*, 15519-15526.
[27] A. Paracchino, N. Mathews, T. Hisatomi, M. Stefik, S. D. Tilley, M. Grätzel, *Energy Environ. Sci.* **2012**, *5*, 8673-8681.
[28] C.-Y. Chiang, Y. Shin, S. Ehrman, *Energy Procedia* **2014**, *61*, 1799-1802.
[29] Z. Han, L. Shen, W. W. Brennessel, P. L. Holland, R. Eisenberg, *J. Am. Chem. Soc.* **2013**, *135*, 14659-14669.
[30] A. Mazzeo, S. Santalla, C. Gaviglio, F. Doctorovich, J. Pellegrino, *Inorg. Chim. Acta* **2021**, *517*, 119950.
[31] M. Wang, L. Chen, L. C. Sun, *Energy Environ. Sci.* **2012**, *5*, 6763-6778.
[32] P. W. Du, R. Eisenberg, *Energy Environ. Sci.* **2012**, *5*, 6012-6021.
[33] Y. Yan, B. Y. Xia, B. Zhao, X. Wang, *J. Mater. Chem. A* **2016**, *4*, 17587-17603.
[34] L. Yuan, C. Han, M.-Q. Yang, Y.-J. Xu, *Int. Rev. Phys. Chem.* **2016**, *35*, 1-36.
[35] X. Li, J. Li, F. Kang, *Ionics.* **2019**, *25*, 1045-1055.
[36] C. O'meara, M. P. Karushev, I. A. Polozhentceva, S. Dharmasena, H. Cho, B. J. Yurkovich, S. Kogan, J.-H. Kim, *ACS Appl. Mater. Interfaces* **2018**, *11*, 525-533.
[37] M. Novozhilova, E. Smirnova, M. Karushev, A. Timonov, V. Malev, O. Levin, *Russ. J. Electrochem.* **2016**, *52*, 1183-1190.
[38] Z. Han, F. Qiu, R. Eisenberg, P. L. Holland, T. D. Krauss, *Science* **2012**, *338*, 1321-1324.
[39] Y. Yang, M. Wang, L. Xue, F. Zhang, L. Chen, M. S. Ahlquist, L. Sun, *ChemSusChem* **2014**, *7*, 2889-2897.
[40] E. V. Alekseeva, I. A. Chepurnaya, V. V. Malev, A. M. Timonov, O. V. Levin, *Electrochim. Acta.* **2017**, *225*, 378-391.
[41] A. Das, Z. Han, W. W. Brennessel, P. L. Holland, R. Eisenberg, *ACS Catal.* **2015**, *5*, 1397-1406.
[42] P. Pfeiffer, E. Breith, E. Lübbe, T. Tsumaki, *Justus Liebigs Ann. Chem.* **1933**, *503*, 84-130.
[43] A. Erxleben, *Inorg. Chim. Acta.* **2018**, *472*, 40-57.
[44] J. C. Pessoa, I. Correia, *Coord. Chem. Rev.* **2019**, *388*, 227-247.
[45] J. Zhang, L. L. Xu, W.-Y. Wong, *Coord. Chem. Rev.* **2018**, *355*, 180-198.
[46] V. Brabec, O. Hrabina, J. Kasparkova, *Coord. Chem. Rev.* **2017**, *351*, 2-31.
[47] J. Dong, M. Wang, P. Zhang, S. Yang, J. Liu, X. Li, L. Sun, *J. Phys. Chem. C* **2011**, *115*, 15089-15096.
[48] X. Li, M. Wang, D. Zheng, K. Han, J. Dong, L. Sun, *Energy Environ. Sci.* **2012**, *5*, 8220-8224.
[49] H.-H. Cui, J.-Y. Wang, M.-Q. Hu, C.-B. Ma, H.-M. Wen, X.-W. Song, C.-N. Chen, *Dalton Trans.* **2013**, *42*, 8684-8691.

[50] T. M. Mccormick, B. D. Calitree, A. Orchard, N. D. Kraut, F. V. Bright, M. R. Detty, R. Eisenberg, *J. Am. Chem. Soc.* **2010**, *132*, 15480-15483.
[51] A. Vaneski, J. Schneider, A. S. Susha, A. L. Rogach, *J. Photochem. Photobiol. C Photochem. Rev.* **2014**, *19*, 52-61.
[52] K. Wu, T. Lian, *Chem. Soc. Rev.* **2016**, *45*, 3781–3810.
[53] Z. Han, F. Qiu, R. Eisenberg, P. L. Holland, T. D. Krauss, *Science* **2012**, *338*, 1321-1324.
[54] Y. Xu, Y. Huang, B. Zhang, *Inorg. Chem. Front.* **2016**, *3*, 591-615.
[55] Z.-R. Tang, B. Han, C. Han, Y.-J. Xu, *J. Mater. Chem. A* **2017**, *5*, 2387-2410.
[56] S. Y. Park, H. U. Lee, E. S. Park, S. C. Lee, J.-W. Lee, S. W. Jeong, C. H. Kim, Y.-C. Lee, Y. S. Huh, J. Lee, *ACS Appl. Mater. Interfaces* **2014**, *6*, 3365-3370.
[57] J. S. Jang, U. A. Joshi, J. S. Lee, *J. Phys. Chem. C* **2007**, *111*, 13280–13287.
[58] S. Kumar, T. Nann, *Small* **2006**, *2*, 316–329.
[59] H. Y. Li, D. D. Xi, Y. Niu, C. Wang, F. R. Xu, L. Liang, P. Xu, *J. Inorg. Biochem.* **2019**, *195*, 174-181.
[60] P. K. Dutta, A. K. Asatkar, S. S. Zade, S. Panda, *Dalton Trans.* **2014**, *43*, 1736-1743.
[61] B. Sinha, M. Bhattacharya, S. Saha, *J. Chem. Sci.* **2019**, *131*, 1-10.
[62] S. Sharma, S. K. Ghoshal, *Renew. Sustain. Energy Rev.* **2015**, *43*, 1151-1158.
[63] J. Ran, J. Yu, M. Jaroniec, *Green Chem.* **2011**, *13*, 2708-2713.
[64] V. V. Pavlishchuk, S. V. Kolotilov, E. Sinn, M. J. Prushan, A. W. Addison, *Inorg. Chim. Acta.* **1998**, *278*, 217-222.
[65] R. A. Mendes, J. C. Germino, B. R. Fazolo, E. H. Thaines, F. Ferraro, A. M. Santana, R. J. Ramos, G. L. De Souza, R. G. Freitas, P. A. Vazquez, *J. Adv. Res.* **2018**, *9*, 27-33.
[66] J. Du, G. Liu, F. Li, Y. Zhu, L. Sun, *Adv. Sci.* **2019**, *6*, 1900117.
[67] Q. Jacquet, A. Iadecola, M. Saubanère, H. Li, E. J. Berg, G. L. Rousse, J. Cabana, M.-L. Doublet, J.-M. Tarascon, *J. Am. Chem. Soc.* **2019**, *141*, 11452-11464.
[68] C. Sreekala, I. Jinchu, K. Sreelatha, Y. Janu, N. Prasad, M. Kumar, A. K. Sadh, M. Roy, *IEEE J. Photovolt.* **2012**, *2*, 312-319.
[69] X. Li, J. G. Yu, J. X. Low, Y. P. Fang, J. Xiao, X. B. Chen, *J. Mater. Chem. A* **2015**, *3*, 2485-2534.
[70] Z. Shaghaghi, M. Aligholivand, R. Mohammad-Rezaei, *Int. J. Hydrogen Energy* **2021**, *46*, 389-402.
[71] X. Yao, P.-Y. Ho, S.-C. Yiu, S. Suramitr, W. B. Li, C.-L. Ho, S. Hannongbua, *Dyes Pigm.* **2022**, *205*, 110508.
[72] P. Tian, X. He, L. Zhao, W. Li, W. Fang, H. Chen, F. Zhang, Z. Huang, H. Wang, *Int. J. Hydrogen Energy* **2019**, *44*, 788-800.
[73] P. Tian, X. He, L. Zhao, W. X. Li, W. Fang, H. Chen, F. Q. Zhang, Z. H. Huang, H. L. Wang, *Sol. Energy* **2019**, *188*, 750-759.
[74] H. Y. Wang, C. Y. Gao, R. Li, Z. K. Peng, J. H. Yang, J. Gao, Y. P. Yang, S. H. Li, B. J. Li, Z. Y. Liu, *ACS Sustainable Chem. Eng.* **2019**, *7*, 18744-18752.
[75] Y. Wang, P. Zheng, M. X. Li, Y. R. Li, X. Zhang, J. Chen, X. Fang, Y. J. Liu, X. L. Yuan, X. P. Dai, *Nanoscale* **2020**, *12*, 9669-9679.

[76] R. Acharya, B. Naik, K. Parida, *Beilstein J. Nanotechnol.* **2018**, *9*, 1448-1470.
[77] Y. Zhang, Z. R. Liu, C. Y. Guo, T. X. Chen, C. Guo, Y. Lu, J. D. Wang, *Appl. Surf. Sci.* **2022**, *571*, 151284.
[78] J.-Y. Tang, R.-T. Guo, W.-G. Zhou, C.-Y. Huang, W.-G. Pan, *Appl. Catal. B* **2018**, *237*, 802-810.
[79] D. Jiang, W. Wang, S. Sun, L. Zhang, Y. Zheng, *ACS Catal.* **2015**, *5*, 613-621.
[80] P. Peerakiatkhajohn, J.-H. Yun, S. Wang, L. Wang, *J. Photonics Energy* **2016**, *7*, 012006.
[81] S. Cao, Q. Huang, B. Zhu, J. Yu, *J. Power Sources* **2017**, *351*, 151-159.
[82] F. C. Leng, H. Liu, M. L. Ding, Q.-P. Lin, H.-L. Jiang, *ACS Catal.* **2018**, *8*, 4583-4590.
[83] C. Chen, X. Li, F. Deng, J. Li, *RSC Adv.* **2016**, *6*, 79894-79899.
[84] E. Dmitrieva, M. Rosenkranz, J. S. Danilova, E. A. Smirnova, M. P. Karushev, I. A. Chepurnaya, A. M. Timonov, *Electrochim. Acta.* **2018**, *283*, 1742-1752.
[85] J. Yuan, J. Wen, Y. Zhong, X. Li, Y. Fang, S. Zhang, W. Liu, *J. Mater. Chem. A* **2015**, *3*, 18244-18255.
[86] L. Zhang, X. Hao, Y. Li, Z. Jin, *Appl. Surf. Sci.* **2020**, *499*, 143862.
[87] X. G. Lin, L. Zhu, B. W. Li, D. C. Jiang, H. W. Du, C. H. Zhu, Z. W. Yu, Y. P. Yuan, *J. Alloys Compd.* **2022**, *915*, 165351.
[88] Q.-X. Peng, D. Xue, S.-Z. Zhan, C.-L. Ni, *Appl. Catal. B* **2017**, *219*, 353-361.
[89] C.-B. Li, Y. L. Chu, J. J. He, J. J. Xie, J. W. Liu, N. Wang, J. W. Tang, *ChemCatChem* **2019**, *11*, 6324-6331.
[90] J. Wang, C. Li, Q. Zhou, W. Wang, Y. Hou, B. Zhang, X. Wang, *Dalton Trans.* **2016**, *45*, 5439-5443.
[91] K. Majee, J. Patel, B. Das, S. K. Padhi, *Dalton Trans.* **2017**, *46*, 14869-14879.
[92] S. Rajak, O. Schott, P. Kaur, T. Maris, G. S. Hanan, A. Duong, *RSC Adv.* **2019**, *9*, 28153-28164.
[93] X.-S. Hong, D. Huo, W.-J. Jiang, W.-J. Long, J.-D. Leng, L. Tong, Z.-Q. Liu, *ChemElectroChem* **2020**, *7*, 4956-4962.
[94] C.-B. Li, P. Gong, Y. Yang, H.-Y. Wang, *Catal. Lett.* **2018**, *148*, 3158-3164.
[95] S. Chen, K. Li, F. Zhao, L. Zhang, M. Pan, Y. Z. Fan, J. Guo, J. Y. Shi, C. Y. Su, *Nat. Commun.* **2016**, *7*, 1-8.

Chapter 5: Synthesis, Structures, Characterisations of Metal–Organic Cages, and Their Water-Splitting Hydrogen Generation Experiments in CdS Nanorod System

5.1 Introduction

Because of the fast recombination of photogenerated electron–hole pairs, the photocatalytic activity of traditional water-splitting hydrogen production systems is low and needs to be improved.[1] Metal complexes with heterogeneous carrier materials, such as metal–organic frameworks (MOFs) and covalent–organic frameworks (COFs), have been developed to enhance hydrogen-generation efficiency.[2-6] MOFs and COFs have attracted wide attention because of their excellent properties, including large surface area, and topological structure diversity.[7-10] The porous structure of MOFs enables the reaction molecules attached to their walls to improve catalyst efficiency.[11] However, the carrier shells surrounding the metal-complex catalysts of MOFs reduce the flexibility and accessibility of the photocatalytic centres, thereby decreasing their catalytic activity.[12] Therefore, it is vital to design a stable metal catalyst that has the advantages of MOFs but overcome the drawbacks of them.

Metal–organic cages (MOCs), regarded as inorganic clusters and organic linkers, have been widely developed.[13] Supramolecular assembly of predesigned inorganic and organic building blocks is considered as one of the ideal tools to construct well-defined, nanosized molecular vessels.[14-16] In MOCs, which are a new type of porous crystalline materials, individual nanoscale molecular structures are formed through weak

interactions. These materials are considered to have huge potential when applied in photocatalytic water-splitting.[6, 17, 18] Owing to their MOF-like advantages, easily modifiable MOCs are useful for binding catalyst centres with functional organic linkers. In view of the discrete properties of MOCs, incorporating catalyst molecules with a rigorous design appears to be a practical approach to enhancing catalytic activity and stability. Recently, it has been reported that MOCs can be used as heterogeneous catalysts in photocatalytic reactions by anchoring their catalytic active sites or loading metal nanoparticles, and that they show better performance than nano-MOFs.[19] For example, Wu and co-workers have synthesized [FeFe]-hydrogenase MOCs and employed them in water-splitting hydrogen production, achieving a TON at about 3500 with CdSe QDs and AA (pH=4) for 3 h.[20, 21]

To enhance efficiency in H_2 production, the MOCs should be designed appropriately and possess characteristics such as strong absorption of visible light.[22, 23] In particular, the redox catalytic sites and the photosensitiser should be in close proximity to each other, and the possibility of unwanted electron-transfer reactions were reduced. [24, 25] Inspired by previous studies,[13] two sets of tetrahedral metal−organic cages with triphenylamine or benzene as the framework backbone were synthesized in this study. The framework backbone acts as the supramolecular host and redox catalyst when the MOCs are used for the photocatalytic generation of hydrogen from water (**Fig. 5.1**). The strong coordination ability of the NS chelators has been shown to enhance the stability of the MOCs and provide cobalt or nickel ions with redox potentials, which is suitable for proton reduction.[26, 27]

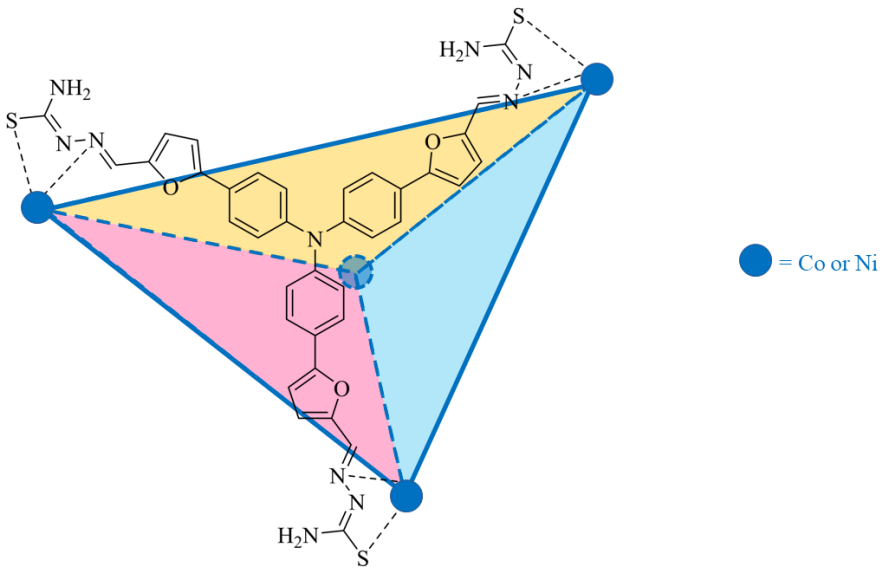

Fig. 5.1. Representative chemical structures of a MOC.

Herein, efficient photocatalytic hydrogen production systems in pure aqueous solution composed of ligand-free CdS NRs and metal–organic cages were presented. The MOCs in this chapter were designed on a small tetrahedral organic framework backbone with nickel or cobalt (**Fig. 5.2** and **Table 5.1**). Furthermore, the photophysical and electrochemical properties of the MOCs and their photocatalytic performance in hydrogen production via water-splitting are also presented and discussed.

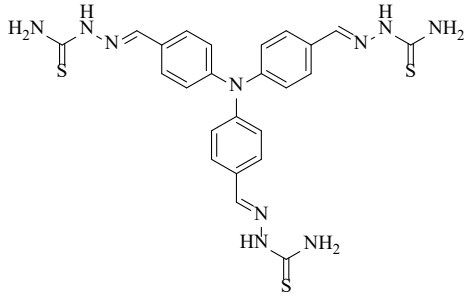

P1

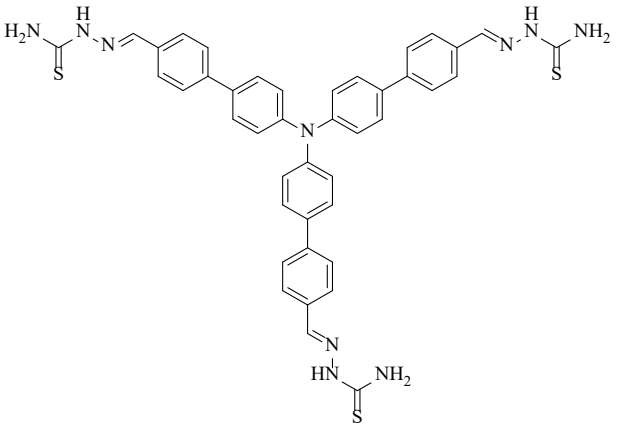

P2

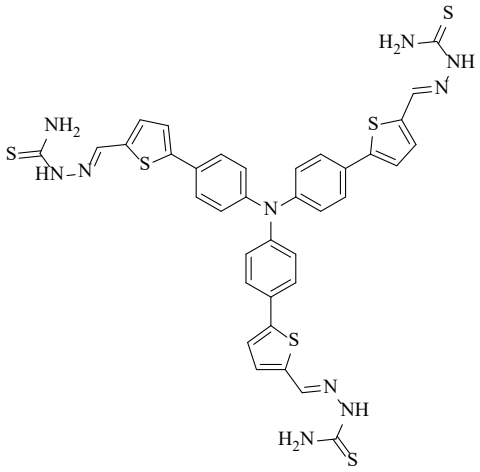

P3

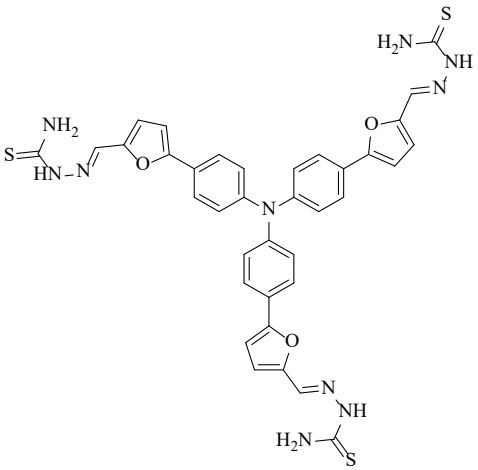

P4

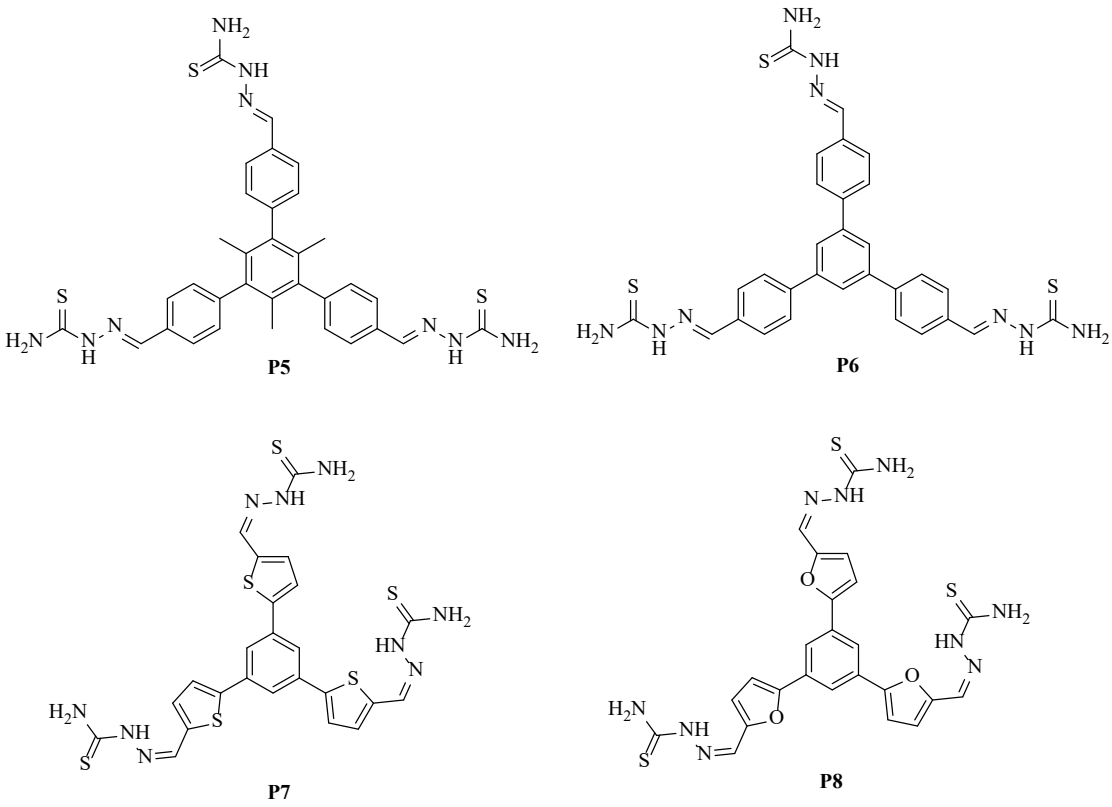

Fig. 5.2. Chemical structures of metal–organic cage precursors **P1**–**P8**.

Table 5.1. Formation of metal–organic cages.

Ligand precursor	Metal	Metal–Organic Cage
P1	**Co**	**MOC1**
P1	**Ni**	**MOC2**
P2	**Co**	**MOC3**
P2	**Ni**	**MOC4**
P3	**Co**	**MOC5**
P3	**Ni**	**MOC6**
P4	**Co**	**MOC7**
P4	**Ni**	**MOC8**

P5	**Co**	**MOC9**
P5	**Ni**	**MOC10**
P6	**Co**	**MOC11**
P6	**Ni**	**MOC12**
P7	**Co**	**MOC13**
P7	**Ni**	**MOC14**
P8	**Co**	**MOC15**
P8	**Ni**	**MOC16**

5.2 Syntheses

5.2.1 Synthesis of MOC aldehyde ligands

MOC aldehyde ligands were generally prepared using the classical Suzuki reaction from 1,3,5-tribromobenzene or tris(4-bromophenyl)amine with corresponding boronic acid and Vilsmeier–Haack reaction with phosphoryl(V) chloride and corresponding organic compounds. The synthetic pathways are shown in **Scheme 5.1**.

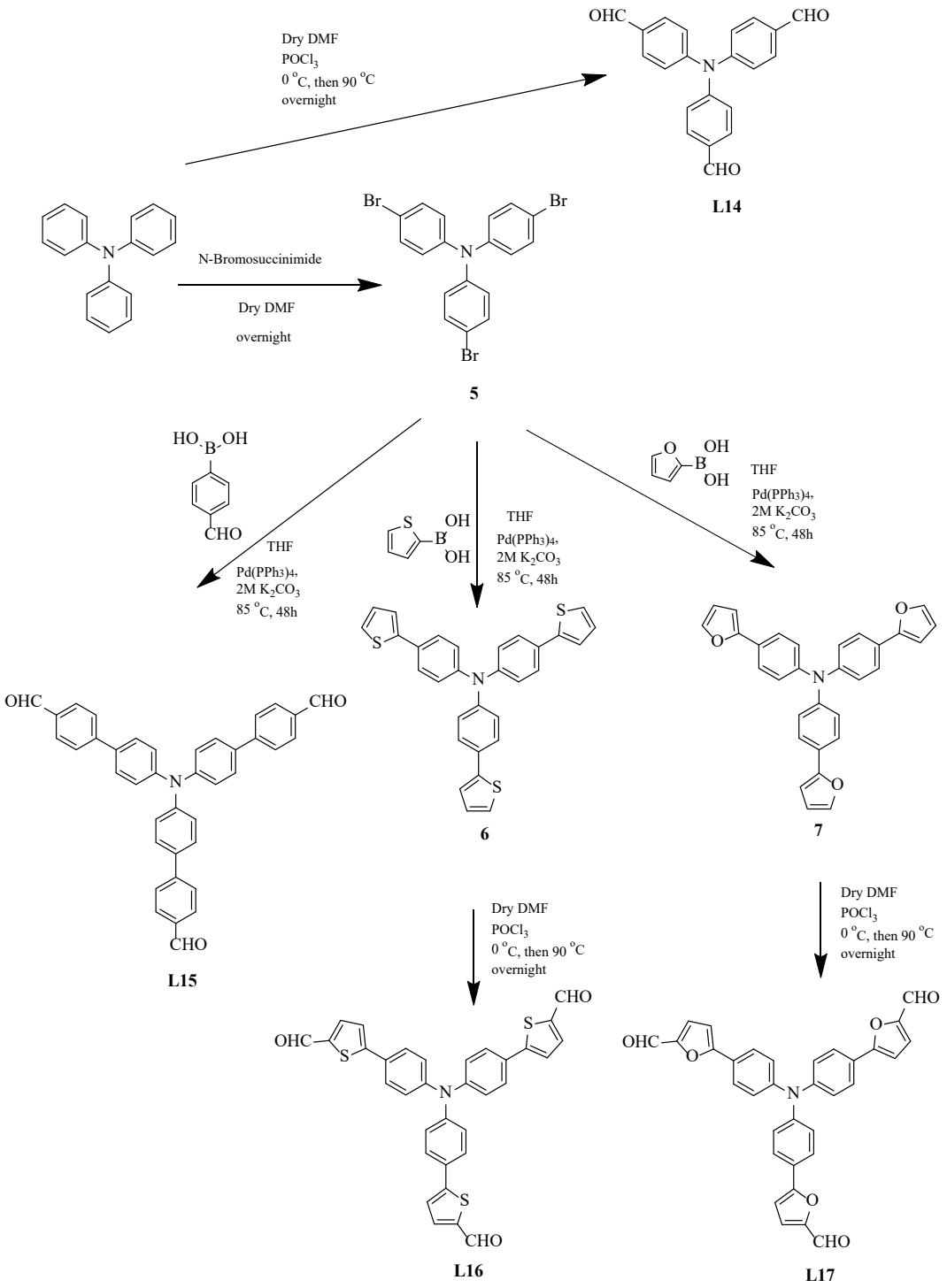
Dry DMF
POCl3
0 °C, then 90 °C
overnight
OHC
CHO
N
CHO
L14
Br
Br
N
Br
N-Bromosuccinimide
Dry DMF
overnight
5
HO
B
OH
CHO
THF
Pd(PPh3)4,
2M K2CO3
85 °C, 48h
S
OH
B
OH
THF
Pd(PPh3)4,
2M K2CO3
85 °C, 48h
O
OH
B
OH
THF
Pd(PPh3)4,
2M K2CO3
85 °C, 48h
OHC
CHO
N
CHO
L15
S
S
N
S
6
O
O
N
O
7
Dry DMF
POCl3
0 °C, then 90 °C
overnight
Dry DMF
POCl3
0 °C, then 90 °C
overnight
OHC
S
CHO
N
S
CHO
L16
OHC
O
CHO
N
O
CHO
L17

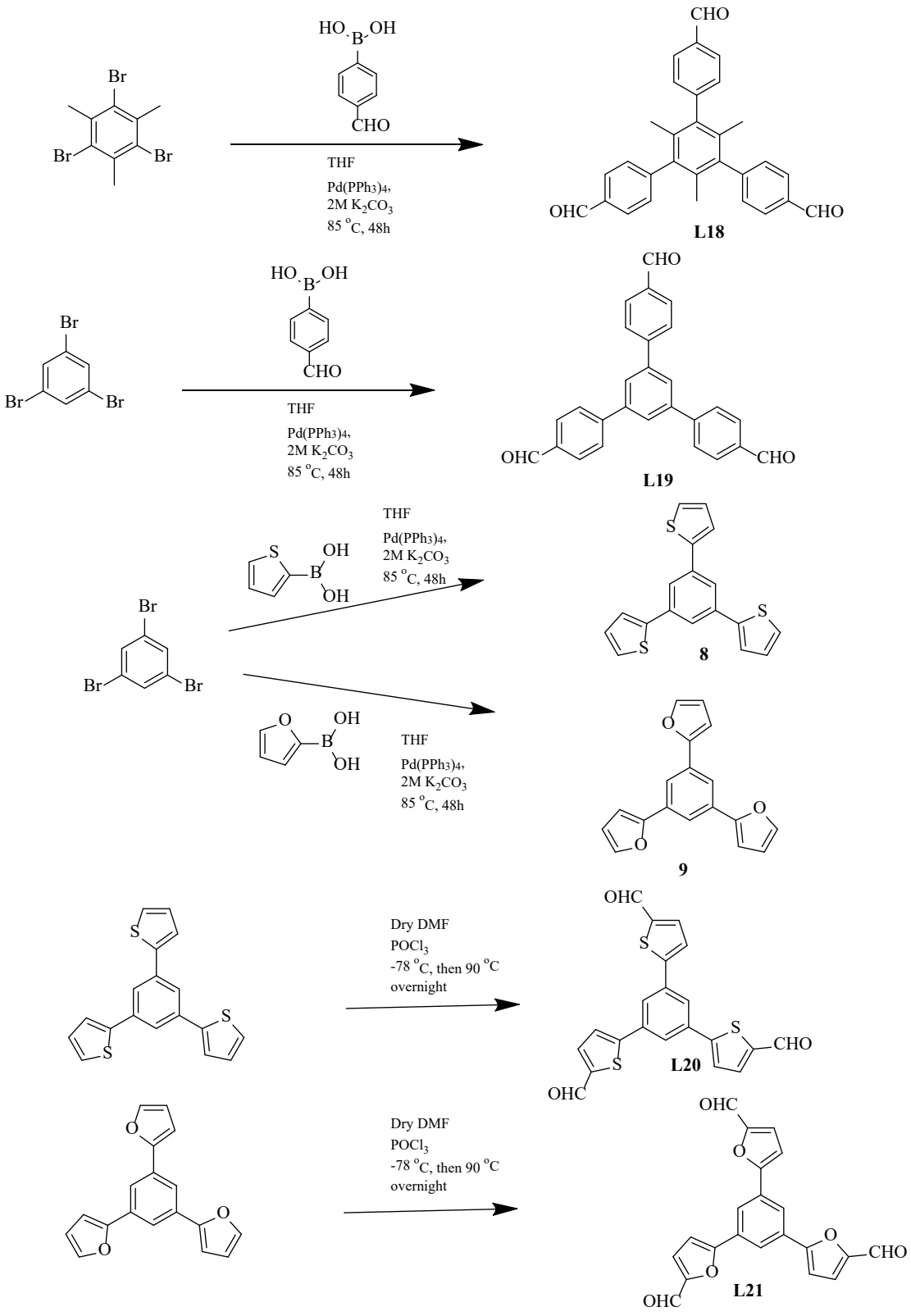

Scheme 5.1. Synthetic pathways of MOC aldehyde ligands.

5.2.2 Synthesis of MOC precursors

The metal–organic cage precursors were prepared according to a previous literature.[13] They were obtained from the reaction of the corresponding aldehyde ligands with thiosemicarbazide in an acetic acid–MeOH solution. **Scheme 5.2** shows the synthetic pathway for precursor **P1** as an example.

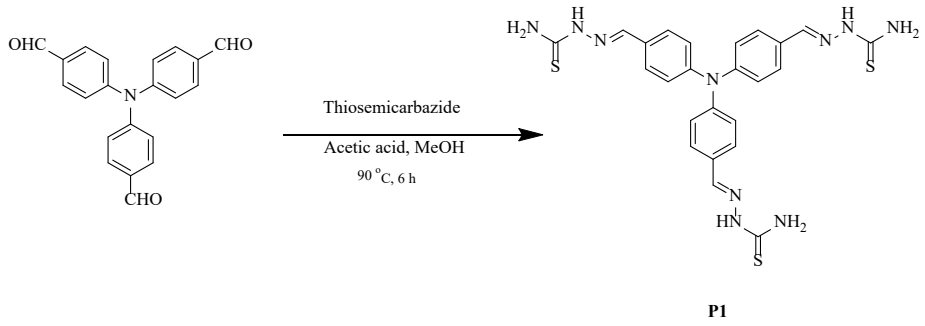

Scheme 5.2. Synthetic pathway of MOC precursor **P1**.

5.2.3 Synthesis of MOCs

The MOCs were synthesised by following a procedure described in a previously published paper.[13] The precursors reacted with $Co(CH_3COO)_2 \cdot 4H_2O$ or $NiNO_3 \cdot 4H_2O$ in a dry DMF solution to form the final MOC. As an example, the synthetic pathway for **MOC1** is shown in **Scheme 5.3**. All MOCs prepared in this study were stable solids in air.

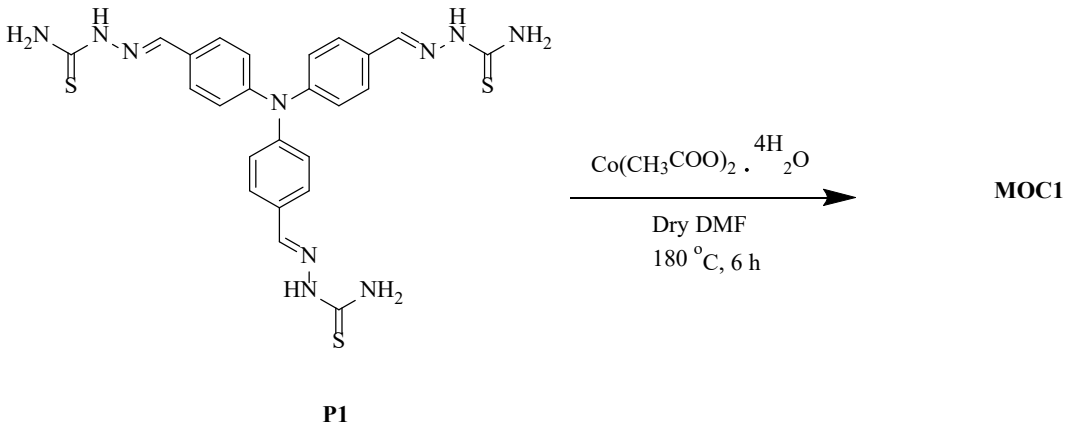

Scheme 5.3. Synthetic pathway of **MOC1**.

5.3 Spectroscopic Characterisation

All MOC aldehyde ligands showed characteristic ^{1}H NMR spectra and indicated a clear structure for each compound. For example, **Fig. 5.3** shows the ^{1}H NMR spectrum of MOC aldehyde ligand **L18** with a singlet at approximately 9.94 ppm attributed to the proton of aldehyde [13].

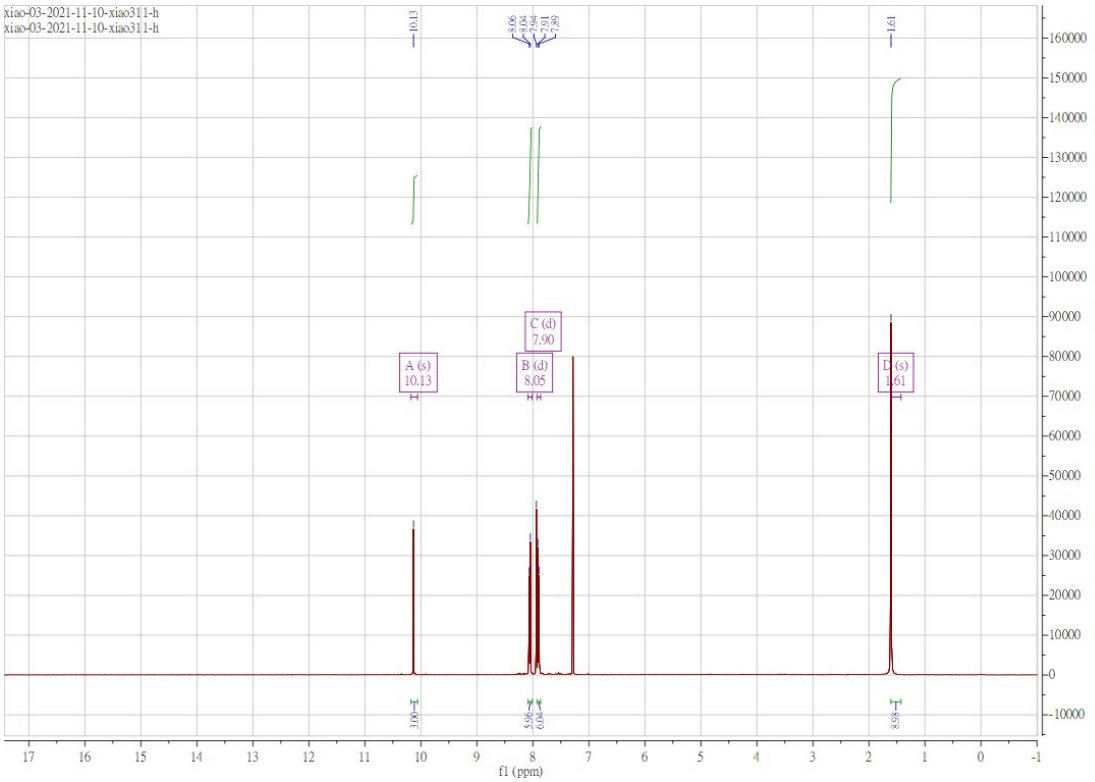

Fig. 5.3. ^{1}H NMR spectrum of MOC aldehyde ligand **L18** in $CDCl_3$.

Owing to the poor solubility of the MOC precursors and final MOCs, only ^{13}C NMR data for the MOC aldehyde ligand could be obtained. The corresponding NMR spectra reveal the structures of these compounds. For example, **Fig. 5.4** shows the ^{13}C NMR spectrum of **L18**.

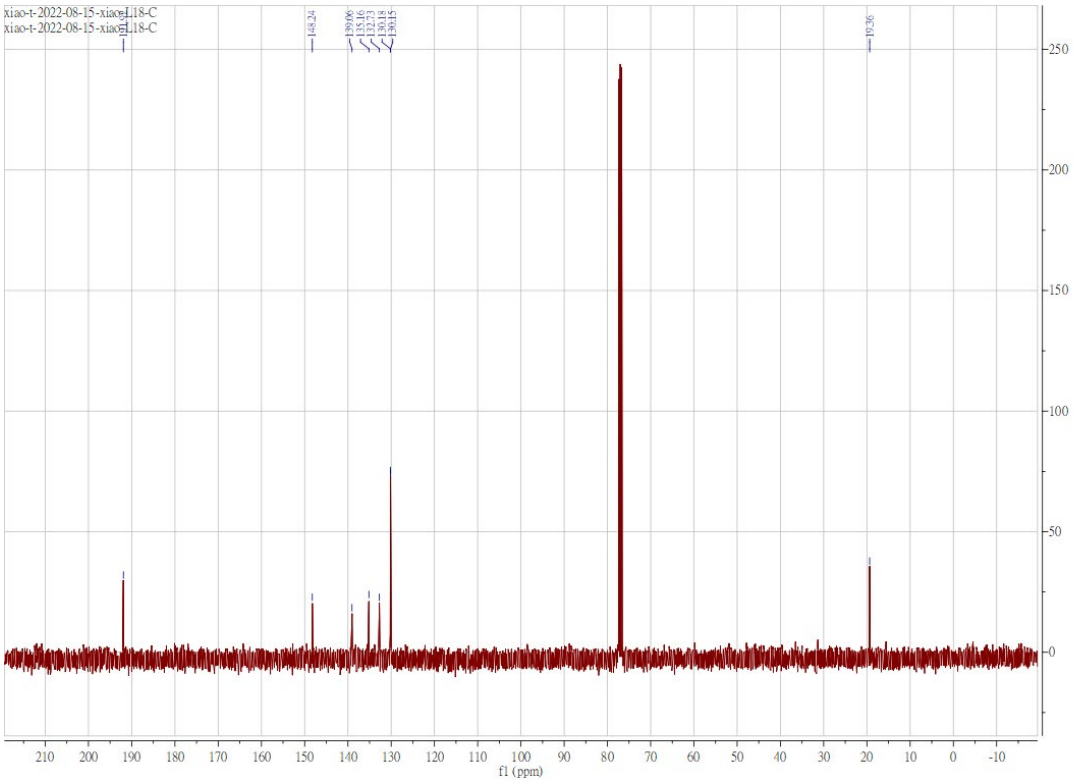

Fig. 5.4. ^{13}C NMR spectrum of MOC aldehyde ligand **L18** in $CDCl_3$.

The MOC precursors were characterised by ^{1}H NMR spectroscopy. **Fig. 5.5** shows the ^{1}H NMR spectrum of MOC precursor **P1**. The appearance of imine proton C(S)−NH signals at 11.40 ppm indicates the structure.[13]

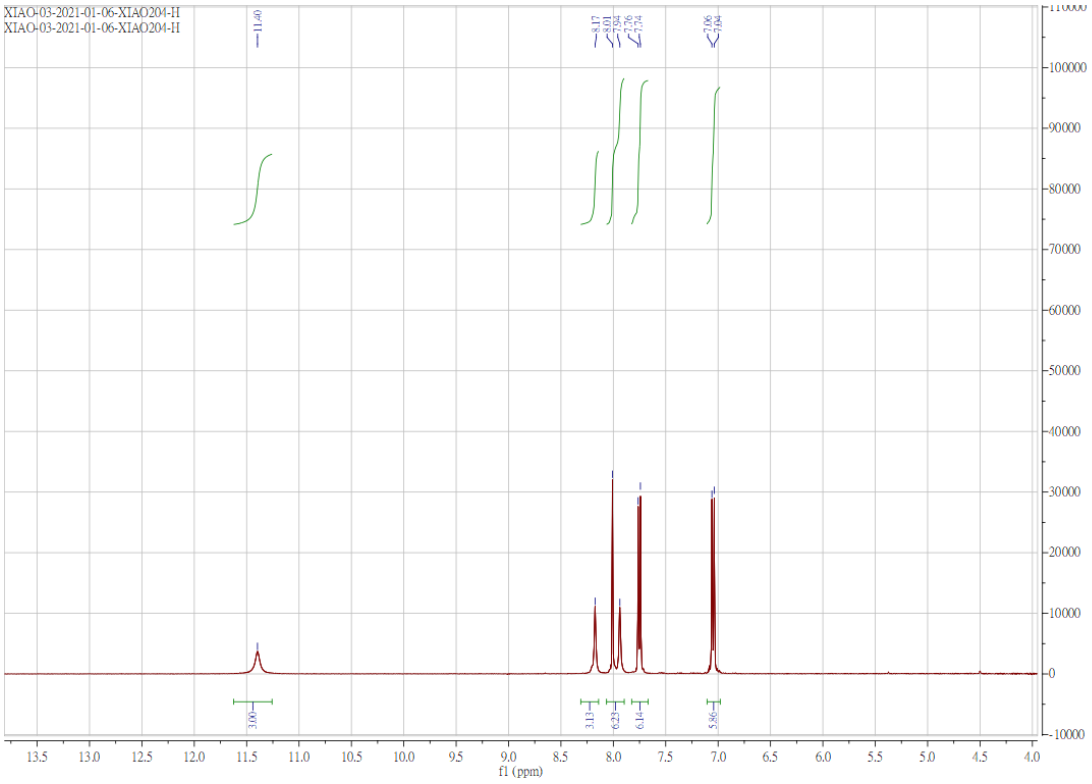

Fig. 5.5. ^{1}H NMR spectrum of MOC precursor **P1** in DMSO-d6.

Due to the poor solubility, only part of the metal–organic cages were confirmed by ^{1}H NMR as well. According to previous literature, others will be confirmed by MS and FTIR.[28] **Fig. 5.6** shows the ^{1}H NMR spectrum of **MOC5**. The disappearance of the imine proton C(S)−NH signals from the precursor suggests that the bidentate moiety was coordinated to a metal ion. [13]

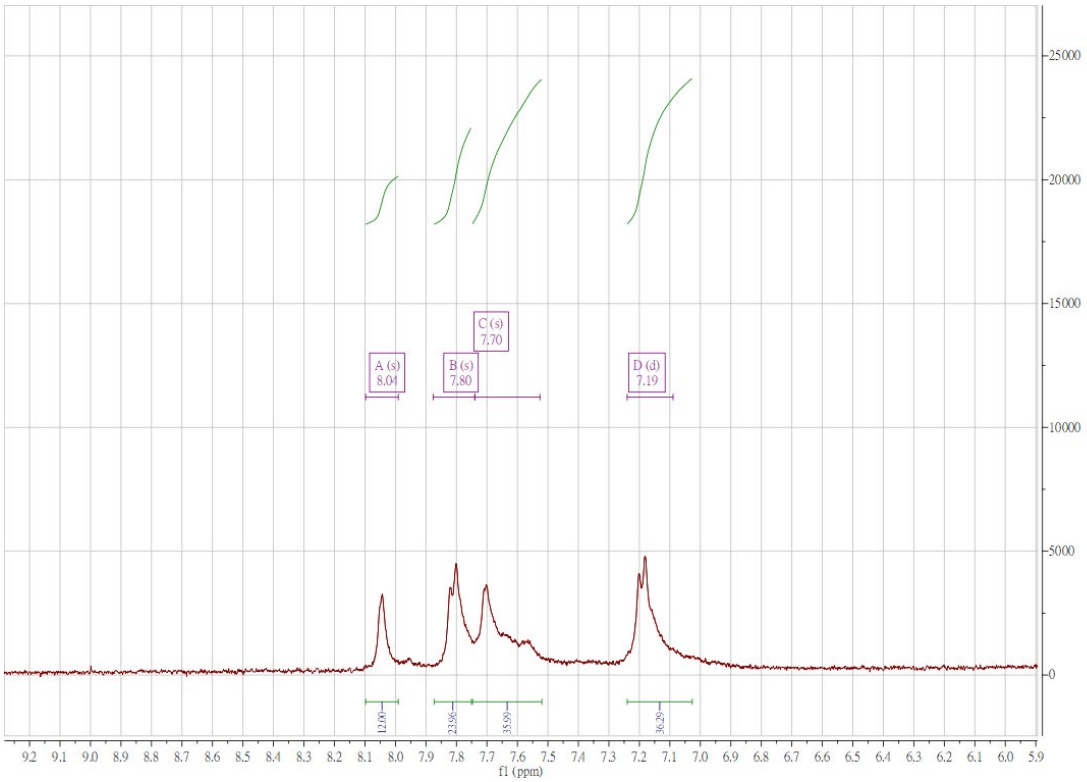

Fig. 5.6. ^{1}H NMR spectrum of **MOC5** in DMSO-d6.

5.4 Mass Spectrum Characterisation

Liquid chromatography–electrospray ionisation quadrupole–time of flight mass spectrum characterisation was performed for the aldehyde ligands, precursors, and the final metal–organic cages to confirm the structures. **Fig. 5.7** to **Fig. 5.9** show the MS results for compound **L18,** MOC precursor **P2** and **MOC7** as examples. The main peaks of the MS results match the calculated molecular ion peaks, indicating correct formation of the structures.

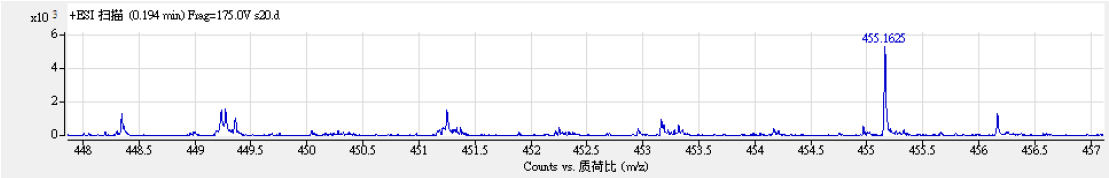

Fig. 5.7. MS result of compound **L18**.

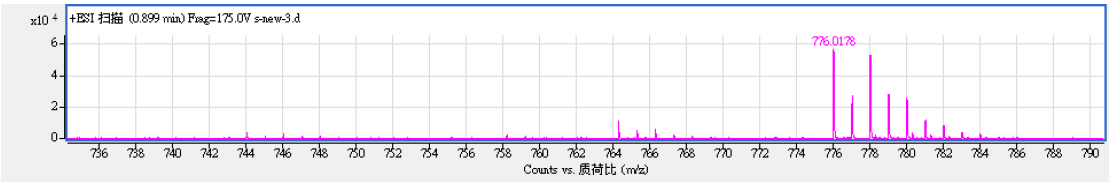

Fig. 5.8. MS result of MOC precursor **P2**.

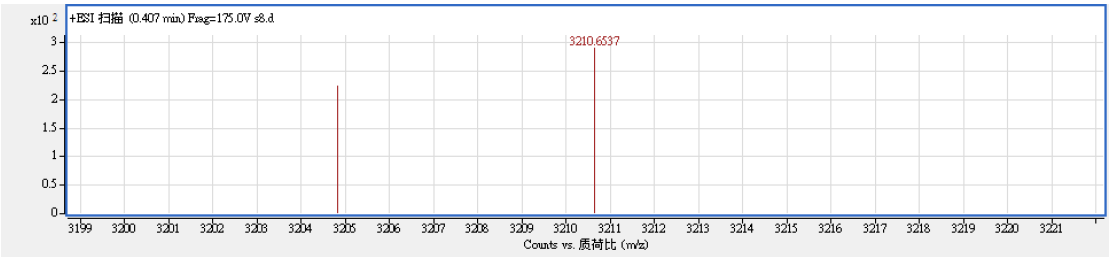

Fig. 5.9. MS result of **MOC7**.

5.5 Fourier-Transform Infrared Characterisation of MOCs

Fourier-transformed infrared (FTIR) characterisation of the selective metal–organic cage **MOC8** was performed to determine its structure. **Fig. 5.10** shows the result of the characterisation, and the corresponding data are presented in **Table 5.2**. The FTIR spectrum of **MOC8** shows two peaks at 615 and 721 cm^{-1}, attributed to the stretching vibration of the Ni-N and S-Ni bonds respectively, which confirms the formation of the expected MOC.

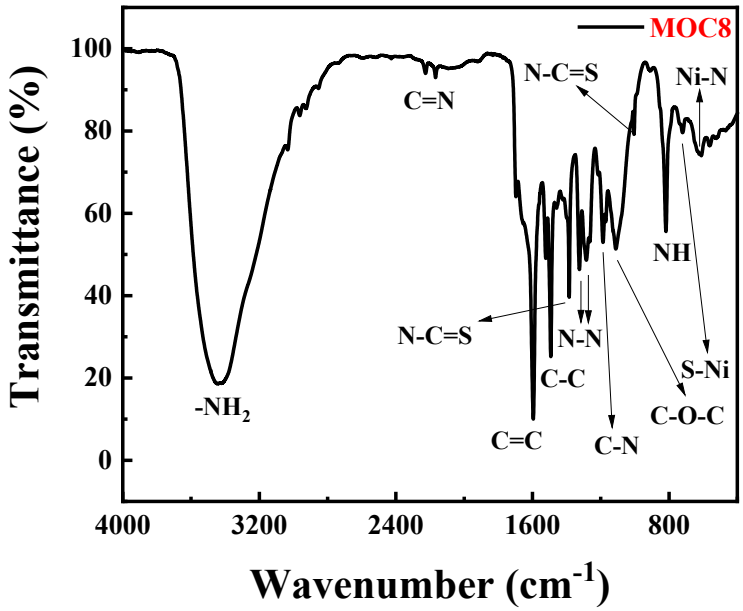

Fig. 5.10. FTIR spectrum of **MOC8**.

Table 5.2. FTIR spectral analysis of **MOC8**.

Band (cm^{-1})	Stretching Vibration Assignment	Reference
≈3449	$–NH_2$	[29]
2918	CH_3	[29]
2222	C=N	[30]
1598	C=C	[31]
1491	C–C	[30, 32]
1383	N–C=S	[33]
1325, 1276	N–N	[34]
1189	C–N	[30]
1107	C–O–C	[35]
996	N–C=S	[33, 36]
819	NH	[30]
721	S–Ni	[37]
615	Ni–N	[30]

5.6 Transmission Electron Microscopy Characterisation of MOCs

A representative MOC, **MOC5**, was investigated using transmission electron microscopy characterisation. A typical TEM image of **MOC5** (**Fig. 5.11**) indicated a cubic structure, in agreement with the structure reported previously.[2] The spatial

distribution of different elements in **MOC5** was determined through elemental mapping analysis (**Fig. 5.12**). The Co distribution characteristics confirmed the formation of the desired structure.

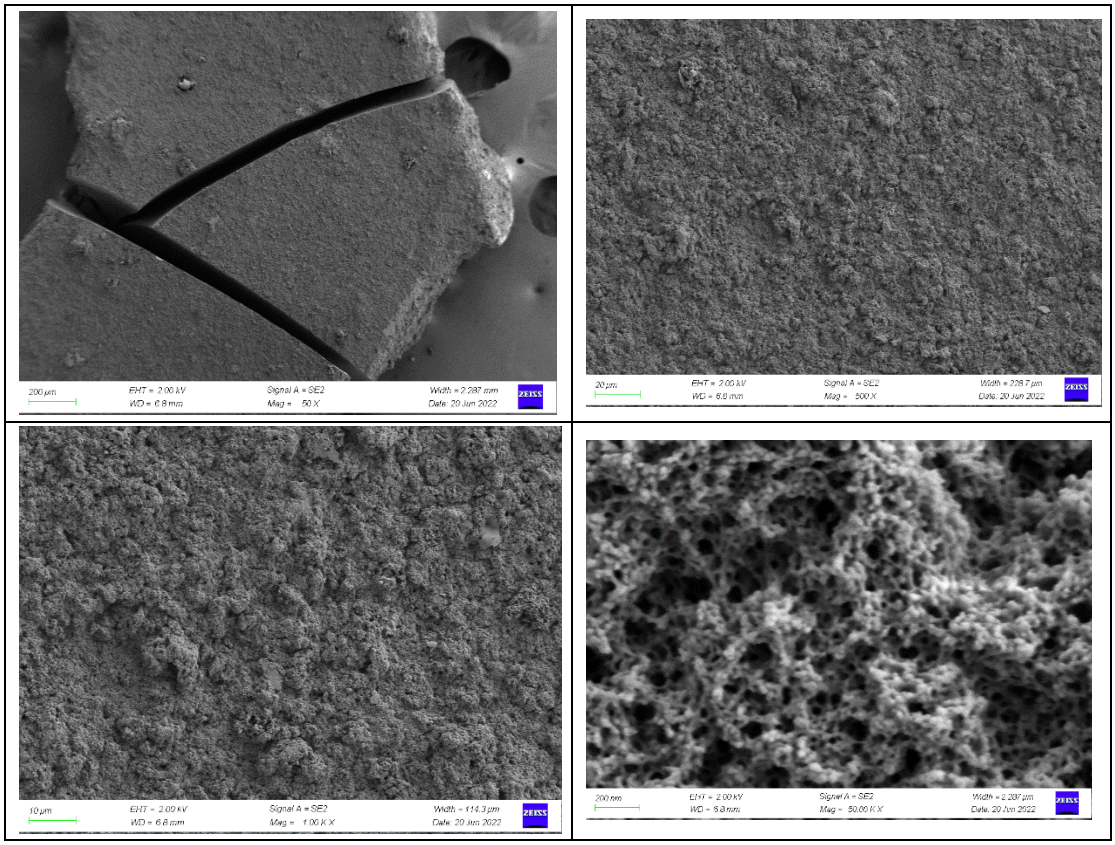

Fig. 5.11. TEM images of **MOC5**.

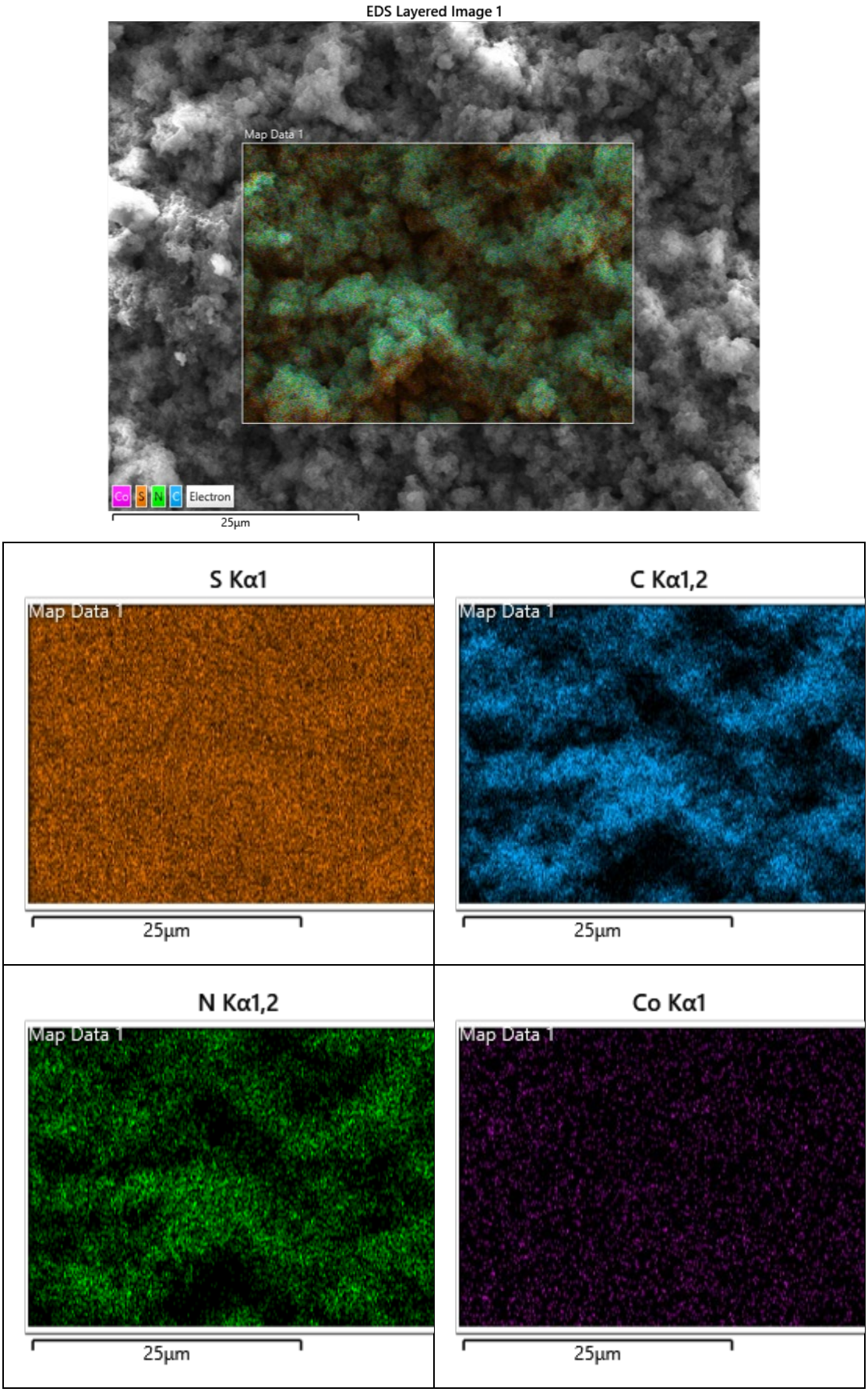

Fig. 5.12. Results of elemental mapping analysis of **MOC5**.

5.7. Photophysical Properties of MOCs

The photophysical properties of all metal–organic cages in DMSO were studied. Photophysical measurements showed that the effect of bonding metals (Ni or Co) on the absorption properties of the MOCs was very marginal. Their UV/Vis absorption spectra are shown in **Fig. 5.13** and **Fig. 5.14**, the corresponding data for which are summarised in **Table 5.3**. The absorption spectra of MOCs were generally dominated by an intense UV band below 330 nm, which was attributed to the ligand-centred π-to-π* transitions of the ligands.[12] Furthermore, broad absorption bands characteristic of metal-to-ligand charge transfer transitions were observed in the visible region.[6, 12] The lowest energy MLCT bands for all metal–organic cages with triphenylamine framework backbone were red-shifted from those without, attributed to the presence of electron donors with extended π-conjugation in the triphenylamine backbone.[38, 39] The ε of the MOC in the visible region is a key factor that determines the light-harvesting capability when it is used for photocatalytic hydrogen generation. All MOCs with triphenylamine had higher ε values than those without, which indicated the superior light-harvesting capability of the former MOCs.

The spectra of **MOC7** exhibit slight red-shifting compared to the spectra of **MOC5** due to the introduction of furan instead of a thiophene functional group in the organic backbone, which has a smaller resonance energy[40] and can enhance electron mobility,[41] indicating the better hydrogen generation performance. A similar observation was made for **MOC13** and **MOC15**. Furthermore, a comparison of the spectra of **MOC9** and **MOC11** showed that the effect of methyl functional groups on

the absorption properties of MOCs was marginal.

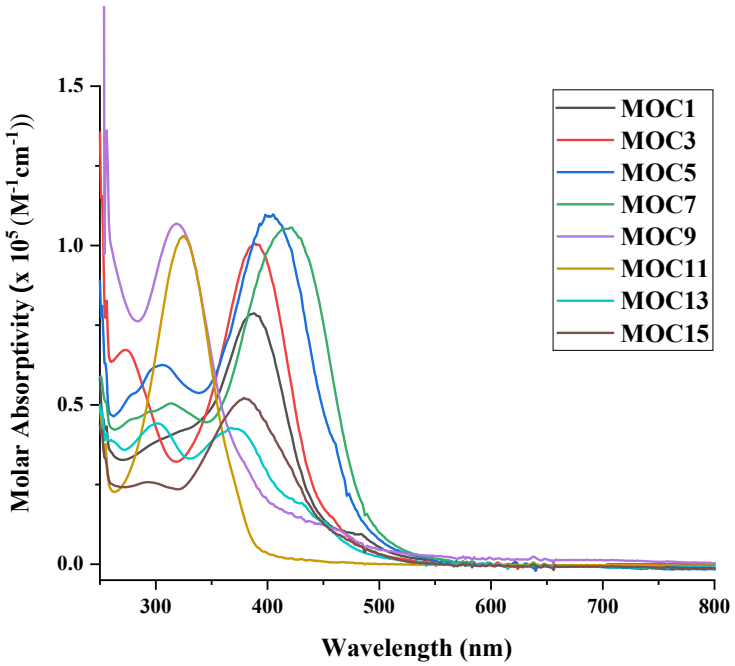

Fig. 5.13. UV/Vis absorption spectra of MOCs with Ni metal in DMSO at 293 K.

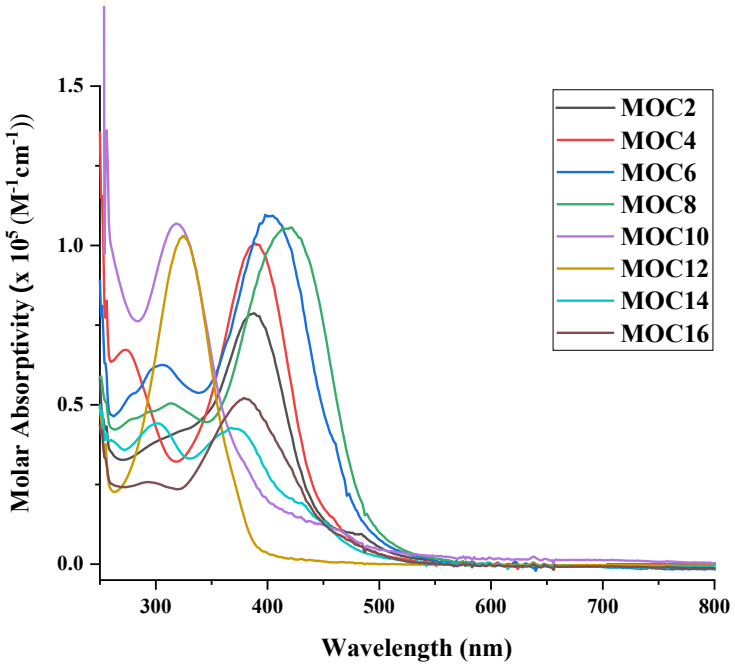

Fig. 5.14. UV/Vis absorption spectra of MOCs with Co metal in DMSO at 293 K.

Table 5.3. UV/Vis absorption parameters of **MOC1** to **MOC16** in DMSO at 293 K.

MOC	λ_{max} /nm (ε /10^5 M^{-1} cm^{-1})
MOC1	306 (0.40), 386 (0.78)
MOC2	305 (0.40), 386 (0.78)
MOC3	273 (0.67), 390 (1.00)
MOC4	273 (0.67), 391 (1.00)
MOC5	305 (0.63), 404 (1.10)
MOC6	305 (0.63), 405 (1.10)
MOC7	315 (0.51), 423 (1.06)
MOC8	314 (0.51), 423 (1.06)
MOC9	316 (1.07), 466 (0.09)
MOC10	316 (1.07), 466 (0.09)
MOC11	327 (1.03)
MOC12	327 (1.03)
MOC13	301 (0.45), 372 (0.43)
MOC14	300 (0.45), 373 (0.43)
MOC15	294 (0.26), 380 (0.52)
MOC16	293 (0.26), 380 (0.52)

5.8. Electrochemical Impedance Spectroscopy Characterisation of MOCs

Electrochemical impedance spectroscopy was used to investigate the charge recombination properties of metal–organic cages according to a previously published procedure.[42, 43] EIS Nyquist plots for **MOC1** to **MOC8** and **MOC9** to **MOC16** are shown in **Figs. 5.15** and **5.16**, respectively. It is known that a smaller arc radius in the Nyquist plot indicates a lower electric charge transfer resistance, which in turn implies better HER performance.[42-45] Overall, the arc radii of **MOC7** and **MOC15** were the smallest in their systems, which suggests that they have better charge carrier transfer properties.[46] These results are consistent with the water-splitting hydrogen production performance (**Fig. 5.19** to **Fig. 5.22**).

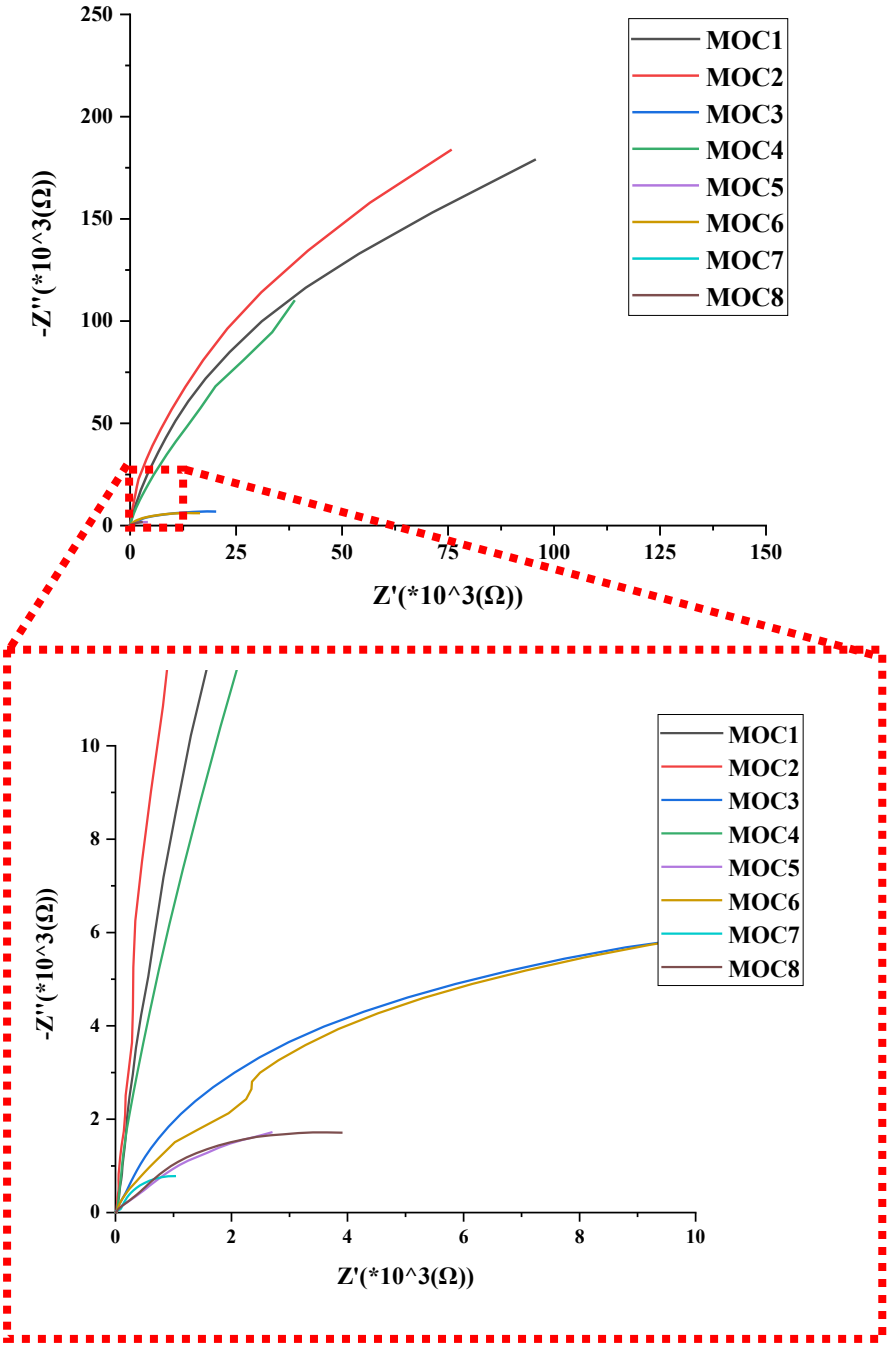

Fig. 5.15. EIS Nyquist plots for **MOC1** to **MOC8**.

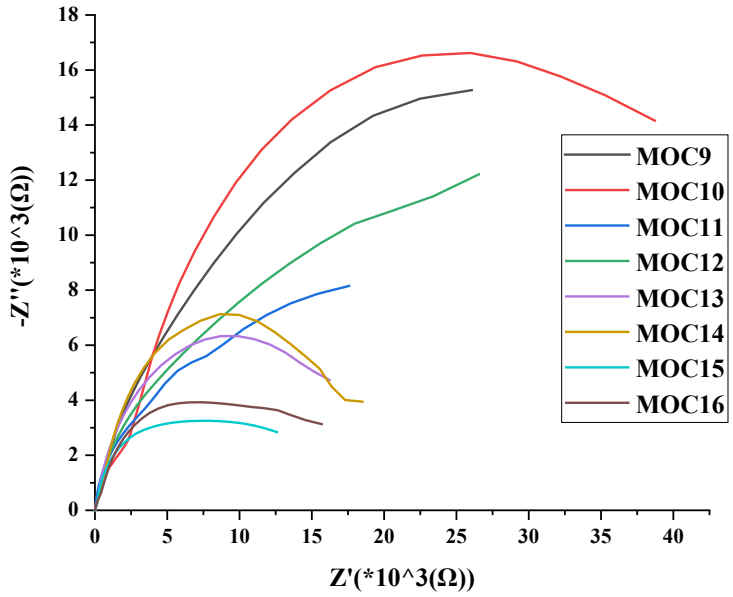

Fig. 5.16. EIS Nyquist plots for **MOC9** to **MOC16**.

5.9. Photocurrent of MOCs

Photocurrent measurement was used to examine the stability and charge separation efficiency of the MOCs.[47] A uniform and fast photocurrent response during the light-on/light-off test showed their stable photocatalytic activity.[48] In particular, a higher photocurrent density indicates better charge separation efficiency,[49] which implies better performance in water-splitting hydrogen generation. Photocurrent measurements were conducted using a previously reported procedure.[50] **Fig. 5.17** and **Fig. 5.18** show the photocurrent responses of **MOC1** to **MOC8** and **MOC9** to **MOC16** under visible light irradiation for six on–off cycles, and they provide clear evidence.[50] Clear photocurrent response were observed during the light-on/light-off test, indicating that the MOCs showed stable photocatalytic activity.[48] **MOC7** and **MOC15** exhibited a significantly higher photocurrent intensity during light-on that decreased with a

noticeable delay during light-off in their systems, indicating superior charge separation efficiency and better hydrogen generation performance.[48, 50-52]

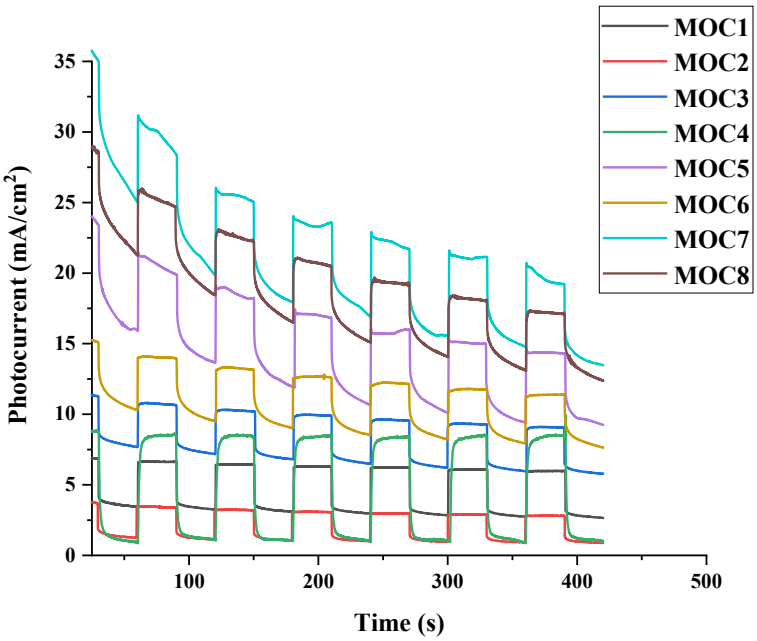

Fig. 5.17. Photocurrent responses of **MOC1** to **MOC8**.

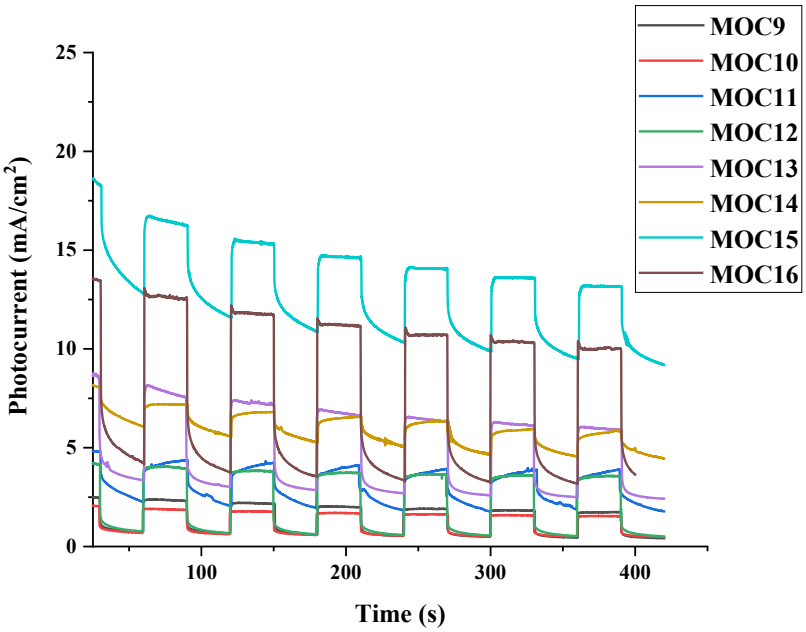

Fig. 5.18. Photocurrent responses of **MOC9** to **MOC16**.

5.10 Light-Driven Hydrogen Generation of MOCs and CdS NRs System

Hydrogen was produced by photocatalytic water-splitting using MOCs as catalysts and CdS NRs as photosentisizer. The procedural reference details for photocatalytic water splitting hydrogen production reaction are described in the experimental section of **Chapter 7**. The photocatalytic water-splitting reaction for hydrogen generation was conducted in 5 mL of AA (0.5 M) solution at a pH of 4.0 and with 10 μM of MOC and 1 mg of CdS NRs. The hydrogen generation curves (vs time) for each sample are shown in **Fig. 5.19** to **Fig. 5.22**, and the corresponding data (TON, TOF, TOF_i and $Activity_i$) are tabulated in **Tables 5.4**–**5.7**.

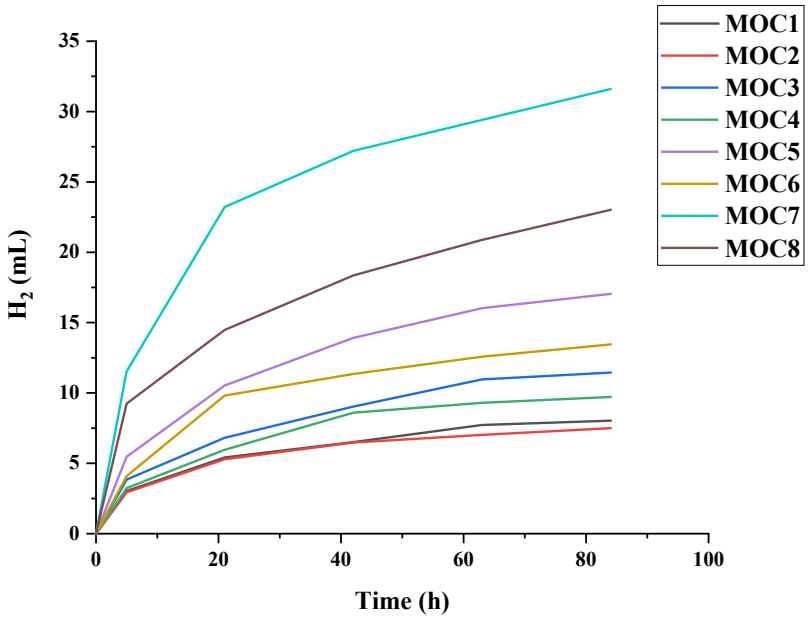

Fig. 5.19. Photocatalytic hydrogen evolution by metal–organic cage **MOC1** to **MOC8** (10 μM) /CdS NR (L/D = 12; 1 mg) /AA (0.5 M) catalysts from H_2O (5 mL) upon irradiation with a 470-nm LED at 19 °C, pH 4.0, and 1 atm initial pressure of N_2:CH_4 (80:20 mol %), with CH_4 as the internal standard for hydrogen quantification via GC.

Table 5.4. Photocatalytic hydrogen evolution by metal–organic cages **MOC1** to **MOC8**/CdS NR (L/D = 12)/ AA catalysts under blue-light irradiation.

MOC	Time /h	H_2 /mL	TON[a]	TOF[b] /h^{-1}	TOF_i[c] /h^{-1}	$Activity_i$[d] /µmol g^{-1} h^{-1}
MOC1	84	8.0	13114	156.1	990.3	247585
MOC2	84	7.5	12238	145.7	959.9	239982
MOC3	84	11.5	18698	222.6	1254.5	313629
MOC4	84	9.7	15869	188.9	1057.5	264384
MOC5	84	17.0	27833	331.3	1786.0	446499
MOC6	84	13.5	21961	261.4	1336.4	334093
MOC7	84	31.6	51592	614.2	3765.4	941362
MOC8	84	23.0	37571	447.3	3017.1	754272

[a] Turnover number for hydrogen calculated as twice the number of moles of hydrogen produced divided by the number of moles of metal–organic cages catalyst. [b] Turnover frequency calculated per hour. [c] Initial turnover frequency for the first 5 h. [d] Photocatalytic activity of the system defined as the number of micromoles of H_2 evolved per mg of CdS NRs loaded per hour.

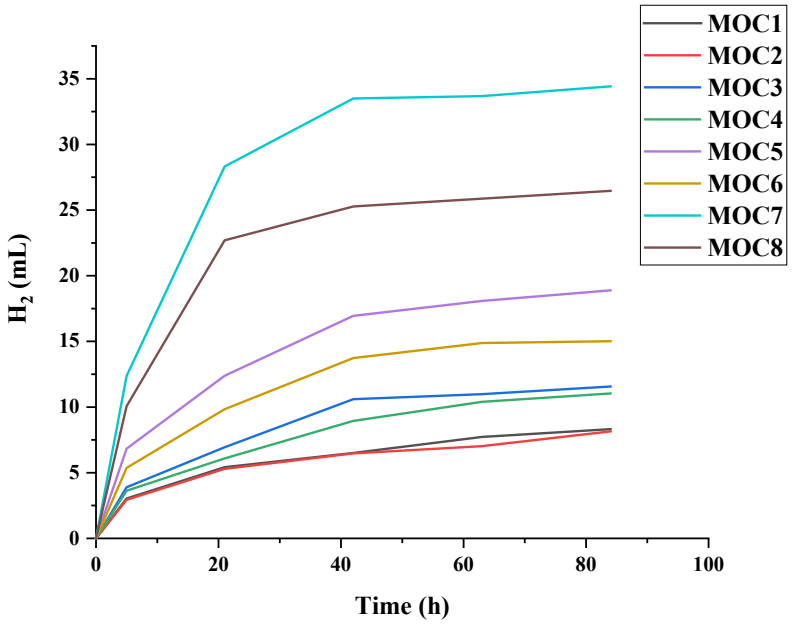

Fig. 5.20. Photocatalytic hydrogen evolution by metal–organic cage **MOC1** to **MOC8**

(10 μM) /CdS NR (L/D = 18; 1 mg) /AA (0.5 M) catalysts from H_2O (5 mL) upon irradiation with a 470-nm LED at 19 °C, pH 4.0, and 1 atm initial pressure of N_2:CH_4 (80:20 mol %), with CH_4 as the internal standard for hydrogen quantification via GC.

Table 5.5. Photocatalytic hydrogen evolution by metal–organic cage **MOC1** to **MOC8** /CdS NR (L/D = 18)/ AA catalysts under blue-light irradiation.

MOC	Time /h	H_2 /mL	TON[a]	TOF[b] /h^{-1}	TOF_i[c] /h^{-1}	$Activity_i$[d] /μmol g^{-1} h^{-1}
MOC1	84	8.3	13589	161.8	990.3	247585
MOC2	84	8.1	13305	158.4	959.9	239982
MOC3	84	11.6	18881	224.8	1270.9	317732
MOC4	84	11.0	18018	214.5	1184.8	296206
MOC5	84	18.9	30829	367.0	2230.7	557671
MOC6	84	15.0	24506	291.7	1753.4	438356
MOC7	84	34.4	56205	669.1	4038.8	1009703
MOC8	84	26.5	43201	514.3	3287.8	821955

[a] Turnover number for hydrogen calculated as twice the number of moles of hydrogen produced divided by the number of moles of metal–organic cages catalyst. [b] Turnover frequency calculated per hour. [c] Initial turnover frequency for the first 5 h. [d] Photocatalytic activity of the system defined as the number of micromoles of H_2 evolved per mg of CdS NRs loaded per hour.

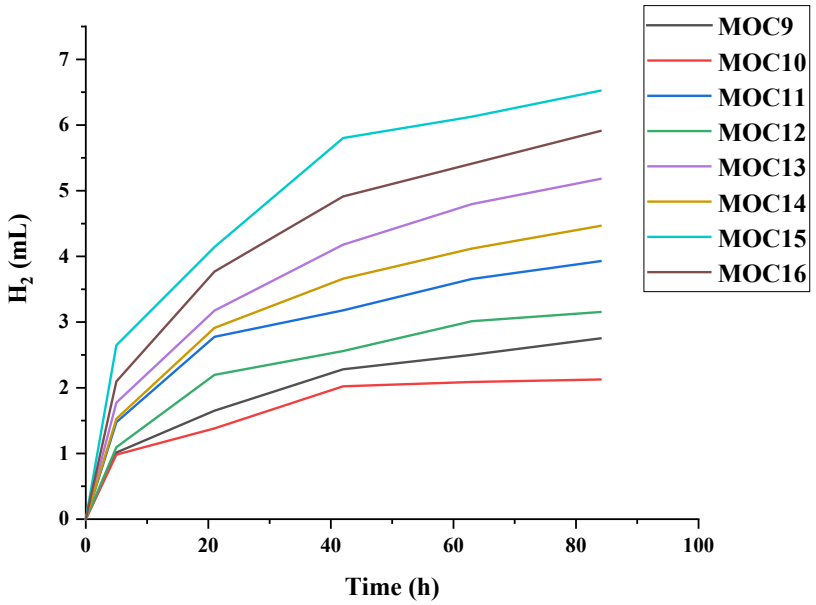

Fig. 5.21. Photocatalytic hydrogen evolution by metal–organic cage **MOC9** to **MOC16**

(10 μM) /CdS NR (L/D = 12; 1 mg) /AA (0.5 M) catalysts from H_2O (5 mL) upon irradiation with a 470-nm LED at 19 °C, pH 4.0, and 1 atm initial pressure of N_2:CH_4 (80:20 mol %), with CH_4 as the internal standard for hydrogen quantification via GC.

Table 5.6. Photocatalytic hydrogen evolution by metal–organic cage **MOC9** to **MOC16** /CdS NR (L/D = 12)/ AA catalysts under blue-light irradiation.

MOC	Time /h	H_2 /mL	TON[a]	TOF[b] /h^{-1}	TOF_i[c] /h^{-1}	$Activity_i$[d] /μmol g^{-1} h^{-1}
MOC9	84	2.8	4494	53.5	331.5	82872
MOC10	84	2.1	3470	41.3	321.1	80263
MOC11	84	3.9	6415	76.4	482.3	120568
MOC12	84	3.2	5150	61.3	357.3	89326
MOC13	84	5.2	8457	100.7	579.4	144849
MOC14	84	4.5	7292	86.8	499.0	124762
MOC15	84	6.5	10651	126.8	864.9	216236
MOC16	84	5.9	9651	114.9	684.4	171109

[a] Turnover number for hydrogen calculated as twice the number of moles of hydrogen produced divided by the number of moles of metal–organic cages catalyst. [b] Turnover frequency calculated per hour. [c] Initial turnover frequency for the first 5 h. [d] Photocatalytic activity of the system defined as the number of micromoles of H_2 evolved per mg of CdS NRs loaded per hour.

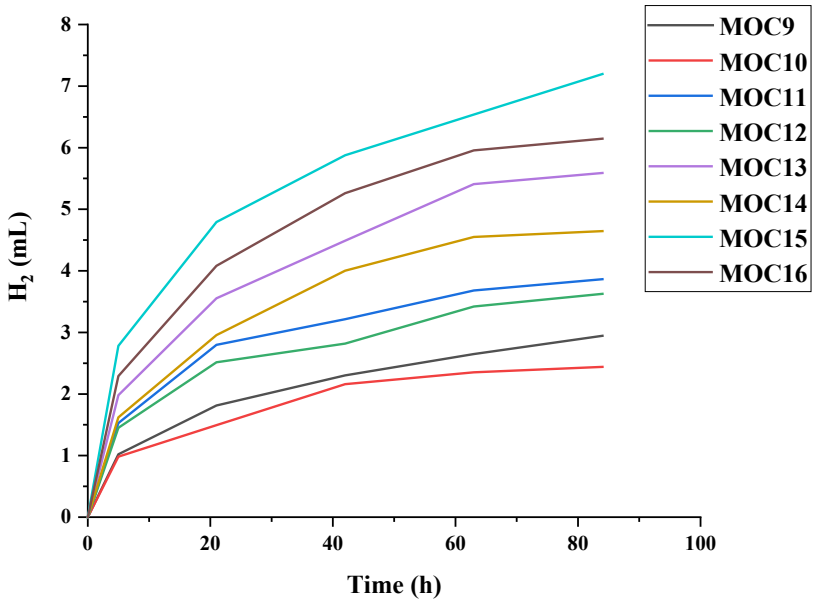

Fig. 5.22. Photocatalytic hydrogen evolution by metal–organic cage **MOC9** to **MOC16**

(10 μM) /CdS NR (L/D = 18; 1 mg) /AA (0.5 M) catalysts from H_2O (5 mL) upon irradiation with a 470-nm LED at 19 °C, pH 4.0, and 1 atm initial pressure of N_2:CH_4 (80:20 mol %), with CH_4 as the internal standard for hydrogen quantification via GC.

Table 5.7. Photocatalytic hydrogen evolution by metal–organic cage **MOC9** to **MOC16** /CdS NR (L/D = 18)/ AA catalysts under blue-light irradiation.

MOC	Time /h	H_2 /mL	TON[a]	TOF[b] /h^{-1}	TOF_i[c] /h^{-1}	$Activity_i$[d] /μmol g^{-1} h^{-1}
MOC9	84	2.9	4809	57.3	333.5	83381
MOC10	84	2.4	3985	47.4	321.1	80263
MOC11	84	3.9	6308	75.1	499.0	124762
MOC12	84	3.6	5921	70.5	473.5	118373
MOC13	84	5.6	9123	108.6	647.1	161783
MOC14	84	4.6	7585	90.3	529.6	132402
MOC15	84	7.2	11751	139.9	908.4	227100
MOC16	84	6.1	10035	119.5	748.1	187023

[a] Turnover number for hydrogen calculated as twice the number of moles of hydrogen produced divided by the number of moles of metal–organic cages catalyst. [b] Turnover frequency calculated per hour. [c] Initial turnover frequency for the first 5 h. [d] Photocatalytic activity of the system defined as the number of micromoles of H_2 evolved per mg of CdS NRs loaded per hour.

Generally, all the MOCs promoted hydrogen generation. MOCs with a triphenylamine backbone were better than those with a benzene ring backbone. Triphenylamine with a donor–π–acceptor (D–π–A) framework can efficiently facilitate intramolecular charge transfer from the ground state to the excited state, broadening the molecular absorption spectrum and enhancing the charge carrier mobility [53-56]. Furthermore, it was found that MOCs with Co were better than those with Ni in water-splitting hydrogen production owing to their superior charge-transfer ability, which has been shown in **Fig. 5.15** to **Fig.5.18**.

For the catalytic systems containing CdS NRs (L/D = 12), those with **MOC7** and **MOC15** produced the largest amount of hydrogen, with TONs of 51592 and 10651 and TOFs of 614.2 h^{-1} and 126.8 h^{-1} over 84 h, respectively, and they were followed by the systems with **MOC8** and **MOC16**, which had TONs of 37571 and 9651, respectively. In the catalytic systems containing longer CdS NRs (L/D = 18), the amount of hydrogen produced was slightly greater. The highest TON values of 56205 and 11751 were obtained with systems containing **MOC7** and **MOC15**, respectively, and they were followed by systems with **MOC8** and **MOC16**, which had TONs of 43201 and 10035, respectively.

In both systems, MOCs with furan produced the largest amount of hydrogen because of their large red-shift[57] and the greatly increased molar extinction coefficients in their UV spectra. In particular, furan has the lowest energy of charge-transfer transition as it has the smallest resonance energy,[40] Compared with a benzene spacer, the introduction of a heterocyclic ring spacer such as furan or thiophene in a triphenylamine or benzene backbone reduces the band gap and broadens the absorption spectra through intramolecular charge-transfer,[58] which can enhance the water-splitting hydrogen production ability.

A control system with only **MOC1** and AA was also conducted for water-splitting hydrogen generation. The experimental results are shown in **Fig. 5.23** and **Table 5.8**. From the results, it is apparent that photocatalytic hydrogen generation with our new MOCs containing CdS NRs was more efficient and stable. Furthermore, we revisited the literature and sorted out the performance data of similar MOCs (**Table 5.9**).

Compared with the MOCs reported in the literature, our MOCs, especially **MOC7**, showed a significant improvement in light-driven hydrogen evolution. These results also indicate that our new MOCs are promising candidates for highly stable and efficient photocatalytic application.

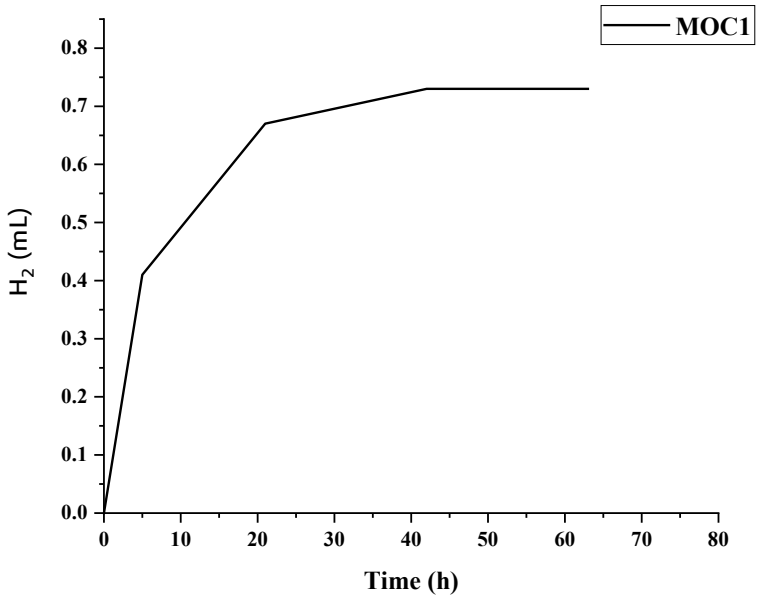

Fig. 5.23. Photocatalytic hydrogen evolution by metal–organic cage **MOC1** (10 μM) /AA (0.5 M) catalysts from H_2O (5 mL) upon irradiation with a 470-nm LED at 19 °C, pH 4.0, and 1 atm initial pressure of N_2:CH_4 (80:20 mol %), with CH_4 as the internal standard for hydrogen quantification via GC.

Table 5.8. Photocatalytic H_2 generation data with **MOC1** under blue light irradiation.

MOC	Time /h	H_2 /mL	TON[a]	TOF[b] /h^{-1}	TOF_i[c] /h^{-1}	$Activity_i$[d] /μmol g^{-1} h^{-1}
MOC1	63	0.73	1192	18.9	133.9	33469

[a] Turnover number (TON) of H_2 was calculated as twice of the number of moles of H_2 produced over the number of moles of metal–organic cages attached to platinized

TiO_2. [b] Turnover frequency (TOF) was calculated per hour. [c] Initial turnover frequency (TOF_i) in the first 5 h. [d] Initial photocatalytic activity ($Activity_i$) is defined as the number of micromoles of H_2 evolved per gram of platinum loaded per hour.

Table 5.9. Performance for light-driven hydrogen evolution based on different MOCs systems.

metal–organic cage	H_2 performance (μmol/g for first 3 h)	SED	Reference
g-C3N4/MOC-Q2	About 20000	Triethanolamine	[28]
15 TBC	About 1500	Triethanolamine	[19]
Zr-Bpydc-$PtCl_2$ MOCs	About 25000	Triethanolamine	[2]
Pt/ZrT-1-NH_2	4024	Acetonitrile	[59]
MOC7 with CdS NRs	408000	AA (pH=4)	This study

The durability of the catalyst is also of considerable importance for water-splitting hydrogen generation. During the cycling experiment, **MOC 1** was performed by every 3 h cyclic tests (**Fig. 5.24**). After four reaction cycles, the hydrogen production performance was sustained and showed only a marginal decline. These results showed the high durability of the MOCs.

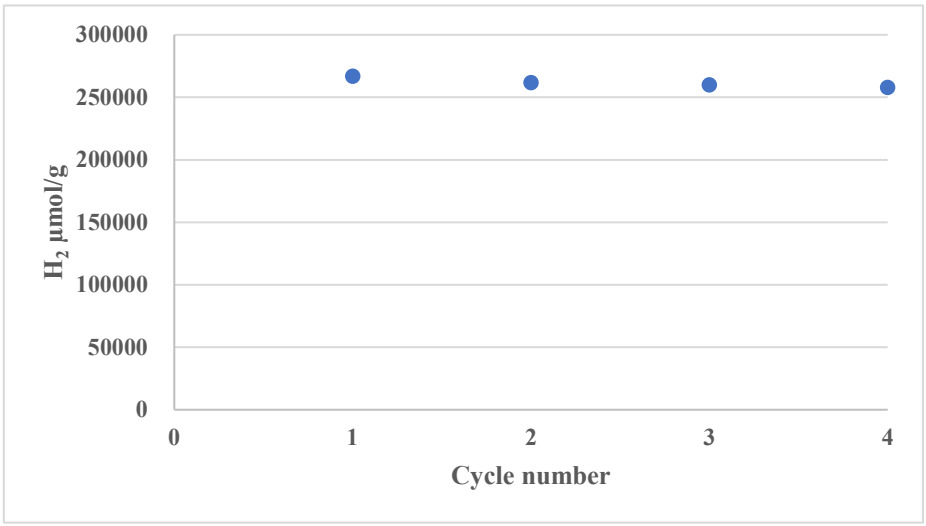

Fig. 5. 24. Cycle durability test for each 3 h on **MOC1** photocatalytic water splitting under visible light irradiation.

Water splitting hydrogen generation reaction with another common system containing fluorescein (FI) have been conducted and the result have been presented in **Fig. 5.25** and **Table 5.10**. From the results, the photocatalytic hydrogen generation of our CdS NRs systems are more efficient with higher stability than that of FI system.

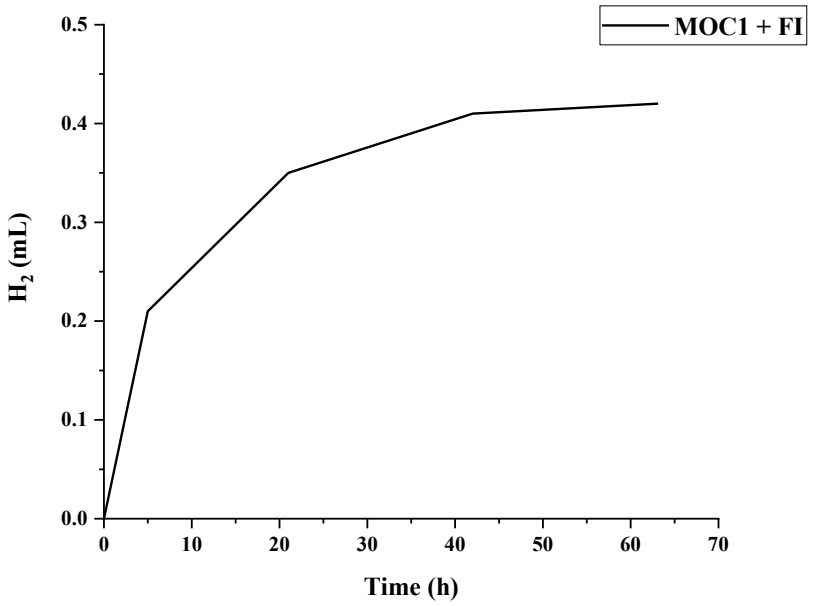

Fig. 5.25. Photocatalytic hydrogen evolution by metal–organic cage **MOC1** (4 μM) / fluorescein (2 mM) from H_2O (5 mL) upon irradiation with a 470-nm LED at 19 °C, pH 4.0, and 1 atm initial pressure of N_2:CH_4 (80:20 mol %), with CH_4 as the internal standard for hydrogen quantification via GC.

Table 5.10. Photocatalytic H_2 generation data with **MOC1** with FI under blue light irradiation

MOC	Time /h	H_2 /mL	TON[a]	TOF[b] /h^{-1}	TOF_i[c] /h^{-1}	$Activity_i$[d] /μmol g^{-1} h^{-1}
MOC1	63	0.42	1714	27.2	171.4	17143

[a] Turnover number (TON) of H_2 was calculated as twice of the number of moles of H_2 produced over the number of moles of metal–organic cages attached to platinized TiO_2. [b] Turnover frequency (TOF) was calculated per hour. [c] Initial turnover frequency (TOF_i) in the first 5 h. [d] Initial photocatalytic activity ($Activity_i$) is defined as the number of micromoles of H_2 evolved per gram of platinum loaded per hour.

5.11. Conclusions

Two sets of metal–organic cages were synthesised and combined with ligand-free CdS NRs to form photocatalytic water-splitting hydrogen generation systems in a fully

aqueous environment. The highest TON and TOF values (56205 h^{-1} and 669.1 h^{-1}, respectively) were obtained for the system containing **MOC7**. The catalytic systems containing **MOC15** achieved a TON of 10651 and a TOF of 126.8 over 84 h, the best among their set of MOCs. MOCs with a triphenylamine framework backbone were better than those with a benzene backbone for water-splitting hydrogen production. This study also indicates that controlling the length of the CdS NRs can potentially optimise the efficiency of MOC/CdS NR/AA photocatalytic water-splitting hydrogen generation systems. What is more, further optimization of water splitting systems will be conducted to enhance the water splitting hydrogen generation.

5.12. References

[1] J.-D. Xiao, Q. Shang, Y. Xiong, Q. Zhang, Y. Luo, S.-H. Yu, H.-L. Jiang, *Angew. Chem. Int. Ed.* **2016**, *55*, 9389-9393.

[2] C. Q. Ji, W. J. Wang, E.-S. M. El-Sayed, G. L. Liu, Y. N. Si, K. Z. Su, Z. F. Ju, F. Wu, D. Q. Yuan, *Appl. Catal. B* **2021**, *285*, 119782.

[3] M. T. Zhao, Y. Huang, Y. W. Peng, Z. Q. Huang, Q. L. Ma, H. Zhang, *Chem. Soc. Rev.* **2018**, *47*, 6267-6295.

[4] H. Liu, C. Xu, D. Li, H.-L. Jiang, *Angew. Chem.* **2018**, *130*, 5477-5481.

[5] G. Liu, Y. Di Yuan, J. Wang, Y. Cheng, S. B. Peh, Y. Wang, Y. Qian, J. Dong, D. Yuan, D. Zhao, *J. Am. Chem. Soc.* **2018**, *140*, 6231-6234.

[6] M. Sun, C. Sun, X. Wang, Z. Su, *Catal. Commun.* **2020**, *137*, 105930.

[7] S. Ott, M. Kritikos, B. Åkermark, L. Sun, *Angew. Chem. Int. Ed.* **2003**, *42*, 3285-3288.

[8] L.-C. Song, S.-Z. Mei, C.-P. Feng, F.-H. Gong, J.-H. Ge, Q.-M. Hu, *Organometallics* **2010**, *29*, 5050-5056.

[9] X. Li, M. Wang, D. Zheng, K. Han, J. Dong, L. Sun, *Energy Environ. Sci.* **2012**, *5*, 8220-8224.

[10] W. Gao, J. Sun, T. Åkermark, M. Li, L. Eriksson, L. Sun, B. Åkermark, *Chem. Eur. J.* **2010**, *16*, 2537-2546.

[11] W. Wang, X.-W. Song, Z. Hong, B. Li, Y. Si, C. Ji, K. Su, Y. Tan, Z. Ju, Y. Huang, C.-N. Chen, D. Q. Yuan. *Appl. Catal. B* **2019**, *258*, 117979.

[12] S. Chen, K. Li, F. Zhao, L. Zhang, M. Pan, Y. Z. Fan, J. Guo, J. Y. Shi, C. Y. Su, *Nat. Commun.* **2016**, *7*, 1-8.

[13] X. Jing, C. He, Y. Yang, C. Duan, *J. Am. Chem. Soc.* **2015**, *137*, 3967-3974.

[14] R. Chakrabarty, P. S. Mukherjee, P. J. Stang, *Chem. Rev.* **2011**, *111*, 6810-6918.

[15] S. Leininger, B. Olenyuk, P. J. Stang, *Chem. Rev.* **2000**, *100*, 853-908.

[16] S. R. Seidel, P. J. Stang, *Acc. Chem. Res.* **2002**, *35*, 972-983.

[17] H. S. Lee, S. Jee, R. Kim, H.-T. Bui, B. Kim, J.-K. Kim, K. S. Park, W. Choi, W. Kim, K. M. Choi, *Energy Environ. Sci.* **2020**, *13*, 519-526.

[18] T.-F. Chen, S.-Y. Han, Z.-P. Wang, H. Gao, L.-Y. Wang, Y.-H. Deng, C.-Q. Wan, Y. Tian, Q. Wang, G. Wang, G.-S. Li, *Appl. Catal. B* **2019**, *259*, 118047.

[19] F. Li, D. K. Wang, Q.-J. Xing, G. Zhou, S.-S. Liu, Y. Li, L.-L. Zheng, P. Ye, J.-P. Zou, *Appl. Catal. B* **2019**, *243*, 621-628.

[20] J. X. Jian, Q. Liu, Z. J. Li, F. Wang, X. B. Li, C. B. Li, B. Liu, Q. Y. Meng, B. Chen, K. Feng, *Nat. Commun.* **2013**, *4*, 1-9.

[21] F. Wang, W.-J. Liang, J.-X. Jian, C.-B. Li, B. Chen, C.-H. Tung, L.-Z. Wu, *Angew. Chem.* **2013**, *125*, 8292-8296.

[22] M. Zhou, S. Bao, A. J. Bard, *J. Am. Chem. Soc.* **2019**, *141*, 7327-7332.

[23] J. Liu, Y. Li, X. Zhou, H. Jiang, H. G. Yang, C. Li, *J. Mater. Chem. A* **2020**, *8*, 17-26.

[24] C. Königstein, *J. Photochem. Photobiol. A. Chem.* **1995**, *90*, 141-152.

[25] Y. Na, J. Pan, M. Wang, L. Sun, *Inorg. Chem.* **2007**, *46*, 3813-3815.

[26] A. Zarkadoulas, E. Koutsouri, C. A. Mitsopoulou, *Coord. Chem. Rev.* **2012**, *256*,

2424-2434.
[27] W. R. Mcnamara, Z. Han, C.-J. Yin, W. W. Brennessel, P. L. Holland, R. Eisenberg, *Proc. Natl. Acad. Sci. U.S.A.* **2012**, *109*, 15594-15599.
[28] C. Y. Lv, S. Qin, Y. Lei, X. A. Li, J. F. Huang, J. M. Liu, *Nanomaterials* **2022**, *12*, 890.
[29] S. Knop, J. Lindner, P. Vöhringer, *Z. Phys. Chem.* **2011**, *225*, 913-926.
[30] J. M. Ramos, M. T. De M. Cruz, A. C. Costa Jr, O. Versiane, C. A. Tellez Soto, *ScienceAsia* **2011**, *37*, 247-255.
[31] T. Fahmy, A. Sarhan, I. A. Elsayed, H. G. Abdelwahed, *Int. J. Eng. Res. Technol.* **2018**, *11*, 1405-1415.
[32] W. Grzesiak, B. Brycki, *Molecules* **2012**, *17*, 12427-12448.
[33] C. Preti, G. Tosi, D. D. Filippo, G. Verani, *Can. J. Chem.* **1974**, *52*, 2021-2028.
[34] F. Zimmermann, T. Lippert, C. Beyer, J. Stebani, O. Nuyken, A. Wokaun, *Appl. Spectrosc.* **2016**, *47*, 986-993.
[35] L. C. Thomas, R. A. Chittenden, *Spectrochim. Acta.* **1964**, *20*, 467-487.
[36] D. M. Wiles, B. A. Gingras, T. Suprunchuk, *Can. J. Chem.* **1967**, *45*, 469-473.
[37] M. Kristl, B. Dojer, S. Gyergyek, J. Kristl, *Heliyon* **2017**, *3*, e00273.
[38] S. X. Wei, X. Q. Lu, X. F. Shi, Z. G. Deng, Y. Shao, L. M. Zhao, W. Y. Guo, C.-M. L. Wu, *Int. J. Photoenergy* **2014**, *2014*, 280196.
[39] X. Yao, P.-Y. Ho, S.-C. Yiu, S. Suramitr, W. B. Li, C.-L. Ho, S. Hannongbua, *Dyes Pigm.* **2022**, *205*, 110508.
[40] K. Kakiage, Y. Aoyama, T. Yano, K. Oya, T. Kyomen, M. Hanaya, *Chem. Commun.* **2015**, *51*, 6315-6317.
[41] Q.-L. Xu, C.-C. Wang, T.-Y. Li, M.-Y. Teng, S. Zhang, Y.-M. Jing, X. Yang, W.-N. Li, C. Lin, Y.-X. Zheng, *Inorg. Chem.* **2013**, *52*, 4916-4925.
[42] P. Tian, X. He, L. Zhao, W. Li, W. Fang, H. Chen, F. Zhang, Z. Huang, H. Wang, *Int. J. Hydrogen Energy* **2019**, *44*, 788-800.
[43] P. Tian, X. He, L. Zhao, W. X. Li, W. Fang, H. Chen, F. Q. Zhang, Z. H. Huang, H. L. Wang, *Sol. Energy* **2019**, *188*, 750-759.
[44] H. Y. Wang, C. Y. Gao, R. Li, Z. K. Peng, J. H. Yang, J. Gao, Y. P. Yang, S. H. Li, B. J. Li, Z. Y. Liu, *ACS Sustainable Chem. Eng.* **2019**, *7*, 18744-18752.
[45] Y. Wang, P. Zheng, M. X. Li, Y. R. Li, X. Zhang, J. Chen, X. Fang, Y. J. Liu, X. L. Yuan, X. P. Dai, *Nanoscale* **2020**, *12*, 9669-9679.
[46] R. Acharya, B. Naik, K. Parida, *Beilstein J. Nanotechnol.* **2018**, *9*, 1448-1470.
[47] Y. Zhang, Z. R. Liu, C. Y. Guo, T. X. Chen, C. Guo, Y. Lu, J. D. Wang, *Appl. Surf. Sci.* **2022**, *571*, 151284.
[48] D. Jiang, W. Wang, S. Sun, L. Zhang, Y. Zheng, *ACS Catal.* **2015**, *5*, 613-621.
[49] P. Peerakiatkhajohn, J.-H. Yun, S. C. Wang, L. Z. Wang, *J. Photonics Energy* **2016**, *7*, 012006.
[50] J.-Y. Tang, R.-T. Guo, W.-G. Zhou, C.-Y. Huang, W.-G. Pan, *Appl. Catal. B* **2018**, *237*, 802-810.
[51] S. Cao, Q. Huang, B. Zhu, J. Yu, *J. Power Sources* **2017**, *351*, 151-159.
[52] F. C. Leng, H. Liu, M. L. Ding, Q. P. Lin, H. L. Jiang, *ACS Catal.* **2018**, *8*, 4583-4590.

[53] X. L. Tang, W. M. Liu, J. S. Wu, C.-S. Lee, J. J. You, P. F. Wang, *J. Org. Chem.* **2010**, *75*, 7273-7278.
[54] R. Chen, G. Zhao, X. Yang, X. Jiang, J. Liu, H. Tian, Y. Gao, X. Liu, K. Han, M. Sun, *J. Mol. Struct.* **2008**, *876*, 102-109.
[55] W. Zhang, B. Li, H. Ma, L. Zhang, Y. Guan, Y. Zhang, X. Zhang, P. Jing, S. Yue, *ACS Appl. Mater. Interfaces* **2016**, *8*, 21465-21471.
[56] B.-G. Kim, K. Chung, J. Kim, *Chem. Eur. J.* **2013**, *19*, 5220-5230.
[57] J. Li, Y. Hao, M. Zhong, L. Tang, J. Nie, X. Zhu, *Dyes Pigm.* **2019**, *165*, 467-473.
[58] A. Kathiravan, V. Srinivasan, T. Khamrang, M. Velusamy, M. Jaccob, N. Pavithra, S. Anandan, K. Velappan, *Phys. Chem. Chem. Phys.* **2017**, *19*, 3125-3135.
[59] M. Sun, Q.-Q. Wang, C. Qin, C.-Y. Sun, X.-L. Wang, Z.-M. Su, *Chem. Eur. J.* **2019**, *25*, 2824-2830.

Chapter 6: Concluding Remarks and Future Work

A series of novel ruthenium(II) complexes used as photosensitisers containing different functional groups were successfully synthesised and fully characterised by NMR and mass spectroscopies. Furthermore, their electrochemical and photophysical properties were investigated. Some selected molecules were structurally analysed using density functional theory calculations. First, attempts were made to synthesise a series of Ru(II) dyes using π-conjugation cyclometalating (C^N) ligands by inserting electron-donating triphenylamine into isoquinoline or pyridine through the thiophene moiety (**Fig. 2.2**), inducing ability of strong intramolecular charge transfer. All the Ru(II) complexes were used as photosensitisers for light-driven water splitting hydrogen production by attaching them to platinised TiO_2 nanoparticles (Pt-TiO_2) in the presence of sacrificial electron donor in an aqueous solution. The relationship between the anchoring groups and their hydrogen production activities was also discussed. An H_2 turnover number (TON) of up to 14 231 was recorded after 236 h of irradiation with the best Ru(II) water-splitting system.

Novel synthetic routes were developed to prepare a new class of iridium(III) dyes with either diethyl [2,2 -bipyridine]-4,4 -dicarboxylate or tetraethyl[2,2 -bipyridine]-4,4 -diylbis(phosphonate) anchoring units. The absorption spectra of these dyes, especially those containing the triphenylamine moiety, were broader with enhanced molar absorptivities (ε) compared to common iridium(III) dyes, such as [**Ir(bpy)$_3$**]$^+$. The energy levels of our new Ir(III) dyes were fine-tuned by chemically modifying the

cyclometalating (C^N) ligands and the anchoring groups. The attractive photophysical and redox properties of the Ir(III) dyes conferred good potential for light-driven hydrogen production. Furthermore, efforts were also made to synthesise Ir(III) dyes with aldehyde functional groups in the C^N ligands (**Fig. 3.2**). A respectable hydrogen TON of 15 509 in a platinised TiO_2 hydrogen-production system was demonstrated with the best Ir(III) water-splitting system.

Furthermore, a series of salen, thiasalen, or salophen earth-abundant metal complexes were successfully synthesised. Different electron-withdrawing or electron-donating functional groups were introduced to determine their influence on hydrogen generation from water splitting (**Fig. 4.2**). Additionally, CdS NRs of various sizes and aspect ratios, having different catalytic activity levels, were examined, suggesting a possible way to improve photocatalytic system efficiency. Furthermore, the proposed mechanisms of different metal complexes during hydrogen generation from water splitting were also discussed. A photocatalytic system containing a metal-salophen complex based on nickel achieved a steady and impressive catalytic activity with a TON of 57 239 and a turnover frequency (TOF) of 436.9 h^{-1} over 131 h under blue-light irradiation.

Finally, work was conducted on the design and synthesis of new metal–organic cages. These metal–organic cages were fully characterised by NMR and mass spectroscopies. Moreover, their photophysical properties and water-splitting performance were investigated. Selected molecules were structurally analysed by Fourier transform infrared (FTIR) spectroscopy to confirm their structures. Furthermore, electrochemical impedance spectroscopy and photocurrents were used to verify their charge separation

and recombination efficiency, and photostability. The cycle durability test was performed for selected metal–organic cages and showed satisfactory results. The water-splitting hydrogen generation reactions of different systems were also investigated. A photocatalytic system containing a metal–organic cages and CdS NRs achieved a steady and impressive catalytic activity with a TON of 57 238 and TOF of 389 h^{-1} over 84 h under blue-light irradiation.

Future work related to this project may focus on employing these materials in biological applications. For example, iridium-based luminophores will be adopted as high-sensitivity and low-response time oxygen sensors.[1] Also, ruthenium and iridium complexes can be designed for luminescence cell imaging for their attractive photophysical properties.[2, 3] Moreover, ruthenium and iridium complexes with Pt-TiO_2 can be applied in water purification, especially for organic dyes, such as methyl orange and rhodamine B.[4, 5] Furthermore, a deep study of metal-organic cages will be conducted, for example, to explore the effects of using different light sources or solvent systems. We will use the 300W Xenon Lamp as the light source to determine the water-splitting hydrogen generation performance. The water-splitting hydrogen generation systems of earth-abundant metal complexes will be optimised to improve the hydrogen generation efficiency, for example, different size of CdS NRs will be applied to the system to determine the best water splitting hydrogen generation performance. Moreover, carbon quantum dots will be used instead of CdS NRs to conduct the water-splitting hydrogen generation experiments for the environmentally friendly reason and better photocatalytic efficiency.

References:

[1] X. Jiang, J. Peng, J. Wang, X. Guo, D. Zhao, Y. Ma, *ACS Appl. Mater. Interfaces* **2016**, *8*, 3591-3600.
[2] H. Huang, S. Banerjee, P. J. Sadler, *ChemBioChem* **2018**, *19*, 1574-1589.
[3] R. Zhang, Z. Ye, Y. Yin, G. Wang, D. Jin, J. Yuan, J. A. Piper, *Bioconjug. Chem.* **2012**, *23*, 725-733.
[4] F. Mousli, A. Chaouchi, M. Jouini, F. Maurel, A. Kadri, M. M. Chehimi, *Catalysts* **2019**, *9*, 578.
[5] Z. Youssef, L. Colombeau, N. Yesmurzayeva, F. Baros, R. Vanderesse, T. Hamieh, J. Toufaily, C. Frochot, T. Roques-Carmes, S. Acherar, *Dyes Pigm.* **2018**, *159*, 49-71.

Chapter 7 Experimental Details

7.1. General Procedures

All reactions were carried out under nitrogen atmosphere with the use of standard Schlenk techniques. Glassware was dried with oven at 140 °C before use. All chemicals and reagents, unless otherwise stated, were purchased from Dieckmann or Sigma and used without further purification. All the reactions were monitored by thin-layer chromatography (TLC) with Merck silica gel pre-coated aluminum plates. Purification of the products were achieved by column chromatography using silica gel (230–400 mesh) or basic aluminum oxide purchased from Dieckmann. TLC was carried out in air at room temperature using laboratory grade solvents as eluents.

7.2. Instrumentation

7.2.1. Nuclear magnetic resonance

^{1}H and ^{13}C NMR spectra were measured in $CDCl_3$, MeOD or DMSO-d6 on a Bruker Ultra-shield 400 MHz FT-NMR spectroscopy and tetramethylsilane (TMS) was used as an internal standard for calibrating the chemical shift.

7.2.2. Mass spectrometry

Matrix-assisted laser desorption ionization time–of–flight (MALDI-TOF) or liquid Chromatography–electrospray ionization–quadrupole–time–of–flight (LC-ESI-Q-TOF) mass spectrometry was performed on an Autoflex Bruker MALDI-TOF or Agilent 6540

system, respectively.

7.2.3. UV–Vis absorption spectra

UV–Vis absorption spectra were recorded on an Agilent Technologies Cary 8454 UV-Vis spectrometer in MeOH, CH_2Cl_2 or DMSO solution at 293 K.

7.2.4. Cyclic voltammetry

Cyclic voltammetry (CV) measurements were performed with a CHI 680D Electrochemical Analyzer/Workstation, using glassy carbon electrode as the working electrode, platinum wire as the counter electrode, and Ag/Ag^+ as the reference electrode, in acetonitrile, DMSO or dichloromethane solution containing 0.1 M tetrabutylammonium hexafluorophosphate at a scan rate of 100 mV s^{-1}.

7.2.5. Electrochemical impedance spectroscopy

Electrochemical impedance spectroscopy characterization was conducted on an electrochemical workstation CHI660E (Shanghai Chenhua, China), using a three-electrode system. Ag/AgCl was served as reference electrode with the platinum electrode as counter electrode, 0.5 M Na_2SO_4 solution as electrolyte. The working electrode was prepared by the following procedure: 10 mg of metal complex was dispersed in 1 mL ethanol and 20 μL Nafion aqueous solution (5 wt%), and was ultrasonically scattered for 2 h. 0.1 mL of this slurry was then added in dropwise on the fluorine-doped tin oxide glass (FTO, 1 cm^2), and the metal complex was attached to the

FTO glass surface after the ethanol evaporated. The spectra were scanned in a frequency range of 0.1 Hz to 100 KHz at room temperature with applied bias potential set at –700 mV. The alternate current amplitude was set at 5 mV. All the experiments were conducted at room temperature.

7.2.6. Inductively coupled plasma optical emission spectroscopy

Inductively coupled plasma optical emission spectroscopy (ICP-OES) was conducted by Agilent Technologies 700 series ICP-OES at room temperature.

7.2.7. Transmission electron microscopy and element mapping

Transmission electron microscopy (TEM) and element mapping were performed with FEI Talos F200S at room temperature.

7.2.8. Scanning electron microscope

Scanning electron microscope (SEM) was performed in Hitachi S-4800 at room temperature.

7.2.9. Photocurrent

Photocurrent measurements were carried out on a CHI 660E electrochemical system (Shanghai Chenhua, China). A typical three-electrode system was immersed in a 0.5 mol/L Na_2SO_4 electrolyte solution. Sample coated FTO conductive glass, Pt wire, and Ag/AgCl were employed as the working, counter, and reference electrodes,

respectively. The working electrode was obtained by dispersing 10 mg of the prepared sample in a mixed solution of ethanol (1 mL) and Nafion (20 μL, 5%), followed by ultrasonic dispersion for 2 h. Afterwards, 0.1 mL of the resulting slurry was dropped on the surface of an FTO glass slide (1 × 1 cm). After evaporating of the ethanol, the complex was applied onto the FTO glass. The spectra were obtained in the frequency range of 0.1 Hz to 100 kHz with an applied bias potential of –700 mV and an AC amplitude of 5 mV. The light power was Xe lamp with 300 W. All of the experiments were conducted at room temperature.

7.2.10. Fourier-transform infrared spectroscopy

Fourier-transform infrared (FT-IR) characterization were determined by Bruker Vector-22 infrared spectroscopy at room temperature, and KBr was used as a blank control.

7.3. Experimental Details for Chapter 2

7.3.1. Computational details

Geometry optimizations of the ruthenium(II) dyes in the ground state and in water solution have been performed with density functional theory (DFT). CAM-B3LYP calculation was performed with DFT using the Gaussian 98 program. The geometries were fully optimized in gas at hybrid DFT levels by CAM-B3LYP functions, which combine Becke's three-parameter exchange function (B3) with the correlation function of Lee, Yang and Parr (LYP). A LanL2DZ basis set was used for Ru. All geometry optimizations were computed in water solution using the CPCM solvation model and

with the 6-311G(d,p) basis set.

7.3.2. Synthesis of ligand compounds

1: To a two-neck round bottom flask containing magnesium (2.200 g, 0.090 mol), 180 mL of dry THF was added by syringe. 2-Bromothiophene (14.020 g, 0.086 mol) was then added under ice bath, which was stirred at 0 °C for 0.5 h. The reaction mixture was further stirred at room temperature for 1.5 h before trimethyl borate (15 mL, 0.135 mol) was added under ice bath. The reaction mixture was then stirred overnight at room temperature under N_2 atmosphere. 2M HCl was added to the mixture under ice bath until the reaction mixture became acidic. After being stirred at 0 °C for another 0.5 h, the resulting mixture was extracted with diethyl ether and brine. The organic layer was dried over sodium sulfate, filtered and concentrated under reduced pressure to give the product as white solid. The titled compound was used in the subsequent reaction without further purification (yield: 8.799 g, 80%).

L1: To a round bottom flask containing 2-bromopyridine (0.9 mL,10.000 mmol) in tetrahydrofuran (250 mL), thiophen-2-ylboronic acid (2.000 g, 15.600 mmol) was added. Tetrakis(triphenylphosphine)palladium(0) (1.155 g, 1.000 mmol) and 2M of potassium carbonate (32 mL, 6.240 mmol) were added to the reaction mixture, which was then heated to 85 °C for 48 h. After being cooled to room temperature, the mixture was extracted with ethyl acetate and brine. The organic layer was dried over sodium sulfate, filtered and concentrated by reduced pressure. The crude product was purified by silica gel column chromatography using dichloromethane/*n*-hexane (1:1, *v/v*) as

eluent to give the final product as a yellow solid (yield: 1.321 g, 86%). ^{1}H NMR (400 MHz, $CDCl_3$) δ 8.62 (d, *J* = 4.8 Hz, 1H), 7.73 (dd, *J* = 18.9, 7.7 Hz, 3H), 7.45 (d, *J* = 4.9 Hz, 1H), 7.24 – 7.08 (m, 2H). ^{13}C NMR (101 MHz, $CDCl_3$) δ 128.2, 127.9, 121.9, 119.1. Found: $[M+H]^+$ 162.0376; 'molecular formula C_9H_7NS ' requires $[M+H]^+$ 162.0372.

L2: To a round bottom flask containing 2-chloro-5-(trifluoromethyl)pyridine (0.454 g, 2.500 mmol) in tetrahydrofuran (250 mL), thiophen-2-ylboronic acid (0.500 g, 3.900 mmol) was added. Tetrakis(triphenylphosphine)palladium(0) (0.288 g, 0.250 mmol) and 2M of potassium carbonate (8 mL, 16.000 mmol) were added to the reaction mixture, which was then heated to 115 °C for 48 h. After being cooled to room temperature, the mixture was extracted with ethyl acetate and brine. The organic layer was dried over sodium sulfate, filtered and concentrated by reduced pressure. The crude product was purified by silica gel column chromatography using dichloromethane/*n*-hexane (2:1, *v/v*) as eluent to give the final product as a yellow solid (yield: 0.498 g, 87%). ^{1}H NMR (400 MHz, $CDCl_3$) δ 8.84 (s, 1H), 7.93 (dd, *J* = 8.3, 1.8 Hz, 1H), 7.78 – 7.72 (m, 2H), 7.49 (dd, *J* = 22.8, 4.4 Hz, 1H), 7.18 (dd, *J* = 4.8, 4.0 Hz, 1H). ^{13}C NMR (101 MHz, $CDCl_3$) δ 155.6, 146.5, 143.2, 133.8, 129.4, 128.3, 126.3, 118.1. Found: $[M]^+$ 229.0038; 'molecular formula $C_{10}H_6F_3NS$ ' requires $[M]^+$ 229.0168.

L3: To a round bottom flask containing 1-chloroisoquinoline (1.636 g, 10.000 mmol) in THF (50 mL), thiophen-2-ylboronic acid (2.000 g, 15.600 mmol) was added. Tetrakis(triphenylphosphine)palladium(0) (1.155 g, 1.000 mmol) and 2 M of potassium

carbonate (32 mL, 62.400 mmol) were then added, and the reaction mixture was heated up to 115 °C for 48 h. After being cooled to room temperature, the mixture was extracted with ethyl acetate and brine. The organic layer was dried over sodium sulfate, filtered and concentrated by reduced pressure. The crude product was purified by silica gel column chromatography using dichloromethane/*n*-hexane (1:1, *v/v*) as eluent to give the target compound as a yellow solid (yield: 1.667 g, 79%). ^{1}H NMR (400 MHz, $CDCl_3$) δ 8.62 – 8.53 (m, 2H), 7.92 (d, *J* = 8.1 Hz, 1H), 7.76 (t, *J* = 7.5 Hz, 1H), 7.66 (dd, *J* = 10.4, 7.0 Hz, 3H), 7.59 (d, *J* = 5.2 Hz, 1H), 7.26 (dd, *J* = 5.0, 3.7 Hz, 1H). ^{13}C NMR (100 MHz, $CDCl_3$): δ 153.5, 142.6, 142.0, 137.2, 130.3, 128.2, 127.8, 127.3, 126.9, 126.3, 120.1. Found: $[M+H]^+$ 212.0533; 'molecular formula $C_{13}H_9NS$ ' requires $[M+H]^+$ 212.0528.

2: To a round bottom flask containing 2-(thiophen-2-yl)pyridine (0.500 g, 3.063 mmol) in dichloromethane (10 mL), n-bromosuccinimide (0.599 g, 3.369 mmol) was added slowly. The reaction mixture was then stirred at room temperature overnight. The mixture was extracted with ethyl acetate and brine. The organic layer was dried over sodium sulfate, filtered and concentrated by reduced pressure. The crude product was purified by silica gel column chromatography using dichloromethane/*n*-hexane (1:1, *v/v*) as eluent to give the final product as a yellow oil (yield: 0.626 g, 84%). ^{1}H NMR (400 MHz, $CDCl_3$) δ 8.56 (d, *J* = 4.7 Hz, 1H), 7.71 (td, *J* = 7.8, 1.6 Hz, 1H), 7.60 (d, *J* = 7.9 Hz, 1H), 7.35 (d, *J* = 3.9 Hz, 1H), 7.19 (dd, *J* = 6.9, 5.3 Hz, 1H), 7.08 (d, *J* = 3.9 Hz, 1H). ^{13}C NMR (101 MHz, $CDCl_3$) δ 151.6, 149.3, 136.9, 130.9, 124.6, 122.2, 118.2, 115.2. Found: $[M+H]^+$ 241.9457; 'molecular formula C_9H_6BrNS ' requires $[M+H]^+$

241.9456.

3: To a round bottom flask containing 1-(thiophen-2-yl)isoquinoline (0.500 g, 2.367 mmol) in dichloromethane (10 mL), *N*-bromosuccinimide (0.505 g, 2.840 mmol) was added slowly. The reaction mixture was stirred at room temperature overnight. The mixture was then extracted with ethyl acetate and brine. The organic layer was dried over sodium sulfate, filtered and concentrated by reduced pressure. The crude product was purified by silica gel column chromatography using dichloromethane/*n*-hexane (2:1, *v/v*) as eluent to give the target product as a yellow oil (yield: 0.295 g, 43%). ^{1}H NMR (400 MHz, $CDCl_3$) δ 8.51 (dd, *J* = 15.7, 6.8 Hz, 2H), 7.89 (d, *J* = 7.7 Hz, 1H), 7.78 – 7.50 (m, 3H), 7.40 (s, 1H), 7.18 (s, 1H). ^{13}C NMR (101 MHz, $CDCl_3$) δ 152.3, 144.8, 142.1, 137.2, 130.4, 130.3, 128.9, 127.9, 127.4, 126.3, 125.8, 120.2, 115.6. Found: $[M+H]^+$ 291.9616 'molecular formula $C_{13}H_8BrNS$ ' requires $[M+H]^+$ 291.9613.

4: To a two-neck round bottom flask containing 4-bromo-*N*,*N*-diphenylaniline (2.000 g, 6.618 mmol), dry THF (50 mL) was added. After being cooled to –78 °C, *n*-butyllithium (3.084 mL from 2.4 M in hexane, 7.402 mmol) was introduced. The reaction mixture was stirred at –78 °C for 20 mins and trimethyl borate (1.057 mL, 9.252 mol) was added by syringe slowly. The mixture was stirred overnight at room temperature under N_2 atmosphere. 2M HCl was added to the mixture under ice bath until the pH became acidic. After being stirred at 0 °C for 30 mins, the resulting mixture was extracted with diethyl ether and brine. The organic layer was dried over sodium

sulfate, filtered and concentrated under reduced pressure. The crude product was purified by silica gel column chromatography using dichloromethane/diethyl ether (4:1, *v/v*) as eluent to give the target product as a white solid. The titled compound was used in the subsequent reaction without further purification (yield: 0.783 g, 44%).

L4: To a round bottom flask containing 2-(5-bromothiophen-2-yl)pyridine (0.429 g, 1.771 mmol) in toluene (50mL), (4-(diphenyl-amino) phenyl)boronic acid (0.799 g, 2.763 mmol) was added. Tetrakis(triphenylphosphine)palladium(0) (0.205 g, 0.177 mmol) and 2M of potassium carbonate (5.526 mL, 11.052 mmol) were added to the reaction mixture, which was then heated to 85 °C for 48 h. After being cooled to room temperature, the mixture was extracted with ethyl acetate and brine. The organic layer was dried over sodium sulfate, filtered and concentrated by reduced pressure. The crude product was purified by silica gel column chromatography using dichloromethane/*n*-hexane (1:1, *v/v*) as eluent to give the final product as a yellow solid (yield: 0.643 g, 89%). ^{1}H NMR (400 MHz, $CDCl_3$) δ 8.61 (d, *J* = 4.7 Hz, 1H), 7.79 – 7.61 (m, 3H), 7.53 (t, *J* = 15.6 Hz, 2H), 7.37 – 7.22 (m, 6H), 7.19 – 7.01 (m, 8H). ^{13}C NMR (101 MHz, $CDCl_3$) δ 147.3, 129.3, 126.5, 124.7, 123.4, 123.3, 121.6. Found: $[M+H]^+$ 405.1424; 'molecular formula $C_{27}H_{20}N_2S$ ' requires $[M+H]^+$ 405.1420.

L5: To a round bottom flask containing 1-(5-bromothiophen-2-yl)isoquinoline (0.400 g, 1.379 mmol) in THF (50 mL), (4-(diphenylamino)phenyl)boronic acid (0.622 g, 2.151 mmol) was added. Tetrakis(triphenylphosphine)palladium(0) (0.159 g, 0.138 mmol) and 2M of potassium carbonate (4 mL, 8.602 mmol) were then introduced. The

reaction mixture was heated up to 85 °C for 48 h. After being cooled to room temperature, the mixture was extracted with ethyl acetate and brine. The organic layer was dried over sodium sulfate, filtered and concentrated by reduced pressure. The crude product was purified by silica gel column chromatography using dichloromethane/*n*-hexane (1:1, *v/v*) as eluent to yield **L2** as a yellow solid (yield: 0.288 g, 46%). ^{1}H NMR (400 MHz, $CDCl_3$) δ 8.68–8.54 (m, 2H), 7.90 (d, *J* = 8.1 Hz, 1H), 7.75 (t, *J* = 7.4 Hz, 1H), 7.69 – 7.52 (m, 5H), 7.33 (dt, *J* = 14.1, 5.1 Hz, 4H), 7.19 – 6.97 (m, 9H). ^{13}C NMR (101 MHz, $CDCl_3$) δ 153.2, 147.3, 141.9, 141.0, 137.1, 130.1, 129.9, 129.3, 127.9, 127.6, 127.2, 126.7, 126.0, 124.6, 123.3, 123.2, 122.7, 119.7. Found: $[M+H]^+$ 455.1585; 'molecular formula $C_{31}H_{22}N_2S$ ' requires $[M+H]^+$ 455.1576.

7.3.3. Synthesis of Ru(II) complexes

Ru1: To a round bottom flask containing $[RuCl_2(p\text{-cymene})]_2$ (0.592 g, 1.183 mmol) in degassed acetonitrile (10 mL), **L1** (0.500 g, 2.367 mmol) and KPF_6 (0.762 g, 4.141 mmol) were introduced. NaOH (0.095 g, 2.367 mmol) was then added, and the reaction mixture was heated up at 45 °C for 20 h. After cooling to room temperature, the reaction mixture was purified by basic aluminum oxide column chromatography using dichloromethane/acetonitrile (1:1, *v/v*) as eluent to afford the ruthenium intermediate $[Ru(CH_3CN)_4(\mathbf{L1})]^+PF_6^-$. This raw product was then further purified by redissolving its solid in dichloromethane and precipitate with *n*-hexane to afford a brown solid. This intermediate was used directly for the next step.

To a flask containing $[Ru(CH_3CN)_4(\mathbf{L1})]^+PF_6^-$ (0.400 g, 0.841 mmol) in MeOH (15

mL), 4,4'-dicarboxylic acid-2,2'-bipyridine (0.378 g, 1.682 mmol) and NaOH (0.135 g, 3.364 mmol) were added. The solution was heated to reflux at 100 °C overnight. The dark purple reaction mixture was then poured in distilled water and acidified with 0.2 M HNO_3 until dark purple precipitate was formed. This dark purple precipitate was collected and purified by silica gel column chromatography using MeOH as eluent. **Ru1** was obtained by further washing with dichloromethane to give a dark purple solid (yield: 0.315 g, 50%). ^{1}H NMR (400 MHz, MeOD) δ 7.22 (d, *J* = 44.1 Hz, 4H), 7.12 – 6.85 (m, 4H), 6.65 (d, *J* = 7.8 Hz, 2H), 6.60 – 6.40 (m, 5H), 6.36 – 6.20 (m, 4H). Found: $[M+K]^+$ 788.9577; 'molecular formula $C_{33}H_{22}N_5O_8RuS$ ' requires $[M+K]^+$ 788.9872.

Ru2: To a flask containing $[Ru(CH_3CN)_4(\mathbf{L1})]^+PF_6^-$ (0. 400 g, 0.772mmol) in MeOH (15 mL), tetraethyl[2,2 -bipyridine]-4,4 -diylbis(phosphonate) (0.918 g, 2.144 mmol) was added. The solution was heated to reflux at 100 °C overnight. After cooling to room temperature, the dark purple reaction mixture was dried and purified by silica gel column chromatography using methanol as eluent. **Ru2** was afforded as a dark purple solid (yield: 0.475 g, 55%). ^{1}H NMR (400 MHz, MeOD) δ 8.66 (d, *J* = 66.3 Hz, 5H), 8.34 (d, *J* = 7.7 Hz, 3H), 8.01 (dd, *J* = 36.5, 32.5 Hz, 8H), 7.39 (s, 2H), 4.71 – 4.04 (m, 16H), 1.52 – 1.32 (m, 24H). Found: $[M+NH_4]^+$ 1136.0243; 'molecular formula $C_{45}H_{58}N_5O_{12}P_4RuS$ ' requires $[M+NH_4]^+$ 1136.2147.

Ru3: This product was synthesized similarly as **Ru1**, in which **L1** was replaced by **L2** to give the final product as a brown-red solid (yield: 0.282 g, 41%). ^{1}H NMR (400 MHz, MeOD) δ 8.80 (s, 3H), 8.15 – 7.93 (m, 6H), 7.86 (d, *J* = 3.5 Hz, 3H), 7.64 (d, *J* = 5.0

Hz, 3H), 7.25 – 7.11 (m, 3H). Found: $[M]^+$ 818.0111; 'molecular formula $C_{34}H_{21}F_3N_5O_8RuS$ ' requires $[M]^+$ 818.0110.

Ru4: This product was synthesized similarly as **Ru2**, in which **L1** was replaced by **L2** to give the target product as a brown-red solid (yield: 0.403 g, 44%). ^{1}H NMR (400 MHz, MeOD) δ 9.08 – 8.74 (m, 5H), 8.26 – 7.94 (m, 4H), 7.94 – 7.53 (m, 7H), 7.39 (s, 1H), 4.53 – 3.95 (m, 16H), 1.54 – 1.22 (m, 24H). Found: $[M]^+$ 1186.1771; 'molecular formula $C_{46}H_{57}F_3N_5O_{12}P_4RuS$ ' requires $[M]^+$ 1186.1677.

Ru5: This product was synthesized similarly as **Ru1**, in which **L1** was replaced by **L3** to give the final product as a brown-red solid (yield: 0.336 g, 50%). ^{1}H NMR (400 MHz, MeOD) δ 9.48 (d, *J* = 5.8 Hz, 1H), 9.14 (d, *J* = 9.6 Hz, 1H), 9.05 (d, *J* = 9.8 Hz, 1H), 8.92 (dd, *J* = 26.3, 16.2 Hz, 2H), 8.12 – 8.01 (m, 2H), 8.00 – 7.81 (m, 5H), 7.81 – 7.57 (m, 5H), 7.49 (d, *J* = 5.7 Hz, 1H), 7.37 (d, *J* = 6.4 Hz, 1H), 7.27 – 7.18 (m, 1H). Found: $[M+K]^+$ 839.0322; 'molecular formula $C_{37}H_{24}N_5O_8RuS$ ' requires $[M+K]^+$ 839.0030.

Ru6: This product was synthesized similarly as **Ru2**, in which **L1** was replaced by **L3** to give the target product as a brown-red solid (yield: 0.442 g, 49%). ^{1}H NMR (400 MHz, MeOD) δ 8.91 (dd, *J* = 13.9, 8.6 Hz, 4H), 8.75 (d, *J* = 14.3 Hz, 2H), 8.20 – 8.08 (m, 3H), 7.83 – 7.78 (m, 3H), 7.72 – 7.64 (m, 4H), 7.57 – 7.50 (m, 2H), 7.36 – 7.20 (m, 2H), 3.98 – 3.74 (m, 16H), 1.67 – 0.98 (m, 24H). Found: $[M]^+$ 1168.1971; 'molecular formula $C_{49}H_{60}N_5O_{12}P_4RuS$ ' requires $[M]^+$ 1168.1961.

Ru7: This product was synthesized similarly as **Ru1**, in which **L1** was replaced by **L4** to give the final product as a brown-red solid (yield: 0.434 g, 52%). ^{1}H NMR (400 MHz, MeOD) δ 8.12 (d, *J* = 5.7 Hz, 3H), 8.00 (d, *J* = 7.5 Hz, 2H), 7.92 – 7.89 (m, 1H), 7.78 (dd, *J* = 18.1, 9.9 Hz, 4H), 7.67 (d, *J* = 7.1 Hz, 2H), 7.49 – 7.42 (m, 3H), 7.38 – 7.26 (m, 6H), 7.19 (d, *J* = 5.5 Hz, 3H), 7.08 (d, *J* = 12.9 Hz, 4H), 6.98 – 6.88 (m, 3H). Found: $[M+H]^+$ 994.1504; 'molecular formula $C_{51}H_{35}N_6O_8RuS$ ' requires $[M+H]^+$ 994.1367.

Ru8: This product was synthesized similarly as **Ru2**, in which **L1** was replaced by **L4** to give the target product as a brown-red solid (yield: 0. 452 g, 43%). ^{1}H NMR (400 MHz, MeOD) δ 8.99 – 8.71 (m, 6H), 8.43 (dd, *J* = 11.7, 6.3 Hz, 1H), 8.21 (dd, *J* = 11.8, 7.6 Hz, 1H), 8.15 (dd, *J* = 9.7, 4.8 Hz, 2H), 7.86 – 7.72 (m, 2H), 7.65 – 7.41 (m, 5H), 7.36 (t, *J* = 7.9 Hz, 1H), 7.21 (dt, *J* = 11.1, 10.3 Hz, 5H), 7.04 – 6.90 (m, 5H), 6.82 – 6.72 (m, 3H), 4.23 (tdd, *J* = 12.1, 6.1, 2.4 Hz, 16H), 1.39 – 1.26 (m, 24H). Found: $[M]^+$ 1361.3008; 'molecular formula $C_{63}H_{71}N_6O_{12}P_4RuS$ ' requires $[M]^+$ 1361.2856.

Ru9: This product was synthesized similarly as **Ru1**, in which **L1** was replaced by **L5** to give the final product as a brown-red solid (yield: 0.351 g, 40%). ^{1}H NMR (400 MHz, MeOD) δ 9.06 (s, 1H), 8.99 – 8.88 (m, 3H), 8.14 (d, *J* = 5.8 Hz, 3H), 7.93 (s, 3H), 7.81 (s, 2H), 7.79 – 7.62 (m, 5H), 7.46 (d, *J* = 8.3 Hz, 2H), 7.41 – 7.19 (m, 6H), 7.10 (dd, *J* = 21.5, 7.6 Hz, 6H), 6.96 (d, *J* = 8.7 Hz, 2H). Found: $[M]^+$1043.1463; 'molecular formula $C_{55}H_{37}N_6O_8RuS$ ' requires $[M]^+$ 1043.1446.

Ru10: This product was synthesized similarly as **Ru2**, in which **L1** was replaced by **L5** to give the target product as a brown-red solid. (yield: 0.458 g, 42%). ^{1}H NMR (400 MHz, MeOD) δ 8.85 (ddt, *J* = 22.5, 14.5, 10.7 Hz, 6H), 8.39–8.30 (m, 1H), 8.22 – 8.08 (m, 3H), 7.82 (ddd, *J* = 17.7, 12.8, 6.2 Hz, 3H), 7.69 – 7.51 (m, 5H), 7.38 – 7.14 (m, 8H), 7.04 (dt, *J* = 20.1, 9.9 Hz, 5H), 6.90 – 6.83 (m, 2H), 4.44 – 4.10 (m, 16H), 1.45 – 1.27 (m, 24H). Found: $[M]^+$ 1411.3030; 'molecular formula $C_{67}H_{73}N_6O_{12}P_4RuS$ ' requires $[M]^+$ 1411.3014.

7.3.4. Light-driven hydrogen generation study with Ru(II) dyes @Pt–TiO_2

7.3.4.1. Calibration curve

Various of proportions of hydrogen and methane were used to plot the calibration curve obtained the area ratio obtained from GC (Agilent 6890 Series GC System with a molecular sieve 5 Å column and thermal conductivity detector).

7.3.4.2. Preparation of platinized TiO_2

To a one-neck round bottom flask containing 1.6 g of titanium oxide powder (anatase, < 25 nm particle size, 99.7% trace metals basis, Sigma-Aldrich) and 0.1 mL of H_2PtCl_6 aqueous solution (8 wt%), 40 mL MeOH was added. The reaction mixture was then subjected to radiation by a 300 W Hg lamp (HF300PD, EYE Lighting) for 24 h with stirring. The mixture was undergone centrifugation at 4000 rpm for 5 minutes and the solid obtained was washed with MeOH three times. The remaining solid was dried

under vacuum in darkness overnight.

7.3.4.3. Adsorption of ruthenium(II) photosensitizer onto platinized TiO_2

To a centrifuge tube containing 20 mg of Pt-TiO_2, 2.5 mL of 50 μM photosensitizer in MeOH solution was added, and the mixture was then sonicated for 30 mins. The solution was decolorized and became clear gradually, while the grey color solid was changed to dark pink. The tube was centrifuged at 4000 rpm for 15 mins and the liquid layer was removed by a dropper. The remaining solid was dried in darkness overnight. The whole dried pellet was directly utilized in the photocatalytic reaction. The dye-loading percentage was estimated by comparing the absorbance of the absorption peaks between the supernatant and the original photosensitizer solution.

7.3.4.4. Light-driven H_2 production studies

To a one-neck pear-shaped round bottom flask containing the dye-adsorbed platinized TiO_2, 5 mL of 0.5 M of AA (pH = 4) was added as the hole scavenger. The flask was then sealed by rubber septa and was purged with a mixture of argon/methane (80:20 mol%) for 15 mins. The methane present in the gas mixture was served as an internal standard for GC analysis of each experiment. The flask was steadily stirred and continuously radiated from the bottom with green (*ca.* 520 nm) or blue (*ca.* 470 nm) light-emitting diodes inside a just-fit container, which blocks the stray light from the environment. The light power was measured using a thermal sensor and power meter (Model: BIM-7203-0100F & BIM-7001; Hangzhou Brolight Technology Co., Ltd.) and

estimated to be 50 mW for each reaction. The produced hydrogen was measured by GC (Agilent 6890 Series GC System with a molecular sieve 5 Å column and thermal conductivity detector) at different time points from the headspace of reaction mixtures and was quantified by the calibration plot. The LED radiation is assumed to be monochromatic at emission intensity maximum (470 nm and 520 nm for blue and green LEDs, respectively).

7.4. Experimental Details for Chapter 3

7.4.1. Computational details

The Gaussian 16 suite of programs was used to optimize the configurations. Structural optimization and molecular orbitals were performed using the b3lyp functional with the 6–311G(d) basis set for non-metal elements and SDD for Ir.

7.4.2. Synthesis of ligand compounds and anchoring functional groups

L6: To a round bottom flask containing 2-bromopyridine (0.8 mL,8.549 mmol) in tetrahydrofuran (250 mL), (5-formylthiophen-2-yl)boronic acid (2.000 g, 12.824 mmol) was added. Tetrakis(triphenylphosphine)palladium(0) (0.988 g, 0.855 mmol) and 2M of potassium carbonate (25.6 mL, 51.295 mmol) were added to the reaction mixture, which was then heated to 85°C for 48 h. After being cooled to room temperature, the mixture was extracted with ethyl acetate and brine. The organic layer was dried over sodium sulfate, filtered and concentrated by reduced pressure. The crude product was purified by silica gel column chromatography using dichloromethane/*n*-hexane (1:1,

v/v) as eluent to give the final product as a yellow solid (yield: 1.405 g, 88%).^{1}H NMR (400 MHz, $CDCl_3$) δ 9.95 (s, 1H), 8.66 (d, *J* = 4.8 Hz, 1H), 7.84 – 7.65 (m, 4H), 7.31 (d, *J* = 1.7 Hz, 1H). ^{13}C NMR (101 MHz, $CDCl_3$) δ 183.2, 153.9, 151.1, 149.9, 144.1, 136.9, 125.1, 123.6, 119.7. Found: $[M+H]^+$ 190.0325; 'molecular formula $C_{10}H_7NOS$ ' requires $[M+H]^+$ 190.0321.

L7: To a round bottom flask containing 1-chloroisoquinoline (1.400 g, 8.549 mmol) in tetrahydrofuran (250mL), (5-formylthiophen-2-yl)boronic acid (2.000 g, 12.824 mmol) was added. Tetrakis(triphenylphosphine)palladium(0) (0.988 g, 0.855 mmol) and 2M of potassium carbonate (25.6 mL, 51.295 mmol) were added to the reaction mixture, which was then heated to 115 °C for 48 h. After being cooled to room temperature, the mixture was extracted with ethyl acetate and brine. The organic layer was dried over sodium sulfate, filtered and concentrated by reduced pressure. The crude product was purified by silica gel column chromatography using dichloromethane/*n*-hexane (1:1, *v/v*) as eluent to give the final product as a white solid (yield: 1.737 g, 85%). ^{1}H NMR (400 MHz, $CDCl_3$) δ 9.92 (d, *J* = 16.3 Hz, 1H), 8.32 (d, *J* = 8.3 Hz, 1H), 7.84 (d, *J* = 8.1 Hz, 1H), 7.77 – 7.63 (m, 5H), 7.59 (s, 1H). ^{13}C NMR (101 MHz, $CDCl_3$) δ 183.0, 182.6, 141.4, 131.2, 128.5, 128.3, 126.9, 126.3, 120.8. Found: $[M]^+$ 239.0219; 'molecular formula $C_{14}H_9NOS$ ' requires $[M]^+$ 239.0399.

Diethyl [2,2 -bipyridine]-4,4 -dicarboxylate: To a round bottom flask containing [2,2 -bipyridine]-4,4 -dicarboxylic acid (0.950 g, 3.893 mmol), concentrated H_2SO_4

(10.5 mL) and ethanol (22.5 mL) was added. The mixture was then heated to 80 °C overnight. After being cooled to room temperature, the mixture was poured on the ice and neutralized to pH equal to 8 with 25% NaOH solution. The mixture was extracted with dichloromethane and brine. The organic layer was dried over sodium sulfate, filtered and concentrated by reduced pressure. The crude product was recrystallized from toluene to give the final product as a white solid (yield: 1.018 g, 87%). ^{1}H NMR (400 MHz, $CDCl_3$) δ 8.96 (s, 2H), 8.89 (s, 2H), 7.92 (s, 2H), 4.47 (t, J = 10.6 Hz, 4H), 1.55 – 1.37 (m, 6H). ^{13}C NMR (101 MHz, $CDCl_3$) δ 165.1, 156.5, 150.1, 138.9, 123.2, 120.5, 61.9, 14.2. Found: $[M+Na]^+$ 323.1045; 'molecular formula $C_{16}H_{16}N_2O_4$ ' requires $[M+Na]^+$ 323.1002.

7.4.3. Synthesis of Ir(III) dyes

Ir1: To a round bottom flask containing **L1** (0.500 g, 3.101 mmol), iridium(III) chloride hydrate (0.365 g, 1.034 mmol) were added with 2-ethoxyethanol: deionized water (3:1, *v/v*, total 8 mL). The reaction mixture was heated at 90 °C for 20 h. The reagent was purified by filtration to give the yellow solid as the iridium dimer Ir_2**L1**$_4Cl_2$. The titled compound was used in the subsequent reaction without further purification.

To a round bottom flask containing iridium dimer Ir_2**L1**$_4Cl_2$ (0.100 g, 0.091 mmol) in dichloromethane: methanol (1:1, *v/v*, total 6 mL), diethyl [2,2 -bipyridine]-4,4 -dicarboxylate (0.068 g, 0.228 mmol) was added. The reaction mixture was then heated to 65 °C for 6 h. After cooling to room temperature, the pH was adjusted to 5 by 1M of HCl. The precipitate product was filtered. The crude product was purified by silica gel

column chromatography using dichloromethane/methanol (1:1, *v/v*) as eluent to give the final product as a yellow solid (yield: 0.061 g, 42%). ^{1}H NMR (400 MHz, $CDCl_3$) δ 9.12 (s, 2H), 8.18 (s, 1H), 8.10 – 7.96 (m, 2H), 7.73 (d, *J* = 26.6 Hz, 4H), 7.54 (d, *J* = 3.5 Hz, 3H), 6.90 (d, *J* = 18.2 Hz, 3H), 6.80 (s, 1H), 6.34 – 6.18 (m, 2H), 3.84 (s, 4H), 0.12 (s, 6H). Found: $[M]^+$ 813.1168; 'molecular formula $C_{34}H_{28}IrN_4O_4S_2$ ' requires $[M]^+$ 813.1174.

Ir2: To a round bottom flask containing iridium dimer Ir_2**L1**$_4Cl_2$ (0.100 g, 0.091 mmol) in dichloromethane: methanol (1:1, *v/v*, total 6 mL), tetraethyl[2,2 -bipyridine]-4,4 -diylbis(phosphonate) (0.098 g, 0.228 mmol) was added. The reaction mixture was then heated to 65 °C for 6 h. After cooling to room temperature, the pH was adjusted to 5 by 1M of HCl. The precipitate product was filtered. The crude product was purified by silica gel column chromatography using dichloromethane/methanol (1:1, *v/v*) as eluent to give the final product as a yellow solid (yield: 0.075 g, 44%). ^{1}H NMR (400 MHz, $CDCl_3$) δ 7.72 – 7.63 (m, 5H), 7.60 – 7.54 (m, 4H), 7.51 – 7.41 (m, 7H), 7.23 – 7.20 (m, 2H), 4.61 – 3.74 (m, 8H), 1.43 – 1.24 (m, 12H). Found: $[M]^+$ 941.1339; 'molecular formula $C_{36}H_{38}IrN_4O_6P_2S_2$ ' requires $[M]^+$ 941.1330.

Ir3: This product was synthesized similarly as **Ir1**, in which **L1** was replaced by **L3** to give the final product as an orange solid (yield: 0.068 g, 41%). ^{1}H NMR (400 MHz, $CDCl_3$) δ 9.00 – 8.82 (m, 6H), 7.94 (d, *J* = 4.8 Hz, 3H), 7.88 – 7.69 (m, 7H), 7.67 – 7.49 (m, 6H), 1.47 (t, *J* = 7.1 Hz, 4H), 1.28 (s, 6H). Found: $[M]^+$ 913.1489; 'molecular

formula $C_{42}H_{32}IrN_4O_4S_2$ ' requires $[M]^+$ 913.1488.

Ir4: This product was synthesized similarly as **Ir2**, in which **L1** was replaced by **L3** to give the target product as an orange solid (yield: 0.083 g, 44%). ^{1}H NMR (400 MHz, $CDCl_3$) δ 8.86 (d, J = 6.9 Hz, 2H), 8.13 – 7.93 (m, 4H), 7.92 – 7.74 (m, 9H), 7.57 (dd, *J* = 8.7, 3.5 Hz, 3H), 7.35 (d, *J* = 6.4 Hz, 2H), 6.40 – 6.32 (m, 2H), 4.51 – 4.09 (m, 8H), 1.39 (d, *J* = 4.1 Hz, 12H). Found: $[M]^+$ 1041.1663; 'molecular formula $C_{44}H_{42}IrN_4O_6P_2S_2$ ' requires $[M]^+$ 1041.1644.

Ir5: This product was synthesized similarly as **Ir1**, in which **L1** was replaced by **L6** to give the final product as an orange solid (yield: 0.059 g, 37%). ^{1}H NMR (400 MHz, $CDCl_3$) δ 9.20 (d, *J* = 5.4 Hz, 2H), 7.99 – 7.86 (m, 7H), 7.79 (dd, *J* = 11.4, 6.8 Hz, 6H), 7.60 (d, *J* = 7.9 Hz, 3H), 2.64 (s, 4H), 2.16 (s, 6H). Found: $[M]^+$ 869.1070; 'molecular formula $C_{36}H_{28}IrN_4O_6S_2$ ' requires $[M]^+$ 869.1073.

Ir6: This product was synthesized similarly as **Ir2**, in which **L1** was replaced by **L6** to give the target product as an orange solid (yield: 0.071 g, 39%). ^{1}H NMR (400 MHz, $CDCl_3$) δ 9.94 – 9.47 (m, 3H), 9.20 (s, 2H), 7.84 (dd, *J* = 57.8, 50.0 Hz, 4H), 7.67 – 7.37 (m, 5H), 6.82 – 6.33 (m, 4H), 4.53 – 3.39 (m, 8H), 1.58 – 0.87 (m, 12H). Found: $[M]^+$ 997.1233; 'molecular formula $C_{38}H_{38}IrN_4O_8P_2S_2$ ' requires $[M]^+$ 997.1229.

Ir7: This product was synthesized similarly as **Ir1**, in which **L1** was replaced by **L7** to

give the final product as a red solid (yield: 0.072 g, 41%). ^{1}H NMR (400 MHz, $CDCl_3$) δ 8.97 (dd, *J* = 25.1, 7.4 Hz, 2H), 7.98 – 7.85 (m, 5H), 7.85 – 7.73 (m, 4H), 7.68 (d, *J* = 6.2 Hz, 1H), 7.19 – 7.06 (m, 10H), 2.46 (s, 4H), 2.02 (s, 6H). Found: $[M]^+$ 969.0983; 'molecular formula $C_{44}H_{32}IrN_4O_6S_2$ ' requires $[M]^+$ 969.1387.

Ir8: This product was synthesized similarly as **Ir2**, in which **L1** was replaced by **L7** to give the target product as a red solid. (yield: 0. 078 g, 39%). ^{1}H NMR (400 MHz, $CDCl_3$) δ 9.04 – 8.87 (m, 2H), 7.94 (dd, *J* = 20.9, 8.0 Hz, 4H), 7.85 – 7.73 (m, 3H), 7.56 (d, *J* = 8.8 Hz, 4H), 7.37 – 7.31 (m, 2H), 7.15 (dd, *J* = 8.6, 2.4 Hz, 7H), 4.18 (ddd, *J* = 17.5, 10.6, 5.2 Hz, 8H), 2.29 (d, *J* = 6.5 Hz, 12H). Found: $[M]^+$ 1097.1545; 'molecular formula $C_{46}H_{42}IrN_4O_8P_2S_2$ ' requires $[M]^+$ 1097.1543.

Ir9: This product was synthesized similarly as **Ir1**, in which **L1** was replaced by **L4** to give the final product as a red solid (yield: 0.099 g, 42%). ^{1}H NMR (400 MHz, $CDCl_3$) δ 7.56 (d, *J* = 8.8 Hz, 13H), 7.38 (s, 10H), 7.21 – 6.92 (m, 21H), 2.29 (d, *J* = 6.4 Hz, 4H), 1.44 (s, 6H). Found: $[M]^+$ 1299.3294; 'molecular formula $C_{70}H_{54}IrN_6O_4S_2$ ' requires $[M]^+$ 1299.3275.

Ir10: This product was synthesized similarly as **Ir2**, in which **L1** was replaced by **L4** to give the target product as a red solid. (yield: 0.109 g, 42%). ^{1}H NMR (400 MHz, $CDCl_3$) δ 8.05 (d, *J* = 2.7 Hz, 3H), 7.84 (dd, *J* = 12.3, 5.3 Hz, 3H), 7.72 – 7.45 (m, 9H), 7.39 (t, *J* = 8.6 Hz, 9H), 7.09 – 7.00 (m, 16H), 6.85 – 6.66 (m, 4H), 4.44 – 3.98 (m, 8H),

1.39 (ddd, *J* = 66.4, 35.8, 15.3 Hz, 12H). Found: $[M]^+$ 1427.3459; 'molecular formula $C_{72}H_{64}IrN_6O_6P_2S_2$ ' requires $[M]^+$ 1427.3431.

Ir11: This product was synthesized similarly as **Ir1**, in which **L1** was replaced by **L5** to give the final product as a brown-red solid (yield: 0.109 g, 43%). ^{1}H NMR (400 MHz, $CDCl_3$) δ 8.99 (s, 6H), 8.89 (d, *J* = 4.9 Hz, 6H), 7.93 (dd, *J* = 4.9, 1.4 Hz, 5H), 7.52 (d, *J* = 8.4 Hz, 4H), 7.12 – 6.94 (m, 27H), 1.28 (s, 4H), 1.10 – 0.44 (m, 6H). Found: $[M]^+$ 1399.3309; 'molecular formula $C_{78}H_{58}IrN_6O_4S_2$ ' requires $[M]^+$ 1399.3589.

Ir12: This product was synthesized similarly as **Ir2**, in which **L1** was replaced by **L5** to give the target product as a brown-red solid. (yield: 0.119 g, 43%). ^{1}H NMR (400 MHz, $CDCl_3$) δ 8.01 – 7.89 (m, 6H), 7.70 (ddd, *J* = 18.9, 14.6, 7.1 Hz, 17H), 7.56 (dd, J = 17.5, 6.8 Hz, 10H), 7.42 – 7.34 (m, 7H), 7.04 – 6.91 (m, 6H), 6.87 (d, *J* = 5.8 Hz, 2H), 4.28 – 4.06 (m, 8H), 1.27 (dd, *J* = 14.2, 7.3 Hz, 12H).Found: $[M]^+$ 1527.3749; 'molecular formula $C_{80}H_{68}IrN_6O_6P_2S_2$ ' requires $[M]^+$ 1527.3746.

7.5. Experimental Details for Chapter 4

7.5.1. Computational details

Geometry optimizations of the complexes in the ground state and in water were performed with density functional theory (DFT). The Gaussian 16 suite of programs were used to optimise and calculate the configurations. Structural optimization was performed using the B3PW91-D3BJ functional with the def2-TZVPP basis set.

7.5.2. Synthesis of CdS NRs

$CdCl_2$•$2.5H_2O$ (2.312 g, 10.125 mmol) and thiourea (2.312 g, 30.375 mmol) were added into a Teflon-lined stainless steel autoclave (50 mL). 30 mL ethylenediamine was added into the autoclave and the reaction mixture was vigorously stirred for an hour. The autoclave was then maintained at 160 °C for 24 or 48 h. After cooling down to room temperature, a yellow precipitate was filtered and washed several times with distilled water and ethanol. The CdS nanorod material was then dried under vacuum overnight. The obtained CdS nanorod (1.234 g for L/D = 12; 1.051 g for L/D = 18) was stored in dark before the photocatalytic reaction.

7.5.3. Synthesis of ligand compounds

L8: A solution of 2-hydroxybenzaldehyde (1.7 mL, 16.377 mmol) in methanol (20 mL) was added dropwise to a solution of ethylenediamine (0.492 g, 8.189 mmol) in methanol (20 mL). The mixture was refluxed for 2 h and the precipitate comprising Schiff base ligand was obtained as a solid product. The solid was then separated by filtration, washed with cold methanol, and dried under vacuum. Finally, the product was recrystallised from methanol to yield an orange solid as the pure ligand (yield: 1.383 g, 63%). ^{1}H NMR (400 MHz, DMSO-d6) δ 13.39 (s, 2H), 8.60 (s, 2H), 7.37 (dd, *J* = 45.8, 6.9 Hz, 4H), 7.00 – 6.63 (m, 4H), 3.93 (s, 4H). ^{13}C NMR (101 MHz, DMSO-d6) δ 167.4, 161.0, 132.8, 132.1, 119.0, 116.9, 59.2; Found: $[M+Na]^+$ 291.1118; 'molecular formula $C_{16}H_{16}N_2O_2$ ' requires $[M+Na]^+$ 291.1104.

L9: This product was synthesized similarly as **L8**, in which ethylenediamine was replaced by benzene-1,2-diamine to give the target product as a yellow solid. (yield: 1.636 g, 63%). ^{1}H NMR (400 MHz, DMSO-d6) δ 12.95 (s, 2H), 8.95 (s, 2H), 7.67 (d, *J* = 7.7 Hz, 2H), 7.49 – 7.33 (m, 6H), 6.98 (t, *J* = 8.1 Hz, 4H). ^{13}C NMR (101 MHz, DMSO-d6) δ 164.5, 160.8, 142.7, 133.9, 132.9, 128.2, 120.2, 119.9, 119.5, 117.1. Found: $[M+H]^+$ 317.1304; 'molecular formula $C_{20}H_{16}N_2O_2$ ' requires $[M+H]^+$ 317.1285.

L10: This product was synthesized similarly as **L8**, in which ethylenediamine was replaced by 3-methylbenzene-1,2-diamine to give the target product as a yellow solid. (yield: 1.789 g, 66%). ^{1}H NMR (400 MHz, DMSO-d6) δ 9.38 (s, 2H), 8.14 – 7.96 (m, 3H), 7.91 (t, *J* = 18.1 Hz, 3H), 7.65 (d, *J* = 8.0 Hz, 2H), 7.33 (t, *J* = 7.3 Hz, 3H), 7.16 (t, *J* = 7.2 Hz, 2H), 1.57 (s, 3H). ^{13}C NMR (101 MHz, DMSO-d6) δ 146.4, 142.6, 138.4, 137.6, 131.6, 130.0, 129.6, 23.5. Found: $[M+H]^+$ 331.1446; 'molecular formula $C_{21}H_{18}N_2O_2$ ' requires $[M+H]^+$ 331.1441.

L11: This product was synthesized similarly as **L8**, in which ethylenediamine was replaced by 4,5-dichlorobenzene-1,2-diamine to give the target product as a yellow solid. (yield: 1.918 g, 61%). ^{1}H NMR (400 MHz, DMSO-d6) δ 12.64 (s, 2H), 8.94 (s, 2H), 7.78 – 7.57 (m, 4H), 7.53 – 7.36 (m, 2H), 7.11 – 6.82 (m, 4H). ^{13}C NMR (101 MHz, DMSO-d6) δ 165.2, 160.7, 134.2, 132.9, 119.9, 119.7, 117.2. Found: $[M]^+$ 384.3087; 'molecular formula $C_{20}H_{14}Cl_2N_2O_2$ ' requires $[M]^+$ 384.0427.

L12: This product was synthesized similarly as **L8**, in which ethylenediamine was replaced by 4,5-dimethylbenzene-1,2-diamine to give the target product as a yellow solid. (yield: 1.747 g, 62%).^{1}H NMR (400 MHz, DMSO-d6) δ 9.38 (s, 2H), 8.10 (s, 2H), 7.89 (dd, *J* = 42.3, 13.6 Hz, 4H), 7.65 (d, *J* = 8.0 Hz, 2H), 7.33 (t, *J* = 7.3 Hz, 2H), 7.16 (t, *J* = 7.2 Hz, 2H), 1.57 (s, 6H). ^{13}C NMR (101 MHz, DMSO-d6) δ 158.8, 142.6, 138.4, 137.6, 122.3, 13.9. Found: $[M+Na]^+$ 367.1426; 'molecular formula $C_{22}H_{20}N_2O_2$ ' requires $[M+Na]^+$ 367.1417.

L13: This product was synthesized similarly as **L8**, in which ethylenediamine was replaced by naphthalene-2,3-diamine to give the target product as a yellow solid. (yield: 1.864 g, 62%). ^{1}H NMR (400 MHz, DMSO-d6) δ 12.91 (s, 2H), 9.08 (s, 2H), 7.94 (s, 4H), 7.75 – 7.65 (m, 2H), 7.59 – 7.37 (m, 4H), 7.14 – 6.82 (m, 4H). ^{13}C NMR (101 MHz, DMSO-d6) δ 164.7, 160.9, 142.9, 134.0, 132.9, 132.8, 128.2, 126.8, 120.0, 119.7, 117.2, 117.1. Found: $[M+Na]^+$ 389.1266; 'molecular formula $C_{24}H_{18}N_2O_2$ ' requires $[M+Na]^+$ 389.1260.

7.5.4. Synthesis of metal complexes

Ni1: A solution of **L8** (0.363 g, 1.364 mmol) in methanol (10 mL) was added dropwise to a solution of nickel(II) acetate (0.241 g, 1.364 mmol) in methanol (10 mL). The mixture was refluxed for 2 h and precipitate was formed. The solid was separated by filtration, washed with cold methanol, and dried under vacuum. Finally, it was

recrystallised from methanol to yield a yellow solid as the pure complex **Ni1** (yield: 0.349 g, 79%). ^{1}H NMR (400 MHz, DMSO-d6) δ 7.91 (s, 2H), 7.27 (d, *J* = 7.6 Hz, 2H), 7.18 (t, *J* = 7.6 Hz, 2H), 6.71 (d, *J* = 8.5 Hz, 2H), 6.52 (t, *J* = 7.3 Hz, 2H), 3.43 (s, 4H). Found: $[M+Na]^+$ 347.0305; 'molecular formula $C_{16}H_{14}N_2NiO_2$ ' requires $[M+Na]^+$ 347.0301.

Ni2: This product was synthesized similarly as **Ni**, in which **L8** was replaced by **L9** to give the target product as a yellow solid. (yield: 0.309 g, 61%). ^{1}H NMR (400 MHz, DMSO-d6) δ 8.93 (d, *J* = 14.7 Hz, 2H), 8.26 – 7.96 (m, 2H), 7.62 (d, *J* = 7.8 Hz, 2H), 7.41 – 7.16 (m, 4H), 6.90 (d, *J* = 8.6 Hz, 2H), 6.68 (t, *J* = 7.3 Hz, 2H). Found: $[M+Na]^+$ 395.0304; 'molecular formula $C_{20}H_{14}N_2NiO_2$ ' requires $[M+Na]^+$ 395.0301.

Ni3: This product was synthesized similarly as **Ni**, in which **L8** was replaced by **L10** to give the target product as a yellow solid. (yield: 0.301 g, 57%).^{1}H NMR (400 MHz, DMSO-d6) δ 8.92 (s, 1H), 8.62 (s, 1H), 8.00 (d, *J* = 7.9 Hz, 1H), 7.59 (d, *J* = 8.0 Hz, 2H), 7.32 (dd, *J* = 9.9, 5.6 Hz, 2H), 7.26 – 7.14 (m, 2H), 6.86 (d, *J* = 8.6 Hz, 2H), 6.65 (dd, *J* = 14.2, 7.1 Hz, 2H), 2.65 (s, 3H). Found: $[M+Na]^+$ 409.0462; 'molecular formula $C_{21}H_{16}N_2NiO_2$ ' requires $[M+Na]^+$ 409.0457.

Ni4: This product was synthesized similarly as **Ni**, in which **L8** was replaced by **L11** to give the target product as a yellow solid. (yield: 0.374 g, 62%).^{1}H NMR (400 MHz, DMSO-d6) δ 8.97 (s, 2H), 8.36 (t, *J* = 9.6 Hz, 2H), 7.56 (d, *J* = 7.9 Hz, 2H), 7.35 (d, *J*

= 7.4 Hz, 2H), 6.92 (d, *J* = 8.6 Hz, 2H), 6.70 (t, *J* = 7.2 Hz, 2H). Found: $[M+Na]^+$ 464.9489; 'molecular formula $C_{20}H_{12}Cl_2N_2NiO_2$ ' requires $[M+Na]^+$ 464.9489.

Ni5: This product was synthesized similarly as **Ni**, in which **L8** was replaced by **L12** to give the target product as a yellow solid. (yield: 0.349 g, 64%).^{1}H NMR (400 MHz, DMSO-d6) δ 8.78 (s, 2H), 7.93 (s, 2H), 7.57 (d, *J* = 7.5 Hz, 2H), 7.31 (s, 2H), 6.88 (d, *J* = 8.5 Hz, 2H), 6.66 (t, *J* = 7.3 Hz, 2H), 2.29 (s, 6H). Found: $[M+Na]^+$ 423.0616; 'molecular formula $C_{22}H_{18}N_2NiO_2$ ' requires $[M+Na]^+$ 423.0614.

Ni6: 2,2'-disulfanediyldibenzaldehyde (0.252 g, 0.842 mmol), Bis(cyclooctadiene)nickel(0) (0.100 g , 0.842 mmo), and ethylenediamine (0.051 g, 0.842 mmol) were mixed in dry methanol and stirred for 5 days at room temperature. The mixture was separated by filtration, washed with cold methanol, and dried under vacuum. Finally, recrystallisation from methanol yielded a dark green solid as the final product. (yield: 0.167 g, 56%). ^{1}H NMR (400 MHz, DMSO-d6) δ 7.92 (s, 2H), 7.27 (dd, *J* = 7.8, 1.4 Hz, 2H), 7.20 – 7.13 (m, 2H), 6.71 (d, *J* = 8.5 Hz, 2H), 6.52 (t, *J* = 7.3 Hz, 2H), 3.43 (s, 4H). Found: $[M+Na]^+$ 378.9848; 'molecular formula $C_{16}H_{14}N_2NiS_2$ ' requires $[M+Na]^+$ 378.9844.

Ni7: This product was synthesized similarly as **Ni6**, in which ethylenediamine was replaced by benzene-1,2-diamine to give the target product as a brown solid. (yield: 0.183 g, 54%). ^{1}H NMR (400 MHz, DMSO-d6) δ 9.45 (s, 2H), 8.31 (s, 2H), 7.97 (d, *J*

= 6.4 Hz, 2H), 7.66 (d, *J* = 6.9 Hz, 2H), 7.53 (s, 2H), 7.35 (s, 2H), 7.16 (s, 2H). Found: $[M+Na]^+$ 426.9844; 'molecular formula $C_{20}H_{14}N_2NiS_2$ ' requires $[M+Na]^+$ 426.9844.

Ni8: This product was synthesized similarly as **Ni6**, in which ethylenediamine was replaced by 3-methylbenzene-1,2-diamine to give the target product as a brown solid. (yield: 0.204 g, 58%). ^{1}H NMR (400 MHz, DMSO-d6) δ 8.91 (s, 1H), 8.61 (s, 1H), 8.00 (d, *J* = 8.0 Hz, 1H), 7.59 (d, *J* = 8.0 Hz, 2H), 7.32 (t, *J* = 7.6 Hz, 2H), 7.28 – 7.15 (m, 2H), 6.86 (d, *J* = 8.6 Hz, 2H), 6.65 (q, *J* = 7.0 Hz, 2H), 2.65 (s, 3H). Found: $[M+Na]^+$ 441.0001; 'molecular formula $C_{21}H_{16}N_2NiS_2$ ' requires $[M+Na]^+$ 441.0001.

Ni9: This product was synthesized similarly as **Ni6**, in which ethylenediamine was replaced by 4,5-dichlorobenzene-1,2-diamine to give the target product as a brown solid. (yield: 0.226 g, 57%). ^{1}H NMR (400 MHz, DMSO-d6) δ 8.51 (s, 2H), 8.10 (s, 2H), 7.93 (s, 2H), 7.52 (s, 2H), 7.34 (s, 2H), 7.16 (s, 2H). Found: $[M+K]^+$ 512.9790; 'molecular formula $C_{20}H_{12}Cl_2N_2NiS_2$ ' requires $[M+K]^+$ 512.8771.

Ni10: This product was synthesized similarly as **Ni6**, in which ethylenediamine was replaced by 4,5-dimethylbenzene-1,2-diamine to give the target product as a brown solid. (yield: 0.221 g, 61%).^{1}H NMR (400 MHz, DMSO-d6) δ 9.38 (s, 2H), 8.10 (s, 2H), 7.94 (d, *J* = 7.4 Hz, 2H), 7.65 (d, *J* = 7.5 Hz, 2H), 7.33 (s, 2H), 7.16 (s, 2H), 2.37 (s, 6H). Found: $[M+Na]^+$ 455.0161; 'molecular formula $C_{22}H_{18}N_2NiS_2$ ' requires $[M+Na]^+$ 455.0157.

Ni11: A solution of ligand **L13** (0.500 g, 1.364 mmol) in methanol (10 mL) was added dropwise to a solution of nickel(II) acetate (0.241 g, 1.364 mmol) in methanol (10 mL). The mixture was refluxed for 2 h and precipitate was formed. The solid was separated by filtration, washed with cold methanol, and dried under vacuum. Finally, it was recrystallised from methanol to yield a yellow solid as the pure complex **1** (yield: 0.471 g, 82%). ^{1}H NMR (400 MHz, DMSO-d6) δ 9.08 (s, 2H), 8.65 (s, 2H), 7.93 (dd, *J* = 6.1, 3.3 Hz, 2H), 7.71 – 7.49 (m, 4H), 7.35 (s, 2H), 6.90 (d, *J* = 8.5 Hz, 2H), 6.70 (t, *J* = 7.3 Hz, 2H). Found: $[M+H]^+$ 423.0461; 'molecular formula $C_{24}H_{16}N_2NiO_2$ ' requires $[M+H]^+$ 423.0638.

Zn1: The synthesis of this product was similar to complex **Ni11**, except that zinc(II) acetate was used instead of nickel(II) acetate to provide a brown-red solid as the target product (yield: 0.491 g, 84%). ^{1}H NMR (400 MHz, DMSO-d6) δ 9.16 (s, 2H), 8.35 (s, 2H), 7.95 (dd, *J* = 6.1, 3.2 Hz, 2H), 7.59 – 7.41 (m, 4H), 7.27 (t, *J* = 7.6 Hz, 2H), 6.73 (d, *J* = 8.5 Hz, 2H), 6.54 (t, *J* = 7.2 Hz, 2H). Found: $[M+Na]^+$ 451.1165; 'molecular formula $C_{24}H_{16}N_2ZnO_2$ ' requires $[M+Na]^+$ 451.0395.

Cu1: This synthesis of this product was similar to complex **Ni11**, except that copper(II) acetate was used instead of nickel(II) acetate to yield the final product as a brown-red solid (yield: 0.489 g, 84%). ^{1}H NMR (400 MHz, DMSO-d6) δ 9.09 (s, 2H), 8.65 (s, 2H), 7.93 (dd, *J* = 6.2, 3.3 Hz, 2H), 7.64 (dd, *J* = 8.0, 1.5 Hz, 2H), 7.57 (dd, *J* = 6.3, 3.2

Hz, 2H), 7.40 – 7.29 (m, 2H), 6.90 (d, J = 8.5 Hz, 2H), 6.70 (t, J = 7.3 Hz, 2H). Found: $[M+H]^+$ 450.0181; 'molecular formula $C_{24}H_{16}N_2CuO_2$ ' requires $[M+Na]^+$ 450.0400.

7.5.5. Light-driven hydrogen generation study with metal complex and CdS NRs

To a one-neck pear-shaped round bottom flask containing 1 mg of CdS NRs and 10 μM of metal complex, 5 mL of 0.5 M of AA (pH = 4) was added as the hole scavenger. The flask was then sealed by rubber septa and was purged with a mixture of argon/methane (80:20 mol%) for 15 mins. The methane present in the gas mixture was served as an internal standard for GC analysis of each experiment. The flask was steadily stirred and continuously radiated from the bottom with blue (*ca.* 470 nm) light-emitting diodes inside a just-fit container, which blocks the stray light from the environment. The light power was measured using a thermal sensor and power meter (Model: BIM-7203-0100F & BIM-7001; Hangzhou Brolight Technology Co., Ltd.) and estimated to be 50 mW for each reaction. The produced hydrogen was measured by GC (Agilent 6890 Series GC System with a molecular sieve 5 Å column and thermal conductivity detector) at different time points from the headspace of reaction mixtures and was quantified by the calibration plot. The LED radiation is assumed to be monochromatic at emission intensity maximum (470 nm for blue and LEDs).

7.6. Experimental Details for Chapter 5

7.6.1. Synthesis of ligand compounds

5: To a round bottom flask containing triphenylamine (1.100 g, 4.445 mmol) in dry

DMF (10 mL), N-bromosuccinimide (3.561 g, 20.003 mmol) in dry DMF (5 mL) was added dropwise. After stirring at room temperature overnight, the reaction mixture was poured into D.I. water at ice-bath. The white precipitate was filtration and dried in oven at room temperature to give the product as white solid. (yield: 1.912 g, 88%). ^{1}H NMR (400 MHz, $CDCl_3$) δ 7.37 (t, J = 8.3 Hz, 6H), 6.95 (d, J = 8.8 Hz, 6H). ^{13}C NMR (101 MHz, $CDCl_3$) δ 146.0, 132.5, 125.6, 116.0. Found: $[M]^+$ 480.8494; 'molecular formula $C_{18}H_{12}Br_3N$ ' requires $[M]^+$ 480.8494.

L14: To a two-neck round bottom flask containing triphenylamine (1.100 g, 4.445 mmol) in dry DMF (30 mL) at 0 ℃, $POCl_3$ (30 mL, 320.890 mmol) was added dropwise. After stirring at 0 ℃ for 60 mins, the reaction mixture was heated at 90 ℃ overnight. After cooling to room temperature, the reaction mixture was poured into ice and neutralized with NaOH and then extracted with chloroform. The organic layer was dried over sodium sulfate, filtered and concentrated by reduced pressure. The crude product was purified by silica gel column chromatography using ethyl acetate /*n*-hexane (1:9, v/v) as eluent to yield **L14** as a yellow solid (yield: 0.673 g, 46%). ^{1}H NMR (400 MHz, $CDCl_3$) δ 9.94 (s, 3H), 7.91 (d, J = 8.5 Hz, 6H), 7.28 (d, J = 8.4 Hz, 6H). ^{13}C NMR (101 MHz, $CDCl_3$) δ 190.5, 151.2, 132.5, 131.5, 124.5. Found: $[M+Na]^+$ 352.0951; 'molecular formula $C_{21}H_{15}NO_3$ ' requires $[M+Na]^+$ 352.0944.

L15: To a round bottom flask containing compound **5** (1.431 g, 2.960 mmol) in tetrahydrofuran (250mL), (4-formylphenyl)boronic acid (2.000 g, 13.341 mmol) was

added. Tetrakis(triphenylphosphine)palladium(0) (0.342 g, 0.296 mmol) and 2M of potassium carbonate (26.5 mL, 53.284 mmol) were added to the reaction mixture, which was then heated to 85 °C for 48 h. After being cooled to room temperature, the mixture was extracted with ethyl acetate and brine. The organic layer was dried over sodium sulfate, filtered and concentrated by reduced pressure. The crude product was purified by silica gel column chromatography using dichloromethane/*n*-hexane (4:1, *v/v*) as eluent to give the final product as a white solid (yield: 1.022 g, 62%). ^{1}H NMR (400 MHz, $CDCl_3$) δ 10.08 (s, 3H), 7.98 (d, *J* = 8.2 Hz, 6H), 7.79 (d, *J* = 8.2 Hz, 6H), 7.63 (d, *J* = 8.6 Hz, 6H), 7.31 (d, *J* = 8.6 Hz, 6H). ^{13}C NMR (101 MHz, $CDCl_3$) δ 147.4, 146.3, 134.9, 134.4, 130.4, 128.4, 127.1, 124.6. Found: $[M]^+$ 557.2004; 'molecular formula $C_{39}H_{27}NO_3$ ' requires $[M]^+$ 557.1985.

6: To a round bottom flask containing tris(4-bromophenyl)amine (1.673 g, 3.472 mmol) in tetrahydrofuran (250mL), compound **1** (2.000 g, 16.631 mmol) was added. Tetrakis(triphenylphosphine)palladium(0) (0.400 g, 0.347 mmol) and 2M of potassium carbonate (31.2 mL, 62.464 mmol) were added to the reaction mixture, which was then heated to 85 °C for 48 h. After being cooled to room temperature, the mixture was extracted with ethyl acetate and brine. The organic layer was dried over sodium sulfate, filtered and concentrated by reduced pressure. The crude product was purified by silica gel column chromatography using dichloromethane/*n*-hexane (1:1, *v/v*) as eluent to give the final product as a white solid (yield: 0.921 g, 54%). ^{1}H NMR (400 MHz, $CDCl_3$) δ 7.55 (d, *J* = 8.6 Hz, 6H), 7.31 – 7.25 (m, 6H), 7.16 (d, *J* = 8.5 Hz, 6H), 7.10 (dd, *J* =

5.0, 3.7 Hz, 3H). ^{13}C NMR (101 MHz, $CDCl_3$) δ 146.5, 144.1, 129.3, 128.0, 126.9, 124.4, 124.2, 122.4. Found: $[M]^+$ 491.0840; 'molecular formula $C_{30}H_{21}NS_3$ ' requires $[M]^+$ 491.0831.

7: This product was synthesized similarly as compound **6**, in which compound **1** was replaced by furan-2-ylboronic acid to give the target product as a yellow solid (yield: 0.876 g, 57%). ^{1}H NMR (300 MHz, $CDCl_3$) δ 7.59 (d, *J* = 8.7 Hz, 6H), 7.47 (d, *J* = 1.3 Hz, 3H), 7.16 (d, *J* = 8.7 Hz, 6H), 6.59 (d, *J* = 3.1 Hz, 3H), 6.49 (dd, *J* = 3.3, 1.8 Hz, 3H). ^{13}C NMR (101 MHz, $CDCl_3$) δ 153.8, 146.3, 141.7, 125.8, 124.8, 124.2, 111.6, 104.1. Found: $[M]^+$ 443.1516; 'molecular formula $C_{30}H_{21}NO_3$ ' requires $[M]^+$ 443.1516.

L16: This product was synthesized similarly as **L14**, in which triphenylamine was replaced by compound **5** to give the target product as a yellow solid (yield: 1.456 g, 57%). ^{1}H NMR (400 MHz, $CDCl_3$) δ 9.91 (s, 3H), 7.77 (d, *J* = 4.0 Hz, 3H), 7.64 (d, *J* = 8.6 Hz, 6H), 7.38 (d, *J* = 3.9 Hz, 3H), 7.22 (d, *J* = 8.6 Hz, 6H). ^{13}C NMR (101 MHz, $CDCl_3$) δ 182.7, 153.6, 147.5, 142.0, 137.6, 128.4, 127.6, 124.6, 123.6. Found: $[M]^+$ 575.0677; 'molecular formula $C_{33}H_{21}NO_3S_3$ ' requires $[M]^+$ 575.0678.

L17: This product was synthesized similarly as **L14**, in which triphenylamine was replaced by compound **6** to give the target product as a yellow solid (yield: 1.335 g, 57%). ^{1}H NMR (400 MHz, $CDCl_3$) δ 9.65 (s, 3H), 7.78 (d, *J* = 8.6 Hz, 6H), 7.35 (d, *J* = 3.7 Hz, 3H), 7.21 (d, *J* = 8.7 Hz, 6H), 6.82 (d, *J* = 3.7 Hz, 3H). ^{13}C NMR (101 MHz,

$CDCl_3$) δ 159.0, 151.8, 147.6, 126.7, 124.4, 107.2. Found: $[M+H]^+$ 528.0180; 'molecular formula $C_{33}H_{21}NO_6$ ' requires $[M+H]^+$ 528.1442.

L18: This product was synthesized similarly as **L15**, in which compound **5** was replaced by 1,3,5-tribromo-2,4,6-trimethylbenzene to give the target product as a yellow solid (yield: 0.704 g, 55%). ^1H NMR (400 MHz, $CDCl_3$) δ 10.13 (s, 3H), 8.05 (d, J = 8.2 Hz, 6H), 7.90 (d, J = 8.2 Hz, 6H), 1.61 (s, 9H). ^{13}C NMR (101 MHz, $CDCl_3$) δ 191.9, 148.2, 139.0, 135.1, 132.7, 130.1, 19.3. Found: $[M+Na]^+$ 455.1625; 'molecular formula $C_{30}H_{24}O_3$ ' requires $[M+Na]^+$ 455.1618.

L19: This product was synthesized similarly as **L15**, in which compound **5** was replaced by 1,3,5-tribromobenzene to give the target product as a yellow solid (yield: 0.658 g, 57%). ^1H NMR (400 MHz, $CDCl_3$) δ 10.11 (s, 3H), 8.23 – 8.14 (m, 9H), 8.06 (d, J = 8.3 Hz, 6H). ^{13}C NMR (101 MHz, $CDCl_3$) δ 191.7, 146.3, 141.6, 135.7, 130.4, 127.9, 126.4. Found: $[M+H]^+$ 391.1932; 'molecular formula $C_{27}H_{18}O_3$ ' requires $[M+H]^+$ 391.1329.

8: This product was synthesized similarly as compound **6**, in which compound **5** was replaced by 1,3,5-tribromobenzene to give the target product as a yellow solid (yield: 0.686 g, 61%). ^1H NMR (400 MHz, $CDCl_3$) δ 7.78 (s, 3H), 7.45 (d, J = 3.1 Hz, 3H), 7.42 – 7.34 (m, 3H), 7.16 (dd, J = 4.9, 3.8 Hz, 3H). ^{13}C NMR (101 MHz, $CDCl_3$) δ 143.5, 135.7, 128.1, 125.4, 123.8, 122.7. Found: $[M+K]^+$ 362.9259; 'molecular formula

$C_{18}H_{12}S_3$ ' requires $[M+K]^+$ 362.9733.

9: This product was synthesized similarly as compound **7**, in which compound **5** was replaced by 1,3,5-tribromobenzene to give the target product as a yellow solid (yield: 0.565 g, 59%). ^{1}H NMR (400 MHz, $CDCl_3$) δ 7.90 (s, 3H), 7.54 (d, J = 1.4 Hz, 3H), 6.80 (d, J = 3.3 Hz, 3H), 6.54 (dd, J = 3.3, 1.8 Hz, 3H). ^{13}C NMR (101 MHz, $CDCl_3$) δ 153.4, 142.3, 131.7, 118.0, 111.7, 105.7. Found: $[M+Li]^+$ 283.0120; 'molecular formula $C_{18}H_{12}O_3$ ' requires $[M+Li]^+$ 283.0941.

L20: This product was synthesized similarly as **L14**, in which triphenylamine was replaced by compound **8** to give the target product as a yellow solid (yield: 1.031 g, 57%). ^{1}H NMR (400 MHz, $CDCl_3$) δ 9.97 (s, 3H), 7.95 (s, 3H), 7.84 (d, J = 4.0 Hz, 3H), 7.56 (d, J = 3.9 Hz, 3H). ^{13}C NMR (101 MHz, $CDCl_3$) δ 143.2, 137.1, 134.8, 128.3, 126.2, 125.1, 124.5. Found: $[M+Li]^+$ 414.9818; 'molecular formula $C_{21}H_{12}O_3S_3$ ' requires $[M+Li]^+$ 415.0104.

L21: This product was synthesized similarly as **L14**, in which triphenylamine was replaced by compound **9** to give the target product as a yellow solid (yield: 0.576 g, 36%). ^{1}H NMR (400 MHz, $CDCl_3$) δ 9.76 (s, 3H), 8.27 (s, 3H), 7.43 (d, J = 3.8 Hz, 3H), 7.11 (d, J = 3.7 Hz, 3H). ^{13}C NMR (101 MHz, $CDCl_3$) δ 182.7, 152.4, 143.2, 137.1, 134.8, 125.1, 124.6. Found: $[M+Na]^+$ 383.0325; 'molecular formula $C_{21}H_{12}O_6$ ' requires $[M+Na]^+$ 383.0526.

7.6.2. Synthesis of ligand precursors

P1: Five drops of acetic acid were added to a mixture of **L14** (0.333 g, 1.000 mmol) and thiosemicarbazine (0.270 g, 3.000 mmol) in a methanol solution. After the mixture was refluxed for 6 h, the yellow precipitate was filtration and dried in oven at room temperature to give the product as yellow solid. (yield: 0.224 g, 41%). ^{1}H NMR (400 MHz, DMSO-d6) δ 11.40 (s, 3H), 8.17 (s, 3H), 7.97 (d, *J* = 28.4 Hz, 6H), 7.75 (d, *J* = 8.7 Hz, 6H), 7.05 (d, *J* = 8.7 Hz, 6H). Found: $[M+K]^+$ 587.1107; 'molecular formula $C_{24}H_{24}N_{10}S_3$ ' requires $[M+K]^+$ 587.0979.

P2: This product was synthesized similarly as **P1**, in which **L14** was replaced by compound **L15** to give the target product as a yellow solid (yield: 0.248 g, 32%). ^{1}H NMR (400 MHz, DMSO-d6) δ 8.64 (s, 12H), 7.56 (s, 12H), 7.20 (s, 12H). Found: $[M]^+$ 776.0178; 'molecular formula $C_{42}H_{36}N_{10}S_3$ ' requires $[M]^+$ 776.2281.

P3: This product was synthesized similarly as **P1**, in which **L14** was replaced by compound **L16** to give the target product as a yellow solid (yield: 0.341 g, 43%). ^{1}H NMR (400 MHz, DMSO-d6) δ 9.90 (s, 3H), 8.05 (d, *J* = 4.0 Hz, 3H), 7.86 – 7.70 (m, 9H), 7.70 (d, *J* = 4.0 Hz, 6H), 7.19 (d, *J* = 8.7 Hz, 9H). Found: $[M+H]^+$ 795.1053; 'molecular formula $C_{36}H_{30}N_{10}S_6$ ' requires $[M+H]^+$ 795.1052.

P4: This product was synthesized similarly as **P1**, in which **L14** was replaced by

compound **L17** to give the target product as a yellow solid (yield: 0.298 g, 40%). ^{1}H NMR (400 MHz, DMSO-d6) δ 11.49 (s, 3H), 8.27 (s, 3H), 7.87 – 7.64 (m, 12H), 7.24 – 7.06 (m, 12H). Found: $[M+H]^+$ 747.1749; 'molecular formula $C_{36}H_{30}N_{10}O_3S_3$ ' requires $[M+H]^+$ 747.1737.

P5: This product was synthesized similarly as **P1**, in which **L14** was replaced by compound **L18** to give the target product as a yellow solid (yield: 0.280 g, 43%). ^{1}H NMR (400 MHz, DMSO-d6) δ 11.44 (s, 3H), 8.20 (s, 3H), 8.03 (s, 3H), 7.89 (d, J = 6.9 Hz, 3H), 7.46 (d, J = 6.6 Hz, 6H), 7.24 – 7.20 (m, 6H), 1.63 – 1.60 (m, 9H). Found: $[M+Na]^+$ 674.0285; 'molecular formula $C_{33}H_{33}N_9S_3$ ' requires $[M+Na]^+$ 674.1913.

P6: This product was synthesized similarly as **P1**, in which **L14** was replaced by compound **L19** to give the target product as a yellow solid (yield: 0.225 g, 37%). ^{1}H NMR (400 MHz, DMSO-d6) δ 10.08 (s, 3H), 8.29 – 8.12 (m, 15H), 8.06 (d, J = 8.3 Hz, 9H). Found: $[M+H]^+$ 610.1798; 'molecular formula $C_{30}H_{27}N_9S_3$ ' requires $[M+H]^+$ 610.1624.

P7: This product was synthesized similarly as **P1**, in which **L14** was replaced by compound **L20** to give the target product as a yellow solid (yield: 0.257 g, 41%). ^{1}H NMR (400 MHz, DMSO-d6) δ 9.98 – 9.98 (m, 3H), 8.19 (s, 6H), 8.14 (d, J = 4.0 Hz, 6H), 8.08 (d, J = 3.9 Hz, 6H). Found: $[M]^+$ 627.0209; 'molecular formula $C_{24}H_{21}N_9S_6$ ' requires $[M]^+$ 627.0239.

P8: This product was synthesized similarly as **P1**, in which **L14** was replaced by compound **L21** to give the target product as a yellow solid (yield: 0.226 g, 39%). ^{1}H NMR (400 MHz, DMSO-d6) δ 11.52 (s, 3H), 8.33 (s, 3H), 8.17 (s, 3H), 8.05 (d, *J* = 21.2 Hz, 6H), 7.45 (d, *J* = 3.6 Hz, 3H), 7.15 (d, *J* = 3.6 Hz, 3H). Found: $[M]^+$ 579.1622; 'molecular formula $C_{24}H_{21}N_9O_3S_3$ ' requires $[M]^+$ 579.0924.

7.6.3. Synthesis of metal-organic cage

MOC1: To a round bottom flask containing **P1** (0.054 g, 0.100 mmol) in dry DMF (5mL), $Co(CH_3COO)_2{\cdot}4H_2O$ (0.024 g, 0.100 mmol) was added. The solution was refluxed at 190 °C for 4 h. After cooling to room temperature, black crystals of **MOC1** were obtained by diffusing methanol into the reaction solution. (yield: 0.025 g, 42%). ^{1}H NMR (400 MHz, DMSO-d6) δ 8.23 – 8.16 (m, 48H), 8.07 (d, *J* = 8.2 Hz, 36H). Found: $[M]^+$ 2418.4895; 'molecular formula $Co_4C_{96}H_{84}N_{40}S_{12}$ ' requires $[M]^+$ 2418.1786.

MOC2: This product was synthesized similarly as **MOC1**, in which $Co(CH_3COO)_2{\cdot}4H_2O$ was replaced by compound $Ni(CH_3COO)_2{\cdot}4H_2O$ to give the target product as a black solid (yield: 0.023 g, 39%). ^{1}H NMR (400 MHz, DMSO-d6) δ 8.23 (s, 36H), 8.10 (s, 48H). Found: $[M]^+$ 2416.2675; 'molecular formula $Ni_4C_{96}H_{84}N_{40}S_{12}$ ' requires $[M]^+$ 2416.1818.

MOC3: This product was synthesized similarly as **MOC1**, in which **P1** was replaced by compound **P2** to give the target product as a black solid (yield: 0.032 g, 38%). ^{1}H NMR (400 MHz, DMSO-d6) δ 7.78 (d, *J* = 29.8 Hz, 72H), 7.60 (s, 24H), 7.55 (s, 36H). Found: $[M]^+$ 3330.5361; 'molecular formula $Co_4C_{168}H_{132}N_{40}S_{12}$ ' requires $[M]^+$ 3330.5565.

MOC4: This product was synthesized similarly as **MOC2**, in which **P1** was replaced by compound **P2** to give the target product as a black solid (yield: 0.032 g, 38%). ^{1}H NMR (400 MHz, DMSO-d6) δ 7.99 (dd, *J* = 10.1, 7.2 Hz, 72H), 7.90 (d, *J* = 12.5 Hz, 60H). Found: $[M]^+$ 3329.4702; 'molecular formula $Ni_4C_{168}H_{132}N_{40}S_{12}$ ' requires $[M]^+$ 3329.5602.

MOC5: This product was synthesized similarly as **MOC1**, in which **P1** was replaced by compound **P3** to give the target product as a black solid (yield: 0.034 g, 40%). ^{1}H NMR (400 MHz, DMSO-d6) δ 8.04 (s, 12H), 7.80 (s, 24H), 7.70 (s, 36H), 7.19 (d, *J* = 7.9 Hz, 36H). Found: $[M]^+$ 3403.1902; 'molecular formula $Co_4C_{144}H_{108}N_{40}S_{24}$ ' requires $[M]^+$ 3403.0316.

MOC6: This product was synthesized similarly as **MOC2**, in which **P1** was replaced by compound **P3** to give the target product as a black solid (yield: 0.035 g, 41%). ^{1}H NMR (400 MHz, DMSO-d6) δ 8.04 (s, 24H), 7.79 (s, 48H), 7.18 (s, 36H). Found: $[M]^+$ 3402.4314; 'molecular formula $Ni_4C_{144}H_{108}N_{40}S_{24}$ ' requires $[M]^+$ 3402.0339.

MOC7: This product was synthesized similarly as **MOC1**, in which **P1** was replaced by compound **P4** to give the target product as a black solid (yield: 0.034 g, 42%).^{1}H NMR (400 MHz, DMSO-d6) δ 8.00 – 7.82 (m, 72H), 7.75 (t, *J* = 18.8 Hz, 24H), 7.27 – 7.15 (m, 12H). Found: $[M]^+$ 3210.6537; 'molecular formula $Co_4C_{144}H_{108}N_{40}S_{12}O_{12}$ ' requires $[M]^+$ 3210.3071.

MOC8: This product was synthesized similarly as **MOC2**, in which **P1** was replaced by compound **P4** to give the target product as a black solid (yield: 0.033 g, 41%).^{1}H NMR (400 MHz, DMSO-d6) δ 7.81 – 7.70 (m, 24H), 7.19 – 7.03 (m, 84H). Found: $[M]^+$ 3209.4507; 'molecular formula $Ni_4C_{144}H_{108}N_{40}S_{12}O_{12}$ ' requires $[M]^+$ 3209.3105.

MOC9: This product was synthesized similarly as **MOC1**, in which **P1** was replaced by compound **P5** to give the target product as a black solid (yield: 0.033 g, 46%). Found: $[M]^+$ 2830.3467; 'molecular formula $Co_4C_{132}H_{120}N_{36}S_{12}$ ' requires $[M]^+$ 2830.4494. FTIR (with KBr): ν(Co-S/Co-N): 525 cm^{-1}.

MOC10: This product was synthesized similarly as **MOC2**, in which **P1** was replaced by compound **P5** to give the target product as a black solid (yield: 0.030 g, 42%). Found: $[M]^+$ 2828.4151; 'molecular formula $Ni_4C_{132}H_{120}N_{36}S_{12}$ ' requires $[M]^+$ 2828.4530. FTIR (with KBr): ν(Ni-S): 670 cm^{-1}.

MOC11: This product was synthesized similarly as **MOC1**, in which **P1** was replaced by compound **P6** to give the target product as a black solid (yield: 0.030 g, 45%). Found: $[M]^+$ 2662.3949; 'molecular formula $Co_4C_{120}H_{96}N_{36}S_{12}$ ' requires $[M]^+$ 2662.2612. FTIR (with KBr): ν(Co-S/Co-N): 505 cm^{-1}.

MOC12: This product was synthesized similarly as **MOC2**, in which **P1** was replaced by compound **P6** to give the target product as a black solid (yield: 0.031g, 46%). Found: $[M]^+$ 2660.2262; 'molecular formula $Ni_4C_{120}H_{96}N_{36}S_{12}$ ' requires $[M]^+$ 2660.2646. FTIR (with KBr): ν(Ni-N): 616 cm^{-1}.

MOC13: This product was synthesized similarly as **MOC1**, in which **P1** was replaced by compound **P7** to give the target product as a black solid (yield: 0.030 g, 44%). Found: $[M]^+$ 2733.7669; 'molecular formula $Co_4C_{96}H_{72}N_{36}S_{24}$ ' requires $[M]^+$ 2733.7358. FTIR (with KBr): ν(Co-S/Co-N): 499 cm^{-1}.

MOC14: This product was synthesized similarly as **MOC2**, in which **P1** was replaced by compound **P7** to give the target product as a black solid (yield: 0.031 g, 45%). Found: $[M]^+$ 2733.8635; 'molecular formula $Ni_4C_{96}H_{72}N_{36}S_{24}$ ' requires $[M]^+$ 2733.7372. FTIR (with KBr): ν(Ni-N): 613 cm^{-1}.

MOC15: This product was synthesized similarly as **MOC1**, in which **P1** was replaced by compound **P8** to give the target product as a black solid (yield: 0.029 g, 45%). Found:

$[M]^+$ 2542.1790; 'molecular formula $Co_4C_{96}H_{72}N_{36}S_{12}O_{12}$ ' requires $[M]^+$ 2542.0114. FTIR (with KBr): ν(Co-S/Co-N): 533 cm^{-1}.

MOC16: This product was synthesized similarly as **MOC2**, in which **P1** was replaced by compound **P8** to give the target product as a black solid (yield: 0.029g, 46%). Found: $[M]^+$ 2540.2184; 'molecular formula $Ni_4C_{96}H_{72}N_{36}S_{12}O_{12}$ ' requires $[M]^+$ 2540.0147. FTIR (with KBr): ν(Ni-N): 630 cm^{-1}.

7.6.4. Light-driven hydrogen generation study with MOC and CdS NRs

To a one-neck pear-shaped round bottom flask containing 1 mg of CdS NRs and 10 μM of MOC, 5 mL of 0.5 M of AA (pH = 4) was added as the hole scavenger. The flask was then sealed by rubber septa and was purged with a mixture of argon/methane (80:20 mol%) for 15 mins. The methane present in the gas mixture was served as an internal standard for GC analysis of each experiment. The flask was steadily stirred and continuously radiated from the bottom with blue (*ca.* 470 nm) light-emitting diodes inside a just-fit container, which blocks the stray light from the environment. The light power was measured using a thermal sensor and power meter (Model: BIM-7203-0100F & BIM-7001; Hangzhou Brolight Technology Co., Ltd.) and estimated to be 50 mW for each reaction. The produced hydrogen was measured by GC (Agilent 6890 Series GC System with a molecular sieve 5 Å column and thermal conductivity detector) at different time points from the headspace of reaction mixtures and was quantified by the calibration plot. The LED radiation is assumed to be monochromatic at emission

intensity maximum (470 nm for blue and LEDs).

Appendix I Nuclear Magnetic Resonance Spectrum

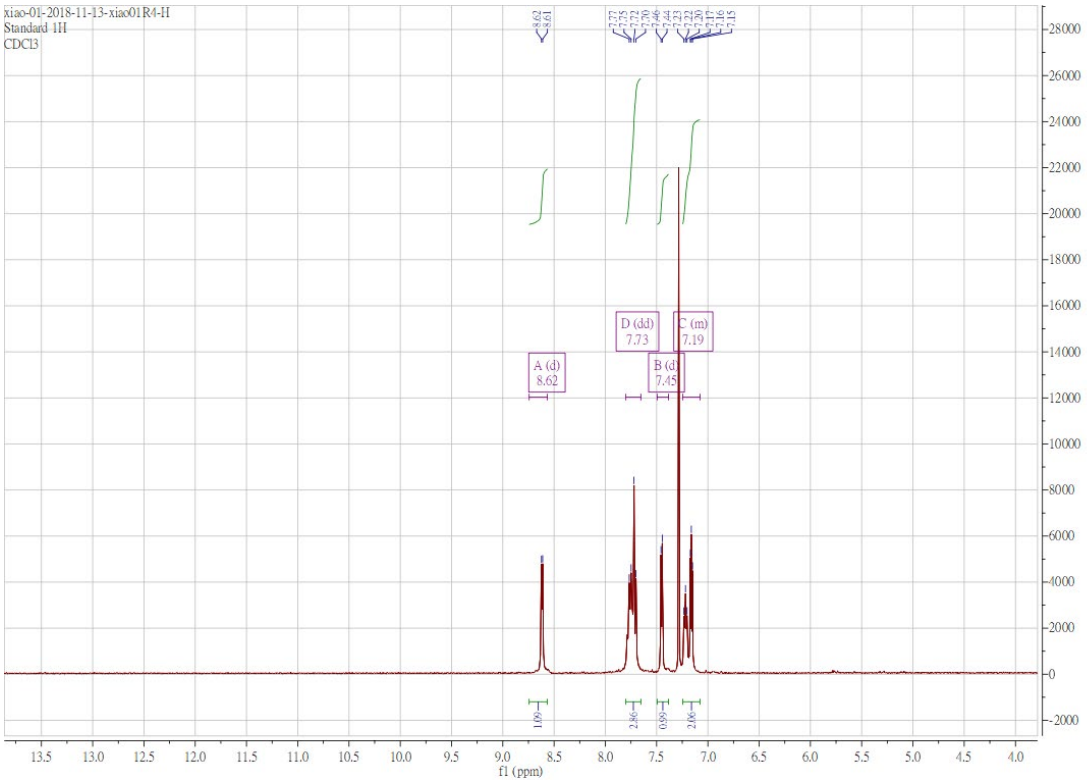

Figure S 1.1. ^{1}H NMR spectrum of **L1** in $CDCl_3$

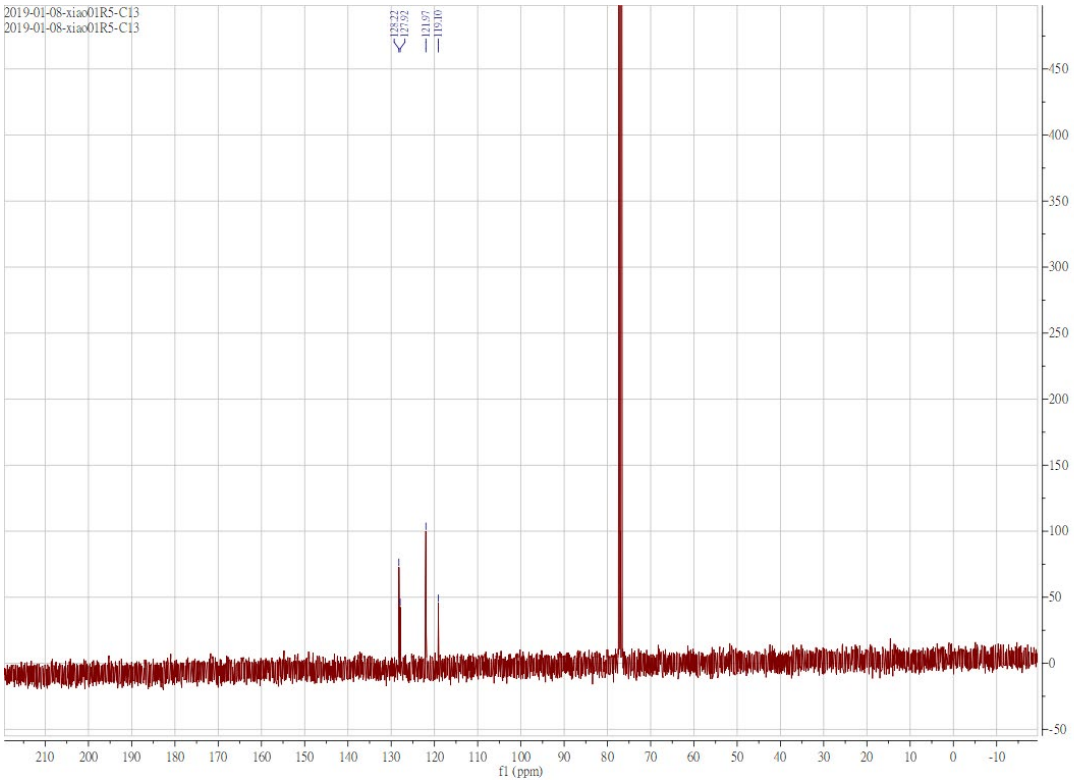

Figure S 1.2. ^{13}C NMR spectrum of spectrum of **L1** in $CDCl_3$

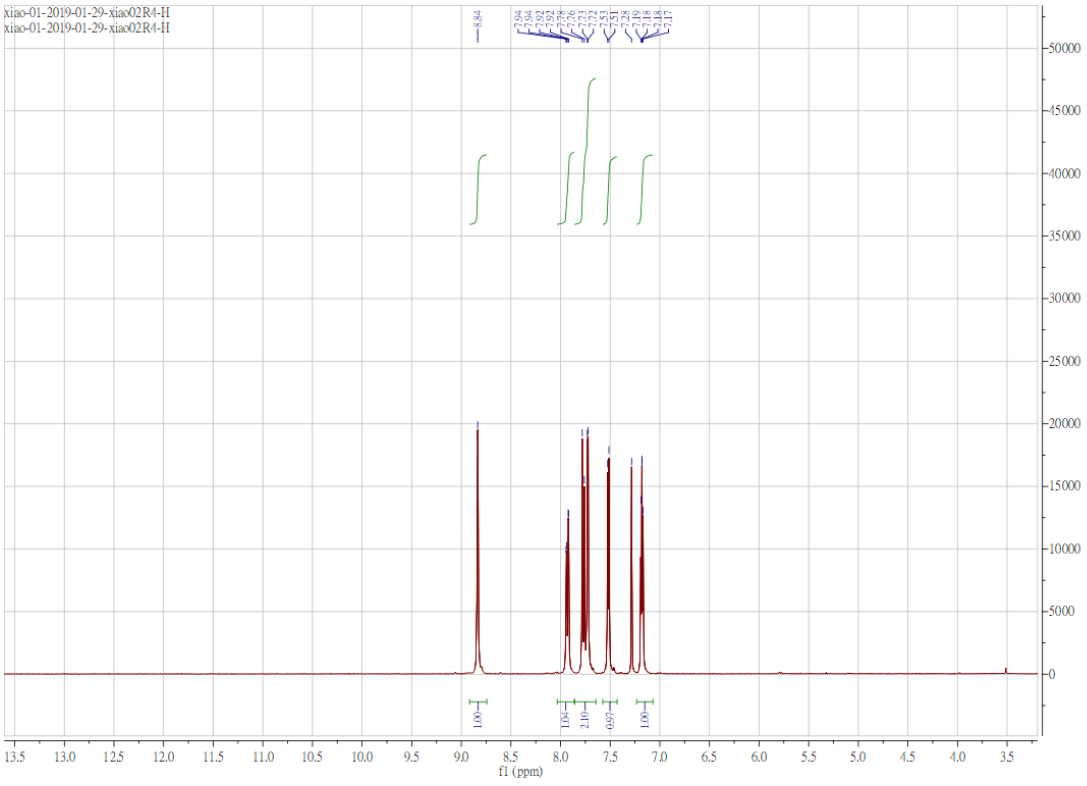

Figure S 1.3. ^{1}H NMR spectrum of **L2** in $CDCl_3$

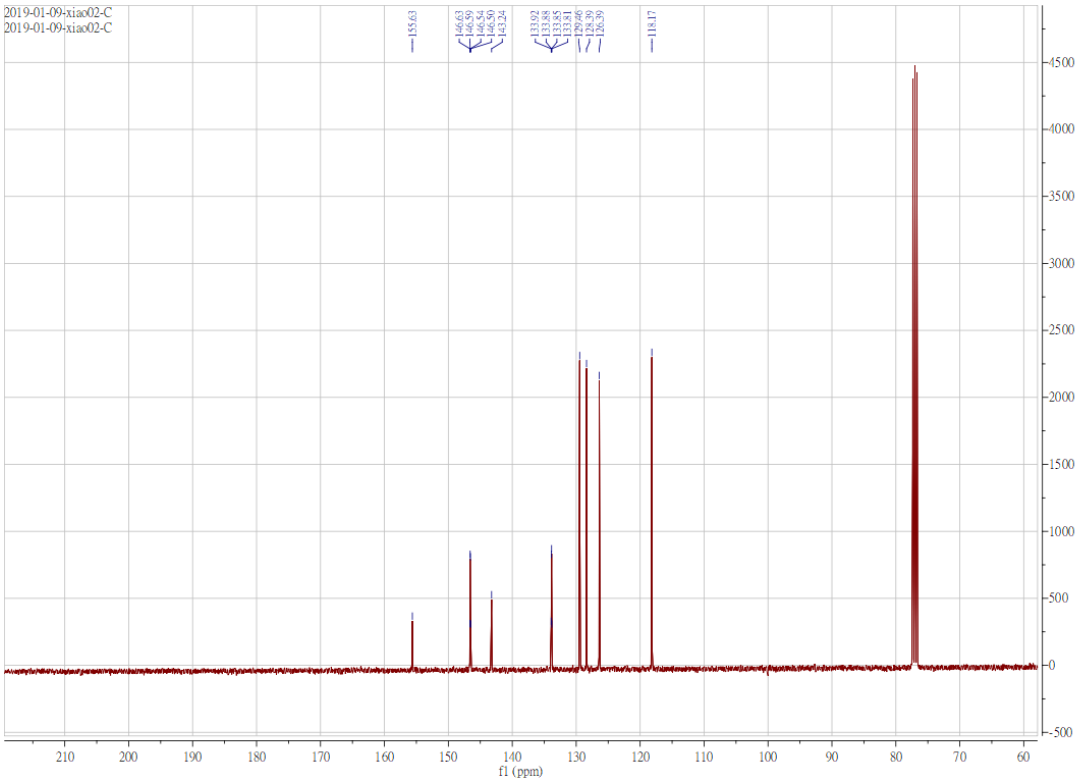

Figure S 1.4. ^{13}C NMR spectrum of spectrum of **L2** in $CDCl_3$

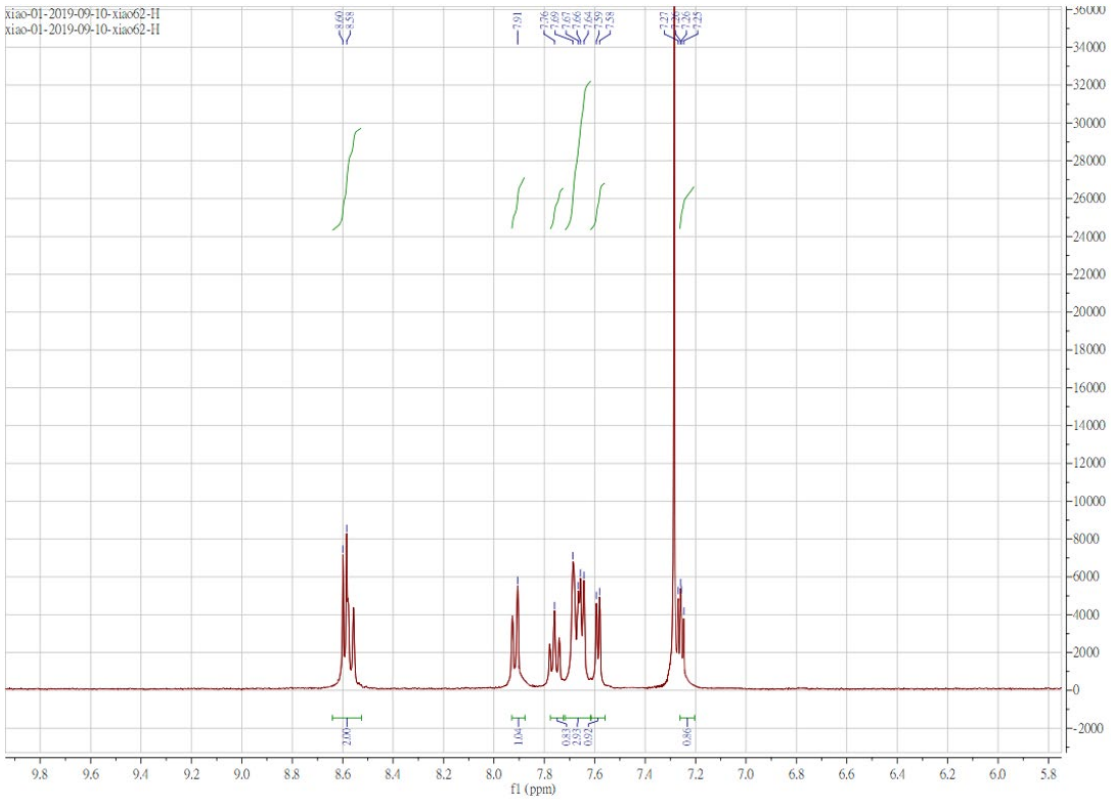

Figure S 1.5. ^{1}H NMR spectrum of **L3** in $CDCl_3$

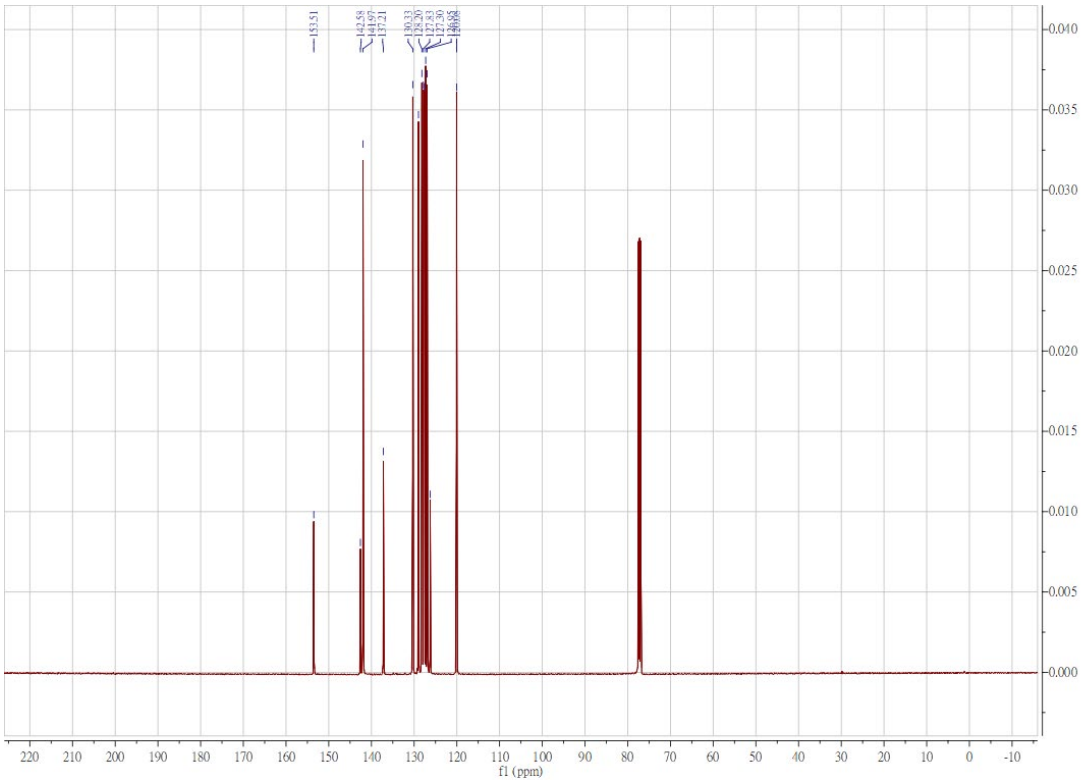

Figure S 1.6. ^{13}C NMR spectrum of **L3** in $CDCl_3$

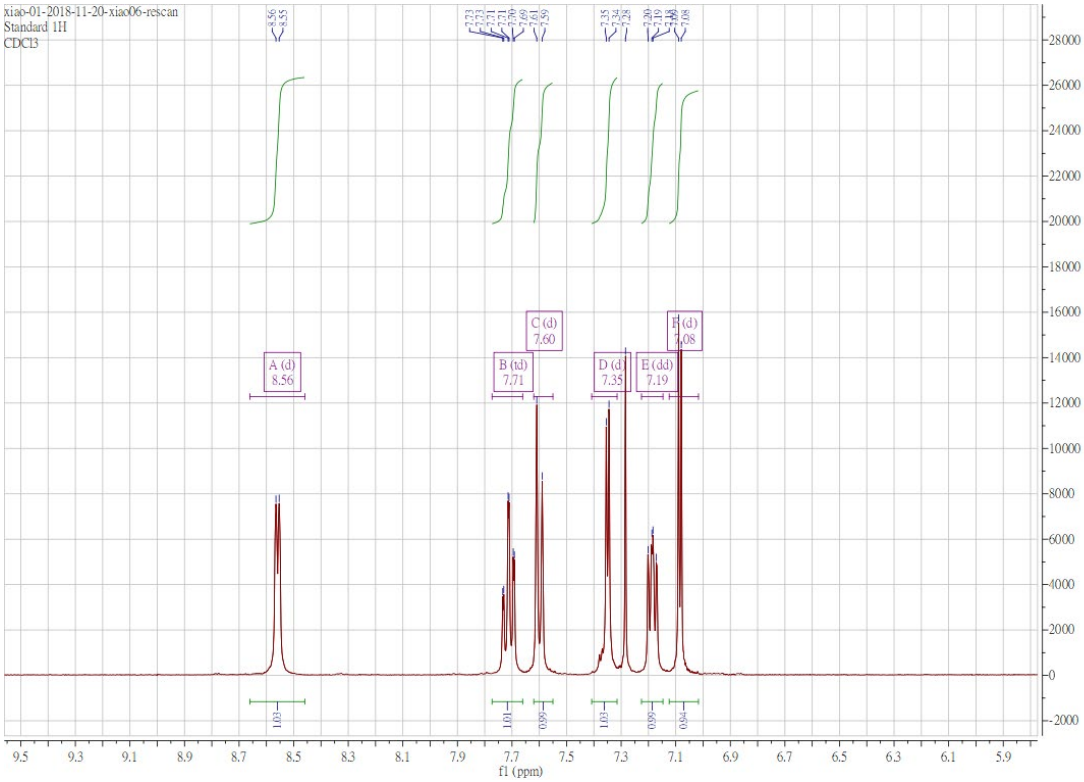

Figure S 1.7. ^{1}H NMR spectrum of **2** in $CDCl_3$

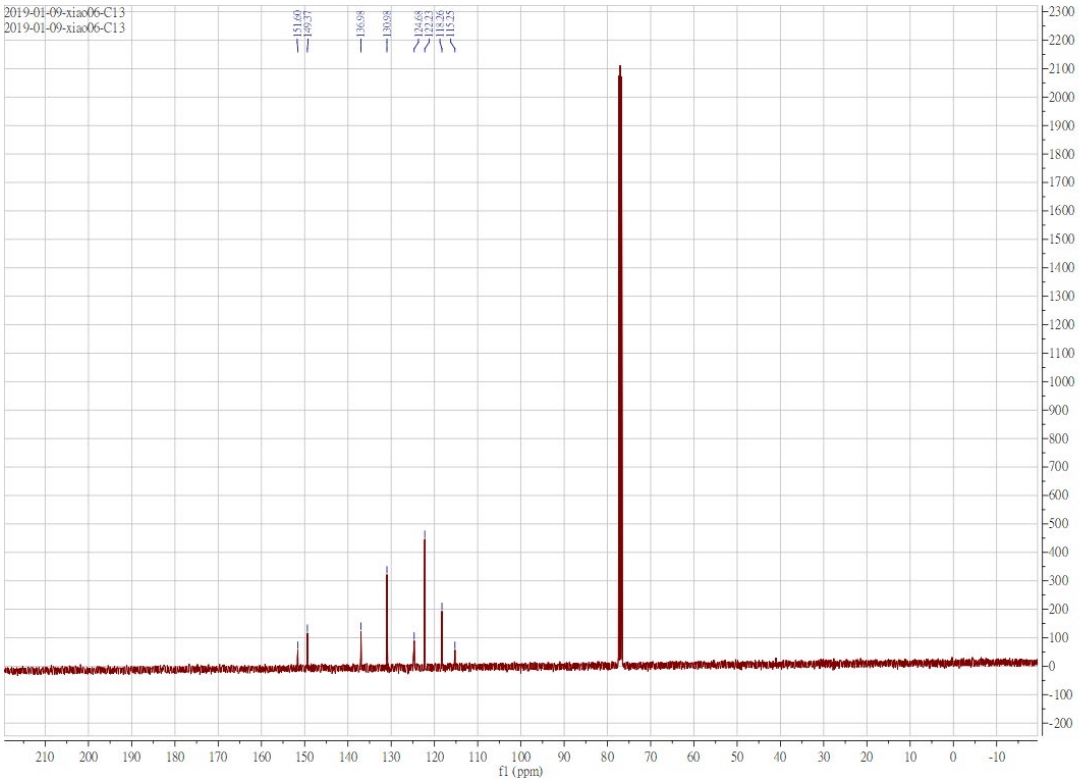

Figure S 1.8. ^{13}C NMR spectrum of **2** in $CDCl_3$

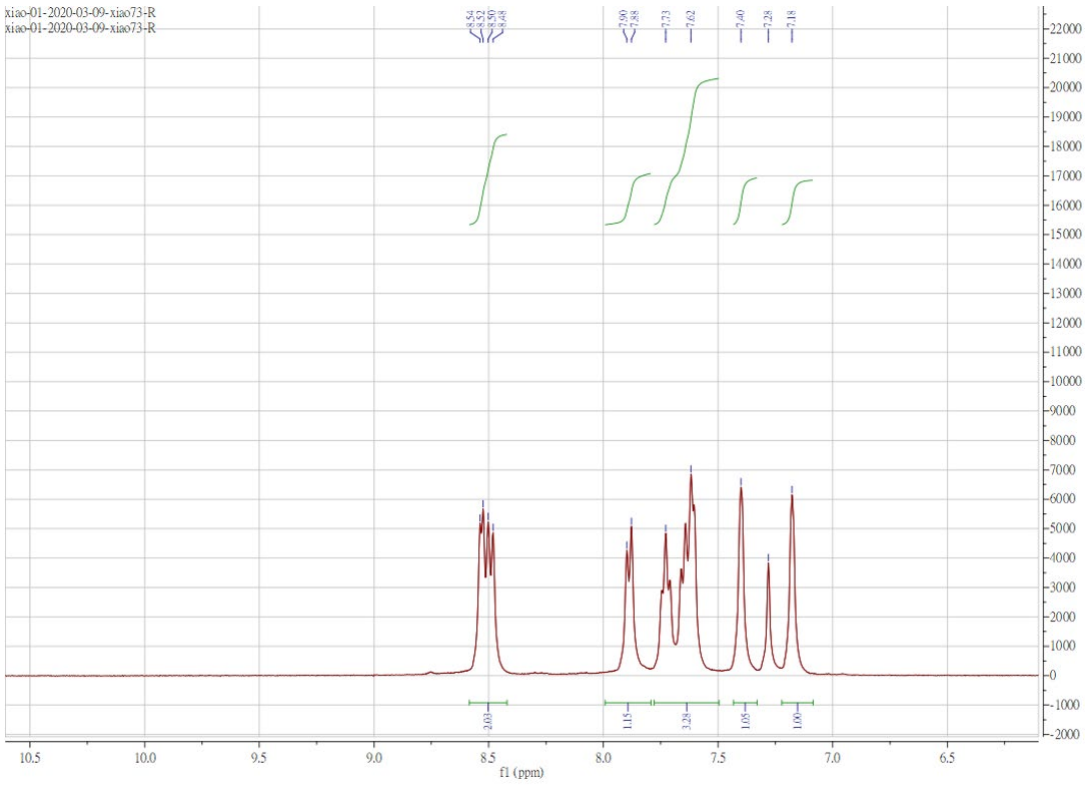

Figure S 1.9. ^{1}H NMR spectrum spectrum of **3** in $CDCl_3$

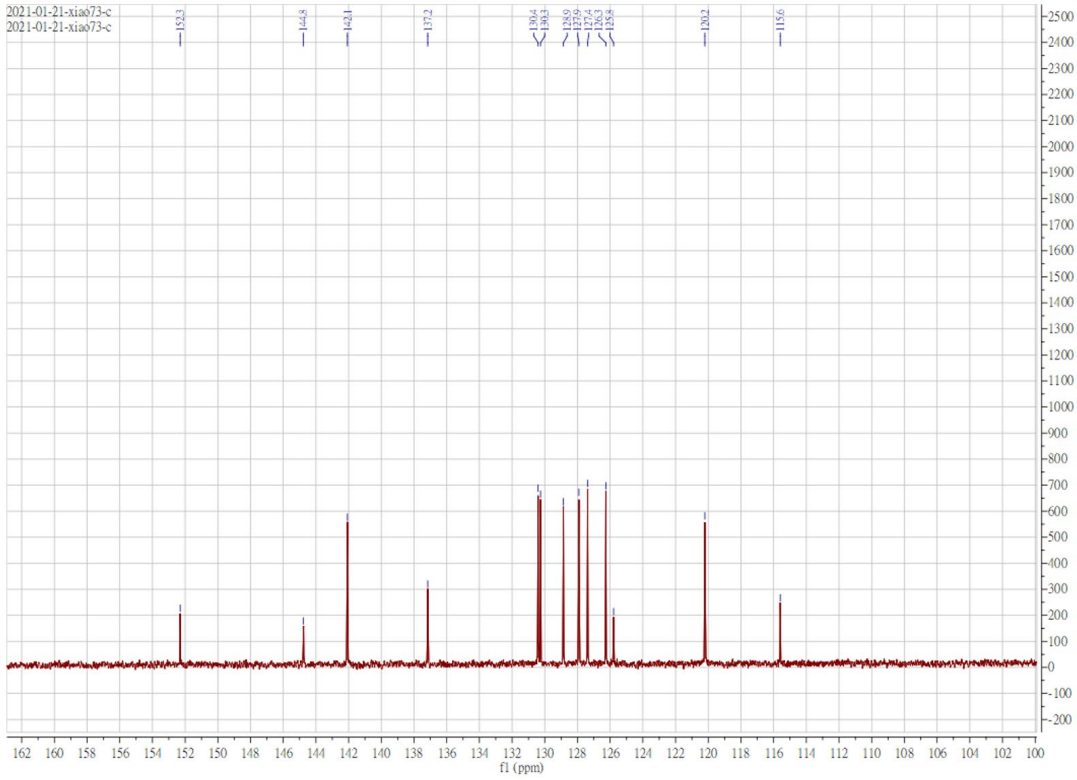

Figure S 1.10. ^{13}C NMR spectrum of **3** in $CDCl_3$

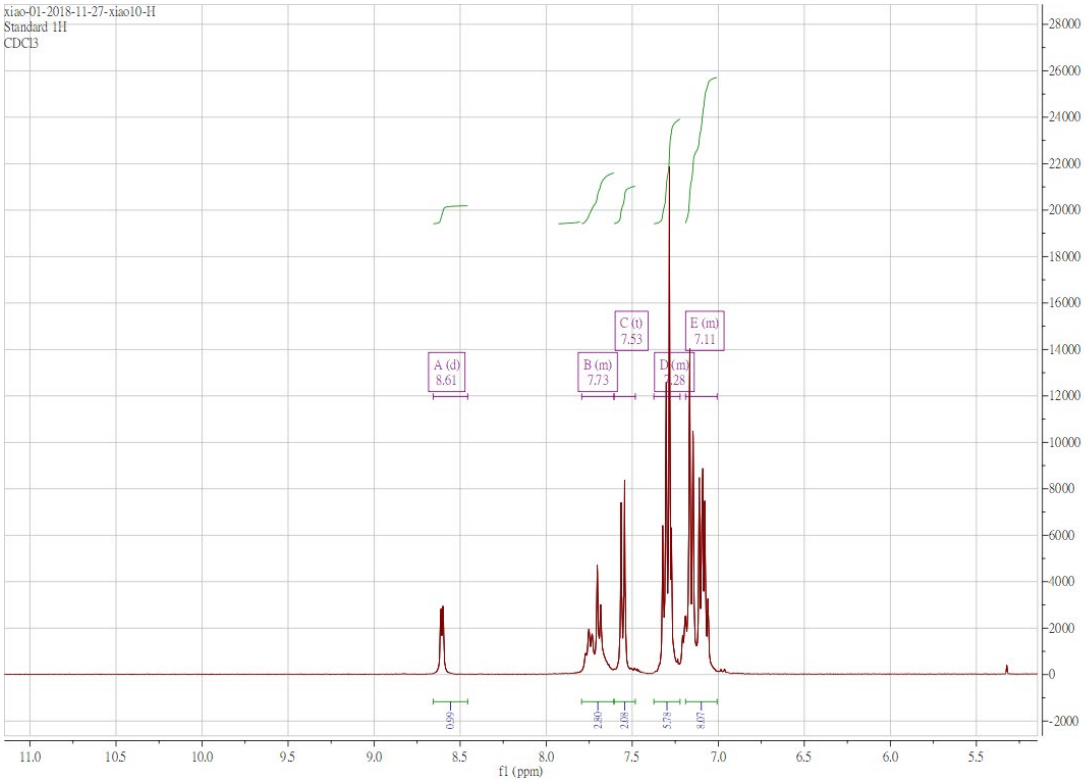

Figure S 1.11. ^{1}H NMR spectrum of **L4** in $CDCl_3$

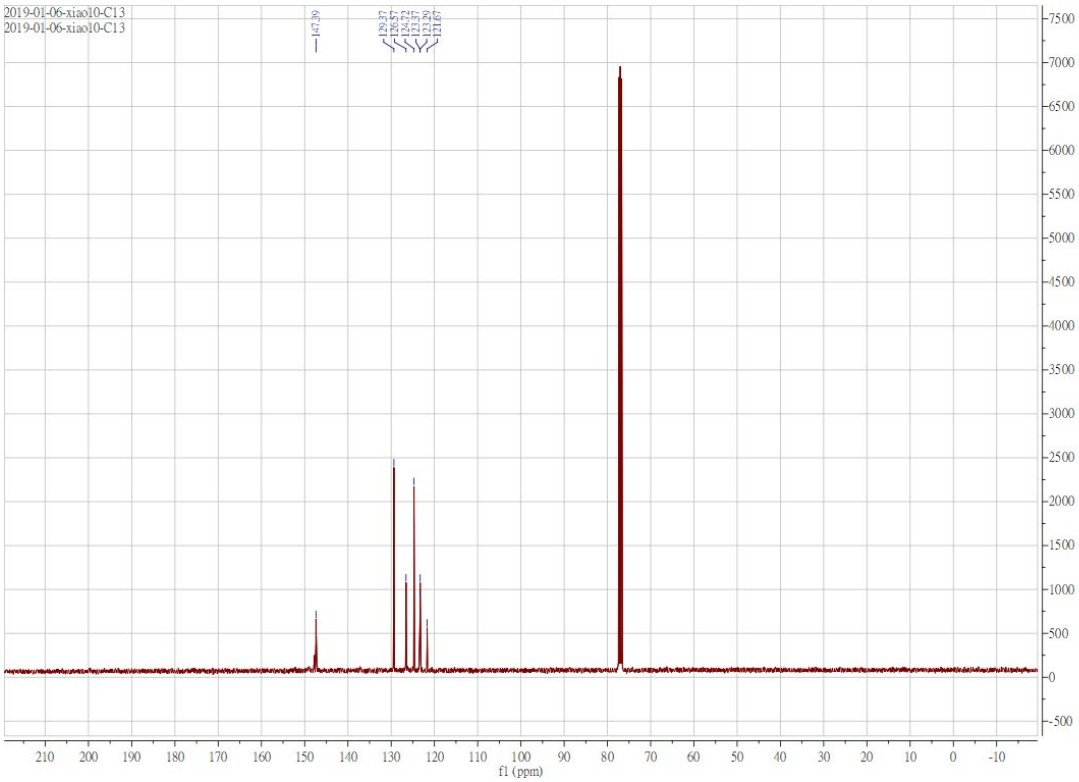

Figure S 1.12. ^{13}C NMR spectrum of **L4** in $CDCl_3$

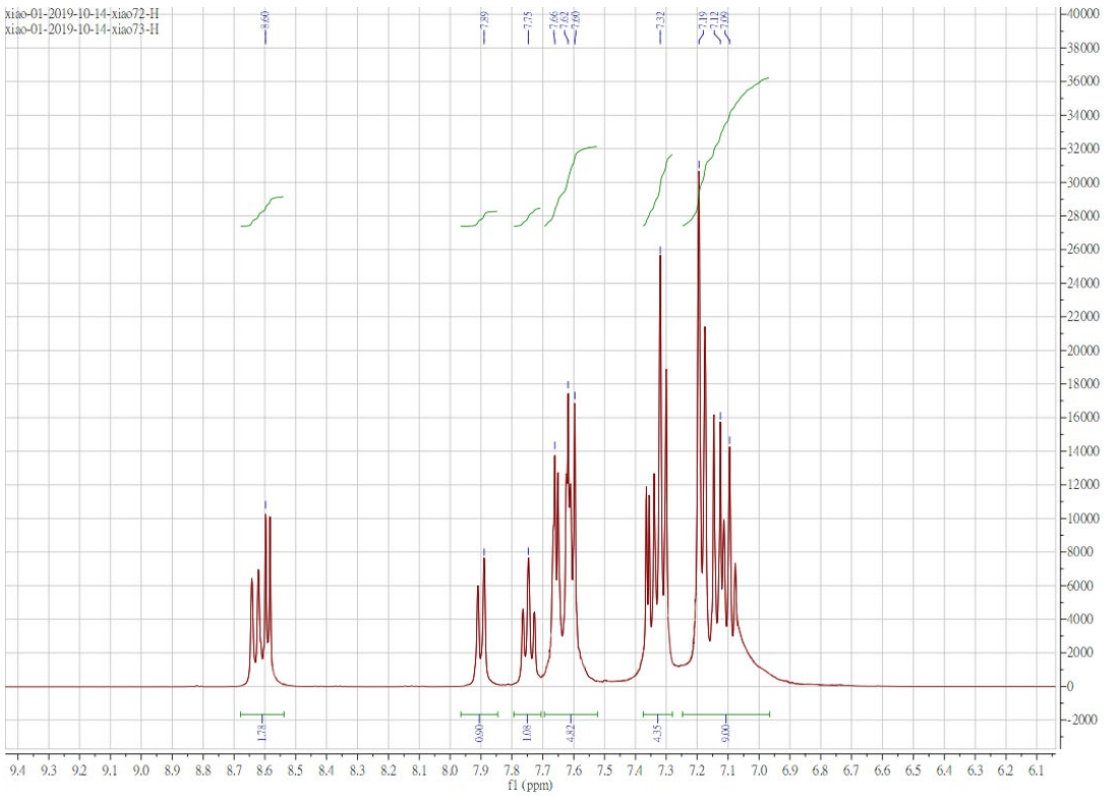

Figure S 1.13. ^{1}H NMR spectrum spectrum of **L5** in $CDCl_3$

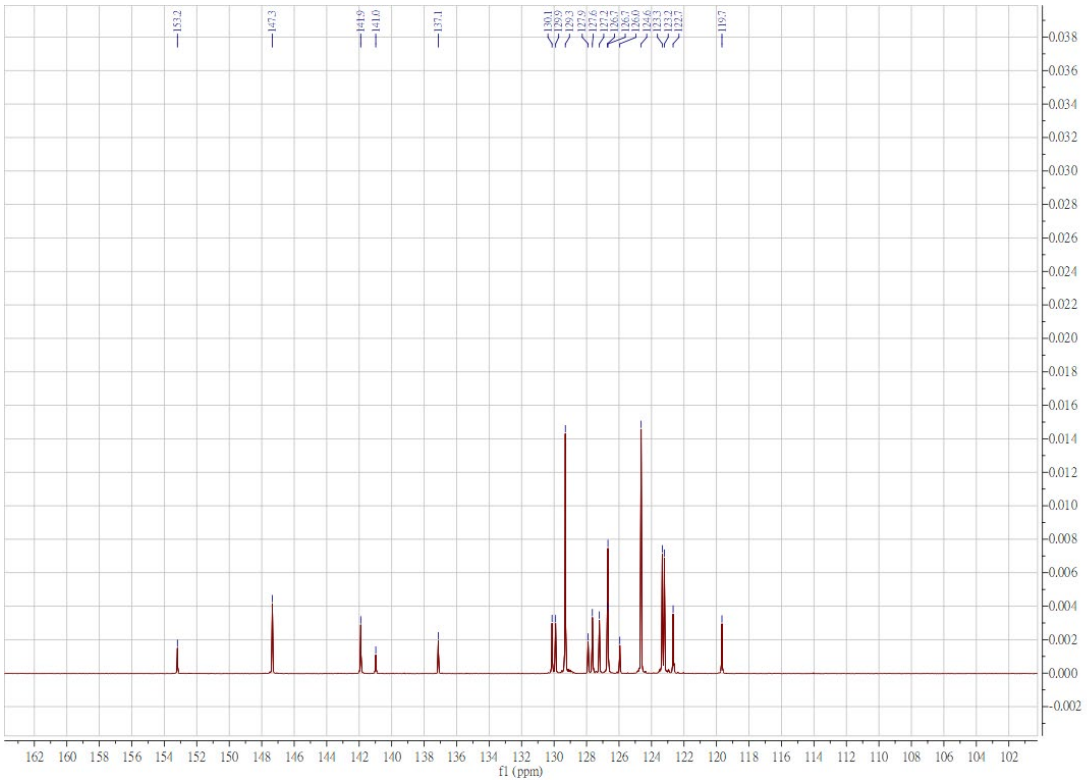

Figure S 1.14. ^{13}C NMR spectrum of **L5** in $CDCl_3$

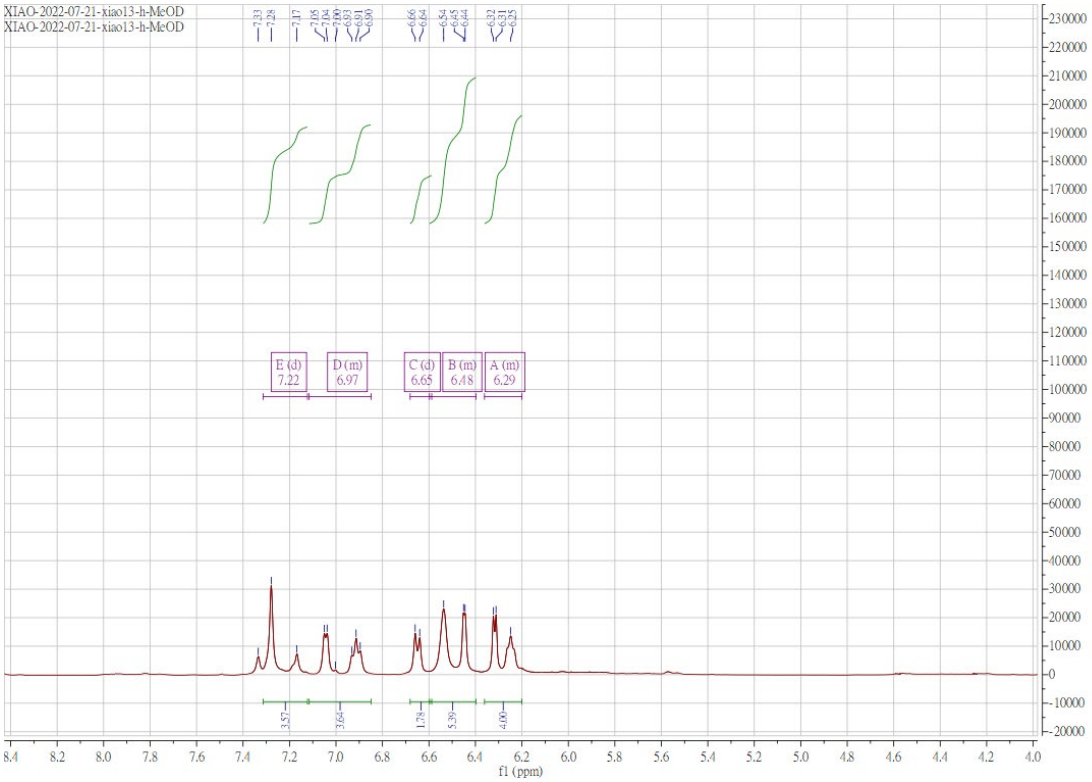

Figure S 1.15. ^{1}H NMR spectrum of **Ru1** in MeOD

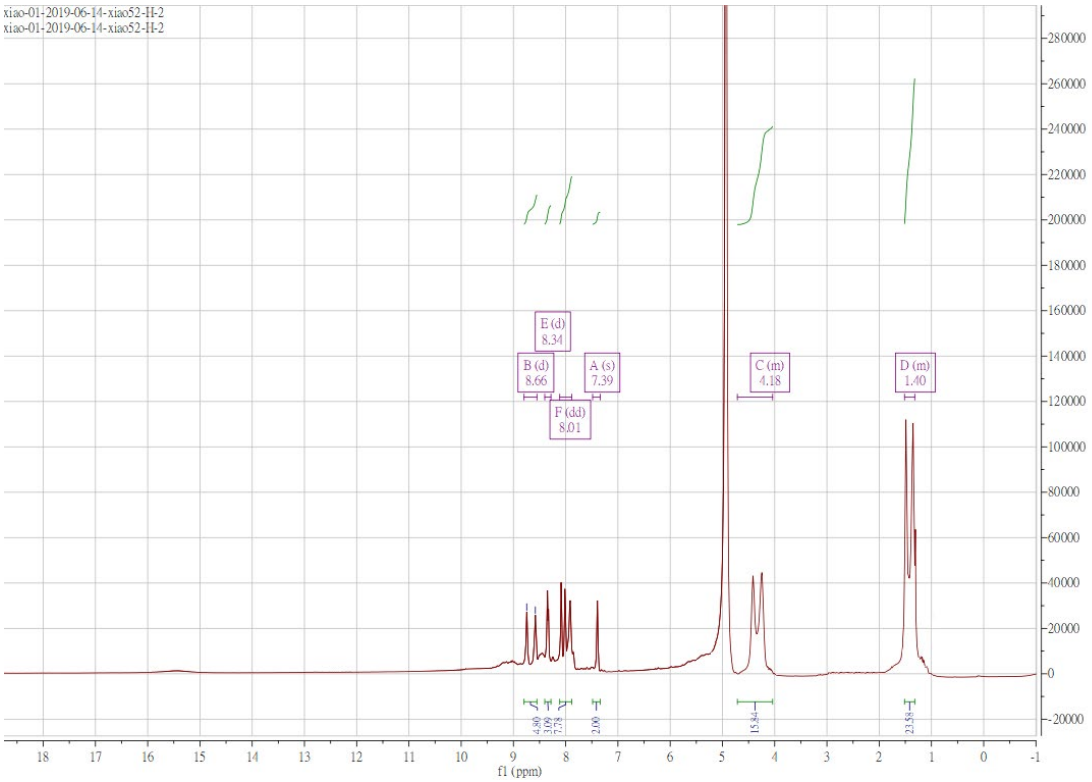

Figure S 1.16. ^{1}H NMR spectrum of **Ru2** in MeOD

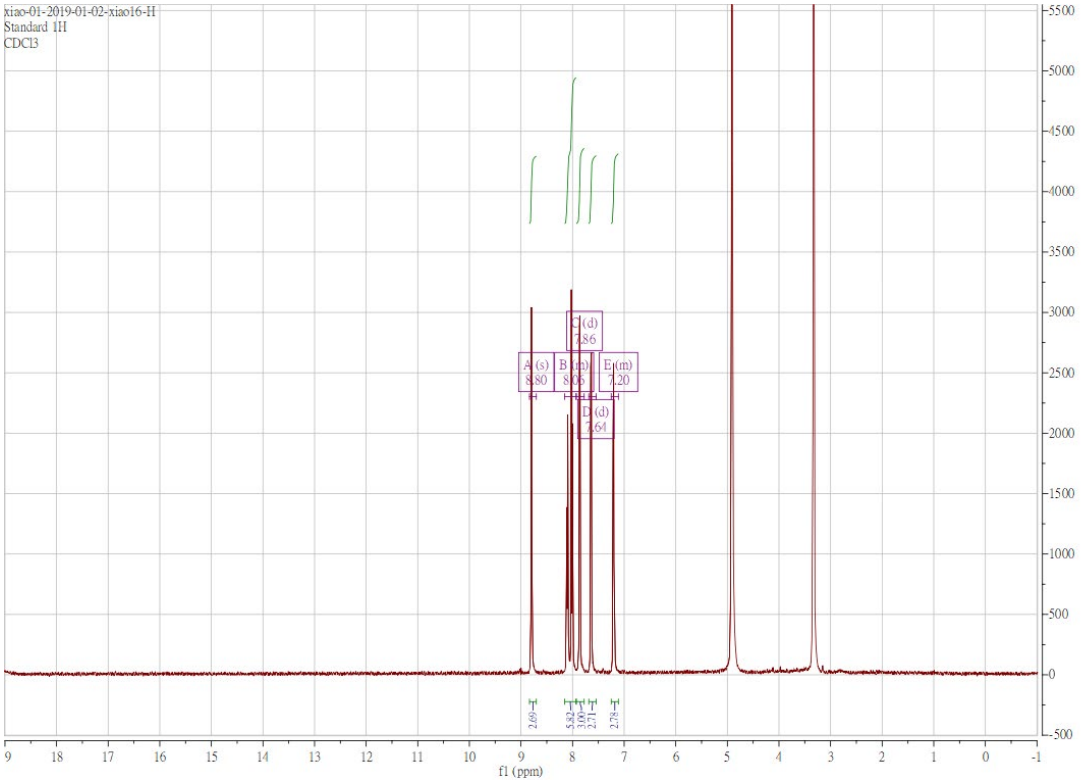

Figure S 1.17. ^{1}H NMR spectrum of **Ru3** in MeOD

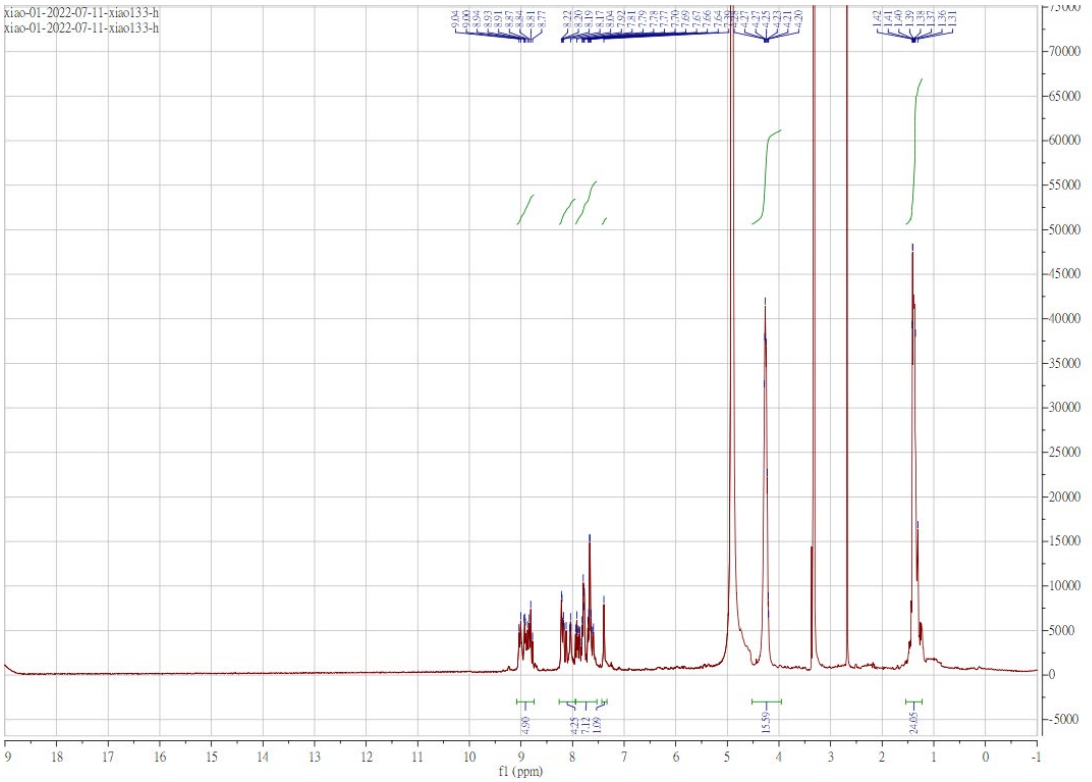

Figure S 1.18. ^{1}H NMR spectrum of **Ru4** in MeOD

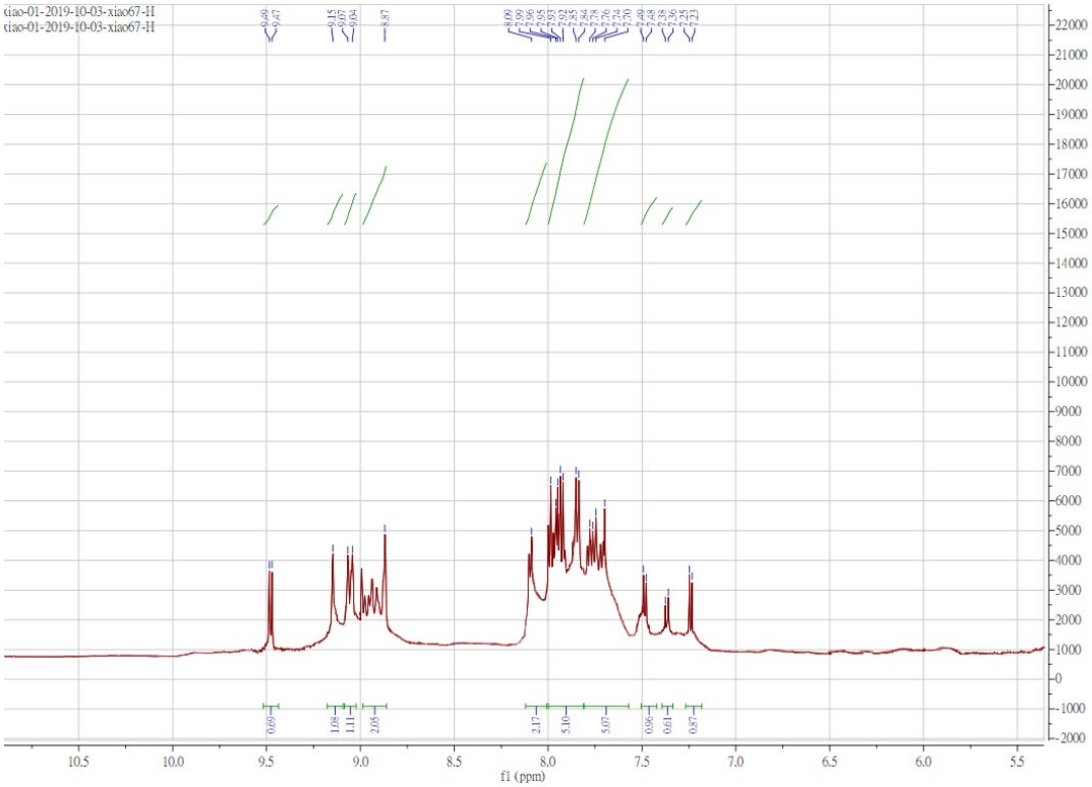

Figure S 1.19. ^{1}H NMR spectrum of **Ru5** in MeOD

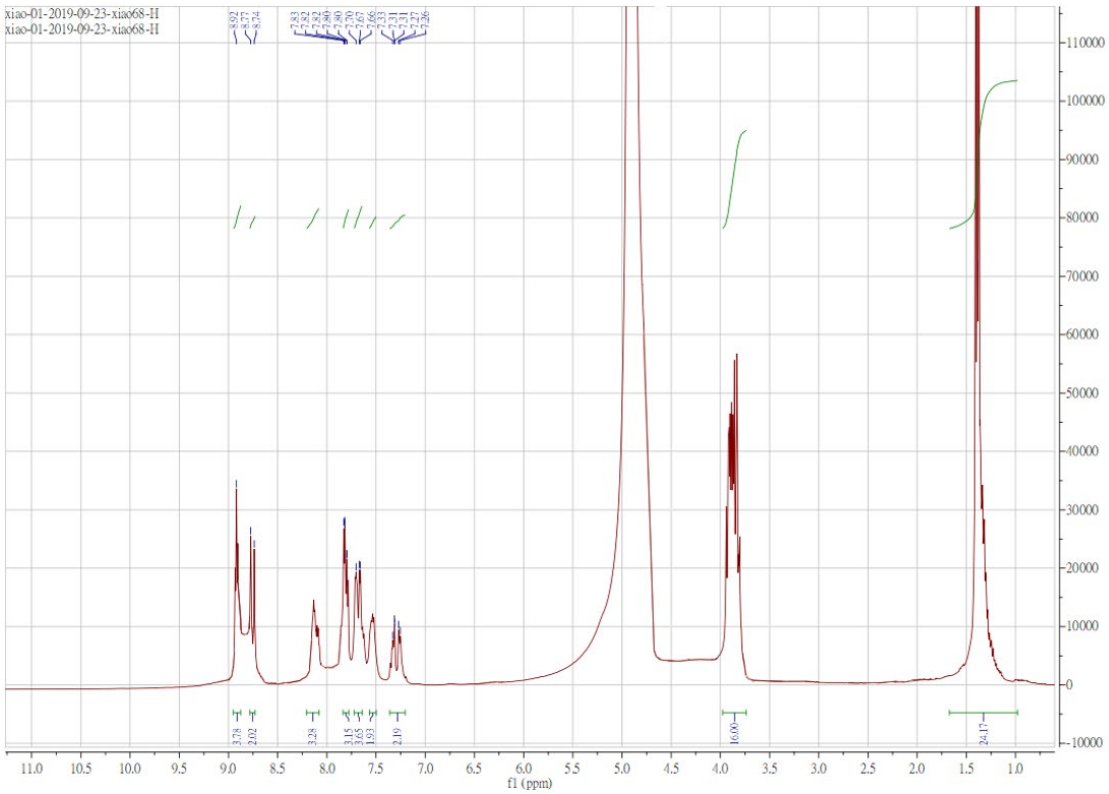

Figure S 1.20. ^{1}H NMR spectrum of **Ru6** in MeOD

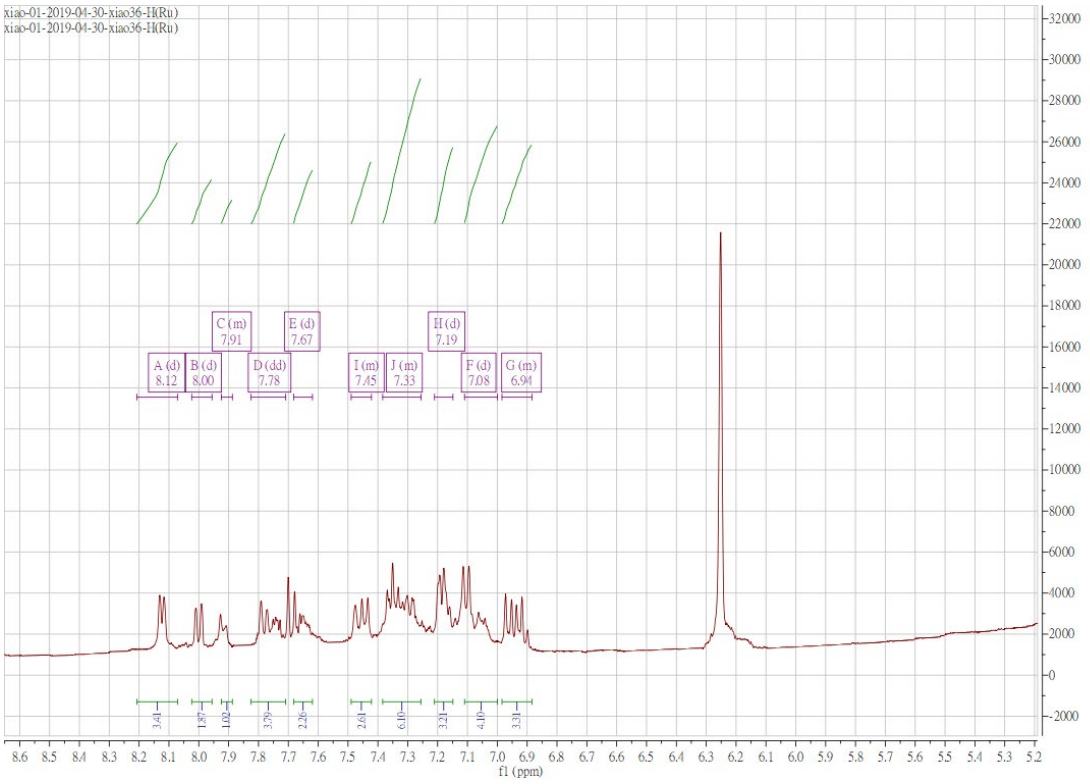

Figure S 1.21. ^{1}H NMR spectrum of **Ru7** in MeOD

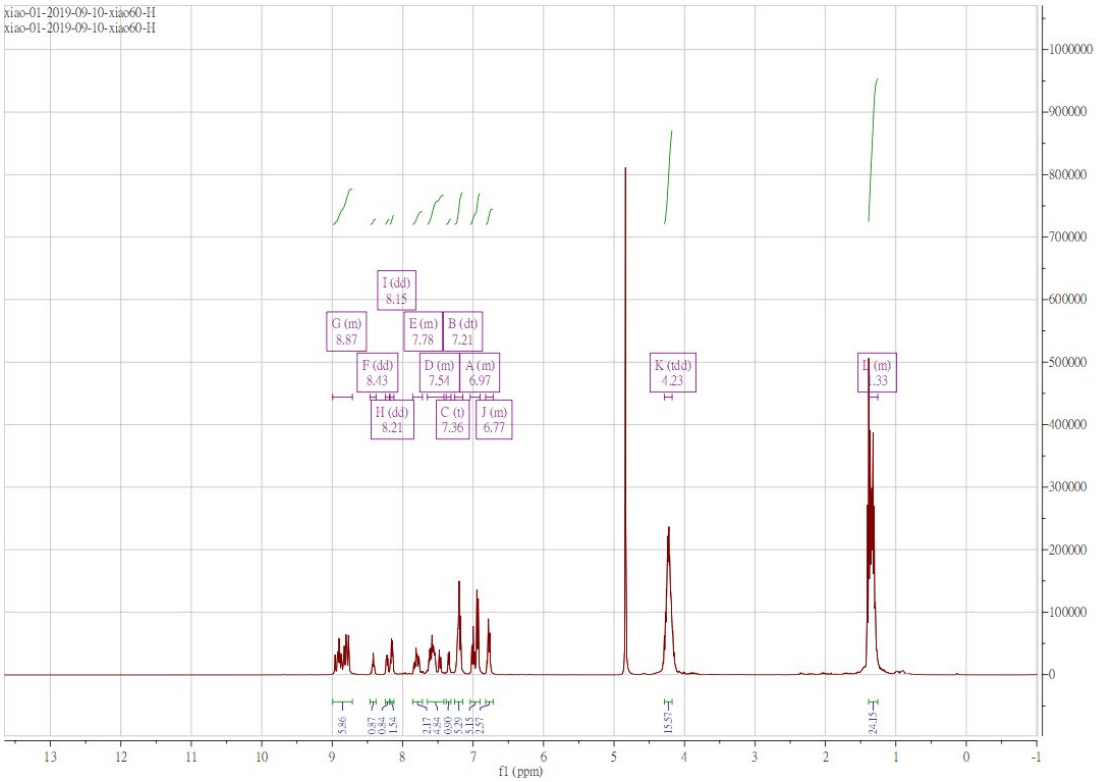

Figure S 1.22. [1]H NMR spectrum of **Ru8** in MeOD

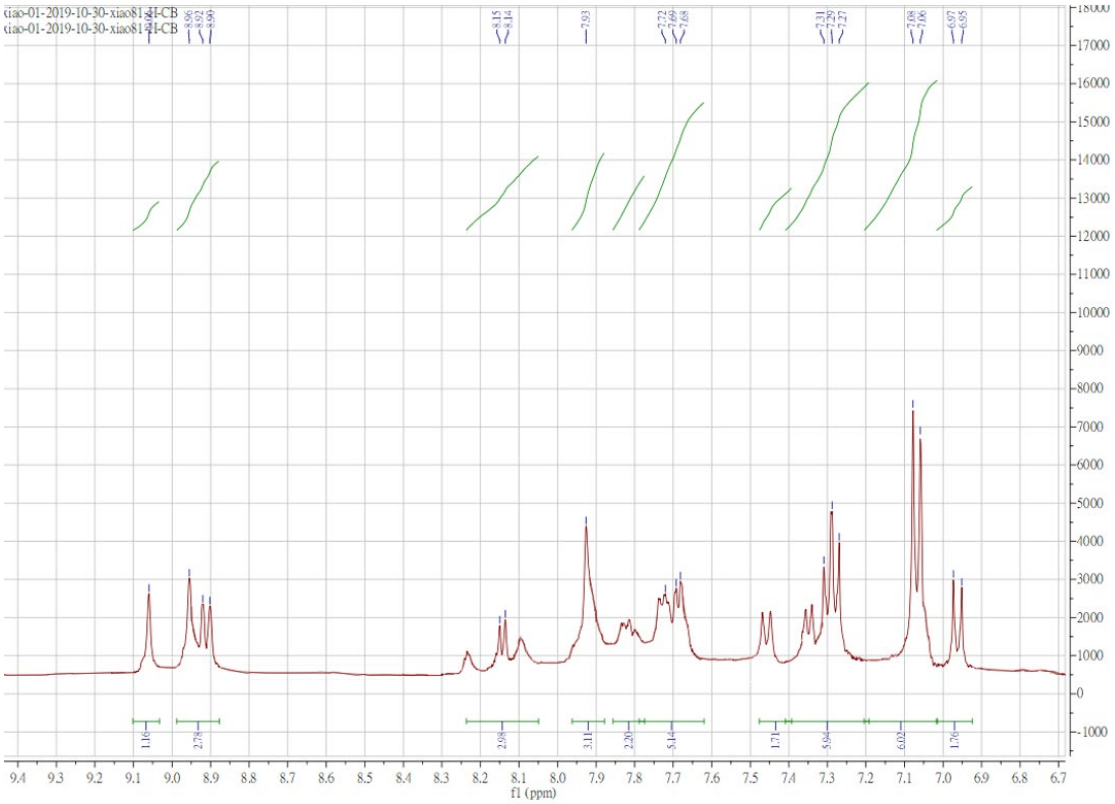

Figure S 1.23. [1]H NMR spectrum of **Ru9** in MeOD

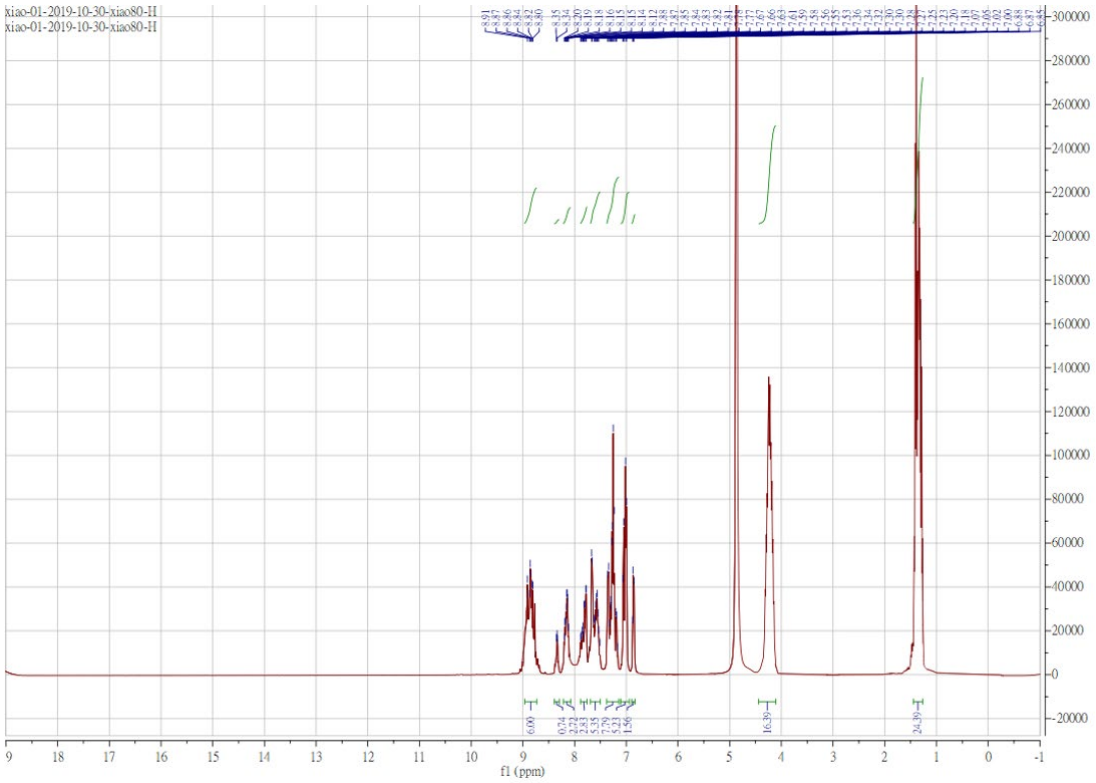

Figure S 1.24. ^{1}H NMR spectrum of **Ru10** in MeOD.

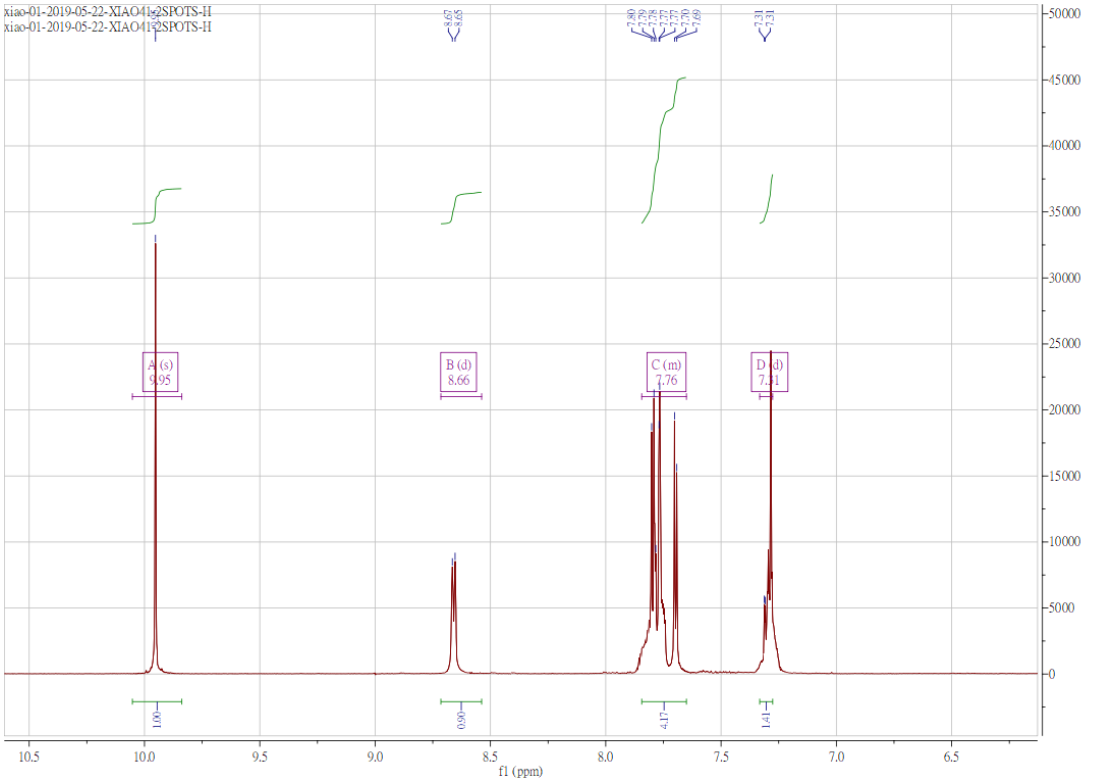

Figure S 1.25. ^{1}H NMR spectrum of **L6** in $CDCl_3$

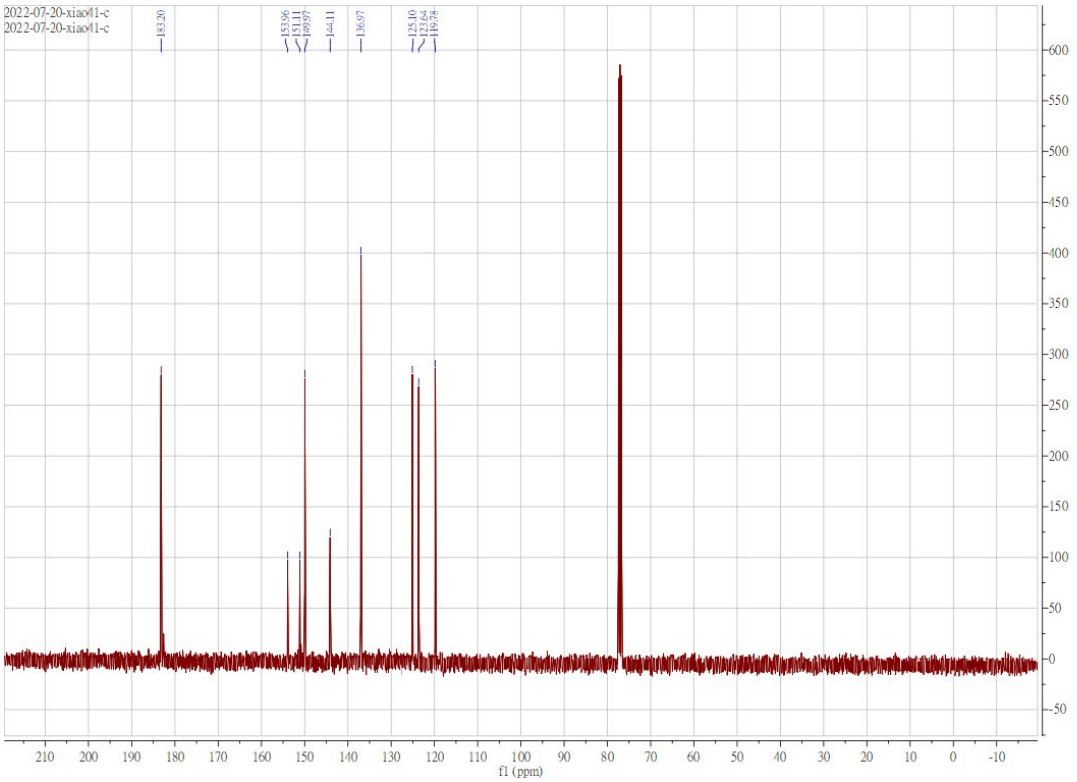

Figure S 1.26. ^{13}C NMR spectrum of **L6** in $CDCl_3$

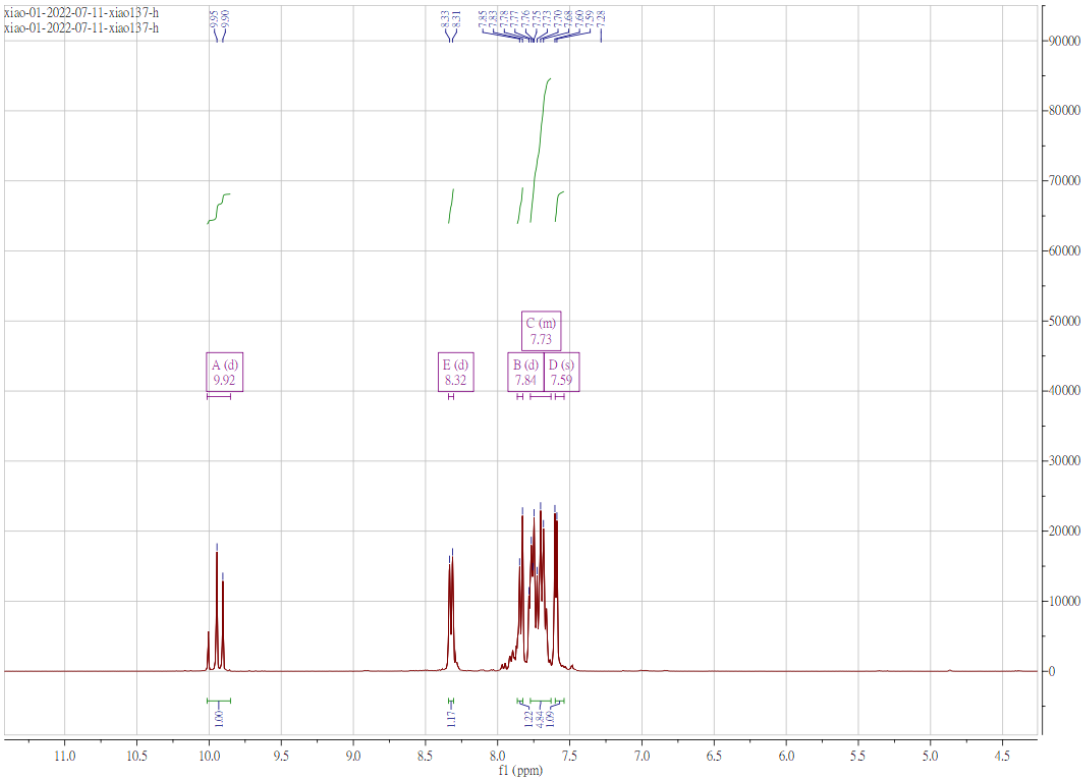

Figure S 1.27. ^{1}H NMR spectrum of **L7** in $CDCl_3$

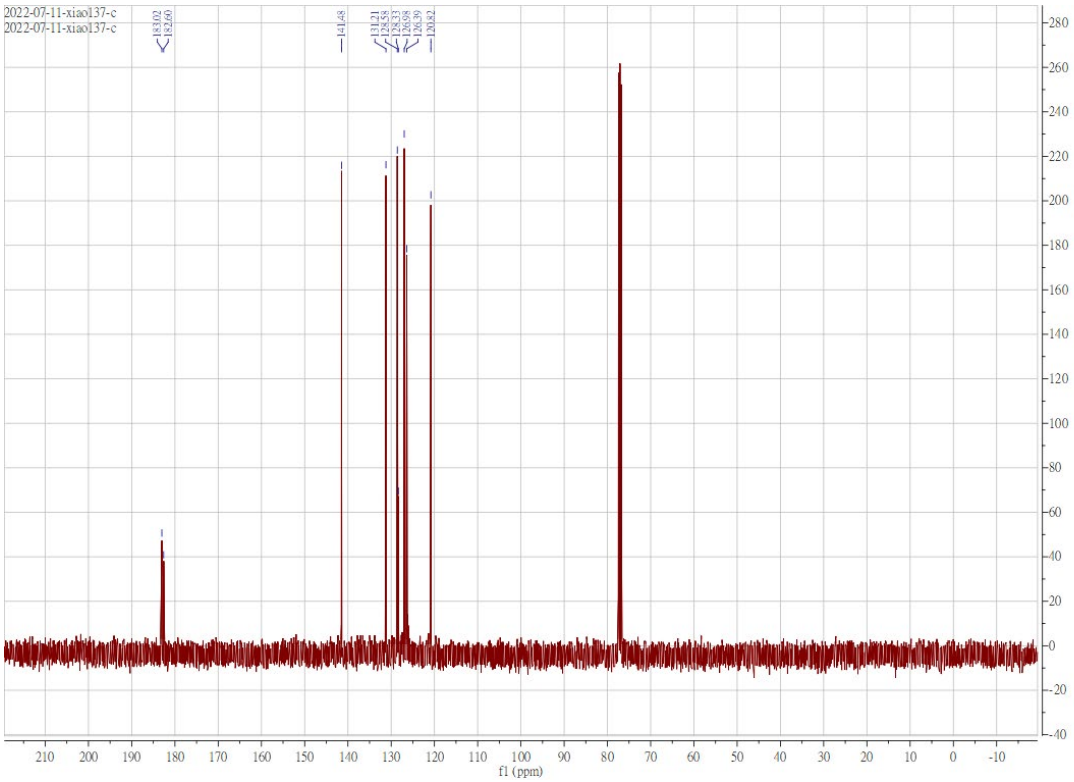

Figure S 1.28. ^{13}C NMR spectrum of **L7** in $CDCl_3$

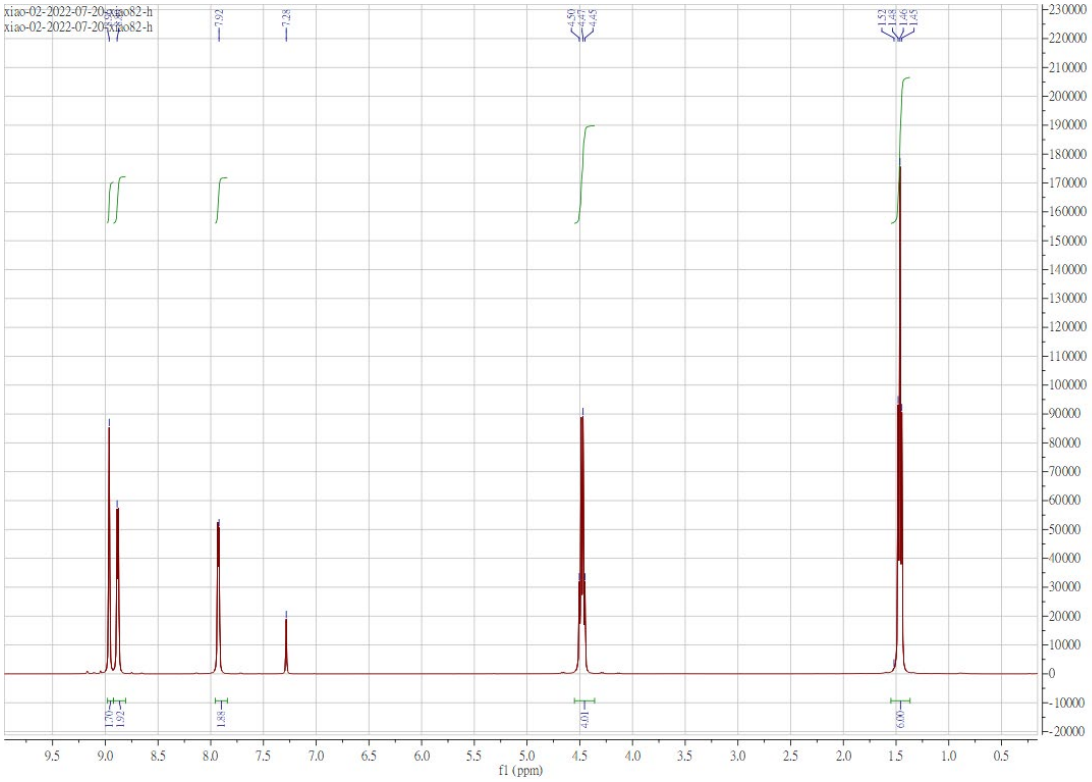

Figure S 1.29. ^{1}H NMR spectrum of diethyl [2,2 -bipyridine]-4,4 -dicarboxylate in $CDCl_3$

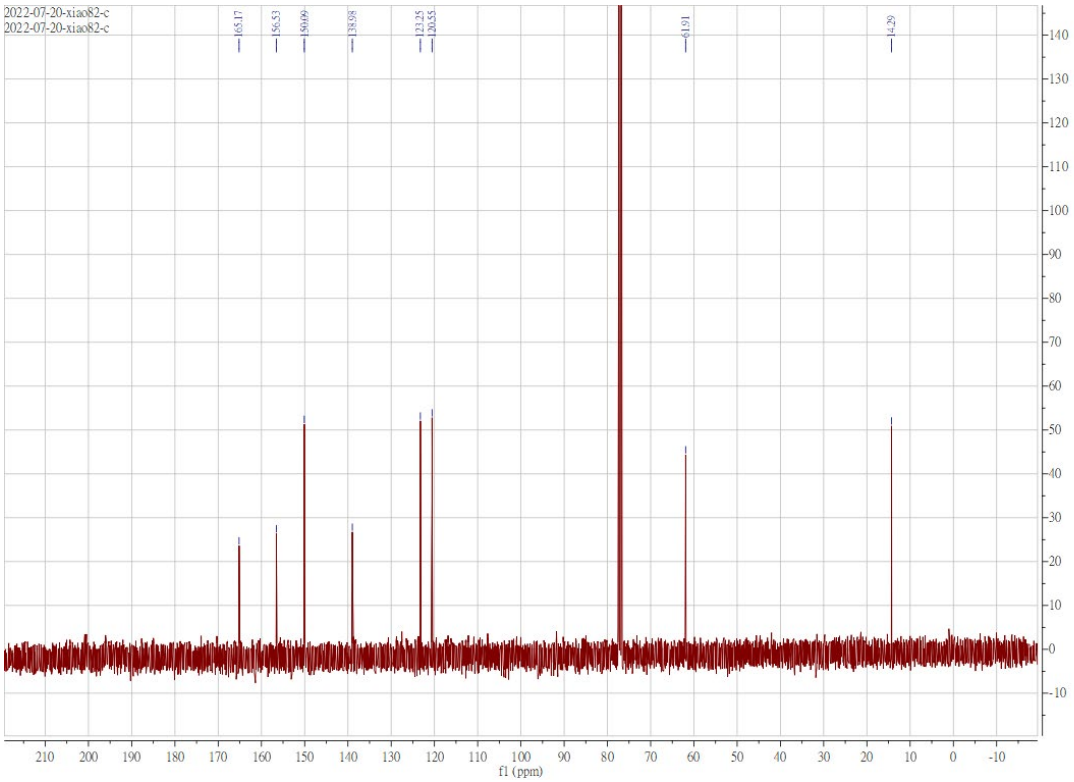

Figure S 1.30. ^{13}C NMR spectrum of diethyl [2,2 -bipyridine]-4,4 -dicarboxylate in $CDCl_3$

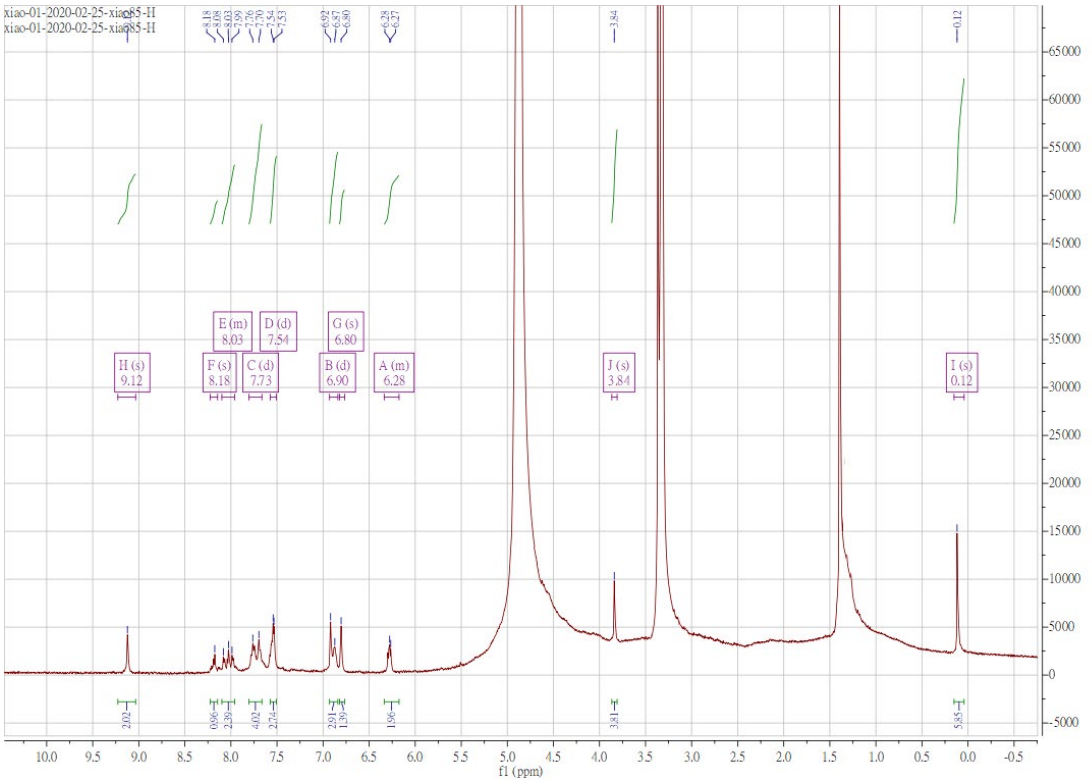

Figure S 1.31. ^{1}H NMR spectrum of **Ir1** in $CDCl_3$

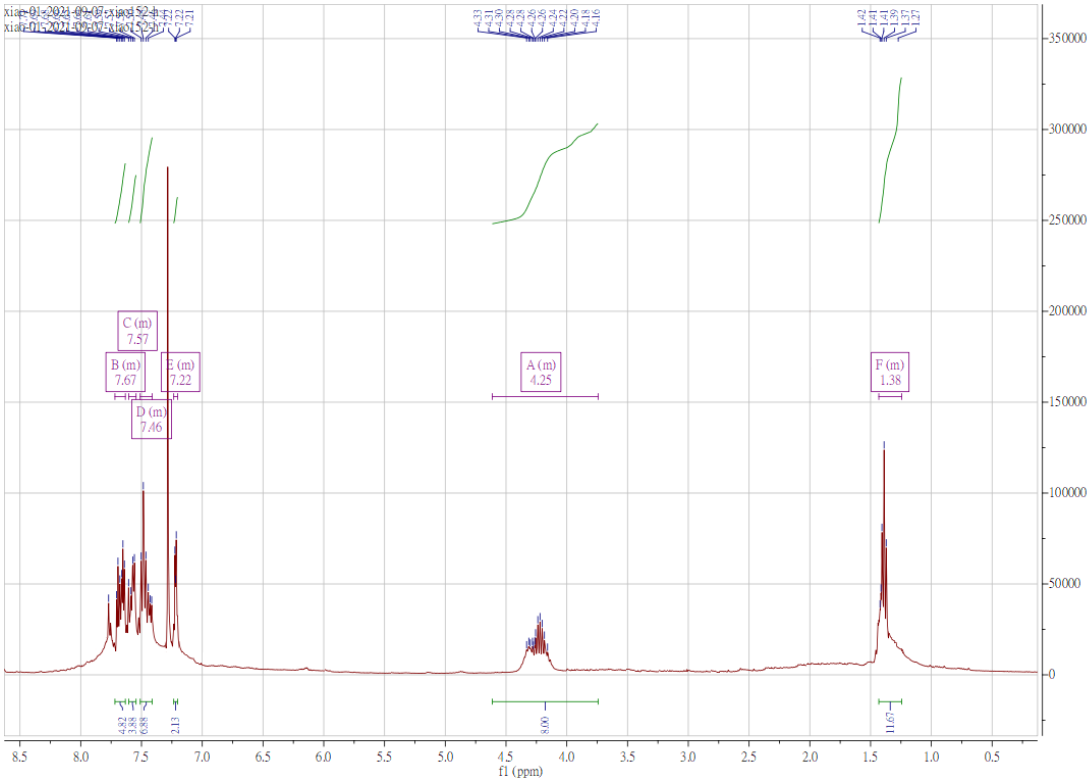

Figure S 1.32. ^{1}H NMR spectrum of **Ir2** in $CDCl_3$

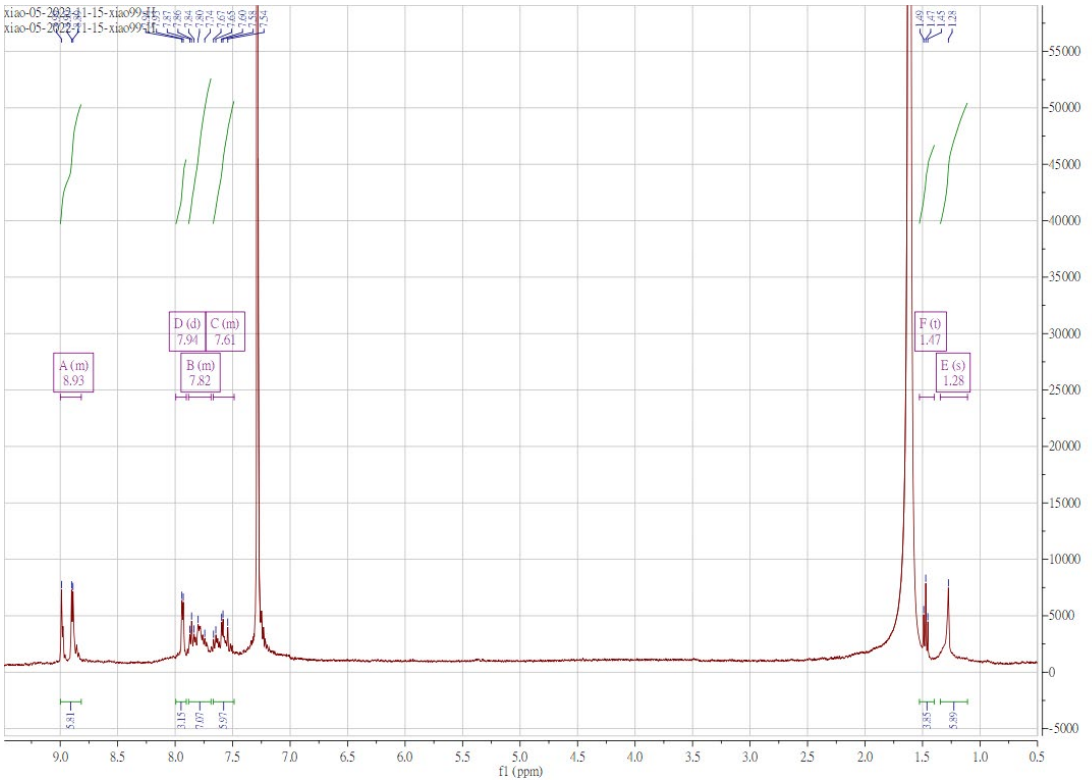

Figure S 1.33. ^{1}H NMR spectrum of **Ir3** in $CDCl_3$

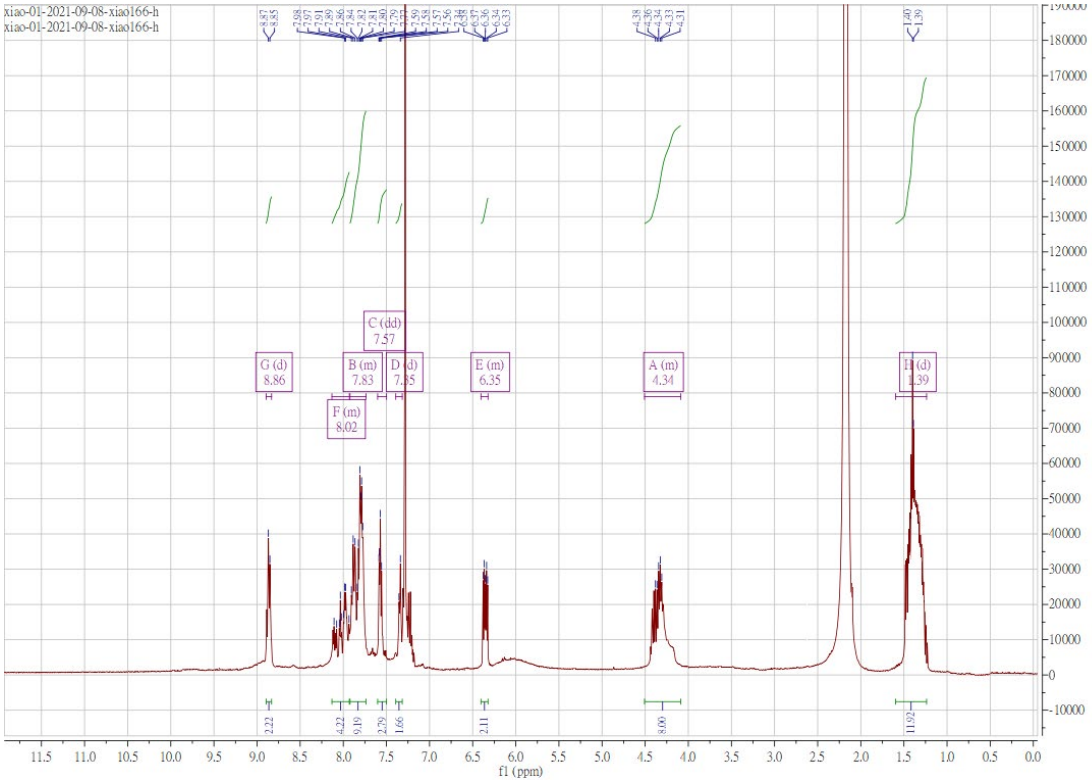

Figure S 1.34. ^{1}H NMR spectrum of **Ir4** in $CDCl_3$

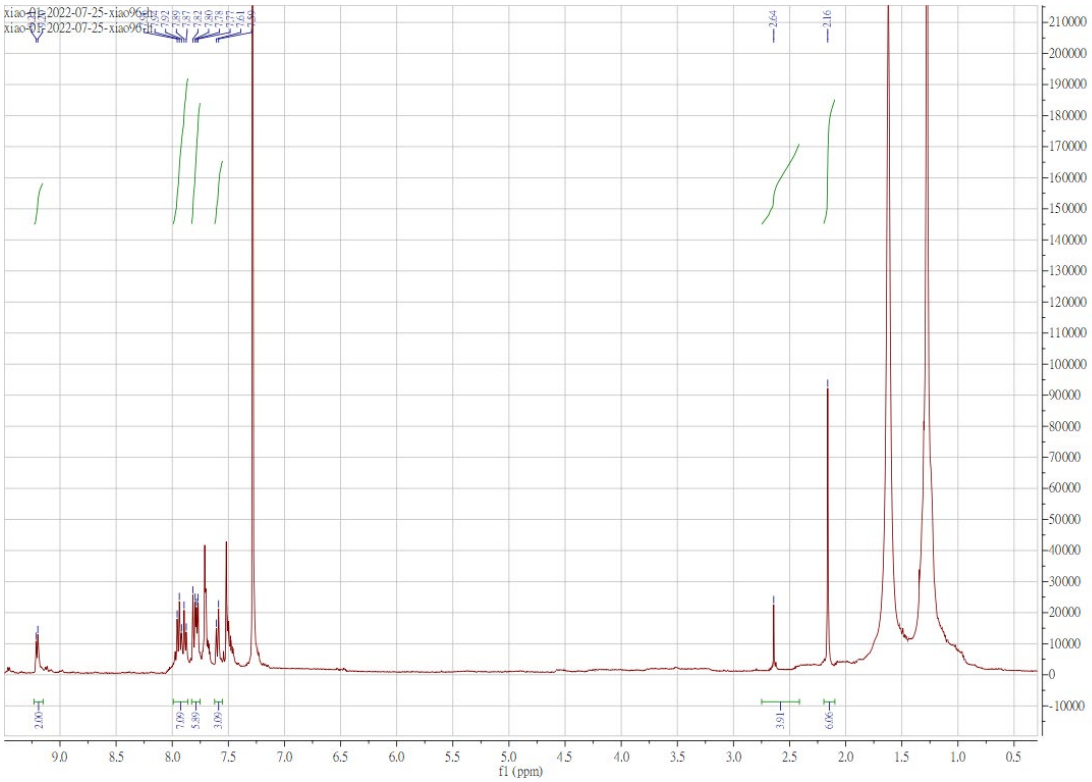

Figure S 1.35. ^{1}H NMR spectrum of **Ir5** in $CDCl_3$

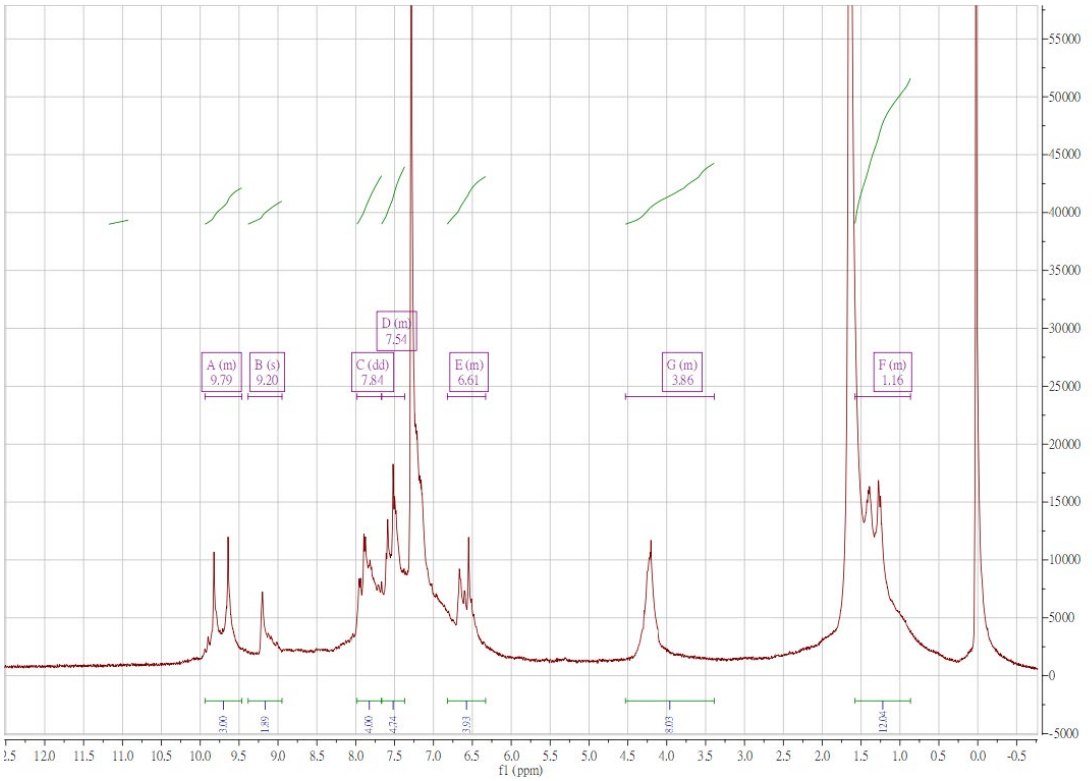

Figure S 1.36. ^{1}H NMR spectrum of **Ir6** in $CDCl_3$

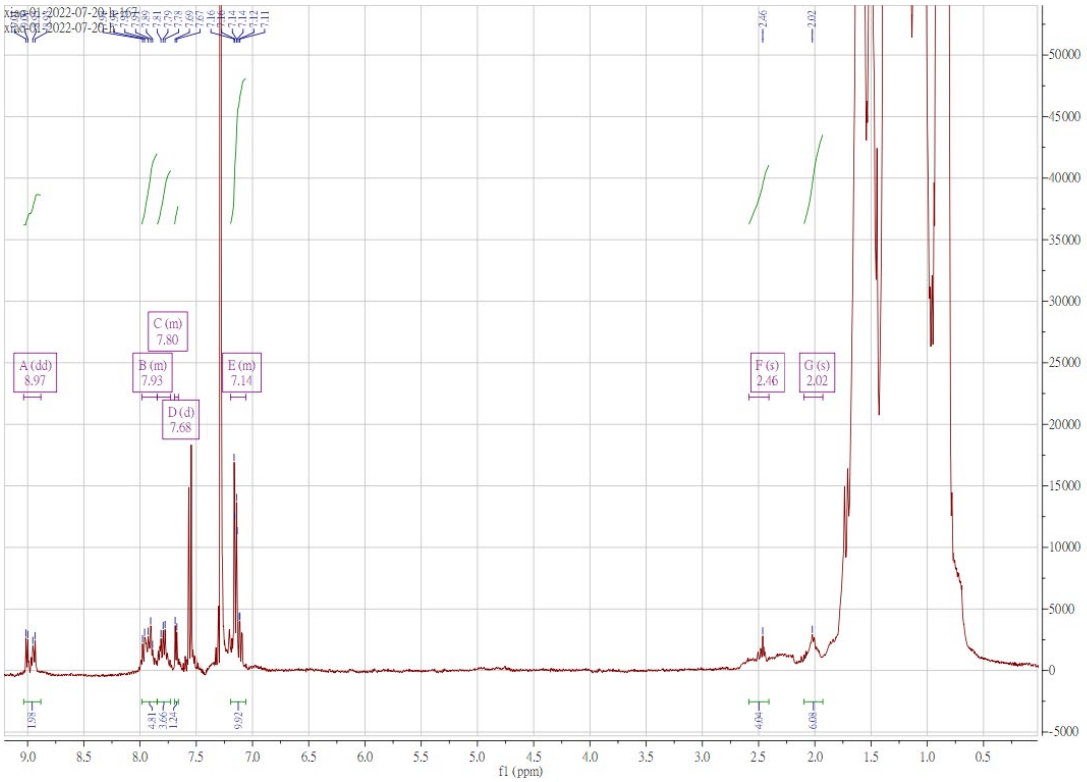

Figure S 1.37. ^{1}H NMR spectrum of **Ir7** in $CDCl_3$

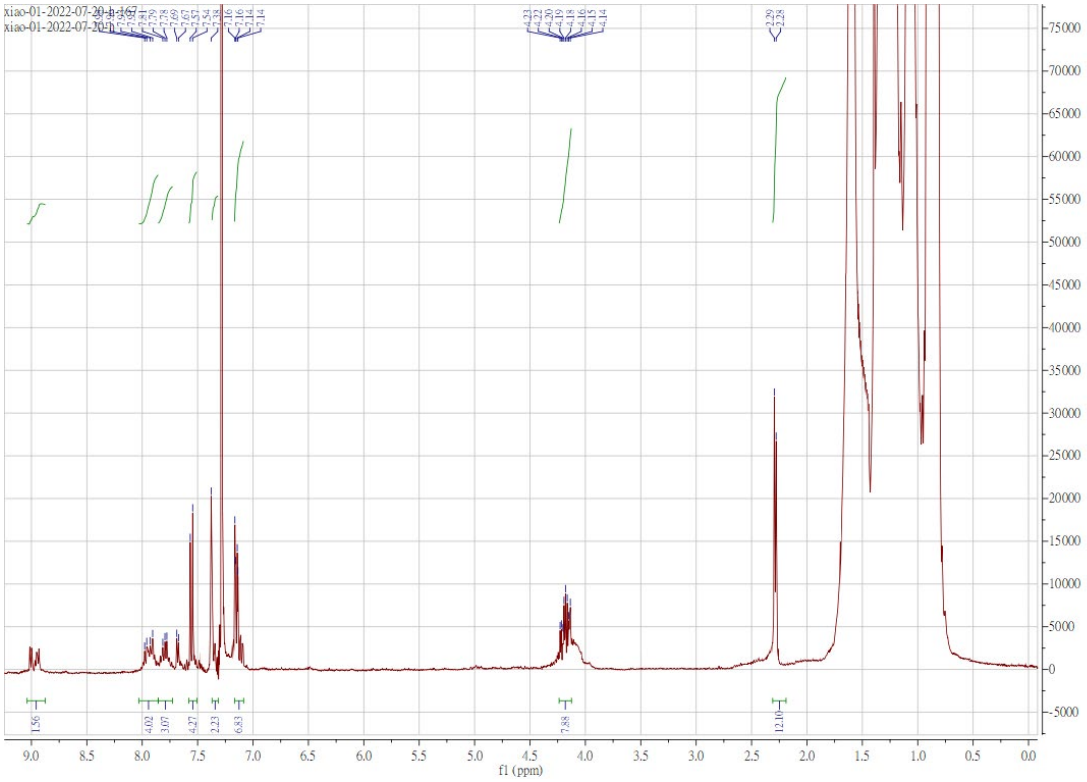

Figure S 1.38. ^{1}H NMR spectrum of **Ir8** in $CDCl_3$

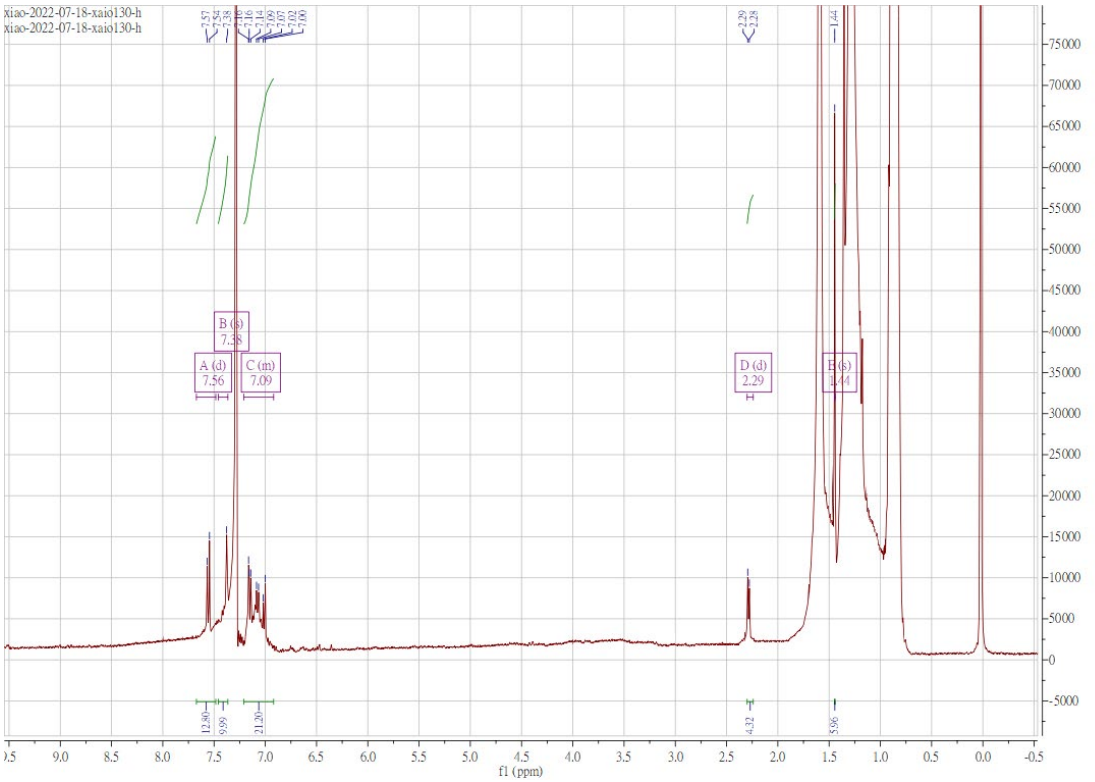

Figure S 1.39. ^{1}H NMR spectrum of **Ir9** in $CDCl_3$

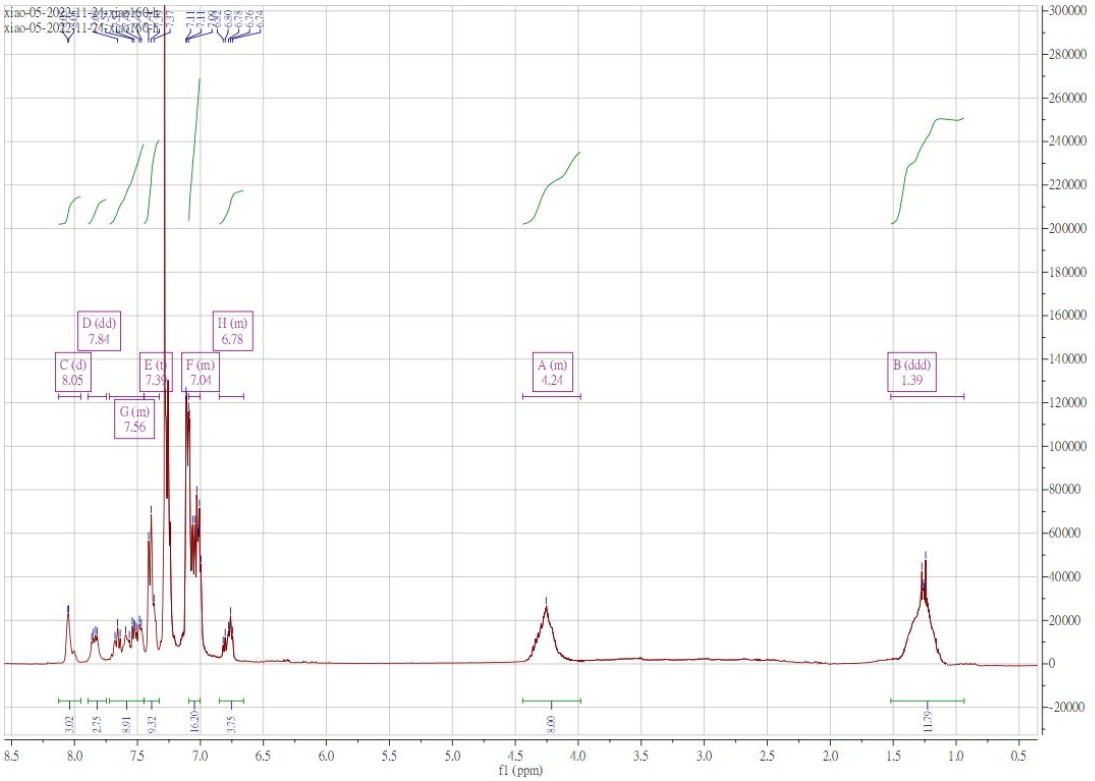

Figure S 1.40. ^{1}H NMR spectrum of **Ir10** in $CDCl_3$

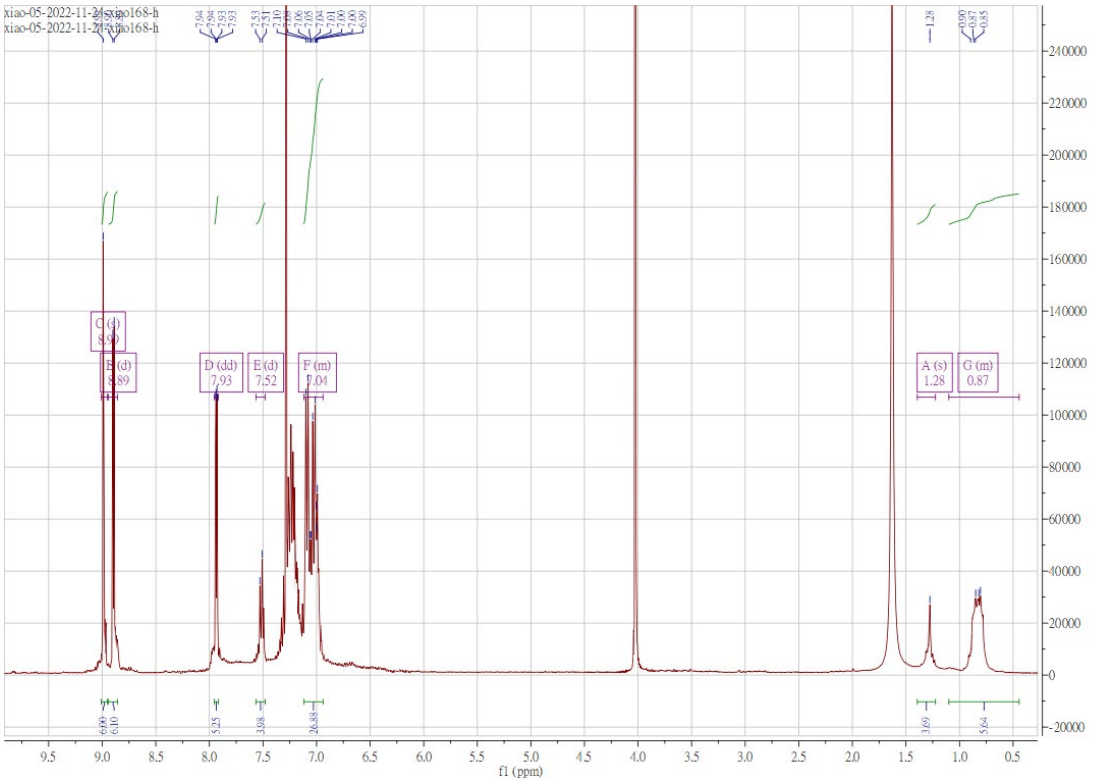

Figure S 1.41. ^{1}H NMR spectrum of **Ir11** in $CDCl_3$

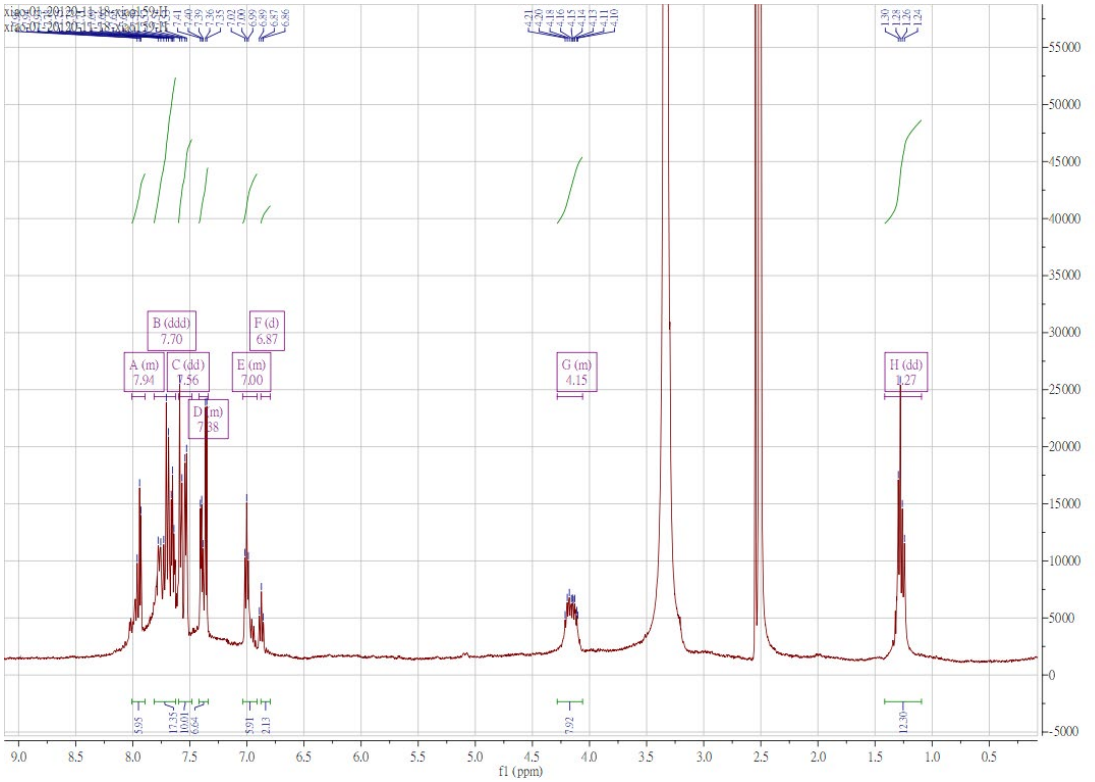

Figure S 1.42. ^{1}H NMR spectrum of **Ir12** in $CDCl_3$

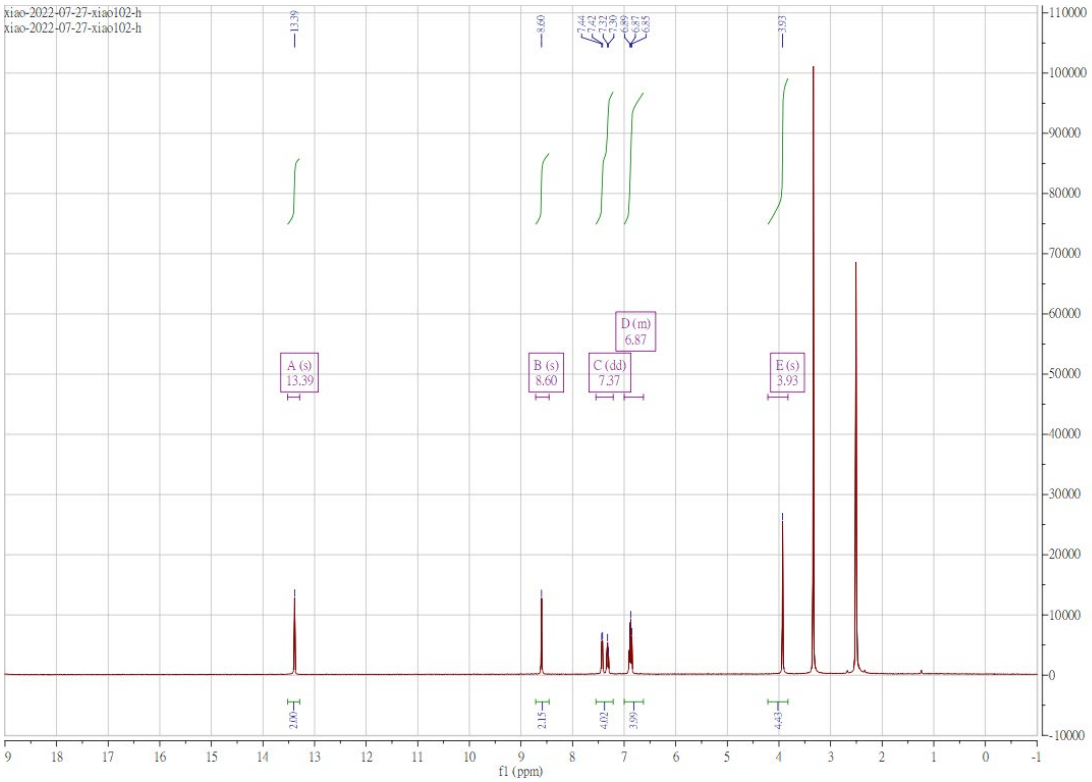

Figure S 1.43. ^{1}H NMR spectrum of **L8** in DMSO-d6

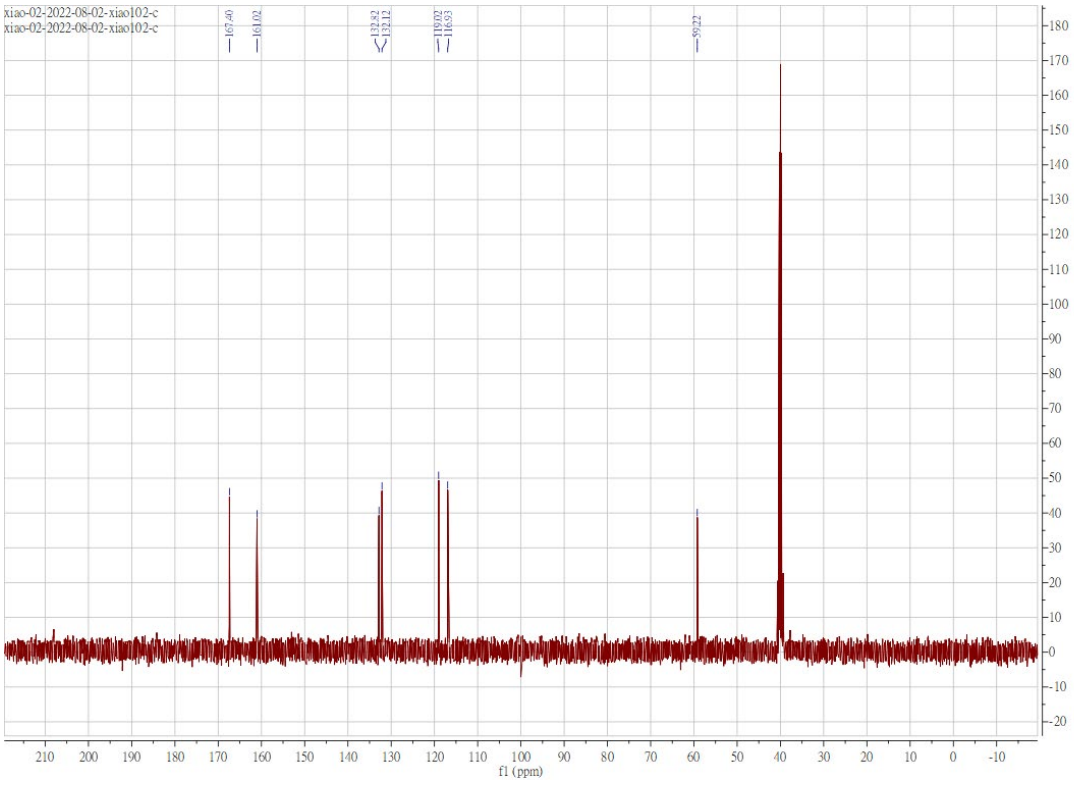

Figure S 1.44. ^{13}C NMR spectrum of **L8** in DMSO-d6

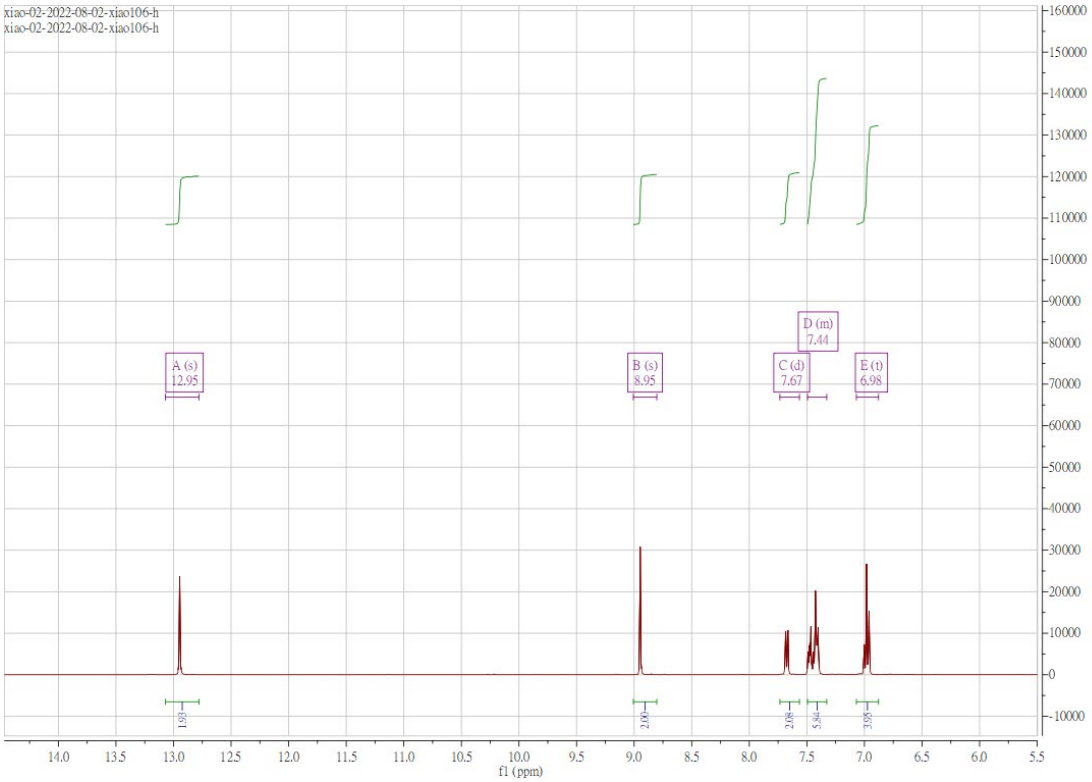

Figure S 1.45. ^{1}H NMR spectrum of **L9** in DMSO-d6

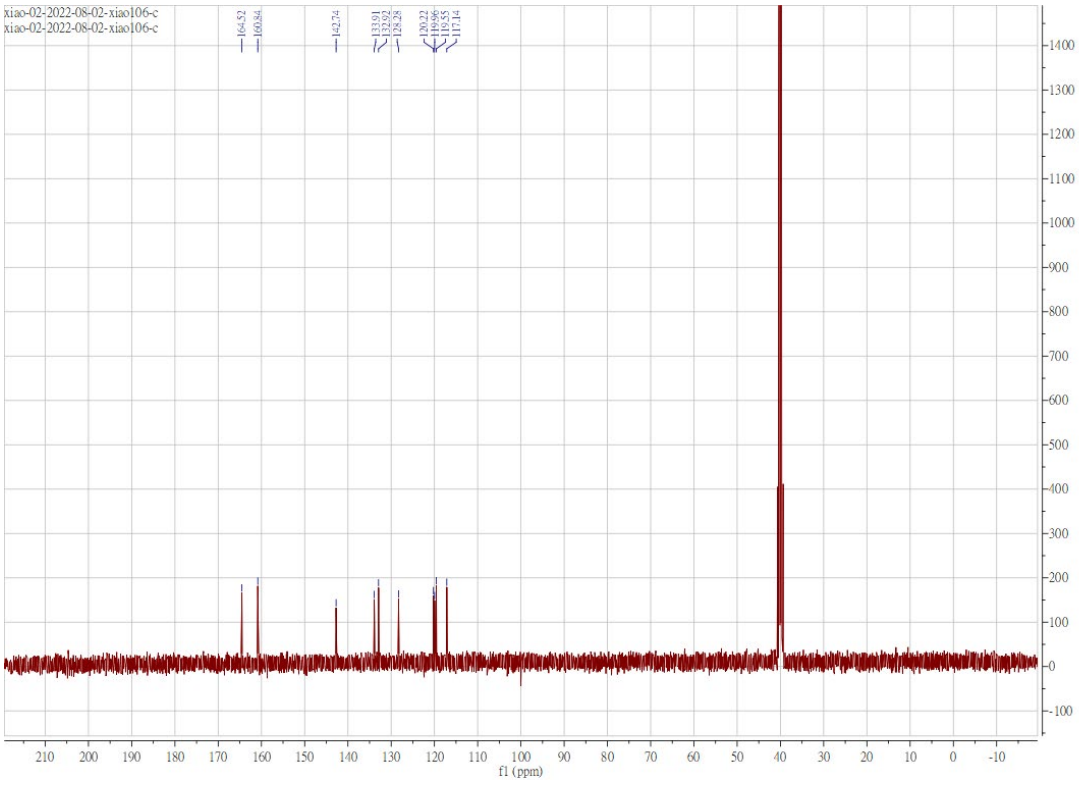

Figure S 1.46. ^{13}C NMR spectrum of **L9** in DMSO-d6

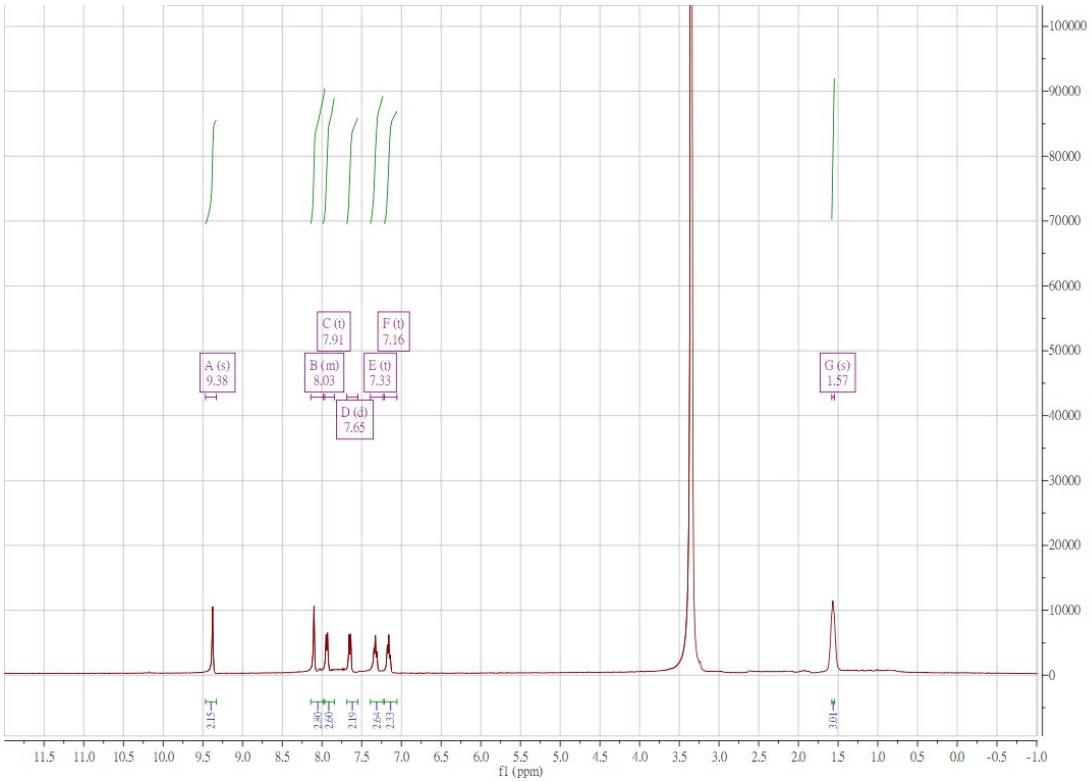

Figure S 1.47. ^{1}H NMR spectrum of **L10** in DMSO-d6

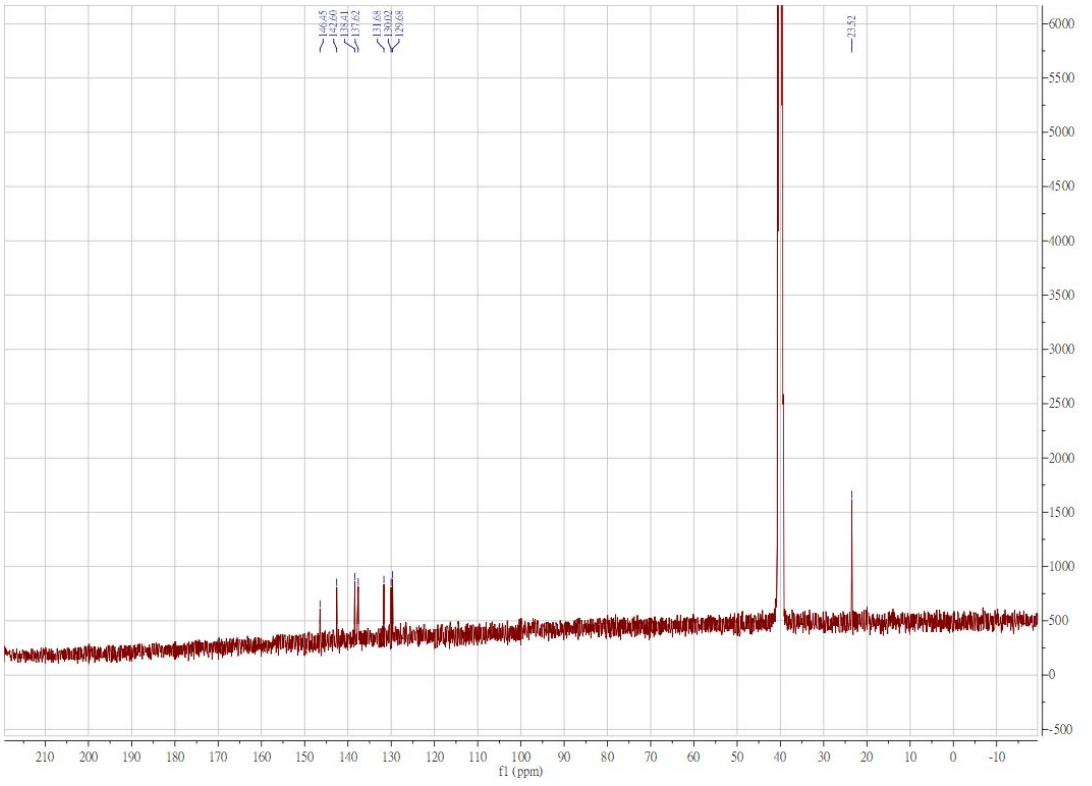

Figure S 1.48. ^{13}C NMR spectrum of **L10** in DMSO-d6

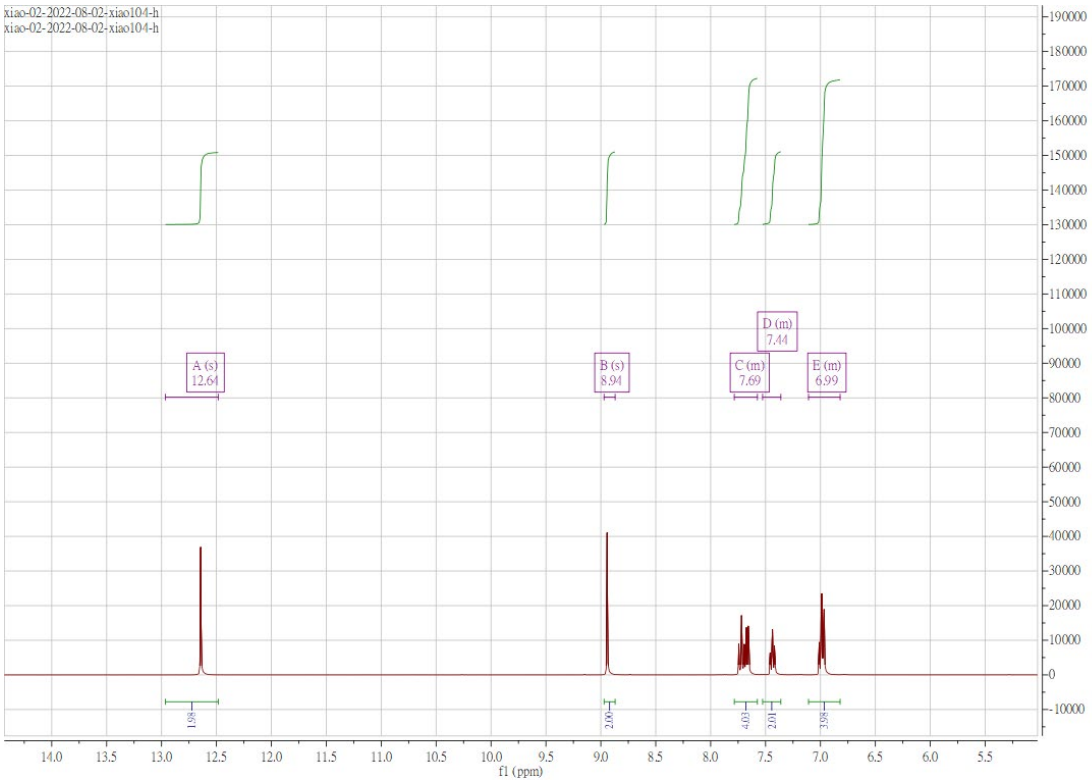

Figure S 1.49. ^{1}H NMR spectrum of **L11** in DMSO-d6

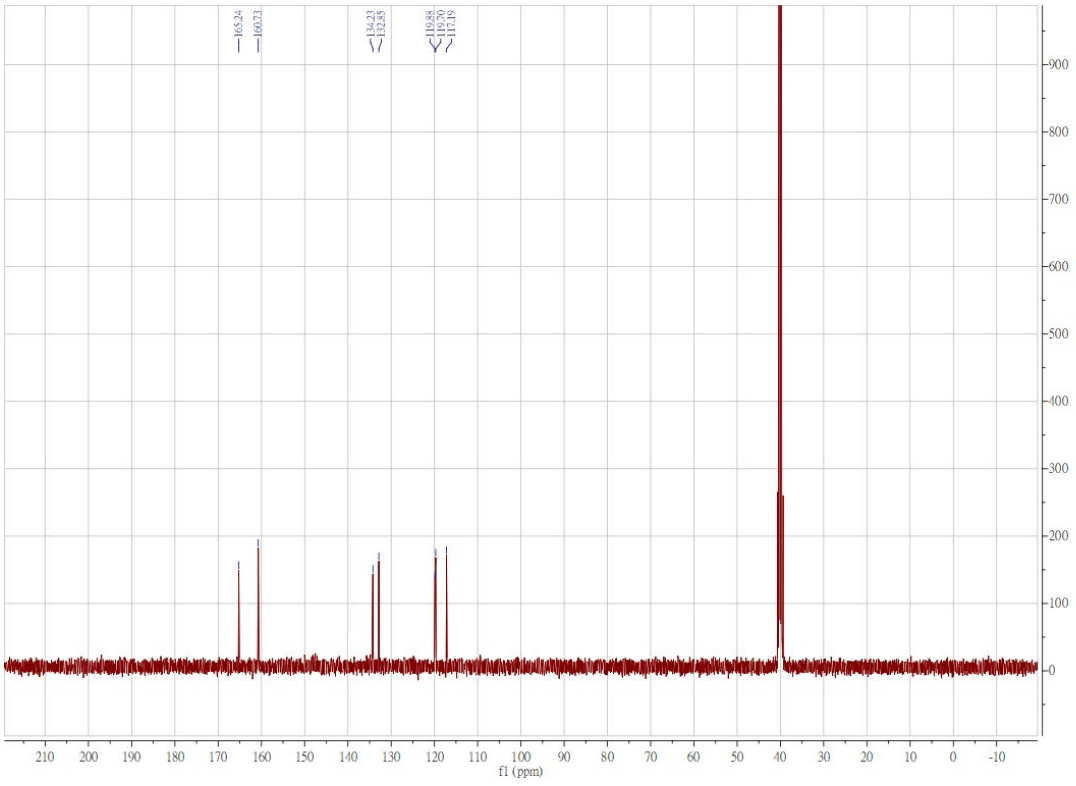

Figure S 1.50. ^{13}C NMR spectrum of **L11** in DMSO-d6

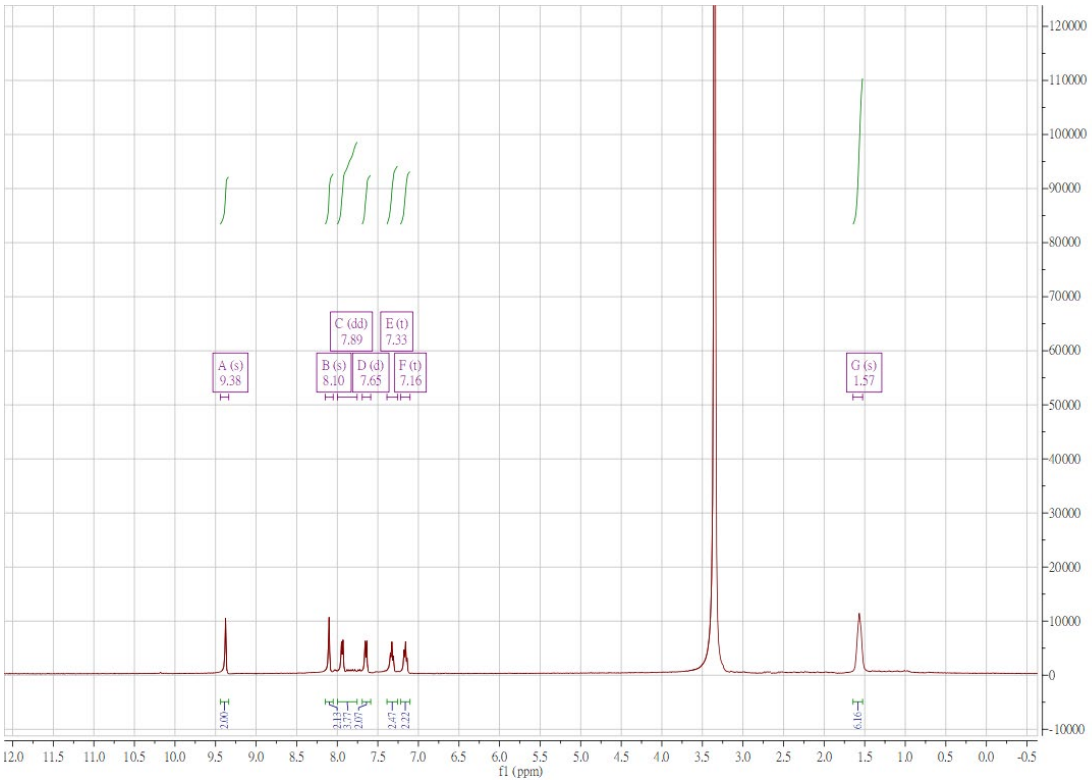

Figure S 1.51. ^{1}H NMR spectrum of **L12** in DMSO-d6

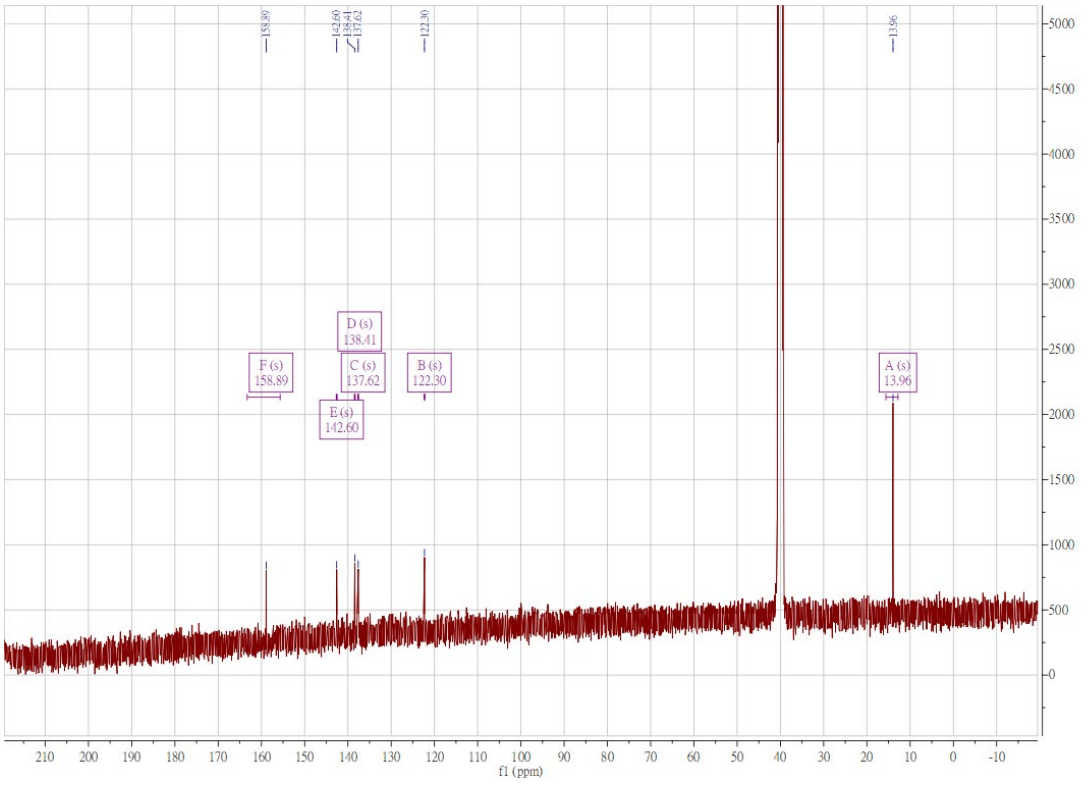

Figure S 1.52. ^{13}C NMR spectrum of **L12** in DMSO-d6

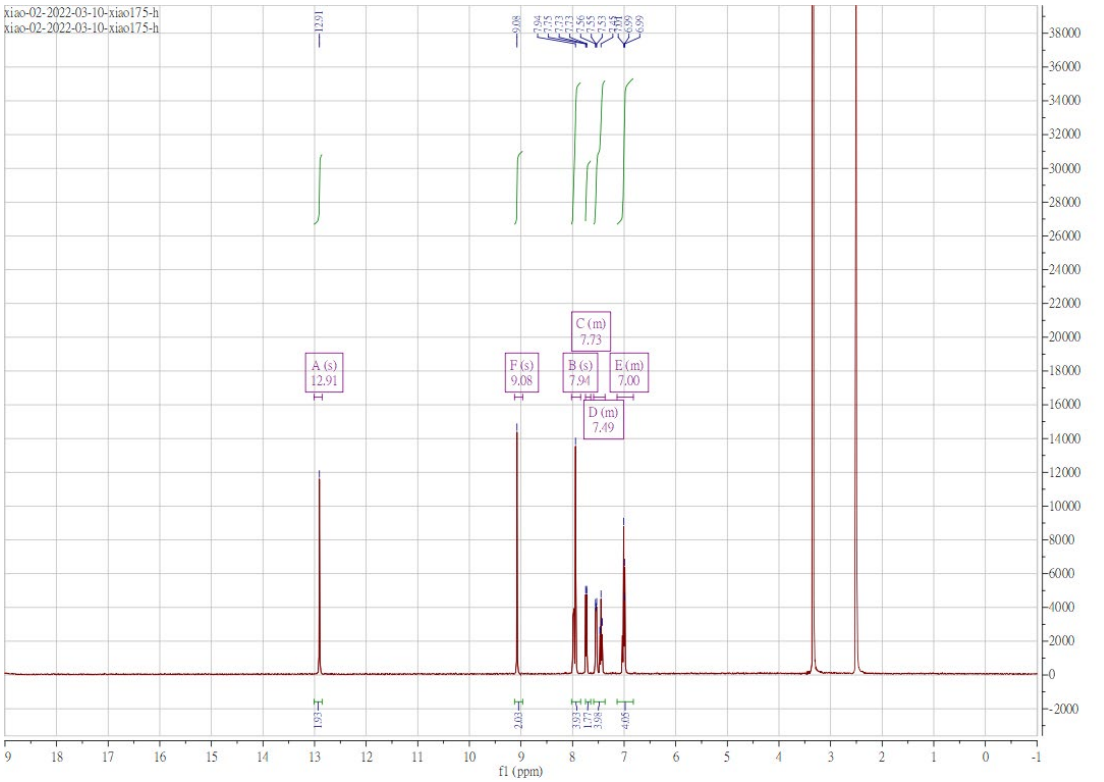

Figure S 1.53. ^{1}H NMR spectrum of **L13** in DMSO-d6

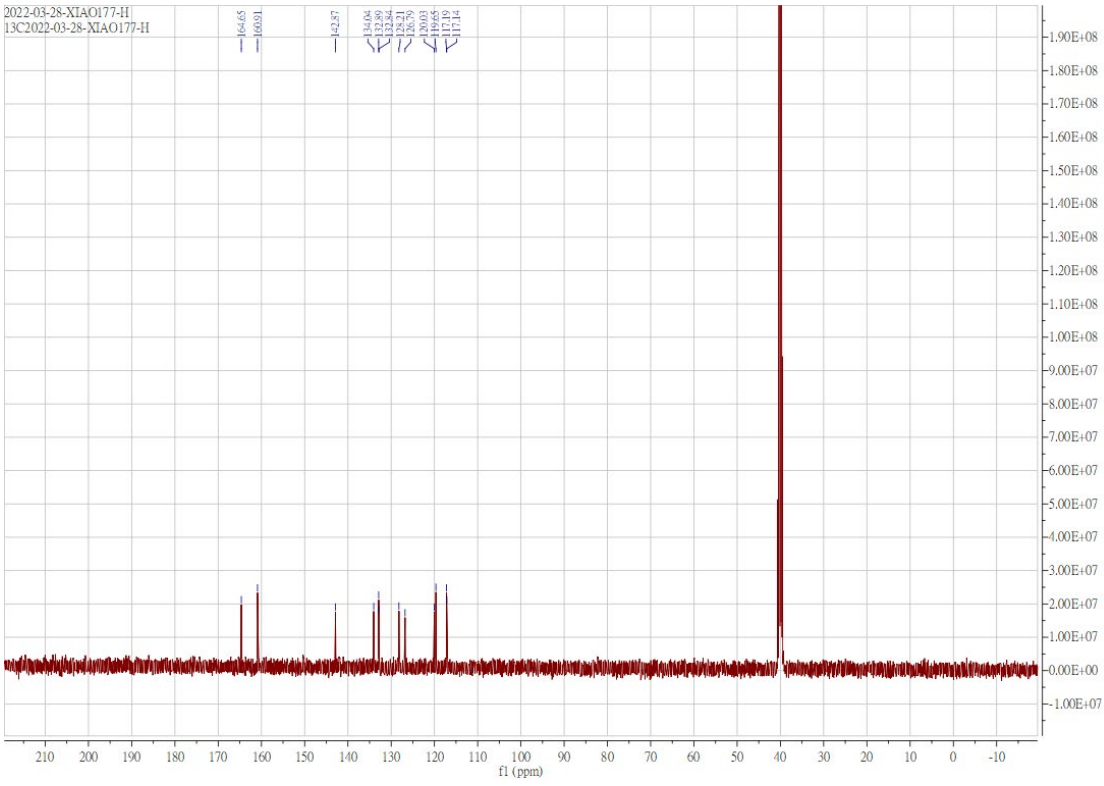

Figure S 1.54. ^{13}C NMR spectrum of **L13** in DMSO-d6

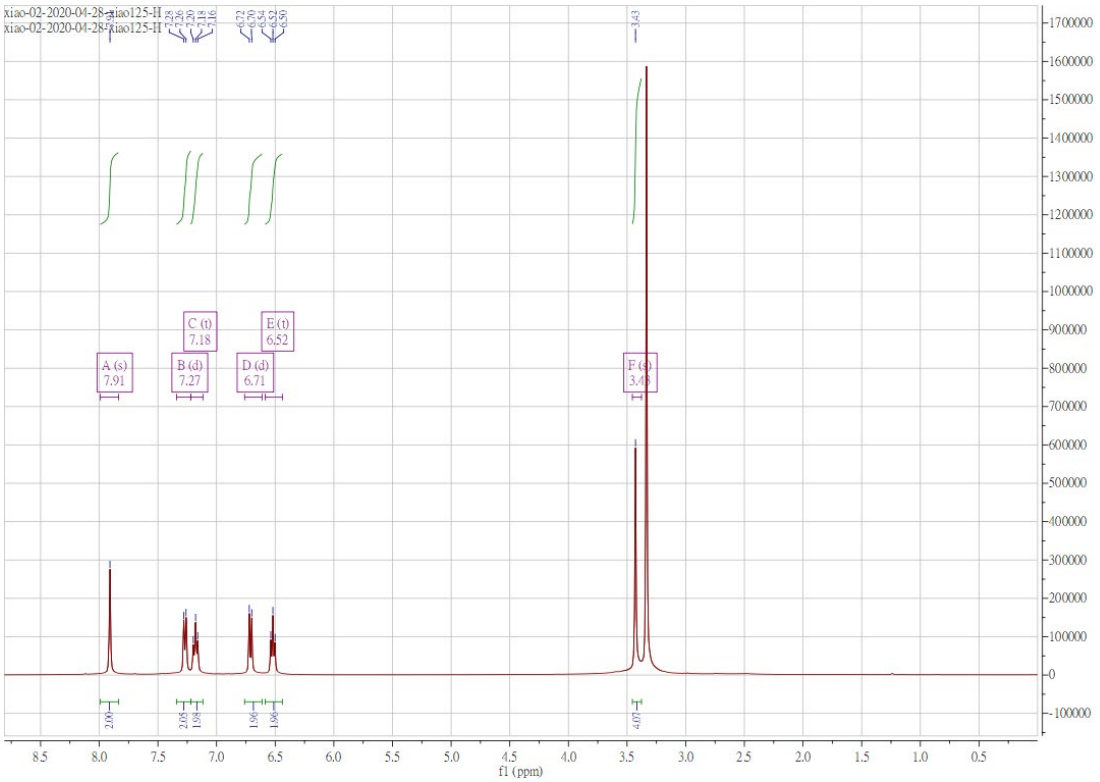

Figure S 1.55. ^{1}H NMR spectrum of **Ni1** in DMSO-d6

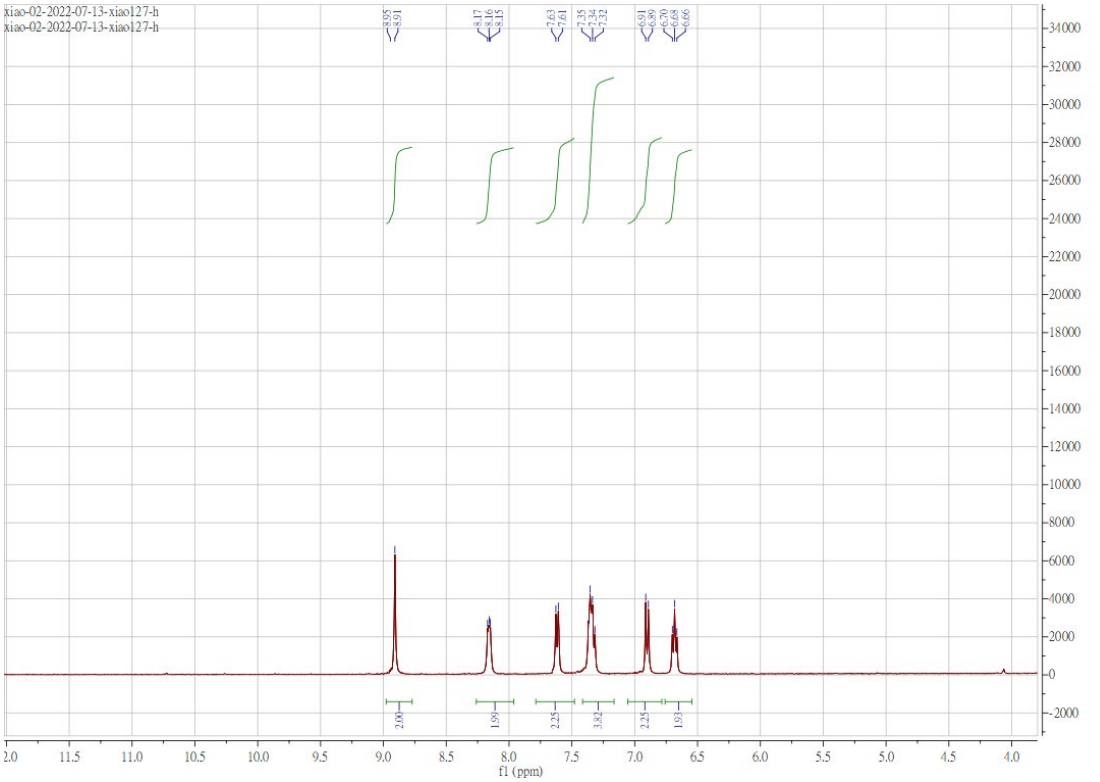

Figure S 1.56. ^{1}H NMR spectrum of **Ni2** in DMSO-d6

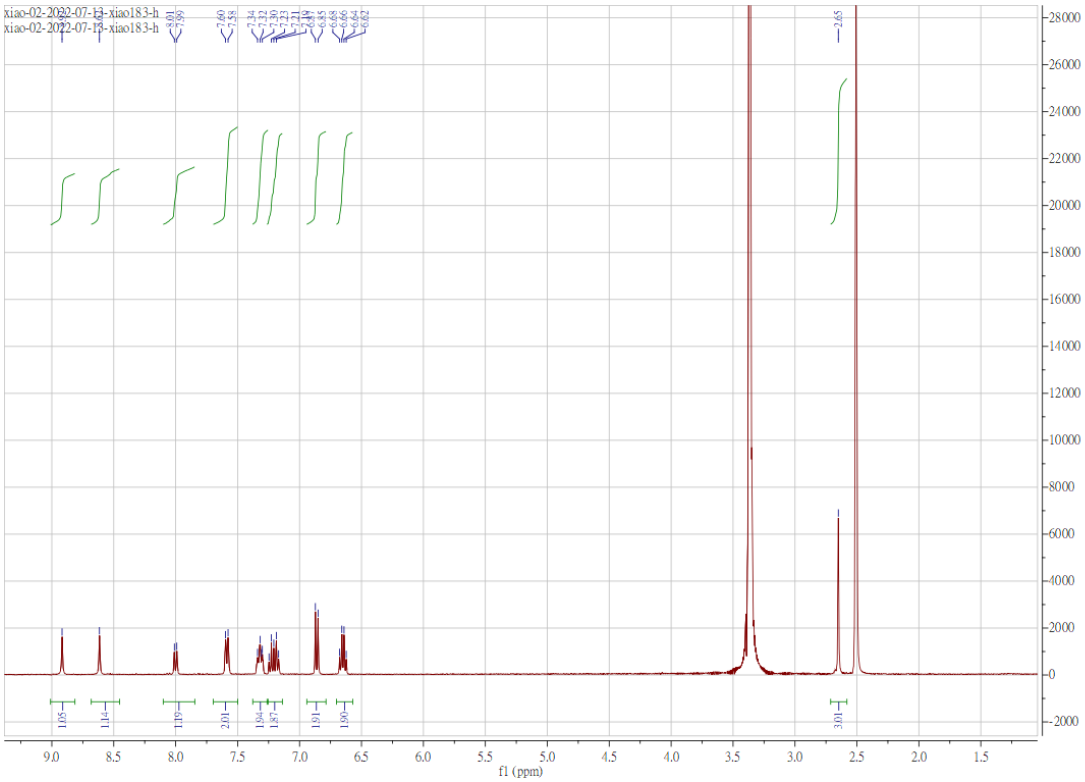

Figure S 1.57. ^{1}H NMR spectrum of **Ni3** in DMSO-d6

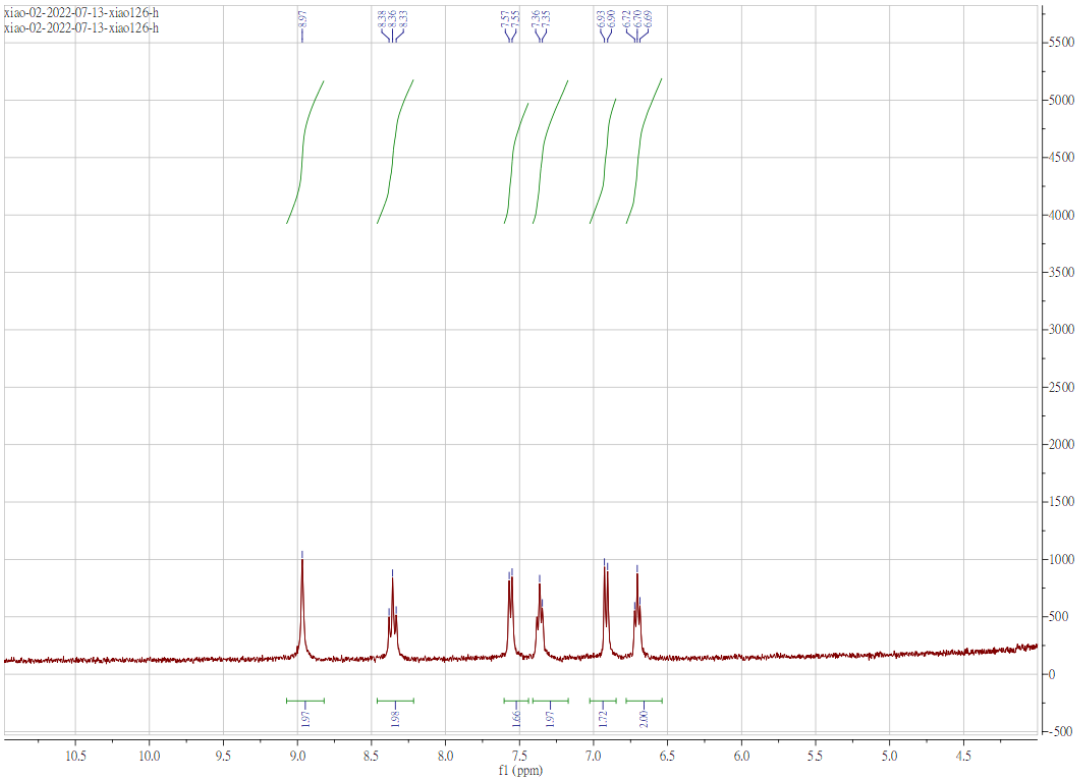

Figure S 1.58. ^{1}H NMR spectrum of **Ni4** in DMSO-d6

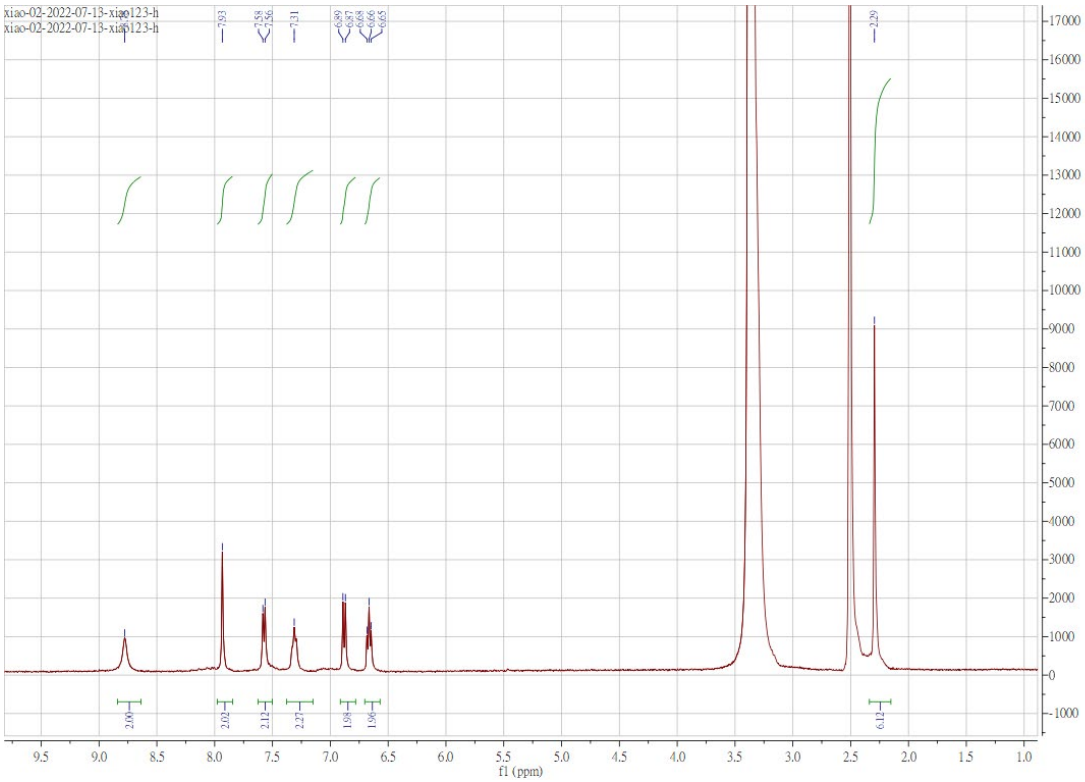

Figure S 1.59. ^{1}H NMR spectrum of **Ni5** in DMSO-d6

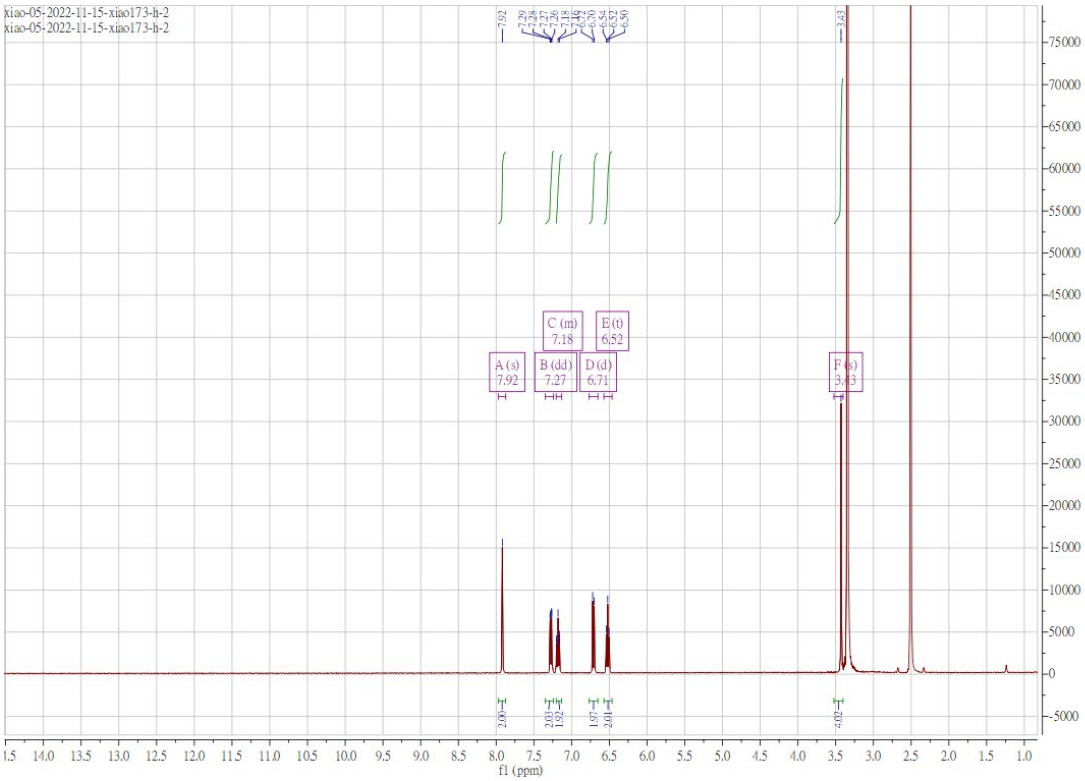

Figure S 1.60. ^{1}H NMR spectrum of **Ni6** in DMSO-d6

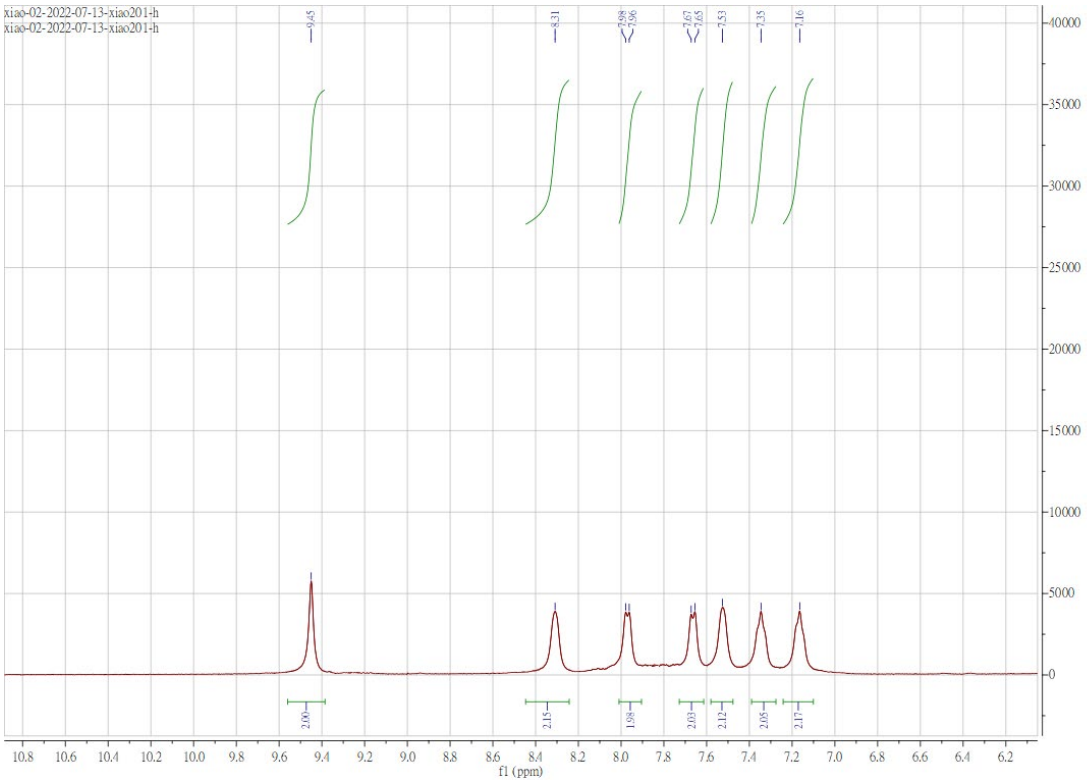

Figure S 1.61. ^{1}H NMR spectrum of **Ni7** in DMSO-d6

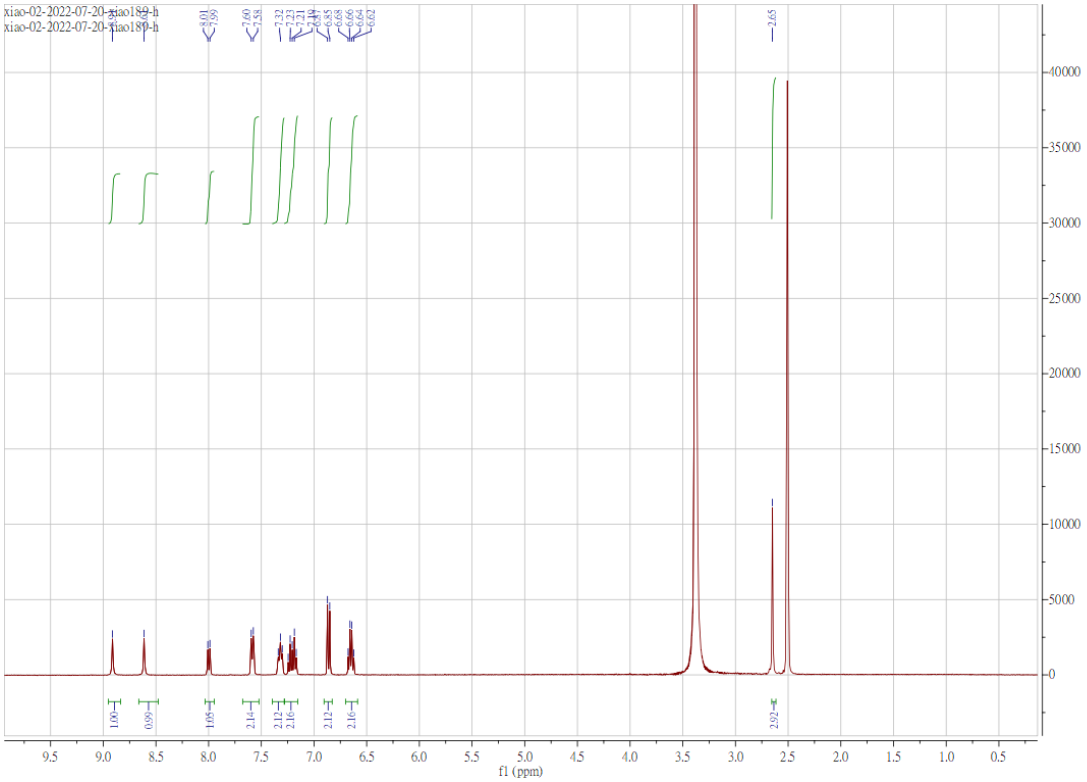

Figure S 1.62. ^{1}H NMR spectrum of **Ni8** in DMSO-d6

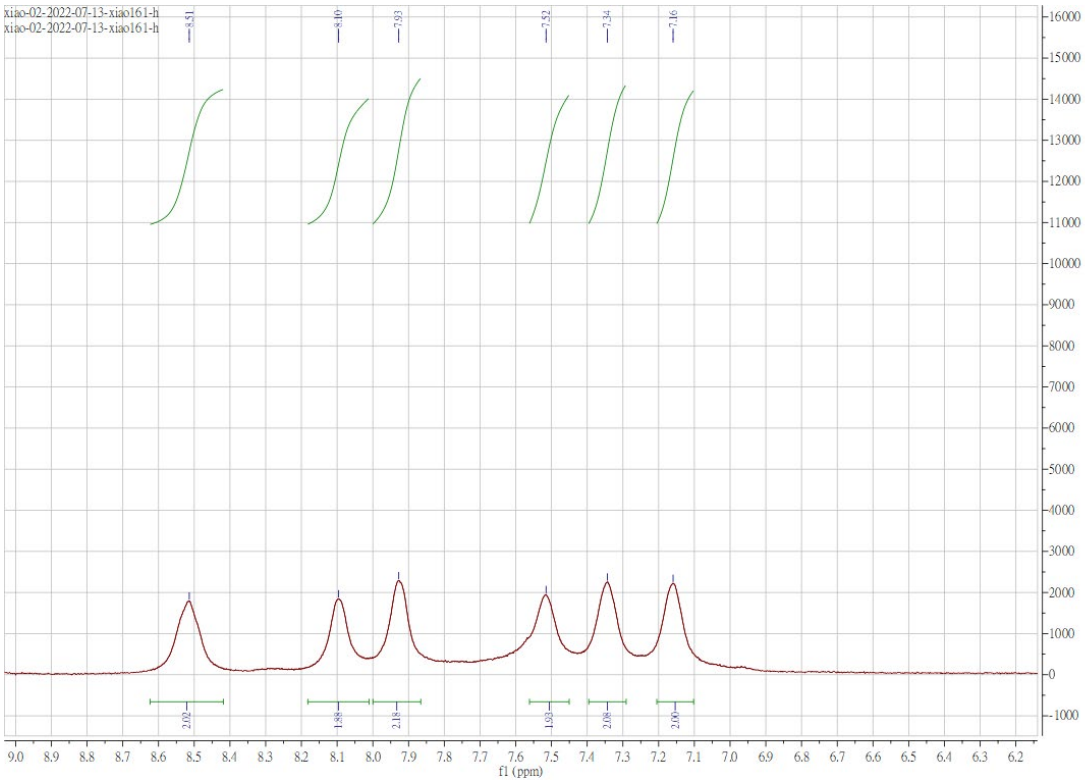

Figure S 1.63. ^{1}H NMR spectrum of **Ni9** in DMSO-d6

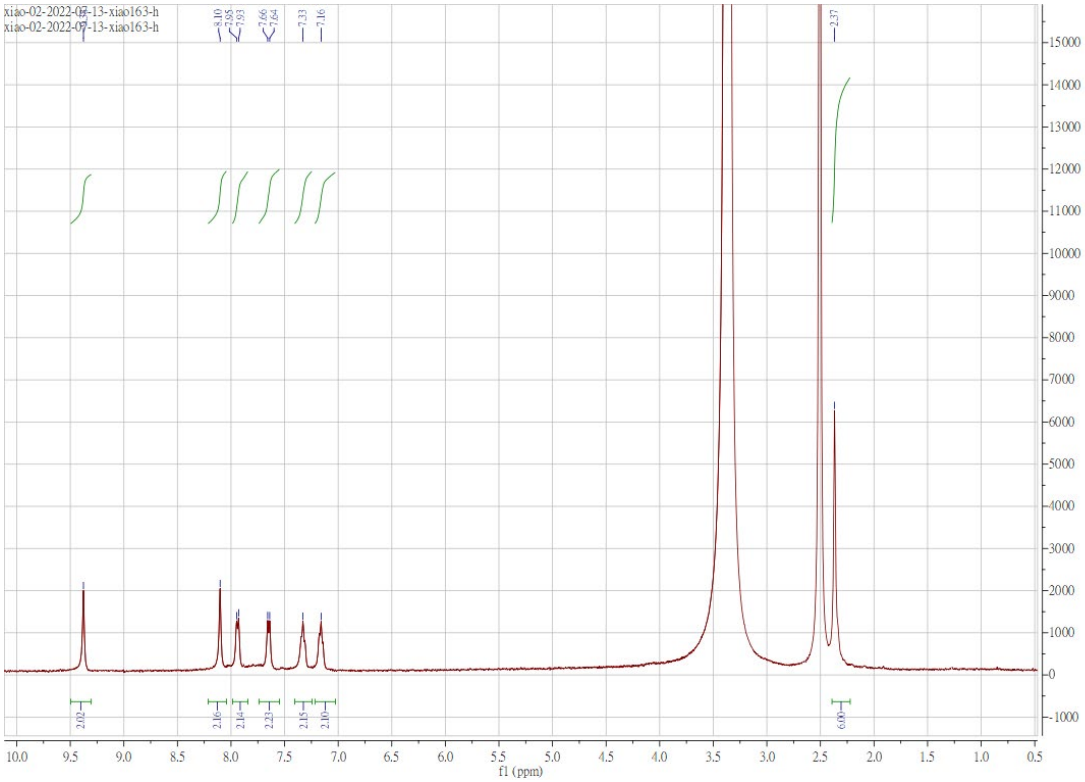

Figure S 1.64. ^{1}H NMR spectrum of **Ni10** in DMSO-d6

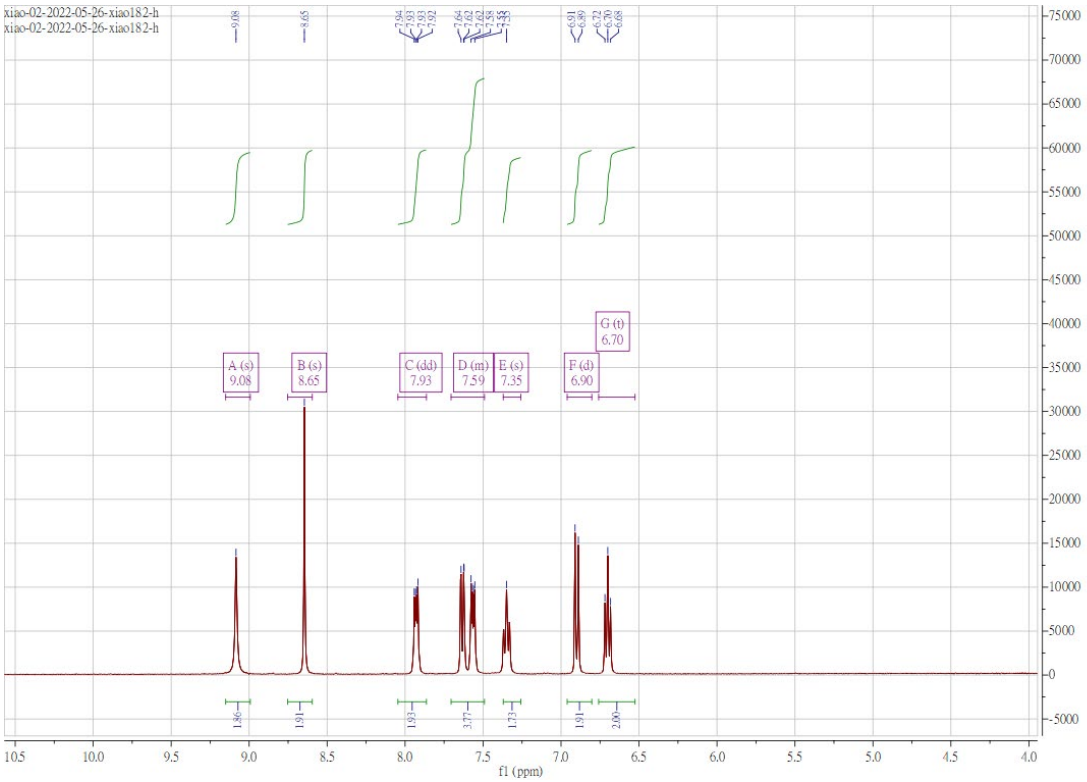

Figure S 1.65. [1]H NMR spectrum of **Ni11** in DMSO-d6

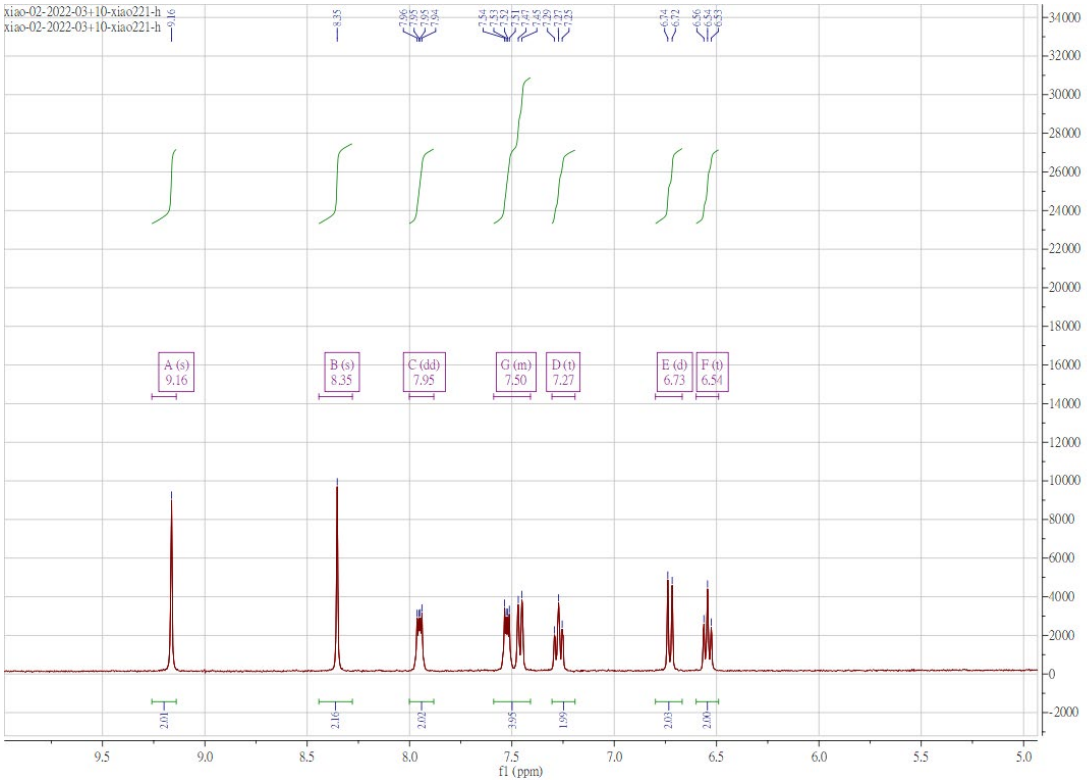

Figure S 1.66. [1]H NMR spectrum of **Zn1** in DMSO-d6

Figure S 1.67. ^{1}H NMR spectrum of **Cu1** in DMSO-d6

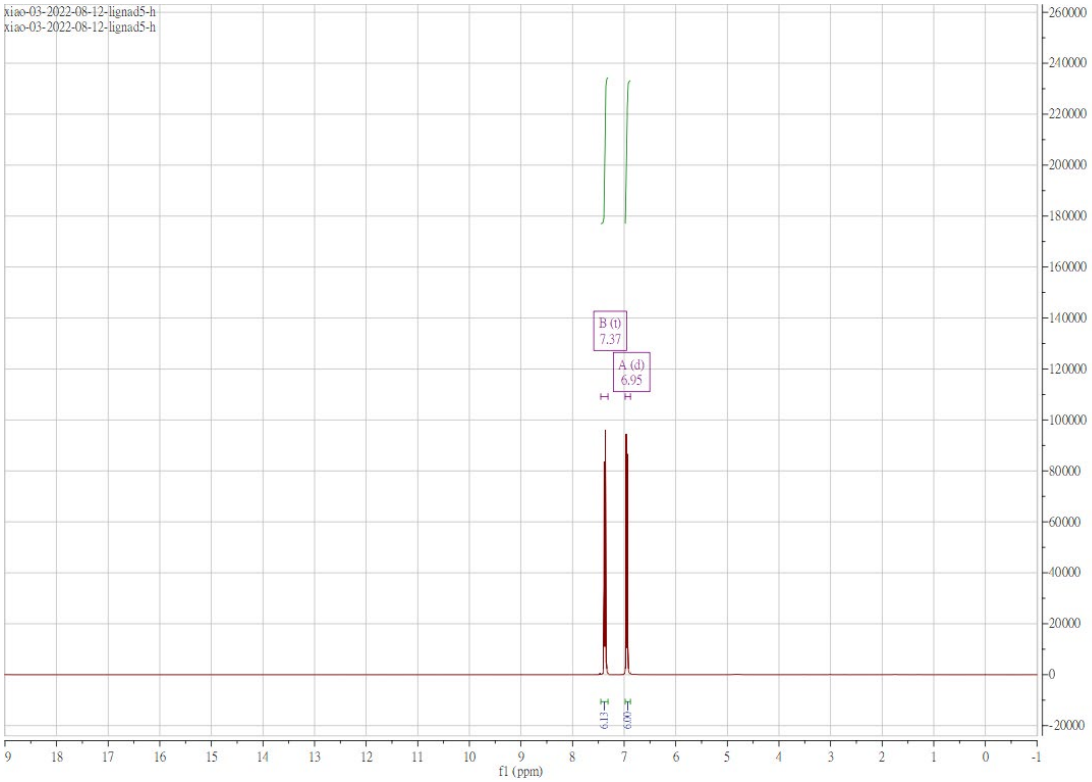

Figure S 1.68. ^{1}H NMR spectrum of **5** in $CDCl_3$

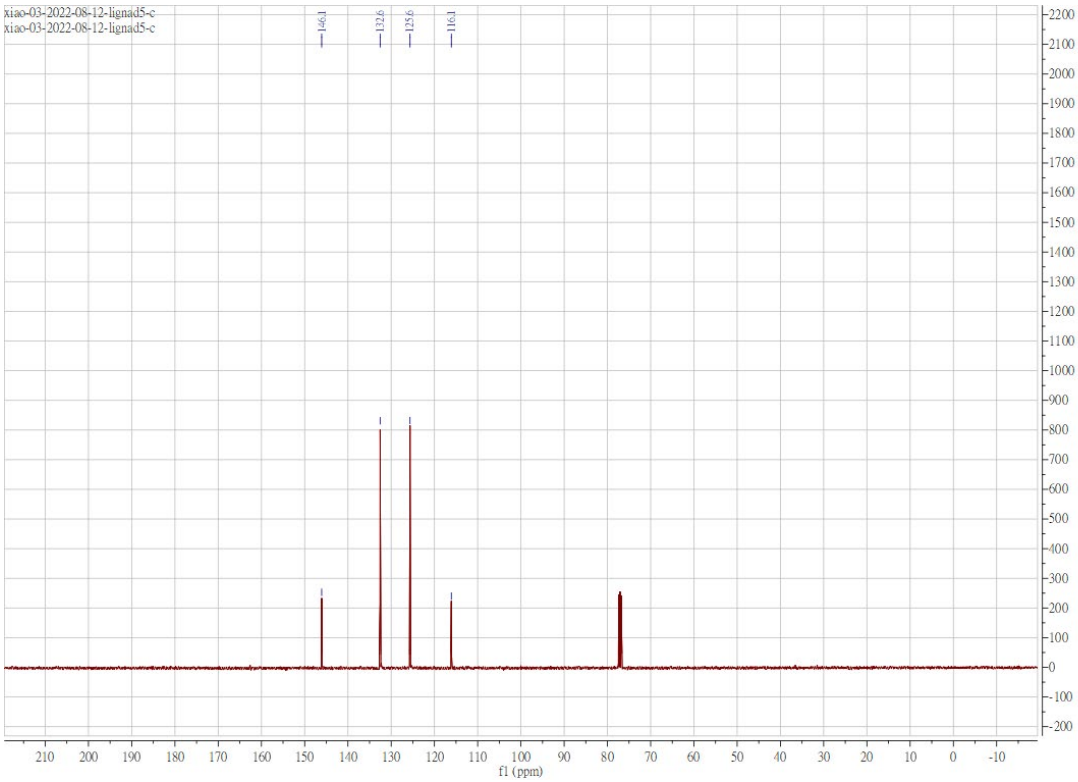

Figure S 1.69. ^{13}C NMR spectrum of **5** in $CDCl_3$

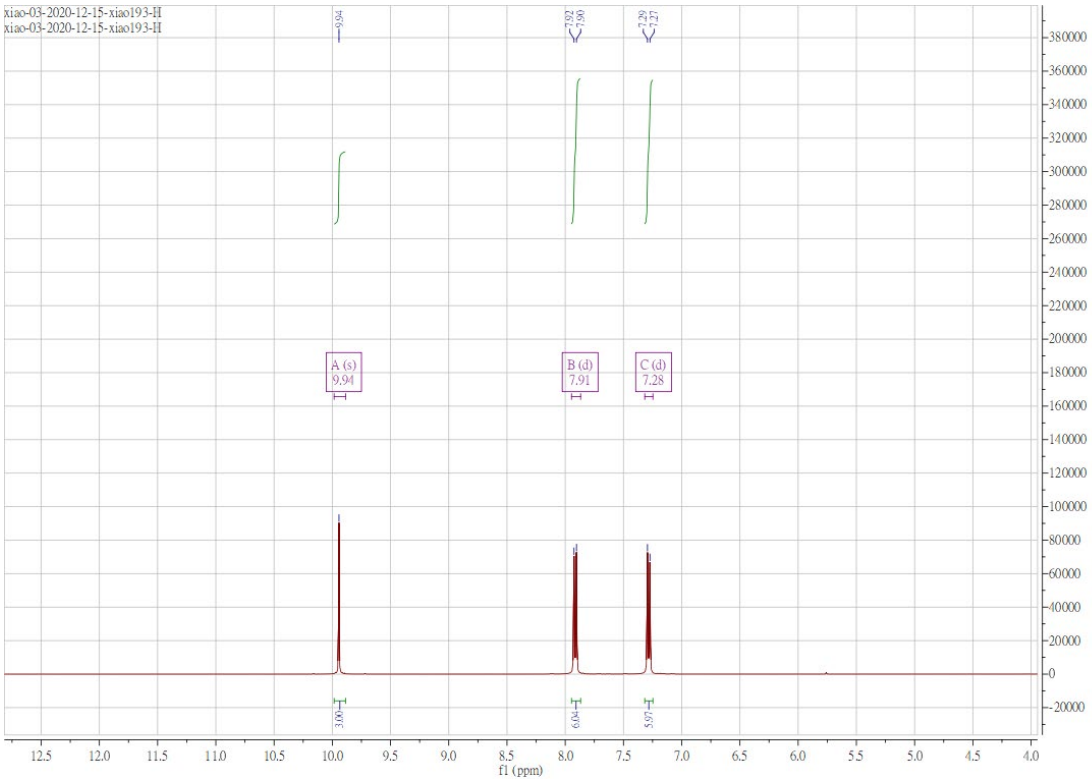

Figure S 1.70. ^{1}H NMR spectrum of **L14** in $CDCl_3$

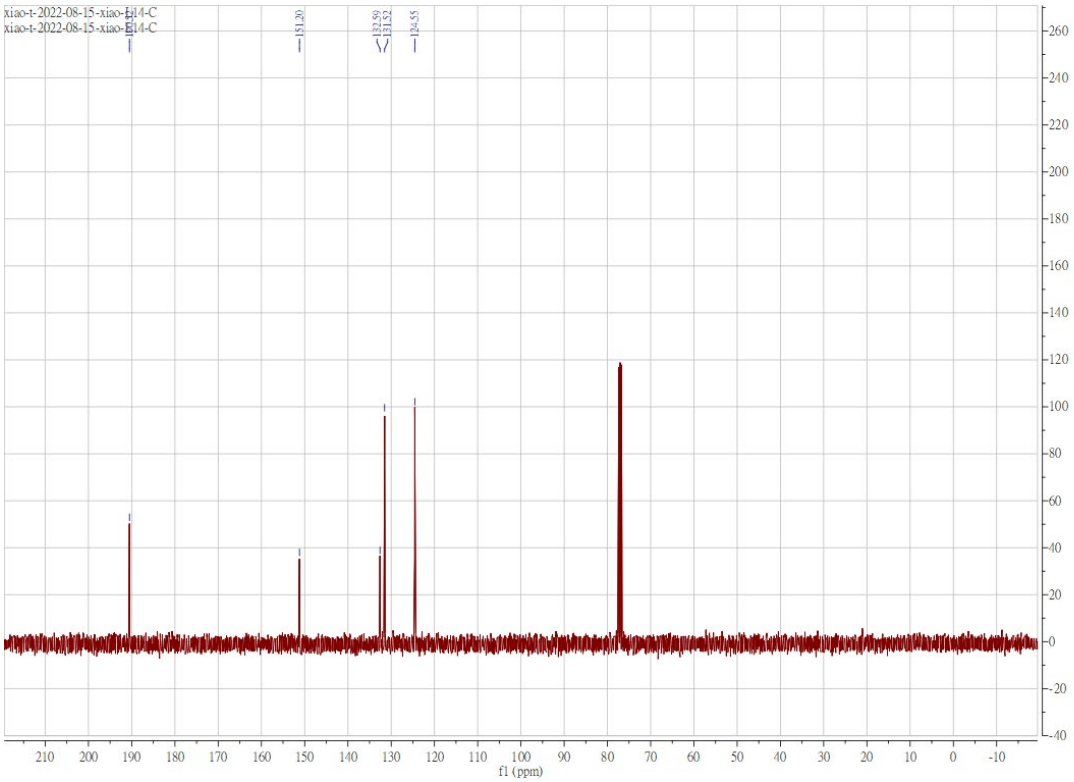

Figure S 1.71. ^{13}C NMR spectrum of **L14** in $CDCl_3$

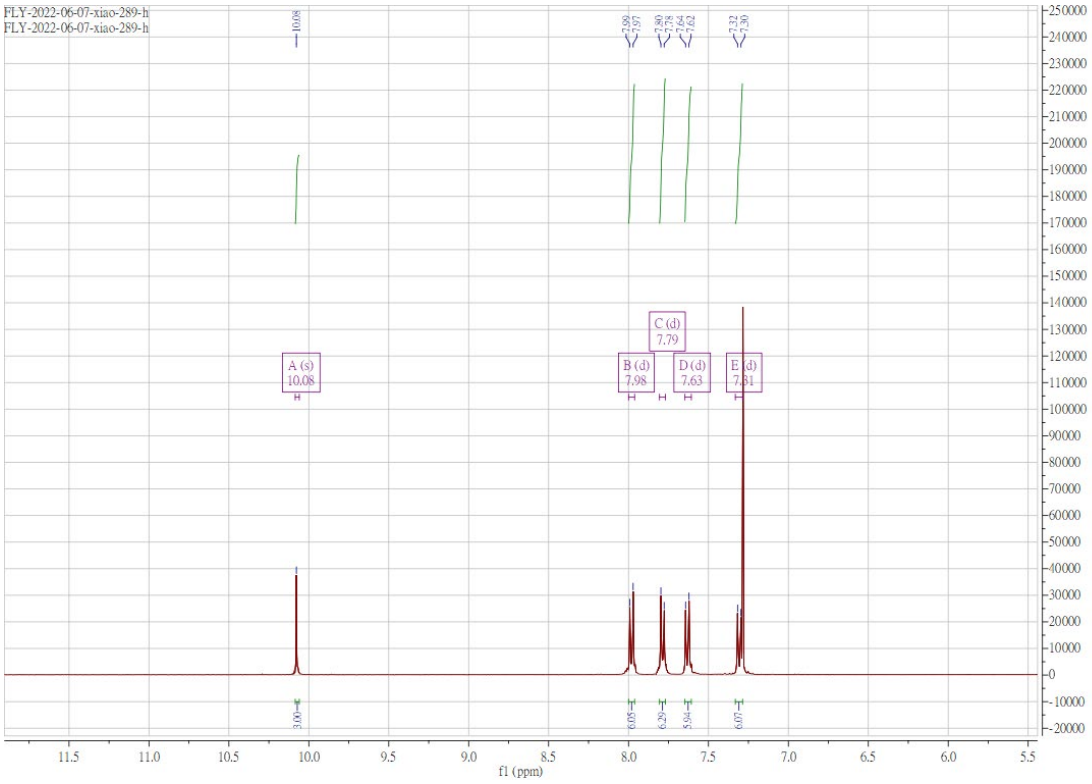

Figure S 1.72. ^{1}H NMR spectrum of **L15** in $CDCl_3$

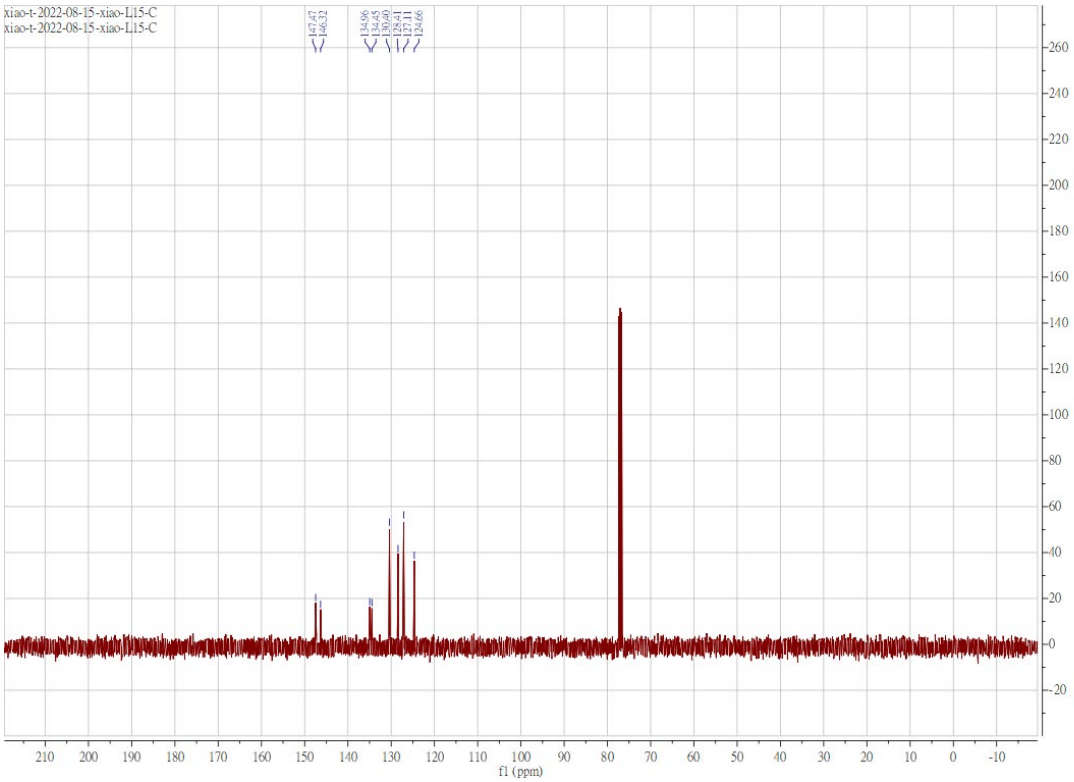

Figure S 1.73. ^{13}C NMR spectrum of **L15** in $CDCl_3$

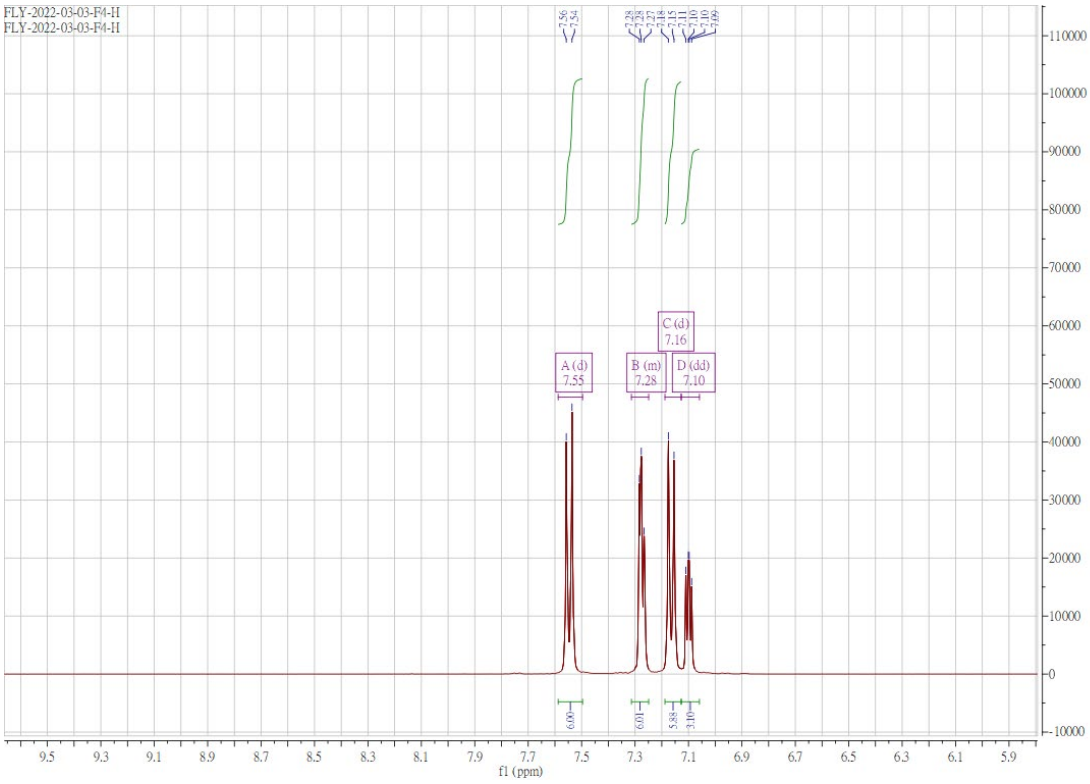

Figure S 1.74. ^{1}H NMR spectrum of **6** in $CDCl_3$

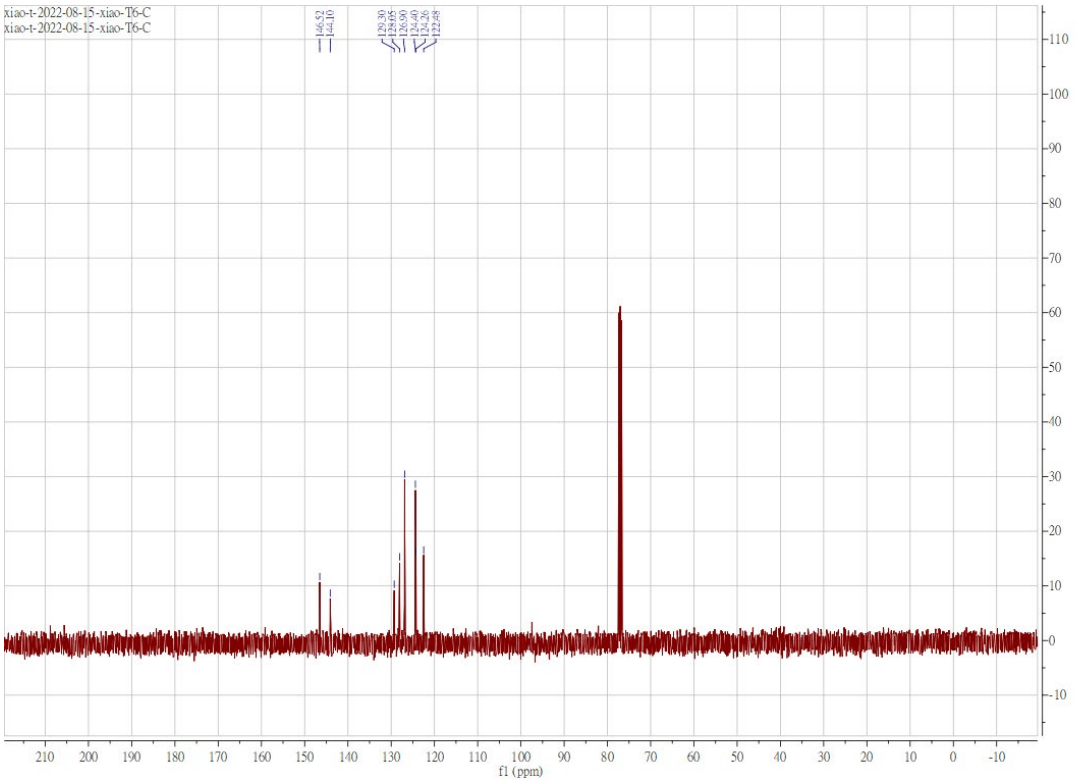

Figure S 1.75. ^{13}C NMR spectrum of **6** in $CDCl_3$

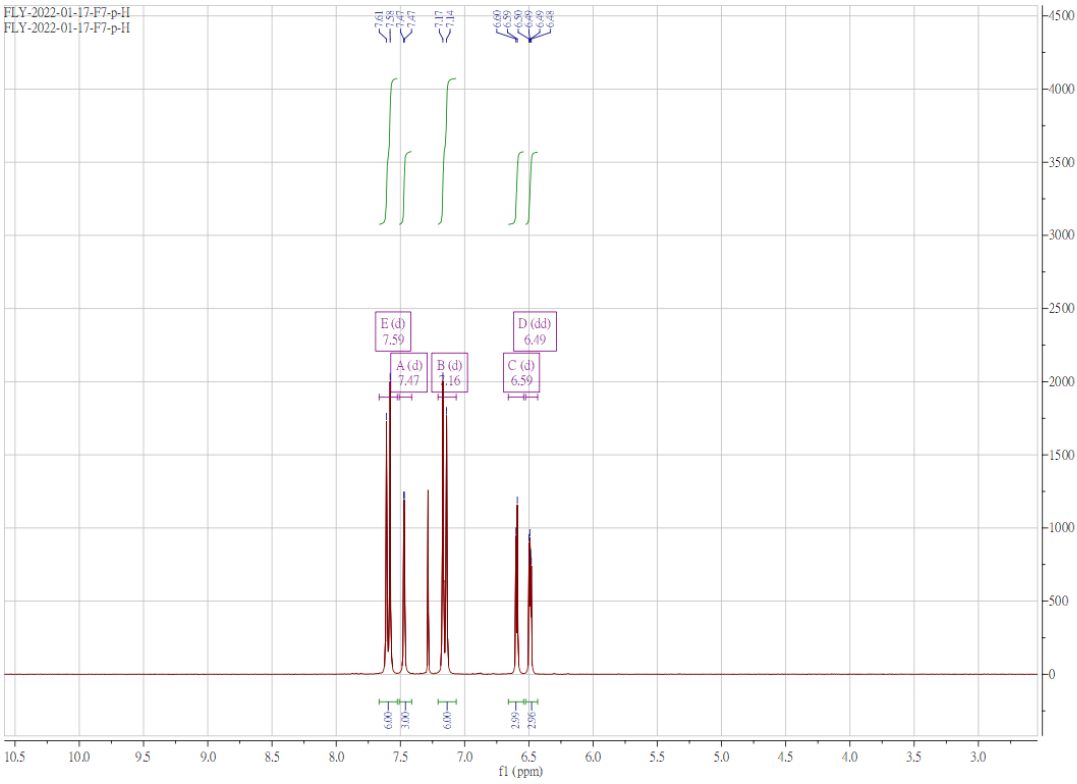

Figure S 1.76. ^{1}H NMR spectrum of **7** in $CDCl_3$

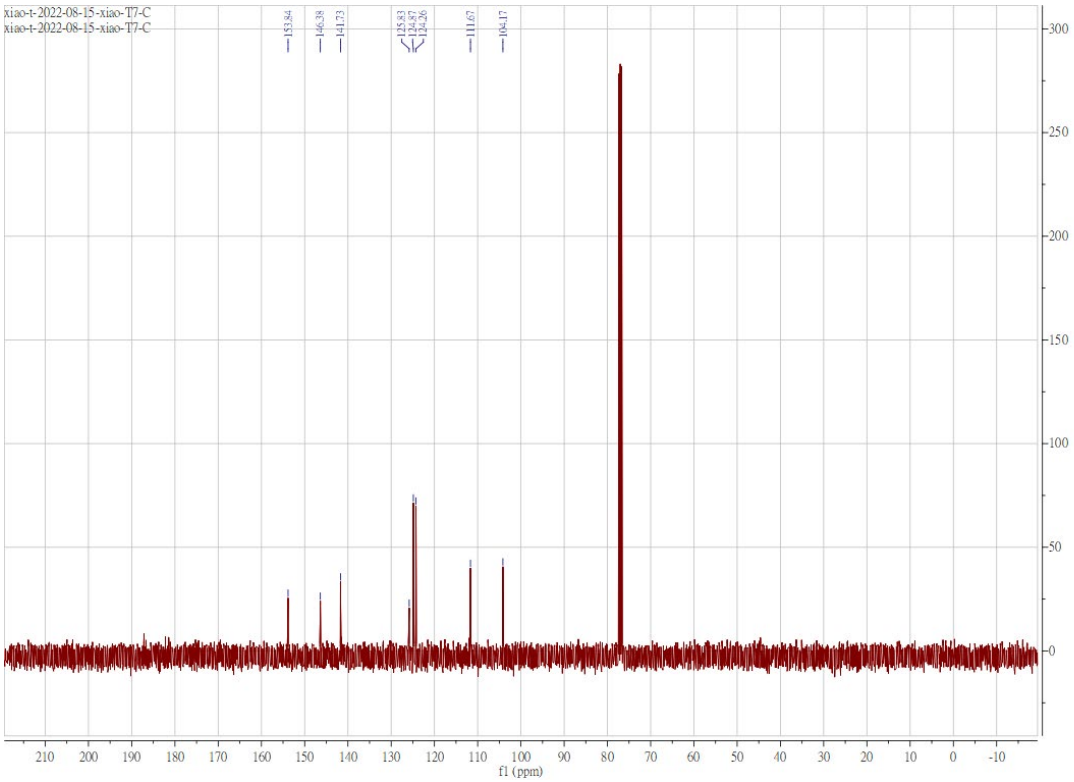

Figure S 1.77. ^{13}C NMR spectrum of **7** in $CDCl_3$

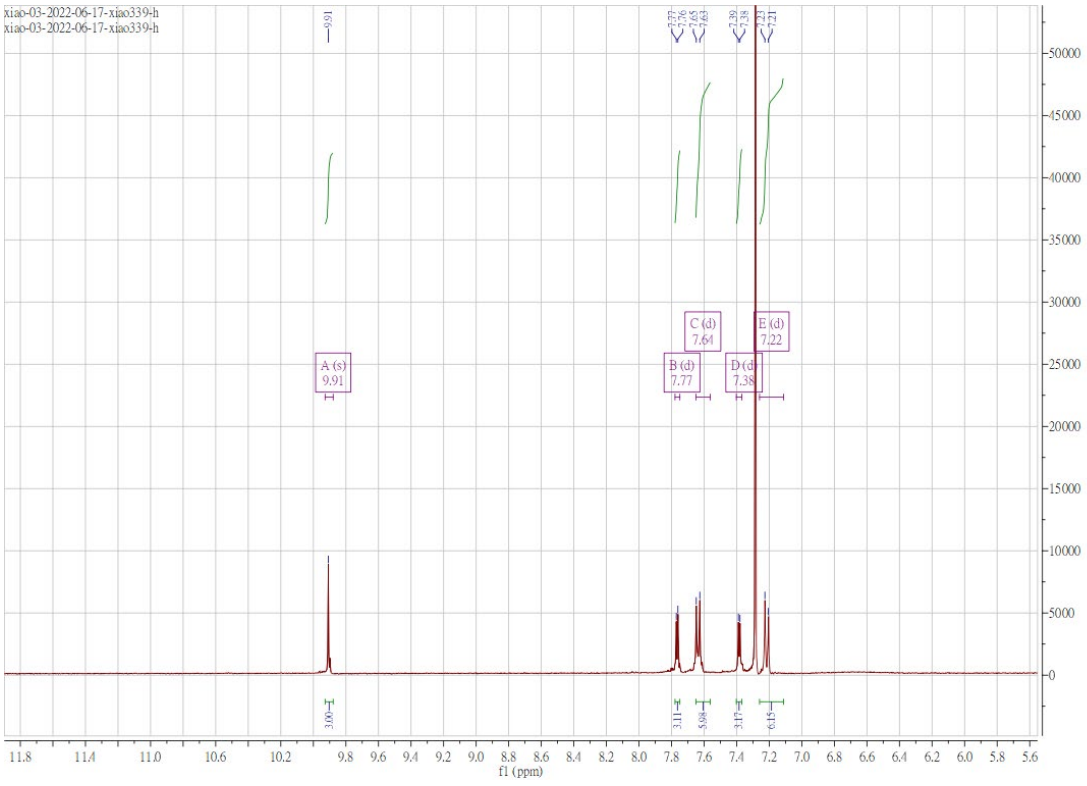

Figure S 1.78. ^{1}H NMR spectrum of **L16** in $CDCl_3$

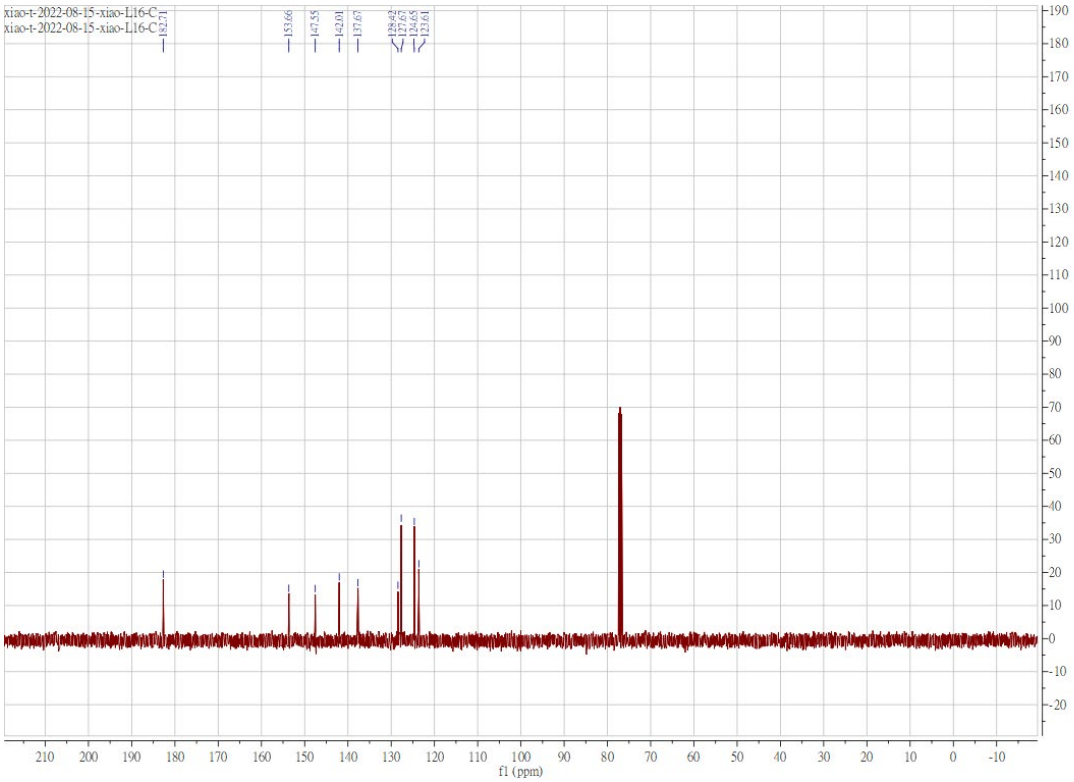

Figure S 1.79. ^{13}C NMR spectrum of **L16** in $CDCl_3$

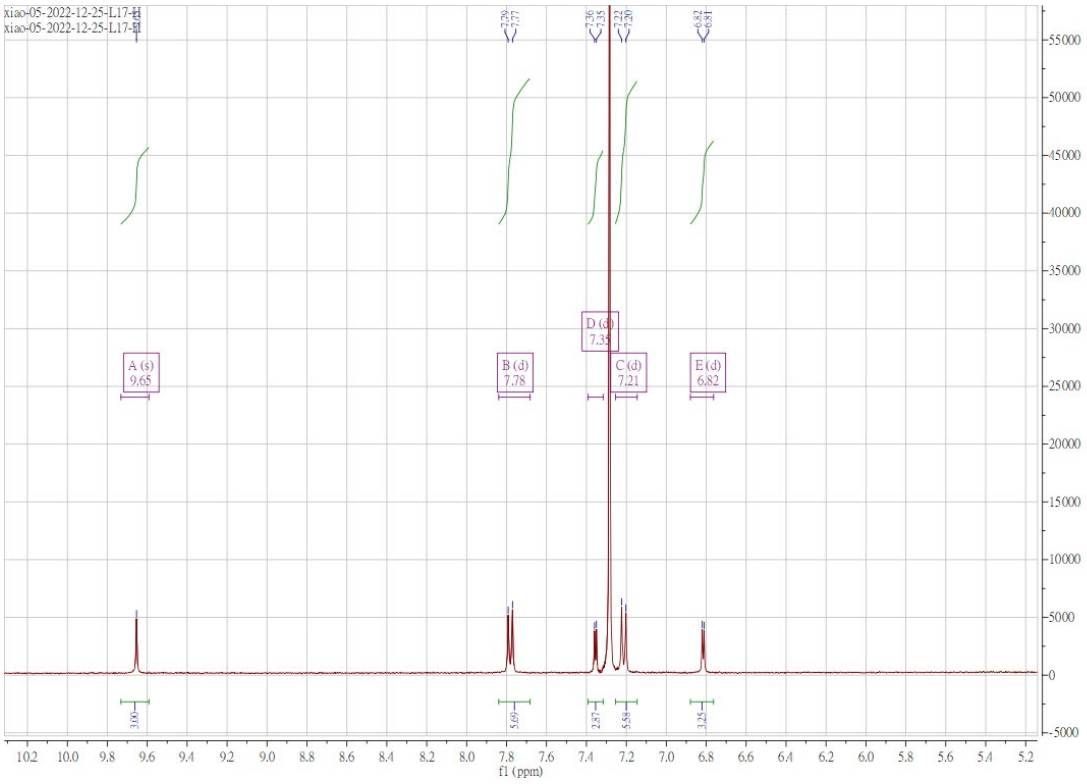

Figure S 1.80. ^{1}H NMR spectrum of **L17** in $CDCl_3$

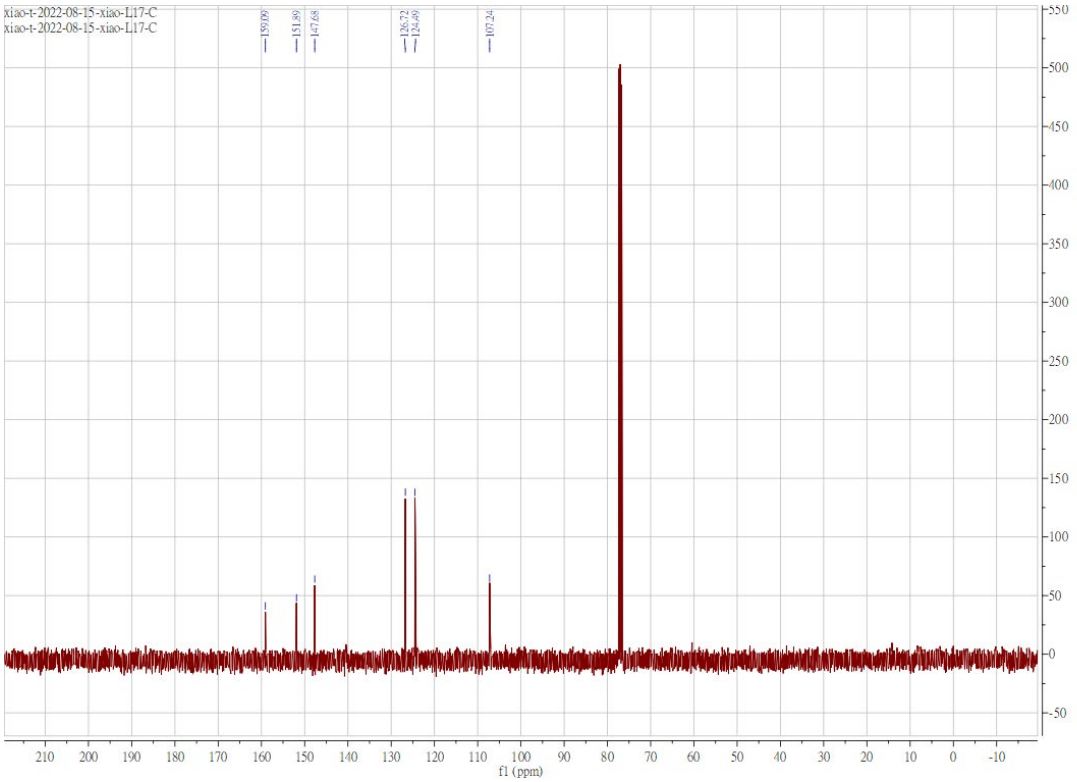

Figure S 1.81. ^{13}C NMR spectrum of **L17** in $CDCl_3$

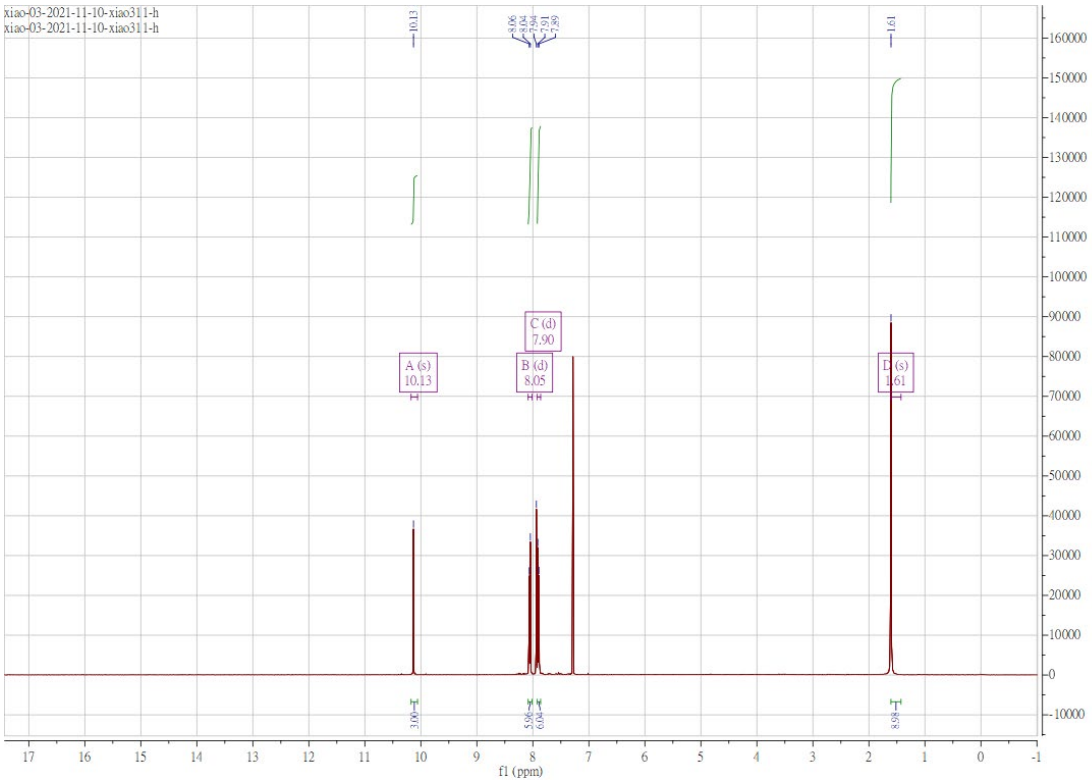

Figure S 1.82. ^{1}H NMR spectrum of **L18** in $CDCl_3$

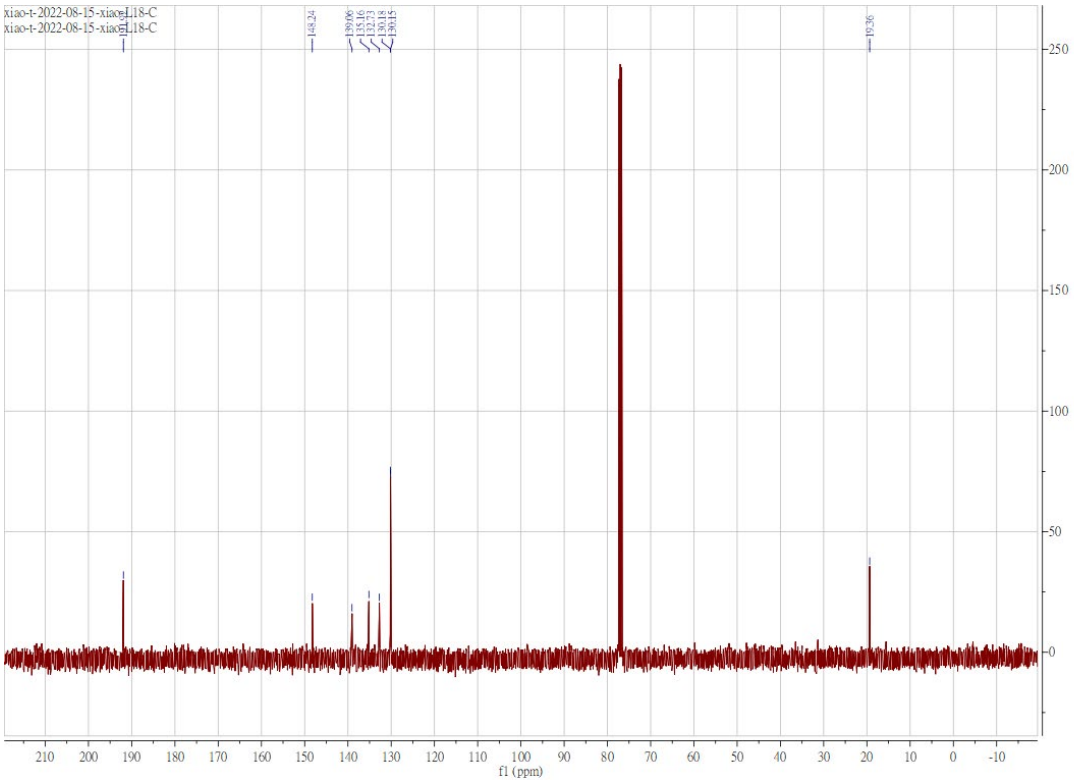

Figure S 1.83. ^{13}C NMR spectrum of **L18** in $CDCl_3$

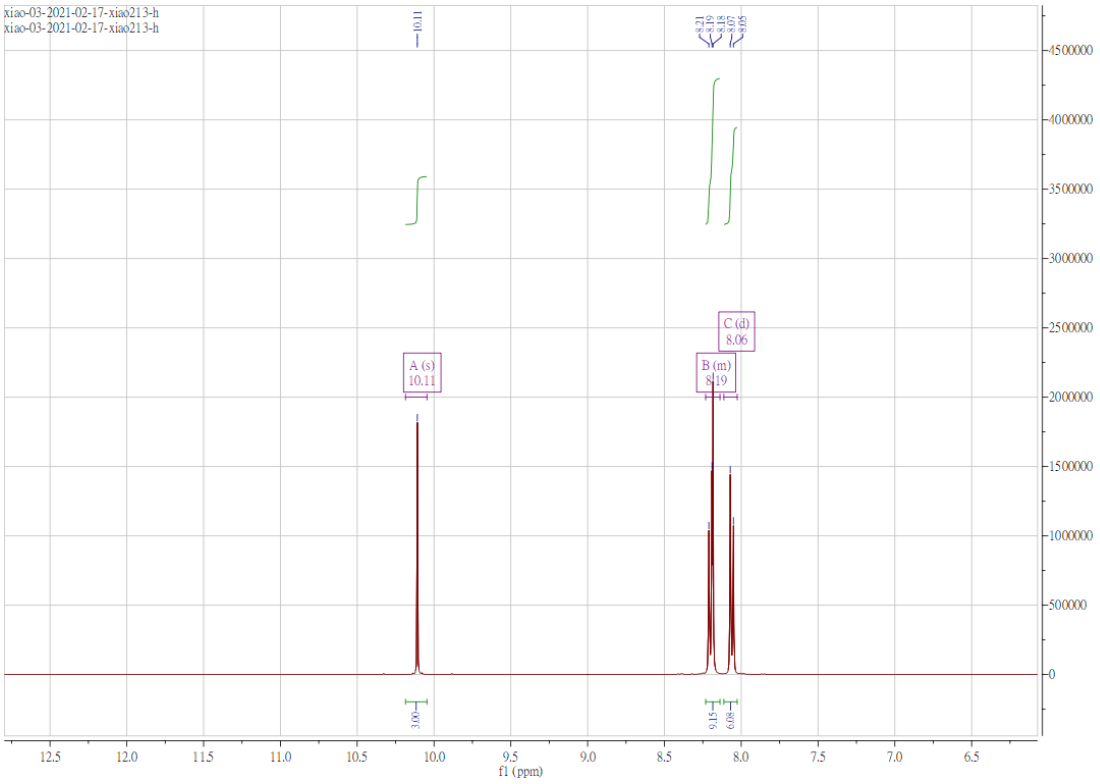

Figure S 1.84. ^{1}H NMR spectrum of **L19** in $CDCl_3$

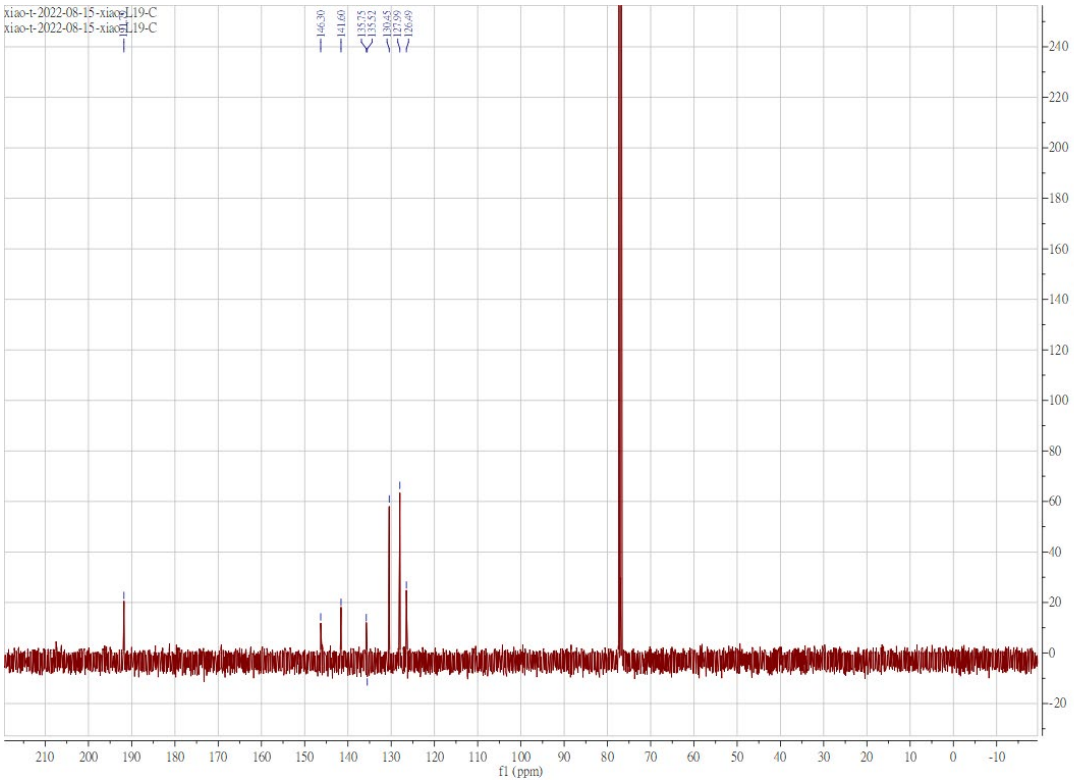

Figure S 1.85. ^{13}C NMR spectrum of **L19** in $CDCl_3$

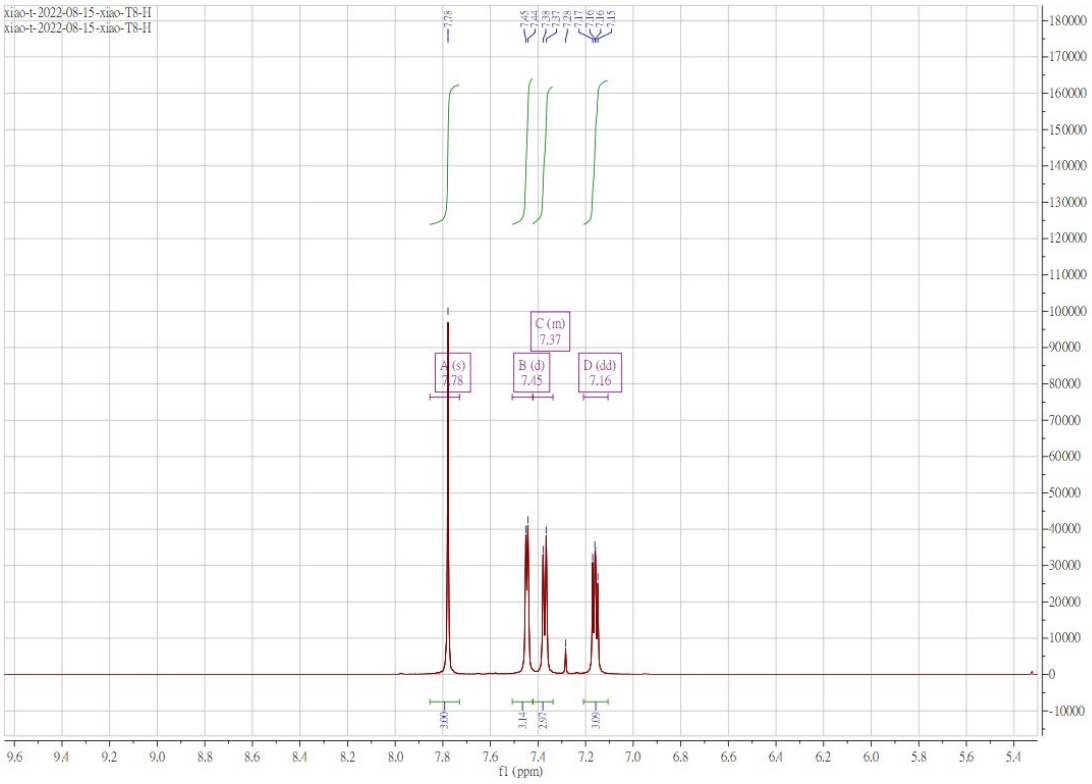

Figure S 1.86. ^{1}H NMR spectrum of **8** in $CDCl_3$

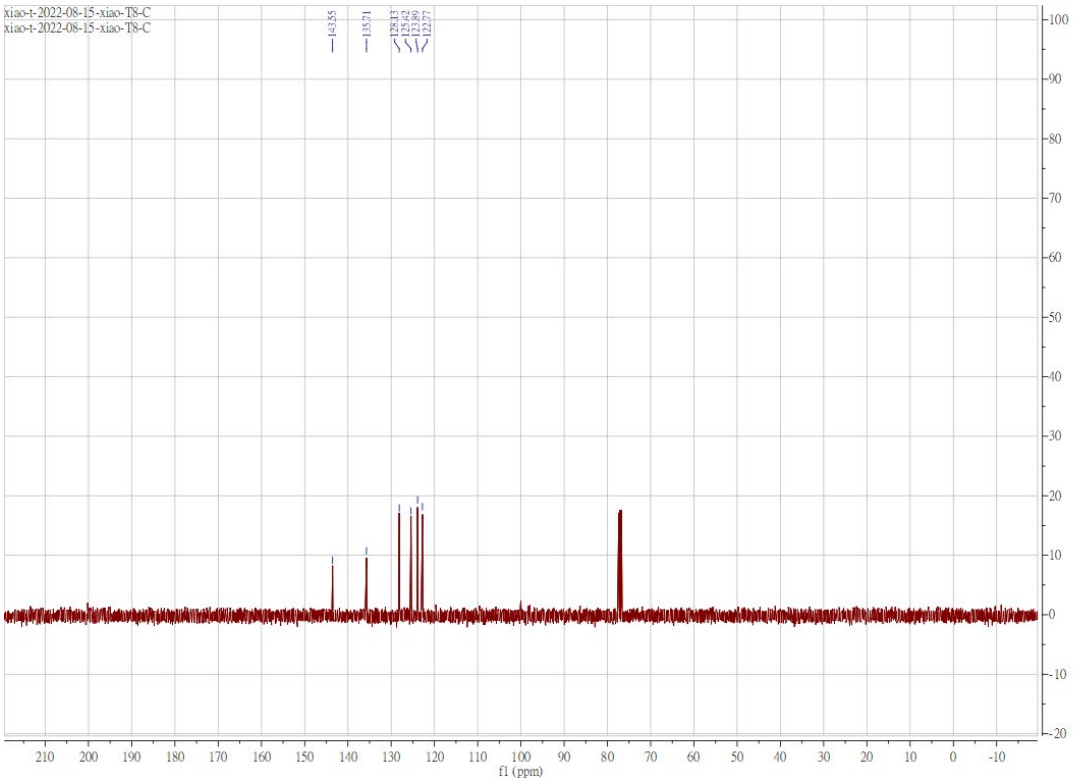

Figure S 1.87. ^{13}C NMR spectrum of **8** in $CDCl_3$

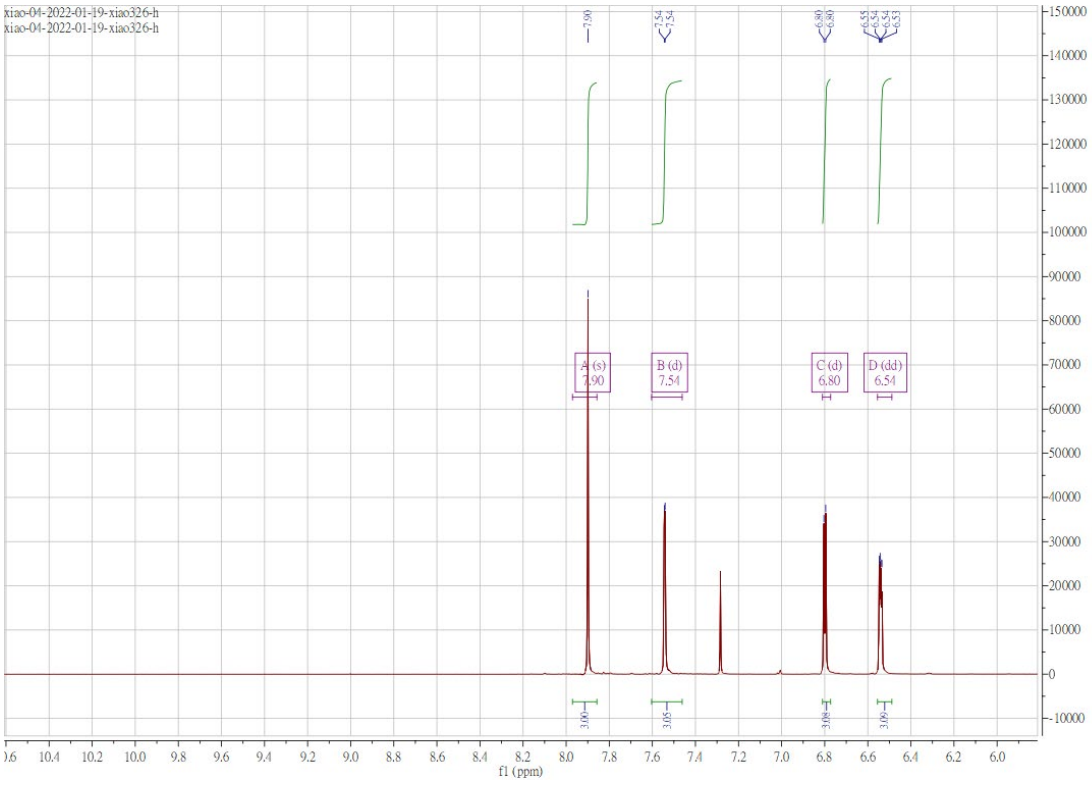

Figure S 1.88. ^{1}H NMR spectrum of **9** in $CDCl_3$

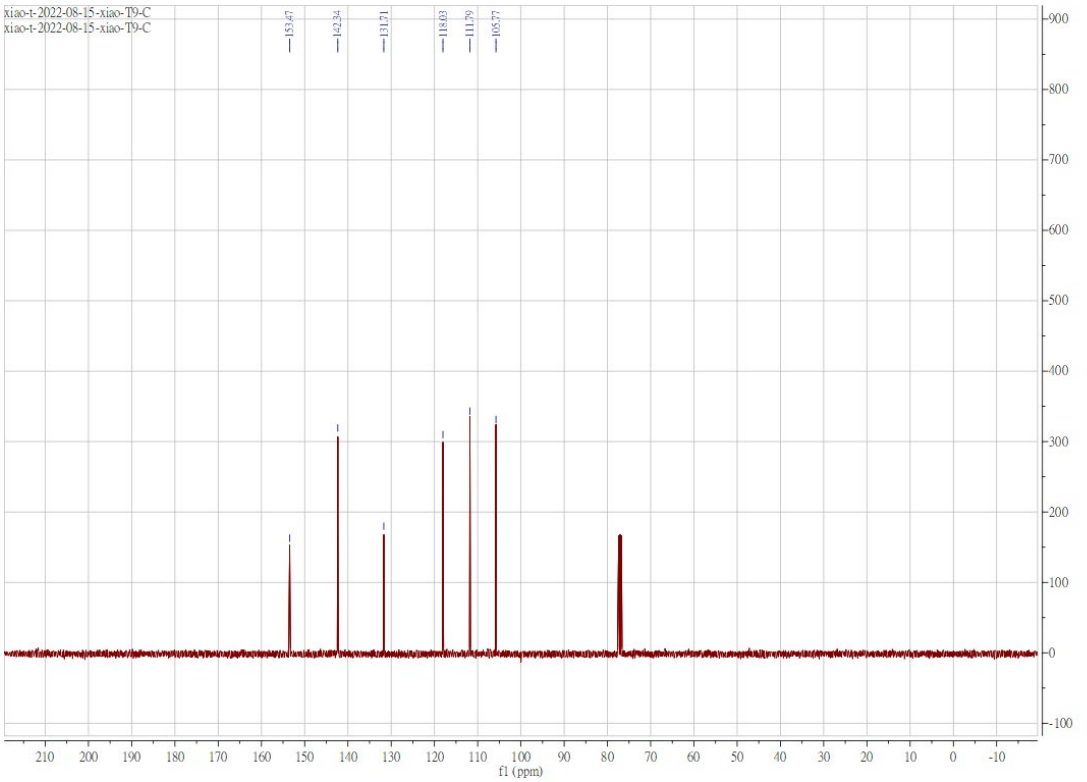

Figure S 1.89. ^{13}C NMR spectrum of **9** in $CDCl_3$

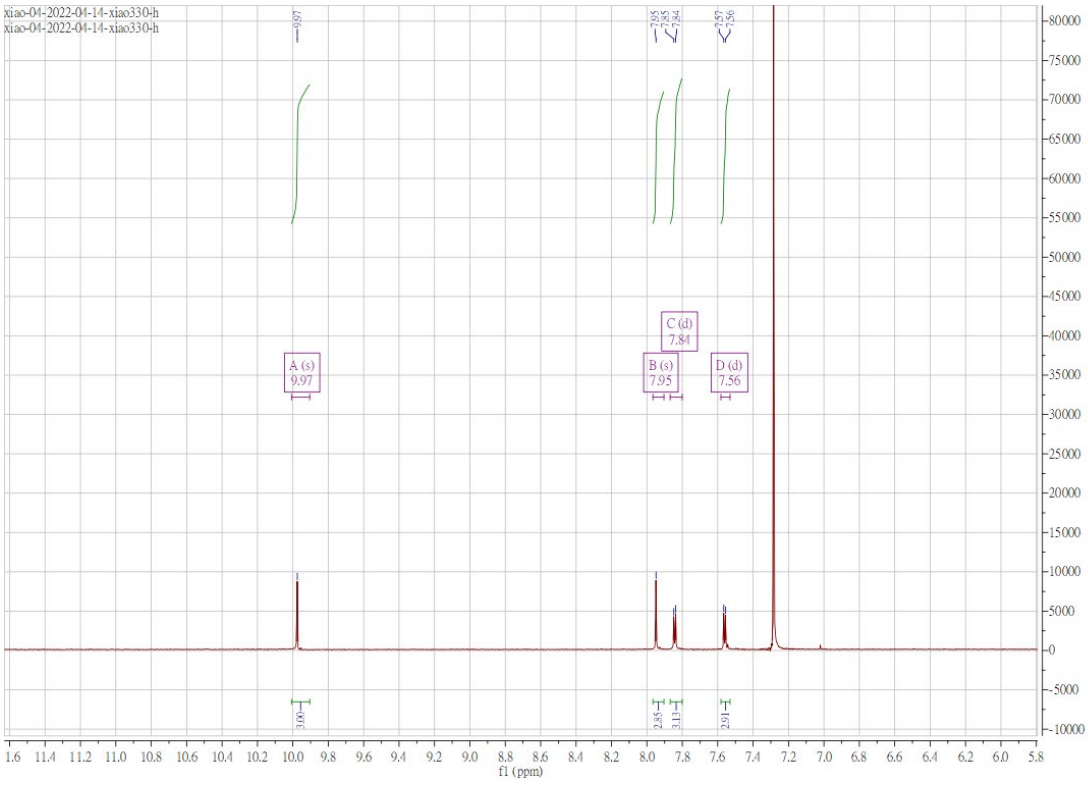

Figure S 1.90. ^{1}H NMR spectrum of **L20** in $CDCl_3$

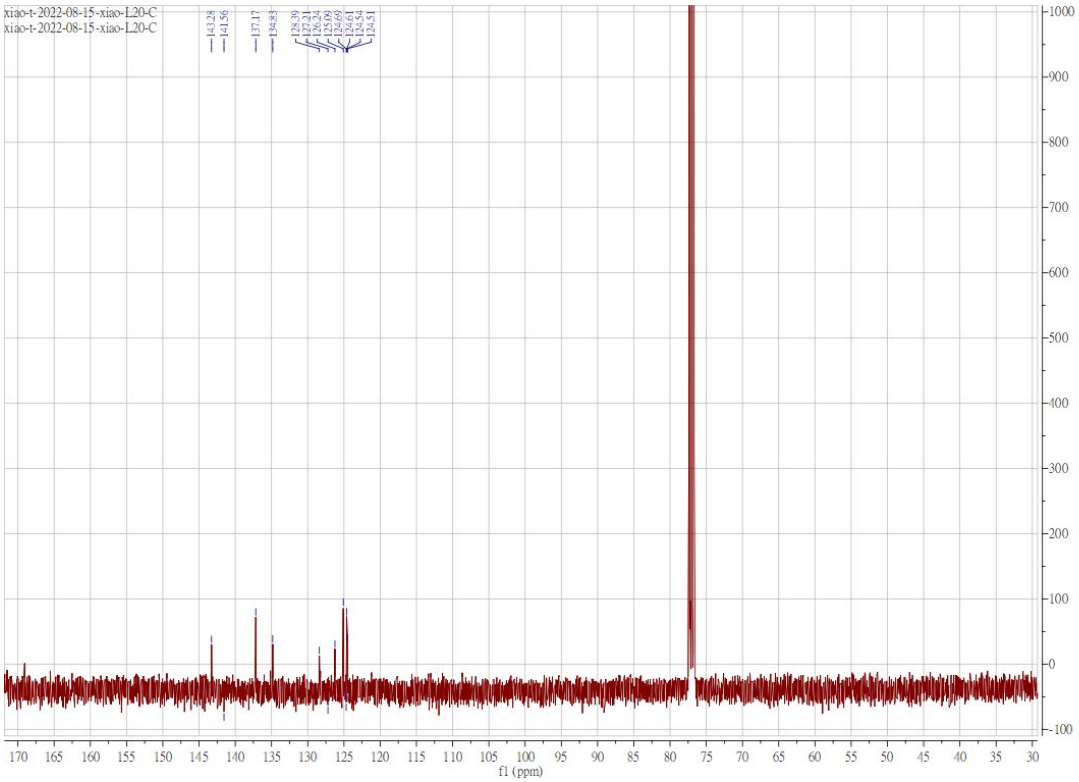

Figure S 1. 91. ^{13}C NMR spectrum of **L20** in $CDCl_3$

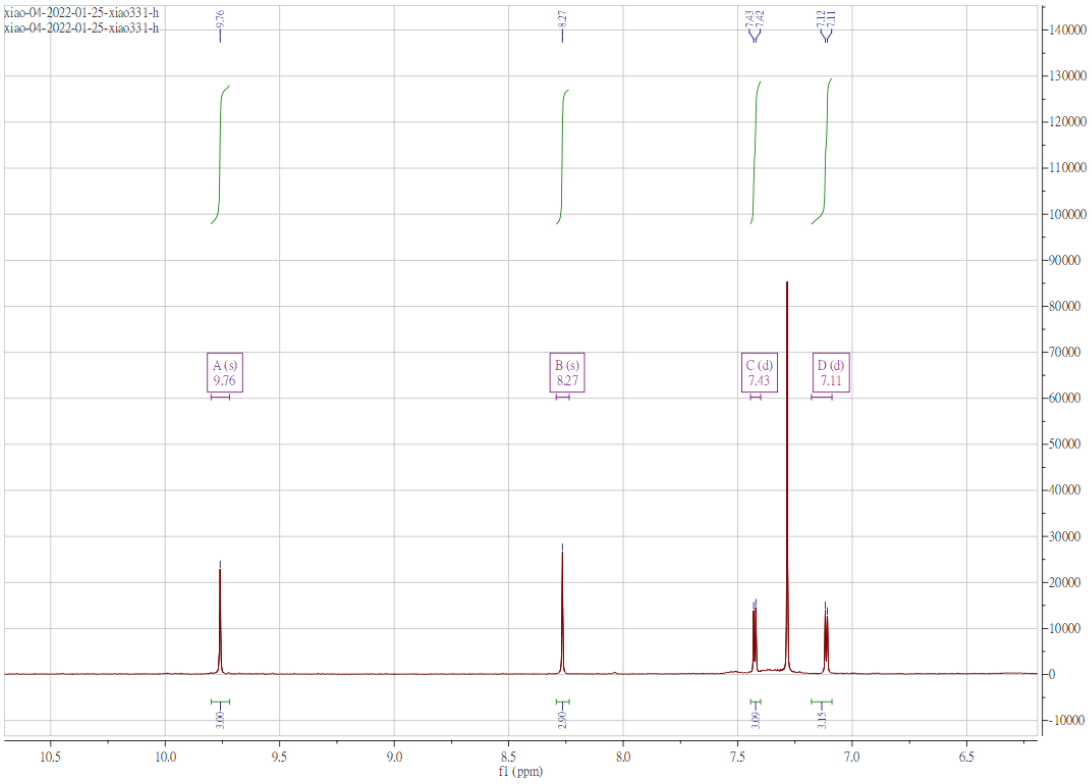

Figure S 1.92. ^{1}H NMR spectrum of **L21** in $CDCl_3$

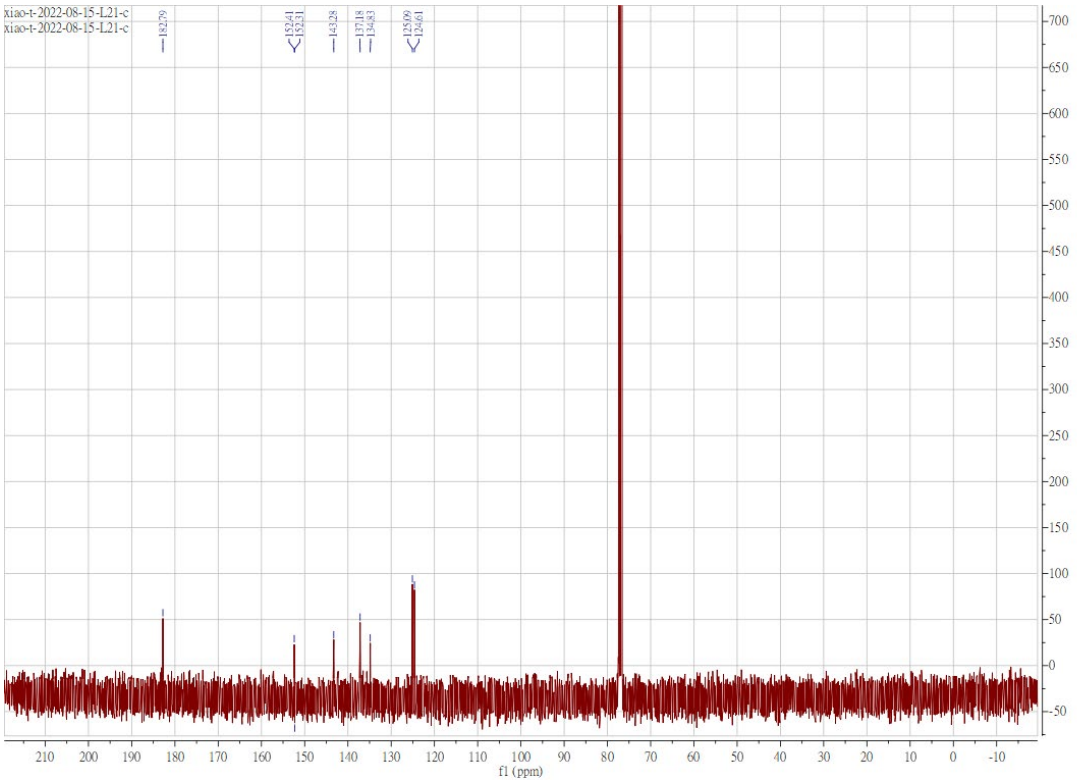

Figure S 1.93. ^{13}C NMR spectrum of **L21** in $CDCl_3$

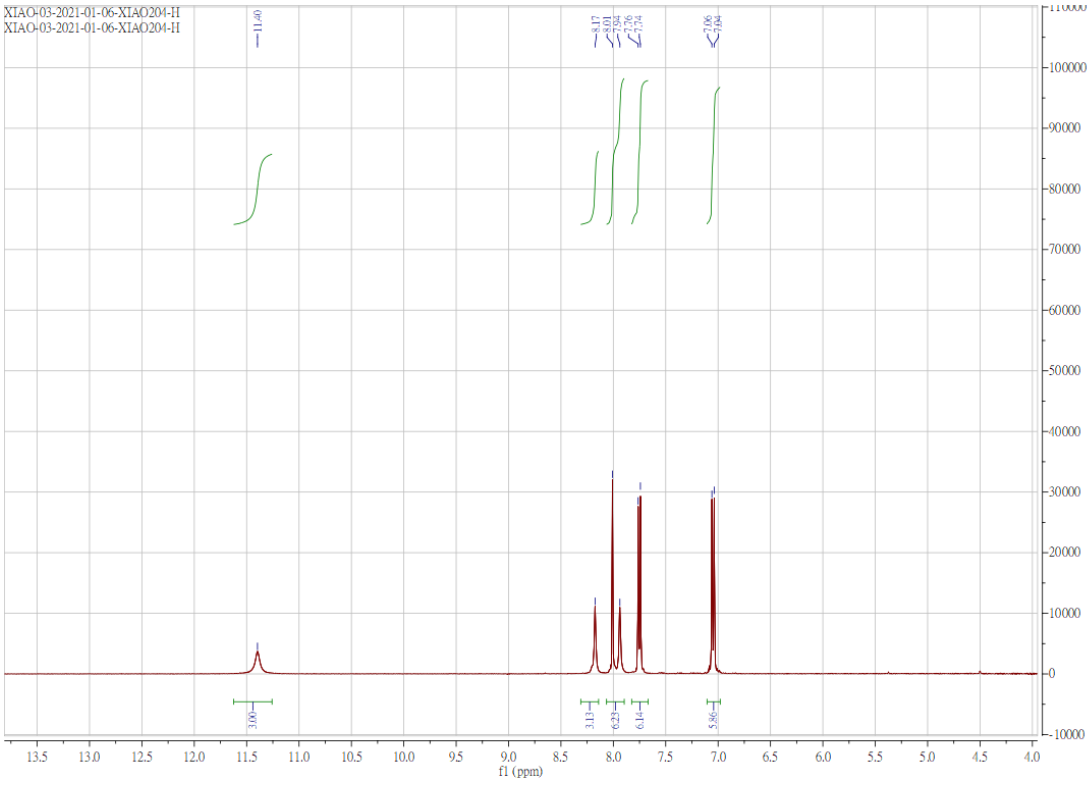

Figure S 1.94. ^{1}H NMR spectrum of **P1** in DMSO-d6

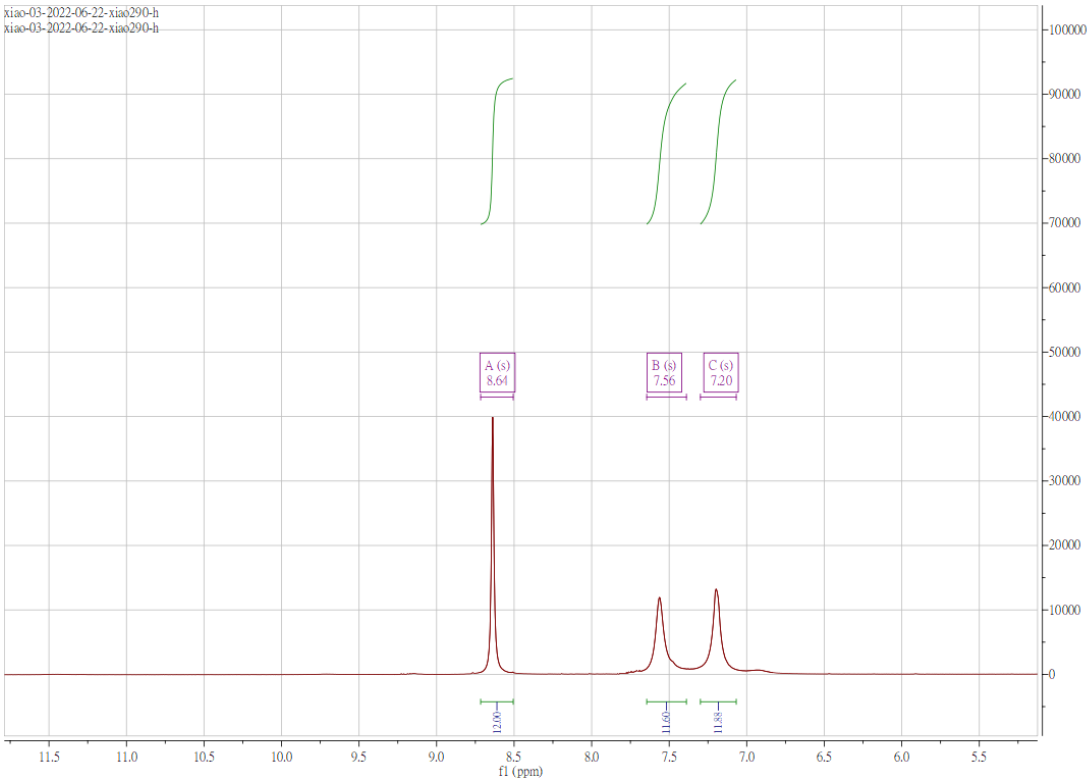

Figure S 1.95. [1]H NMR spectrum of **P2** in DMSO-d6

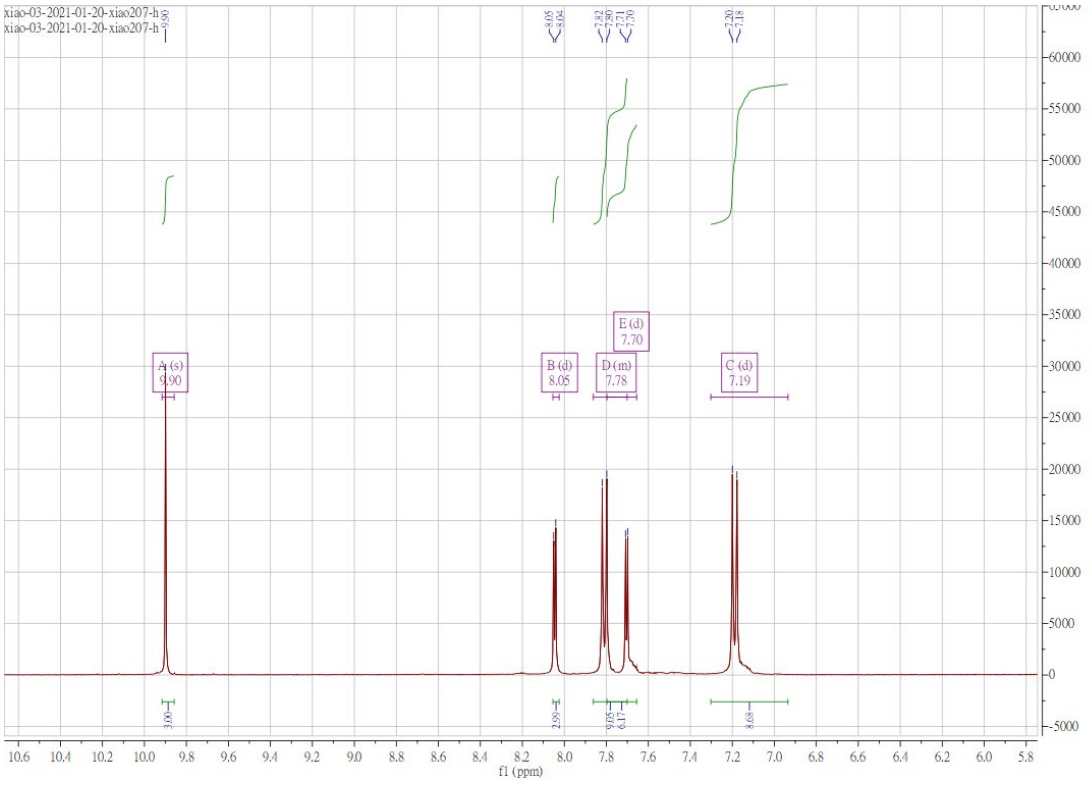

Figure S 1.96. [1]H NMR spectrum of **P3** in DMSO-d6

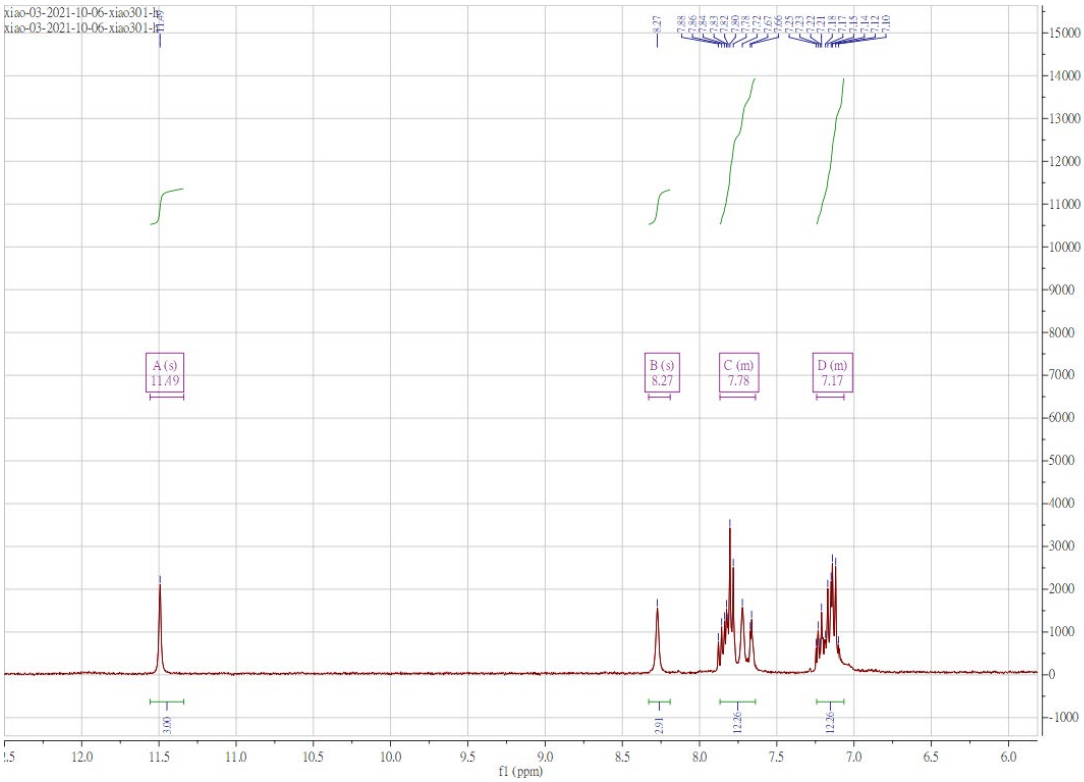

Figure S 1.97. ^{1}H NMR spectrum of **P4** in DMSO-d6

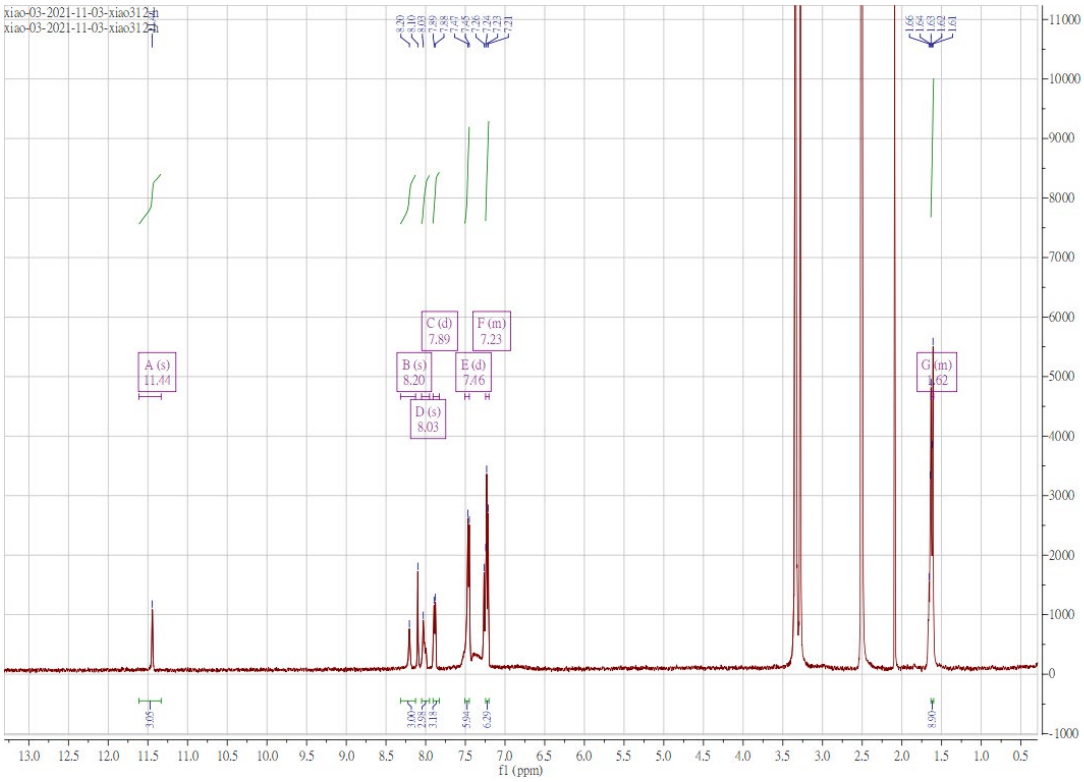

Figure S 1.98. ^{1}H NMR spectrum of **P5** in DMSO-d6

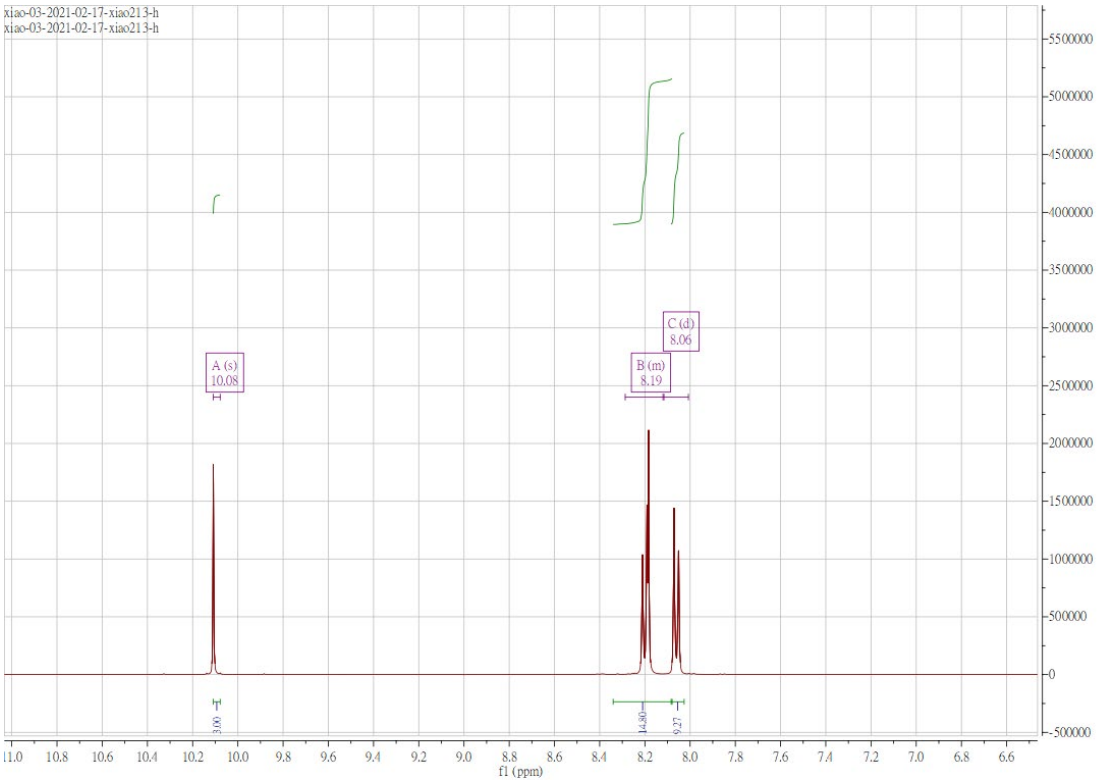

Figure S 1.99. [1]H NMR spectrum of **P6** in DMSO-d6

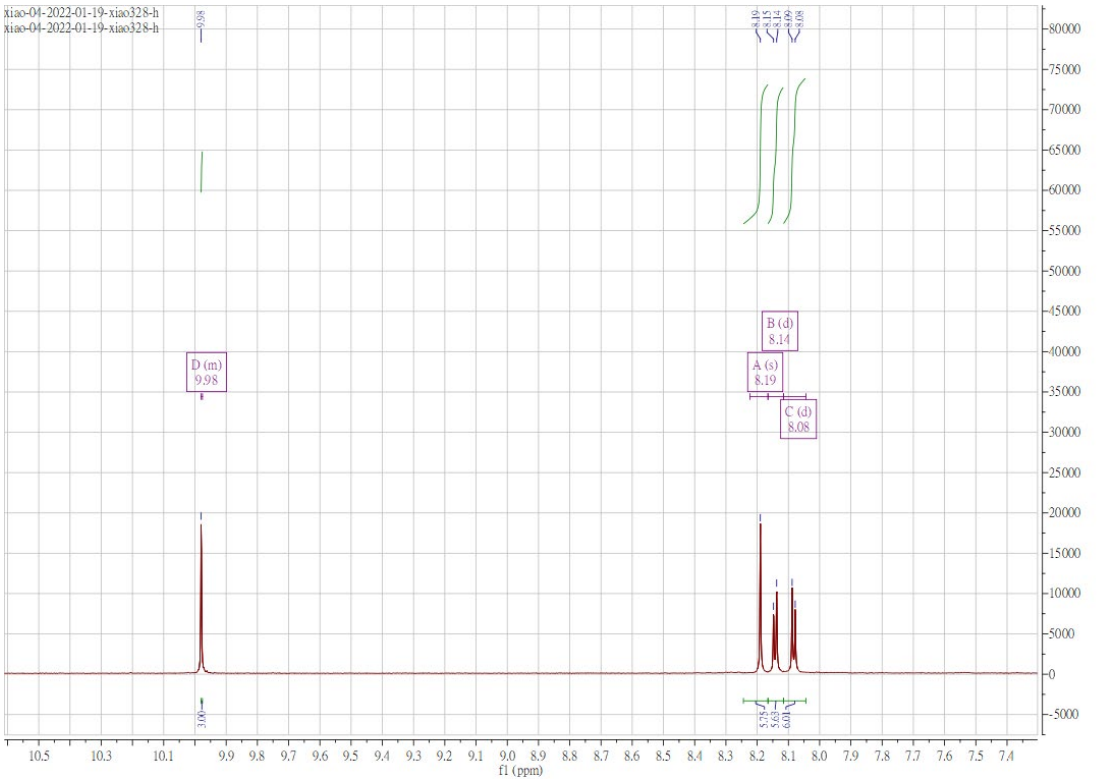

Figure S 1.100. [1]H NMR spectrum of **P7** in DMSO-d6

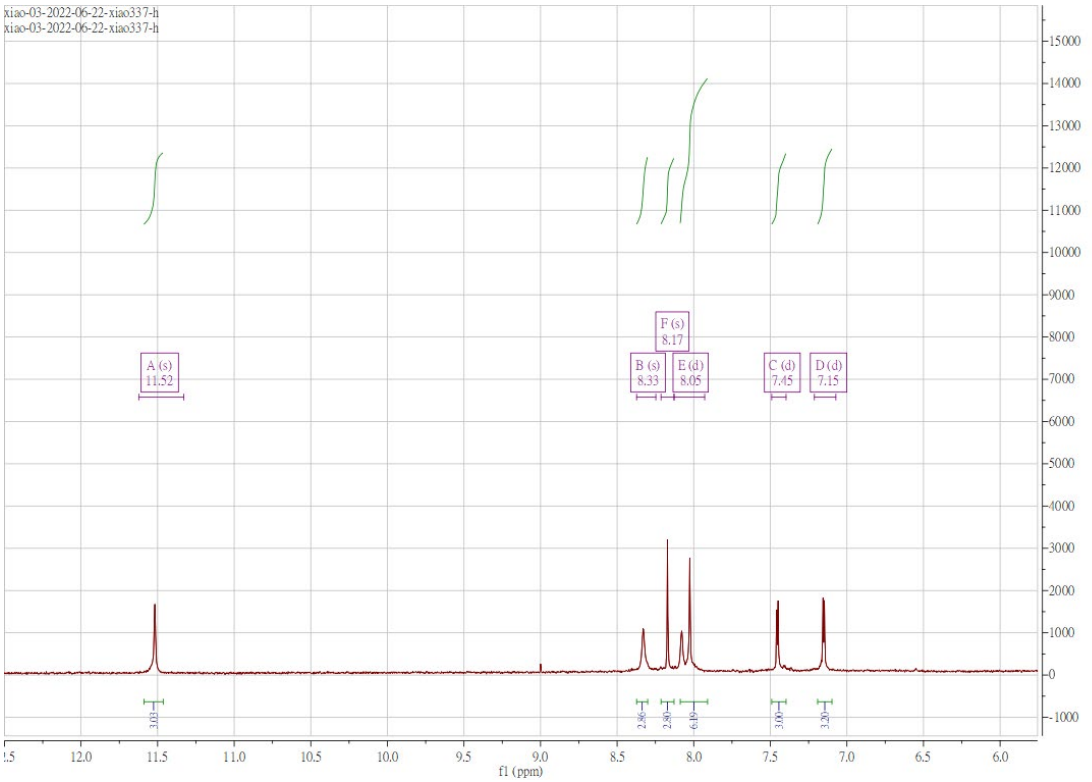

Figure S 1.101. [1]H NMR spectrum of **P8** in DMSO-d6

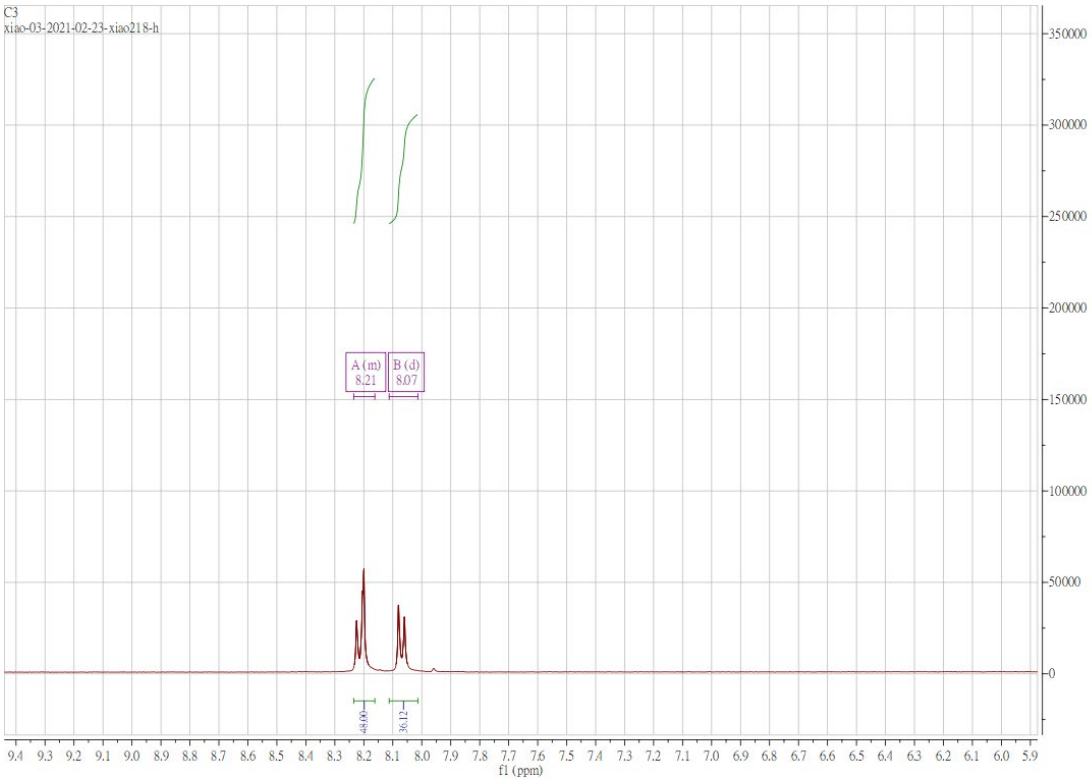

Figure S 1.102. [1]H NMR spectrum of **MOC1** in DMSO-d6

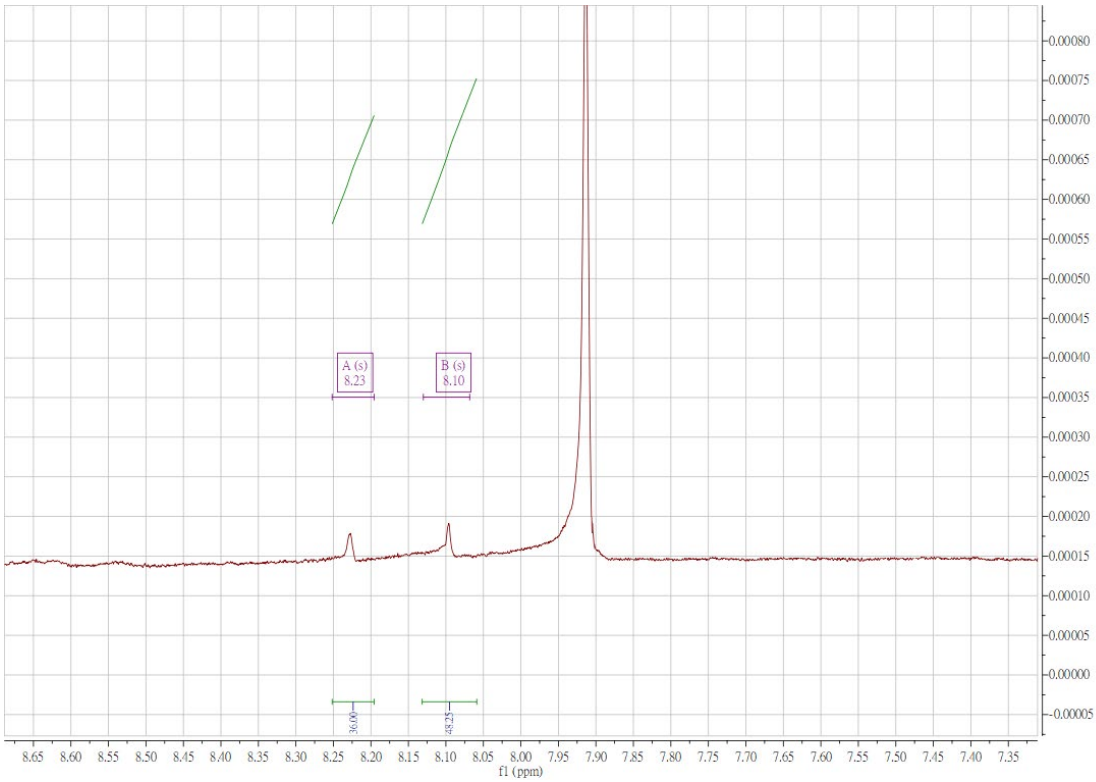

Figure S 1.103. [1]H NMR spectrum of **MOC2** in DMSO-d6

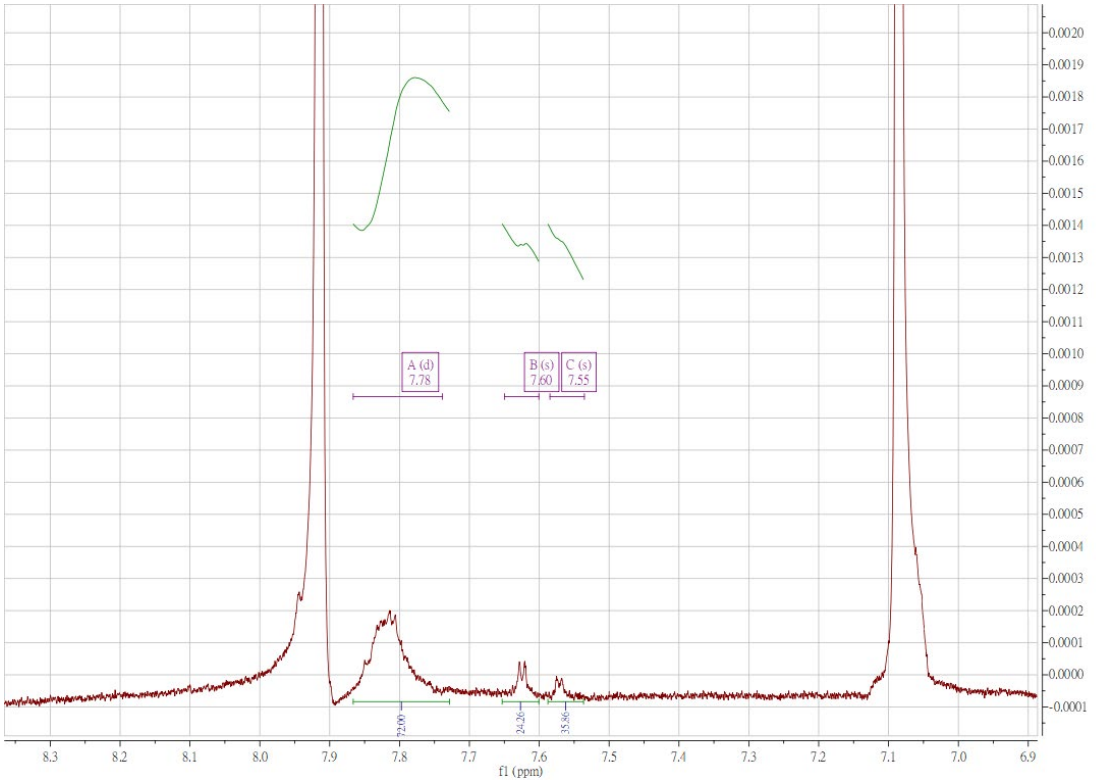

Figure S 1.104. [1]H NMR spectrum of **MOC3** in DMSO-d6

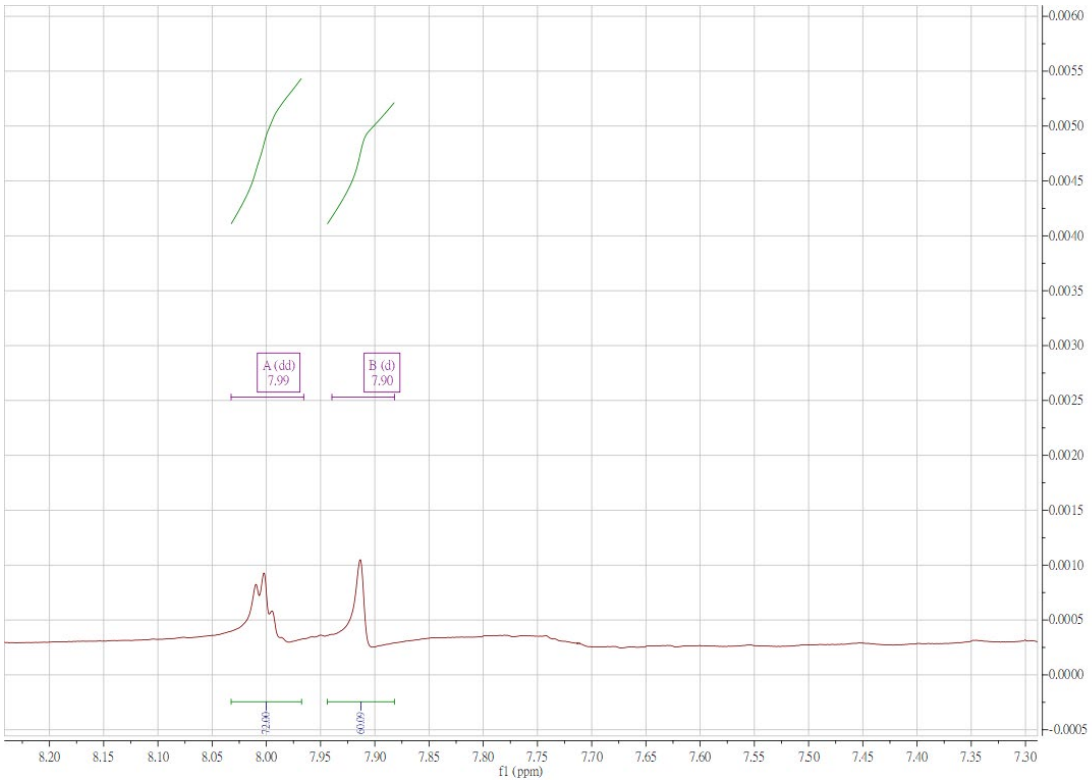

Figure S 1.105. ^{1}H NMR spectrum of **MOC4** in DMSO-d6

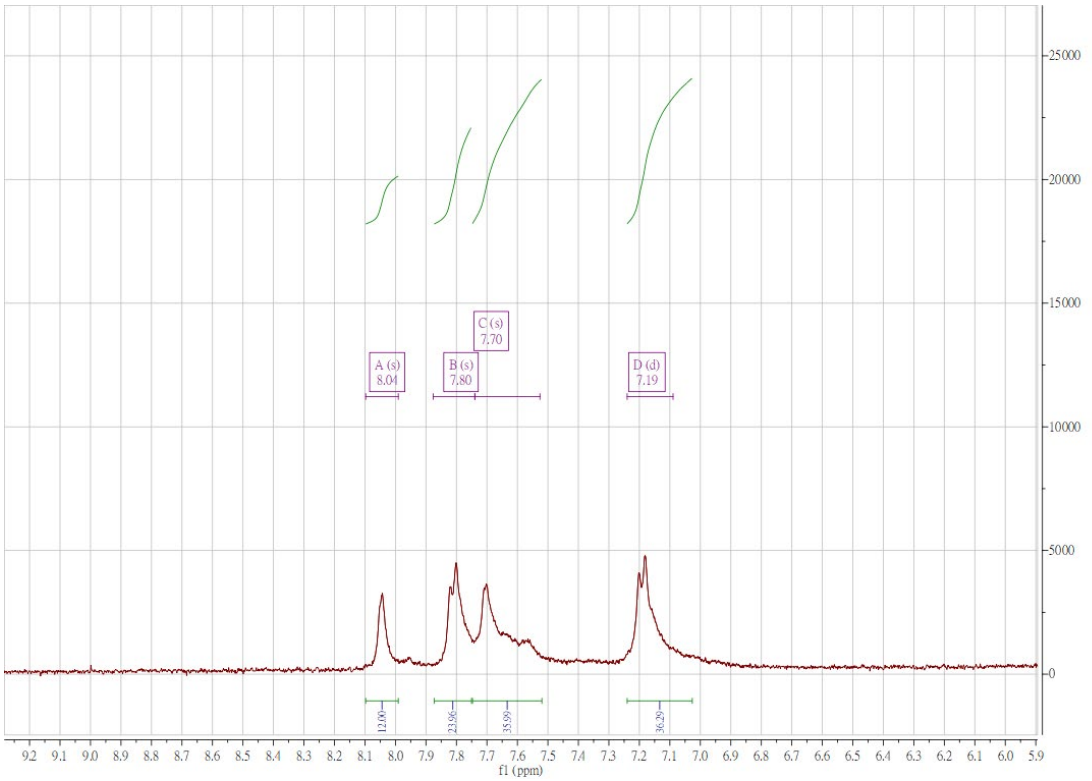

Figure S 1.106. ^{1}H NMR spectrum of **MOC5** in DMSO-d6

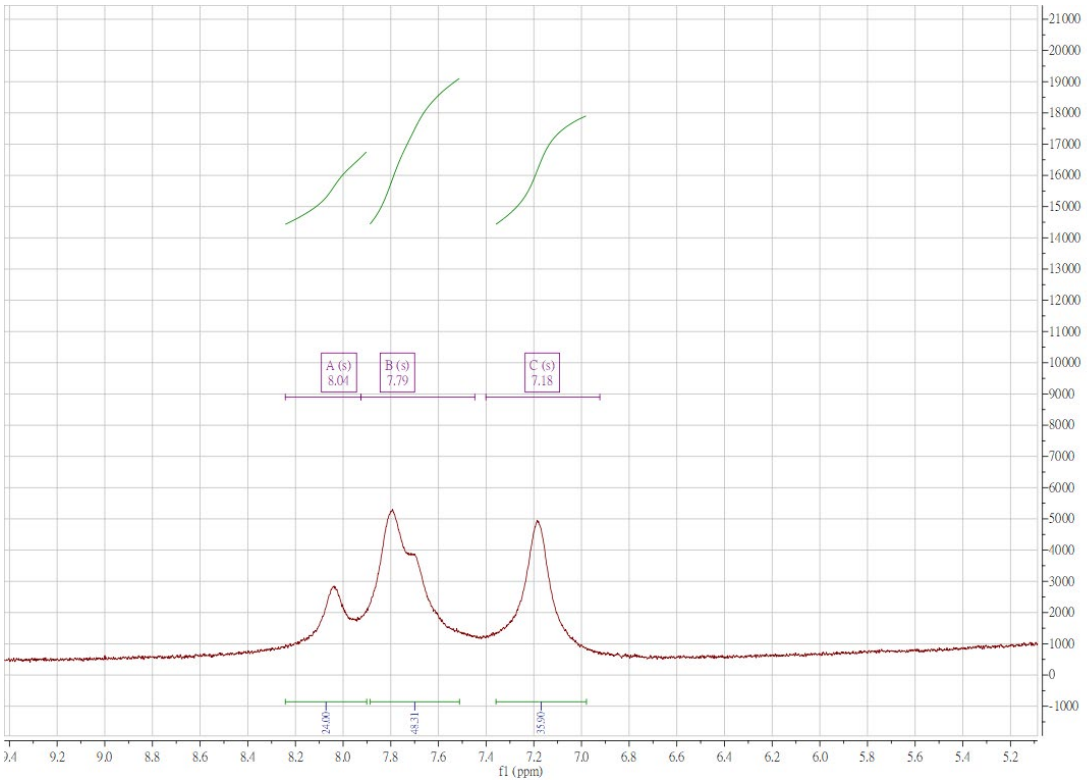

Figure S 1.107. [1]H NMR spectrum of **MOC6** in DMSO-d6

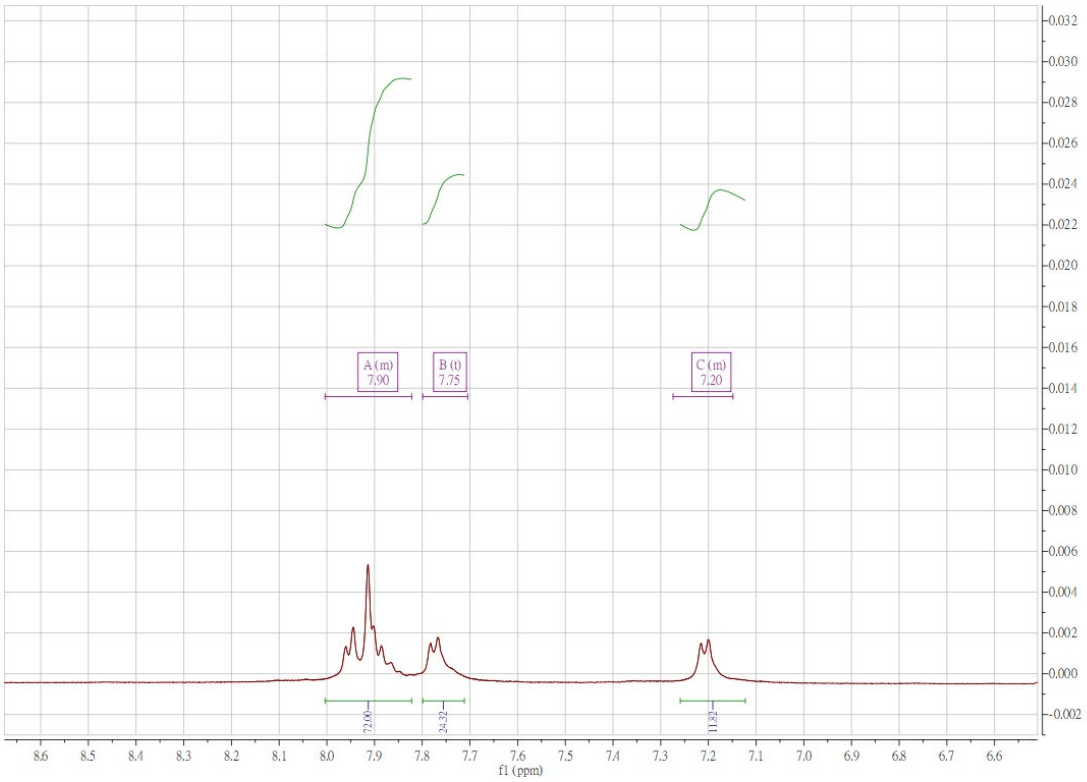

Figure S 1.108. [1]H NMR spectrum of **MOC7** in DMSO-d6

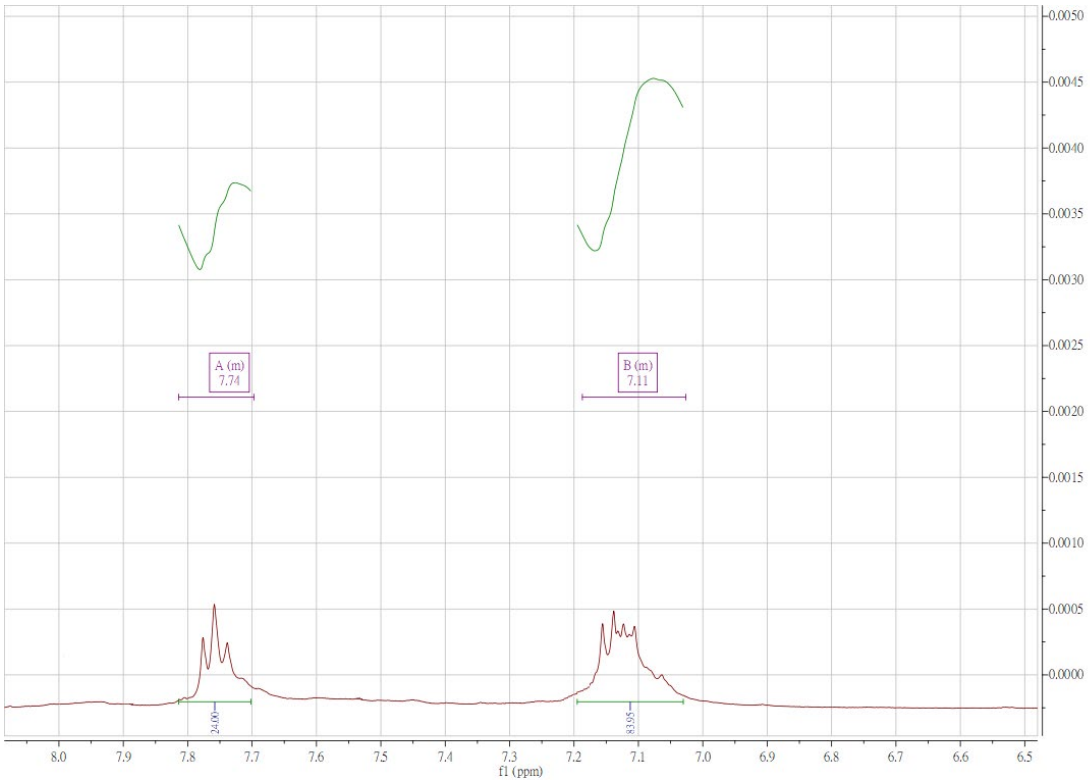

Figure S 1.109. ^{1}H NMR spectrum of **MOC8** in DMSO-d6

Appendix II Mass Spectrum Results

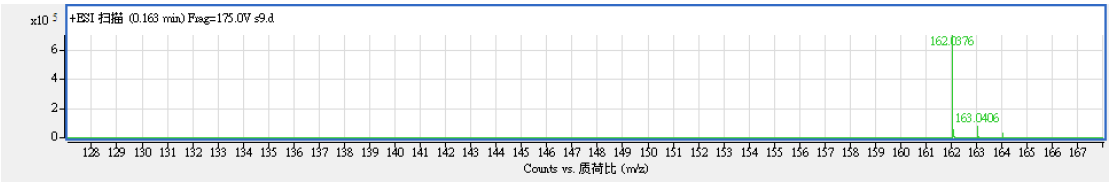

Figure S. 2.1. MS result of **L1**

Figure S. 2.2. MS result of **L2**

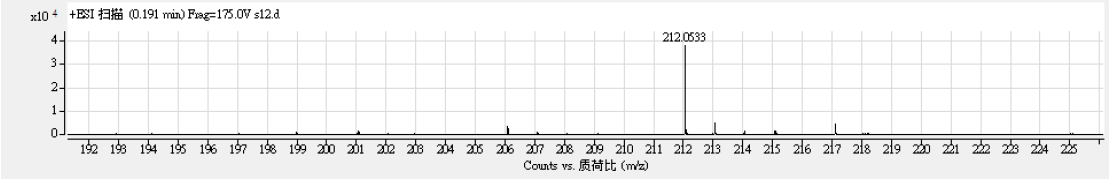

Figure S. 2.3. MS result of **L3**

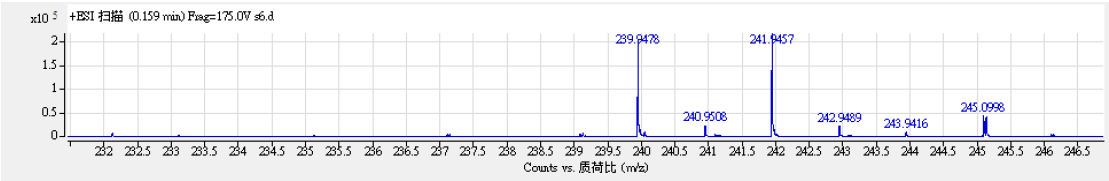

Figure S. 2.4. MS result of **2**

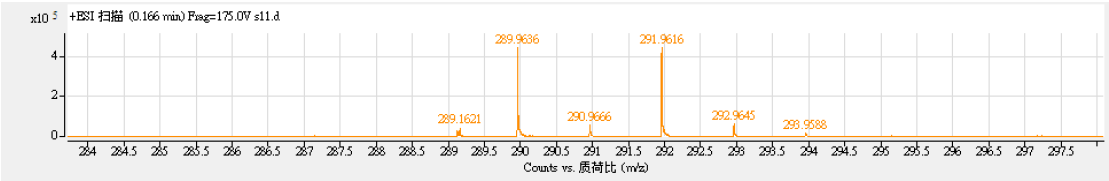

Figure S. 2.5. MS result of **3**

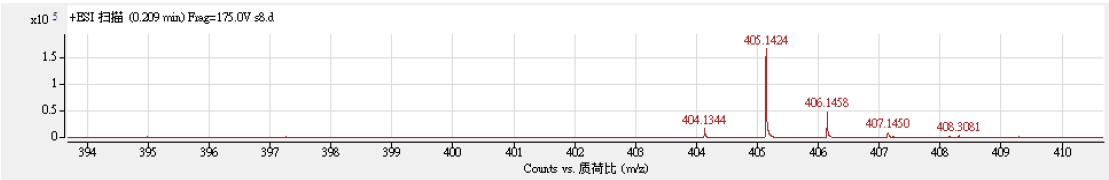

Figure S. 2.6. MS result of **L4**

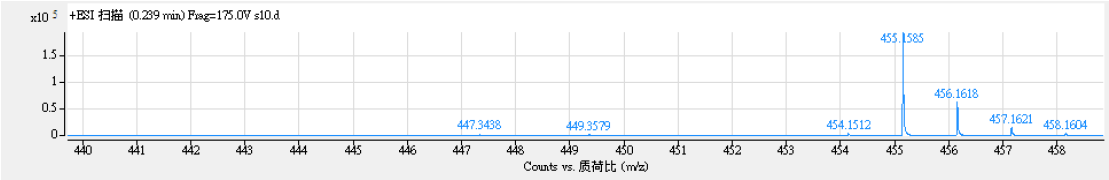

Figure S. 2.7. MS result of **L5**

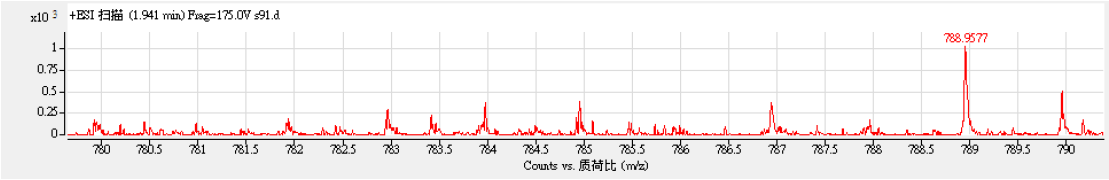

Figure S. 2.8. MS result of **Ru1**

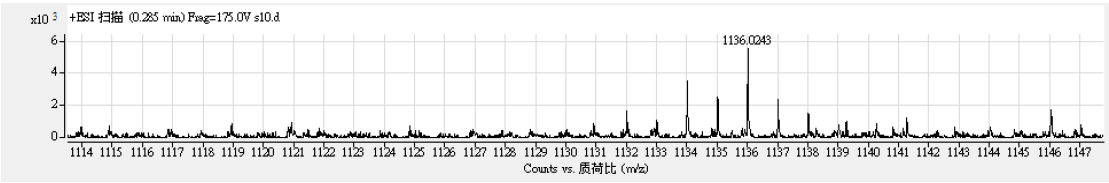

Figure S. 2.9. MS result of **Ru2**

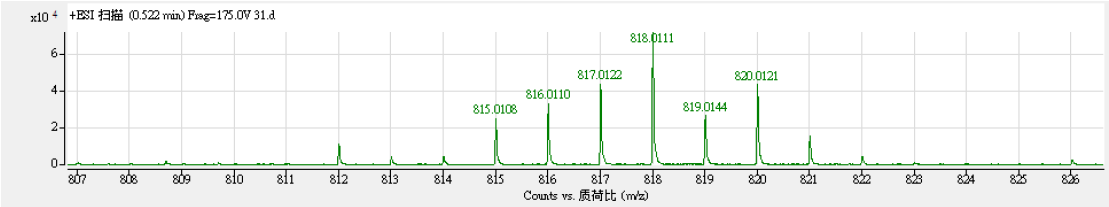

Figure S. 2.10. MS result of **Ru3**

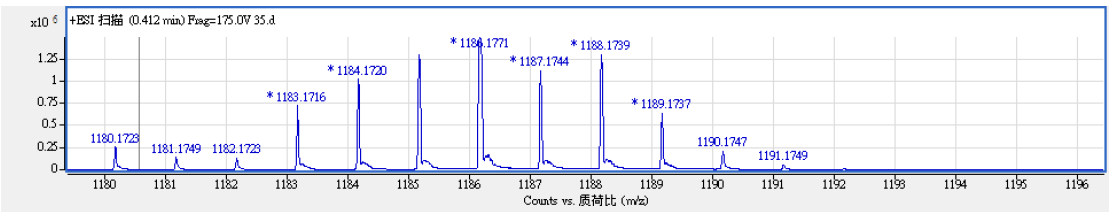

Figure S. 2.11. MS result of **Ru4**

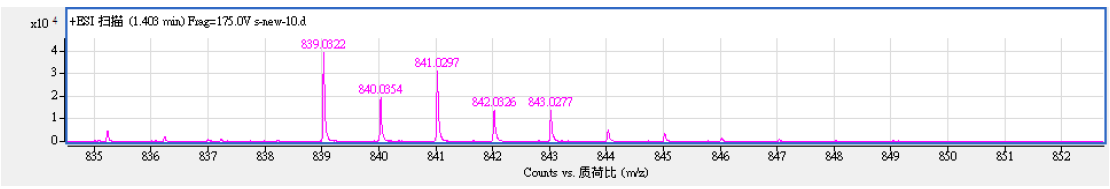

Figure S. 2.12. MS result of **Ru5**

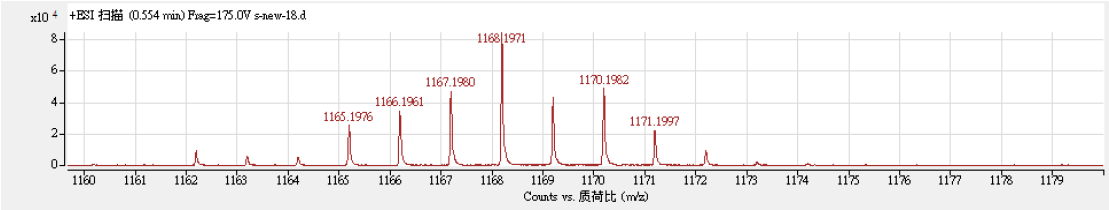

Figure S. 2.13. MS result of **Ru6**

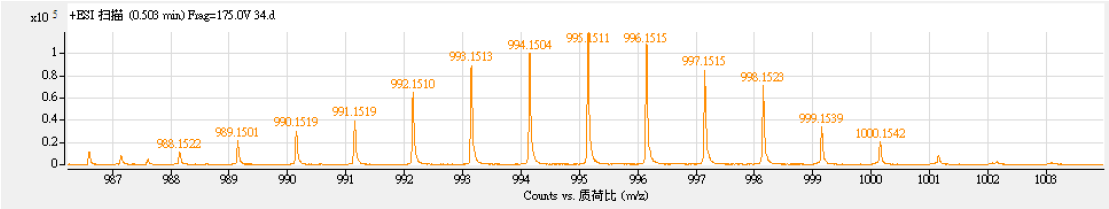

Figure S. 2.14. MS result of **Ru7**

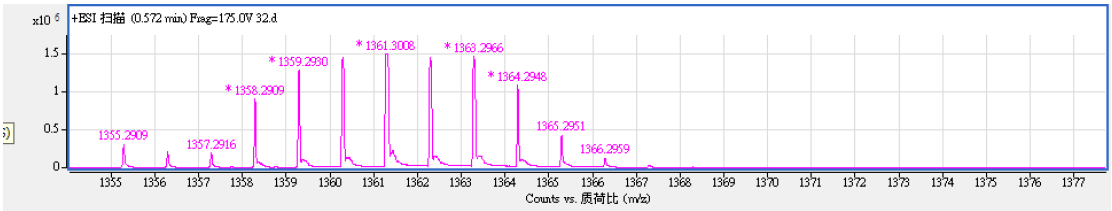

Figure S. 2.15. MS result of **Ru8**

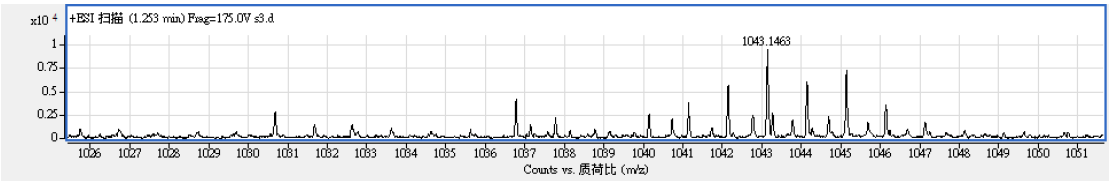

Figure S. 2.16. MS result of **Ru9**

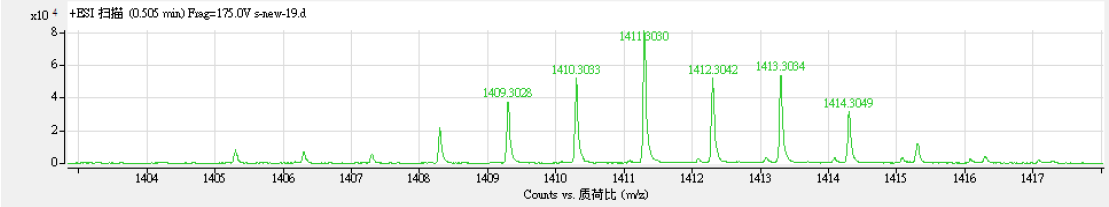

Figure S. 2.17. MS result of **Ru10**

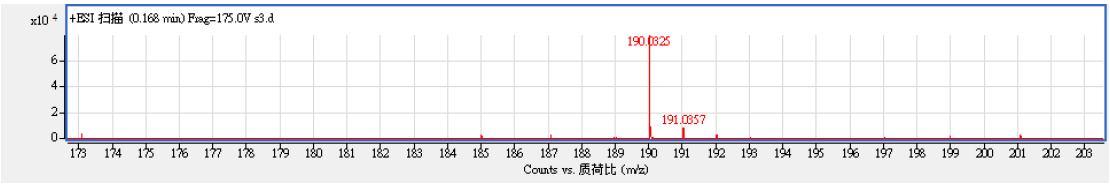

Figure S. 2.18. MS result of **L6**

Figure S. 2.19. MS result of **L7**

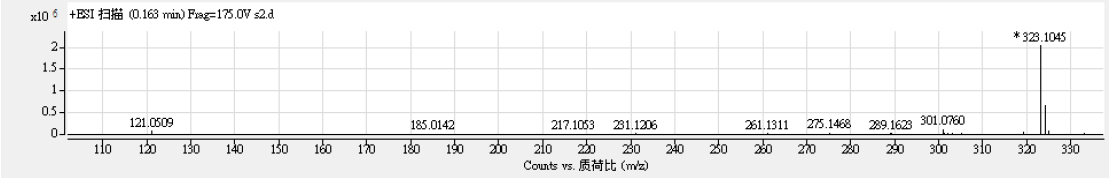

Figure S. 2.20. MS result of diethyl [2,2 -bipyridine]-4,4 -dicarboxylate

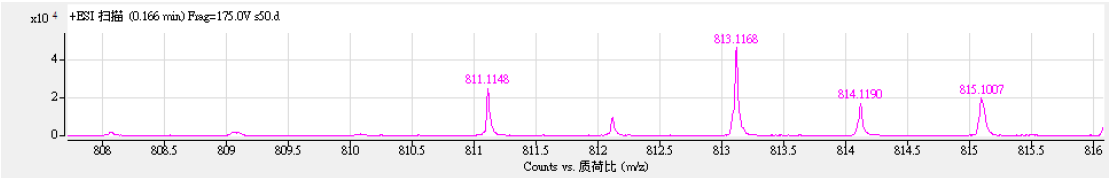

Figure S. 2.21. MS result of **Ir1**

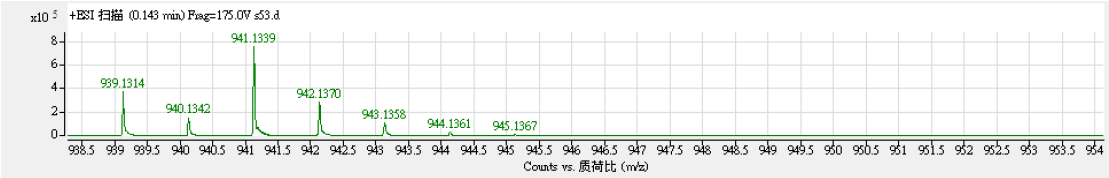

Figure S. 2.22. MS result of **Ir2**

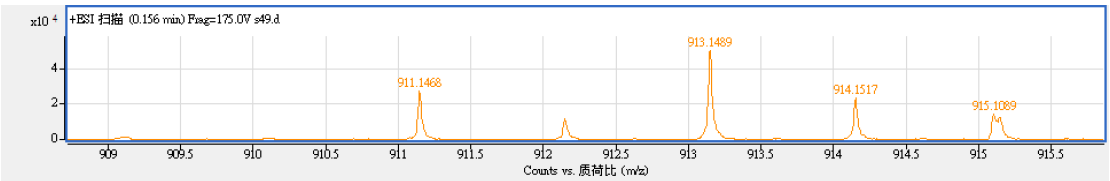

Figure S. 2.23. MS result of **Ir3**

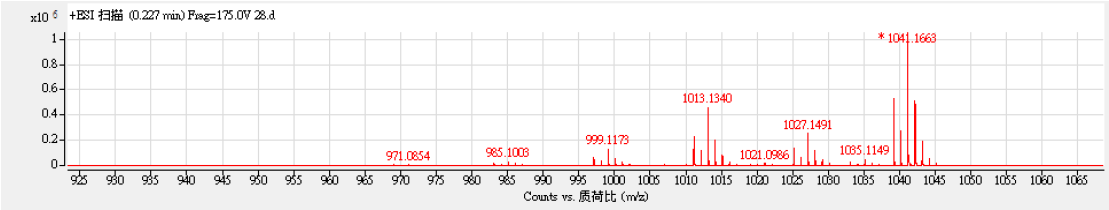

Figure S. 2.24. MS result of **Ir4**

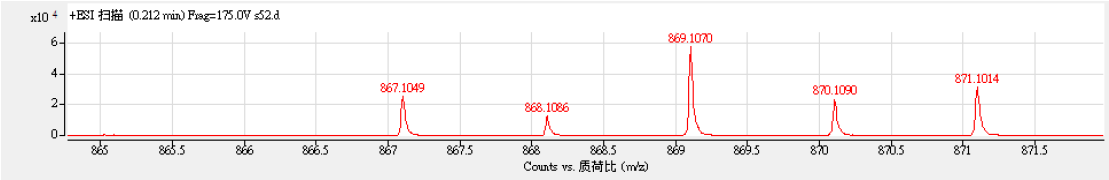

Figure S. 2.25. MS result of **Ir5**

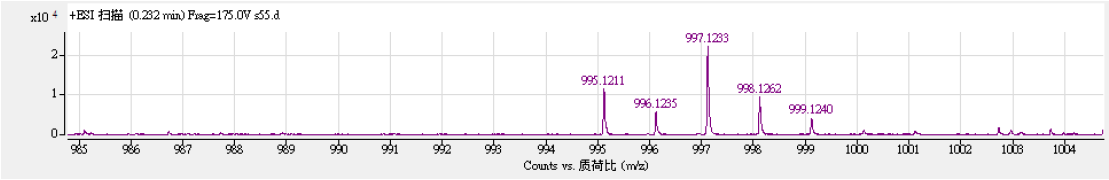

Figure S. 2.26. MS result of **Ir6**

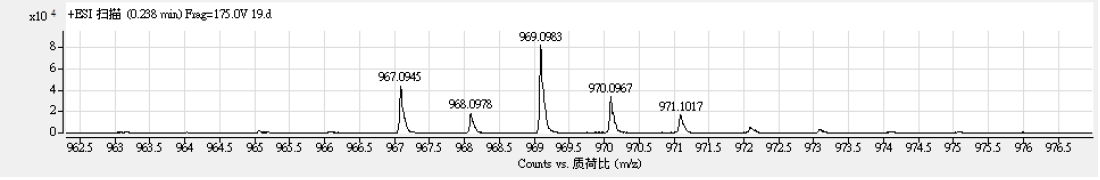

Figure S. 2.27. MS result of **Ir7**

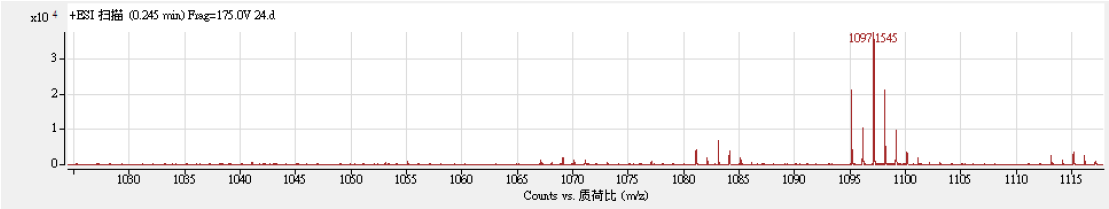

Figure S. 2.28. MS result of **Ir8**

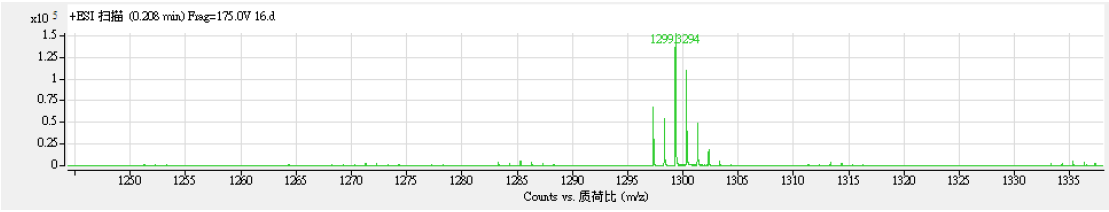

Figure S. 2.29. MS result of **Ir9**

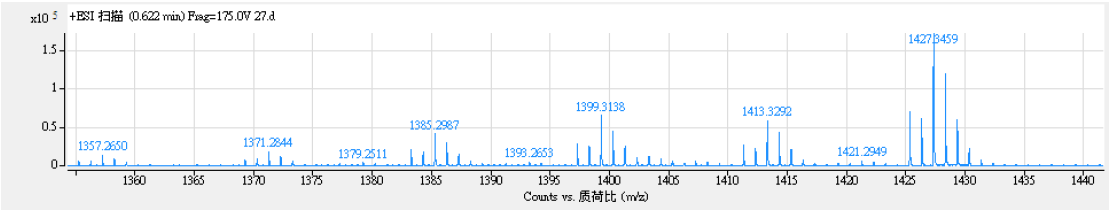

Figure S. 2.30. MS result of **Ir10**

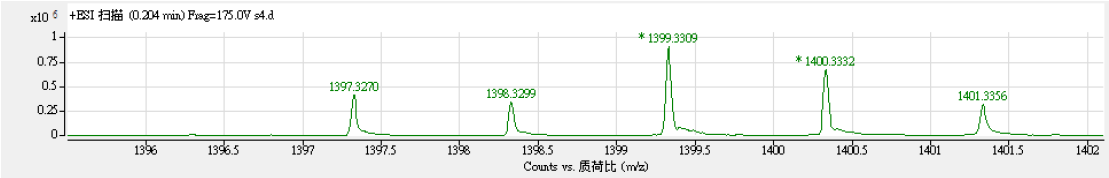

Figure S. 2.31. MS result of **Ir11**

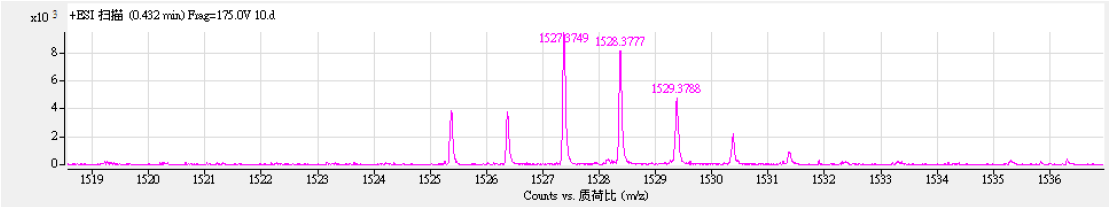

Figure S. 2.32. MS result of **Ir12**

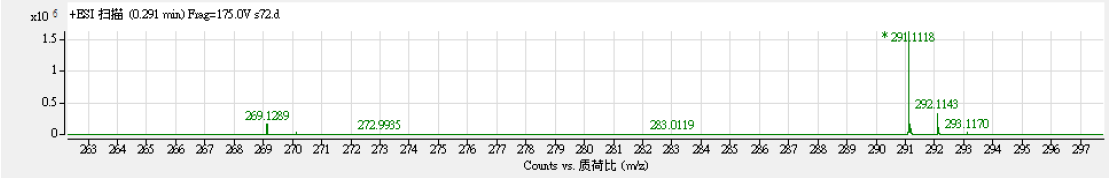

Figure S. 2.33. MS result of **L8**

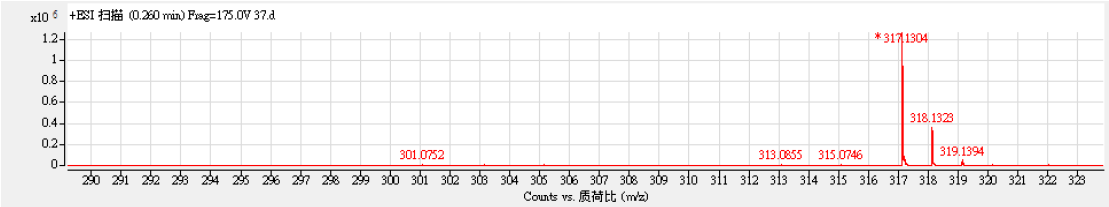

Figure S. 2.34. MS result of **L9**

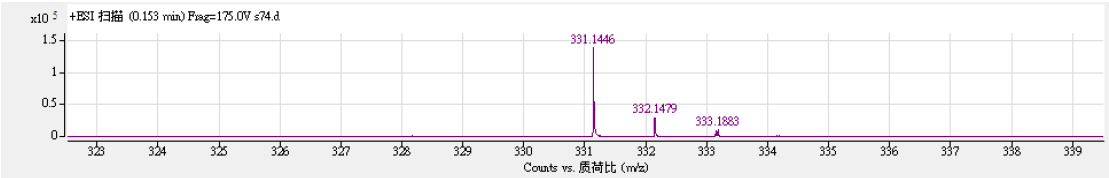

Figure S. 2.35. MS result of **L10**

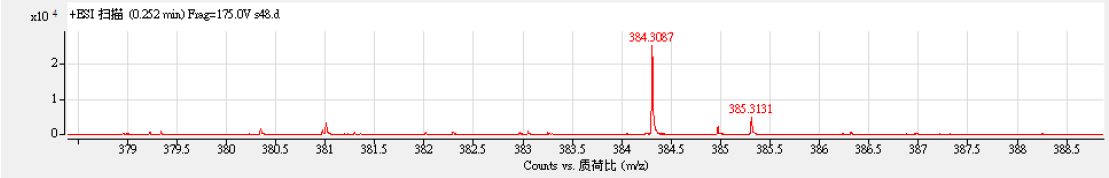

Figure S. 2.36. MS result of **L11**

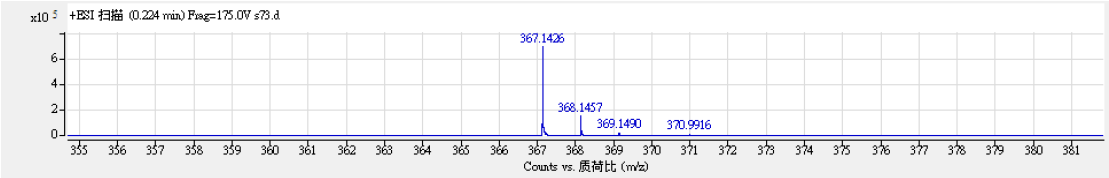

Figure S. 2.37. MS result of **L12**

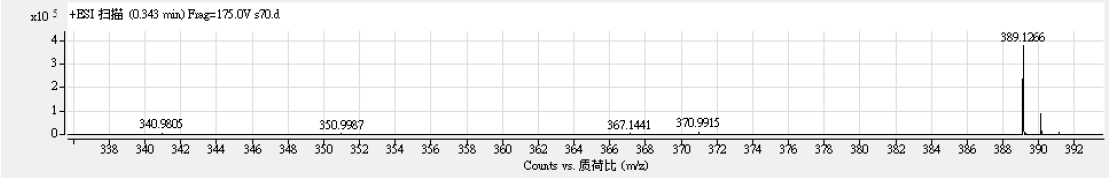

Figure S. 2.38. MS result of **L13**

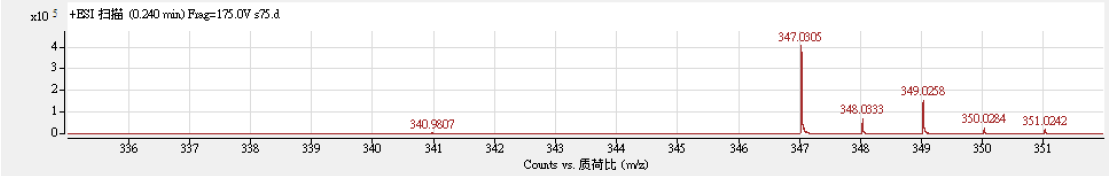

Figure S. 2.39. MS result of **Ni1**

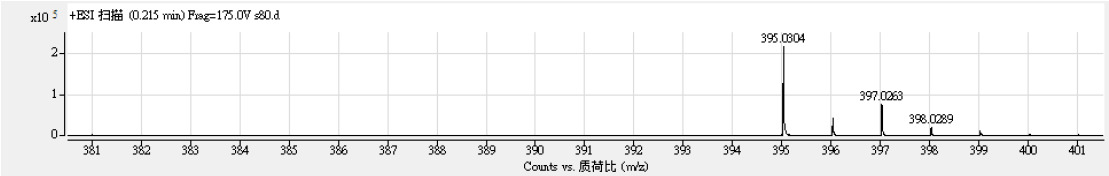

Figure S. 2.40. MS result of **Ni2**

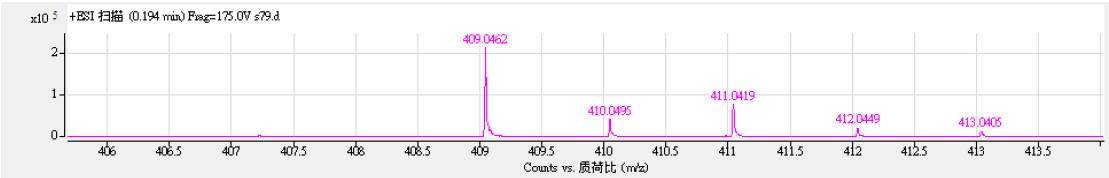

Figure S. 2.41. MS result of **Ni3**

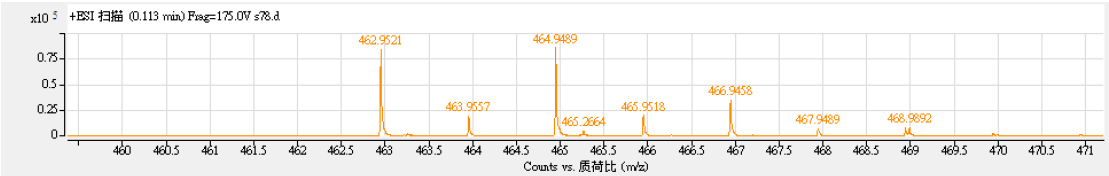

Figure S. 2.42. MS result of **Ni4**

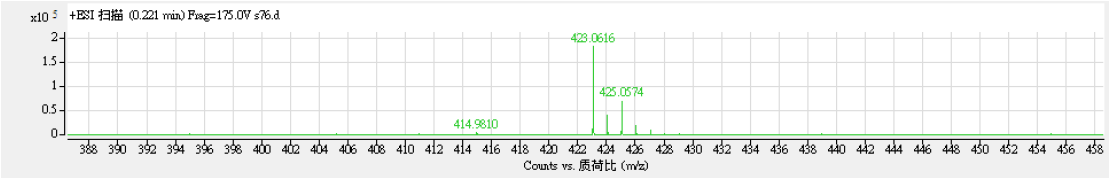

Figure S. 2.43. MS result of **Ni5**

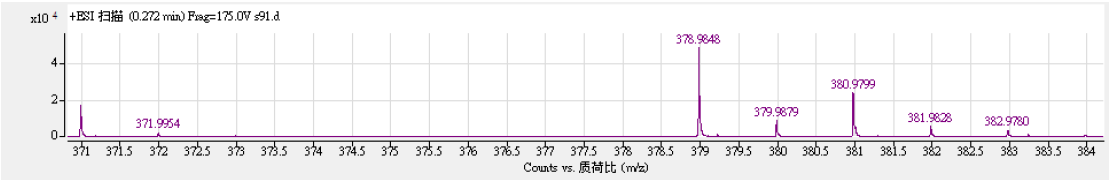

Figure S. 2.44. MS result of **Ni6**

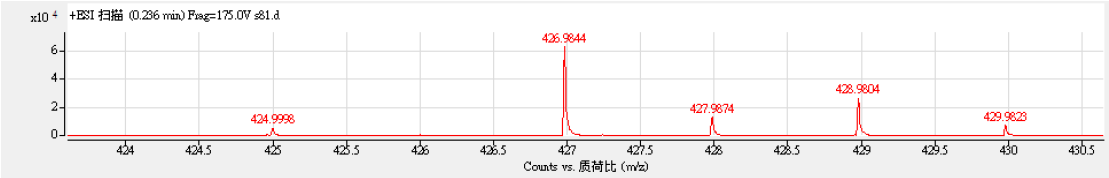

Figure S. 2.45. MS result of **Ni7**

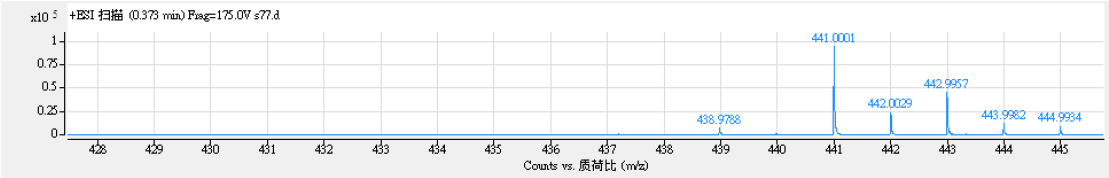

Figure S. 2.46. MS result of **Ni8**

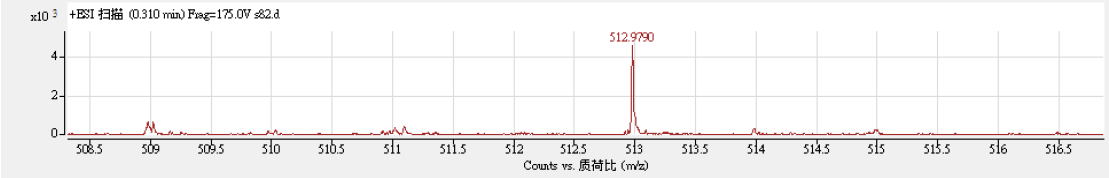

Figure S. 2.47. MS result of **Ni9**

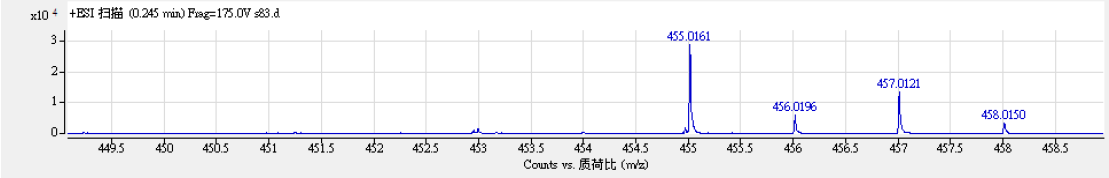

Figure S. 2.48. MS result of **Ni10**

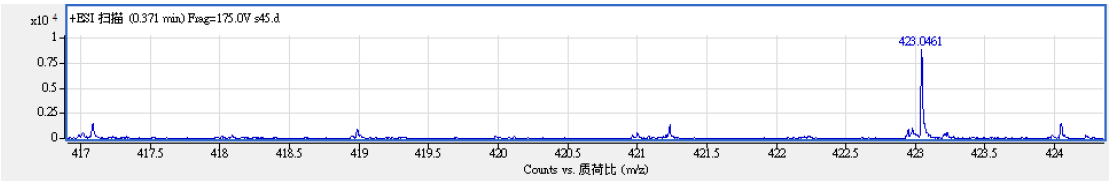

Figure S. 2.49. MS result of **Ni11**

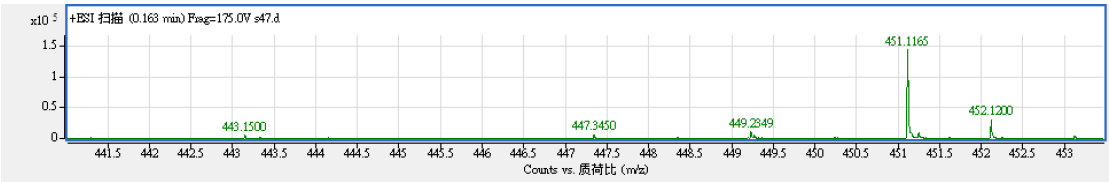

Figure S. 2.50. MS result of **Zn1**

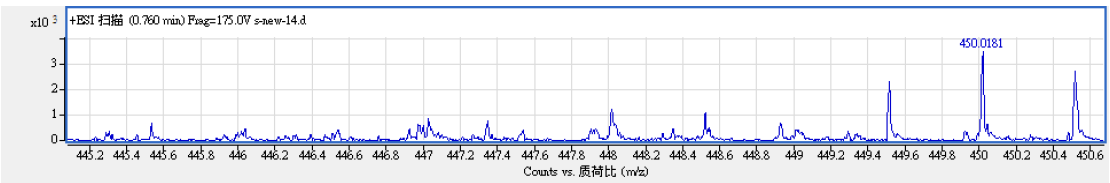

Figure S. 2.51. MS result of **Cu1**

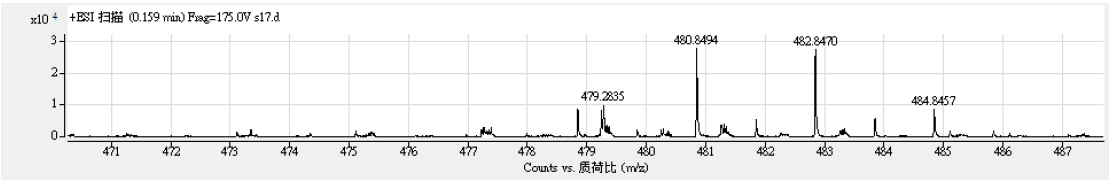

Figure S. 2.52. MS result of **5**

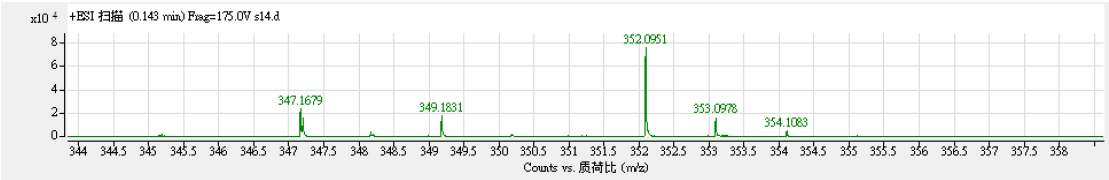

Figure S. 2.53. MS result of **L14**

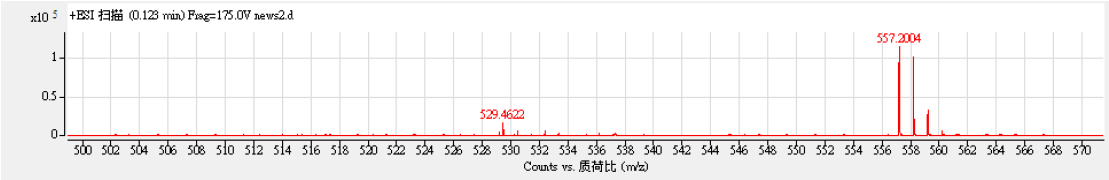

Figure S. 2.54. MS result of **L15**

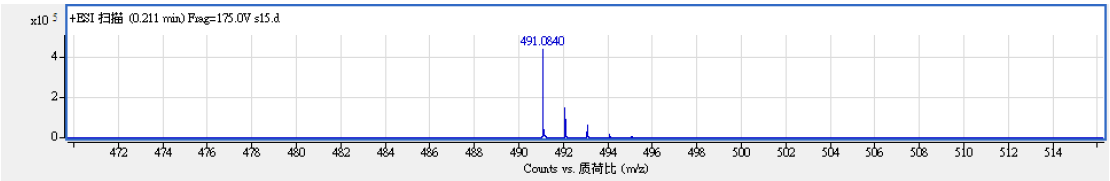

Figure S. 2.55. MS result of **6**

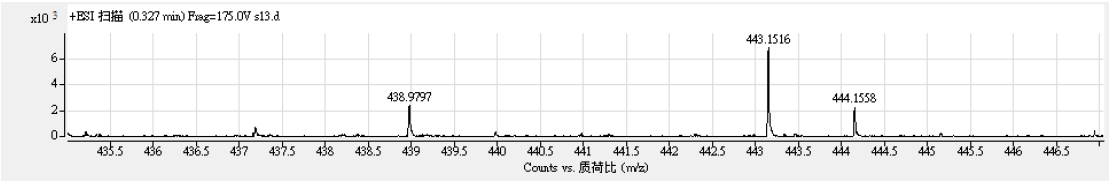

Figure S. 2.56. MS result of **7**

Figure S. 2.57. MS result of **L16**

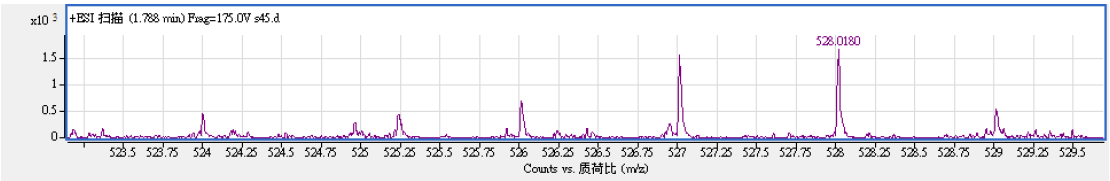

Figure S. 2.58. MS result of **L17**

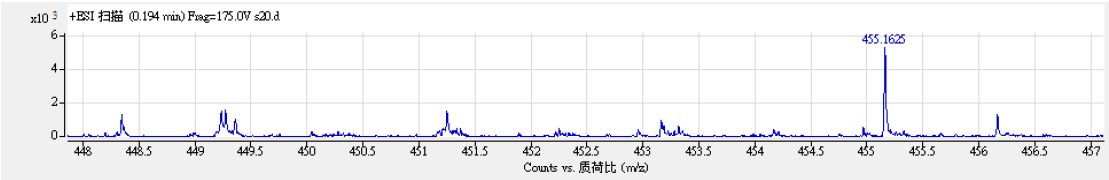

Figure S. 2.59. MS result of **L18**

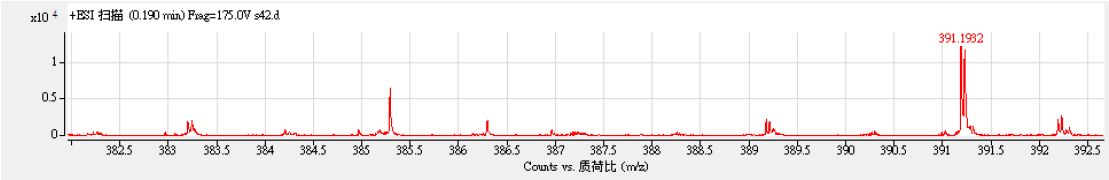

Figure S. 2.60. MS result of **L19**

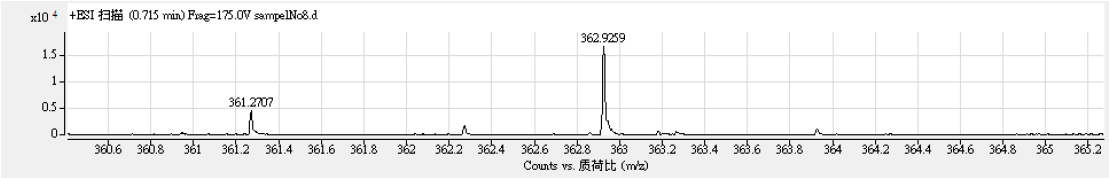

Figure S. 2.61. MS result of **8**

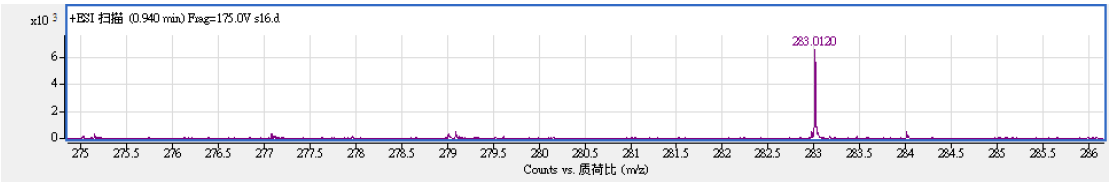

Figure S. 2.62. MS result of **9**

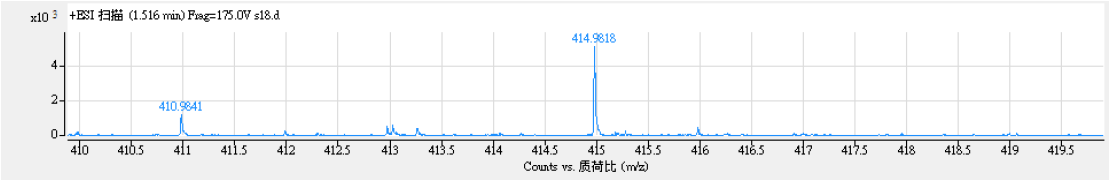

Figure S. 2.63. MS result of **L20**

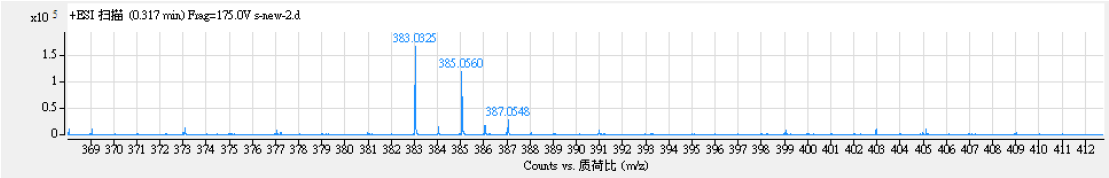

Figure S. 2.64. MS result of **L21**

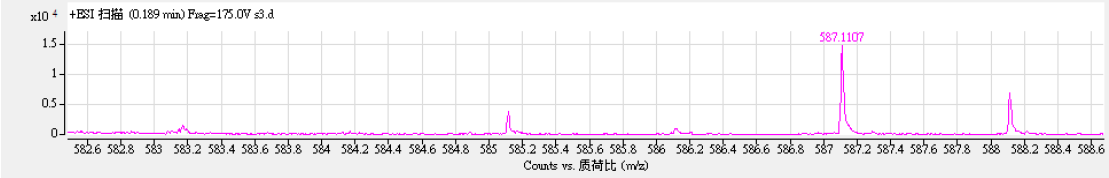

Figure S. 2.65. MS result of **P1**

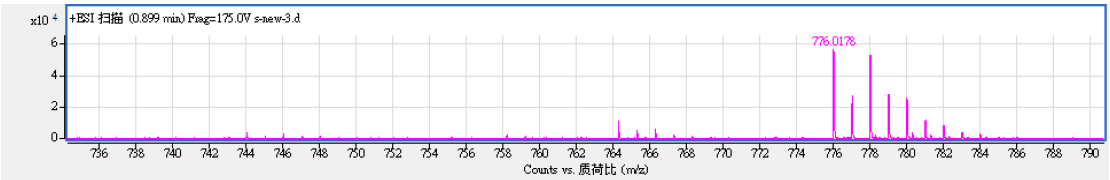

Figure S. 2.66. MS result of **P2**

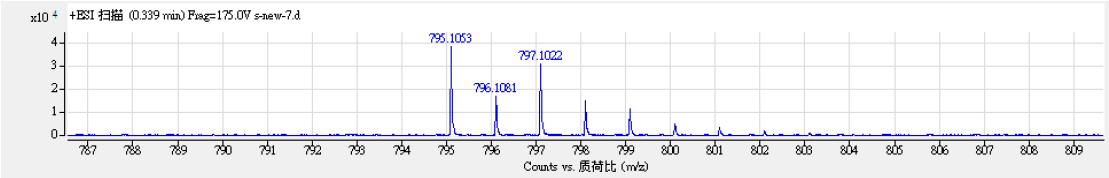

Figure S. 2.67. MS result of **P3**

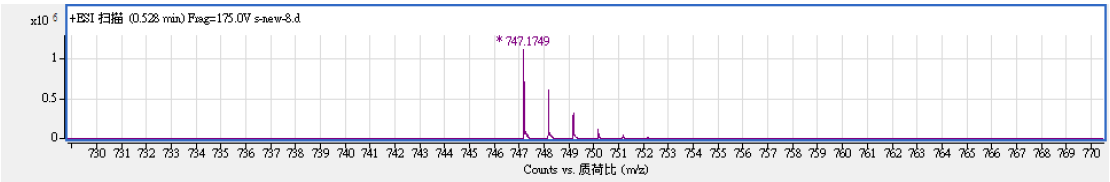

Figure S. 2.68. MS result of **P4**

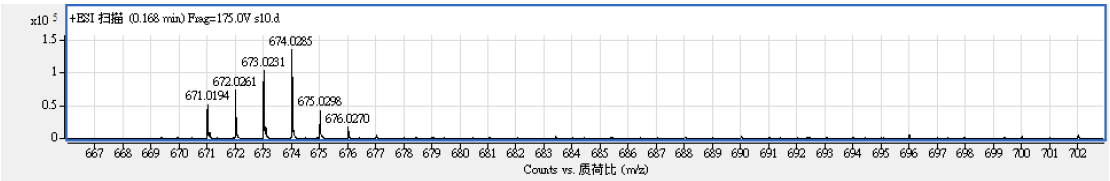

Figure S. 2.69. MS result of **P5**

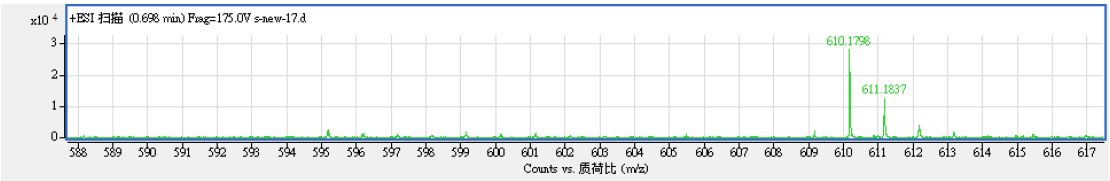

Figure S. 2.70. MS result of **P6**

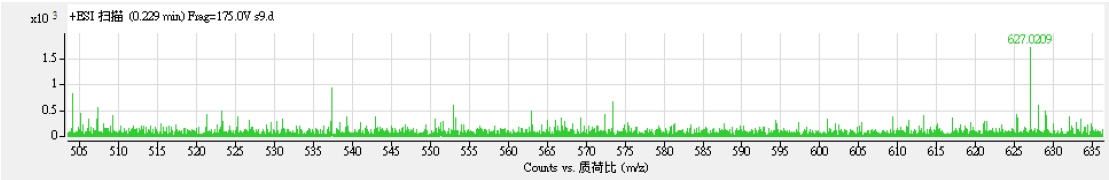

Figure S. 2.71. MS result of **P7**

Figure S. 2.72. MS result of **P8**

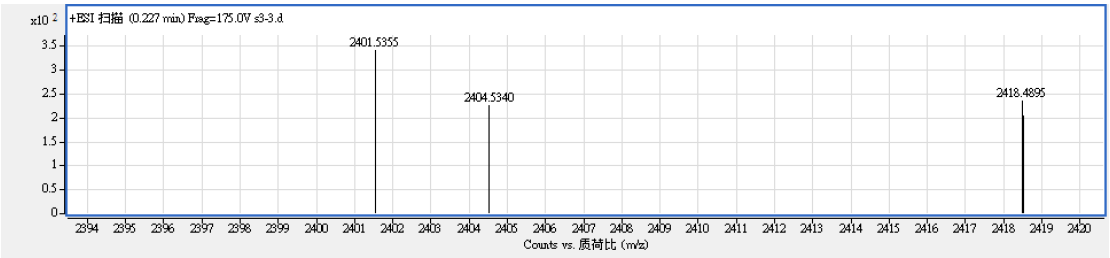

Figure S. 2.73. MS result of **MOC1**

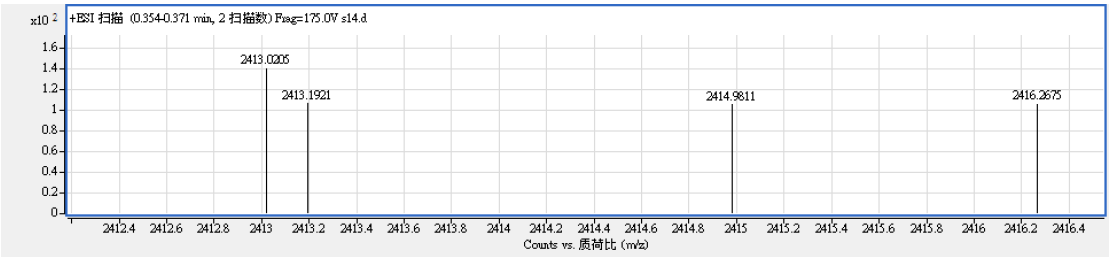

Figure S. 2.74. MS result of **MOC2**

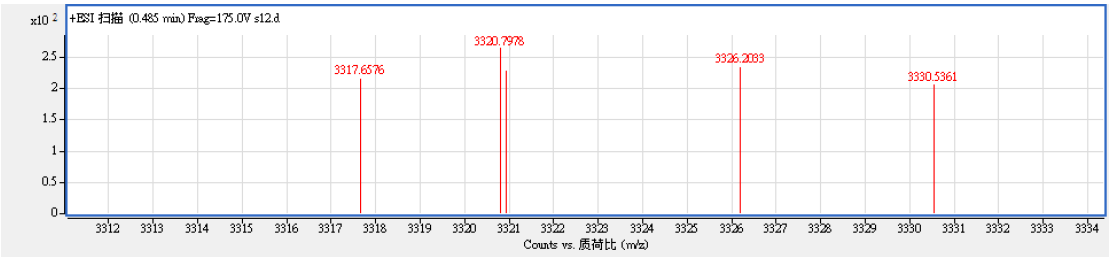

Figure S. 2.75. MS result of **MOC3**

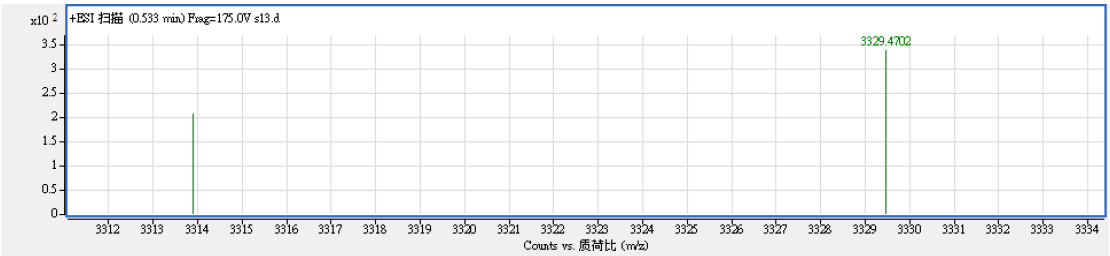

Figure S. 2.76. MS result of **MOC4**

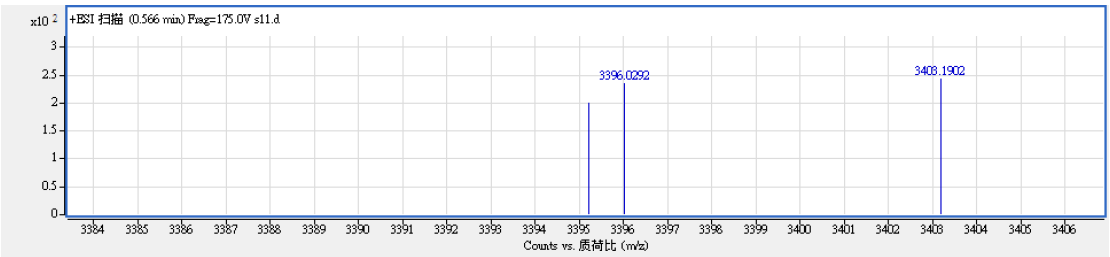

Figure S. 2.77. MS result of **MOC5**

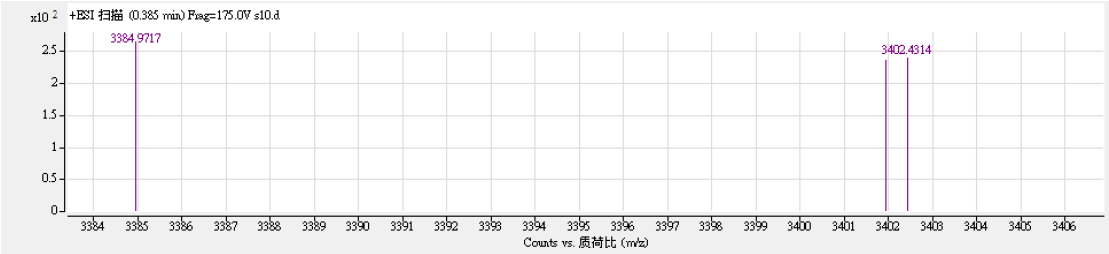

Figure S. 2.78. MS result of **MOC6**

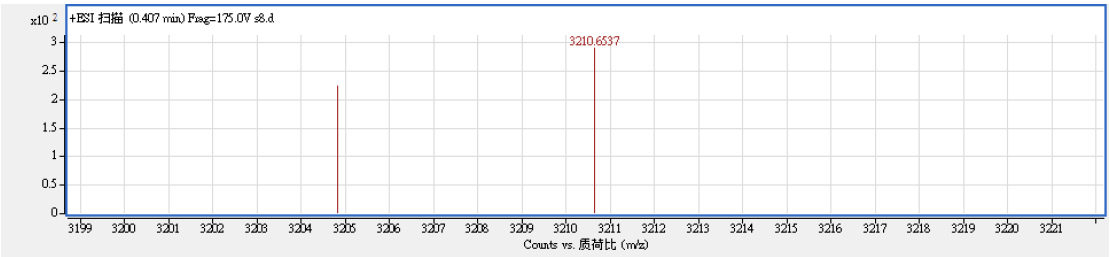

Figure S. 2.79. MS result of **MOC7**

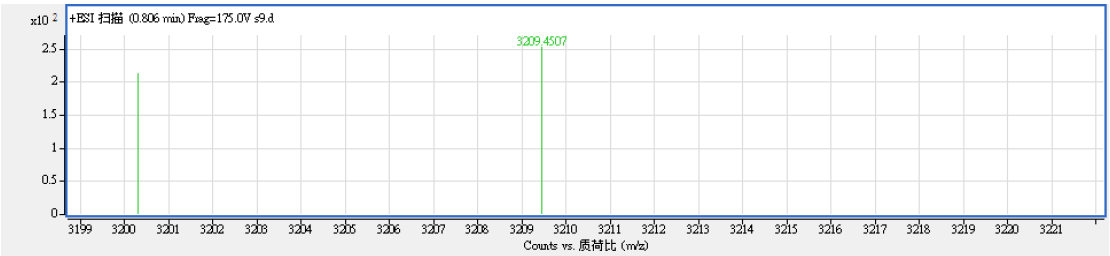

Figure S. 2.80. MS result of **MOC8**

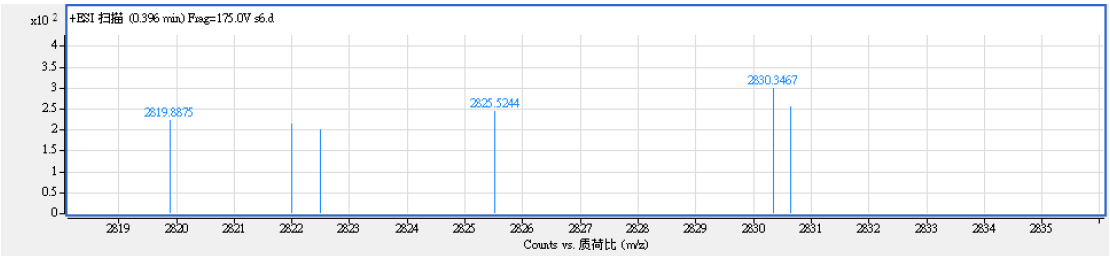

Figure S. 2.81. MS result of **MOC9**

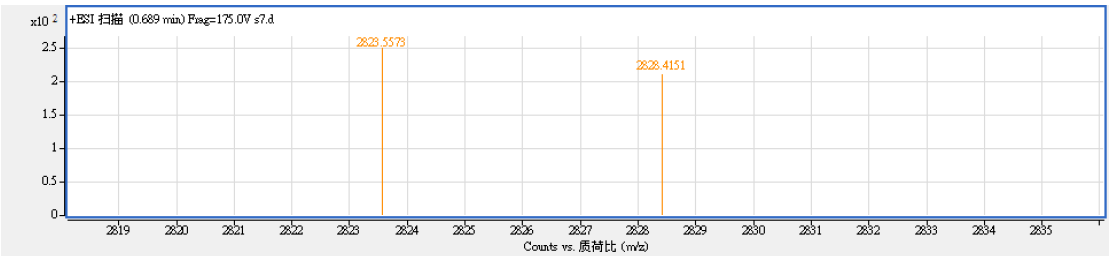

Figure S. 2.82. MS result of **MOC10**

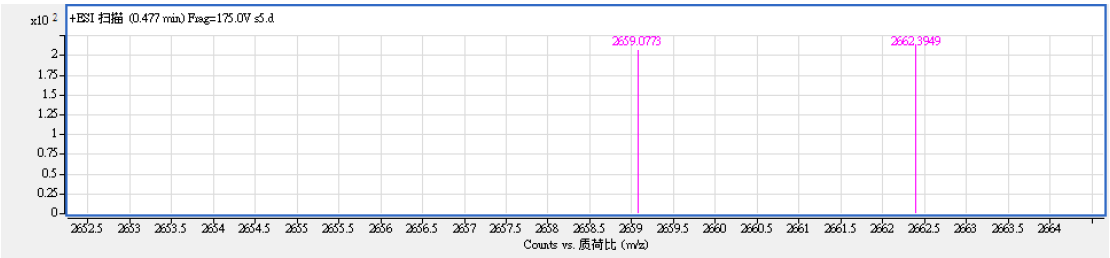

Figure S. 2.83. MS result of **MOC11**

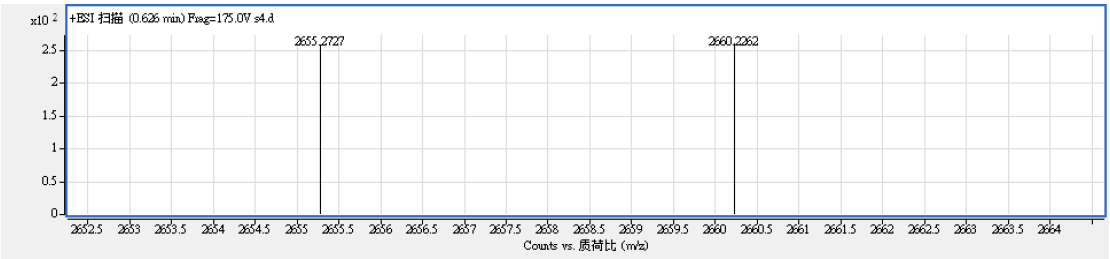

Figure S. 2.84. MS result of **MOC12**

Figure S. 2.85. MS result of **MOC13**

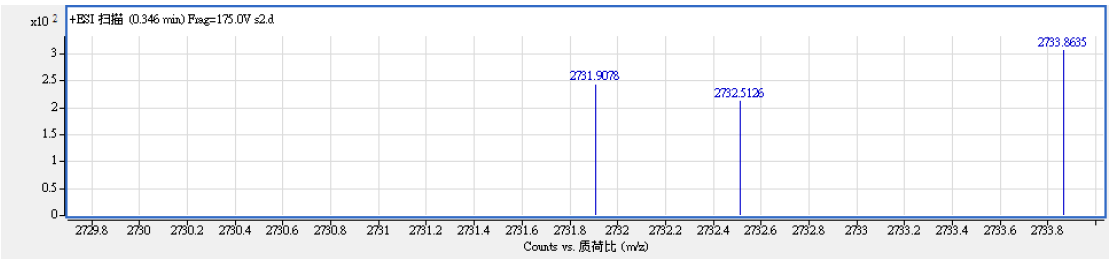

Figure S. 2.86. MS result of **MOC14**

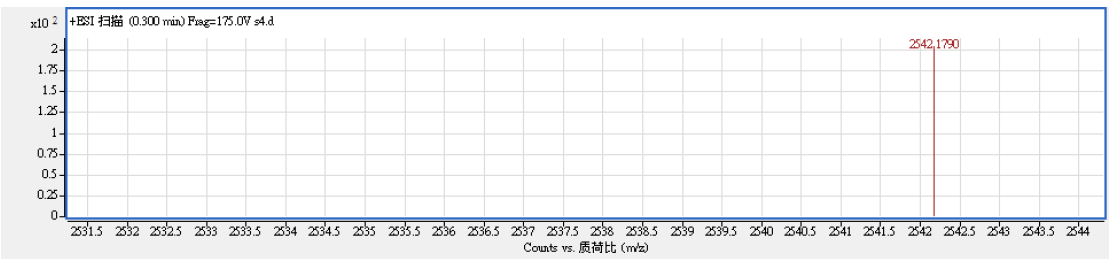

Figure S. 2.87. MS result of **MOC15**

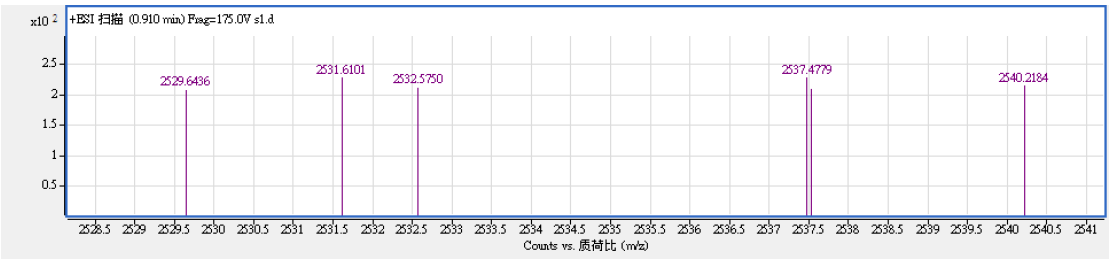

Figure S. 2.88. MS result of **MOC16**

Appendix III. Fourier-Transform Infrared Spectroscopy Results

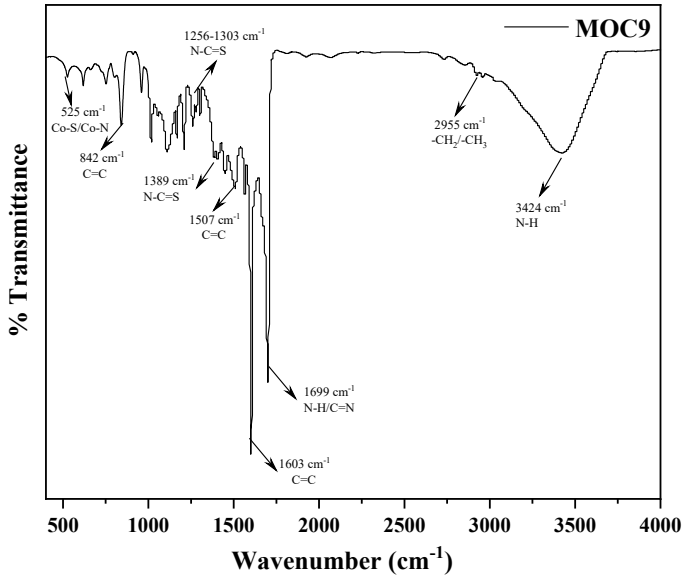

Figure S. 3.1. FTIR spectrum of **MOC9**.

Table S. 3.1. FTIR spectral analysis of **MOC9**.

Band (cm^{-1})	Stretching Vibration Assignment	Reference
3424	N-H	[1, 2]
2955	$-CH_2/-CH_3$	[1, 2]
1699	N-H/C=N	[3, 4]
1603	C=C	[3, 4]
1565	C=C	[3, 4]
1507	C=C	[3, 4]
1445	N-C=S	[5]
1389	N-C=S	[3, 5]
1303	N-C=S	[5]
1256	N-C=S	[5]
1209	N-C=S	[5]
1113	N-C=S	[5]
842	C=C	[3]
751	C=C	[3]

525	Co-S/Co-N	[6, 7]

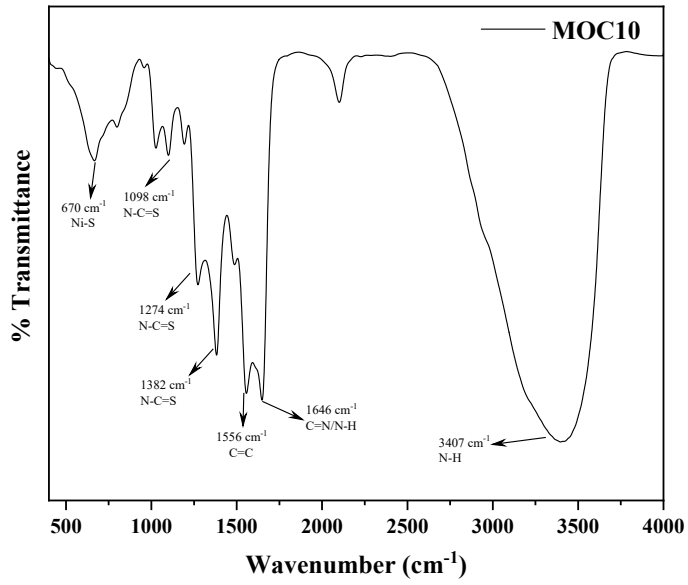

Figure S. 3.2. FTIR spectrum of **MOC10**.

Table S. 3.2. FTIR spectral analysis of **MOC10**.

Band (cm^{-1})	**Stretching Vibration Assignment**	**Reference**
3407	N-H	[1, 2]
1646	N-H/C=N	[3, 4]
1556	C=C	[3, 4]
1485	N-C=S	[5]
1382	N-C=S	[5]
1274	N-C=S	[5]
1098	N-C=S	[5]
800	C=C	[3]
670	Ni-S	[8]

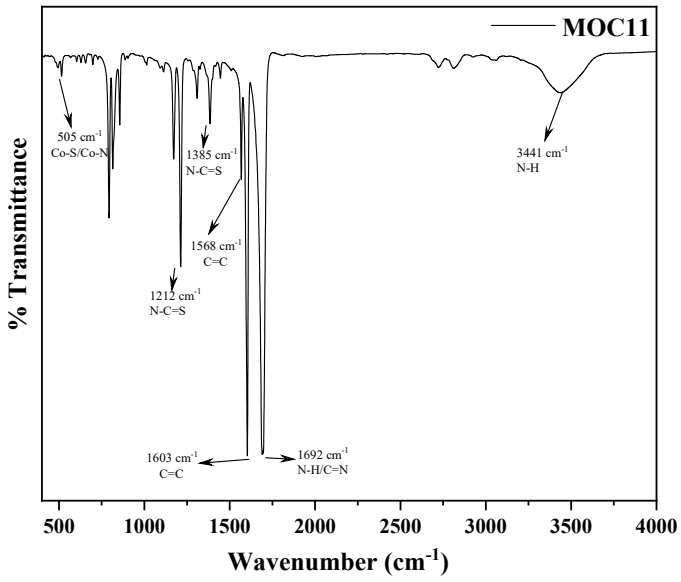

Figure S. 3.3. FTIR spectrum of **MOC11**.

Table S. 3.3. FTIR spectral analysis of **MOC11**.

Band (cm^{-1})	**Stretching Vibration Assignment**	**Reference**
3441	N-H	[1, 2]
1692	N-H/C=N	[3, 4]
1603	C=C	[3, 4]
1568	C=C	[3, 4]
1385	N-C=S	[5]
1212	N-C=S	[5]
854	C-H	[3]
812	C=C	[3]
792	C=C	[3]
505	Co-S/Co-N	[6, 7]

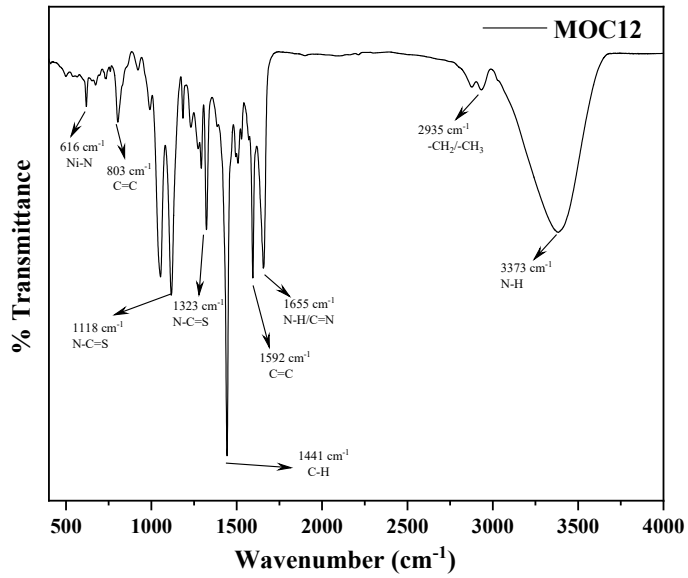

Figure S. 3.4. FTIR spectrum of **MOC12**.

Table S. 3.4. FTIR spectral analysis of **MOC12**.

Band (cm^{-1})	**Stretching Vibration Assignment**	**Reference**
3373	N-H	[1, 2]
2935	$-CH_3$ /$-CH_2$	[3, 4]
2873	$-CH_3$ /$-CH_2$	[3, 4]
1655	N-H/C=N	[3, 4]
1592	C=C	[3, 4]
1504	C=C	[3, 4]
1441	N-C=S	[5]
1323	N-C=S	[5]
1291	N-C=S	[5]
1232	N-C=S	[5]
1118	N-C=S	[5]
803	C=C	[3]
616	Ni-N	[9]

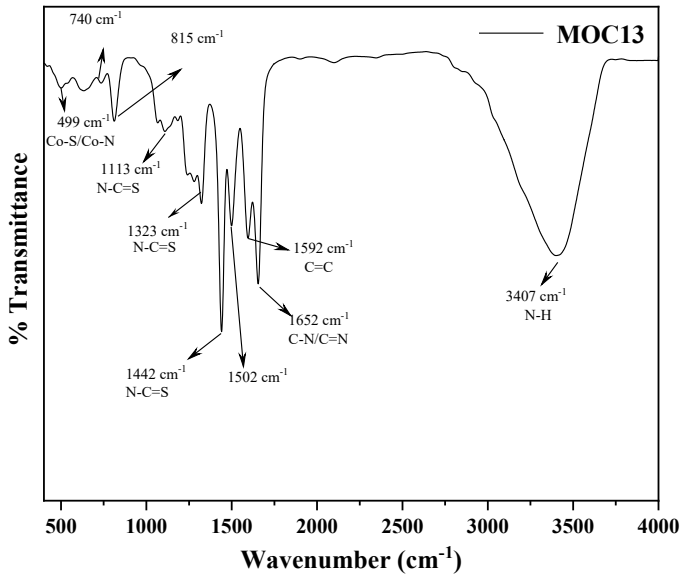

Figure S. 3.5. FTIR spectrum of **MOC13**.

Table S. 3.5. FTIR spectral analysis of **MOC13**.

Band (cm^{-1})	**Stretching Vibration Assignment**	**Reference**
3407	N-H	[1, 2]
1652	C-N/C=N	[3, 4]
1592	C=C	[3, 4]
1502	Thiophene ring	[10]
1442	N-C=S	[5]
1323	N-C=S	[3, 5]
1113	N-C=S	[5]
815	Thiophene ring	[10]
740	C=C	[3]
499	Co-S/Co-N	[6, 7]

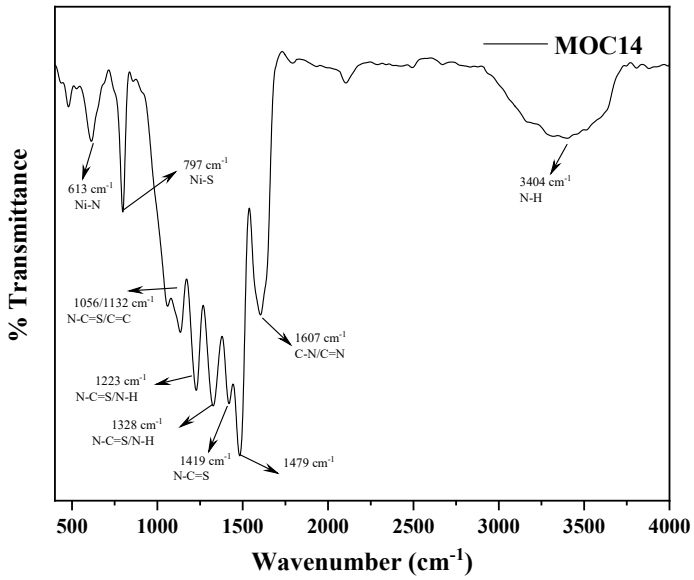

Figure S. 3.6. FTIR spectrum of **MOC14**.

Table S. 3.6. FTIR spectral analysis of **MOC14**.

Band (cm^{-1})	Stretching Vibration Assignment	Reference
3404	N-H	[1, 2]
1607	C-N/C=N	[3, 4]
1479	Thiophene ring	[10]
1419	N-C=S	[5]
1328	N-C=S/N-H	[3, 5]
1223	N-C=S/N-H	[3, 5]
1132	N-C=S/C=C	[5]
1056	N-C=S/C=C	[5]
797	Ni-S	[8]
613	Ni-N	[9]

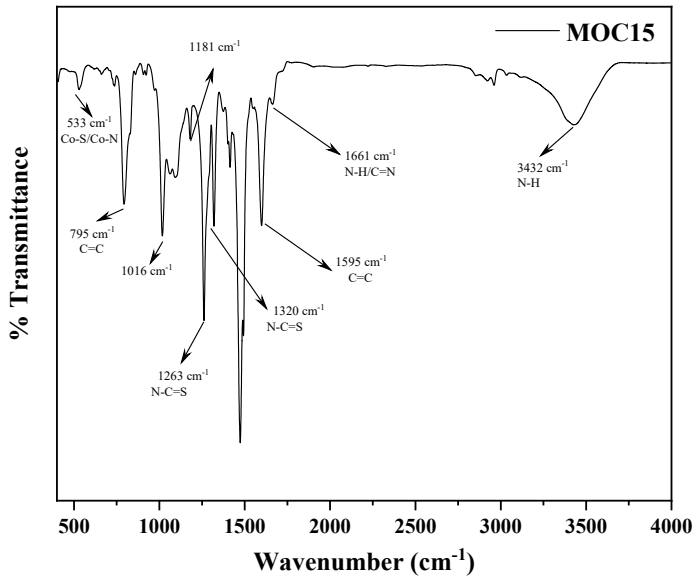

Figure S. 3.7. FTIR spectrum of **MOC15**.

Table S. 3.7. FTIR spectral analysis of **MOC15**.

Band (cm^{-1})	Stretching Vibration Assignment	Reference
3432	N-H	[1, 2]
1661	N-H/C=N	[3, 4]
1595	C=C	[3, 4]
1473	N-C=S	[5]
1320	N-C=S	[5]
1263	N-C=S	[5]
1181	furan ring	[11]
1101	furan ring	[11]
1016	furan ring	[11]
795	C=C	[3]
533	Co-S/Co-N	[6, 7]

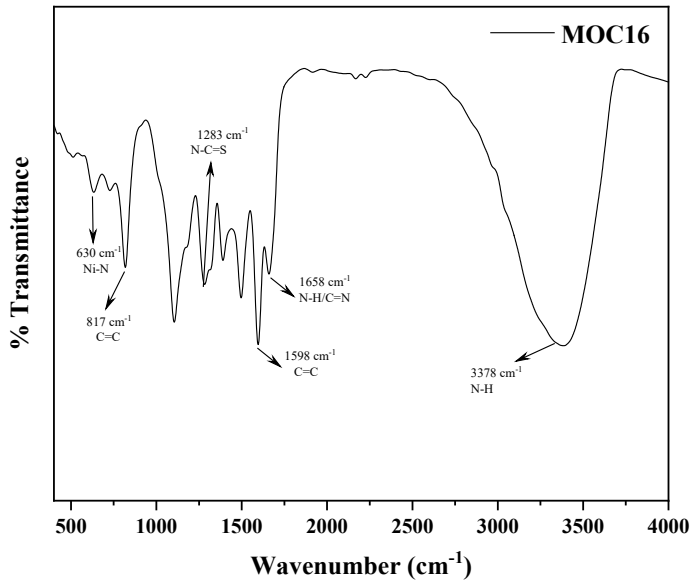

Figure S. 3.8. FTIR spectrum of **MOC16**.

Table S. 3.8. FTIR spectral analysis of **MOC16**.

Band (cm^{-1})	Stretching Vibration Assignment	Reference
3378	N-H	[1, 2]
1658	N-H/C=N	[3, 4]
1598	C=C	[3, 4]
1496	N-C=S	[5]
1391	N-C=S	[5]
1283	N-C=S	[5]
1107	furan ring	[11]
817	C=C	[3]
732	furan ring	[11]
630	Ni-N	[9]

Reference

[1] N. Alizadeh, A. Salimi, R. Hallaj, F. Fathi, F. Soleimani, *J. Nanobiotechnol.* **2018**, *16*, 1-14.

[2] Z. Y. Sun, G. P. Cao, H. Lv, L. Zhao, T. Liu, L. Montastruc, N. Iordan, *J. Appl. Polym. Sci.* **2009**, *114*, 3882-3888.

[3] Y. Wang, W. Z. Zhang, X. M. Wu, C. Y. Luo, Q. G. Wang, J. H. Li, L. Hu, *Synth. Met.* **2017**, *228*, 18-24.

[4] P. B. Liu, Y. Huang, X. Zhang, *Compos. Sci. Technol.* **2015**, *107*, 54-60.

[5] M. Kadir, R. Ramli, M. Yusof, N. Ismail, N. Ngah, N. Haris, *Data Brief* **2019**, *27*, 104651.

[6] M. Hafeez, S. Afyaz, A. Khalid, P. Ahmad, M. U. Khandaker, M. U. K. Sahibzada, I. Ahmad, J. Khan, F. A. Alhumaydhi, T. B. Emran, *J. King Saud Univ. Sci.* **2022**, *34*, 102028.

[7] X. Y. Li, J. A. Li, Y. Shi, M. M. Zhang, S. Y. Fan, Z. F. Yin, M. C. Qin, T. T. Lian, X. Y. Li, *J. Colloid Interface Sci.* **2018**, *528*, 45-52.

[8] M. Kristl, B. Dojer, S. Gyergyek, J. Kristl, *Heliyon* **2017**, *3*, e00273.

[9] A. Lang, A. Yelisseyev, N. Pokhilenko, J. Steeds, A. Wotherspoon, *J. Cryst. Growth* **2004**, *263*, 575-589.

[10] C. Ehrendorfer, H. Neugebauer, A. Neckel, P. Bäuerle, *Synth. Met.* **1993**, *55*, 493-498.

[11] S. D. Jackson, A. S. Canning, E. M. Vass, S. R. Watson, *Ind. Eng. Chem. Res.* **2003**, *42*, 5489-5494.

Appendix IV UV/Vis spectrums for determining of the dye loading percentage

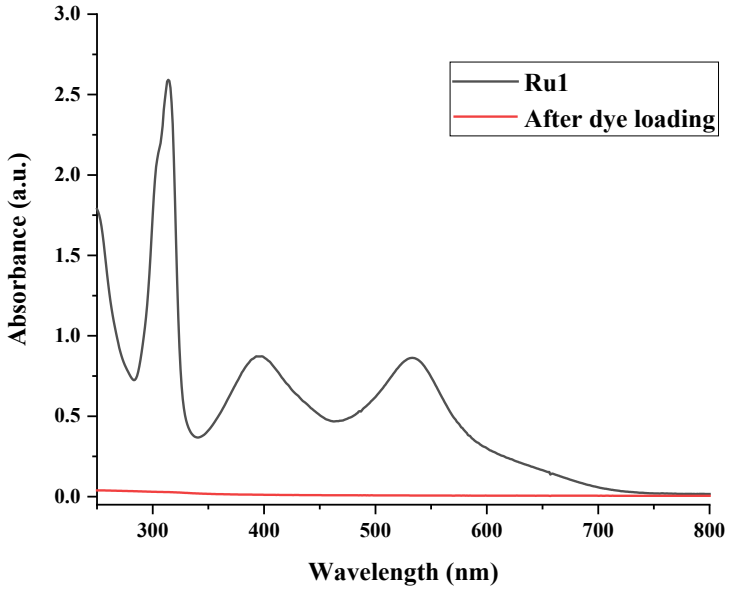

Figure S 4.1. UV/Vis absorption spectra of **Ru1** before and after dye loading in MeOH solution at 293 K.

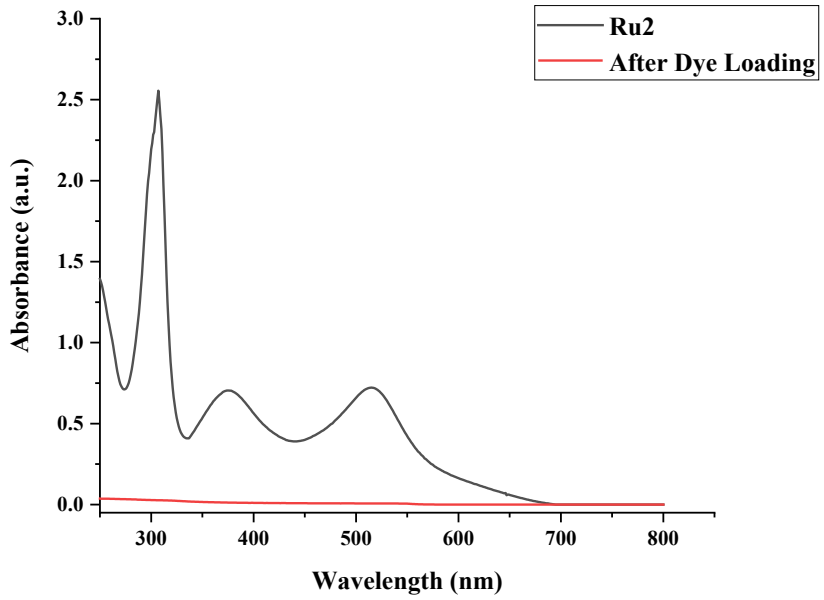

Figure S 4.2. UV/Vis absorption spectra of **Ru2** before and after dye loading in MeOH solution at 293 K.

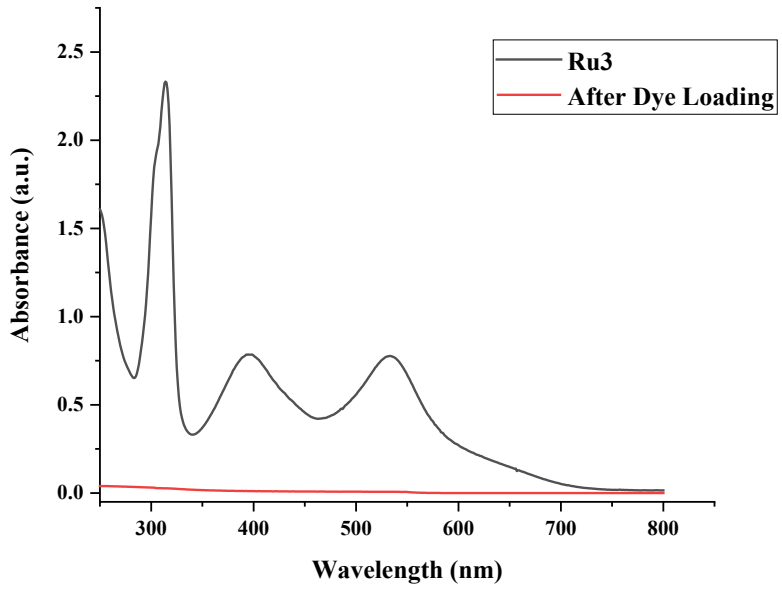

Figure S 4.3. UV/Vis absorption spectra of **Ru3** before and after dye loading in MeOH solution at 293 K.

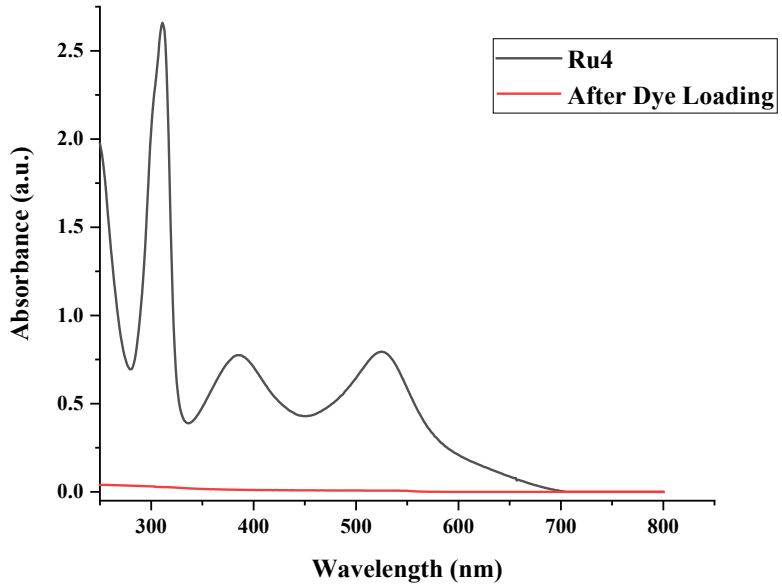

Figure S 4.4. UV/Vis absorption spectra of **Ru4** before and after dye loading in MeOH solution at 293 K.

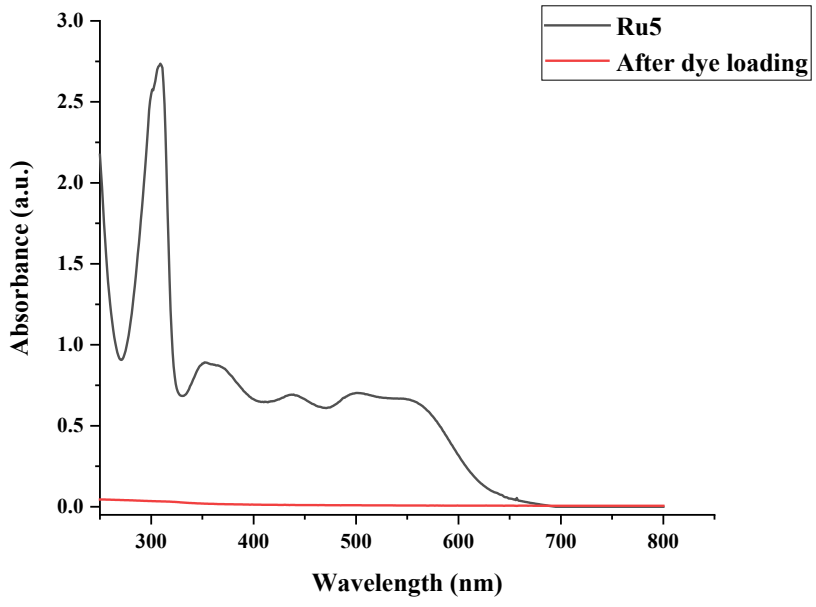

Figure S 4.5. UV/Vis absorption spectra of **Ru5** before and after dye loading in MeOH solution at 293 K.

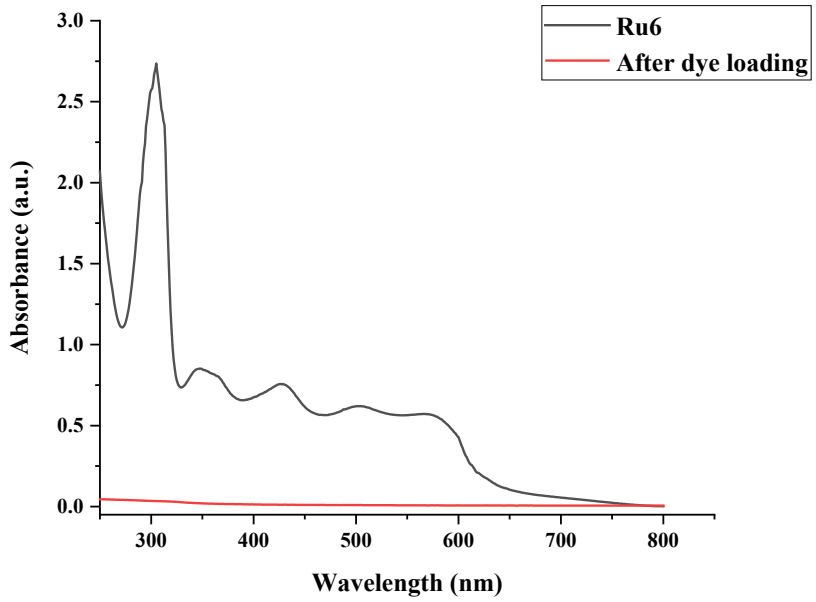

Figure S 4.6. UV/Vis absorption spectra of **Ru6** before and after dye loading in MeOH solution at 293 K.

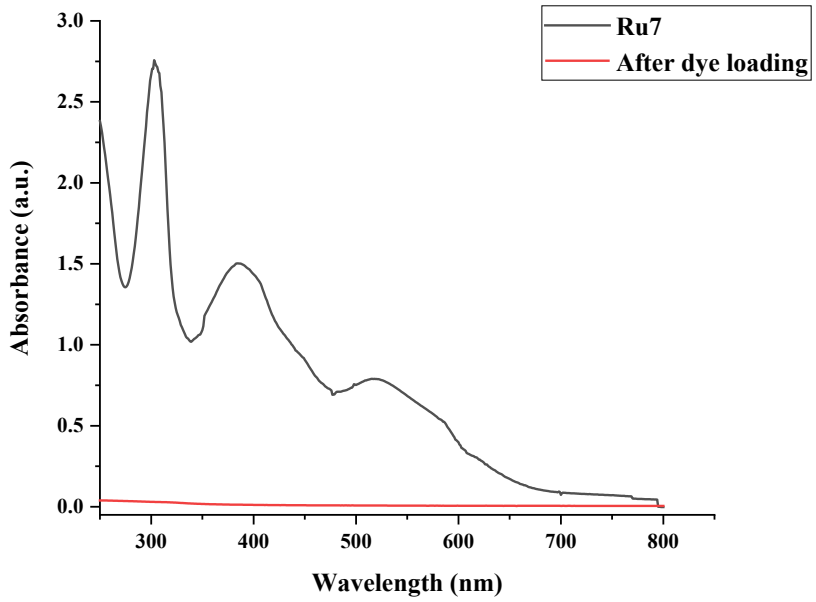

Figure S 4.7. UV/Vis absorption spectra of **Ru7** before and after dye loading in MeOH solution at 293 K

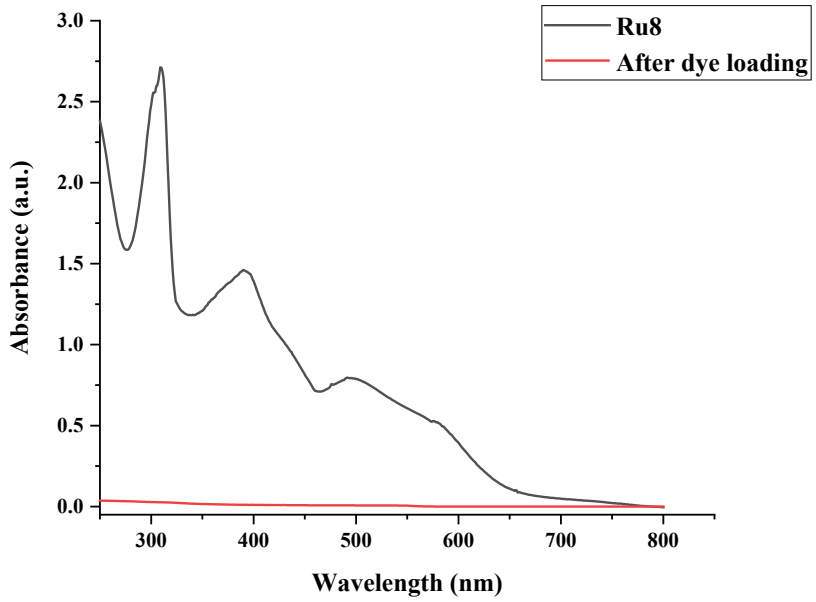

Figure S 4.8. UV/Vis absorption spectra of **Ru8** before and after dye loading in MeOH solution at 293 K

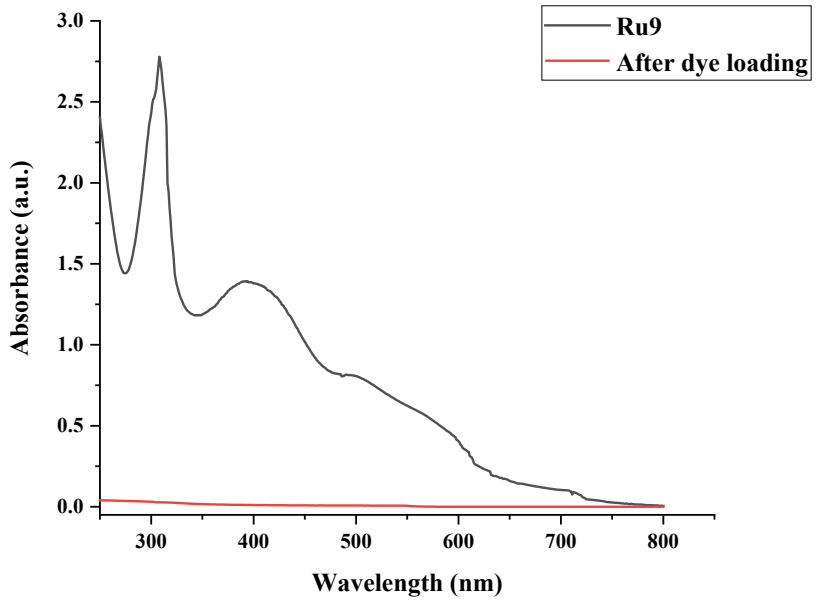

Figure S 4.9. UV/Vis absorption spectra of **Ru9** before and after dye loading in MeOH solution at 293 K

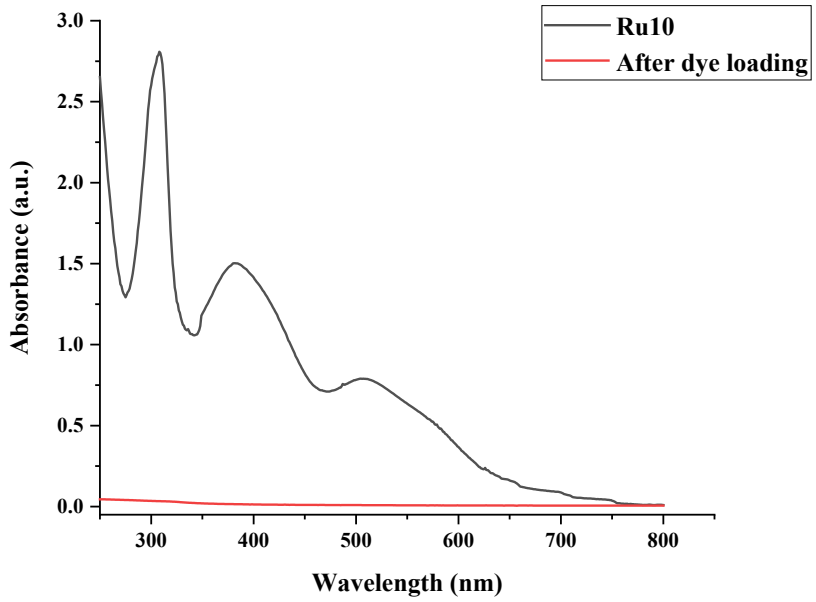

Figure S 4.10. UV/Vis absorption spectra of **Ru10** before and after dye loading in MeOH solution at 293 K

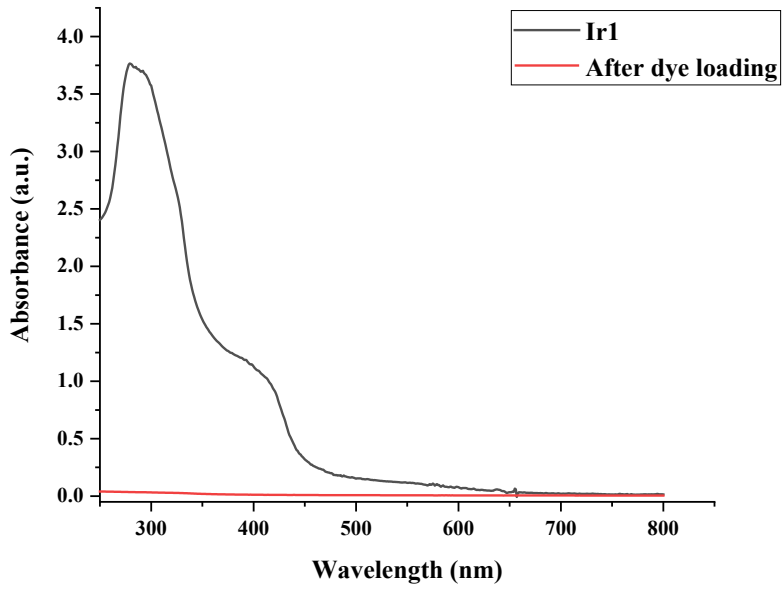

Figure S 4.11. UV/Vis absorption spectra of **Ir1** before and after dye loading in CH_2Cl_2 solution at 293 K

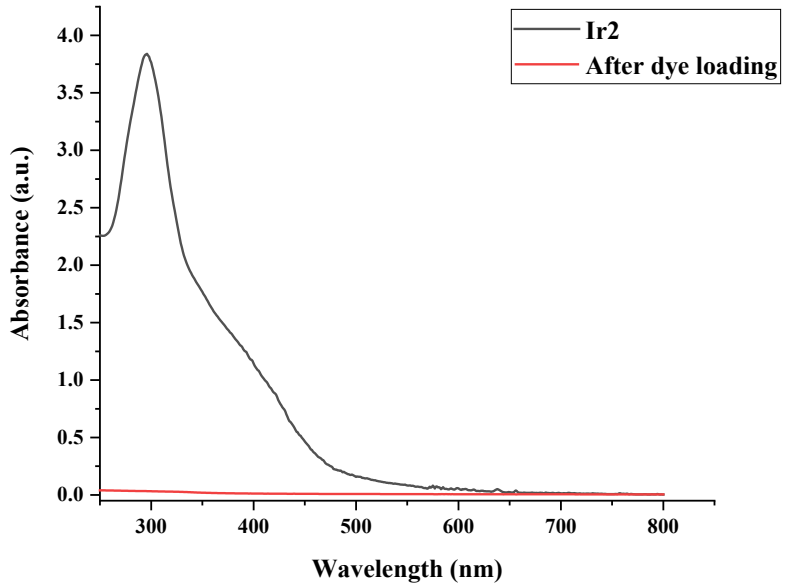

Figure S 4.12. UV/Vis absorption spectra of **Ir2** before and after dye loading in CH_2Cl_2 solution at 293 K

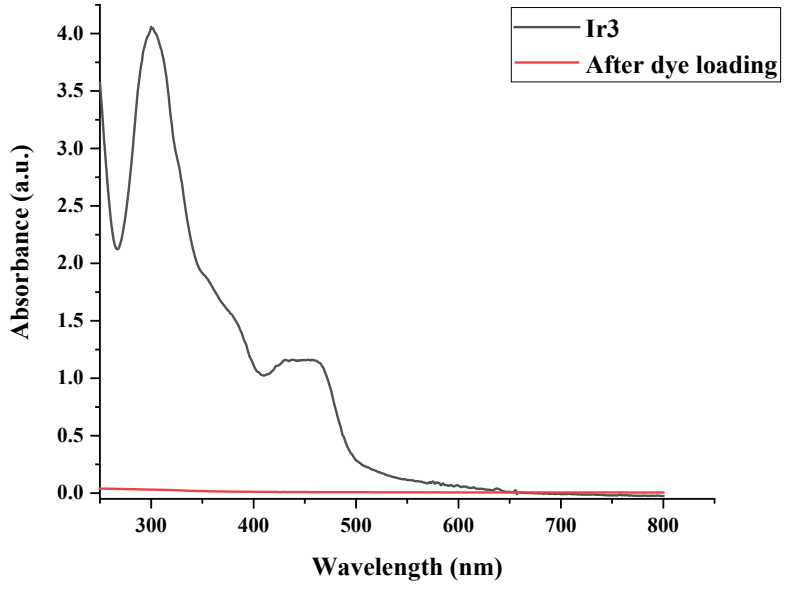

Figure S 4.13. UV/Vis absorption spectra of **Ir3** before and after dye loading in CH_2Cl_2 solution at 293 K

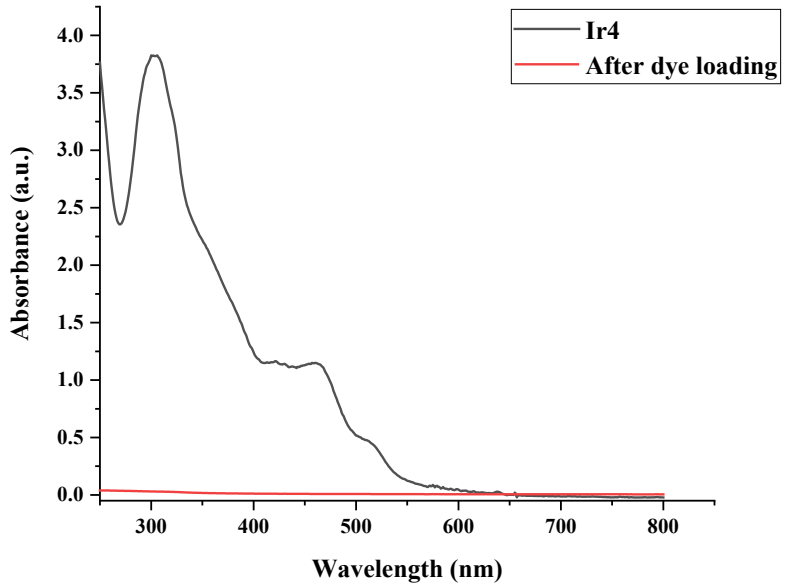

Figure S 4.14. UV/Vis absorption spectra of **Ir4** before and after dye loading in CH_2Cl_2 solution at 293 K

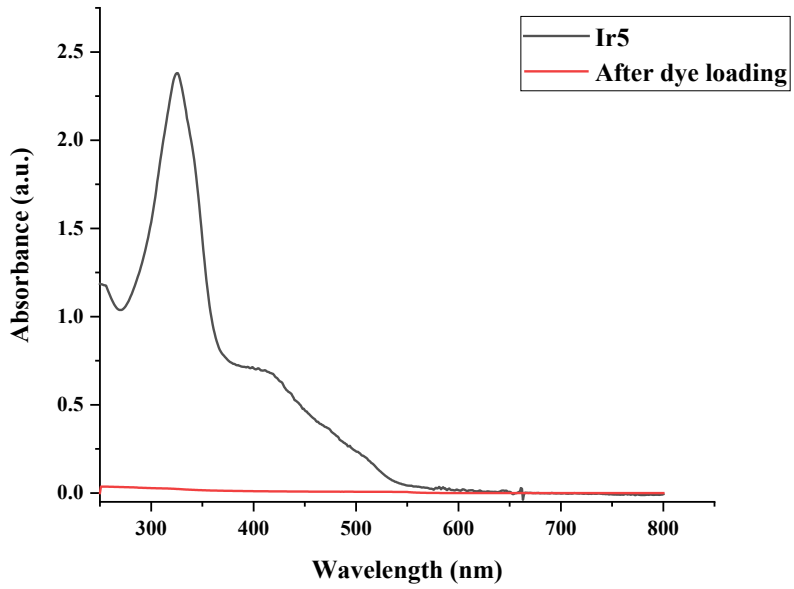

Figure S 4.15. UV/Vis absorption spectra of **Ir5** before and after dye loading in CH_2Cl_2 solution at 293 K

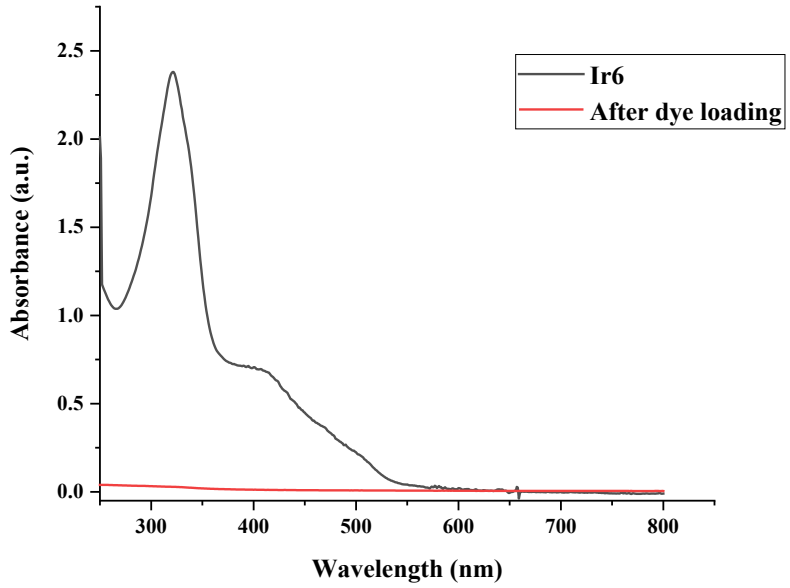

Figure S 4.16. UV/Vis absorption spectra of **Ir6** before and after dye loading in CH_2Cl_2 solution at 293 K

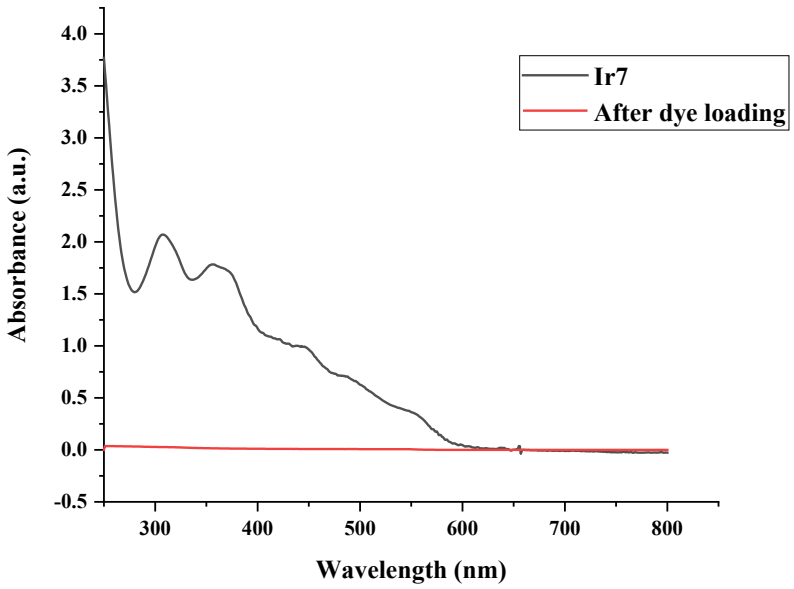

Figure S 4.17. UV/Vis absorption spectra of **Ir7** before and after dye loading in CH_2Cl_2 solution at 293 K

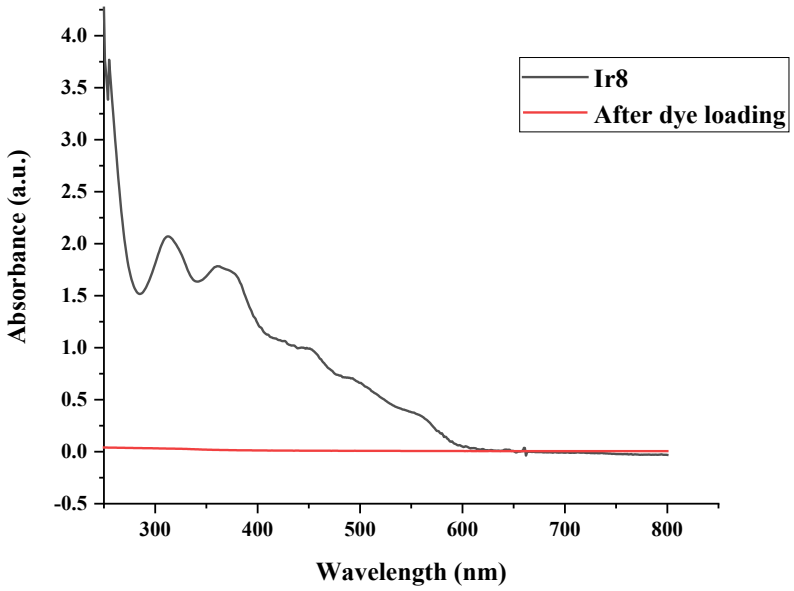

Figure S 4.18. UV/Vis absorption spectra of **Ir8** before and after dye loading in CH_2Cl_2 solution at 293 K

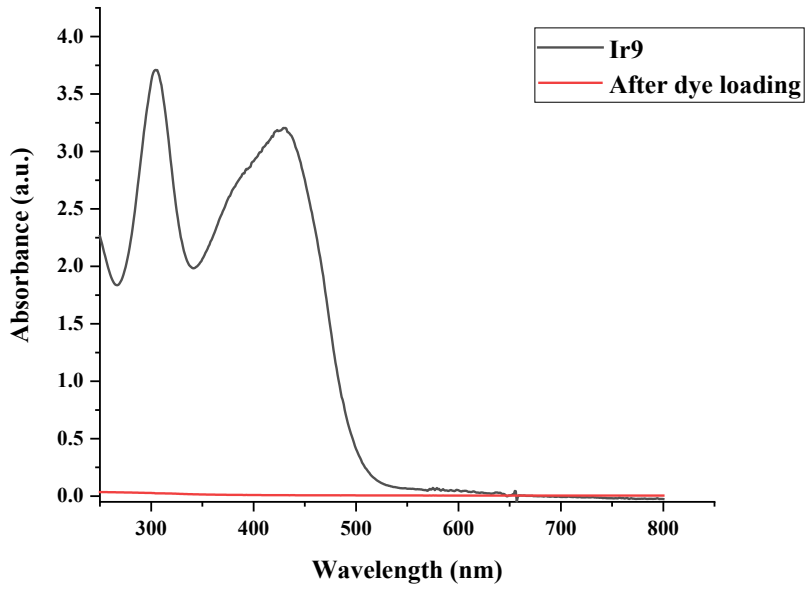

Figure S 4.19. UV/Vis absorption spectra of **Ir9** before and after dye loading in CH_2Cl_2 solution at 293 K

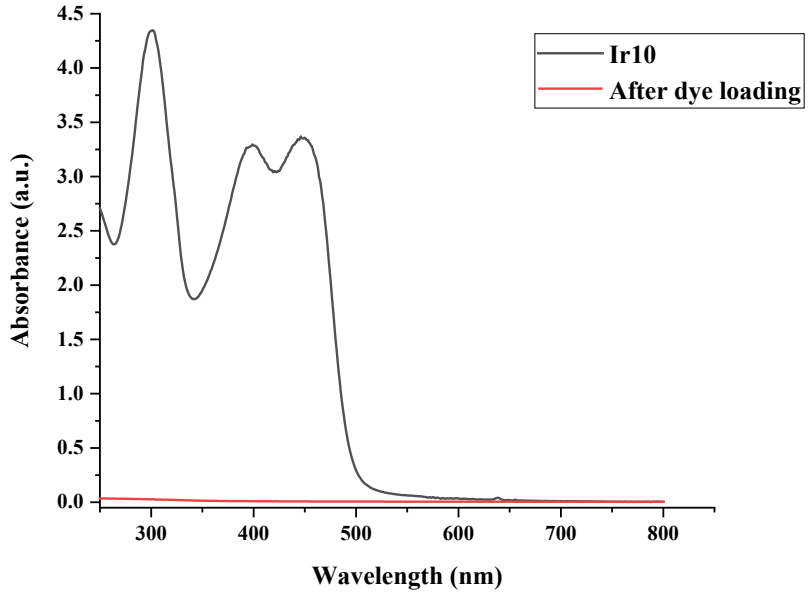

Figure S 4.20. UV/Vis absorption spectra of **Ir10** before and after dye loading in CH_2Cl_2 solution at 293 K

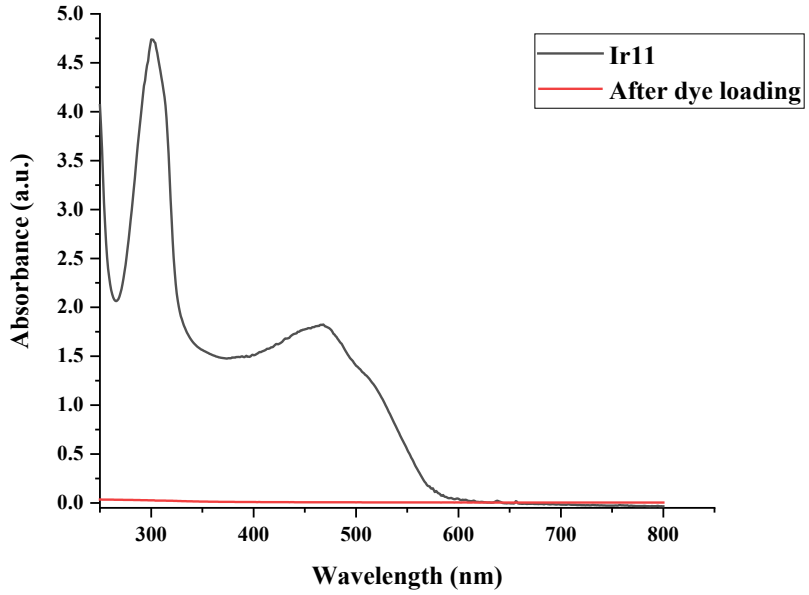

Figure S 4.21. UV/Vis absorption spectra of **Ir11** before and after dye loading in CH_2Cl_2 solution at 293 K

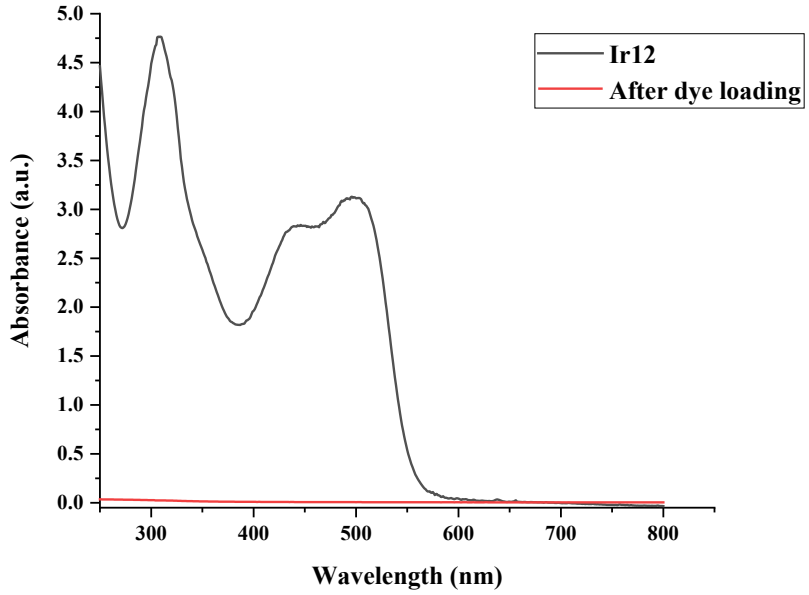

Figure S 4.22. UV/Vis absorption spectra of **Ir12** before and after dye loading in CH_2Cl_2 solution at 293 K